Universität Paderborn
Fakultät für Naturwissenschaften

Experimental and theoretical spectroscopy on molecular transition metal based systems for sustainable chemistry

Dissertation

Vorgelegt von

Lorena Fritsch

Zur Erlangung des akademischen Grades
Doktor der Naturwissenschaften (Dr. rer. nat.)
im Department Chemie

Paderborn 2024

Promotionskommission

Prof. Dr. Michael Tiemann	Kommissionsvorsitzender
Prof. Dr. Matthias Bauer	Erstgutachter
Prof. Dr. Thomas Kühne	Zweitgutachter
Prof. Dr. Nieves Lopez Salas	Drittprüferin

Einreichung:	22. April 2024
Verteidigung:	28. Mai 2024

Ein Experte ist jemand, der alle Fehler gemacht hat,
die man in einem bestimmten Gebiet machen kann.

Niels Bohr

Eidesstattliche Erklärung

Hiermit versichere ich, die vorliegende Arbeit selbständig angefertigt und keine anderen als die von mir angegebenen Hilfsmittel verwendet zu haben. Wörtliche und sinngemäße Zitate wurden als solche gekennzeichnet und die Genehmigungen zur Veröffentlichung der urheberrechtlich geschützten Publikationen wurden eingeholt.

Paderborn, 22. April 2024 — Lorena Fritsch

Abstract

Transition metal (TM) complexes play a major role in various sustainable processes. In order to understand their functional principles and to strive for an optimization of the processes, an insight into the geometric and electronic structure is necessary. The aim of this work is to use experimental spectroscopy and theoretical calculations to gain deep insights into the properties of transition metal complexes. Four different transition metal-based systems from the field of coordination chemistry are investigated not only using X-ray absorption and emission spectroscopy, but also employing methods established for photoactive systems, such as UV-Vis spectroscopy, photoluminescence spectroscopy and cyclic voltammetry. In order to understand and explain the experimental observations, calculations based on density functional theory (DFT) are applied.

By combining these methods, it can be shown how a ruthenium complex exhibits altered luminescence behaviour after amine functionalization in the backbone. The observed strong decrease in the quantum yield can be attributed to stabilization and destabilization of different excited states, so that a non-luminescent relaxation pathway can be populated at room temperature.

Due to their intrinsically low ligand field splitting, these relaxation pathways via metal-centered states are typically also found in iron complexes. In order to be able to specifically change the energy landscape of these, various backbone functionalizations are introduced in N-phenylpyrazole-based iron(III) complexes and their influences are investigated. Cyclic voltammetry, UV-Vis spectroscopy, X-ray absorption near edge structure (XANES) and valence-to-core X-ray emission spectroscopy (VtC-XES) provide insights into the electronic structure and the effects of the various electron-withdrawing and electron-pushing substituents.

The strongly electron-pushing ligands of a tridentate cyclometallated iron(III) complex lead to the metal center being both chemically reduced and oxidized and thus an isostructural complex can be realized in three oxidation states. In order to localize these processes at the metal center and exclude ligand-based redox processes, element-specific X-ray methods, in particular XANES and core-to-core X-ray emission spectroscopy (CtC-XES), are used. These reveal both the oxidation state-dependent occupation of the d orbitals and the associated spin state on the iron atom to confirm all three oxidation states.

Not only the electronic structure, but also the associated geometric structure can be analyzed using X-ray spectroscopy. It is shown how XANES and VtC-XES, rather unpopular methods in the field of complex chemistry, can be used to detect and characterize hydride ligands in copper complexes.

KURZZUSAMMENFASSUNG

Übergangsmetallkomplexe (ÜM) spielen eine große Rolle in verschiedenen nachhaltigen Prozessen. Um die Funktionsprinzipien zu verstehen und eine Optimierung der Prozesse anzustreben, ist ein Einblick in die geometrische und elektronische Struktur notwendig. Ziel dieser Arbeit ist der Einsatz experimenteller Spektroskopie und quantenmechanischer Rechnungen, um ein tiefes Verständnis der Eigenschaften von Übergangsmetallkomplexen zu erhalten. Dazu werden vier unterschiedliche ÜM-basierte Systeme aus dem Bereich der Koordinationschemie mit Hilfe der Röntgenabsorbptions- und Emissionsspektroskopie, sowie mit für photoaktive Systeme etablierten Methoden, wie der UV-Vis- oder Photolumineszenzspektroskopie untersucht. Um die experimentellen Beobachtungen zu verstehen und erklären zu können, werden Rechnungen basierend auf Dichtefunktionaltheorie (DFT) Niveau, angewandt.

Durch die Kombination dieser Methoden kann gezeigt werden, wie sich die Relaxationseigenschaften eines initial lumineszenten Rutheniumkomplex nach Aminfunktionalisierung verändern. Die starke Abnahme der Quantenausbeute ist dabei auf stabilisierte und destabilisierte Energieniveaus, insbesondere der angeregten Zustände, zurückzuführen, sodass ein nicht-lumineszenter Relaxationsweg bei raumtemperatur populiert werden kann.

Aufgrund ihrer intrinsisch geringeren Ligandenfeldaufspaltung sind diese Relaxationswege über metallzentrierte Zustände typischerweise auch bei Eisenkomplexen wiederzufinden. Zur gezielten veränderung der Energielandschaft, werden verschiedene Rückgratfunktionalisierungen bei N-Phenylpyrazol basierten Eisen(III)-Komplexen eingeführt und deren Einflüsse untersucht. UV-Vis-Spektroskopie, X-ray absorption near edge structure (XANES) und Valence-to-Core X-ray emission spectroscopy (VtC-XES) liefern dabei Einblicke in die Auswirkungen der verschiedenen elektronenziehenden und -schiebenden Substituenten.

Die stark elektronenschiebenden Liganden eines dreizähnigen zyklometallierten Eisen(III)-Komplexes führen dazu, dass das Metallzentrum sowohl chemisch reduziert, als auch oxidiert werden kann, wodurch ein isostruktureller Komplex in drei Oxidationsstufen realisiert werden kann. Um diese Prozesse am Metallzentrum zu lokalisieren und ligandbasierte Redoxprozesse auszuschließen, werden auch hier elementspezifische Röntgenmethoden, besonders XANES und Core-to-Core X-ray emission spectroscopy (CtC-XES) eingesetzt. Diese decken die oxidationsstufenabhängige Besetzung der d Orbitale sowie den resultierenden Spinzustand am Eisenatom auf und bestätigen so alle drei Oxidationsstufen.

Nicht nur die elektronische Struktur, sondern auch die damit zusammenhängende geometrische Struktur kann mit Hilfe von Röntgenspektroskopie untersucht werden. Es wird gezeigt, wie die im Bereich der Komplexchemie eher weniger verbreitete Methoden XANES und VtC-XES zum Nachweis und der Untersuchung von Hydriden in Kupferkomplexen dienen können.

Danksagung

Zuerst danke ich Matthias Bauer für die Chance zur Promotion in seinem Arbeitskreis, in welchem ich ein interdisziplinäres Themengebiet finden konnte, das mir sehr viel Spaß machte zu bearbeiten. Ich möchte mich bei ihm auch für den freundlichen und entspannten Umgang und die vielen fachlichen und außerfachlichen Unterhaltungen sowie für die Möglichkeit zur Teilnahme an diversen Messzeiten und inner- sowie außereuropäischen Konferenzen bedanken. Mein Dank gilt außerdem Thomas Kühne für die Übernahme des Zweitgutachtens und die Diskussionen über Wissenschaft, sowie das Austeilen und Einstecken von spitzen Bemerkungen.

Auch dem Fonds der chemischen Industrie des Verbandes der Chemischen Industrie e.V. möchte ich für eine zweijährige finanzielle Unterstützung dieser Promotion danken.

Ein besonderer Dank gilt Patrick Müller, der meine Themengebietsfindung deutlich geprägt hat und mir das nötige Wissen zur Röntgenspektroskopie und zu DFT-Rechnungen mit den Grundlagen beginnend vermittelt hat. Er war oft mein erster Ansprechpartner bei fachlichen Problemen und zugleich ein guter Freund für Gespräche innerhalb und außerhalb der Chemie. Zudem danke ich Yannik Vukadinovic, der mir gerade zu Beginn der Promotion die Arbeitsweisen im Labor aber auch die Photochemie nähergebracht hat. Bei ihm, sowie bei Tanja Hirschhauen, Michal Nowakowski, Jakob Steube und Pia Rehsies möchte ich mich für die fruchtbare Zusammenarbeit bei den hier gezeigten Publikationen bedanken.

Auch allen anderen ehemaligen und derzeitigen Kollegen danke ich für die fachlichen Diskussionen aber auch die lustige und freundschaftliche Atmosphäre, sowohl auf als auch abseits der Arbeit, auf Messzeiten oder Dienstreisen mit anschließendem Urlaub.

Zum Abschluss möchte ich mich bei meiner Familie und meinen Freunden bedanken, die mir während des gesamten Studiums und der Zeit der Promotion immer Verständnis entgegengebracht, sich trotz der für Fachfremde abstrakt wirkenden Inhalte für meine Arbeit interessiert und für viele schöne Erinnerungen außerhalb der akademischen Welt gesorgt haben, bedanken.

List of beamtimes

Deutsches Elektronensynchrotron (DESY)

P64
- April 11-17 2019
- August 28 - September 2 2020
- June 9-15 2022
- June 6-11 2023
- June 11-17 2020
- October 5-10 2021
- March 2-8 2023
- December 4-11 2023

P65
- April 12-17 2019
- September 6-9 2021

European Synchrotron Radiation Facility (ESRF)

ID26
- June 13-19 2018
- March 3-9 2021
- March 29 - April 4 2022

European XFEL

FXE
- June 02-06 2021
- October 4-10 2022

List of publications

Publications in journals

1. L. Fritsch, M. Nowakowski and M. Bauer. Hard X-ray Absorption and Emission Spectroscopy – Method and Applications in organometallic chemistry. *Organometallics* **2024**, submitted.

2. L. Fritsch, P. Rehsies, W. Barakat, D. P. Estes and M. Bauer. Detection and Characterization of Hydride Ligands in Copper Complexes by Hard X-ray Spectroscopy. *Chemistry - A European Journal* **2024**, accepted, DOI: 10.1002/chem.202400357.

3. L. Fritsch, Y. Vukadinovic, M. Lang, R. Naumann, M.-S. Bertrams, A. Kruse, R. Schoch, P. Müller, A. Neuba, P. Dierks, S. Lochbrunner, C. Kerzig, K. Heinze and M. Bauer. Chemical and photophysical properties of amine functionalized bis-NHC-pyridine-Ru^{II} complexes. *ChemPhotoChem* **2024**, *8*, e202300281.

4. T. Hirschhausen, L. Fritsch, F. Lux, J. Steube, R. Schoch, A. Neuba, H. Egold and M. Bauer. Iron(III)-Complexes with N-Phenylpyrazole-Based Ligands. *Inorganics* **2023**, *11, 7,* 282.

5. J. Steube, L. Fritsch, A. Kruse, O. Bokareva, S. Demeshko, H. Elgabarty, R. Schoch, M. Alaraby, S. Hohloch , T. D. Kühne, F. Meyer, O. Kühn, S. Lochbrunner and M. Bauer. Isostructural cyclometalated iron complex in three oxidation states. *Inorganic Chemistry* **2023**, in revision.

6. A. Rogolino, J. B. G. Filho, L. Fritsch, J. D. Ardisson, M. A. R. da Silva, G. Ali Atta Diab, I. Fernandes Silva, C. André Ferreira Moraes, Moacir Rossi Forim, Matthias Bauer, Thomas D. Kühne, Markus Antonietti, and Ivo F. Teixeira. Direct Synthesis of Acetone by Aerobic Propane Oxidation Promoted by Photoactive Iron(III) Chloride under Mild Conditions. *ACS Catalysis* **2023**, *13, 13*, 8662–8669.

7. U. Chakraborty, P. Bügel, L. Fritsch, F. Weigend, M. Bauer and A. Jacobi von Wangelin. Planar Iron Hydride Nanoclusters: Combined Spectroscopic and Theoretical Insights into Structures and Building Principles. *ChemistryOpen* **2021**, *10, 2,* 265-271.

8. Y. Vukadinovic, L. Burkhardt, A. Päpcke, A. Miletic, L. Fritsch, B. Altenburger, R. Schoch, A. Neuba, S. Lochbrunner and M. Bauer. When Donors Turn into Acceptors: Ground and Excited State Properties of Fe^{II} Complexes with Amine-Substituted Tridentate Bis-imidazole-2-ylidene Pyridine Ligands. *Inorganic Chemistry* **2020**, *59, 13,* 8762–8774.

9. B. J. Gregori, F. Schwarzhuber, S. Pöllath, J. Zweck, L. Fritsch, R. Schoch, M. Bauer and A. Jacobi von Wangelin. Stereoselective Alkyne Hydrogenation by using a Simple Iron Catalyst. *ChemSusChem* **2019**, *12, 16,* 3864-3870.

Talks

1. L. Fritsch, M. Bauer: 'Characterization of Coordination Compounds by Hard X-ray Spectroscopy'. Koordinationschemikertreffen, Innsbruck, February 26, 2024.

Poster presentations

1. L. Fritsch, Y. Vukadinovic, M. Bauer: 'Chemical and photophysical properties of amine functionalized bis-NHC-pyridine-Ru^{II} complexes'. Central European Conference on Photochemistry, Bad Hofgastein, February 18, 2024.
2. L. Fritsch, Y. Vukadinovic, M. Bauer: 'Amine Donors heavily influence luminescence properties of bis-NHC-pyridine-Ru^{II} complexes'. International Conference on Photochemistry, Sapporo, Japan, July 27, 2023.
3. L. Fritsch, Y. Vukadinovic, M. Bauer: 'Amine Donors heavily influence luminescence properties of bis-NHC-pyridine-Ru^{II} complexes'. SPP 2102 Meeting, Rostock, March 30, 2023.
4. L. Fritsch, J. Steube, M. Bauer: 'X-ray spectroscopic investigation of cyclometalated iron complexes as promising photosensitizers'. Central European Conference on Photochemistry, Bad Hofgastein, February 15, 2022.

TABLE OF CONTENTS

CHAPTER 1

INTRODUCTION

1.1 Outline

Transition metal (TM) complexes can be utilized in various sustainable reactions, such as photosensitizers in photocatalytic water splitting, as catalysts for the hydrogenation of CO_2 or C-H bond activation and functionalization processes.[1–5] In order to investigate and improve these reactions, insight into the geometric and electronic structure of the active metal center is necessary to understand the working principles. The aim of this work is the combination of experimental spectroscopy and theoretical calculations to get deep insights into the properties of TM complexes. For this purpose, the type of spectroscopy must be specifically adapted to the respective system and its associated questions.

The geometric structure of most complexes is commonly investigated by X-ray scattering, vibrational spectroscopy, or nuclear magnetic resonance (NMR) spectroscopy. While these standard methods are suitable for most systems, in some cases they reach their limits. For hydride ligands, the small X-ray scattering form-factor hides the hydride electron density next to the heavy TM. Furthermore, ligands, solvents, or co-reactants, can interfere with complex associated vibrations[6,7] and paramagnetic substances provide broad and shifted signals in the NMR spectra. Hard X-ray spectroscopy can overcome most of those limitations since it is element specific and almost no restrictions on the state of the sample or environmental variables exist. On the one hand, the excitation of the TM 1s electron into unoccupied metal orbitals can be probed for geometry and oxidation state identification. On the other hand, the emission process of the valence electrons can provide information about the ligand orbitals, also including hydride ligands. Also, the electronic structure of metal hydrides, potential photosensitizers or photoactive complexes can be examined with the help of hard X-rays. In particular, the spin state and the associated oxidation state can be investigated with X-ray absorption and emission methods. Additionally, especially photoactive complexes are primarily investigated using optical methods based on UV-Vis spectroscopy

and electrochemical methods to observe optical properties and redox potentials. The analysis of all these spectroscopic methods can often only be carried out phenomenologically or based on literature reports for similar systems. This is where the potential of (time-dependent) density functional theory (TD-)DFT becomes evident, which can be used to precisely analyze the orbital levels and simulate the experimental spectra to gain additional information. This work specifically showcases the potential of combining optical and X-ray based spectroscopic methods with TD-DFT calculations across four distinct projects.

1.2 Methods

1.2.1 Tutorial: Hard X-ray Absorption and Emission Spectroscopy – Method and Applications in organometallic chemistry

For the determination of the geometric and the electronic structure different analytical methods can be applied. In this work the focus is especially on X-ray absorption and emission spectroscopy whereas (TD-)DFT calculations have contributed to the understanding of these. Although X-ray spectroscopy methods are well established, they are not regularly applied in the field of organometallic chemistry. In order to make the method more appealing for chemists in this area, a tutorial, explaining the theoretical background and the stepwise procedure for analysis but also showing exemplary applications, was created.

Participations in this publication

L. Fritsch: Writing - Introduction, Physical Background, Data reduction and analysis (XANES, XES), Limitations (RD), Applications (HERFD-XANES and VtC-XES)
M. Nowakowski: Writing - Instrumentation, Data reduction and analysis (EXAFS), Limitations (SA), Applications (EXAFS characterizations and mechanistic studies)
M. Bauer: Writing - Review and Editing.

Reprinted from
Hard X-ray Absorption and Emission Spectroscopy – Method and Applications in organometallic chemistry
L. Fritsch, M. Nowakowski, M. Bauer, *Organometallics*, **2024**, submitted.

Hard X-ray Absorption and Emission Spectroscopy – Method and Applications in organometallic chemistry

Lorena Fritsch,[†,1] Michal Nowakowski,[†,1] and Matthias Bauer[1,2] *

[1] Institute of Inorganic Chemistry, Paderborn University, 33098 Paderborn, Germany

[2] Center for Sustainable Systems Design, Paderborn University, 33100 Paderborn, Germany

* Author to whom correspondence should be addressed.

[†] These authors contributed equally to this work.

Supporting Information Placeholder

ABSTRACT: This tutorial introduces hard X-ray absorption and emission spectroscopy as powerful tools to answer questions in organometallic chemistry. Although the methods are well established, they are not yet regularly applied, but they are becoming increasingly important. By providing a concise introduction to the methods, along with their theoretical and experimental backgrounds, and by showcasing selected examples, this work aims to make hard X-ray spectroscopy more appealing to researchers in the field of organometallic chemistry.

1. INTRODUCTION

X-ray absorption and emission spectroscopy (XAS, XES) are established methods in fields such as heterogeneous catalysis, materials science, geology, or physics,[1–5] and gain more and more importance in organometallic chemistry due to their unique opportunities to provide structural details. As such, they nicely complement the more standard method portfolio of NMR, EPR, and Mößbauer spectroscopy or X-ray diffraction. They are the only techniques that can give information about electronic and structural properties independent of the state of aggregation and, as such, even in the presence of reactants under reaction conditions: they provide information about the oxidation state, distance, and type of neighboring atoms, geometry, and spin state, as well as HOMO (highest occupied molecular orbital) and LUMO (lowest unoccupied molecular orbital) details. They are thus highly suited to unravel structural details of organometallic compounds not provided by other methods and to study their reactions and dynamic behavior. We want to provide a comprehensive tutorial for researchers in the field of organometallic science. Therefore, first, the physical foundations of the methods and essential instrumentation are introduced, followed by data analysis in a step-by-step description. In the second part, instructive examples relevant to metalorganic research using hard X-ray spectroscopy will be discussed.

2. PHYSICAL BACKGROUND

Both XAS and XES are element-specific methods that make use of X-rays. In general, X-rays are short wavelength electromagnetic radiation ranging approximately from 10 nm to 10 pm or from 125 eV to 125 keV.[6] The range can be divided into soft and hard X-rays, whereas the boundary is not strictly defined but lies in an area around few keV.[7] In this tutorial, only spectroscopy with hard X-rays in the K-edge energy regime of 3d transition metals is discussed in detail. In order to create a spectroscopic signal, the binding energy of transition metal 1s core electrons has to be compensated by the absorption of an X-ray photon. Since core states are involved, the energy between different elements is usually separated enough to probe only one type of element with a specific energy, even in elemental mixtures. Additionally, there are almost no limitations with respect to the sample environment in this energy range since air, solvents, and window materials are quasi-transparent. Thus, it is possible to irradiate the sample under diverse conditions with different experimental cell designs.

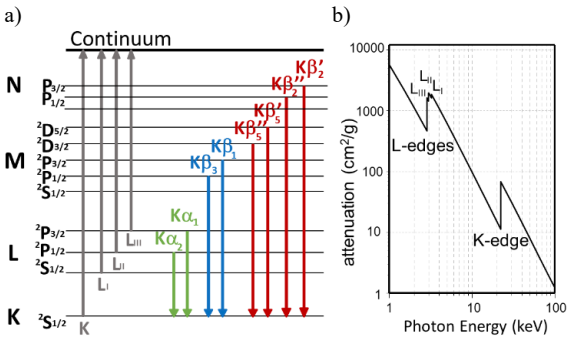

Figure 1. a) Selected absorption edges (black) and K-edge emission bands (blue). b) Exemplary Ru K- and L- absorption edges (Figure created with[8]).

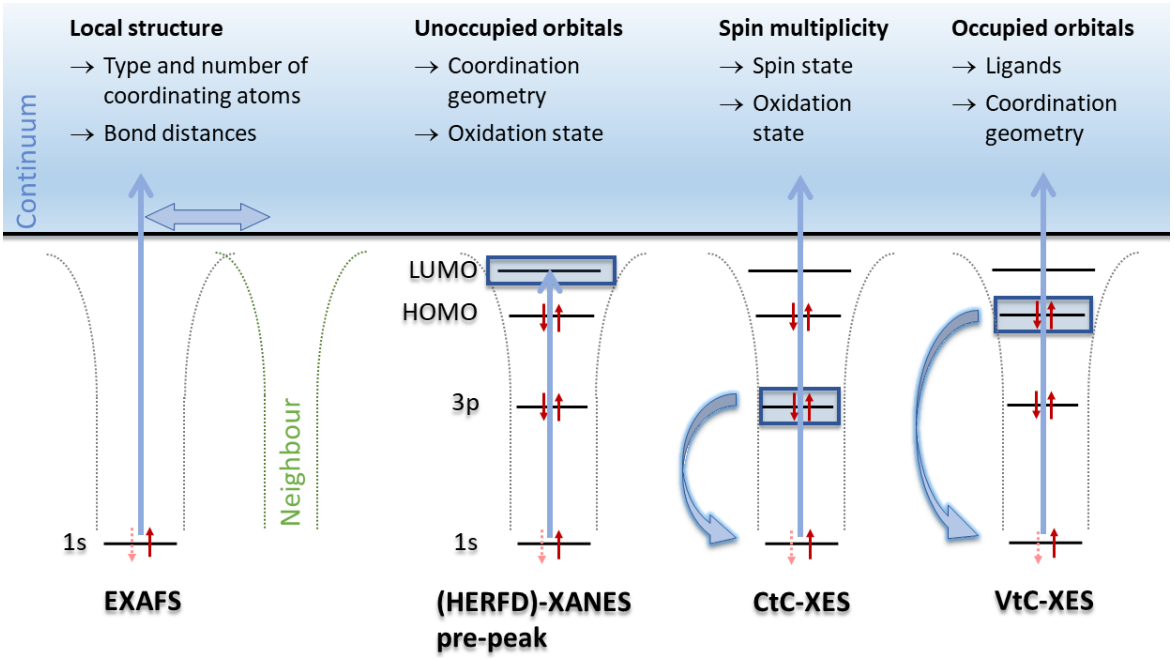

Figure 2. Schematic representation of the main K-edge transitions discussed in this tutorial using the example of a 3d metal. EXAFS and XANES refer to Chapter 2.1, while VtC-XES, CtC-XES, and HERFD-XANES refer to Chapter 2.2.

When the sample absorbs X-ray energy higher than the 1s binding level, electrons are excited into empty bound states or continuum levels at higher incident energies, and finally, photoelectrons are created. The absorption leads to a sharp increase in the absorption probability, also called absorption edge. Depending on the principal and orbital quantum numbers of the origin orbital of the excited electron, absorption edges are designated differently (see Figure 1).[6] The strong rise resulting from a 1s excitation is called K-edge. Transition metal K-edge energies for 3d and 4d metals range from 4.492 keV (Sc) to 26.711 keV (Cd) and are thus covered by most hard X-ray synchrotron beamlines, such as ID26 (2.4-27 keV)[9] or BM30 (4.8-40 keV)[10] at ESRF, P64 and P65 at DESY (4-44 keV)[11,12], 6-2b at SLAC (5-18 keV)[13], BALDER at MAX IV (2.4-40 keV)[14] or I18 (2-20.5 keV)[15], B18 (2-35 keV)[16] and B20 (4.5 -20 keV)[17] at Diamond Light Source. The typical absorption and emission experiments outlined in the following can be performed within this energy range. This tutorial will focus on K-edge spectroscopy, especially for 3d transition metals as used in many organometallic studies. Special attention will be paid to the static X-ray absorption near edge spectroscopy (XANES) and the extended X-ray absorption fine structure (EXAFS), the emission methods: Core-to-Core (CtC) or $K\beta_{1,3}$, Valence-to-Core (VtC) or $K\beta_{2,5}$, and high energy resolution fluorescence detected (HERFD)-XANES. The corresponding transitions are depicted in Figure 2 and are explained in more detail in the following sections.

2.1 X-ray absorption spectroscopy (Figure 2 left) provides information about the oxidation state, coordination geometry, and ligand environment of complex organometallic compounds in the solid, solution, or gas phase. It is the only spectroscopic method that directly provides bond lengths. Absorption of monochromatic high-energy X-rays leads to the excitation of a core electron to an unoccupied LUMO state or the continuum, depending on the incident energy of the photon. Thus, the beam which passes through a homogeneous sample of the thickness t is attenuated. The linear absorption coefficient μ(E) can be determined by recording $I_0(E)$ and $I(E)$ as the incident and transmitted X-ray intensities in the function of the incoming energy E. According to Lambert-Beer's law:[18]

$$I(E) = I_0(E)e^{-\mu(E)t} \qquad (1)$$

Depending on the energy, typical changes in the absorption coefficient occur. It decreases continuously smooth with higher energies due to a decrease in the probability of absorption, which is directly proportional to the absorption coefficient. It can be approximated as a relation between the atomic number Z and the X-ray energy E ($\mu \sim Z^4/E^3$), leading to a decrease of about $1/E^3$. As the binding energy of the core-electrons E_0 is exceeded, an abrupt increase of the absorption coefficient named absorption edge is observed. With increasing energy E of the incident X-ray beam, the excess energy E-E_0 is transferred to the created photoelectron that propagates away from the absorbing atom with the wavelength λ and wave vector k.[6]

$$\lambda = \frac{2\pi}{k} \quad where \quad k = \sqrt{\frac{2m}{\hbar^2}(E - E_0)} \qquad (2)$$

Due to the interference of the outgoing photoelectron wave and the wave backscattered at neighboring atoms, a fine structure with oscillations in the absorption coefficient can be observed after the absorption edge. Three characteristic regions can accordingly be found in XAS spectra as shown in Figure 3a: The pre-edge part, the edge region typically whin 40 eV above

the edge, and the EXAFS region, which can continue for more than 1000 eV above the absorption edge.[6]

The Pre-edge region is often included in the XANES region and shows a decreasing absorption probability with incoming energy until the energy of a specific transition is reached. This signal is called the pre-edge feature or just "pre-peak". It is usually assigned to $1s \rightarrow nd$ transitions, but in fact, the LUMO levels are the final states here. Thus, they are better described as $1s \rightarrow nd/(n+1)p$ transitions.[19] Since $s \rightarrow d$ transitions are dipole-forbidden, only weak quadrupole transitions are possible for pure d states.[7] However, coordination symmetry-dependent hybridization of metal-p with metal-d orbitals results in an increased intensity of this signal by partial dipole transition character. In this way, the pre-peak contains information about the coordination geometry in metal complexes. Additionally, the shape of the pre-peak provides information about spin states when more than one d-orbital as the final state is available. In this case, multiplet effects become visible, leading to different shapes due to the final state energy splitting as a function of crystal field strength given by the Tanabe-Sugano diagrams.[20] Last, the energy of a pre-peak can provide information about the oxidation state. The core orbitals of 3d metals are more influenced by the effective nuclear attraction force than the valence orbitals, leading to a shift to higher signal energies for higher oxidation states and *vice versa*. However, different ligand environments can significantly influence this shift because the ligand properties affect the valence energy levels, changing the effective nuclear charge as well. Thus, pre-peaks should be compared with care if different coordination environments are present.

The XANES region comprises the rising edge and the "white line." The term "white line" originates from the early days of XAS when spectra were recorded in photographic films and

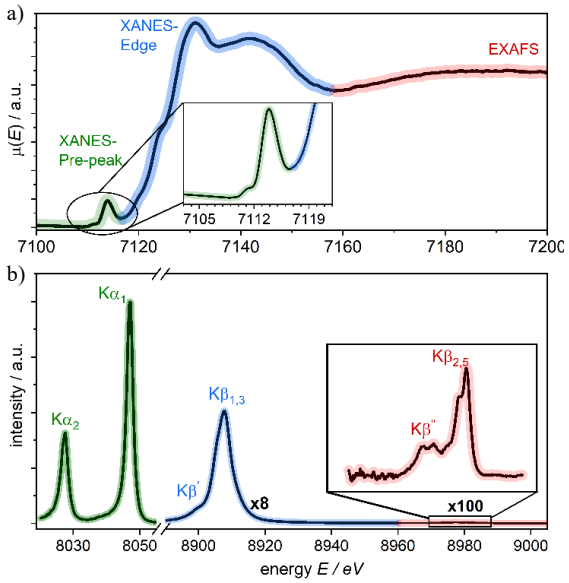

Figure 3. a) X-ray absorption spectrum of a Fe complex with pre-edge (green and zoom in), XANES (blue), and EXAFS (red) part. b) X-ray emission spectra of a Cu complex. $K\alpha_{1,2}$ (green), $K\beta_{1,3}$ (blue) and $K\beta_{2,5}$. Spectra with given multiplication factors to display the intensity ratios.

the most intense absorption appeared as the brightest areas in the film.[21] It denotes the first resonance after the absorption edge. The intense features here can be mainly attributed to dipole-allowed 1s→4p excitations. The most common usage of the XANES region is an oxidation state analysis using the edge position. Several approaches exist to determine the edge position (E_0, Figure 4a) from experimental data. The local maximum of the first derivative can be used,[22] but it must be noted that the determined value is beamline-dependent and can be affected by pre-edges and ligand contributions. The same limitations apply basically to the even more straightforward approach in which the absorption threshold is read out at exactly 50 % of the jump. An oxidation state change by one is typically accompanied by an edge shift of ~1-2 eV but can amount to 5 eV if ligands and local geometry change.[23] For further details and an example of this procedure, see the data analysis section. It is also possible to enhance spectral resolution by collecting high energy resolution fluorescence detected (HERFD-) XANES spectra, which is explained in the X-ray emission section.

The EXAFS region at higher energies results from 1s→continuum transitions and is characterized by oscillations that continue well above the edge. The ejected photoelectron can be understood as a spherical wave with respective μ(E) monotonically decreasing as an energy function for isolated atoms (Figure 4a). For X-ray absorbing atoms in a complex, the variation of absorption coefficient is caused by the interference of the outgoing photoelectron wave with the incoming one at the position of the absorber (Figure 4b).[6] By analysis of these modulations, the type, number, distance to a metal center, and disorder of the neighboring atoms can be obtained. Thus, this technique is especially valuable for structural analyses of chemical systems where diffraction methods are not applicable,

e.g., in solution or non-crystalline samples. It has, however, to be emphasized that coordinating atoms that are neighbors early (Z<19) in the periodic table cannot be distinguished by EXAFS spectroscopy, and very light ligands such as hydrides are EXAFS silent as they do not contribute visibly to the EXAFS oscillations.[24–26] To isolate the oscillatory fine structure from the spectra, an atomic background μ_0(E) is subtracted from the measured absorption coefficient. This atomic background cannot be calculated a priori and must be identified in a heuristic way. The difference is normalized to this background at E_0, yielding the isolated EXAFS oscillations $\chi(E)$:

$$\chi(E) = \frac{\mu(E) - \mu_0(E)}{\mu_0(E_0)} \tag{3}$$

This expression can be converted from E dependence to k dependence by Eq. 2 to obtain $\chi(k)$. Using the single scattering approximation, Stern, Sayers, and Lylte found an expression for $\chi(k)$, now called the standard EXAFS equation (eq. 4): [6]

$$\chi(k) = \sum_j N_j S_i(k) F_j(k) \exp\left(-2\sigma_j{}^2 k^2\right) \exp\left(-\frac{2r_j}{\lambda_j(k)}\right) \frac{\sin\left(2kr_j + \phi_{ij}(k)\right)}{kr^2{}_j} \tag{4}$$

- N_j: Number of atoms in coordination shell *j*. One coordination shell is built from the same type of atoms at a similar distance.
- $S_i(k)$: Amplitude-reducing factor - accounts mainly for multiple excitations (so-called many-body effects) in the absorbing atom *i*. The photoelectron loses kinetic energy by imparting energy to another atom's electron and appears at a higher binding energy in the spectrum.
- $F_j(k)$: Backscattering amplitude from each neighboring atom in coordination shell j.
- σ_j^2: Mean square half-path displacement for scattering path j – describes the static and dynamic disorders of the system (Debye-Waller-like factor). The static disorder results from varying distances between atoms of the same coordination shell and the absorbing atom. The dynamic disorder is caused by lattice vibrations dependent on temperature.
- $exp\left(-\frac{2r_j}{\lambda_j(k)}\right)$ accounts for the photoelectron lifetime decrease due to inelastic interactions with nearby environment and is characterized by inelastic mean free path length $\lambda_j(k)$.
- $1/kr_j^2$: Reflects the decrease in intensity of the outgoing photoelectron wave with distance r_j to the absorber. Thus, the nearest neighbors dominate EXAFS, and contributions from more distant shells are represented weakly.
- $sin(2kr_j+\phi_{ij}(k))$: Sinusoidal oscillations as a function of interatomic distances and the phase shift $\phi_{ij}(k)$.

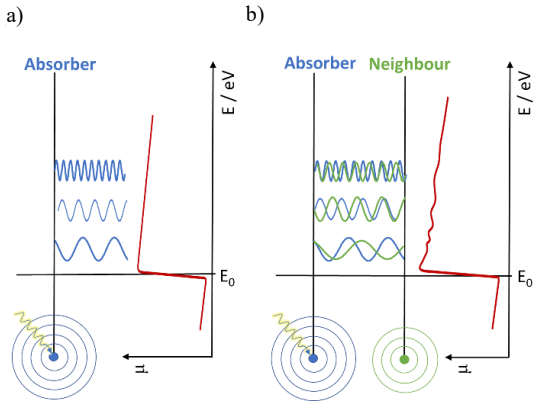

Figure 4. Schematic representation of the absorption process and the resulting absorption spectrum of an isolated atom (a) and an absorbing atom surrounded by neighboring atoms (b).

This approximation is adequate in many circumstances. It simplifies the theoretical description, assuming the EXAFS region is dominated by single scattering effects of the electron wave propagating through a largely constant electronic potential, and multiple scattering is important only under certain conditions. In contrast, XANES is dominated by multiple scattering due to the low kinetic energy of the photoelectron. The more sophisticated approach assumes the possibility of scattering the photoelectron wave on multiple atoms before returning to the source atom. In the frame of Multiple Scattering theory [27–30], such multiple scattering paths can be linear or triangle; all other paths can usually be neglected. Scattering paths are calculated *ab-initio* based on the initial structural model, for example, with the FEFF, GNXAS, or Excurve software,[31] and fitted to the experimental spectra. The most important benefit of the multiple scattering approach is a more detailed insight into the Debye-Waller factors and local angles in multiple scatters.[28,32,33] For linear ligands such as CO and CN^-, so-called forward-scattering due to the colinear arrangement of M-CO and M-CN must be considered in the fit procedure to achieve correct coordination numbers.[34,35] Insights on theoretical EXAFS equation fitting to the data are discussed in detail in the *Data reduction and analysis* section.

2.2 X-ray emission spectroscopy (Figure 2 right) describes the detection of emissive relaxation following an absorption process to access information, especially about the electronic structure and ligand environment. After the photoabsorption, two relaxation channels mainly compete. In the radiative pathway, called X-ray emission, an electron of a higher energy level fills the core hole. The excess energy is released as X-ray fluorescence, according to the Energy Conservation Rule. On the contrary, in the non-radiative Auger effect, one electron refills the core level, and the excess energy is carried by a second electron, which is promoted into the continuum.[6] The ratio of both competitive processes (fluorescence vs. Auger) increases with transition energy: for elements heavier than the gallium radiation pathway dominates[36]. X-ray fluorescence detection is standard for molecular materials since detecting Auger electrons is only possible for near-surface regions or interfaces and requires UHV conditions, which makes in-situ studies very challenging. Thus, we only address the fluorescence relaxation methods here.

The described fluorescence can also be considered as a two-step photon in/photon out process or inelastic scattering process. A few words about the underlying physics might be appropriate here. In a second-order perturbation picture with one photon absorbed (annihilated) and one created, the obtained cross-section is the Kramers-Heisenberg formula[37] and can be simplified as follows.[38]

$$\frac{\partial^2\sigma}{\partial E\partial\Omega} = {r_e}^2\frac{\omega_{out}}{\omega_{in}}\sum_f\left|\sum_n\frac{\langle f|T^*|n\rangle\langle n|T|g\rangle}{E_g-E_f+\hbar\omega_{in}-i\Gamma_n/2}\right|^2\cdot\delta(E_g-E_f+\hbar\omega_{in}-\hbar\omega_{out}) \quad (5)$$

The formula provides the double differential cross section σ of the emission of a photon with energy $\hbar\omega_{out}$ after the excitation of a photon with energy $\hbar\omega_{in}$. $|g\rangle$ is the ground state, $|n\rangle$ is an intermediate state, and $|f\rangle$ is the final state. E_g and E_f represent the energy in each state, respectively. r_e describes the electron, radius, and δ delta function that conserves energy. T and T^* are transition operators, and Γ_n represents the line broadening based on the lifetime of the core hole, i.e., the transition state *n*. δE denotes energy, and $\delta\Omega$ the solid angle. The formula describes various scattering techniques, including resonant and non-resonant X-ray emission spectroscopy.[39] If the 1s electron is excited well above the edge, the emission does not change with excitation energy (non-resonant XES). However, suppose the incident energy is tuned in the vicinity of the absorption edge. In that case, the fluorescence intensity is strongly modulated by the absorption probability and is called resonant inelastic X-ray scattering (RIXS) or resonant X-ray emission spectroscopy (RXES).[40–42] The fluorescence lines are designated differently depending on the orbital from which the relaxing electron originates (see Figure 1a). The resulting spectra, including the intensity ratios, are given in Figure 3a.

The Kα line is the lowest energy emission in K-edge spectroscopy. The 1s core hole is filled by an electron of the L-shell (2p). Due to the different spin quantum numbers at the 2p level, two lines are observed according to the total angular momentum: $K\alpha_1$ ($2p_{3/2}$) and $K\alpha_2$ ($2p_{1/2}$). These transitions show the highest fluorescence yield due to maximal overlap between the initial and final state and, thus, the highest intensity (see Figure 3).[43] Therefore, it is beneficial for detecting HERFD-XANES spectra (vide infra). 2p-3d exchange interaction broadens the full width at half maximum (FWHM) of the $K\alpha_1$line with increasing valence shell spin state. Thus, it can, in principle, be used to determine the oxidation state in organometallic complexes. However, it must be noted that for precise determination, the core hole effects need to be taken into account. This issue becomes less important in covalent compounds due to the screening effects of ligand electrons.[44]

The Kβ line reflects transitions from higher energy core (3p) and valence(3d) orbitals to the 1s orbital and is chemically more sensitive. Compared to the Kα line, the p-d overlap and exchange interactions are larger and stronger. For the $K\beta_{1,3}$ or Kβ mainline transition (Figure 3b), the spin-orbit interaction is much weaker (~ 1 eV) than for Kα (~ 10 eV).[41] Thus, the observed splitting does not originate from spin-orbit coupling but is due to modulations of the exchange integrals between the 3p hole and the valence electrons in the final state. It can be understood in a multiplet framework yielding two peaks assigned to $K\beta_{1,3}$ as the main peak and Kβ' as the low-energy shoulder (Figure 5).[40,45] In the case of a d^5 high spin system, the intermediate states after photoionization are $^{5,7}S$ if the continuum electron is excluded. For the final states, the selection rules ΔS=0 and ΔL=0,±1 apply, making $^{5,7}P$ final states conceivable. While the ^7S intermediate state can only relax into one ^7P state, there are two possible ^5P final states to relax the ^5S intermediate state. One of those contains a 3p electron with antiparallel spin with respect to the 3d electrons, characterized by increased energy compared to the ^7P state. The low-energy ^5P state originates from symmetry mixing in the core hole excited state, which can be viewed as a spin flip in the 3d shell due to the interaction with a core hole.[39] The significant energy difference between the ^7P (and low-energy ^5P) state, which is responsible for the $K\beta_{1,3}$ line, and the high-energy ^5P state, which is responsible for the Kβ' signal, finally explains the shape of this emission line for high-spin systems. In low-spin systems, the energy difference between the final states ^3H and ^1H is significantly smaller, so both signals strongly overlap, and only a low-energy shoulder is detectable. Thus, it is also apparent that the Kβ mainline is also sensitive to covalency effects, which strongly influence the valence electrons.[46,47]

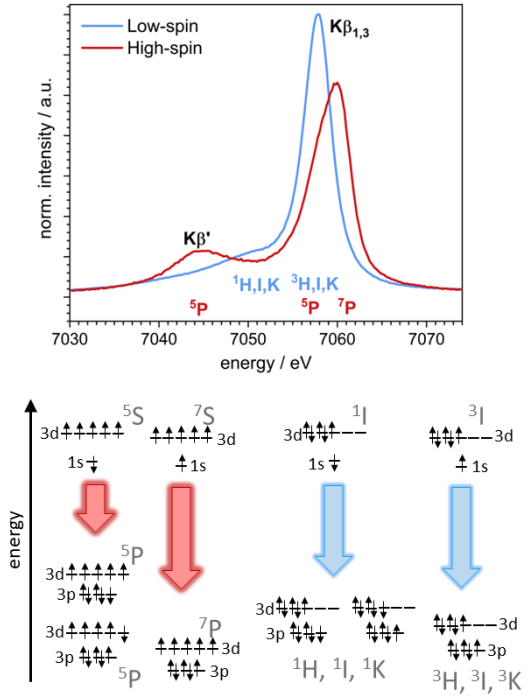

Figure 5. Top: Exemplary $K\beta_{1,3}$ spectra of a Fe^{III} low spin and a Fe^{III} high spin complex. Bottom: Resulting multiplets (top: initial state, bottom: final state) leading to the respective energy splitting.[19]

Furthermore, weak signals on the high-energy side close to the absorption edge energy are visible. They arise from transitions between the valence orbitals (HOMO levels) and the metal 1s shell and are named $K\beta_{2,5}$ or Valence-to-Core (VtC) transitions. They consist of the higher intensity $K\beta_{2,5}$ peak and the Kβ" satellite. Since the valence orbitals of organometallic complexes usually have high d-character, the hybridization with ligand orbitals leads to a detectable intensity, which is still about 100 times lower than for dipole-allowed and energetically lower-lying $K\beta_{1,3}$ transitions. While the $K\beta_{2,5}$ peak emerges from the transitions of electrons in the valence molecular orbitals (ligand p- and metal p- and d-character), the latter arise from molecular orbitals with mainly ligand s-character with metal p- and d-contribution. The splitting between both is based on the differences in binding energy between the ligand s and p orbitals, which makes it possible to distinguish between ligands with similar atomic numbers like O, N, and C. As such, VtC-XES is able to overcome some limitations of EXAFS. Even light elements, especially hydrogen in hydride complexes, can be detected and investigated by VtC-XES.[48–51] Thus, information can be provided not just about the electronic structure like in $K\beta_{1,3}$ but also about the atomic structure like ligand type and geometry. For the analysis, ground state DFT calculations play a significant role, as they usually accurately reproduce the spectra. Thus, VtC-XES is a method with high potential for characterizing electronic structures in metal complexes.[52,53]

HERFD-XANES, as mentioned above, can be obtained by recording the intensity of various emission processes while sweeping the incident energy over an absorption edge.[54] In the range of hard X-rays, it can be assumed that there is a sufficient proportionality between the measured intensity of the fluorescence process, described by the Kramers-Heisenberg formula (1.5), and the linear absorption coefficient.[55] According to the Heisenberg Uncertainty Principle, the energy resolution of an experiment is limited by the lifetime of the final state. Extracting information from pre-peak and the edge in conventional transition metal K-edge XANES spectra can be imprecise due to this core-hole lifetime broadening of the 1s electron hole, which smears out pre-peak and edge signals. The HERFD-XANES spectrum is recorded indirectly *via* distinct secondary fluorescence processes whose final state is a 2p (Kα) or a 3p (Kβ) core hole, having an elongated lifetime with respect to 1s.[56] An example of a HERFD-XANES compared to a conventional XANES spectrum is given in Figure 6.

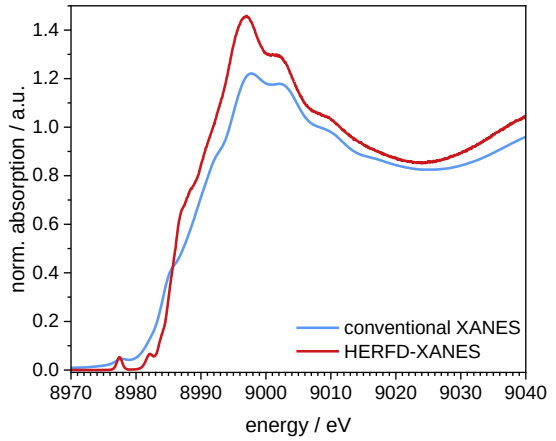

Figure 6. Comparison of conventional and HERFD-XANES spectra of a Cu^{II} compound.

3. INSTRUMENTATION

3.1 Synchrotron as an X-ray radiation source. A synchrotron is an X-ray source used primarily for scientific purposes. A general scheme of synchrotrons is shown in Figure 7. Electrons are generated by the electron gun (A), which consists of a hot tungsten rod (2800 K) from which thermal electrons are ejected and accelerated in the electric field. Next, the electrons are directed to the linear accelerator (B), accelerated to MeV energies, and directed to the first circular accelerator, the Booster (C). Here, they gain energy of a few GeV and are injected into the storage ring (D).[57] Bending magnets are used to maintain a circular orbit and serve as radiation sources. On straight fragments, insertion devices in the form of wigglers and undulators are installed, where the electron beam interacts with periodically changing external magnetic fields to generate strong and coherent X-ray radiation beams. During the interaction with magnetic fields, electrons lose energy, which must be replenished to slow down the decrease in ring current. For that, superconducting radio-frequency cavities are installed. Modern synchrotrons work in top-up mode to compensate for the current loss, where electrons are frequently injected into the ring in small doses to maintain current changes

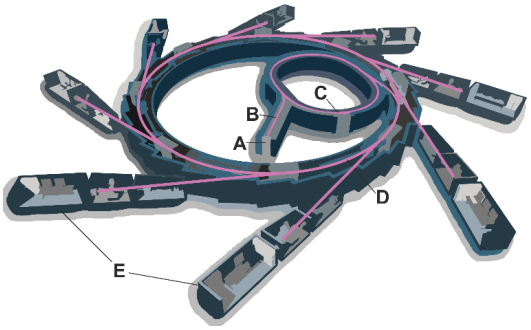

Figure 7. Schematic of 3rd generation synchrotrons with the most important elements marked.

in 1-2 % of the designed value. It must be stressed that an ultra-high vacuum (UVH) is maintained in all synchrotron components to avoid electron scattering on gas particles. In the outer tangential arms (E), synchrotron radiation is utilized.

3.2 Sources and properties of synchrotron radiation (SR). *Synchrotron radiation* is generated in bending magnets and insertion devices due to the interaction of relativistic electron bunches with external magnetic fields and is emitted tangentially to the direction of movement of charged particles. Except for the required high stability, the properties of synchrotron radiation are:[7,58]

1) Very high intensity, over 12 rows of magnitude higher than conventional X-ray tube source,
2) Broad and tunable energy range: from infrared to hard X-ray radiation
3) Small collimation angle, thus high flux, brilliance, and coherence of the emitted radiation
4) Discrete temporal structure
5) High degree of radiation polarization in the plane of the accumulation ring

Sources of synchrotron radiation. Bending magnets have a dual function in synchrotrons. Their primary task is maintaining the circular trajectory of electrons in the storage ring. Additionally, they act as sources of synchrotron radiation. They produce a broad spectrum of radiation in short pulses. Such a source can be characterized by a critical wavelength λ_c below and over which 50% of the radiation flux power is emitted. Figure 8a) presents a bending magnet's scheme, temporal pulse pattern, and emittance profile. A single bending magnet produces a short pulse of a broad energy range. On the contrary, insertion devices are divided into two types: wigglers and undulators. Both consist of stacked pairs of superconducting magnets with alternate polarity and produce much more intense radiation than bending magnets. Electron bunches entering a device are forced to oscillate in the plane of the device with a changing magnetic field. With every wiggle, a portion of the radiation is emitted. The final properties of the emitted radiation are determined by the device's parameters: total length, number of magnet pairs, the distance between the magnets, magnetic field strength, and electron energy. Wigglers can be understood as the equivalent of a series of bending magnets stacked together (Figure 8b). The relative oscillation amplitude is large enough that the narrow emission cone leaves the detector plane, adding the radiation incoherently. Thus, the observed radiation's temporal structure is like a series of pulses from bending magnets. However, the total brightness of an N-magnet pair wiggler is N- times higher than that of a single bending magnet. The difference between a wiggler and an undulator (Figure 8c) is subtle but crucial. The electron oscillation amplitude is smaller in undulators, and electron wiggles have a smaller curvature angle than the natural emittance angle. As a result, radiation emitted from every wiggle interferes with each other, forming a coherent beam that maintains its collimation in both horizontal and vertical axes. Therefore, the undulator produces a radiation N^2 times more intense than BM with a very narrow energetic profile.[59]

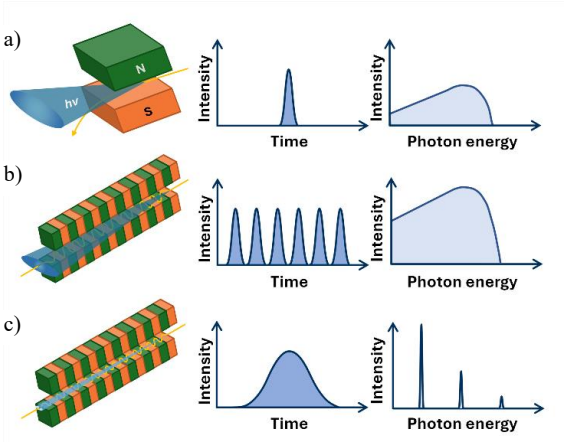

Figure 8. X-ray sources/ insertion devices at the synchrotron and their emittance profile: a) bending magnet, b) wiggler, c) undulator.

2.3 Hard X-ray beamline optics. Every beamline can be divided into optical and experimental parts. This section will present typical optical parts to produce monochromatic hard X-rays and provides technical language to new experimentalists. Vital elements of every beamline are shown in Figure 9, which shows the hard X-ray spectroscopy beamline P64 of Petra III, DESY (Hamburg) [60].

Slits. The beam is formed when the radiation enters the optic area through the entrance slit. Slits form the beam shape, quench the scattered radiation, and divide the beamline into sections where it is technically easier to maintain UHV. The slit window on the beam path is composed of weakly interacting material, like Kapton® or Beryllium.

Double crystal monochromator (DCM). Monochromators are used to obtain a beam with a narrow energy profile. Usually, a Double Crystal Monochromator (DCM) composed of two parallel Si or Ge monocrystals of the same crystal lattice cut is used on a hard X-ray beamline. This arrangement is chosen to achieve a better energy resolution and allow the X-rays to exit the optics with only a slight offset from the storage ring plane. Energy selection is achieved by diffracting the incoming beam on the crystal surface according to the Bragg law:

$$n\lambda = 2dsin(\theta) \tag{6}$$

λ is the wavelength to be selected, d is the crystal lattice plane, and θ is the required incidence angle or Bragg angle. The n is a natural number defining the order of reflection. First-order reflections are chosen, although higher-order reflections might and can cause artifacts in the spectra.

Mirrors. The typical following elements on the beam path are mirrors. They focus the beam in horizontal and vertical directions and act as a filter to eliminate higher harmonics from the monochromator. An optimal design contains two toroidal or cylindric Kirkpatrick-Baetz mirrors aligned at 90° to each other, with the beam hitting their planes at an angle smaller than the critical angle. The most common material used in mirror manufacturing is Si or SiO_2 coated with layers of heavy metals, like Pt, Rh, Ni, and Au, depending on the dedicated working energy of the beamline. For example, at the P64 beamline in DESY, the source is a 2 m undulator, and the dedicated energy range is 4-44 keV.[11]

2.4 The experiment. As described above, the main task of the monochromator is to select the energy from the incoming beam utilizing the Bragg condition. After passing through the system of mirrors and slits, the formed beam enters the experimental area. Although numerous experiments could be conducted, we will focus on two types: X-ray absorption (XAS) and X-ray emission spectroscopy (XES). For XAS, three ways of measuring μ(E) are typically applied:[61,62] transmission, total fluorescence yield (TFY), and total electron yield (TEY).[63] Since total electron yield detection is highly surface sensitive and requires ultra-high vacuum, it is not further discussed here. On the other hand, in XES, there are two types of measurements depending on which geometric solution is chosen: Johann (scanning) and von Hamos (energy dispersive). XES geometries can also be used to perform high-resolved fluorescence-detected XANES (HERFD XANES).

Transmission XAS. The simplest experimental setup is the transmission mode shown schematically in Figure 10a). This method measures the beam intensity using ionization chambers before (I_0) and after (I) interaction of the beam with the sample S. According to eq. 7, the absorption coefficient can be derived as a function of the incident beam energy μ(E):

$$\mu(E)d = \ln\left({}^{I}/_{I_0}\right) \tag{7}$$

To calculate the gas composition in the ionization chambers, freeware software like Hephaestus (Demeter)[64] or XAFSmass[65] can be used. The choice of the gas composition depends on the probed energy range. The transmission method can be applied for thin, homogenous, and low-concentrated samples. A sample that is too concentrated will absorb too much beam to be detected by the second ionization chamber. The ideal range of observed edge jumps to allow reliable EXAFS analysis is

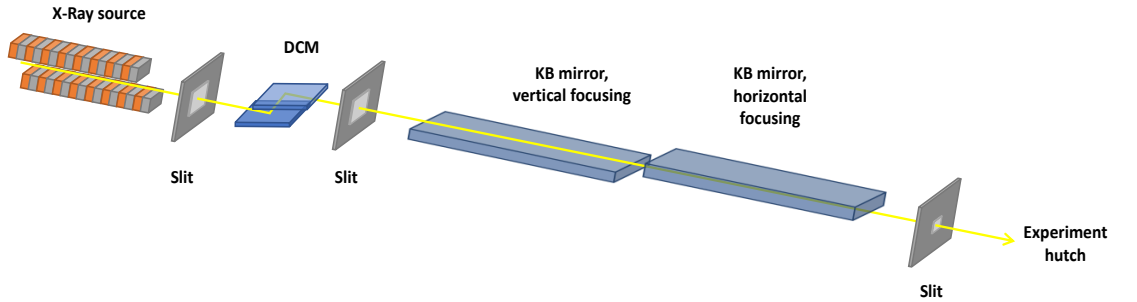

Figure 9. General scheme of a hard X-ray spectroscopic beamline with undulator X-ray source and the most important elements marked. The order and details of the elements might vary, depending on the individual solutions.

around $\mu(E)d = 0.3 - 1.5$.[66] It is worth noting that the thickness and concentration have convoluted effects. Thus, there is reasonable flexibility in sample preparation concerning concentration and sample thickness combinations.

Fluorescence XAS. For inhomogeneous and low concentrated samples with an edge jump below 0.2, fluorescence detection is advantageous,[67] schematically shown in Figure 10 a). Total fluorescence yield XAS is slightly more complicated in an experimental sense due to the detectors used and additional physical effects that need to be considered. Emitted X-ray fluorescence intensity upon creating a core hole is directly proportional to the number of created vacancies, i.e., the absorption coefficient, and the following ratio applies:

$$\mu(E) \approx {I_f}/{I_0} \tag{8}$$

Here I_f is the fluorescence intensity recorded by the detector. In the experiment, the beam hits the sample at a 45° angle, while the detector is typically also oriented at 45° to the sample, thus at 90° to the incoming beam. During the beam's interaction with the sample, elastic scattering is produced. According to the Klein-Nishina formula[68], the lowest yield of the elastic scattering to the background can be achieved when the beam and the detector are at 90°. For signal detection, a simple avalanche photodiode, a passivated implanted planar silicon (PIPS),[69,70] a silicon drift detector (SDD),[71] or a hyper pure germanium detector[72] can be used.

Scanning XES. X-ray emission spectroscopy records a relation between the X-ray fluorescence intensity and its energy. Therefore, the applied setup must have a detection resolution of 1 eV. Although standard X-ray photon counting detectors used in XAS cannot accomplish this task, the addition of analyzing crystals allows for obtaining a spectral resolution of around 1 eV. In standard applications for XES, the analyzer is composed of a grid of analyzer crystals. They have very narrow diffraction solid angles, but a matrix of such crystals can effectively compensate for that.[73–75] Typically, analyzers are bent spherically or in the dispersive axis direction[76]. Figure 10 shows two different spectrometer geometries – 10 b) shows a scanning X-ray spectrometer with spherically bent analyzer crystals, where the source, analyzer, and detector are on a Rowland circle (dashed line). The proposed solution is called Johann or Johannsson spectrometer.[77] In Johann's geometry, the analyzing crystals are bent in the plane of the Rowland circle. However, they do not match the curvature of the circle, which causes a loss of the spectral resolution.[76] The Johansson geometry provides analyzing crystals with the curvatures of the Rowland circle. Spectrometers based on the Rowland circle work in scanning mode: with fixed incident energy, the emission is recorded by stepwise changes of the Bragg angle (movement of the analyzers and diode along the Roland geometry). With this, the energy of the X-rays diffracted by the analyzer is varied. They also provide the highest intensities of the recorded X-ray fluorescence.

Energy dispersive XES. In the energy dispersive von Hamos geometry (Figure 10c), the analyzer is cylindrically bent perpendicular to the dispersive plane. Theoretically, the energy resolution is the same as in scanning XES geometry, but due to deviations from a point source, a slightly reduced resolution is observed in practice. Energy dispersive area detectors are used for signal detection, allowing for measuring the full XES spectrum in a "single shot". Current applications of the von Hamos spectrometers span from synchrotron experiments, both static and time-resolved, to free electron lasers.[78–85] Energy-dispersive spectrometers can significantly facilitate HERFD-XANES and XES acquisition at the expense of spectral resolution and signal quality.

High energy resolution fluorescence detected XANES. Closely connected to X-ray emission spectroscopy is HERFD-XANES, as described above. To record HERFD-XANES spectra, the intensity of a single fluorescence channel, selected with the analyzer crystals, is monitored with a resolution smaller than the lifetime broadening while sweeping the incident energy of the double crystal monochromator. Usually, the maximum of the Kα or Kβ main line is used for this purpose.[86]

Ultrafast pump-probe X-spectroscopy. While time-resolved experiments are most known for ultrafast serial X-ray crystallography,[87–90] X-ray emission and absorption experiments can also be conducted in a similar scheme. The experiments can be carried out using synchrotron pulsed beam patterns for processes slower than 100 ps or dedicated X-ray free electron lasers if a better time resolution is required.[91] The described methods can, in principle, all be implemented for such measurements, i.e., both XAS [92–94] and XES.[95] From an experimental point of view, the drawback here is the basically mandatory application of a liquid jet for sample delivery. Only in this case can radiation damage by the intense X-ray (and optical) laser pulses be avoided (sec. 2.5).

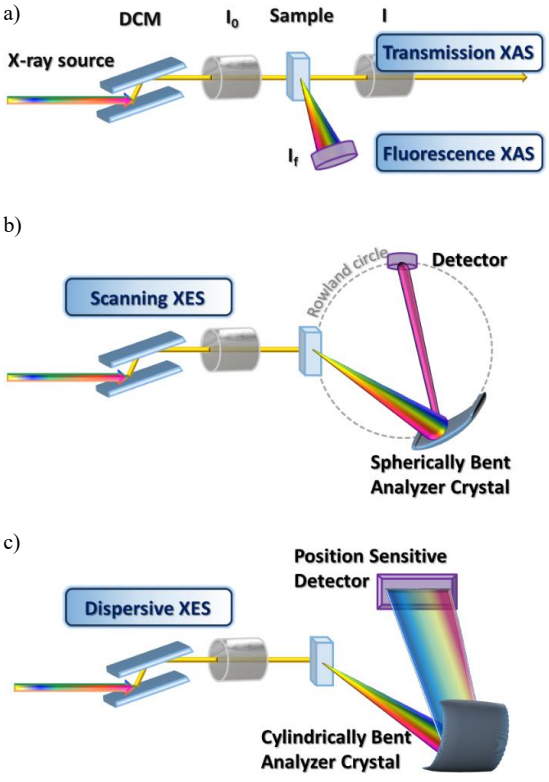

Figure 10. Schematic representation of the a) transmission XAS and TFY XAS. b) Scanning Johann or Johannsson type XES spectrometer and c) Dispersive von Hamos XES spectrometer.

2.5 Sample delivery systems. X-ray spectroscopy is element-selective and bulk-sensitive. Therefore, one can probe numerous types of samples in all states of matter. For metalorganic purposes, typically solid and liquid samples are used, and thus, we will focus on such systems and present selected experimental approaches.

Supported wafers. The simplest way to prepare a homogenous sample is to prepare a wafer or pellet. Solid samples in that form can be used for transmission and fluorescence measurements. Transmission pellet samples are prepared as a mixture of the sample with a binder, for example, BN or cellulose. While preparation of BN supported samples requires a bit of experience, cellulose is an easier to handle alternative, although it is not as inert as BN. For the investigation of sensitive samples, preparation can be conducted in glove boxes using degassed and dried binders. Such wafers provide a significant degree of flexibility regarding absorber concentration and sample environment control. The required amount of substance can be calculated using, for example, the program XAFSMass.[65]

Solid powders. If the sample amount is too low to prepare a good pellet or the concentration plays an essential role in the measurement, a pure powder sample can be measured. The powder must be as homogenous as possible, and small particle sizes are required. To seal sensitive samples, they can be prepared between two layers of Kapton®. Alternatively, the powder sample can be glued on a Kapton® tape or formed into a thin layer by solvent evaporation. Ultimately, very sensitive samples can be stored and measured in silica capillaries. However, capillary effects can change total sample thickness and density, thus affecting the spectra.

Liquid cells. Next to solid samples for fundamental characterization, liquid cells play a crucial role in metalorganic applications. Figure 11 displays various cell types for measurements in solution.[96] For metalorganic systems, the preferred cell body material is inert. Thus, Teflon® or PEEK are the best choices, while stainless steel or other metals should be avoided as they might interfere with the chemical reaction under investigation. As a prerequisite for X-ray experiments on potentially sensitive complexes, Schlenk conditions need to be enabled. Thus, the cells need to allow the application of vacuum and inert gas atmospheres. Cell (1) in Figure 11 is a commonly used design for this purpose. Kapton® is used as a highly X-ray transparent window material. Although it is considered chemically inert, it always has to be kept in mind that very high X-ray intensities or radical reactions could induce reactive species from the polyimide Kapton®. Since Teflon is especially a rather ductile material, the window can be effectively pressed onto the cell body, resulting in an effective sealing that allows vacuum pressures down to 10^{-3} mbar. The gas atmosphere can be supplied via HPLC fittings, and reactants can be added under stirring via a septum. Cell type (2) can be used to allow measurements under elevated pressure. To maintain a flat window with increased pressure inside the cell, the windows for the X-ray need to be minimized. Instead of a septum, an additional HPLC fitting is used to add reactive gases or liquids. Cell (1) can be used for transmission and fluorescence measurements, while type (2) can only be applied in fluorescence experiments, which allows a flexible operation in both conventional and XERFD-XANES or XES experiments. Several cell designs exist for electrochemical experiments, one is shown as (3) in Figure 11.[97] It is configured in a three-electrode geometry to provide a flexible exchange of electrode types and application of inert gas. Compared to optical spectro-electrochemical cells, the sample volume in X-ray absorption and emission experiments cannot be that small; therefore, measurements in such cells need to be considered as bulk electrolysis experiments, which could intrinsically suffer from the known problems such as back reactions or incomplete redox product formation. If successful, such measurements can be important since reference spectra for different oxidation states can be generated in cases where no solid reference compounds are available. Moreover, potential reaction intermediates can be prepared and investigated. This is even more vital for a reliable understanding of results from the ultra-fast pump-probe experiment.[98–100] Metal-to-ligand (MLCT) or ligand-to-metal (LMCT) charge transfer states formally contain an oxidized or reduced metal center. Thus, in selected cases, the simulation of XAS/XES spectra of these states can be achieved by generation of the oxidized or reduced species in-situ with the described X-ray spectro-electrochemical cell. Since the results of XAS and XES provide only one spectroscopic dimension, combinations with other spectroscopic techniques can help to avoid misinterpretations if carried out on the same sample spot. An example of such a multi-dimensional measurement cell is type (4).[101] Optical absorption spectra are recorded with the help of fiber technique simultaneously to XAS data. While all other cells described use stirring to achieve sample exchange in the beam, experimental cell (4) is an example of a flow cell.

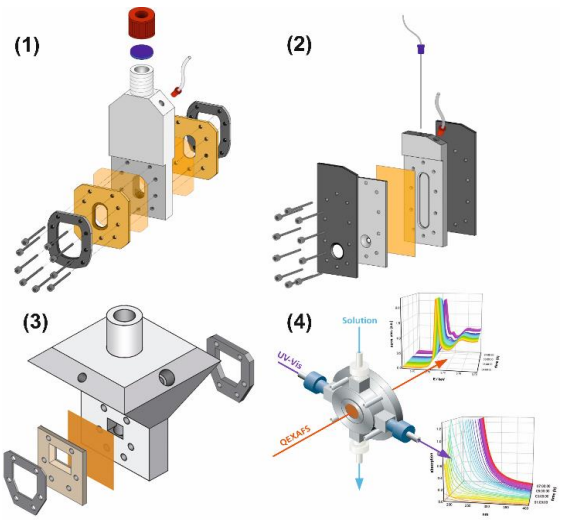

Figure 11. Different cells for hard X-ray measurements of metal-organic reactions in solution. (1) Cell for measurements under Schlenk conditions. (2) Cell for measurements under elevated pressure. (3) Electrochemical cell. (4) Cell for simultaneous measurement of optical absorption data. Reproduced from Ref.[8] with permission from the Royal Society of Chemistry.

Liquid jet. As indicated above, a liquid jet is widely applied, especially in time-resolved pump-probe experiments, to study photochemical reactions.[86,102,103] It consists of three essential elements: a sample delivery system, which includes a sample source, tubing, and HPLC pump, an injector with nozzle and catcher, and a recirculation system. The sample is pumped via an HPLC pump to the injecting system under high pressure through a flat or circular nozzle of several µm to hundreds µm

diameter.[104–106] After the interaction with the X-ray beam, the sample is collected and can be recirculated by another pump for reuse unless radiation damage is observed. Such systems have three main benefits: controllable sample exchange rate, high spectral reproducibility, and relatively short contact between the sample and the setup. However, liquid jet systems in standard X-ray spectroscopy applications consume large volumes of samples (>20 ml). Additionally, due to the small nozzle diameters and their ease of getting clogged, the sample solution must be filtered to remove all solid contaminations. The speed of the liquid jet must be adjusted to the X-ray source repetition rate to allow the jet's recovery before the next pulse excites the sample again.

4. HOW TO DO DATA REDUCTION AND ANALYSIS

4.1 X-ray absorption near edge spectroscopy.

XANES reduction. The raw XAS data must be reduced in several steps to obtain normalized XANES functions that can be further used for analysis, as shown in Figure 12. A) Pre-edge removal: In this step, the contribution of lower-energy edges and Compton-scattering to the absorption coefficient below the absorption edge is removed by approximation of the pre-edge region, for example, by a Victoreen-spline or polynomials. The adjusted function is extrapolated beyond the edge and subtracted from the measured data. B) E_0 determination: E_0 provides an estimation of the threshold energy required for the excitation of the core electron into the continuum. Several approaches exist to determine this value. Since none of them provide a physically exact value, it should be mentioned here that the same determination method should be applied for reference complexes. The simplest method is to use the energy at an edge jump of 0.5 in the normalized spectra. Another way is to use the first maximum of the 1st derivative.[107] C) Normalization: The edge jump is approximated by a value $\Delta\mu_0$ at the energy E_0. The spectrum is normalized by this factor, resulting in a normalized absorption of 1.

XANES analysis. The XANES spectrum is a fingerprint of the molecule – it contains convoluted electronic and structural information about the local environment of the X-ray absorbing metal center. Typical chemical analysis uses these fingerprinting properties by comparing the sample spectrum under investigation with known reference spectra. If a mixture of species for which the XANES spectra are available is present, quantitative analysis can be carried out with linear combination fitting.[111–113]

The XANES spectrum can be represented as a combination of electronic transitions modeled by pseudo-Voigt functions overlapping with an edge step function defined by:[108]

$$I_{step} = H\left[0.5 + {}^{1}/_{\pi}\arctan\left(\frac{E-E_{Fermi}}{{}^{\Gamma_L}/_{2}}\right)\right] \quad (9)$$

where H is the normalization factor accounting for the edge height, Γ_L is the core-hole lifetime at the studied edge, E_{Fermi} is the compound's Fermi level, and E is an independent energy variable. With this definition, the XANES spectrum can be decomposed to pseudo-Voight with individual intensities and widths, and the step function is modeled by an arctan function and provides quantitative insight into the electronic structure.

Finally, this deconvolution allows for a precise comparison with theoretical calculations to account for densities of states (s, p, d),[31,109,110] or molecular orbitals using the TD-DFT approach implemented in ORCA.[111,112] The pre-edge transitions at the K-edge of metal complexes can be described reasonably by TD-DFT calculations as the excited final state is treated in analogy to UV/Vis spectroscopy, but the donor space is limited to the 1s orbital.[113] Since such DFT calculations are gaining considerable importance and a thorough XANES analysis of XAS data on organometallic compounds basically requires such theoretical insights as well, the following paragraphs give a brief overview of how to run a calculation and analyze transitions using the ORCA program package. A typical input file is shown in Figure 13. Generally, an input geometry is needed, for example, from X-ray or geometry-optimized structures. To perform a geometry optimization, at least a functional, a basis set and the keyword "OPT" must be chosen. A typical low-cost selection for a 1st row transition metal (TM) complex could be the BP86 functional[114] together with the def2-TZVP basis set, whereas newer composite methods like PBEh-3c[115], B97-3c[116] or r^{2}scan-3c[117] (including functional, basis set and corrections like D4 dispersion correction) work well, especially for large chemical systems. In general, it is advisable to use a dispersion correction like "D4"[118] and, for heavy elements (fourth row and beyond), the zeroth-order regular approximation for relativistic effects "ZORA"[119]. To check if the final geometry is at least a global minimum on the energy landscape, it is possible to calculate the vibrational frequencies with the "FREQ" keyword and check them for the absence of negative values.

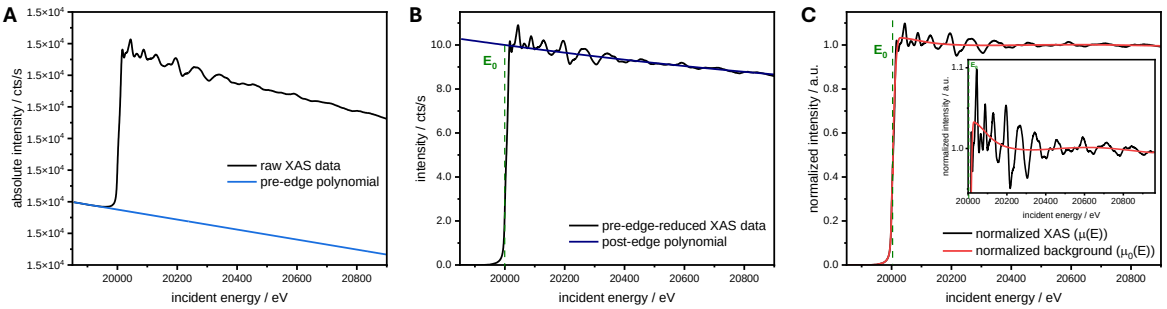

Figure 12. Background removal and normalization procedure for XAS spectra: A) Pre-edge polynomial (blue) subtraction; B) Post-edge polynomial (blue) subtraction and normalization at E0; C) Normalized XAS spectrum with background function (red). Insert: Background function includes very low-frequency oscillations.

The optimized geometry can now serve as the input geometry for calculating the pre-peak transitions. Also, here, a functional and a basis set must be defined. To select this, parameters used for similar systems in the literature can be applied, or different functionals can be tested and selected depending on their fit to an experimental spectrum. In general, hybrid functionals lead to a good result here since adding the Hartree-Fock exchange reduces the self-interaction error and gives higher accuracy for the corresponding core-excited state transitions.[120] For example, the meta-hybrid functional TPSSh[121] with a moderate amount of Hartree-Fock (HF) exchange of 10 % has been frequently reported to calculate the structural and electronic properties of 3d TM complexes.[122–124] In the case of core-level spectroscopy, it is recommended to increase the accuracy by using triple-ζ basis sets like CP(PPP)[125] for the metal center, for all other atoms Ahlrich's all-electron def2-TZVP[126,127] can be applied. Additionally, for organometallic molecules, higher convergency criteria ("TightSCF") are typically used. To speed up the calculation, RI-approximations can be applied (default) where additional basis sets like def2/J[128] are required. For later orbital analysis, the keyword "normalprint" is needed. In the TD-DFT input block, the donor and acceptor orbital range for an "OrbWin[0]" and b "OrbWin[1]" (in the case of open-shell systems) orbital sets can be selected. The metal 1s orbital, which typically has the number 0 as it is the orbital with the lowest energy, is selected as the donor orbital for the transitions, which shall be calculated. The acceptor orbital range can be chosen, including all other virtual orbitals (-1). Furthermore, there is the possibility of including quadrupole transitions which becomes more important for heavy elements, since quadrupole oscillator strength increases due to the cubic dependence on the transition energies. The calculated spectra in the output file can be extracted with a fixed broadening using the mapspc command in ORCA or an energy-correlated broadening, which is preferred to estimate better the lifetime broadening with programs like MOAnalyzer.[129] Using mapspc next to the spectrum also, the transitions are extracted as sticks with a certain transition dipole moment. Note that the total energy of the calculated transitions is usually underestimated due to shortcomings in DFT and must be shifted to fit the experimental spectrum. Also, the total intensity must be adjusted, e.g., to the pre-peak intensity. To investigate the nature of the spectral features, the transitions are analyzed in relation to their orbital contribution. This can be extracted from the Löwdin orbital population analysis in the output file. It gives the percentual contribution of a specific atomic orbital (AO) to a molecular orbital (MO), which can be summed up using, e.g., MOAnalyzer.

```
Exemplary input for geometry optimization

! r2scan-3c OPT D4 FREQ
*xyzfile 0 1 guess_Fe_complex.xyz

Exemplary input for XANES calculations

! TPSSh def2-TZVP def2/J D4 TightSCF normalprint
%basis  newgto Fe "CP(PPP)" end
end
%tddft
    OrbWin[0] = 0,0,-1,-1 # Selecting the alpha set
    #OrbWin[1] = 0,0,-1,-1 beta set - only for open shell
    NRoots 25   # number of calculated transitions
    DoQuad true # includes quadrupole contributions
end
*xyzfile 0 1 optimized_Fe_complex.xyz

Exemplary input for XES calculations

! TPSS def2-TZVP def2/J D4 TightSCF normalprint
%basis  newgto Fe "CP(PPP)" end
end
%xes
    CoreOrb 0 # acceptor orbital(s) for α and β spin
              #(for open shell 0,1)
    OrbOp 0   # acceptor orbital spin  α (=0) and β (=1)
              #(for open shell 0,1)
    #DoSOC true   includes spin-orbit-coupling
    #CoreOrbSOC 0,1   acceptor orbitals defined for SOC
end
*xyzfile 0 1 optimized_Fe_complex.xyz
```

Figure 13. ORCA input example for geometry optimization and XAS, XES calculation for a closed shell iron complex.

3.2 Extended X-ray absorption fine structure.

EXAFS signal extraction. Oscillations above the absorption edge contain information about the geometric structure of studied complexes. To isolate the EXAFS signal in energy space χ(E), first, an atomic background function must be subtracted from the normalized XAS spectrum (Figure 12 C) according to equation 10:

$$\chi(E) = \frac{\mu(E)-\mu_0(E)}{\Delta\mu_0(E_0)} \qquad (10)$$

where $\mu(E)$ is the XAS signal, $\Delta\mu_0$ is the value of the edge jump at the absorption edge position (E_0), and $\mu_0(E)$ is the background function. Simplified, this background describes the absorption fine structure of an atom in its surroundings, where the effects of the neighbor atoms are "switched off". Caused by the scattering of the photoelectron from valence electrons and more unspecific background factors, this atomic background contains low-frequency oscillations that cannot be measured independently or calculated from first principles. However, it can be approximated by a spline. Different splines are tried using different approaches to achieve the optimal removal of low-frequency contributions in the EXAFS oscillations.

Next, function $\chi(E)$ is transformed into k-space $\chi(k)$ via equation 11 (Figure 14 A):

$$k = \sqrt{\frac{2m(E-E_0)}{\hbar^2}} \qquad (11)$$

Here, m is electron rest mass, $\hbar$ is Dirac constant, and E_0 is described above (Figure 12 C). It is obvious, and shown in Figure 14 A, that the k-weighting procedure affects the oscillations in $\chi(k)$ differently in various regions. The aim is to minimize EXAFS extraction artifacts and reduce the EXAFS signal's physical damping at higher k values. To obtain the pseudo-radial distribution of the EXAFS signal, $\chi(k)$ must be Fourier-transformed (Figure 14 B[130]). Next to a better visual effect on the different backscattering shells, Fourier transformation acts as a noise filter. The efficiency of the filter can be controlled by performing a backward Fourier transform operation and comparing the obtained signal $\chi(q)$ (Figure 14 C, red) with the original $\chi(k)$. Fourier-transformed EXAFS can be further analyzed by fitting multiparameter EXAFS equation,[131,132] of which single-electron single-scattering[133] and more advanced multiple-scattering approaches [28,32] are worth mentioning. EXCURVE,[134] Artemis,[64] and LARCH[135] codes can be used for EXAFS analysis, to mention a few.

Alternatively, there are approaches beyond the Fourier transform that use wavelet transform instead.[136]

EXAFS fitting. The main problem with EXAFS analysis with standard EXAFS equation is connected to mathematical restrictions of the multiparameter fitting. Equation 1.4 presents an EXAFS equation that describes all possible scatters from all neighboring atoms in the sample. In practice, fit usually includes atoms at distances no more than 4.5 -5.0 Å. The analysis is restricted to the most intense scatters obtained from theoretical calculations. At least three parameters describe every scatter: R, σ, and N. On average, the final fit contains at least 10 paths, translating to 30 parameters. The maximal number of parameters included in the fitting procedure must be smaller than the number of free points calculated from the Nyquist criterion:

$$N_{max} = \frac{2\Delta k \Delta R}{\pi} \quad (12)$$

Where Δk and ΔR are fit ranges in k- and R-spaces. For typical fit ranges in metalorganic chemistry of 2.0-12.0 Å^{-1} and 1.0-5.0 Å, N_{max} is 25.5. The situation when the number of independent points is smaller than the required number of fitted parameters requires additional parametrization of the fitted variables. Proper parametrization requires good-quality initial structure and *a-priori* knowledge about the sample. General rules of parametrization and setting constraints are shown, for example, in refs.[109,132] The fit result quality is estimated by the R-factor,[109,137] where data and fit are compared in terms of functional overlap. On the other hand, the reduced chi-squared χ^2 is a minimized chi-square fitting metric divided by the number of unused points. This factor cannot be used separately to a single fit but allows quantitative comparison between different fit models. Generally, as long as not only a structure needs to be confirmed but an unknown structure needs to be identified, different models arising from chemical knowledge should be tested against each other using both statistical parameters of R-factor and reduced χ^2.

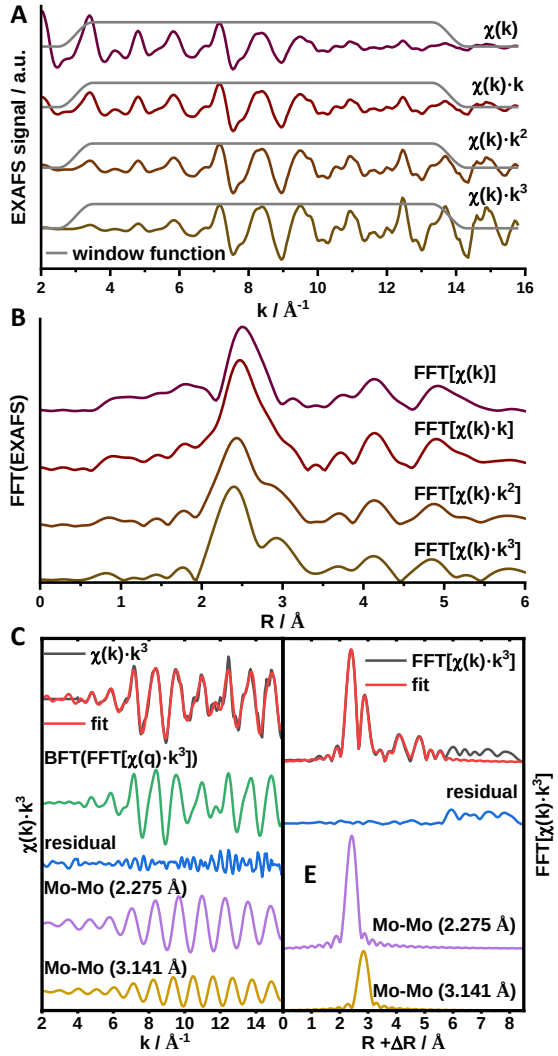

Figure 14. EXAFS analysis steps for Mo foil: A) Background subtraction from normalized XAS spectrum from Fig. 12 C with k-weighting from none to 3. In grey, a window function used in Fourier Transform is shown; B) Fourier-transformed EXAFS for different k-weights; D-E) EXAFS fitting results for k^3 weighting in range of 1-5.5 Å: C) k-space data and fit (black and red) compared to Fourier-filtered EXAFS (green), residual function (blue) and two the most intense Mo-Mo scatters; E) Fitting results in R-space: data and fit (black and red) compared to residuals (blue) and two the most important Mo-Mo scatters.

3.3 X-ray emission spectroscopy.

$K\alpha_{1,2}$ emission lines. The intense $K\alpha_{1,2}$ emission lines originate from 2p→1s transitions. Due to the strong 2p spin-orbit coupling, the lines of 3rd row transition metals are separated by 5-23 eV. Due to strong 3p and 3s electron screening, the effect of the bonding situation and covalency effects on the position and width of Kα emission lines are nearly negligible.[138–140] In a nutshell, the position and FWHM of the line are affected by the effective number of unpaired 3d electrons ($3d_{eff}$) upon creating a 1s electron core hole.[138,141] While this effect is least severe for covalent compounds, it can only be accounted for by theoretical calculations[142], which makes $K\alpha_{1,2}$ emission lines of inferior importance for chemical applications in organometallic chemistry.

$K\beta_{1,3}$ emission lines. For the analysis of the $Kb_{1,3}$ signal, a comparison with reference systems is a common approach. For this purpose, the spectra can be area normalized, and the splitting of the signals can be compared. Although calculations can also be performed using multiplet theory or DFT on RAS-CI/ CAS-CI[143] level with programs like CTM4XAS[144] or ORCA,[111,112] there is no straightforward approach for all kinds of complexes yet.

$K\beta_{2,5}$ signal extraction and analysis. VtC offers a high sensitivity to electronic and structural details of metalorganic complexes. As the VtC signal appears on the high energy side of the Kβ main line, the data can be normalized to the area of the whole Kβ region. To extract the isolated VtC-XES signal, the main line needs to be extrapolated by a Pseudo-Voigt or exponential decay function and subtracted from the spectrum (Figure 15a). [52,145] For analysis of VtC-XES spectra, quantum chemical calculations are necessary. For this purpose, ligand field multiplet theory (LFMT) or DFT can be applied. In the first case, the chemical environment is only represented by empirical parameters; therefore, DFT, which calculates the electronic structure *ab-initio*, is recommended especially for organometallic complexes.[38]

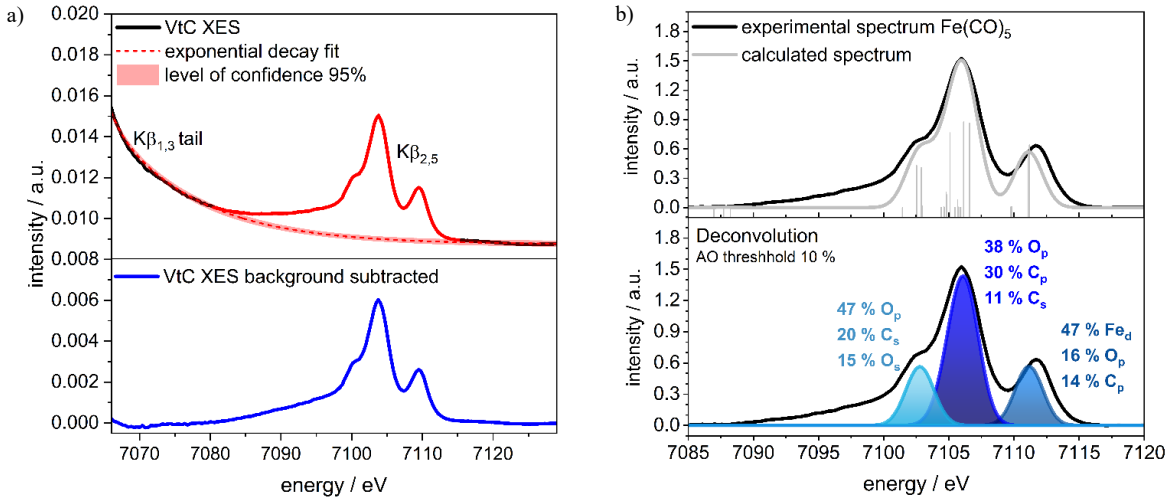

Figure 15. a) Raw experimental VtC spectrum, exponential decay fit of the Kβ mainline background, and resulting corrected VtC spectrum after subtraction of the background. b) Top: Comparison and analysis of an experimental and a calculated VtC spectrum (broadening 2.5 eV). Calculated transitions are shown as sticks. Bottom: Contribution of different atomic orbitals to the acceptor molecular orbitals involved in the respective transitions in the region

DFT calculated transitions approximated as one-electron processes, utilizing the ground-state DFT wavefunction, without any electronic relaxation as a response to the perturbation, typically give a good result for VtC spectra, whereas approximate treatment of electronic relaxation did not improve the agreement.[146] Here also, ORCA is the most established program package used for calculations on organometallic complexes with modules for calculating XES spectra,[111,147,148] but also NWChem[149,150] or codes like FEFF[151] and FDMNES[152], traditionally employed for XAS calculations include modules for XES calculations. For the use of ORCA, most of the keywords can be taken from the TD-DFT calculation part (Figure 13). In the XES input block, the metal 1s orbital (0) can be selected as the acceptor orbital for the transitions, which shall be calculated ("CoreOrb"). For open-shell systems, 0,1 must be chosen for 1s a and 1s b orbital. Then, the spin of the acceptor orbitals must be selected, where 0 corresponds to α and 1 to β spin. In addition, there are further possibilities for calculating the quadrupole overlap or the spin-orbit coupling, which play a minor role for 1st row transition metal complexes. As mentioned before, the calculated spectra in the output file can be extracted and analyzed. Ligand- or atom-projected VtC-XES spectra are created by taking only specific donor orbitals with a significant population of a given atom or fragment into account. Since there can be a considerable number of AO for large molecules, which makes it elaborate, to sum up, programs like MOAnalyzer[129] sum up the contributions to a MO and allow to plot ligand- or atom-projected spectra. This is shown in Figure 15 b) for the example of $Fe(CO)_5$.

5. LIMITATIONS

5.1 Radiation Damage. Over the last few years, the X-ray intensities on synchrotron sources increased, not to mention the very high X-ray intensity at free electron lasers. Any measurements using high-intensity X-rays should be critically evaluated concerning potential radiation damage. Thus, compounds under investigation must be tested before the actual measurements to address their beam stability, which manifests as changes in spectral shapes. This is particularly relevant for organometallic compounds, which can exhibit low chemical stability anyway. It is suspected that the absorbed energy is dissipated by thermal vibration (heating) or covalent bond breaking. Additionally, radicals formed by this primary process can lead to damage in a secondary process.[153]

Figure 16 shows the result of a radiation damage test. For such tests, time resolutions must be as high as possible, even at the expense of data quality. A possible approach is to measure (HERFD-)XANES spectra on the same spot of a sample to observe the time during which the sample does not change, which finally defines the time for real measurements on one sample spot. Radiation damage is manifested by an intensity and structure deviation in the white line, a change in pre-peak intensity, or a shift of the absorption edge to different energies. As a matter of experience, XES spectra are less sensitive to radiation damage. If sample stability in the beam is too short, the X-ray dose can be reduced by shortening the exposure time per point or attenuating the beam intensity. Another attempt is to cool the sample with a cryostat to around 30-100 K to reduce free radical mobility.[154–156] However, if the sample is cooled to very low temperatures, X-ray-induced excited-spin-state trapping (HAXIESST) can occur. This is the X-ray pendant to the LIESST, describing an X-ray-induced spin crossover into an excited spin state, which is stabilized by low temperatures typically lower than 80 K.[157,158]

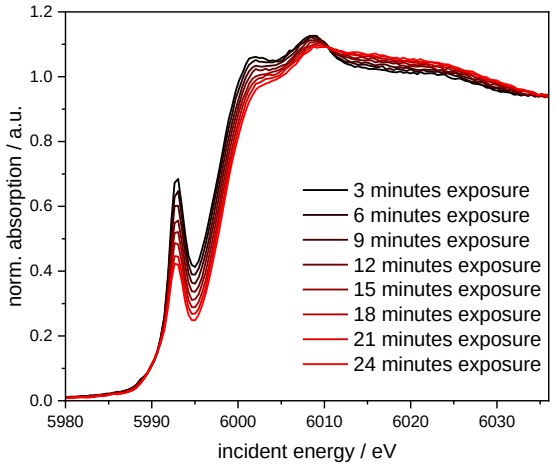

Figure 16. Comparison of XANES spectra of a solid chromium complex sample pallet taken on the same spot within 180 sec per spectrum. The measurements were done at the P65 beamline, Petra III (DESY).

4.2 Self-absorption effect. As indicated in equation 8, μ(E) measured in fluorescence is only approximated by the ratio of the signals on the fluorescence and incident ion chambers. This ratio is correct only in the limited case of very thin or very dilute samples. In all other cases, the oscillating character of μ(E) also causes energy-dependent changes in the penetration depth. The X-ray penetration depth is reduced for maxima of μ(E), while for minima, it is increased, and accordingly, the oscillations are damped. Additionally, to be able to measure fluorescence radiation, the fluorescent X-rays have to travel from the emitting atom through the sample to the detector. All other atoms in this way attenuate X-rays; therefore, the fluorescence intensity, and thus oscillations of μ(E), is damped, as shown in Figure 17.[159,160] The self-absorption effect is well described by mathematical terms [161–164] and can be efficiently removed from experimental data if the sample composition, incident beam, and detection angles are known.

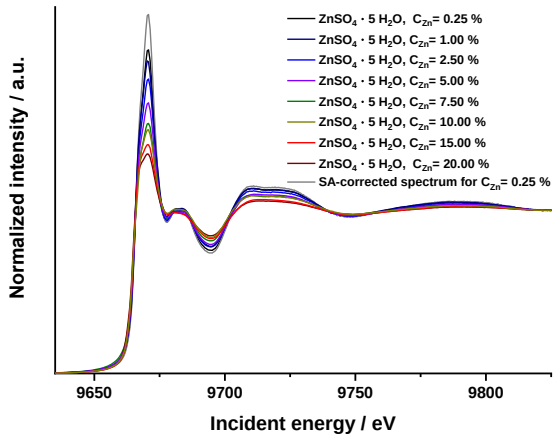

Figure 17. XANES spectra of $ZnSO_4 \cdot 5H_2O$ in cellulose measured in fluorescence mode for a 1 mm sample thickness with varied absorber concentration from 0.25 % to 20 % of dry sample mass. The results are compared to the SA-free spectrum (black). The measurements were done at the P65 beamline, Petra III (DESY).

6. APPLICATIONS

6.1 XANES studies

XANES measurements are typically employed to determine oxidation states. Since the absorption edge position depends not only on the oxidation state but also on the coordinating atoms, it is ideally applied as an oxidation state measure for identical coordinating atoms or, in a relative way, towards well-defined references.

Valence tautomeric transition of bis(o-dioxolene) cobalt complex in solid state and solution[165]

In the following example, the valence tautomer transition in a bis(dioxolene)cobalt complex functionalized with a 2,2,6,6-tetramethylpiperidin-1-oxyl moiety in the iminopyridine ligand is investigated. Valence tautomerism (VT, Figure 18a), a reversible intramolecular electron transfer, is particularly interesting for developing single-molecule switches that can be activated by external stimuli such as temperature, pressure, or light. The study highlights that conventional methods like single-crystal X-ray diffraction often cannot be applied when the crystal structure is damaged during the transition or when the sample is in solution. To overcome these challenges, two complementary spectroscopic techniques were employed: Fourier Transform Infrared Spectroscopy (FTIR), which is sensitive to ligand-related processes, and Co K-edge X-ray Absorption Spectroscopy (XAS), which provides structural and electronic information around the Co center.

Redox-isomer interconversion induced by temperature changes was analyzed in both solid state and toluene solution. The XANES analysis demonstrated a notable shift in the absorption edge towards higher energies, along with changes in pre-edge intensity and overall spectral shape upon cooling (Figure 18b). These changes were consistent across solid and solution samples and can be attributed to the transition from a Co^{II} to a Co^{III} valence state. Principal Component Analysis (PCA) of the series of spectra in Figure 1b confirms that the entire series can be adequately described by only two independent components that vary in proportion with temperature (Figure 17c). Additionally, a hysteresis of around 50 K was observed between the cooling and heating cycles in the solid sample, consistent with previous magnetic susceptibility measurements.[166] This suggests that the cause of the hysteresis is likely due to the phase transition in the solid state rather than the tautomeric transition itself.

Further investigations using EXAFS, DFT calculations, and FTIR could validate the observations and lead to a more detailed examination of the electronic and geometric structure of the different species.

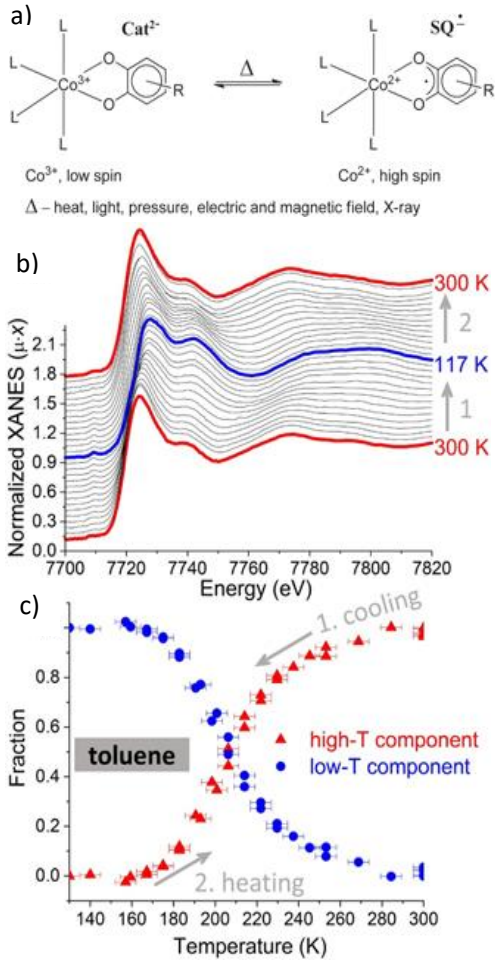

Figure 18. a) General scheme of VT equilibrium in Co-complexes. b) Co K-edge XANES measured upon cooling and subsequent heating of the Co 1 toluene solution. Red and blue curves indicate spectra acquired at the highest and lowest temperatures correspondingly. c) Concentrations of the two principal components (referred to as the low-temperature and high-temperature phases) derived from PCA. Reproduced from Ref. with permission from the Royal Society of Chemistry.

6.2 EXAFS - characterization and mechanistic studies

While XANES spectroscopy is typically used to investigate the electronic structure and oxidation states of transition metal complexes, EXAFS studies are mainly used to determine the local geometric structure. For pure metal complexes, single crystal X-ray diffraction is the gold standard for structure determination, and EXAFS can only play a supportive role. We will thus focus here on examples where EXAFS is mandatory to answer specific questions or where it plays a crucial role in a methodic context.

Identification of interactions of Molybdenum macrocyclization catalysts with confined supports[167]

Confined spaces allow the mimicking of enzyme catalyst characteristics by creating active pockets or channels with defined geometric parameters into which a catalytically active metal complex can be immobilized.[168] The characterization of metal complexes after immobilizing, for example, on mesoporous silica support is challenging. Here, EXAFS's element specificity and short-range order sensitivity are a tremendous advantage, as the molecular nature of immobilized catalysts can be probed. Additionally, in ideal cases, EXAFS also allows the identification of complex-support interactions, which can be crucial for mechanistic investigations. For example, Figure 19 shows the Fourier-transformed EXAFS functions of a molybdenum imido-alkylidene-NHC complex immobilized on an SBA-15 support with a pore diameter of 6.2 nm compared to its pure form.[169] The experiment was conducted at P65 beamline[170] in DESY using transmission mode. For the solid samples, to avoid radiation damage, each spectrum was collected from a fresh sample. The investigation of such samples is not straightforward due to the low metal concentrations of a few µmol per gram support. In the EXAFS analysis the structural integrity of the complex could be confirmed, but with a more compact shape as deduced from contracted bond distances. In the fit procedure, a Mo-Si pair could be adjusted and interpreted as interactions of the complex with the support wall. The silicon backscatterer replaced the Mo-F contributions in the pure complex as the nona-fluoro tert-butoxide groups are exchanged by oxo-mediated support interactions. The Mo-Si contribution was also partially responsible for the modified XANES shape.

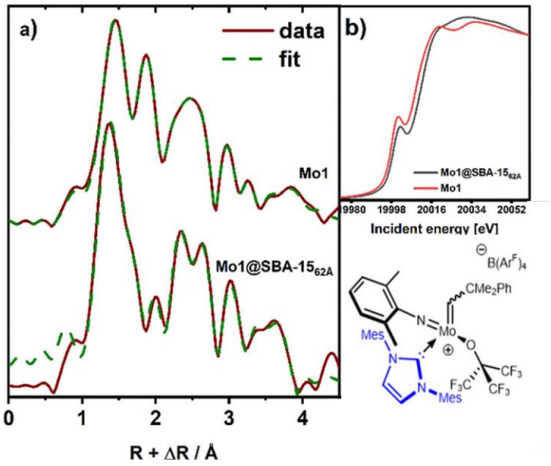

Figure 19. (a) Fourier-transformed EXAFS signal (red) and corresponding fitting results (green dashed) of the molybdenum imido-alkylidene-NHC complex and immobilized on a SBA-15 support. (b) XANES spectra reveal differences in the white line and edge position between the samples. (Reprinted with permission from Ref.[169] Copyright 2021 American Chemical Society.)

Investigation of structures formed from precursors in solution[171]

Although this example is strictly speaking from the field of coordination chemistry rather than metalorganic chemistry, it nicely demonstrated the potential of EXAFS spectroscopy to investigate and identify structures formed in solution from a particular precursor. $FeCl_3 \cdot 6H_2O$ is used as a catalyst in the homogeneous Michael reaction of α,β-unsaturated ketones with 2-oxocyclopentanecarboxylate, where the latter is both reactant and solvent. In contrast to $Fe(ClO_4)_3 \cdot 9H_2O$, $FeCl_3 \cdot 6H_2O$ shows

reduced activity. XAS could nicely give the reason for this observation. Figure 20 shows the XANES spectra of $FeCl_3 \cdot 6H_2O$ in 2-oxocyclopentanecarboxylate compared to solid $FeCl_3 \cdot 6H_2O$. It is obvious that the prepeak in solution is significantly increased in comparison to $FeCl_3 \cdot 6H_2O$, which is characterized by an octahedral coordination geometry. Since it is well known that iron chloride can form tetrahedral tetrachloro-ferrates, the solution structure is compared to $[FeCl_4]^-$ as well. The latter shows a more intense prepeak than $FeCl_3 \cdot 6H_2O$ in solution. Also, in Figure 20, the Fourier-transformed EXAFS functions of $FeCl_3 \cdot 6H_2O$ in solution are compared to the spectrum of $Fe(ClO_4)_3 \cdot 9H_2O$ in 2-oxocyclopentane-carboxylate, which is formed by 6-fold oxygen coordination composed of two bis-diketonate ligands and two water molecules. It is obvious that the spectrum of $FeCl_3 \cdot 6H_2O$ in solution is somehow the average of $[FeCl_4]^-$ and the FeO_6 spectrum formed by $Fe(ClO_4)_3 \cdot 9H_2O$ in solution. The obtained coordination numbers in the fit were 3.4 Fe-O pairs and 2.2 Fe-Cl single scatters, which led to the conclusion of a $[FeO_6][FeCl_4]$ contact ion pair, in which half of the iron centers are removed from the catalytically active iron pool by poisoning with chloride.

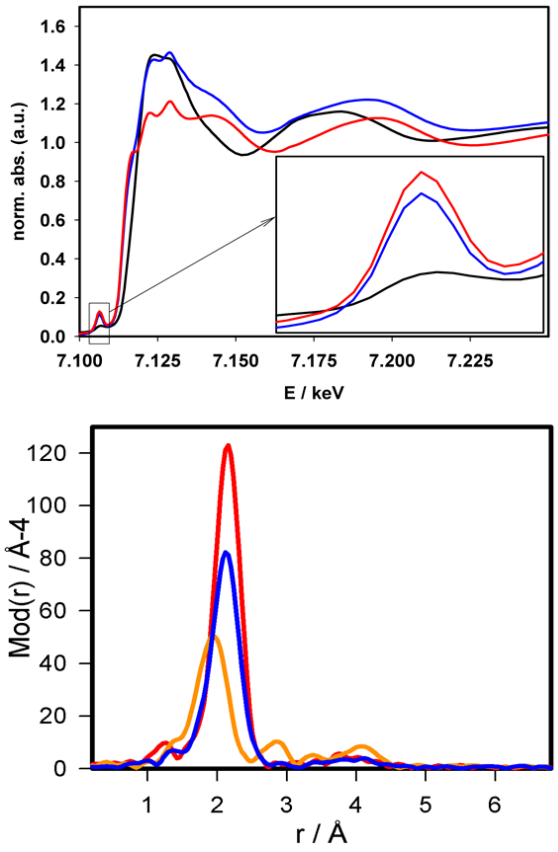

Figure 20. (top) XANES spectra of solid $FeCl_3 \cdot 6H_2O$ (black), $FeCl_3 \cdot 6H_2O$ in 2-oxocyclopentanecarboxylate (blue), and solid $[FeCl_4]^-$ (red). (b) Fourier transformed EXAFS functions of a FeO_6 coordination composed of two oxocyclopentanecarboxylate and two H_2O ligands (orange), $[FeCl_4]^-$ (red), and of $FeCl_3 \cdot 6H_2O$ in 2-oxocyclopentanecarboxylate (blue).

In-operando study of stereoselective chromium-catalyzed semi-hydrogenation of alkynes[172]

As the next example, the unique properties of EXAFS when it comes to identifying in situ-generated active species for catalytic transformations from coordination or metalorganic compounds are presented. The selective hydrogenation of alkynes is an important synthetic reaction as it can produce alkene precursors for numerous industrial reactions. While chromium catalysts are recognized to be effective in oxidation[173] and polymerization reactions[174], very little is known about chromium-catalyzed hydrogenations. Analogously to chemoselective hydrogenation of alkynes by $Fe(acac)_2$ with diisobutylaluminium hydride (DIBAL−H)[175], a commercially available $Cr(acac)_3$ can be used as a precursor for the formation of the catalytically active species by activation with diisobutylaluminium hydride (DIBAL−H). The Fourier-transformed EXAFS functions of the activation of $Cr(acac)_3$ with increasing equivalents of DIBAL-H are shown in Figure 21. The trend shows a significant reduction of the Cr-O contributions below 2 Å, indicating the expected reduction process. Surprisingly, no Cr-Cr contribution appeared, which would be expected if the reduction would cause Cr^0 particles to be formed. Formally, three equivalents are required for the complete reduction of Cr0, indicating that ligand reduction is also involved. Since the solutions were measured immediately after preparation, they present an early stage of the reaction, and by electron microscopy, the formation of Cr nanoparticles could be shown at a later stage.

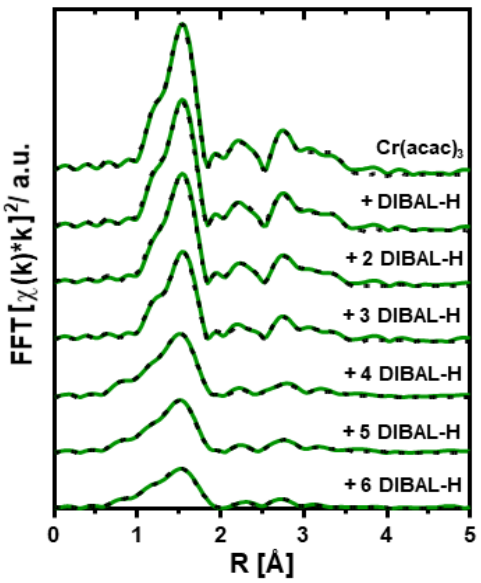

Figure 21. Experimental (solid green) and theoretical (dashed black) Fourier transformed EXAFS spectra of the activation of $Cr(acac)_3$ precursor by 1-6 equivalents DIBAL-H.

5.3 HERFD-XANES and VtC-XES studies

In contrast to conventional XANES and EXAFS, HERFD-XANES, and VtC-XES are more sensitive to the electronic states of organometallic compounds or specific ligands, as will be explained with selected examples below.

HERFD-XANES probes of electronic structures of iron(II/III) carbene complexes[176]

Due to their long charge transfer lifetimes, iron carbene complexes are interesting candidates as photocatalysts or photosensitizers based on non-noble metals.[177,178] To further improve their properties for these purposes, it is essential to know what influence the ligands have on the electronic structure of the metal center. To determine this influence, HERFD-XANES measurements of three different carbene complexes (Figure 22) were performed together with multiconfigurational restrict active space (RAS) calculations, which provide electronic-structure information about the occupation of valence orbitals, the orbital covalency, oxidation state, and the site symmetry. Three pseudo-octahedral low spin iron complexes $[Fe^{II}(bpy)(btz)_2]^{2+}$, $[Fe^{III}(btz)_3]^{3+}$, and $[Fe^{III}(phtmeimb)_2]$ (bpy = 2,2′-bipyridine, btz = 3,3′-dimethyl-1,1′-bis(p-tolyl)-4,4′-bis(1,2,3-triazol-5-ylidene and phtmeimb = [phenyl(tris(3-methylimidazol-2-ylidene))borate]$^-$) have been investigated regarding the position and the intensity of the pre-peaks. As expected for the spectra of high energy resolution, two pre-peaks were observed for the Fe^{III} species, which can be assigned to transitions into the unoccupied t_{2g} and e_g orbitals of a low-spin d^5 configuration. For the Fe^{II} species, only one pre-peak exists due to the d^6 low-spin state, which allows transitions only into the e_g orbitals. The e_g signal of the Fe^{II} complex $[Fe^{II}(bpy)(btz)_2]^{2+}$ (7113.6 eV) is located at lower energies than in the Fe^{III} species $[Fe^{III}(btz)_3]^{3+}$ and $[Fe^{III}(phtmeimb)_2]$ (7114.3 eV): This is due to the contraction of the 3d shell in the core-excited states.

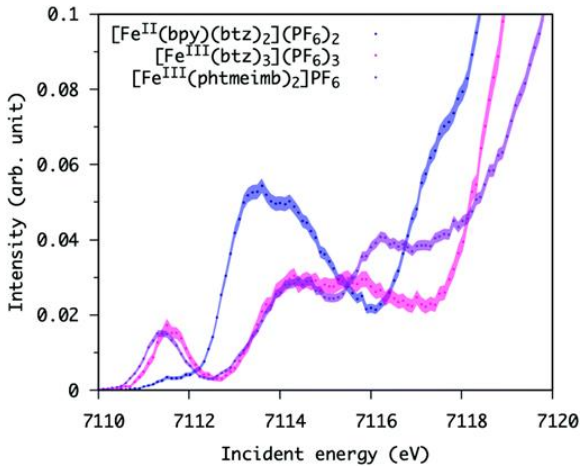

Figure 22. Experimental HERFD-XANES pre-edge features of $[Fe^{II}(bpy)(btz)_2]^{2+}$ (blue), $[Fe^{III}(btz)_3]^{3+}$ (pink) and $[Fe^{III}(phtmeimb)_2]$ (purple). The transparent filled curves represent the 2σ confidence environment of the measurement, including statistical error and normalization error. Reproduced from Ref.[176] with permission from the Royal Society of Chemistry.

Moreover, the energy difference between the e_g and t_{2g} signals in Fe^{III} complexes is a direct probe of the ligand-field strength in the systems. As can be assumed, this was largest for $[Fe^{III}(phtmeimb)_2]^{1+}$ since the strong σ donating ligand is known to lead to a large ligand field splitting. In addition, the pre-peak intensity can be analyzed in terms of symmetry. The heteroleptic complex $[Fe^{II}(bpy)(btz)_2]^{2+}$ has a less symmetric environment than the homoleptic tridentate Fe^{III} complexes, which is reflected in the calculated Fe 4p contribution to the e_g orbitals of ~2% and less than 0.2%, for $[Fe^{III}(btz)_3]^{3+}$ and $[Fe^{III}(phtmeimb)_2]$, respectively. This leads to a much higher intensity of the e_g-based pre-peak for the Fe^{II} complex. In summary, HERFD-XANES, together with theoretical calculations, provide a tool to predict and compare the properties of different complexes. This can strongly support the search for new systems with improved characteristics.

Electronic Structure of the Hieber Anion $[Fe(CO)_3(NO)]^-$ [179]

In coordination chemistry, the NO-Ligand is well-known for its non-innocent character.[180] According to textbook knowledge, either a linear (NO^+) or a bent (NO^-) binding mode is possible, influencing the electronic structure at the metal center differently. Whereas the first case would lead to a formal reduction of the metal, the second case would increase the formal oxidation state. As an organometallic complex, the Hieber anion shows catalytic activities in different organic reactions, while the isoelectronic $Fe(CO)_4^{2-}$ shows only poor activity. Formally, both have the same oxidation state of -II. Still, due to differences in catalytic behavior and unusual N-O bond length and IR signals, there was a debate about the "physical" electronic structure in terms of oxidation state.[181] Hard X-ray spectroscopy reveals many spectral similarities of the Hieber anion $[Fe(CO)_3(NO)]^-$ and $Fe(CO)_4^{2-}$ in contrast to the Fe(0) reference $Fe(CO)_5$.[179]. Whereas the K-edges (Figure 22a) of the first two compounds are nearly identical, the latter shows a shift of 1.6 eV, indicating a change in oxidation state. The VtC-XES spectra show an additional NO signal for the Hieber anion in the region of the ligand-based cross-over peaks around 7100 eV, demonstrating the ligand sensitivity of this method (Figure 22b). However, in the region of the d-orbital-based transitions at 7112 eV, there is again an overlap of the two formal Fe(-II) species, and the formally Fe(0) complex $Fe(CO)_5$ shows a significantly lower intensity. Although this indicates a similar electronic structure of the Hieber anion and $Fe(CO)_4^{2-}$, the geometrical differences must also be considered. While the two species mentioned above have C_{3v} symmetry, $Fe(CO)_5$ has D_{3h} symmetry, which could cause spectral differences due to differences in the selection rules.

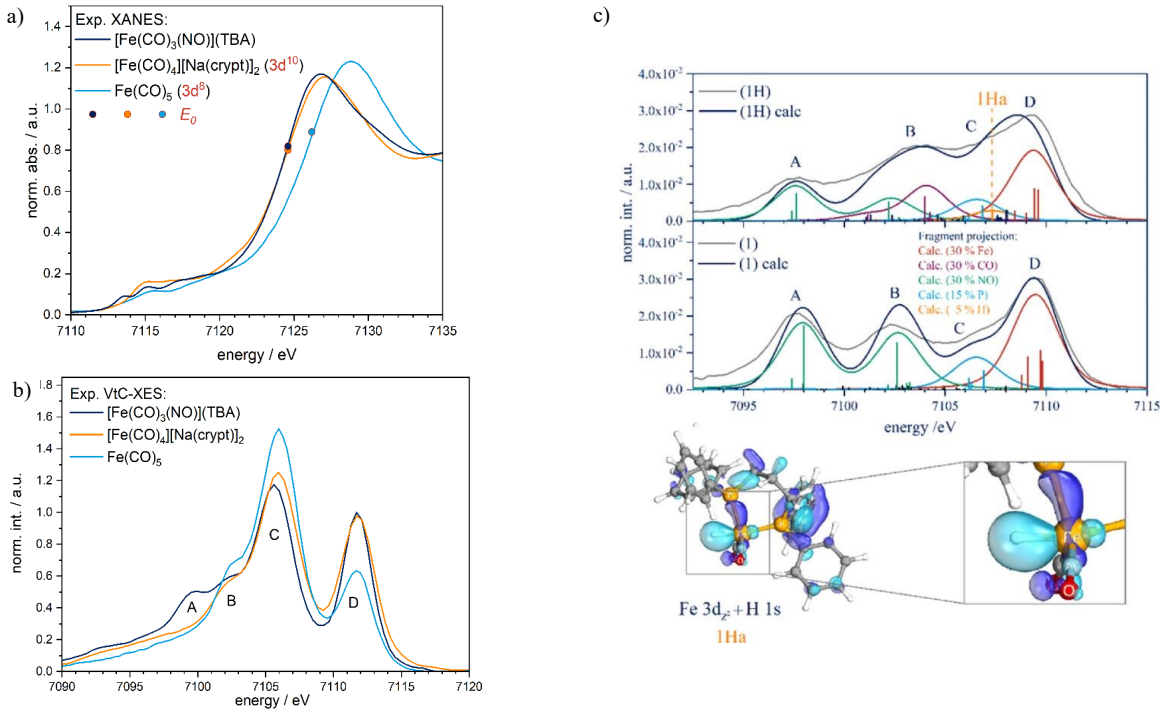

Figure 23. a) Experimental XANES and b) VtC spectra of the Hieber anion, $Fe(CO)_4^{2-}$ and $Fe(CO)_5$. ((Reprinted with permission from Ref. XX. Copyright 2020 American Chemical Society.). c) Comparison of experimental (gray) and theoretical (blue) Fe K-edge VtC-XES spectra for 1 (bottom) and 1H (top), including contributions of individual fragment projections. (Reprinted with permission from Ref.[179] Copyright 2017 American Chemical Society.)

Detection and Characterization of Hydride Ligands in Iron Complexes by High-Resolution Hard X-ray Spectroscopy and Implications for Catalytic Processes[49]

To understand the working principle of metal complexes catalyzing, e.g., molecular hydrogen formation or hydrogen transfer, experimental methods are necessary to access geometric and electronic changes in the corresponding in situ environment. However, most spectroscopic or scattering methods like Mößbauer, NMR, EPR, neutron diffraction, or X-ray scattering, have limitations with respect to the sample environment or the sample itself, such as the need for paired or unpaired electrons, selective deuteration, or the small scattering amplitude of hydrogen.[182,183] X-ray absorption and emission spectroscopy were recently shown to have considerable potential to overcome these limitations since high-energetic X-rays used for transition metal K-edge spectroscopy are not absorbed by light elements. In this study, a combination of high-energy resolution fluorescence-detected X-ray absorption near-edge structure (HERFD-XANES) and valence-to-core X-ray emission spectroscopy (VtC-XES) is used together with (TD-)DFT calculations to investigate two hydride catalysts [Fe(CO)(dppp)H(NO)] **1H** (dppp=1,3-bis(diphenyl-phosphine)propane) and $[Fe(CO)H(NO)(PPh_3)_2]$ **2H** in comparison with anhydride analogs $[Fe(dppe)(NO)_2]$ **1** (dppe = 1,3-bis(diphenylphosphine)ethane) and $[Fe(NO)_2(PPh_3)_2]$ **2**.

The hydride effects on the LUMOS are investigated by HERFD-XANES, where two pre-peaks at around 7114 eV and 7116 eV are observed in all complexes. For the hydride complexes, the low-energy signal shows a blue shift and an intensity decrease. In contrast, the high-energy signal shows a red shift and an intensity increase in contrast to the non-hydride complexes. With the help of TD-DFT calculations, the changes in the first pre-peak for the hydride complexes could be attributed to a lower number of possible transitions in total but an additional high energy signal with a hydride content of 5%. However, the changes in the second pre-peak could be attributed to the CO ligands also introduced for the hydride complexes.

The VtC spectra reflecting the HOMOS show an even more apparent fingerprint concerning the hydride ligands (see Figure 23 c). For **1** and **1H**, DFT calculations show an assignment of the NO 2s-orbitals to signal A as a typical fingerprint, a superposition of NO 2p- and CO 2p-orbitals for signal B[123] and Fe 3d-based donor orbitals typical for signal D[148] where the intensity ratios correspond to the number of ligands in the respective complexes. In the case of the anhydride complex, signal C is solely attributed to the P 3p- and Fe 3d-orbital interaction. However, for the hydride complex, this signal is superimposed by transition Ha (see Figure 23), which leads to a drastic intensity increase in this band. Signal Ha is characterized by transitions from the bonding interaction between the Fe $3d_z^2$- and the H 1s-orbital. The same assignment can be found for complexes **2** and **2H,** whereas here, two different hydride-based transitions (Ha and Hb) in the region of

signals B and C lead to an intensity increase and shift. To verify these findings, simulations for different Fe-H bond lengths were applied in a scan procedure. Elongation of the Fe-H bond transforms the hydride-influenced features to similar energies and intensities of the non-hydride references. Thus, it could be shown that both HERFD-XANES and VtC-XES exhibit distinctive hydride signals, which could be characterized with the help of (TD-)DFT calculations. This makes the methods highly suitable for detecting hydrides in coordination compounds and following changes in catalytic reaction progress.

Valence-selective HERFD-XANES[184,185]

X-ray absorption spectroscopy (XAS) can provide detailed insight into transition metal complexes' electronic and geometric structures. HERFD-XANES detected by the intense $K\alpha_{1,2}$ or $K\beta_{1,3}$ lines can be used to eliminate lifetime broadening effects for a better resolution. However, the spectrum always shows the influence of the entire coordination environment. XAS spectra can be measured by monitoring the fluorescence of a specific valence-to-core X-ray emission signal to achieve ligand-selective EXAFS spectra. For this purpose, a full resonant X-ray emission (RXES) plane should be detected. Afterward, the emission spectrometer can be set to the energy of a ligand-specific VtC-XES feature, and the incident energy can be varied to obtain the XAS spectrum, as shown in Figure 24. DeBeer and Co-workers investigated the four Mn model compounds $[Mn(CN)_4N]^{2-}$, $[Mn(CN)_5N]^{3-}$, $[Mn(taml)O]^{1-}$, and MnO_4^{2-}. Significant changes in the absolute pre-edge intensities are seen if detected by different emission features. While the HERFD-XANES detection at the Kβ" feature leads to a slight decrease, the detection at a specific $K\beta_{2,5}$ feature substantially increases signal intensity. One could assume that this effect might result from the line sharpening due to decreased lifetime broadening; however, the peak area also changes, which would not be the case for line sharpening effects. Thus, the differences might be traced to the different 2s and 2p orbital contributions. Since the $K\beta_{2,5}$ is dominated by 2p, this mediated the 3d/4p mixing responsible for high pre-peak intensities. *Vice versa*, the absence of 2p contribution for Kβ" leads to a decrease. The exact physical mechanisms underlying these spectra are still unclear, and further investigation is needed.

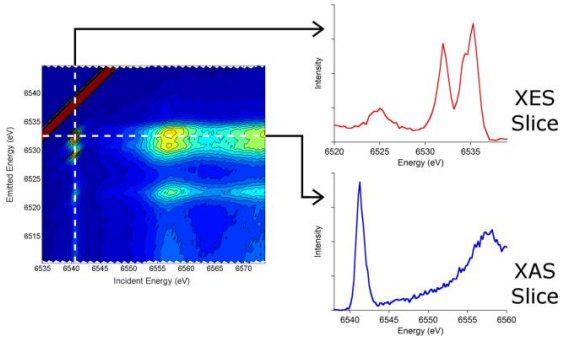

Figure 24. An RXES plane for $[Mn(CN)_4N]^{2-}$ is shown along with "slices" through the plane. A horizontal cut through the plane at constant emitted energy yields a VtC-detected XAS (i.e., HERFD) spectrum, while a vertical slice at constant incident energy gives a resonant X-ray emission spectrum. Reprinted with permission from Ref.[185] Copyright 2021 American Chemical Society.

6. CONCLUSION AND OUTLOOK

With this tutorial, the theoretical and experimental basics of X-ray absorption and emission spectroscopy were introduced to provide a reliable foundation for experienced and new users in the field and students interested in the topic. With the provided background, identification of the best suited hard X-ray methods for particular questions in organometallic chemistry can be identified, and the experiment can be planned and conducted. Finally, introducing the first steps in the different data analyses allows for a smooth use of the available programs.

The presented examples demonstrated the versatility of XAS and XES in organometallic chemistry research. Important areas that can be addressed are the local geometric structure of complexes, oxidation states, and their dynamic changes, and details of the electronic structure in different physical states, such as solids, liquids, and solutions.

In conclusion about the methods, a few statements should provide a final guide through the selection of methods.

1) In cases where crystals suitable for single-crystal measurements are available, EXAFS and XANES are considered auxiliary methods for confirming structures and oxidation states.

2) If the translational symmetry of a crystal is broken, for example, in amorphous samples, by dissolving complexes in liquids or immobilization in supports, EXAFS is the only method providing structural information in an element-specific manner, i.e., any interfering structural effects can be eliminated. If the analysis is based on a defined structure, the structural integrity or newly formed structures can be identified.

3) For conventional XAS, the time resolution is sufficient to follow chemical reactions catalyzed by organometallic or coordination compounds. Thus, operando studies are usually possible.

4) There are limitations of XAS: Neighbors in the periodic table as coordinating atoms and very light back scatterers cannot be distinguished by EXAFS, and many factors influence the absorption edge energy and, thus, are not always a reliable measure for the oxidation state. In such cases, emission-based techniques should be considered, such as VtC-XES to increase the sensitivity to different ligands and CtC-XES to determine the d-electron spin density.

5) In cases where the electronic structure of the complex is at the core of interest, high-resolution emission-based methods VtC-XES and HERFD-XANES should be applied. While a higher chemical specificity characterizes VtC-XES, HERFD-XANES allows a much better time resolution. Ideally, they are combined to address LUMO and HOMO states.

Next to this advice, the tutorial will not be finished without mentioning that all methods can be applied to photoinduced reactions on a very short time scale at free electron lasers.[186] Although this topic is beyond the scope of this tutorial, it should be emphasized here that this opens up the field of light-induced sustainable reactions using metalorganic complexes to X-ray spectroscopy.

AUTHOR INFORMATION

Corresponding Author

Prof. Dr. Matthias Bauer - Faculty of Science, Chemistry Department and Centre for Sustainable Systems Design, Paderborn University, 33098 Paderborn, Germany. ORCID: 0000-0002-9294-6076 **E-mail:** matthias.bauer@upb.de

Authors

Lorena Fritsch - Department of Chemistry, University of Paderborn, Warburger Straße 100, Paderborn D-33098, Germany. ORCID: 0000-0002-3990-6278

Michal Nowakowski - Department of Chemistry, University of Paderborn, Warburger Straße 100, Paderborn D-33098, Germany. ORCID: 0000-0002-3734-7011

BIOGRAPHY

Matthias Bauer is a Professor of Inorganic Chemistry and holds the chair for Inorganic chemistry of sustainable processes with a focus on X-ray spectroscopy at the University of Paderborn (Germany). He studied chemistry in Stuttgart, where he also received his PhD in Physical Chemistry. After a Postdoc in Stuttgart at the European Synchrotron Radiation Facility (Grenoble, France) and the Karlsruhe Institute for Technology, he was an Assistant Professor at the Technical University of Kaiserslautern (Germany). His work focuses on the development and investigation of systems for sustainable chemistry, such as photochemistry and hydrogen production, using synchrotron and free electron lasers as core methods.

Michal Nowakowski is a postdoctoral researcher in Matthias Bauer's Group at Paderborn University. He studied biophysics and physics at Jagiellonian University in Krakow (Poland). He received his PhD in 2019 under Prof. Wojciech M. Kwiatek at the Institute of Nuclear Physics in Krakow, working on X-ray spectroscopy. The same year, he started his postdoctoral position in Paderborn. His current work focuses on the advancements in X-ray absorption and emission spectroscopies for chemical applications and steady and ultrafast X-ray spectroscopy investigations in sustainable catalysis using synchrotron and XFEL sources.

Lorena Fritsch is currently a PhD candidate under the supervision of Matthias Bauer at Paderborn University, where she focuses on spectroscopic studies of molecular transition metal systems for sustainable chemistry. She completed her master's degrees in chemistry and chemistry education in 2021, working on the examination of the electronic structure of iron complexes via high-resolution X-ray spectroscopy. Lorena's work was supported by a Kekulé Scholarship from the Fonds der Chemischen Industrie.

ACKNOWLEDGMENT

M.B. kindly acknowledges financial support from the German BMBF in the frame of project 05K24PPA. M.B. and M.N. thank the Deutsche Forschungsgemeinschaft in frame of the CRC 1333/2 (Project C10). L.F. thanks the Fonds der Chemischen Industrie for a Kekulé Scholarship.

REFERENCES

(1) Bare, S. R.; Kelly, S. D.; Ravel, B.; Greenlay, N.; King, L.; Mickelson, G. E. Characterizing Industrial Catalysts Using in Situ XAFS under Identical Conditions. *Phys Chem Chem Phys* **2010**, *12* (27), 7702–7711. https://doi.org/10.1039/B926621F.

(2) Bertagnolli, H.; Ertel, T. S. X-Ray Absorption Spectroscopy of Amorphous Solids, Liquids, and Catalytic and Biochemical Systems - Capabilities and Limitations. *Angew Chem, Int Ed* **1994**, *33* (1), 45–66. https://doi.org/10.1002/anie.199400451.

(3) Hawthrone, Frank. C. *Spectroscopic Methods in Mineralogy and Geology*; Mineralogical Society of America: Washington, D.C., 1988; Vol. 18.

(4) Iwasawa, Y. *X-Ray Absorption Fine Structure for Catalysts and Surfaces*; World Scientific, 1996; Vol. 2. https://doi.org/10.1142/2807.

(5) Lengeler, B. Applications of X-Ray Absorption Spectroscopy in Materials Science: Status and New Trends. *Z Phys B: Condens Matter Quanta* **1985**, *61* (4), 421–427. https://doi.org/10.1007/BF01303547.

(6) Teo, B. K. *EXAFS: Basic Principles and Data Analysis*; Springer Berlin Heidelberg: Berlin, Heidelberg, 1986. https://doi.org/10.1007/978-3-642-50031-2.

(7) Bunker, G. *Introduction to XAFS*; Cambridge University Press, 2011. https://doi.org/10.1017/CBO9780511809194.

(8) Berger, M. J.; Hubbell, J. H.; Seltzer, S. M.; Chang, J.; Coursey, J. S.; Sukumar, R.; Zucker, D. S.; Olsen, K. *XCOM: Photon Cross Sections Database*. https://physics.nist.gov/PhysRefData/Xcom/html/xcom1.html (accessed 2024-03-11).

(9) Gauthier, C.; Solé, V. A.; Signorato, R.; Goulon, J.; Moguiline, E. The ESRF Beamline ID26: X-Ray Absorption on Ultra Dilute Sample. *J Synchrotron Radiat* **1999**, *6* (Pt 3), 164–166. https://doi.org/10.1107/S0909049598016835.

(10) Proux, O.; Biquard, X.; Lahera, E.; Menthonnex, J. J.; Prat, A.; Ulrich, O.; Soldo, Y.; Trvisson, P.; Kapoujyan, G.; Perroux, G.; Taunier, P.; Grand, D.; Jeantet, P.; Deleglise, M.; Roux, J. P.; Hazemann, J. L. FAME A New Beamline for X-Ray Absorption Investigations of Very Diluted Systems of Environmental, Material and Biological Interests. *Phys Scr* **2005**, 970. https://doi.org/10.1238/Physica.Topical.115a00970.

(11) Caliebe, W. A.; Murzin, V.; Kalinko, A.; Görlitz, M. High-Flux XAFS-Beamline P64 at PETRA III. *AIP Conf Proc* **2019**, *2054*, 60031. https://doi.org/10.1063/1.5084662.

(12) Welter, E.; Chernikov, R.; Herrmann, M.; Nemausat, R. A Beamline for Bulk Sample X-Ray Absorption Spectroscopy at the High Brilliance Storage Ring PETRA III. *AIP Conf Proc* **2019**, 040002. https://doi.org/10.1063/1.5084603.

(13) Sokaras, D.; Weng, T.-C.; Nordlund, D.; Alonso-Mori, R.; Velikov, P.; Wenger, D.; Garachtchenko, A.; George, M.; Borzenets, V.; Johnson, B.; Rabedeau, T.; Bergmann, U. A Seven-Crystal Johann-Type Hard x-Ray Spectrometer at the Stanford Synchrotron Radiation Lightsource. *Rev Sci Instrum* **2013**, *84* (5), 053102. https://doi.org/10.1063/1.4803669.

(14) Klementiev, K.; Norén, K.; Carlson, S.; Clauss, K. G. V. S.; Persson, I. The BALDER Beamline at the MAX IV Laboratory. *J Phys Conf Ser* **2016**, *712*, 012023. https://doi.org/10.1088/1742-6596/712/1/012023.

(15) Mosselmans, J. F. W.; Quinn, P. D.; Dent, A. J.; Cavill, S. A.; Moreno, S. D.; Peach, A.; Leicester, P. J.; Keylock, S. J.; Gregory, S. R.; Atkinson, K. D.; Rosell, J. R. I18 – the Microfocus Spectroscopy Beamline at the Diamond Light Source. *J Synchrotron Radiat* **2009**, *16* (6), 818–824. https://doi.org/10.1107/S0909049509032282.

(16) Dent, A. J.; Cibin, G.; Ramos, S.; Smith, A. D.; Scott, S. M.; Varandas, L.; Pearson, M. R.; Krumpa, N. A.; Jones, C. P.; Robbins, P. E. B18: A Core XAS Spectroscopy Beamline for Diamond. *J Phys Conf Ser* **2009**, *190*, 012039. https://doi.org/10.1088/1742-6596/190/1/012039.

(17) Diaz-Moreno, S.; Hayama, S.; Amboage, M.; Freeman, A.; Sutter, J.; Duller, G. I20; the Versatile X-Ray Absorption Spectroscopy Beamline at Diamond Light Source. *J Phys Conf Ser* **2009**, *190*, 012038. https://doi.org/10.1088/1742-6596/190/1/012038.

(18) Ingle, J. D.; Crouch, S. R. *Spectrochemical Analysis*; Prentice Hall: Englewood Cliffs, 1988.

(19) Yamamoto, T. Assignment of Pre-Edge Peaks in K-Edge X-Ray Absorption Spectra of 3d Transition Metal Compounds: Electric Dipole or Quadrupole? *X-Ray Spectrometry* **2008**, *37* (6), 572–584. https://doi.org/10.1002/xrs.1103.

(20) van Bokhoven, J. A.; Lamberti, C. *X-Ray Absorption and X-Ray Emission Spectroscopy*; John Wiley & Sons, Ltd: Chichester, UK, 2016. https://doi.org/10.1002/9781118844243.

(21) Stumm von Bordwehr, R. A History of X-Ray Absorption Fine Structure. *Ann Phys (Paris)* **1989**, *14* (4), 377–465. https://doi.org/10.1051/anphys:01989001404037700.

(22) Chantler, C. T. X-Ray Absorption Spectroscopy Definitions. In *International Tables for Crystallography*; 2021; Vol. I. https://doi.org/10.1107/s1574870720003785.

(23) Shulman, G. R.; Yafet, Y.; Eisenberger, P.; Blumberg, W. E. Observations and Interpretation of X-Ray Absorption Edges in Iron Compounds and Proteins. *PNAS* **1976**, *73* (5), 1384–1388. https://doi.org/10.1073/pnas.73.5.1384.

(24) Sayers, D. E.; Stern, E. A.; Lytle, F. W. New Technique for Investigating Noncrystalline Structures: Fourier Analysis of the Extended X-Ray—Absorption Fine Structure. *Phys Rev Lett* **1971**, *27* (18), 1204–1207. https://doi.org/10.1103/PhysRevLett.27.1204.

(25) Lee, P. A.; Pendry, J. B. Theory of the Extended X-Ray Absorption Fine Structure. *Phys. Rev. B* **1975**, *11* (8), 2795–2811. https://doi.org/10.1103/PhysRevB.11.2795.

(26) Gurman, S. J.; Pettifer, R. F. EXAFS Study of the Structure of Amorphous and Crystalline Arsenic Oxide. *Philosophical Magazine B* **1979**, *40* (5), 345–359. https://doi.org/10.1080/13642817908246378.

(27) Rehr, J. J. Theoretical Approaches to X-Ray Absorption Fine Structure. *Rev Mod Phys* **2000**, *72* (3), 621–654. https://doi.org/10.1103/RevModPhys.72.621.

(28) Rehr, J. J.; Albers, R. C. Scattering-Matrix Formulation of Curved-Wave Multiple-Scattering Theory: Application to x-Ray-Absorption Fine Structure. *Phys Rev B* **1990**, *41* (12), 8139–8149. https://doi.org/10.1103/PhysRevB.41.8139.

(29) Hove, M. A. Van; Rehr, J. J.; Schattke, W. Development of the Scattering Theory of X-Ray Absorption and Core Level Photoemission. **2002**, *126*, 67–76.

(30) Rehr, J. J.; Kas, J. J.; Prange, M. P.; Sorini, A. P.; Takimoto, Y.; Vila, F. Ab Initio Theory and Calculations of X-Ray Spectra. *C R Phys* **2009**, *10* (6), 548–559. https://doi.org/10.1016/j.crhy.2008.08.004.

(31) Rehr, J. J.; Kas, J. J.; Vila, F. D.; Prange, M. P.; Jorissen, K. Parameter-Free Calculations of X-Ray Spectra with FEFF9. *Physical Chemistry Chemical Physics* **2010**, *12* (21), 5503–5513. https://doi.org/10.1039/b926434e.

(32) Gurman, S. J.; Binsted, N.; Ross, I. A Rapid, Exact Curved-Wave Theory for EXAFS Calculations. II. The Multiple-Scattering Contributions. *Journal of Physics C: Solid State Physics* **1986**, *19* (1), 1845–1861. https://doi.org/10.1088/0022-3719/17/1/019.

(33) Ankudinov, A.; Ravel, B. Real-Space Multiple-Scattering Calculation and Interpretation of x-Ray-Absorption near-Edge Structure. *Phys Rev B Condens Matter Mater Phys* **1998**, *58* (12), 7565–7576. https://doi.org/10.1103/PhysRevB.58.7565.

(34) Muñoz-Páez, A.; Díaz-Moreno, S.; Sánchez Marcos, E.; Rehr, J. J. Importance of Multiple-Scattering Phenomena in XAS Structural Determinations of $[Ni(CN)_4]^{2-}$ in Condensed Phases. *Inorg Chem* **2000**, *39* (17), 3784–3790. https://doi.org/10.1021/ic000274n.

(35) Crüsemann, R.; Bökman, F.; Fritzsche, V.; Bertagnolli, H. A Multiple Scattering EXAFS Study of Organometallic Compounds: $W(CO)_6$ and (1,3,5-Trimethylbenzene)$W(CO)_3$. *Chem Phys* **1995**, *194* (1), 81–90. https://doi.org/10.1016/0301-0104(95)00056-T.

(36) Attwood, D. *Soft X-Rays and Extreme Ultraviolet Radiation: Principles and Applications*; Cambridge University Press, 1999. https://doi.org/10.1017/CBO9781139164429.

(37) Kramers, H. A.; Heisenberg, W. Über Die Streuung von Strahlung Durch Atome. *Z. Angew. Phys.* **1925**, *31* (1), 681–708. https://doi.org/10.1007/BF02980624.

(38) Rovezzi, M.; Glatzel, P. Hard X-Ray Emission Spectroscopy: A Powerful Tool for the Characterization of Magnetic Semiconductors. *Semicond Sci Technol* **2014**, *29* (2), 023002. https://doi.org/10.1088/0268-1242/29/2/023002.

(39) Glatzel, P.; Alonso-Mori, R.; Sokaras, D. Hard X-Ray Photon-in/Photon-out Spectroscopy: Instrumentation, Theory and Applications. In *X-Ray Absorption and X-Ray Emission Spectroscopy*; van Bokhoven, J. A., Lamberti, C., Eds.; John Wiley & Sons, Ltd: Chichester, UK, 2016; pp 125–153. https://doi.org/10.1002/9781118844243.ch6.

(40) Glatzel, P.; Bergmann, U. High Resolution 1s Core Hole X-Ray Spectroscopy in 3d Transition Metal Complexes—Electronic and Structural Information. *Coord Chem Rev* **2005**, *249* (1–2), 65–95. https://doi.org/10.1016/j.ccr.2004.04.011.

(41) Bergmann, U.; Glatzel, P. X-Ray Emission Spectroscopy. *Photosynth Res* **2009**, *102* (2–3), 255–266. https://doi.org/10.1007/s11120-009-9483-6.

(42) Carra, P.; Fabrizio, M.; Thole, B. T. High Resolution X-Ray Resonant Raman Scattering. *Phys Rev Lett* **1995**, *74* (18), 3700–3703. https://doi.org/10.1103/PhysRevLett.74.3700.

(43) Wang, X.; Groot, F. M. F.; Cramer, S. P. Spin-Polarized X-Ray Emission of 3d Transition-Metal Ions: A Comparison via Kβ Detection. *Phys Rev B* **1997**, *56* (8), 4553–4564. https://doi.org/10.1103/PhysRevB.56.4553.

(44) Glatzel, P.; Bergmann, U. High Resolution 1s Core Hole X-Ray Spectroscopy in 3d Transition Metal Complexes—Electronic and Structural Information. *Coord Chem Rev* **2005**, *249* (1–2), 65–95. https://doi.org/10.1016/j.ccr.2004.04.011.

(45) Tsutsumi, K. The X-Ray Non-Diagram Lines Kβ' of Some Compounds of the Iron Group. *J Physical Soc Japan* **1959**, *14* (12), 1696–1706. https://doi.org/10.1143/JPSJ.14.1696.

(46) Groot, F. High-Resolution X-Ray Emission and X-Ray Absorption Spectroscopy. *Chem Rev* **2001**, *101* (6), 1779–1808. https://doi.org/10.1021/cr9900681.

(47) Pollock, C. J.; Delgado-Jaime, M. U.; Atanasov, M.; Neese, F.; DeBeer, S. Kβ Mainline X-Ray Emission Spectroscopy as an Experimental Probe of Metal-Ligand Covalency. *J Am Chem Soc* **2014**, *136* (26), 9453–9463. https://doi.org/10.1021/ja504182n.

(48) Chandrasekaran, P.; Chiang, K. P.; Nordlund, D.; Bergmann, U.; Holland, P. L.; DeBeer, S. Sensitivity of X-Ray Core Spectroscopy to Changes in Metal Ligation: A Systematic Study of Low-Coordinate, High-Spin Ferrous Complexes. *Inorg Chem* **2013**, *52* (11), 6286–6298. https://doi.org/10.1021/ic3021723.

(49) Burkhardt, L.; Holzwarth, M.; Plietker, B.; Bauer, M. Detection and Characterization of Hydride Ligands in Iron Complexes by High-Resolution Hard X-Ray Spectroscopy and Implications for Catalytic Processes. *Inorg Chem* **2017**, *56* (21), 13300–13310. https://doi.org/10.1021/acs.inorgchem.7b02063.

(50) Chakraborty, U.; Bügel, P.; Fritsch, L.; Weigend, F.; Bauer, M.; Jacobi von Wangelin, A. Planar Iron Hydride Nanoclusters: Combined Spectroscopic and Theoretical Insights into Structures and Building Principles. *ChemistryOpen* **2021**, *10* (2), 265–271. https://doi.org/10.1002/open.202000307.

(51) Swarbrick, J. C.; Kvashnin, Y.; Schulte, K.; Seenivasan, K.; Lamberti, C.; Glatzel, P. Ligand Identification in Titanium Complexes Using X-Ray Valence-to-Core Emission Spectroscopy. *Inorg Chem* **2010**, *49* (18), 8323–8332. https://doi.org/10.1021/ic100755t.

(52) Gallo, E.; Glatzel, P. Valence to Core X-Ray Emission Spectroscopy. *Adv Mater* **2014**, *26* (46), 7730–7746. https://doi.org/10.1002/adma.201304994.

(53) Smolentsev, G.; Soldatov, A. V; Messinger, J.; Merz, K.; Weyhermüller, T.; Bergmann, U.; Pushkar, Y.; Yano, J.; Yachandra, V. K.; Glatzel, P. X-Ray Emission Spectroscopy to Study Ligand Valence Orbitals in Mn Coordination Complexes. *J Am Chem Soc* **2009**, *131* (36), 13161–13167. https://doi.org/10.1021/ja808526m.

(54) Glatzel, P.; Sikora, M.; Smolentsev, G.; Fernández-García, M. Hard X-Ray Photon-in Photon-out Spectroscopy. *Catal Today* **2009**, *145* (3–4), 294–299. https://doi.org/10.1016/j.cattod.2008.10.049.

(55) Glatzel, P.; Weng, T.-C.; Kvashnina, K.; Swarbrick, J.; Sikora, M.; Gallo, E.; Smolentsev, N.; Mori, R. A. Reflections on Hard X-Ray Photon-in/Photon-out Spectroscopy for Electronic Structure Studies. *J Electron Spectros Relat Phenomena* **2013**, *188*, 17–25. https://doi.org/10.1016/j.elspec.2012.09.004.

(56) Eisenberger, P.; Platzman, P. M.; Winick, H. X-Ray Resonant Raman Scattering: Observation of Characteristic Radiation Narrower than the Lifetime Width. *Phys Rev Lett* **1976**, *36* (11), 623–626. https://doi.org/10.1103/PhysRevLett.36.623.

(57) Balerna, A.; Mobilio, S. Introduction to Synchrotron Radiation. In *Synchrotron Radiation Basics, Methods and Applications*; Mobilio, S., Boscherini, F., Meneghini, C., Eds.; Springer Berlin Heidelberg: Berlin, Heidelberg, 2015; pp 3–28. https://doi.org/10.1007/978-3-642-55315-8.

(58) Margaritondo, G. Characteristics and Properties of Synchrotron Radiation; Mobilio, S., Boscherini, F., Meneghini, C., Eds.; Springer Berlin Heidelberg: Berlin, Heidelberg, 2015; pp 29–63. https://doi.org/10.1007/978-3-642-55315-8.

(59) Aquilanti, G.; Vaccari, L.; Rikkert Plaisier, J.; Goldoni, A. Instrumentation at Synchrotron Radiation Beamlines. In *Synchrotron Radiation Basics, Methods and Applications*; Mobilio, S., Boscherini, F., Meneghini, C., Eds.; Springer Berlin Heidelberg: Berlin, Heidelberg, 2015; pp 64–104. https://doi.org/10.1007/978-3-642-55315-8.

(60) *P64 Advanced X-ray Absorption Spectroscopy - beamline layout*. http://photon-science.desy.de/facilities/petra_iii/beamlines/p64_advanced_xafs/beamline_layout/index_eng.html (accessed 2019-01-15).

(61) Newville, M. Fundamentals of XAFS. *ReVision* **2004**, 43. https://doi.org/10.2138/rmg.2014.78.2.

(62) Fornasini, P. Introduction to X-Ray Absorption Spectroscopy. In *Synchrotron Radiation: Basics, Methods and Applications*; Mobilio, S., Boscherini, F., Meneghini, C., Eds.; Springer: Bologna, 2015; pp 181–211. https://doi.org/10,1007/978-3-642-55315-8_6.

(63) Erbil, A.; Cargill, G. S.; Frahm, R.; Boehme, R. F. Total-Electron-Yield Current Measurements for near-Surface Extended x-Ray-Absorption Fine Structure. *Phys Rev B* **1988**, *37* (5), 2450. https://doi.org/10.1103/PhysRevB.37.2450.

(64) Ravel, B.; Newville, M. ATHENA, ARTEMIS, HEPHAESTUS: Data Analysis for X-Ray Absorption Spectroscopy Using IFEFFIT. *J Synchrotron Radiat* **2005**, *12* (4), 537–541. https://doi.org/10.1107/S0909049505012719.

(65) Klementiev, K. *XAFSmass 1.5.0*. https://doi.org/10.5281/zenodo.10235107.

(66) Stern, E. A.; Kim, K. Thickness Effect on the Extended-x-Ray-Absorption-Fine-Structure Amplitude. *Phys Rev B* **1981**, *23* (8), 3781–3787. https://doi.org/10.1103/PhysRevB.23.3781.

(67) Jaklevic, J.; Kirby, J. A.; Klein, M. P.; Robertson, A. S.; Brown, G. S.; Eisenberger, P. Fluorescence Detection of Exafs: Sensitivity Enhancement for Dilute Species and Thin Films. *Solid State Commun* **1977**, *23* (9), 679–682. https://doi.org/10.1016/0038-1098(77)90548-8.

(68) Klein, O.; Nishina, Y. Über Die Streuung von Strahlung Durch Freie Elektronen Nach Der Neuen Relativistischen Quantendynamik von Dirac. *Z Angew Phys* **1929**, *52* (11–12), 853–868. https://doi.org/10.1007/BF01366453.

(69) Clark, A. H.; Steiger, P.; Bornmann, B.; Hitz, S.; Frahm, R.; Ferri, D.; Nachtegaal, M. Fluorescence-Detected Quick-Scanning X-Ray Absorption Spectroscopy. *J Synchrotron Radiat* **2020**, *27* (3), 681–688. https://doi.org/10.1107/S1600577520002350.

(70) Teng, Z.; Song, M. Low-Energy Continuous Filtered X-Ray Measurement and Dosimetry with a PIPS Detector. *Radiat Phys Chem* **2021**, *179*, 109241. https://doi.org/10.1016/j.radphyschem.2020.109241.

(71) Lechner, P.; Fiorini, C.; Hartmann, R.; Kemmer, J.; Krause, N.; Leutenegger, P.; Longoni, A.; Soltau, H.; Stötter, D.; Stötter, R.; Strüder, L.; Weber, U. Silicon Drift Detectors for High Count Rate X-Ray Spectroscopy at Room Temperature. *Nucl Instrum Methods Phys Res A* **2001**, *458* (1–2), 281–287. https://doi.org/10.1016/S0168-9002(00)00872-X.

(72) Protic, D.; Stohlker, T.; Krings, T.; Mohos, I.; Spillmann, U. Two-Dimensional Microstrip Germanium Detector for the Spectroscopy of Hard X-Ray Transitions. *IEEE Trans Nucl Sci* **2005**, *52* (6), 3194–3198. https://doi.org/10.1109/TNS.2005.862932.

(73) Sette, F.; Ruocco, G.; Krisch, M.; Bergmann, U.; Masciovecchio, C.; Mazzacurati, V.; Signorelli, G.; Verbeni, R. Collective Dynamics in Water by High Energy Resolution Inelastic X-Ray Scattering. *Phys Rev Lett* **1995**, *75* (5), 850–853. https://doi.org/10.1103/PhysRevLett.75.850.

(74) Baron, A. Q. R.; Tanaka, Y.; Goto, S.; Takeshita, K.; Matsushita, T.; Ishikawa, T. An X-Ray Scattering Beamline for Studying Dynamics. *J Phys Chem Solids* **2000**, *61* (3), 461–465. https://doi.org/10.1016/S0022-3697(99)00337-6.

(75) Szlachetko, J.; Nachtegaal, M.; de Boni, E.; Willimann, M.; Safonova, O.; Sa, J.; Smolentsev, G.; Szlachetko, M.; van Bokhoven, J. A.; Dousse, J.-Cl.; Hoszowska, J.; Kayser, Y.; Jagodzinski, P.; Bergamaschi, A.; Schmitt, B.; David, C.; Lücke, A. A von Hamos X-Ray Spectrometer Based on a Segmented-Type Diffraction Crystal for Single-Shot x-Ray Emission Spectroscopy and Time-Resolved Resonant Inelastic x-Ray Scattering Studies. *Rev Sci Instrum* **2012**, *83* (10). https://doi.org/10.1063/1.4756691.

(76) Gog, T.; Casa, D. M.; Said, A. H.; Upton, M. H.; Kim, J.; Kuzmenko, I.; Huang, X.; Khachatryan, R. Spherical Analyzers and Monochromators for Resonant Inelastic Hard X-Ray Scattering: A Compilation of Crystals and Reflections. *J Synchrotron Radiat* **2013**, *20* (1), 74–79. https://doi.org/10.1107/S0909049512043154.

(77) Johann, H. H. Die Erzeugung Lichtstarker Röntgenspektren Mit Hilfe von Konkavkristallen. *Z Angew Phys* **1931**, *69* (3–4), 185–206. https://doi.org/10.1007/BF01798121.

(78) Sá, J.; Czapla-Masztafiak, J.; Lipiec, E.; Kayser, Y.; Kwiatek, W.; Wood, B.; Deacon, G. B.; Berger, G.; Dufrasne, F.; Fernandes, D. L. A.; Szlachetko, J. The Use of Resonant X-Ray Emission Spectroscopy (RXES) for the Electronic Analysis of Metal Complexes and Their Interactions with Biomolecules. *Drug Discov Today Technol* **2015**, *16*, 1–6. https://doi.org/10.1016/j.ddtec.2015.07.001.

(79) Nowakowski, M.; Czapla-Masztafiak, J.; Szlachetko, J.; Kwiatek, W. M. Electronic Structure of Fe, α-Fe2O3and Fe(NO3)3 × 9 H2O Determined Using RXES. *Chem Phys* **2017**, *493*, 49–55. https://doi.org/10.1016/j.chemphys.2017.06.002.

(80) Sá, J.; Czapla-Masztafiak, J.; Lipiec, E.; Kayser, Y.; Fernandes, D. L. A.; Szlachetko, J.; Dufrasne, F.; Berger, G. Resonant X-Ray Emission Spectroscopy of Platinum(II) Anticancer Complexes. *Analyst* **2016**, *141* (4), 1226–1232. https://doi.org/10.1039/C5AN02490K.

(81) Alonso-Mori, R.; Kern, J.; Sokaras, D.; Weng, T.; Nordlund, D.; Tran, R.; Delor, J.; Yachandra, V. K.; Yano, J.; Bergmann, U. A Multi-Crystal Wavelength Dispersive x-Ray Spectrometer A Multi-Crystal Wavelength Dispersive x-Ray Spectrometer. *Review of Scientific Instruments* **2012**, *83* (073114). https://doi.org/10.1063/1.4737630.

(82) Zakrzewska, K.; Kollbek, K.; Sikora, M.; Kapusta, C.; Szlachetko, J.; Sitarz, M.; Ziabka, M.; Radecka, M. Importance of the Electronic Structure of Modified TiO2 in the Photoelectrochemical Processes of Hydrogen Generation. *Int J Hydrogen Energy* **2015**, *40* (1), 815–824. https://doi.org/10.1016/j.ijhydene.2014.09.097.

(83) Milne, C. J.; Penfold, T. J.; Chergui, M. Recent Experimental and Theoretical Developments in Time-Resolved X-Ray Spectroscopies. *Coord Chem Rev* **2014**, *277–278* (February), 44–68. https://doi.org/10.1016/j.ccr.2014.02.013.

(84) Szlachetko, J.; Nachtegaal, M.; Sá, J.; Dousse, J.-C.; Hoszowska, J.; Kleymenov, E.; Janousch, M.; Safonova, O. V.; König, C.; van Bokhoven, J. A. High Energy Resolution Off-Resonant Spectroscopy at Sub-Second Time Resolution: (Pt(Acac)2) Decomposition. *Chem Commun* **2012**, *48* (88), 10898. https://doi.org/10.1039/c2cc35086f.

(85) Szlachetko, J.; Sá, J. Rational Design of Oxynitride Materials: From Theory to Experiment. *Cryst Eng Comm* **2013**, *15* (14), 2583. https://doi.org/10.1039/c3ce26909d.

(86) Bauer, M. HERFD-XAS and Valence-to-Core-XES: New Tools to Push the Limits in Research with Hard X-Rays? *Phys Chem Chem Phys* **2014**, *16* (27), 13827–13837. https://doi.org/10.1039/C4CP00904E.

(87) Stellato, F.; Oberthür, D.; Liang, M.; Bean, R.; Gati, C.; Yefanov, O.; Barty, A.; Burkhardt, A.; Fischer, P.; Galli, L.; Kirian, R. A.; Meyer, J.; Panneerselvam, S.; Yoon, C. H.; Chervinskii, F.; Speller, E.; White, T. A.; Betzel, C.; Meents, A.; Chapman, H. N. Room-Temperature Macromolecular Serial Crystallography Using Synchrotron Radiation. *IUCrJ* **2014**, *1* (4), 204–212. https://doi.org/10.1107/S2052252514010070/IT5001SUP1.PDF.

(88) Kupitz, C.; Basu, S.; Grotjohann, I.; Fromme, R.; Zatsepin, N. A.; Rendek, K. N.; Hunter, M. S.; Shoeman, R. L.; White, T. A.; Wang, D.; James, D.; Yang, J. H.; Cobb, D. E.; Reeder, B.; Sierra, R. G.; Liu, H.; Barty, A.; Aquila, A. L.; Deponte, D.;

Kirian, R. A.; Bari, S.; Bergkamp, J. J.; Beyerlein, K. R.; Bogan, M. J.; Caleman, C.; Chao, T. C.; Conrad, C. E.; Davis, K. M.; Fleckenstein, H.; Galli, L.; Hau-Riege, S. P.; Kassemeyer, S.; Laksmono, H.; Liang, M.; Lomb, L.; Marchesini, S.; Martin, A. V.; Messerschmidt, M.; Milathianaki, D.; Nass, K.; Ros, A.; Roy-Chowdhury, S.; Schmidt, K.; Seibert, M.; Steinbrener, J.; Stellato, F.; Yan, L.; Yoon, C.; Moore, T. A.; Moore, A. L.; Pushkar, Y.; Williams, G. J.; Boutet, S.; Doak, R. B.; Weierstall, U.; Frank, M.; Chapman, H. N.; Spence, J. C. H.; Fromme, P. Serial Time-Resolved Crystallography of Photosystem II Using a Femtosecond X-Ray Laser. *Nature 2014 513:7517* **2014**, *513* (7517), 261–265. https://doi.org/10.1038/nature13453.

(89) Brändén, G.; Neutze, R. Advances and Challenges in Time-Resolved Macromolecular Crystallography. *Science (1979)* **2021**, *373* (6558). https://doi.org/10.1126/science.aba0954.

(90) Meents, A.; Wiedorn, M. O.; Srajer, V.; Henning, R.; Sarrou, I.; Bergtholdt, J.; Barthelmess, M.; Reinke, P. Y. A.; Dierksmeyer, D.; Tolstikova, A.; Schaible, S.; Messerschmidt, M.; Ogata, C. M.; Kissick, D. J.; Taft, M. H.; Manstein, D. J.; Lieske, J.; Oberthuer, D.; Fischetti, R. F.; Chapman, H. N. Pink-Beam Serial Crystallography. *Nat Commun* **2017**, *8* (1), 1281. https://doi.org/10.1038/s41467-017-01417-3.

(91) Vanko, G.; Bordage, A.; Glatzel, P.; Gallo, E.; Rovezzi, M.; Gawelda, W.; Galler, A.; Bressler, C.; Doumy, G.; March, A. M.; Kanter, E. P.; Young, L.; Southworth, S. H.; Canton, S. E.; Uhlig, J.; Smolentsev, G.; Sundstrom, V.; Haldrup, K.; Van Driel, T. B.; Nielsen, M. M.; Kjaer, K. S.; Lemke, H. T. Spin-State Studies with XES and RIXS: From Static to Ultrafast. *J Electron Spectros Relat Phenomena* **2013**, *188*, 166–171. https://doi.org/10.1016/J.ELSPEC.2012.09.012.

(92) Farrell, R.; Vanderpuye, K.; Entine, G.; Squillante, M. R. High Resolution, Low Energy Avalanche Photodiode X-Ray Detectors. *IEEE Trans Nucl Sci* **1991**, *38* (2), 144–147. https://doi.org/10.1109/23.289288.

(93) Baron, A. Q. R.; Rüffer, R.; Metge, J. A Fast, Convenient, X-Ray Detector. *Nucl Instrum Methods Phys Res A* **1997**, *400* (1), 124–132. https://doi.org/10.1016/S0168-9002(97)00936-4.

(94) Kishimoto, S.; Adachi, S.; Taniguchi, T.; Ikeno, M.; Shimazaki, S.; Tanaka, M.; Mitsui, T. Si-APD Array Detectors with 2 Ns Pulse-Pair Resolving Time and Sub-Ns Resolution for Synchrotron X-Ray Measurements. *Nucl Instrum Methods Phys Res A* **2011**, *650* (1), 98–100. https://doi.org/10.1016/J.NIMA.2010.12.165.

(95) Khakhulin, D.; Otte, F.; Biednov, M.; Bömer, C.; Choi, T.-K.; Diez, M.; Galler, A.; Jiang, Y.; Kubicek, K.; Lima, F. A.; Rodriguez-Fernandez, A.; Zalden, P.; Gawelda, W.; Bressler, C. Ultrafast X-Ray Photochemistry at European XFEL: Capabilities of the Femtosecond X-Ray Experiments (FXE) Instrument. *Appl Sci* **2020**, *10* (3), 995. https://doi.org/10.3390/app10030995.

(96) Schoch, A.; Burkhardt, L.; Schoch, R.; StühRenberg, K.; Bauer, M. Hard X-Ray Spectroscopy: An Exhaustive Toolbox for Mechanistic Studies (?). *Faraday Discuss* **2019**, *220*, 113–132. https://doi.org/10.1039/C9FD00070D.

(97) Antonio, M. R.; Soderholm, L.; Song, I. Design of Spectroelectrochemical Cell for in Situ X-Ray Absorption Fine Structure Measurements of Bulk Solution Species. *J Appl Electrochem* **1997**, *27* (7), 784–792. https://doi.org/10.1023/A:1018464526864.

(98) Naumova, M.; Khakhulin, D.; Rebarz, M.; Rohrmüller, M.; Dicke, B.; Biednov, M.; Britz, A.; Espinoza, S.; Grimm-Lebsanft, B.; Kloz, M.; Kretzschmar, N.; Neuba, A.; Ortmeyer, J.; Schoch, R.; Andreasson, J.; Bauer, M.; Bressler, C.; Gero Schmidt, W.; Henkel, G.; Rübhausen, M. Structural Dynamics upon Photoexcitation-Induced Charge Transfer in a Dicopper(I)–Disulfide Complex. *Physical Chemistry Chemical Physics* **2018**, *20* (9), 6274–6286. https://doi.org/10.1039/C7CP04880G.

(99) Cannizzo, A.; Milne, C. J.; Consani, C.; Gawelda, W.; Bressler, Ch.; van Mourik, F.; Chergui, M. Light-Induced Spin Crossover in Fe(II)-Based Complexes: The Full Photocycle Unraveled by Ultrafast Optical and X-Ray Spectroscopies. *Coord Chem Rev* **2010**, *254* (21–22), 2677–2686. https://doi.org/10.1016/j.ccr.2009.12.007.

(100) Veen, R. M. van der; Bressler, C.; Milne, C. J.; Pham, V.-T.; Nahhas, A. El; Lima, F. A.; Gawelda, W.; Borca, C. N.; Abela, R.; Chergui, M. Retrieving Photochemically Active Structures by Time-Resolved EXAFS Spectroscopy. *J Phys Conf Ser* **2009**, *190*, 012054. https://doi.org/10.1088/1742-6596/190/1/012054.

(101) Prestipino, C.; Mathon, O.; Hino, R.; Beteva, A.; Pascarelli, S. Quick-EXAFS Implementation on the General Purpose EXAFS Beamline at ESRF. *J Synchrotron Radiat* **2011**, *18* (2), 176–182. https://doi.org/10.1107/S0909049510046546.

(102) Shimada, H.; Fukao, T.; Minami, H.; Ukai, M.; Fujii, K.; Yokoya, A.; Fukuda, Y.; Saitoh, Y. Structural Changes of Nucleic Acid Base in Aqueous Solution as Observed in X-Ray Absorption near Edge Structure (XANES). *Chem Phys Lett* **2014**, *591*, 137–141. https://doi.org/10.1016/j.cplett.2013.11.026.

(103) Ledbetter, K.; Reinhard, M. E.; Kunnus, K.; Gallo, A.; Britz, A.; Biasin, E.; Glownia, J. M.; Nelson, S.; Van Driel, T. B.; Weninger, C.; Zederkof, D. B.; Haldrup, K.; Cordones, A. A.; Gaffney, K. J.; Sokaras, D.; Alonso-Mori, R. Excited State Charge Distribution and Bond Expansion of Ferrous Complexes Observed with Femtosecond Valence-to-Core x-Ray Emission Spectroscopy. *J Chem Phys* **2020**, *152* (7). https://doi.org/10.1063/1.5139441.

(104) Kjær, K. S.; Van Driel, T. B.; Harlang, T. C. B.; Kunnus, K.; Biasin, E.; Ledbetter, K.; Hartsock, R. W.; Reinhard, M. E.; Koroidov, S.; Li, L.; Laursen, M. G.; Hansen, F. B.; Vester, P.; Christensen, M.; Haldrup, K.; Nielsen, M. M.; Dohn, A. O.; Pápai, M. I.; Møller, K. B.; Chabera, P.; Liu, Y.; Tatsuno, H.; Timm, C.; Jarenmark, M.; Uhlig, J.; Sundstöm, V.; Wärnmark, K.; Persson, P.; Németh, Z.; Szemes, D. S.; Bajnóczi, É.; Vankó, G.; Alonso-Mori, R.; Glownia, J. M.; Nelson, S.; Sikorski, M.; Sokaras, D.; Canton, S. E.; Lemke, H. T.; Gaffney, K. J. Finding Intersections between Electronic Excited State Potential Energy Surfaces with Simultaneous Ultrafast X-Ray Scattering and Spectroscopy. *Chem Sci* **2019**, *10* (22), 5749–5760. https://doi.org/10.1039/c8sc04023k.

(105) Göries, D.; Dicke, B.; Roedig, P.; Stübe, N.; Meyer, J.; Galler, A.; Gawelda, W.; Britz, A.; Geßler, P.; Sotoudi Namin, H.; Beckmann, A.; Schlie, M.; Warmer, M.; Naumova, M.; Bressler, C.; Rübhausen, M.; Weckert, E.; Meents, A. Time-Resolved Pump and Probe x-Ray Absorption Fine Structure Spectroscopy

at Beamline P11 at PETRA III. *Review of Scientific Instruments* **2016**, *87* (5). https://doi.org/10.1063/1.4948596.

(106) Ukai, M.; Yokoya, A.; Fujii, K.; Saitoh, Y. X-Ray Absorption Spectrum for Guanosine-Monophosphate in Water Solution in the Vicinity of the Nitrogen K-Edge Observed in Free Liquid Jet in Vacuum. *Radiat Phys Chem* **2008**, *77* (10–12), 1265–1269. https://doi.org/10.1016/j.radphyschem.2008.05.051.

(107) Chantler, C. T. X-Ray Absorption Spectroscopy Definitions. *International Tables for Crystallography* **2021**, *I*, 1–9. https://doi.org/10.1107/s1574870720003785.

(108) Stöhr, J. Analysis of K-Shell Excitation Spectra by Curve Fitting. In *NEXAFS Spectroscopy*; Lotsch, H. K. V., Ertl, G., Gomer, R., Mills, D. L., Eds.; Springer-Verlag Berlin Heidenberg: Berlin, 1996; pp 211–238. https://doi.org/10.1007/978-3-662-02853-7.

(109) Newville, M.; IUCr. EXAFS Analysis Using FEFF and FEFFIT. *urn:issn:0909-0495* **2001**, *8* (2), 96–100. https://doi.org/10.1107/S0909049500016290.

(110) Bourke, J. D. X-Ray Absorption Spectroscopy and Related Techniques The FDMX Code. In *international tables Int. Tables Crystallogr. I*; 2021. https://doi.org/10.1107/S1574870720003316.

(111) Neese, F. The ORCA Program System. *Wiley Interdiscip Rev Comput Mol Sci* **2012**, *2* (1), 73–78. https://doi.org/10.1002/wcms.81.

(112) Neese, F. Software Update: The ORCA Program System—Version 5.0. *Wiley Interdiscip Rev Comput Mol Sci* **2022**, *12* (5). https://doi.org/10.1002/wcms.1606.

(113) DeBeer George, S.; Petrenko, T.; Neese, F. Prediction of Iron K-Edge Absorption Spectra Using Time-Dependent Density Functional Theory. *J Phys Chem A* **2008**, *112* (50), 12936–12943. https://doi.org/10.1021/jp803174m.

(114) Becke, A. D. Density-Functional Exchange-Energy Approximation with Correct Asymptotic Behavior. *Phys Rev A (Coll Park)* **1988**, *38* (6), 3098–3100. https://doi.org/10.1103/PhysRevA.38.3098.

(115) Grimme, S.; Brandenburg, J. G.; Bannwarth, C.; Hansen, A. Consistent Structures and Interactions by Density Functional Theory with Small Atomic Orbital Basis Sets. *J Chem Phys* **2015**, *143* (5). https://doi.org/10.1063/1.4927476.

(116) Brandenburg, J. G.; Bannwarth, C.; Hansen, A.; Grimme, S. B97-3c: A Revised Low-Cost Variant of the B97-D Density Functional Method. *J Chem Phys* **2018**, *148* (6). https://doi.org/10.1063/1.5012601.

(117) Grimme, S.; Hansen, A.; Ehlert, S.; Mewes, J.-M. R2SCAN-3c: A "Swiss Army Knife" Composite Electronic-Structure Method. *J Chem Phys* **2021**, *154* (6), 064103. https://doi.org/10.1063/5.0040021.

(118) Caldeweyher, E.; Bannwarth, C.; Grimme, S. Extension of the D3 Dispersion Coefficient Model. *J Chem Phys* **2017**, *147* (3), 034112. https://doi.org/10.1063/1.4993215.

(119) van Lenthe, E.; van der Avoird, A.; Wormer, P. E. S. Density Functional Calculations of Molecular Hyperfine Interactions in the Zero Order Regular Approximation for Relativistic Effects. *J Chem Phys* **1998**, *108* (12), 4783–4796. https://doi.org/10.1063/1.475889.

(120) Besley, N. A.; Gilbert, A. T. B.; Gill, P. M. W. Self-Consistent-Field Calculations of Core Excited States. *J Chem Phys* **2009**, *130* (12), 124308. https://doi.org/10.1063/1.3092928.

(121) Staroverov, V. N.; Scuseria, G. E.; Tao, J.; Perdew, J. P. Comparative Assessment of a New Nonempirical Density Functional: Molecules and Hydrogen-Bonded Complexes. *J Chem Phys* **2003**, *119* (23), 12129–12137. https://doi.org/10.1063/1.1626543.

(122) Bauer, M. HERFD-XAS and Valence-to-Core-XES: New Tools to Push the Limits in Research with Hard X-Rays? *Phys Chem Chem Phys* **2014**, *16* (27), 13827–13837. https://doi.org/10.1039/C4CP00904E.

(123) Vollmers, N. J.; Müller, P.; Hoffmann, A.; Herres-Pawlis, S.; Rohrmüller, M.; Schmidt, W. G.; Gerstmann, U.; Bauer, M. Experimental and Theoretical High-Energy-Resolution X-Ray Absorption Spectroscopy: Implications for the Investigation of the Entatic State. *Inorg Chem* **2016**, *55* (22), 11694–11706. https://doi.org/10.1021/acs.inorgchem.6b01704.

(124) Krewald, V.; Lassalle-Kaiser, B.; Boron, T. T.; Pollock, C. J.; Kern, J.; Beckwith, M. A.; Yachandra, V. K.; Pecoraro, V. L.; Yano, J.; Neese, F.; DeBeer, S. The Protonation States of Oxo-Bridged Mn ^{IV} Dimers Resolved by Experimental and Computational Mn K Pre-Edge X-Ray Absorption Spectroscopy. *Inorg Chem* **2013**, *52* (22), 12904–12914. https://doi.org/10.1021/ic4008203.

(125) Neese, F. Prediction and Interpretation of the 57Fe Isomer Shift in Mössbauer Spectra by Density Functional Theory. *Inorganica Chim Acta* **2002**, *337*, 181–192. https://doi.org/10.1016/S0020-1693(02)01031-9.

(126) Schäfer, A.; Horn, H.; Ahlrichs, R. Fully Optimized Contracted Gaussian Basis Sets for Atoms Li to Kr. *J Chem Phys* **1992**, *97* (4), 2571–2577. https://doi.org/10.1063/1.463096.

(127) Weigend, F.; Ahlrichs, R. Balanced Basis Sets of Split Valence, Triple Zeta Valence and Quadruple Zeta Valence Quality for H to Rn: Design and Assessment of Accuracy. *Phys Chem Chem Phys* **2005**, *7* (18), 3297. https://doi.org/10.1039/b508541a.

(128) Weigend, F. Accurate Coulomb-Fitting Basis Sets for H to Rn. *Physical Chemistry Chemical Physics* **2006**, *8* (9), 1057–1065. https://doi.org/10.1039/b515623h.

(129) Delgado-Jaime, M. U.; DeBeer, S. Expedited Analysis of DFT Outputs: Introducing Moanalyzer. *J Comput Chem* **2012**, *33* (27), 2180–2185. https://doi.org/10.1002/jcc.23028.

(130) Bauer, M.; Bertagnolli, H. The Amplitude Reduction Factor and the Cumulant Expansion Method: Crucial Factors in the Structural Analysis of Alkoxide Precursors in Solution. *J Phys Chem B* **2007**, *111* (49), 13756–13764. https://doi.org/10.1021/jp076386i.

(131) Koningsberger, D. C.; Mojet, B. L.; Van Dorssen, G. E.; Ramaker, D. E. XAFS Spectroscopy; Fundamental Principles and Data Analysis. *Top Catal* **2000**, *10* (3–4), 143–155. https://doi.org/10.1023/A:1019105310221/METRICS.

(132) Ravel, B. Quantitative EXAFS Analysis. In *X-Ray Absorption and X-Ray Emission Spectroscopy*; Wiley, 2016; pp 281–302. https://doi.org/10.1002/9781118844243.ch11.

(133) Gurman, S. J.; Binsted, N.; Ross, I. A Rapid, Exact Curved-Wave Theory for EXAFS Calculations. *J Phys C: Solid State Phys.* **1984**, *17* (1), 143–151. https://doi.org/10.1088/0022-3719/17/1/019.

(134) Feiters, M. C.; Strange, R. W.; Binsted, N. EXCURVE. In *International Tables for Crystallography*; John Wiley & Sons, Ltd, 2020. https://doi.org/https://doi.org/10.1107/S1574870720003262.

(135) Newville, M. Larch: An Analysis Package for XAFS and Related Spectroscopies. *J Phys Conf Ser* **2013**, *430* (1). https://doi.org/10.1088/1742-6596/430/1/012007.

(136) Muñoz, M.; Argoul, P.; Farges, F. Continuous Cauchy Wavelet Transform Analyses of EXAFS Spectra: A Qualitative Approach. *Am Min* **2003**, *88* (4), 694–700. https://doi.org/10.2138/am-2003-0423.

(137) Corker, J.; Lefebvre, F.; Lécuyer, C.; Dufaud, V.; Quignard, F.; Choplin, A.; Evans, J.; Basset, J. M. Catalytic Cleavage of the C-H and C-C Bonds of Alkanes by Surface Organometallic Chemistry: An EXAFS and IR Characterization of a Zr-H Catalyst. *Science (1979)* **1996**, *271* (5251), 966–969. https://doi.org/10.1126/SCIENCE.271.5251.966.

(138) Pollock, C. J.; Delgado-Jaime, M. U.; Atanasov, M.; Neese, F.; Debeer, S. Kβ Mainline X-Ray Emission Spectroscopy as an Experimental Probe of Metal-Ligand Covalency. *J Am Chem Soc* **2014**, *136* (26). https://doi.org/10.1021/ja504182n.

(139) Glatzel, P.; Bergmann, U. High Resolution 1s Core Hole X-Ray Spectroscopy in 3d Transition Metal Complexes — Electronic and Structural Information. *Coord Chem Rev* **2005**, *249*, 65–95. https://doi.org/10.1016/j.ccr.2004.04.011.

(140) Glatzel, P.; Sikora, M.; Smolentsev, G.; Fernández-García, M. Hard X-Ray Photon-in Photon-out Spectroscopy. *Catal Today* **2009**, *145* (3–4), 294–299. https://doi.org/10.1016/j.cattod.2008.10.049.

(141) Lee, N.; Petrenko, T.; Bergmann, U.; Neese, F.; Debeer, S. Probing Valence Orbital Composition with Iron Kβ X-Ray Emission Spectroscopy. *J Am Chem Soc* **2010**, *132* (28), 9715–9727. https://doi.org/10.1021/ja101281e.

(142) Kawai, J.; Suzuki, C.; Adachi, H.; Konishi, T.; Gohshi, Y. Charge-Transfer Effect on the Linewidth of Fe *K* α X-Ray Fluorescence Spectra. *Phys Rev B* **1994**, *50* (16), 11347–11354. https://doi.org/10.1103/PhysRevB.50.11347.

(143) Castillo, R. G.; Henthorn, J. T.; McGale, J.; Maganas, D.; DeBeer, S. Kβ X-Ray Emission Spectroscopic Study of a Second-Row Transition Metal (Mo) and Its Application to Nitrogenase-Related Model Complexes. *Angew Chem, Int Ed* **2020**, *59* (31), 12965–12975. https://doi.org/10.1002/anie.202003621.

(144) Stavitski, E.; de Groot, F. M. F. The CTM4XAS Program for EELS and XAS Spectral Shape Analysis of Transition Metal L Edges. *Micron* **2010**, *41* (7), 687–694. https://doi.org/10.1016/j.micron.2010.06.005.

(145) Müller, P.; Neuba, A.; Flörke, U.; Henkel, G.; Kühne, T. D.; Bauer, M. Experimental and Theoretical High Energy Resolution Hard X-Ray Absorption and Emission Spectroscopy on Biomimetic Cu2S2 Complexes. *J Phys Chem A* **2019**, *123* (16), 3575–3581. https://doi.org/10.1021/acs.jpca.9b00463.

(146) Lee, N.; Petrenko, T.; Bergmann, U.; Neese, F.; Debeer, S. Probing Valence Orbital Composition with Iron K X-Ray Emission Spectroscopy. *J Am Chem Soc* **2010**, No. 15, 9715–9727. https://doi.org/10.1021/ja101281e.

(147) Geoghegan, B. L.; Liu, Y.; Peredkov, S.; Dechert, S.; Meyer, F.; DeBeer, S.; Cutsail, G. E. Combining Valence-to-Core X-Ray Emission and Cu K-Edge X-Ray Absorption Spectroscopies to Experimentally Assess Oxidation State in Organometallic Cu(I)/(II)/(III) Complexes. *J Am Chem Soc* **2022**, *144* (6), 2520–2534. https://doi.org/10.1021/jacs.1c09505.

(148) Delgado-Jaime, M. U.; DeBeer, S.; Bauer, M. Valence-to-Core X-Ray Emission Spectroscopy of Iron-Carbonyl Complexes: Implications for the Examination of Catalytic Intermediates. *Chem Eur J* **2013**, *19* (47), 15888–15897. https://doi.org/10.1002/chem.201301913.

(149) Valiev, M.; Bylaska, E. J.; Govind, N.; Kowalski, K.; Straatsma, T. P.; Van Dam, H. J. J.; Wang, D.; Nieplocha, J.; Apra, E.; Windus, T. L.; de Jong, W. A. NWChem: A Comprehensive and Scalable Open-Source Solution for Large Scale Molecular Simulations. *Comput Phys Commun* **2010**, *181* (9), 1477–1489. https://doi.org/10.1016/j.cpc.2010.04.018.

(150) Zhang, Y.; Mukamel, S.; Khalil, M.; Govind, N. Simulating Valence-to-Core X-Ray Emission Spectroscopy of Transition Metal Complexes with Time-Dependent Density Functional Theory. *J Chem Theory Comput* **2015**, *11* (12), 5804–5809. https://doi.org/10.1021/acs.jctc.5b00763.

(151) Rehr, J. J.; Kas, J. J.; Vila, F. D.; Prange, M. P.; Jorissen, K. Parameter-Free Calculations of X-Ray Spectra with FEFF9. *Phys Chem Chem Phys* **2010**, *12* (21), 5503. https://doi.org/10.1039/b926434e.

(152) Bunău, O.; Ramos, A. Y.; Joly, Y. The FDMNES Code; 2021. https://doi.org/10.1107/S1574870720003304.

(153) Sliz, P.; Harrison, S. C.; Rosenbaum, G. How Does Radiation Damage in Protein Crystals Depend on X-Ray Dose? *Structure* **2003**, *11* (1), 13–19. https://doi.org/10.1016/S0969-2126(02)00910-3.

(154) Hopkins, J. B.; Thorne, R. E. Quantifying Radiation Damage in Biomolecular Small-Angle X-Ray Scattering. *J Appl Crystallogr* **2016**, *49* (3), 880–890. https://doi.org/10.1107/S1600576716005136.

(155) Stanley, H. B.; Banerjee, D.; van Breemen, L.; Ciston, J.; Liebscher, C. H.; Martis, V.; Merino, D. H.; Longo, A.; Pattison, P.; Peters, G. W. M.; Portale, G.; Sen, S.; Bras, W. X-Ray Irradiation Induced Reduction and Nanoclustering of Lead in Borosilicate Glass. *Cryst Eng Comm* **2014**, *16* (39), 9331–9339. https://doi.org/10.1039/C4CE00937A.

(156) Christensen, J.; Horton, P. N.; Bury, C. S.; Dickerson, J. L.; Taberman, H.; Garman, E. F.; Coles, S. J. Radiation Damage in Small-Molecule Crystallography: Fact Not Fiction. *IUCrJ* **2019**, *6* (4), 703–713. https://doi.org/10.1107/S2052252519006948.

(157) Vankó, G.; Renz, F.; Molnár, G.; Neisius, T.; Kárpáti, S. Hard-X-Ray-Induced Excited-Spin-State Trapping. *Angew Chem, Int Ed* **2007**, *46* (28), 5306–5309. https://doi.org/10.1002/anie.200604432.

(158) Gütlich, P.; Hauser, A.; Spiering, H. Thermal and Optical Switching of Iron(II) Complexes. *Angew Chem, Int Ed* **1994**, *33* (20), 2024–2054. https://doi.org/10.1002/anie.199420241.

(159) Meirer, F.; Pepponi, G.; Streli, C.; Wobrauschek, P.; Kregsamer, P.; Zoeger, N.; Falkenberg, G. Parameter Study of Self-Absorption Effects in Total Reflection X-Ray Fluorescence-X-Ray Absorption Near Edge Structure Analysis of Arsenic. *Spectrochim Acta Part B At Spectrosc* **2008**, *63* (12), 1496–1502. https://doi.org/10.1016/j.sab.2008.05.004.

(160) Goulon, J.; Goulon-Ginet, C.; Cortes, R.; Dubois, J. M. On Experimental Attenuation Factors of the Amplitude of the EXAFS Oscillations in Absorption, Reflectivity and Luminescence Measurements. *J Phys France* **1982**, *43* (3), 539–548. https://doi.org/10.1051/jphys:01982004303053900.

(161) Tröger, L.; Arvanitis, D.; Baberschke, K.; Michaelis, H.; Grimm, U.; Zschech, E. Full Correction of the Self-Absorption in Soft-Fluorescence Extended x-Ray-Absorption Fine Structure. *Phys Rev B* **1992**, *46* (6), 3283–3289. https://doi.org/10.1103/PhysRevB.46.3283.

(162) Meirer, F.; Pepponi, G.; Streli, C.; Wobrauschek, P.; Kregsamer, P.; Zoeger, N.; Falkenberg, G. Parameter Study of Self-Absorption Effects in Total Reflection X-Ray Fluorescence-X-Ray Absorption Near Edge Structure Analysis of Arsenic. *Spectrochim Acta Part B At Spectrosc* **2008**, *63* (12), 1496–1502. https://doi.org/10.1016/j.sab.2008.05.004.

(163) Booth, C. H.; Bridges, F. Improved Self-Absorption Correction for Fluorescence Measurements of Extended XRay Absorption FineStructure. *Phys Scr* **2005**, *T115*, 202–204. https://doi.org/10.1238/Physica.Topical.115a00202.

(164) Haskel, D. FLUO: Correcting XANES for Self-Absorption in Fluorescence Measurements. 1999.

(165) Guda, A. A.; Chegerev, M.; Starikov, A. G.; Vlasenko, V. G.; Zolotukhin, A. A.; Bubnov, M. P.; Cherkasov, V. K.; Shapovalov, V. V; Rusalev, Y. V; Tereshchenko, A. A.; Trigub, A. L.; Chernyshev, A. V; Soldatov, A. V. Valence Tautomeric Transition of Bis(o-Dioxolene) Cobalt Complex in Solid State and Solution. *J Phys: Condens Matter* **2021**, *33* (21), 215405. https://doi.org/10.1088/1361-648X/abe650.

(166) Zolotukhin, A. A.; Bubnov, M. P.; Arapova, A. V.; Fukin, G. K.; Rumyantcev, R. V.; Bogomyakov, A. S.; Knyazev, A. V.; Cherkasov, V. K. Valence–Tautomeric Interconversion in a Bis(Dioxolene)Cobalt Complex with Iminopyridine Functionalized by a TEMPO Moiety. Phase Transition Coupled with Monocrystal Destruction. *Inorg Chem* **2017**, *56* (24), 14751–14754. https://doi.org/10.1021/acs.inorgchem.7b02597.

(167) Benedikter, M.; Musso, J.; Kesharwani, M. K.; Leonard Sterz, K.; Elser, I.; Ziegler, F.; Fischer, F.; Plietker, B.; Frey, W.; Kastner, J.; Winkler, M.; van Slageren, J.; Nowakowski, M.; Bauer, M.; Buchmeiser, M. R. Charge Distribution in Cationic Molybdenum Imido Alkylidene N-heterocyclic Carbene Complexes: A Combined X-ray, XaS, XeS, DFT, Mössbauer, and Catalysis Approach. *ACS Catal* **2020**, *10* (24), 14810–14823. https://doi.org/10.1021/acscatal.0c03978.

(168) Ziegler, F.; Teske, J.; Elser, I.; Dyballa, M.; Frey, W.; Kraus, H.; Hansen, N.; Rybka, J.; Tallarek, U.; Buchmeiser, M. R. Olefin Metathesis in Confined Geometries: A Biomimetic Approach toward Selective Macrocyclization. *J Am Chem Soc* **2019**, *141* (48), 19014–19022. https://doi.org/10.1021/jacs.9b08776.

(169) Ziegler, F.; Kraus, H.; Benedikter, M. J.; Wang, D.; Bruckner, J. R.; Nowakowski, M.; Weißer, K.; Solodenko, H.; Schmitz, G.; Bauer, M.; Hansen, N.; Buchmeiser, M. R. Confinement Effects for Efficient Macrocyclization Reactions with Supported Cationic Molybdenum Imido Alkylidene *N* -Heterocyclic Carbene Complexes. *ACS Catal* **2021**, *11* (18), 11570–11578. https://doi.org/10.1021/acscatal.1c03057.

(170) Welter, E.; Chernikov, R.; Herrmann, M.; Nemausat, R. A Beamline for Bulk Sample X-Ray Absorption Spectroscopy at the High Brilliance Storage Ring PETRA III. *AIP Conf Proc* **2019**, *2054* (January), 1–6. https://doi.org/10.1063/1.5084603.

(171) Bauer, M.; Kauf, T.; Christoffers, J.; Bertagnolli, H. Investigations into the Metal Species of the Homogeneous Iron(III) Catalyzed Michael Addition Reactions. *Phys Chem Chem Phys* **2005**, *7* (13), 2664. https://doi.org/10.1039/b501204j.

(172) Gregori, B. J.; Nowakowski, M.; Schoch, A.; Pöllath, S.; Zweck, J.; Bauer, M.; Jacobi von Wangelin, A. Stereoselective Chromium-Catalyzed Semi-Hydrogenation of Alkynes. *Chem Cat Chem* **2020**, *12* (21), 5359–5363. https://doi.org/10.1002/cctc.202000994.

(173) Muzart, J. Chromium-Catalyzed Oxidations in Organic Synthesis. *Chem Rev* **1992**, *92* (1), 113–140. https://doi.org/10.1021/cr00009a005.

(174) Bariashir, C.; Huang, C.; Solan, G. A.; Sun, W. H. Recent Advances in Homogeneous Chromium Catalyst Design for Ethylene Tri-, Tetra-, Oligo- and Polymerization. *Coord Chem Rev* **2019**, *385*, 208–229. https://doi.org/10.1016/J.CCR.2019.01.019.

(175) Gregori, B. J.; Schwarzhuber, F.; Pöllath, S.; Zweck, J.; Fritsch, L.; Schoch, R.; Bauer, M.; Jacobi von Wangelin, A. Stereoselective Alkyne Hydrogenation by Using a Simple Iron Catalyst. *Chem Sus Chem* **2019**, 3864–3870. https://doi.org/10.1002/cssc.201900926.

(176) Guo, M.; Prakash, O.; Fan, H.; de Groot, L. H. M.; Hlynsson, V. F.; Kaufhold, S.; Gordivska, O.; Velásquez, N.; Chabera, P.; Glatzel, P.; Wärnmark, K.; Persson, P.; Uhlig, J. HERFD-XANES Probes of Electronic Structures of Iron(II/III) Carbene Complexes. *Phys Chem Chem Phys* **2020**, *22* (16), 9067–9073. https://doi.org/10.1039/C9CP06309A.

(177) Kjær, K. S.; Kaul, N.; Prakash, O.; Chábera, P.; Rosemann, N. W.; Honarfar, A.; Gordivska, O.; Fredin, L. A.; Bergquist, K.-E.; Häggström, L.; Ericsson, T.; Lindh, L.; Yartsev, A.; Styring, S.; Huang, P.; Uhlig, J.; Bendix, J.; Strand, D.; Sundström, V.; Persson, P.; Lomoth, R.; Wärnmark, K. Luminescence and Reactivity of a Charge-Transfer Excited Iron Complex with Nanosecond Lifetime. *Science (1979)* **2019**, *363* (6424), 249–253. https://doi.org/10.1126/science.aau7160.

(178) Chábera, P.; Liu, Y.; Prakash, O.; Thyrhaug, E.; Nahhas, A. El; Honarfar, A.; Essén, S.; Fredin, L. A.; Harlang, T. C. B.; Kjær, K. S.; Handrup, K.; Ericson, F.; Tatsuno, H.; Morgan, K.; Schnadt, J.; Häggström, L.; Ericsson, T.; Sobkowiak, A.; Lidin, S.; Huang, P.; Styring, S.; Uhlig, J.; Bendix, J.; Lomoth, R.; Sundström, V.; Persson, P.; Wärnmark, K. A Low-Spin Fe(Iii) Complex with 100-Ps Ligand-to-Metal Charge Transfer Photoluminescence. *Nature* **2017**, *543* (7647), 695–699. https://doi.org/10.1038/nature21430.

1.2.2 UV-VIS spectroscopy

Similar to X-ray absorption spectroscopy, UV/Vis spectroscopy is also an electron spectroscopy. Here, valence electrons are excited into unoccupied orbitals by absorption of UV/Vis radiation. The intensity of the incident monochromatic beam (I_0) is – depending on the wavelength – attenuated, as it passes through a sample. With the intensity (I) measured after the sample, Beer-Lambert law gives the extinction E_λ by forming the decadic logarithm of the quotient from both intensities:

$$E_\lambda = log(I_0/I)_\lambda = \epsilon_\lambda cd \tag{1.1}$$

The extinction forms the basis for analyzing the UV/Vis spectra as the photon energy of the absorbed light corresponds to the energy levels of the different 'vertical' transitions (Franck-Condon principle). Typically, the extinction coefficient ϵ_λ independent of concentration (c) and path length (d) is plotted against the wavelength or the wavenumber. The value of the extinction coefficient depends on the probability of the transitions at a respective wavelength. Due to the Frank-Condon principle, only the 'vertical' transitions have to be considered since the electron transfer between different states takes place so quickly (less than 10^{-15} s)[8] that the distance between the atomic nuclei does not change during excitation. However, due to energy uncertainty, superimposed vibrational and rotational energy levels in molecules or the interaction with solvents, the discrete absorption lines are broadened forming absorption bands in the spectrum.

Time-dependent perturbation theory describes the transitions between two stationary states, e.g. the ground state Ψ_g and an excited state Ψ_a whereas Ψ describes the one-electron state functions defined by the location of the electron and the orientation of its spin. In this case the perturbation operator is the electric dipole operator $\vec{\mu}_{el}$ since only the electric dipole interaction is of importance when the spatial distribution of the atoms and molecules is significantly smaller than the wavelength of the electromagnetic radiation, as is the case here. The expected value for a specific transition is the transition dipole moment $\vec{\mu}_{g,a}$, describing the redistribution of electron density within a molecule during the electronic transition. The square of the magnitude of the transition dipole moment is proportional to the probability and therefore also the intensity $I_{a,g}$ of a spectral transition between states a and g.[9]

$$I_{a,g} \propto \left|\vec{\mu}_{g,a}\right|^2 = \left|\langle \Psi_a^* | \vec{\mu}_{el} | \Psi_g \rangle\right|^2 \tag{1.2}$$

From this it can be concluded that a transition is only allowed and has a certain intensity if the transition dipole moment is larger than zero. If it is zero, the transitions are forbidden.

The calculation of the matrix elements is very complex, but based on equation 1.2 selection rules can be established that provide information on whether the transition between two states of a system are allowed (high intensity) or forbidden (no intensity). However, it should be noted that prohibitions are often 'softened' by various effects such as geometric distortions or spin-orbit coupling (SOC) so that forbidden transitions can still be observed with low intensity. An important selection rule can be derived by considering the orbital motion and the spin of an electron separately since for light elements, including 3d metals, the SOC is so weak that the interaction is negligible . This results in the spin selection rule, which states that transitions between states of different spin multiplicities are forbidden and only transitions between states with the same spin are allowed. Furthermore, the Laporte rule applies, according to which the parity (even, odd) of the excited state has to differ from that of the ground state in the case of permitted transitions. This also explains the low intensity of ligand field (d-d) transitions in centrosymmetric TM complexes whereas for non-centrosymmetric complexes the p-d hybridization leads to a higher intensity.[10,11]
The possible electronic transitions in complexes can be differentiated due to the character of the donor and acceptor orbital. The mentioned ligand-field transitions have mainly metal d-character and are thus metal centered (MC) states. Furthermore charge transfer (CT) transitions can occur, whereby these can appear from the metal to the ligand (MLCT) or from the ligand to the metal (LMCT). Furthermore its also possible that the electron is transferred from a bonding orbital of the ligand into an antibonding orbitals of the same ligand as an intra-ligand charge transfer (ILCT) or to another ligand as a ligand-ligand charge transfer (LLCT).[10]

1.2.3 Photoluminescence spectroscopy

Photoluminescence is the process following the absorption of photons by re-emission of photons of longer wavelengths. When a complex is excited by UV-Vis photons, valence electrons are promoted from the ground state to higher energy levels, leaving behind electron vacancies. Subsequently, the excited electrons undergo relaxation processes that can be illustrated using the Jablonski diagram (Figure 1.1a), depicting the electronic states of a molecule and the transitions between these states. After excitation from the ground state S_0 into a vibrational excited state S_n, the compound may undergo various radiative (straight lines) or non-radiative processes (waved lines). This can lead to vibrational relaxation (VR) into the vibronic ground state of the same excited state, internal conversion (IC) to a different state with the same spin multiplicity, or intersystem crossing (ISC) which is a transition between different spin states as shown from the lowest singlet excited state S_1 to the lowest triplet excited state T_1. Finally, the molecule can also relax vibrationally from here or can emit radiation through the transition from these states to different vibrational states of

S_0. If this is a spin-allowed transition, it is referred to as fluorescence; if the transition is associated with a change in electron spin and is therefore forbidden, it is referred to as phosphorescence. The luminescence lifetime τ indicates the average time that a molecule remains in an excited state before it returns to its ground state. With values typically around 10^{-8} s, the fluorescence lifetime is significantly shorter than the phosphorescence lifetimes which can be in the ms range or even longer, since a spin flip is necessary to decay into the ground state.[8]

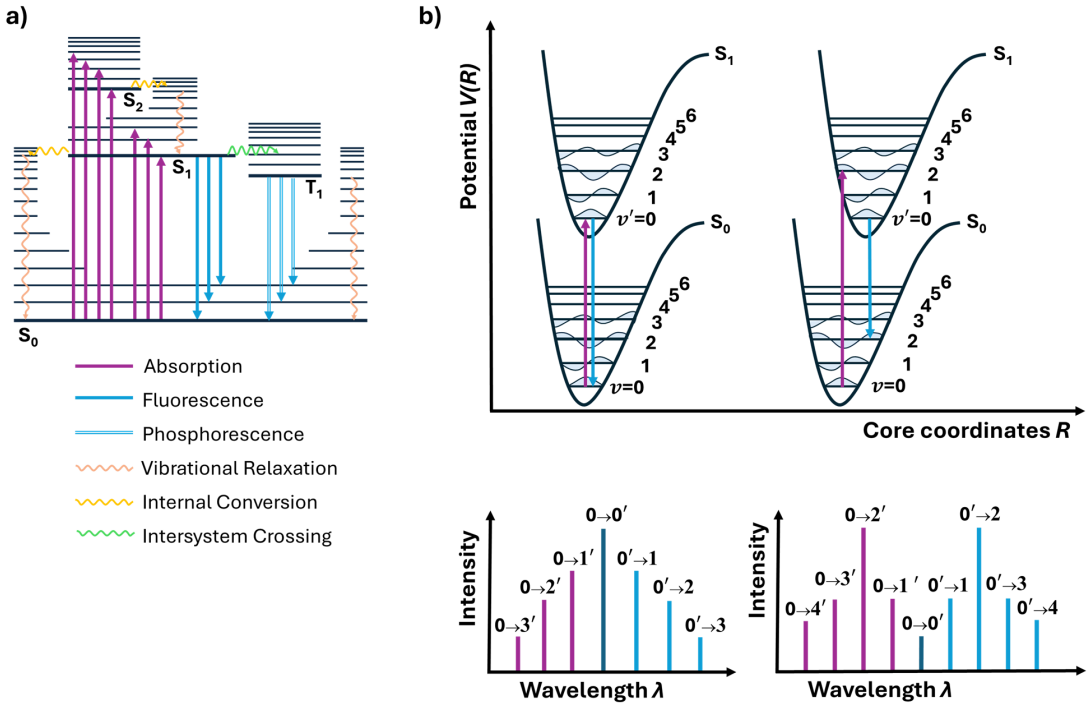

Figure 1.1: a) Jablosnki diagram. b) Shematic representation of the potential energy hypersurfaces with the corresponding vibrational levels of the first two electronic states S_0 and S_1 and the resulting symmetry and intensity of the luminescence transitions of a diatomic molecule with two different equilibrium distances of the ground and excited state.

As for the absorption, the intensity of the bands result from the squares of the overlap integrals of the vibronic wave functions in the excited and ground state. Thus, the luminescence spectrum is basically a mirror image of the absorption spectrum as the oscillator characteristics of S_0 and S/T_1 are comparable. However, due to energy loss through VR or solvent relaxation the luminescence spectrum is bathochromically shifted compared to the absorption spectrum (Stokes shift).[12] This depends primarily on the different equi-

librium distances between the nuclei in the ground and excited states. If this is small, then the Stokes shift is small and vice versa (compare Fig. 1.1b). However, the emission is independent of the excitation wavelength since Kasha's rule states that photon emission occurs only from the lowest excited state of a given multiplicity in appreciable yield.[13] This quantum yield is an important feature for characterisation. The luminescence quantum yield Φ_l indicates what proportion of the initially absorbed photons n_{abs} is finally emitted by luminescence photons n_l and is typically determined using reference substances.[14]

$$\Phi = \frac{n_l}{n_{abs}} \tag{1.3}$$

As fluorescence spectroscopy is a very sensitive analytical technique, even very low concentrations of impurities can interfere with the spectrum of the actual substance. In the same way, impurities can cause the luminescence to quench and thus significantly reduce the quantum yield. One quenching mechanism is dynamic quenching, in which the luminophore collides with the quencher within the lifetime of the excited state and the excitation energy is released in the form of heat. This process can be described using the Stern-Volmer equation for dynamic quenching (1.4) where I_0 and I is the luminescence intensity without and with quencher, [Q] is the quencher concentration, K_{dyn} is the Stern-Volmer constant, k_q is the quenching rate and τ_0 and τ is the lifetime without and with quenching.[8] Examples of quenchers are amines, halogens, acrylamide and also oxygen, which is why the solvent is typically degassed, especially in the case of metal-organic complexes with long living excited triplet states.[8] However, the spin conservation rule requires that the total spin momentum of the system is maintained.

$$\frac{I_0}{I} = \frac{\tau_0}{\tau} = 1 + K_{dyn}[Q] = 1 + k_q \tau_0 [Q] \tag{1.4}$$

Another quenching process is static quenching, in which luminophores and quenchers can build less luminescent complexes. This happens in the ground state and does not rely on diffusion or collision but only on the concentrations of the quencher Q and the luminophore L as it can be seen from the Stern-Volmer equation for static quenching (1.5)

$$\frac{I_0}{I} = 1 + K_{stat}[Q] \quad \text{with} \quad \mathrm{K}_{stat} = \frac{[L-Q]}{[L][Q]} \tag{1.5}$$

In a Stern-Volmer graph, the intensity ratio is plotted against the quencher concentration. In the case of pure dynamic or static quenching, a linear relationship is obtained whose slope increases (dynamic quenching) or decreases (static quenching) with increasing temperature. Mixing processes can also be present in which a non-linear relationship is obtained.

1.2.4 Density Functional Theory

Density functional theory (DFT) has become the cornerstone for calculating the quantum mechanical ground states of large many-electron systems, prized for its cost-efficiency and accuracy. DFT simplifies quantum mechanical calculations by determining observables directly from the electron density, eliminating the need to solve the Schrödinger equation for the wave function explicitly. The basis of this approach is the assumption of a correlation between the molecular properties and the electron density, which was already made by Thomas and Fermi in the 1920s. Later in the 1960s two theorems were established by Hohenberg and Kohn showing that this approach would lead to an exact solution. The first H.-K. theorem states that the external potential of a system, and thus also the ground state energy, is uniquely determined by an unknown functional of the density. The second theorem states that the ground state energy can be calculated according to the variational principle where only the electron density of the ground state leads to the minimum value of the energy. For simplification, the Born-Oppenheimer approximation is used, so that the kinetic energy of the nuclei can be neglected, and the nucleus-nucleus repulsion is assumed to be constant. The electronic energy E of the system, which depends on the density $[\rho(r)]$, is then composed of three different terms.

$$E[\rho(r)] = T_e[\rho(r)] + V_{ee}[\rho(r)] + V_{eK}[\rho(r)] \tag{1.6}$$

T_e describes the kinetic energy of the electrons, V_{ee} the electron-electron interaction and V_{eK} the electron-nucleus attraction. In the case of the electron-electron interaction, a further distinction can be made between the classical Coulomb repulsion U_H, and the non-classical interaction E_{NC} whereas the terms for V_{eK} and U_H are defined by established physical principles.

$$E[\rho(r)] = T_e[\rho(r)] + U_H[\rho(r)] + E_{NC}[\rho(r)] + V_{eK}[\rho(r)] \tag{1.7}$$

$$U_H[\rho(r)] = \frac{1}{2}\int\int \frac{\rho(r1)\rho(r2)}{|r_1 - r_2|} dr_1 dr_2 \tag{1.8}$$

$$V_{eK}[\rho(r)] = -\sum_{l=1}^{N-k} \int \frac{Z_l \rho(r)}{|r - R_l|} \tag{1.9}$$

Z describes the nuclear charge whereas r and R describe the position vector of the electron and nucleus, respectively. The difficulty therefore lies in the description of the kinetic energy T_e and the non-classical electron-electron interaction (exchange energy) E_{NC}. In 1927 Thomas and Fermi used the approach to describe the dominating kinetic energy as a homogeneous electron gas and neglected the exchange energy. Here, no orbitals were considered, which has the advantage that the density is only dependent on three spatial

coordinates. Although this simplifies the expression, the model is not able to describe chemical bonds. In 1964, Kohn and Sham presented an approach that characterizes modern DFT. A part of the kinetic energy is described by a fictitious system of non-interacting electrons, which has the same density as the real system. This is achieved by calculating the kinetic energy via a single slater determinant of orbitals $\{\phi_i\}$.[15]

$$T_s[\{\phi_i\}] = -\frac{1}{2}\sum_{i=1}^{n}\int \phi_i^*(r)\nabla^2\phi_i(r)dr \tag{1.10}$$

Since T_s is still unequal to the total kinetic energy T_e, the unknown difference is summarized together with the unknown E_{NC} to the exchange-correlation functional E_{XC}.

$$E_{XC}[\rho(r)] = T[\rho(r)] - T_s[\{\phi_i\}] + E_{NC}[\rho(r)] \tag{1.11}$$

This functional is unknown and many different non- and semi-empirical functionals have been developed to approximate the values as accurate as possible. However, the improvement is not straight forward in DFT since not always adding additional terms leads to a better description of all types of interaction. Therefore, a suitable functional must be selected for different systems and applications (e.g. spectra calculation), which can be determined, for example, by a good match with experimental data.

For simulating spectra it is possible to approximate the transition energies using the energy difference between the orbital energies of the ground state DFT description and calculate the transition probability for each transition. For VtC-XES this method is known to lead to good results.[16,17] However, for XANES Pre-peak or optical absorption simulations, time-dependent DFT (TD-DFT) has shown to be more suitable in the context of excitation processes.[18] TD-DFT rests on the Runge-Gross theorem, which establishes a one-to-one correspondence between the time-dependent external potential and the time-dependent electron density.[19] With that the static ground-state properties described by DFT can be extended to the time domain, taking into account how the electron density of a systems changes with a time-dependant external perturbation.

CHAPTER 2

CHEMICAL AND PHOTOPHYSICAL PROPERTIES OF AMINE FUNCTIONALIZED BIS-NHC-PYRIDINE-Ru^{II} COMPLEXES

Photoactive coordination compounds are promising candidates for the development of a wide variety of materials. Especially after Fujishima and Honda were able to carry out water splitting with the help of sunlight in 1972, the idea of utilising sunlight for chemical reactions is attractive, particularly against the background of energy shortages. Many polypyridine Ruthenium(II) complexes are known for their outstanding photophysical properties of their long-lived triplet metal-to-ligand charge transfer (MLCT) state. Here, different ligands influence the properties, whereby backbone modifications can also help to tailor the properties for a specific use. However, this requires an understanding of the influence of various ligands and substitutes. In this study the influence of an amine functionalization in the emissive bis-NHC-pyridine-Ru^{II} complex was investigated by single crystal diffraction, electrochemistry, optical spectroscopy and transient absorption spectroscopy. It was shown that in particular the quantum yield decreases significantly, while photostability increases. This could be explained with the help of (TD-)DFT calculations, showing the stabilization of a dark metal centered (MC) state and the destabilization of the emissive MLCT state in comparison to the non-functionalized complex.

Participations in this publication

L.Fritsch: Methodology, Writing - Original Draft, DFT Calculations and Analysis, Supporting Synthesis (Ref. 1);
Y. Vukadinovic: Synthesis (C1-C3), Writing – Prior Draft;
M. Lang, A. Kruse: Transient Absorption Spectroscopy, Writing – Review and Editing;
R. Naumann: Variable Temperature Emission Spectroscopy, ^{1}O Phosphorescence Measurem.;
M.-S. Bertrams: Nanosecond Laser Flash Photolysis Measurements;
R. Schoch: Single-Crystal Measurements and Analyses;
P. Müller: Prior DFT Calculations;
A. Neuba: Spectroelectrochemistry Measurements;
P. Dierks: Supporting Synthesis (Ref. 3);
S. Lochbrunner, C. Kerzig & K. Heinze: Writing – Review and Editing;
M. Bauer: Conceptual design of the study, Writing – Review and Editing, Project Administration.

Reprinted from
Chemical and photophysical properties of amine functionalized bis-NHC-pyridine-Ru^{II} complexes
Lorena Fritsch, Yannik Vukadinovic, Moritz Lang, Robert Naumann, Maria-Sophie Bertrams, Ayla Kruse, Roland Schoch, Patrick Müller, Adam Neuba, Philipp Dierks, Stefan Lochbrunner, Christoph Kerzig, Katja Heinze, and Matthias Bauer*, *ChemPhotoChem*, **2023**, *55(22)*, 11694-11706, DOI:10.1002/cptc.202300281.

Supplementary Information for this publication is found in the Appendix A.1.

Check for updates

ChemPhotoChem

Research Article
doi.org/10.1002/cptc.202300281

Chemistry Europe
European Chemical Societies Publishing

www.chemphotochem.org

Chemical and photophysical properties of amine functionalized bis-NHC-pyridine-Ru^{II} complexes

Lorena Fritsch,[a] Yannik Vukadinovic,[a] Moritz Lang,[c] Robert Naumann,[b] Maria-Sophie Bertrams,[b] Ayla Kruse,[c] Roland Schoch,[a] Patrick Müller,[a] Adam Neuba,[a] Philipp Dierks,[a] Stefan Lochbrunner,[c] Christoph Kerzig,[b] Katja Heinze,[b] and Matthias Bauer*[a]

The effects of backbone amine functionalization in three new homoleptic C^N^C type ruthenium(II) complexes bearing a tridentate bis-imidazole-2-ylidene pyridine ligand framework are characterized and studied by single crystal diffraction, electrochemistry, optical spectroscopy and transient absorption spectroscopy in combination with ab initio DFT calculations. Functionalization by dimethylamine groups in 4-position of the pyridine backbone significantly influences the properties of the complexes as revealed by comparison with the unfunctionalized references. As a result of the amine functionalization, a higher molar absorption coefficient of the MLCT bands, a decreased photoluminescence quantum yield at room temperature together with a shortened excited state lifetime but an improved photostability is observed. Introduction of electron donating and withdrawing groups at the NHC unit modifies the electronic and optical properties, such as the oxidation potential, absorption and emission properties, and the lifetimes of the excited states.

Introduction

Photoactive materials are designed to respond reversibly and precisely to an external stimulus. This field of research has received massive attention due to the high potential arising from developed materials in information technology, communication, or material science.[1] Frequently, heavy metal ions like Ru^{II}, Os^{II} or Ir^{III} are used for this purpose because of the excellent photophysical properties of their triplet metal-to-ligand charge transfer (^{3}MLCT) excited states.[2] Many of these complexes emit in the visible region under ambient conditions with excited state lifetimes in the microsecond range.[3] In the last decades, the investigation of Ru^{II} complexes containing polypyridyl ligands has been in the focus of research and resulted in a detailed understanding of their photochemical behavior. Five different possibilities exist for the depopulation of the ^{3}MLCT states:[4] (a) tunneling into high-energy vibrational levels of the singlet ground state (^{1}GS); (b) thermally activated decay into a triplet metal centered (^{3}MC) state followed by surface crossing at a minimum energy crossing point (MECP); (c) thermally activated surface crossing from the ^{3}MLCT state to the ^{1}GS; (d) decay via non-emissive charge transfer states, and (e) phosphorescence. [Ru(bpy)$_3$]$^{2+}$ (bpy: 2,2′-bipyridine) or [Ru(tpy)$_2$]$^{2+}$ (tpy: 2,2′:6′2″-terpyridine) are prominent examples for Ru^{II} complexes. Contrary to [Ru(bpy)$_3$]$^{2+}$, [Ru(tpy)$_2$]$^{2+}$ shows at room temperature (r.t.) only weak luminescence[5] and a short excited state lifetime because of the lower bite angle of the tridentate ligand reducing the ligand field splitting. This enables deactivation over a dark ^{3}MC state, i.e. decay pathway (b) mentioned above.[6] However, with the tridentate terpyridine ligand, isomer and chirality effects can be circumvented, and chemically more stable complexes are typically obtained.

Thus, such compounds were subject to numerous efforts in order to modify the terpyridine ligand and to tune the photophysical properties of respective Ru^{II} complexes.[7] The syntheses of different Ru^{II} complexes with tridentate ligands have been described in the literature, and their optical properties have been analyzed thoroughly.[8–13] Both homo- and heteroleptic complexes are used for photocatalytic applications, but ligand modifications in homoleptic complexes are studied less frequently.[14] One approach which gained prominence in the design of iron photosensitizers recently[15] but received less attention in ruthenium chemistry, is the use of N-heterocyclic carbenes (NHCs) to increase the ligand field splitting and thus to reduce the chance of deactivation by process (b). These very strong σ-donors destabilize the MC states. In addition, the

[a] L. Fritsch, Dr. Y. Vukadinovic, Dr. R. Schoch, Dr. P. Müller, A. Neuba, Dr. P. Dierks, Prof. Dr. M. Bauer
Department of Chemistry, Paderborn University
Institute of Inorganic Chemistry and Center for Sustainable Systems Design (CSSD)
Warburger Straße 100, 33098 Paderborn, Germany
E-mail: matthias.bauer@upb.de
Homepage: http://www.chemie.upb.de/bauer

[b] Dr. R. Naumann, M.-S. Bertrams, Prof. Dr. C. Kerzig, Prof. Dr. K. Heinze
Department of Chemistry, Johannes Gutenberg University Mainz
Duesbergweg 10–14, 55128 Mainz, Germany

[c] Dr. M. Lang, A. Kruse, Prof. Dr. S. Lochbrunner
Department Science and Technology of Life, Light and Matter, University of Rostock, Institute of Physics
Albert-Einstein-Straße 23, 18059 Rostock, Germany

Supporting information for this article is available on the WWW under https://doi.org/10.1002/cptc.202300281

ChemPhotoChem

Research Article
doi.org/10.1002/cptc.202300281

Chemistry Europe
European Chemical Societies Publishing

combination of the strong σ-donating carbenes with a suitable π-acceptor, such as pyridine, stabilize the MLCT states. Thus, the probability of non-radiative deactivation through dark MC states is reduced.[16]

The interplay of both effects makes tridentate C^N^C ligands a versatile structure motif for a multitude of purposes. Furthermore, modification of the pyridine backbone in such ligand systems can have extensive effects on the photophysical behavior of the complexes as shown by addition of aromatic systems, carboxy-substituted pyridines or pyrazine derivatives.[9,10,13] In general, substitution of the pyridine in 4-position by an electron withdrawing group stabilizes the orbital energies relative to the unsubstituted complex. Here the antibonding lowest unoccupied molecular orbitals (LUMOs) are stabilized to a larger extent than the bonding highest occupied molecular orbitals (HOMOs) leading to a smaller HOMO-LUMO gap. However, functionalization with donating amines bearing a free electron pair has not yet been investigated for this ligand motif in Ru complexes, although comparable terpyridine complexes have shown a reduction of the HOMO-LUMO gap and thus absorption in the low energy spectral range.[12] In addition amines offer numerous possibilities to further functionalize the photoactive ruthenium core.[17] Besides the modified π-acceptor capability of pyridine by amine substitution in the backbone, an interplay in the variation of the properties of the σ-donating NHCs is of interest. Based on our previous work on amine functionalization in combination with electron donating and withdrawing groups at the NHC units of the prototype tridentate C^N^C ligand bis(imidazole-2-ylidene)pyridine (**LR1**) for Fe^{II} complexes,[18] we present the Ru^{II} analogue here.

In this study, the effect of the electron donating dimethylamine substituent in the pyridine backbone of **LR1** and **LR3** on the ground and excited state properties of the corresponding $[RuL_2]^{2+}$ complexes **Ref. [1]** and **Ref. [3]**, respectively is investigated by electrochemistry, optical, and ultrafast spectroscopy in combination with density functional theory (DFT). In order to vary the σ-donor and π-acceptor strengths at the NHC units, [Ru(bip^{NMe2})$_2$] (**C1**, bip = (pyridine-2,6-diyl)bis(1-methyl-imidazol-2-ylidene), [Ru(bdmip^{NMe2})$_2$] (**C2**, bdmip = (pyridine-2,6-diyl)bis(1,4,5-trimethyl-imidazol-2-ylidene)), and [Ru(bbp^{NMe2})$_2$] (**C3**, bbp = pyridine-2,6-diyl)bis(1-methyl-benzimidazol-2-ylidene)) were used (the pro-ligand structures **L1**, **L2**, **L3** and **LR1**, **LR3** are shown in Scheme 1).

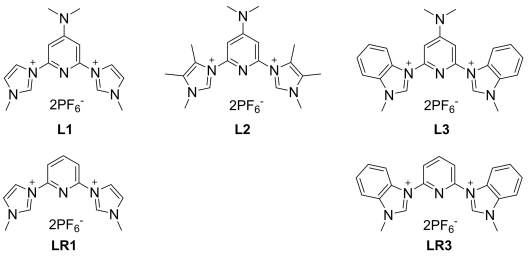

Scheme 1. Schematic structures of pro-ligands **L1**-**L3** of homoleptic complexes **C1**–**C3** and reference ligands **LR1** and **LR3** of reference complexes **Ref. [1]** and **Ref. [3]**.

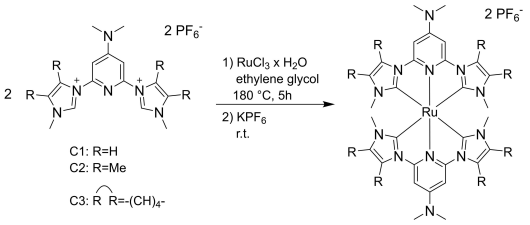

Scheme 2. Reaction conditions of complexation for **C1**–**C3**.

Results and Discussion

Synthesis and crystal structure

The cationic pro-ligands **L1**-**L3** are prepared following a procedure previously described.[14] The subsequent complex synthesis of **C1**–**C3** was carried out according to the synthetic protocol of Son *et al.* starting from $RuCl_3$ and the respective pro-ligand (Scheme 2).[8] Anion metathesis and purification by column chromatography gave the complexes as bright yellow powders. Composition and purity of the compounds were determined by single crystal diffraction analyses, multinuclear NMR spectroscopy in combination with mass spectrometry, IR and elemental analysis. For the detailed experimental protocol see Supporting Information, chapter 2.

The key structural parameters of **C1**–**C3** obtained from single crystal diffraction are discussed in comparison to **Ref. [1]** since no crystal structure of **Ref. [3]** is available. As an example, the crystal structure of **C1** is shown in Figure 1. The structures of **C2** and **C3** are displayed in the Supporting Information (Figure S2 and S3). The Ru–N bond lengths of in average 2.018(2) Å in **C2**, 2.020(2) Å in **C1**, and 2.031(1) Å in **C3** increase slightly depending on the NHC character. Thus, the benzimidazole-2-ylidene containing complex **C3** has the longest and the dimethylimidazole-2-ylidene complex **C2** the shortest Ru–N bond whereas **C1** only show minor deviations from **C2** within

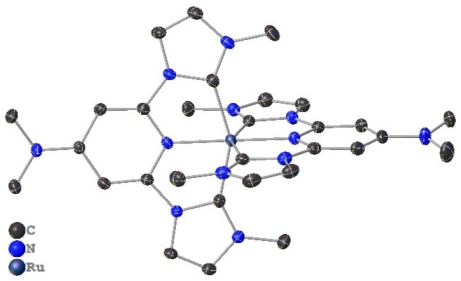

Figure 1. Single crystal structure of complex cation **C1**. Atoms are shown with anisotropic displacement parameters as ellipsoids at 50% probability level. Hydrogen atoms and counter ions are omitted for clarity.

the instrument error. Nevertheless this finding supports the expected σ-donor strength of the respective NHC part of the ligand. For **Ref. [1]** an average Ru–N bond length of 2.019(2) Å, which is nearly identical to **C1**, is observed. Therefore, the amine functionalization does not seem to have any structural effect here. For the Ru–C bond length only a shortening within the 3σ-error for the amine substituted complexes **C1**–**C3**, with average values between 2.042(2) Å and 2.044(4) Å, in contrast to **Ref. [1]** with an average Ru–C distance of 2.051(2) Å is observed. The N–Ru–N trans angle hardly differ from 178.70(7) to 179.21(7) for **C1**–**C3** with the size of the NHC unit. However, for the unsubstituted reference **Ref. [1]**, a significant smaller angle of 175.78(6) was observed, deviating most from an ideal octahedral geometry. The C–Ru–C angle shows very small deviations following the Ru–C bond length, whereas **C2** has an angle of 153.20(8) and **C3** of 153.86(7) . Overall, the amine substitution slightly reduces Ru–C bond lengths and thus stabilizes the Ru–C bond. Furthermore, for all substituted complexes a less distorted octahedral structure can be found in contrast to the reference. All coordination bond lengths are summarized in Table 1 and further details of the crystal structure analysis can be found in the Supporting Information (Chapter 3).

Table 1. Trans-coordination angles and bond lengths for complex **C1**–**C3** and the reference complex **Ref. [1]**.

	C1	C2	C3	Ref. [1][8]
Ru–N[a]	2.019(2) 2.021(2)	2.015(2) 2.021(2)	2.030(1) 2.032(1)	2.018(2) 2.020(2)
Ru–N av[b]	2.020(2)	2.018(2)	2.031(1)	2.019(2)
Ru–C[a]	2.036(2) 2.043(2) 2.044(2) 2.051(2)	2.037(2) 2.039(2) 2.041(2) 2.049(2)	2.037(3) 2.043(3) 2.046(2) 2.052(2)	2.048(2) 2.049(2) 2.053(2) 2.055(2)
Ru–C av[b]	2.044(2)	2.042(2)	2.044(3)	2.051(2)
N–Ru–N[c]	178.70(7)	178.85(6)	179.21(7)	175.78(6)
C–Ru–C[c]	153.41(9) 153.60(9)	153.01(8) 153.39(8)	154.33(7) 153.38(7)	153.81(8) 153.56(8)
C–Ru–C av[d]	153.51(9)	153.20(8)	153.86(7)	153.69(8)

[a] bond length [Å]. [b] average bond length [Å]. [c] trans bond angle [ ]. [d] average trans bond angle [ ].

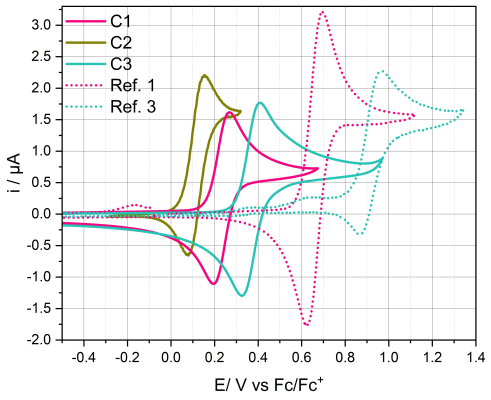

Figure 2. Cyclic voltammograms (oxidative scans) of complexes **C1**–**C3** and **Ref. 1**/**Ref. 3**. recorded in MeCN (c = 1 mmol/L) at r.t. using [n-Bu_4N][PF_6] (0.1 mol/L) as supporting electrolyte at 100 mV·s^{-1}. Potentials are shown against the Fc/Fc^+ couple.

Electrochemical behavior

Cyclic voltammograms of complexes **C1**–**C3** and **Ref. [1]**/**Ref. [3]** are depicted in Figure 2. The full scan ranges are given in the Supplementary Information (Figure S4). For all complexes a single reversible oxidation in the range between 0.1 V and 0.4 V versus Fc/Fc^+ is observed which can be ascribed to the Ru^{III}/Ru^{II} one-electron redox pair (for further details see Supplementary Information, chapter 4 and Figure S5). The summarized electrochemical data displayed in Table 2 show a half-step potential of 0.11 V for **C2**, 0.23 V for **C1** and 0.37 V for **C3**. The amine substitution has a significant effect on the oxidation potential, which is cathodically shifted compared to the reference complexes **Ref. [1]** (0.67 V) and **Ref. [3]** (0.92 V). This shift can be explained by the reduced π-accepting properties of the amine substituted pyridine, causing a destabilization of the Ru localized t_2g orbitals (HOMOs). For the same reason, ligand localized π* orbitals (LUMOs) are also destabilized compared to **Ref. [1]** and **Ref. [3]**, shifting the ligand reduction potentials to more negative values, moving out of the potential range for MeCN as solvent in the electrochemical experiments.

Different NHC ligands influence the redox potential significantly.[19] The Ru^{III}/Ru^{II} redox process in the benzimidazole complexes **C3** and **Ref. [3]** appears at higher potentials than in the imidazole complexes **C1** and **Ref. [1]**. The decreased π-donor and increased π-acceptor function of the benzimida-

Table 2. Optical absorption and electrochemical data for **C1**–**C3** and the reference complexes.

	C1	C2	C3	Ref. [1]	Ref. [3]
$\lambda_{abs,max}$ (nm)[a]	379 352 242	391 355 239	384 370 300 283	384 345 273 237	378 295
ε (M^{-1}·cm^{-1})	41200 34500 93900	44300 28800 96300	36500 34300 44800 76000	19200 14800 30100 43000	16700 98200
$\lambda_{em,max,\ 77K}$ (nm)[b]	486 510	501 524	474 497	–	–
$\lambda_{em,max,r.t.}$ (nm)[b]	515 585	535 620	497 557	541	524
$E_{1/2}^{ox}$(V)[d]	0.23	0.11	0.37	0.67	0.92
ΔE (mV)	68	63	79	71	100

[a] Measured in MeCN at 298 K. [b] Measured in BuCN at 77 K and excitation at 354 nm (**C1**), 390 nm (**C2**), 354 nm (**C3**). [c] Measured in MeCN at 298 K and excitation at 380 nm. [d] Potentials are quoted vs. Fc/Fc^+ and recorded in MeCN (c = 1 mM) using [n-Bu_4N][PF_6] (0.1 M) as supporting electrolyte at 100 mV·s^{-1} at 25 C.

ChemPhotoChem

Research Article
doi.org/10.1002/cptc.202300281

Chemistry Europe
European Chemical Societies Publishing

zole-2-ylidene stabilizes the HOMOs compared to imidazole-2-ylidene, explaining the shift. The four-fold methyl substitution in the ligand of **C2** further increases the electron density at the ruthenium centre compared to **C1** due to the stronger π-donor and weaker π-acceptor capabilities, which destabilizes the HOMOs.

To obtain a more detailed view on the oxidation process, UV/Vis spectro-electrochemical investigations were performed (Figure S6). The observed isosbestic points confirm that there are only two species involved. Fully reversible Ru^{III}/Ru^{II} redox processes for C1 and C3 can be observed, while for C2, there is no complete electrochemical re-reduction, although this was observed in the CV. This may be due to the significantly longer time scale at which the potential is applied in the spectro-electrochemical measurements. Under these conditions the complex might build another species which can't be transferred in the initial state.

The progressive oxidation of the Ru^{II} species can be observed by the decreased intensity of the typical MLCT band at 300–400 nm. The resulting Ru^{III} species possesses a corresponding ligand-to-metal charge transfer (LMCT) transition, which appears in the range of 600–900 nm.[20] The ligand-centered transitions below 300 nm are not significantly affected by the oxidation process.

UV/Vis Spectroscopy

The UV/Vis- absorption spectra of the Ru^{II} complexes recorded in MeCN solutions ($1 \cdot 10^{-5}$ M) are shown in Figure 3. The data agreement with those of related compounds[9] and are summarized in Table 2. The complexes exhibit intense bands in the UVB below 315 nm and the UVA/blue region (> 315 nm), assigned to ligand-based π-π* transitions and MLCT dπ-pπ* transitions, respectively.[21] Within the MLCT region (315–450 nm) two absorption bands are present at ~360 nm and ~385 nm. The splitting between both decreases from **C2** (2600 cm^{-1}) to **C1** (2000 cm^{-1}) to **C3** (1000 cm^{-1}). A weak redshift of the low-energy tail of the MLCT band, starting from **C3** to **C1** to **C2** can be observed in line with the calculated HOMO-LUMO gaps (vide infra, Figure 5) and the electrochemical properties. The references show a similar behavior even if the molar absorption coefficients of the MLCT bands are lower by a factor of ~2: for **Ref. [1]** a significant splitting (2900 cm^{-1}) is visible, whereas for **Ref. [3]** only one band is visible. Interestingly, amine substitution at the pyridine does not appear to cause a significant shift in the MLCT band of the functionalized complexes compared to the unsubstituted **Ref. [1]** and **Ref. [3]**, in contrast to what was observed for methoxy functionalization at the pyridine ligand of comparable C^N^C iron complexes and can be expected due to variations in the HOMO-LUMO gaps.[22] Related Fe^{II} complexes show the same spectral behavior, and it is known that the higher energy MLCT band is assigned to a Fe–NHC charge transfer, whereas the MLCT band at lower energies corresponds to a Fe-pyridine charge transfer.[18] A corresponding quantum chemical analysis of the Ru complexes will be presented below.

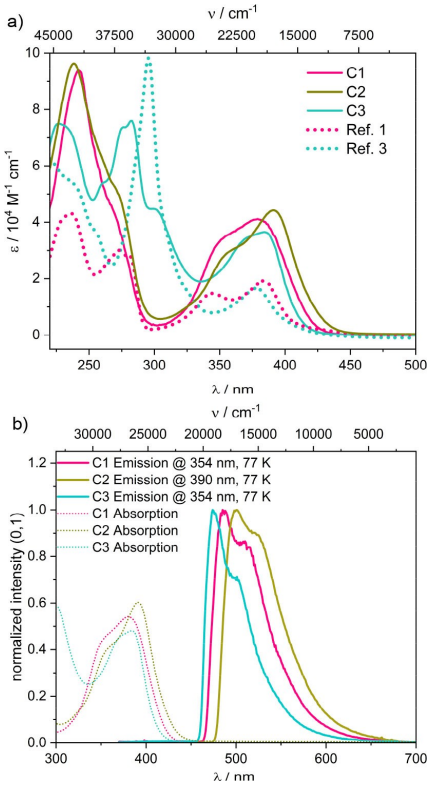

Figure 3. a) Optical absorption spectra of complexes **C1**–**C3** in MeCN at 25 C compared to the references. Right: Normalized emission spectra of the complexes **C1**–**C3** in frozen nBuCN at 77 K in comparison to a cutout of the normalized optical absorption spectra in MeCN at 25 C.

Luminescence Properties

Photoluminescence spectra of **C1**–**C3** at 77 K are shown in Figure 3. The emission band at 77 K has a maximum at 486 nm (**C1**), 501 nm (**C2**) and 474 nm (**C3**) resulting in an observed energy difference between absorption and emission maxima of 5800 cm^{-1}, 5600 cm^{-1}, 4900 cm^{-1}, respectively. It follows the order observed for the MLCT absorption bands. Such emission bands, with vibronic fine structure have been reported previously for $[Ru^{II}(bpy)_3]^{2+}$ complexes and can be assigned to the typical phosphorescence of the ^{3}MLCT state[23] after intersystem crossing from the ^{1}MLCT state. Since both reference complexes **Ref. [1]** and **Ref. [3]** show pronounced r.t. luminescence (Figure S8) at 541 nm and 524 nm, respectively and emission quantum yields of ~0.9% in deoxygenated MeCN solutions, it was a surprising observation that the amine substituted complexes **C1**–**C3** show only very weak r.t. emission.

Temperature-dependent luminescence spectra were measured to investigate thermal effects on the emissive behavior

(Figures S10/11). No sudden changes are detected, but a constant intensity decrease indicates a thermally activated non-radiative deactivation process. With increasing temperature, a shift to lower energies becomes visible, i.e. the low-energy band becomes progressively dominant. The step at the glass transition point around 110 K, indicates the increased solvent mobility and the loss of rigidochromic effects.[24]

At r.t. **C1**–**C3** each show two weak emission bands with maxima/shoulders at 515 nm and 585 nm (**C1**), 535 nm and 620 nm (**C2**) and 497 nm and 557 nm (**C3**) (Figure S8). The observed shift in contrast to the frozen solution further substantiates a ^{3}MLCT character.[25] The low-energy band is quenched in presence of $^3O_2$. This quenching results in the formation of $^1O_2$ as proven by the characteristic emission at 1270 nm (Figure S7). The formation of $^1O_2$ is also indicative of a triplet state.[26] However, this band shows a lower emission energy than the associated reference complexes **Ref. [1]** and **Ref. [3]**, which would suggest a stabilization of the MLCT state for the amine substituted complexes, whereas the opposite is shown in the Quantum-chemical calculations section. Thus, we assume that the lower-energy emission band is not associated to the complexes **C1**–**C3** but to an emissive trace impurity whereas the high energy band can be assigned to the amine substituted complexes. Excitation spectra with detection at the low- and high-energy side of the bands differ as well (Figure S11).

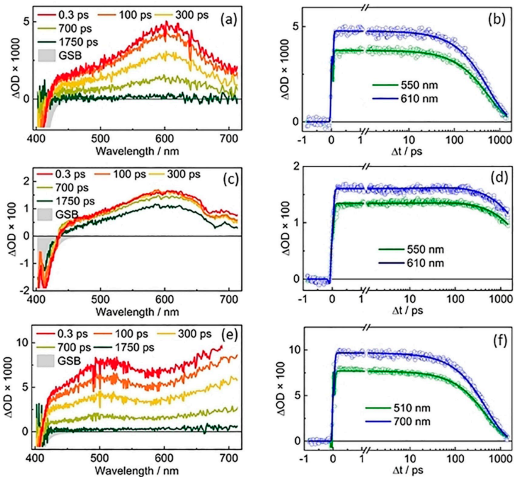

Figure 4. Ultrafast pump-probe measurements of **C1**–**C3** in MeCN with optical excitation at 400 nm. Left panels: Transient absorption spectra at the given delay times for **C1** (a), **C2**(c), and **C3** (e). The shaded areas indicate where GSB contributes to the signal. Right panels: Measured time traces (circles) at the respective two specified probe wavelengths and corresponding decay curves (lines) obtained by a global fit with a time constant of 560 ps for **C1** (b), 4 ns for **C2** (d) and of 490 ps for **C3** (f), respectively.

Excited state dynamics

Due to the very low r.t. quantum yields, attempts to determine the lifetime of the emissive states by time resolved emission measurements using a streak camera failed. Therefore, details of the excited state dynamics could only be investigated with the aid of transient absorption (TA) spectroscopy (Figure 4, Figure S12). An ultrafast pump-probe setup with a time resolution of about 100 fs was used applying pulses with a center wavelength of 400 nm, obtained by frequency doubling the output of a Ti:sapphire amplifier system, for excitation and a white light continuum for probing.[27] The polarizations of the pump and probe pulses were set to magic angle to avoid signal contributions caused by rotational diffusion.

TA spectra at selected delay times between excitation and probe are shown in Figure 4a) for **C1**, 4c) for **C2** and 4e) for **C3** in MeCN. For **C1**–**C3** a positive signal in the visible range was detected, which is attributed to the excited state absorption (ESA) of the corresponding ^{3}MLCT state. The steep signal drop below 420 nm indicates the onset of the ground state bleach (GSB) merging into the positive ESA signal (see Figure 4a), c), e)). This is in good accordance with the chronoamperometric spectra (see Figure S6). Upon electrochemical oxidation, the ruthenium cation is oxidized to Ru^{III}. Also, in the MLCT state, where one electron is shifted from the ruthenium metal center to the ligand, the ruthenium cation is formally oxidized to Ru^{III}, but in addition the ligand is reduced. The absorption changes due to electrochemical oxidation should therefore resemble partially the transient absorption spectrum. And indeed, the positive absorbance changes at wavelengths above 500 nm is observed in both the chronoamperometric spectra as well as the transient absorption spectra. Differences in the spectral shape might be related to the reduction of the ligand in the MLCT state. Unfortunately, this reduction turned out to be irreversible in the chronoamperometric experiments and corresponding spectral changes could not be recorded.

The temporal evolution of the transient absorption spectra was analyzed by a global fit. The time evolution of the signals of **C1**, **C2** and **C3** can be reproduced by a monoexponential decay. The associated time constants are 560 ps, 4 ns, and 490 ps for **C1**, **C2** and **C3**, respectively (see Figure 4b), d), and f)), are assigned to the lifetimes of the ^{3}MLCT state of the respective complex. The ^{3}MLCT excited state lifetime of **Ref. [1]** was determined to be 820 ns through emission lifetime measurements in a previous study.[8] Using nanosecond laser flash photolysis (ns-LFP)[28] the transient absorption spectrum of **Ref. [1]** with a broad maximum in the visible region and a characteristic GSB could be measured after excitation with 355 nm pulses (Figure S21). A ^{3}MLCT lifetime of 2.4 µs was obtained under our conditions (MeCN, 20 C). The excited state lifetime of **Ref. [3]** was also examined by time resolved emission and transient absorption measurements and determined to be 920 ns (see Figures S14/S15). Therefore, the addition of the dimethylamine functionality shortens the lifetime by more than three orders of magnitude. Comparative ns-LFP measurements of **C1** and **Ref. [1]** with semi-quantitative detection of the TA signals provided further evidence for the efficient and ultrafast deactivation of excited **C1** (Figure S22). This can be explained by the destabilization of the ^{3}MLCT state and a consequently

ChemPhotoChem
Research Article
doi.org/10.1002/cptc.202300281
Chemistry Europe
European Chemical Societies Publishing

faster transfer to the ^{3}MC state. Surprisingly, the trend of an elongated ^{3}MLCT lifetime due to a larger π-system in the benzimidazole complex **C3** in contrast to **C1**, as it is described for the iron complex with carboxylic acid instead of amine functionalization, could not be reproduced for the ruthenium complex which shows that an interaction of substituents at different positions might also play a role.[19] Furthermore, the lifetime of **C2** of ~4 ns is approximately eight times longer than that of **C1** and **C3**. The addition of the methyl groups thus prolongs the excited state lifetime and partially compensates the weakened π-acceptor properties of the pyridine due to the amine.

Ref. [1] and **C1** are sufficiently photostable for comparative ns-LFP measurements and for a reliable photostability assay using a 390 nm LED as light source (Figure S24). Upon excitation of the MLCT band **C1** is more photostable than its reference compound by more than one order of magnitude. Considering that the lifetime of **C1** is still sufficiently long for several photophysical and photochemical applications and the advantageous increase in the molar absorption coefficients of the MLCT band, the dimethylamine group in the C^N^C ligands might be regarded as a useful design principle when fast photobleaching must be avoided.

Quantum-chemical calculations

To understand the significant influence of the amine substitution at the pyridine ring, molecular properties were investigated by means of (time-dependent) density functional theory (DFT) calculations on **C1**–**C3** and the respective references **Ref. [1]** and **Ref. [3]**. B97-3c DFT-optimized molecular geometries predict a distorted octahedral structure in the electronic ground state (^{1}GS) for all complexes which is in good agreement with the experimentally observed bond lengths and angles given in Table S5. To illustrate the electronic properties and the energy difference of the molecular orbitals caused by the amine functionalization, TD-DFT calculations on the PBE0 level were conducted using the ZORA-def2-TZVP basis set, the relativistic approximation ZORA and the continuum solvent model CPCM of MeCN. The resulting energies and the composition of the frontier orbitals are shown in Figure 5. A further analysis of the orbitals can be found in Table S6 and Figure S18. In each case, the HOMO is composed of Ru d-orbitals (around 40%) in combination with π-orbitals of the ligands.

Both references possess a HOMO with additional NHC character (around 40%) and a LUMO dominated by the accepting pyridine (around 55%). For the amine substituted complexes this varies with the specific substitution at the NHC. While **C2** behaves most similarly to the references due to the electron-donating effect of the methyl groups at the NHC and also exhibits a HOMO with 40% NHC and a LUMO with 44% pyridine contribution, this ratio is reversed for non-methylated

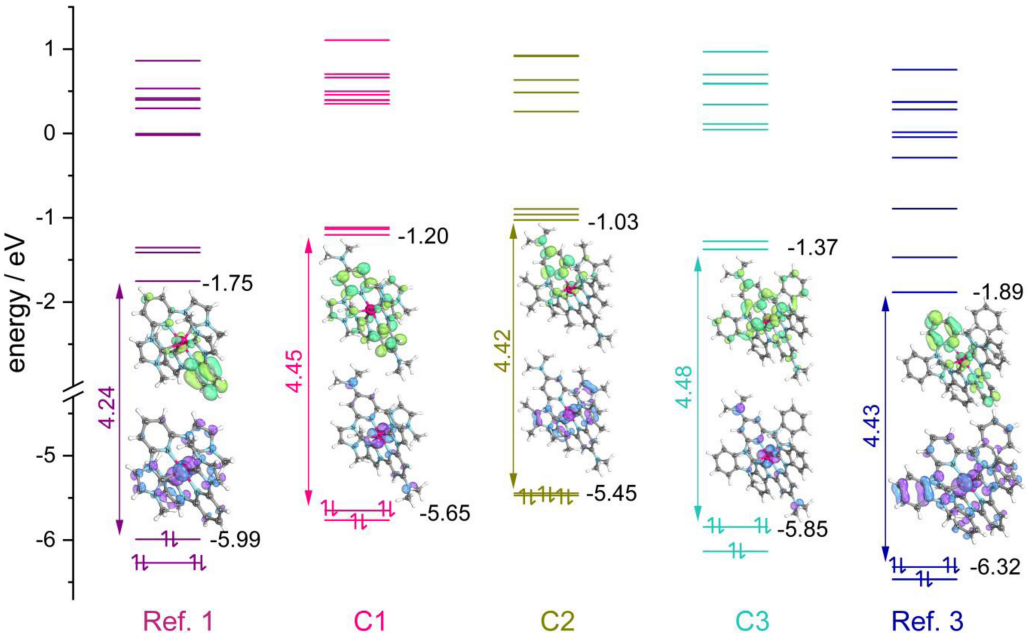

Figure 5. Molecular orbital levels of complexes **C1**–**C3** and the references in MeCN obtained from TD-DFT calculations. Theoretical HOMO-LUMO gaps are given in between the HOMO and LUMO of each complex as well as the spatial distribution.

C1. Here, the LUMO is still pyridine dominated with 48%, but the HOMO has only 12% NHC contribution. This effect is further enhanced for **C3**, where even the LUMO has only 22% pyridine, but 47% NHC contribution. Thus, a stepwise inversion of the ligand-based orbital components of the HOMOs and LUMOs is observed. This can be explained by the fact that the NHC donor properties are weakened by the benzimidazole, and at the same time the donor properties of the pyridines are increased by the amine in accordance with the electron donating properties of the $-NMe_2$ group. In contrast, the opposite effect is seen for the acceptor properties. The electron donating effect of the amine consequently destabilizes all frontier orbitals. Especially the energy of the metal-centered HOMOs reflects this trend as can be seen from the cyclic voltammetry results. The reference complexes both show more stabilized HOMOs than the amine substituted complexes due to the better π-accepting ability of the unfunctionalized pyridines. This results in a significant shift of $+0.44$ eV and $+0.55$ eV of the experimental oxidation potentials between **C1** and **C3** and their respective references **Ref. [1]** and **Ref. [3]**. The calculations reproduce these findings quite well with energy differences of $+0.33$ eV and $+0.44$ eV respectively. Also, the HOMO energy of the amine substituted complexes shows an increasing destabilization with a change of in total $+0.40$ eV from **C2** (-5.45 eV) to **C1** (-5.65 eV) to **C3** (-5.85 eV). The trend of these theoretical values is in the same order of magnitude as the increase of in total 0.26 eV found in the experiment. For all complexes the stabilizing and destabilizing effects of the substituents are stronger for the occupied orbitals resulting in slightly different HOMO-LUMO gaps for the three complexes **C2**, **C1**, and **C3** with 4.42 eV, 4.45 eV, and 4.48 eV, respectively. These rather small changes correspond to a change of only 4 nm in the UV/Vis spectra (Figure 3) which might be visible as a slight blue shift in the same order.

Furthermore, the first 150 vertical transitions together with their oscillator strength were calculated using the PBE0 functional to reproduce the absorption spectra (Figure S19/Table S7). The intense bands in the UV region at 240 nm and 275 nm can be assigned to several ligand centered (LC) transitions, typical for ruthenium polypyridine complexes.[29] Since the pyridine part of the ligands still has better acceptor properties than the NHC part even after amine functionalization, the accepting orbitals of the most intense transitions all have a higher pyridine than NHC contribution, whereas the composition of the donor orbitals is more distributed over both ligand parts. Above 325 nm the calculations describe all transitions mainly as MLCT transitions. However, the experiment shows two distinct bands, and the calculation does not reproduce the intensity of those features very well. The use of other functionals, such as B3LYP does not lead to an improvement (Figure S19). Having a closer look into the origin of the transitions (Table S6/S7) it becomes apparent that the donor orbitals of the lower energy band transitions consist of Ru d-orbitals with a z-component while the higher energy transitions originate from Ru d_{xy} orbitals. This results in a higher pyridine proportion for the donor orbitals of the low energy band and a higher NHC proportion for the high energy feature, consistent with the findings for the corresponding iron complexes.[18] However, for the accepting LUMOs no such trend is found. The orbitals are more delocalized over the molecule, consistent with the literature for similar Ru complexes.[30] To shed further light into the excited state landscape the lowest triplet states of **C1**–**C3** were optimized. As seen from Figure 6, the spin density of the lowest triplet state is localized at the Ru center and one pyridine-amine unit predicting a pyridine based ^{3}MLCT as emissive state in all cases supporting the results discussed above.

The extremely low emission quantum yield at r.t. and the short ^{3}MLCT lifetimes compared to the reference complexes suggest that also thermally accessible efficient dark relaxation pathways are present. Excitation energies calculated by PBE0 TD-DFT can be used to estimate the excited state energies (Figure 6). The calculated values only reflect the vertical transitions at the Franck-Condon (FC) geometry and do not take into account different vibronic levels and the shape of the potential energy surfaces (PES) along the reaction coordinate, which leads to an overestimation especially for the ^{3}MC states. However, they allow a relative comparison of the functionalized complexes with the references to determine the different luminescence behavior.

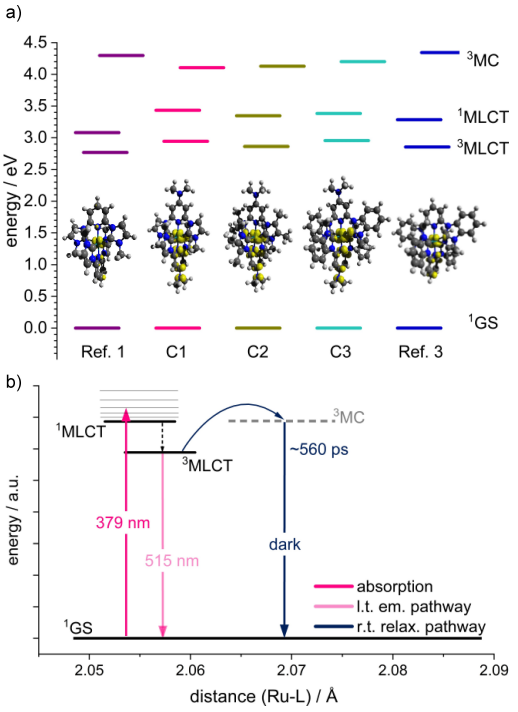

Figure 6. a) Visualization of the TD-DFT calculated vertical excitation energies (Table S8) at the optimized ground state geometry (FC) and spin density plots of the lowest b97-3c optimized (opt) triplet states of **C1**–**C3** and **Ref. 1**/**3**. b) Absorption and potential relaxation pathways using **C1** as an example. Position of the relaxed ^{3}MC state is shown arbitrarily since the ^{3}MC state could not be geometry optimized by DFT.

ChemPhotoChem | Research Article doi.org/10.1002/cptc.202300281 | Chemistry Europe European Chemical Societies Publishing

In general, amine substitution destabilizes the MLCT states and stabilizes the MC states. This results in a decreased energy gap between the lowest ^{3}MLCT and ^{3}MC states from 1.53 eV and 1.49 eV for **Ref. [1]** and **Ref. [3]** to 1.16 eV, 1.27 eV and 1.25 eV for **C1**, **C2** and **C3**, respectively (FC geometry). For $[Ru(bpy)_3]^{2+}$ the thermal activation barrier between ^{3}MLCT and ^{3}MC was determined to be about 0.31 eV (trans ^{3}MC) or 0.45 eV (cis ^{3}MC).[31] Thus, taking into account the overestimation of the MC energy, the reduction of the energy gap of about 0.3 eV is very likely to enable the thermal deactivation path via the dark ^{3}MC state. **C2**, which exhibits the longest ^{3}MLCT lifetime of the three amine substituted complexes, also has the largest ^{3}MC-^{3}MLCT energy gap which supports the relevance of the gap for the deactivation and the photophysical properties. Additionally, the calculated ^{3}MLCT absorption energy of **Ref. [1]** and **Ref. [3]** is 2.77 eV and 2.87 eV, respectively corresponding to a wavelength of 448 nm and 432 nm. This overestimates the experimental emission energy by ~4000 cm^{-1} (90 nm) due to the aforementioned reasons. Using the same approach, the emission bands for **C1**, **C2** and **C3** (2.94 eV/422 nm, 2.86 eV/434 nm, 2.96 eV/419 nm) are expected to be around 512 nm, 524 nm and 509 nm which substantiates the assignment of the r.t. high-energy emission band to the complex emission.

Conclusions

Three new amine functionalized bis-NHC-pyridine ruthenium(II) complexes have been synthesized and characterized. The use of an amine in the pyridine backbone was previously described for analogue weakly emissive $[Ru(tpy)_2]^{2+}$ and non-emissive $[Fe(bip^{NMe2})_2]^{2+}$ complexes and has now been transferred to a corresponding and originally luminescent tetra-carbene ruthenium complex. The amine substitution on the pyridine decreases the push-pull effect associated with the σ-donating NHC and π-accepting pyridine and thereby weakens particularly the pyridine π-acceptor and strengthens the σ-donating properties significantly. As a result, all relevant frontier orbitals are destabilized. This is manifested in the lower oxidation potentials of the substituted complexes compared to the unfunctionalized references. The effect has an even larger impact on the ligand centered LUMOs leading to a slight increase of the HOMO-LUMO gaps. Different substituents at the NHC backbone, modifying its σ-donor and π-acceptor strength, also show an influence. The improved π-donor properties in **C2** due to methyl substitution destabilize especially the metal-based HOMOs, whereas the better π-acceptor properties of the benzyl functionalization in **C3** stabilize them.

Amine functionalization strongly impacts the excited state energy landscape since especially the emission properties change drastically. The r.t. luminescence is nearly fully quenched due to much shorter ^{3}MLCT excited state lifetimes, i.e. faster non-radiative decay. DFT calculations could show that destabilization of the ^{3}MLCT and stabilization of the ^{3}MC states occurs in the amine substituted complexes and could facilitate a dark ^{3}MC relaxation channel. The quenching is weakened by electron donating and slightly strengthened by electron withdrawing groups at the NHC, which is reflected by the excited state lifetimes. However, even if the luminescence properties are quenched in the amine functionalized complexes, they possess a higher photostability in combination with a doubled extinction coefficient for the ^{1}MLCT absorption band.

Experimental Section

Synthesis

General Method for the Synthesis of Ru-NHC complexes: Under argon atmosphere the ligand (2 mmol) and $RuCl_3 \cdot H_2O$ (1 mmol) were propounded in ethylene glycol (10 mL) and the reaction mixture was heated to 180 C for 5 h. After cooling to r.t. a saturated aqueous solution of KPF_6 was added to the mixture resulting in precipitation of the Ru(II) complex. After stirring for another 2 h the suspensions were filtered, and the crude product was purified by column chromatography (Al_2O_3/MeCN).

$[Ru(bip^{NMe2})_2][PF_6]_2$ (C1): Yield: 64% (0.64 mmol); yellow powder. **^{1}H-NMR** (500 MHz, acetonitrile-d3, 30 C, δ [ppm]): 7.94 (d, $^3J_{HH}$ = 1.7 Hz, 4H, CH); 7.03 (s, 4H, CH); 6.94 (d, $^3J_{HH}$ = 1.73 Hz, 4H, CH); 2.67 (s, 12H, CH_3); 2.13 (s, 12H, CH_3). **^{13}C-NMR** (125 MHz, acetonitrile-d3, 30 C, δ [ppm]): 192.6 (Cq); 156.4 (Cq); 151.4 (Cq); 123.4 (CH); 115.9 (CH); 89.4 (CH); 39.8 (CH_3); 35.1 (CH_3). **ESI-MS** (m/z(%)) (MeCN): 333.10 (100) [M^{2+}]; 811.17 (4) [M^{2+} + PF6$^-$]. **IR** (ATR, $\tilde{\nu}$ [cm^{-1}]): 3182 w, 3153 w, 2945 w, 2361 w, 2336 w, 1634 m, 1574 w, 1515 m, 1505 w, 1481 w, 1447 w, 1403 m, 1344 m, 1280 w, 1267 m, 1242 w, 1178 w, 1126 w, 1088 w, 1009 w, 937 m, 876 w, 837 s, 823 s, 804 s, 729 m, 716 m, 684 s, 595 w, 555 s, 488 w, 463 w, 438 w, 381 w, 361 w, 306 w, 281 w, 221 w. **elemental analysis** calculated for $C_{30}H_{36}F_{12}RuN_{12}P_2$: C: 37.70; H: 3.80; N: 17.59; found: C: 37.78; H: 4.13; N: 17.65.

$[Ru(bdmip^{NMe2})_2][PF_6]_2$ (C2): Yield: 68% (0.68 mmol) **^{1}H-NMR** (700 MHz, acetonitrile-d3, 30 C, δ [ppm]): 7.12 (s, 4H, CH); 3.25 (s, 12H, CH_3); 2.64 (s, 12H, CH_3); 2.54 (s, 12H, CH_3); 1.99 (s, 12H, CH_3). **^{13}C-NMR** (176 MHz, acetonitrile-d3, 30 C, δ [ppm]): 193.0 (Cq); 156.0 (Cq); 153.6 (Cq); 127.8 (Cq); 123.9 (Cq); 91.4 (CH); 40.4 (CH_3); 33.3 (CH_3); 11.87 (CH_3); 8.75 (CH_3). **ESI-MS** (m/z(%)) (MeCN): 389.17 (100) [M^{2+}]; 923.31 (18) [M^{2+} + PF_6^-]. **IR** (ATR, $\tilde{\nu}$ [cm^{-1}]): 3170 w, 3116 w, 2935 w, 1616 m, 1571 w, 1537 m, 1444 w, 1394 w, 1332 w, 1226 m, 1180 w, 1139 w, 1097 w, 1068 w, 989 w, 825 s, 740 m, 676 w, 638 w, 555 s, 281 m, 225 w. **elemental analysis**: calculated for $C_{34}H_{44}F_{12}RuN_{12}P_2$: C: 40.36; H: 4.38; N: 16.61; found: C: 40.44; H: 4.70; N: 16.82.

$[Ru(bbp^{NMe2})_2][PF_6]_2$ (C3): Yield: 60% (0.60 mmol) **^{1}H-NMR** (500 MHz, acetonitrile-d3, 30 C, δ [ppm]): 8.26 (d, $^3J_{HH}$ = 8.3 Hz, 4H, CH); 7.48 (t, $^3J_{HH}$ = 8.3 Hz 4H, CH); 7.41 (s, 4H, CH); 7.43 (t, $^3J_{HH}$ = 9.0 Hz, 4H, CH); 7.31 (d, $^3J_{HH}$ = 7.98 Hz, 4H, CH); 3.54 (s, 12H, CH_3); 2.92 (s, 12H, CH_3). **^{13}C-NMR** (125 MHz, acetonitrile-d3, 30 C, δ [ppm]): 202.4 (Cq); 156.6 (Cq); 151.9 (Cq); 136.5 (Cq); 131.1 (Cq); 124.4 (CH); 123.7 (CH); 111.9 (CH); 110.5 (CH); 90.7 (CH); 40.1 (CH_3); 32.3 (CH_3). **ESI-MS** (m/z(%)) (MeCN): 433.14 (100) [M^{2+}]; 426.13 (32) [M^{2+}−CH_3]; 288.7 (7) [M^{3+}].**IR** (ATR, $\tilde{\nu}$ [cm^{-1}]): 3656 w, 2941 w, 2875 w, 1639 m, 1598 w, 1531 m, 1496 m, 1461 m, 1440 m, 1390s, 1334 m, 1317 m, 1292 m, 1232 w, 1182 w, 1161 m, 1091 m, 1022 w, 937 w, 827 s, 784 s, 732 s, 669 m, 630 w, 586 w, 555 s, 428 m, 347 m, 256 m. **elemental analysis** calculated for $C_{46}H_{44}F_{12}RuN_{12}P_2$: C: 47.80; H: 3.84; N: 14.54; found: C: 47.57; H: 3.90; N: 14.65.

$[Ru(bip)_2][PF_6]_2$ (Ref.1): Yield: 25% (0.37 mmol) **^{1}H-NMR** (500 MHz, acetonitrile-d3, 30 C, δ [ppm]): 8.22 (t, 2H, $^3J_{HH}$ = 8.2 Hz, CH) 8.00 (d, 4H, $^3J_{HH}$ = 2.3 Hz, CH); 7.84 (d, 4H, $^3J_{HH}$ = 8.2 Hz, CH); 7.00 (d, 4H, $^3J_{HH}$ = 2.5 Hz, CH); 2.61 (s, 12H, CH_3).

$[Ru(bbp)_2][PF_6]_2$ (Ref.3): **^{1}H-NMR** Yield: 64 % (0.13 mmol) (700 MHz, d_6-acetone) δ (ppm): 8.82 (d, 4H, $^3J_{HH}$ = 8.3 Hz, CH); 8.74 (dd, 2H, $^3J_{HH}$ = 8.9 Hz, $^3J_{HH}$ = 7.8 Hz, CH); 8.56 (d, 4H, $^3J_{HH}$ = 8.4 Hz, CH); 7.85–7.55 (m, 4H, CH); 7.48–7.45 (m, 8H, CH); 3.04 (s, 12H, CH_3). **^{13}C-NMR** (176 MHz, d_6-acetone) δ (ppm): 201.1 (s, Cq, 4C, C); 153.3 (s, Cq, 4C, C); 140.5 (s, 2C, CH); 137.4 (s, Cq, 4C, C); 132.4 (s, Cq, 4C, C); 125.9 (s, 4C, CH); 125.2 (s, 4C, CH); 113.2 (s, 4C, CH); 111.9 (s, 4C, CH); 108.7 (s, 4C, CH); 33.2 (s, 4C, CH_3). **ESI-MS (pos)** (m/z in MeCN) calculated for $[C_{42}H_{34}N_{10}Ru]^{2+}$: 390.1000; found: 390.0984. **elemental analysis** calculated for $C_{42}H_{34}F_{12}N_{10}P_2Ru$: C: 47.15; H: 3.20; N: 13.09; found: C: 46.86; H: 3.40; N: 12.79.

Single crystal diffraction

Crystallographic data were recorded using a Bruker SMART CCD area detector equipped three-cycle diffractometer working with graphite monochromated Mo Kα radiation (λ = 0.71073 Å) at 130(2) K. Structure solutions were carried out by direct methods[32] full matrix least-squares refinement based on F2.[32] All non-hydrogen atoms were refined anisotropically, and hydrogen positions were derived from geometrical reasons and afterward refined at idealized positions riding on the carbon atoms with isotropic displacement parameters Uiso(H) = 1.2Ueq(C) and d(C–H) = 0.96 Å. The methyl groups are idealized with tetrahedral angles in a combined rotating and rigid group refinement with the 1.5- fold isotropic displacement parameters of the equivalent Uij of the corresponding carbon atom.

Cyclic Voltammetry

Potentiometric measurements were performed at r.t. using a PGSTAT 101 potentiostat from Metrohm-Autolab in deoxygenated MeCN with an analyte concentration of 10^{-3} M and [n-Bu_4N][PF_6] of 0.1 M as the inert electrolyte. A platinum working electrode (1 mm diameter), a silver/0.01 M AgNO3 and 0.1 M [n-Bu_4N][PF_6] in MeCN reference electrode, and a platinum pin counter electrode were used in a three-electrode configuration. After measurements, ferrocene (FcH) was added as an internal standard to reference against the FcH/FcH^+ redox couple. The resulting voltammograms were analyzed using the software *Nova 2.1.3*. The reversibility of the redox couples was checked by using the criteria from Nicholson and Shain[33] and the Randles–Sevcik equation.[34]

Spectroelectrochemistry

Spectroelectrochemical measurements were performed at r.t. in an optically transparent cell (d = 4 mm) in deoxygenated MeCN/0.1 M [*n*-Bu_4N][PF_6] and a platinum wire mesh working electrode. Spectral changes during oxidations/reductions were recorded on a Varian Cary 50 spectrophotometer.

UV/Vis Spectroscopy

Steady state absorption spectra were recorded at concentrations of 10^{-5} M on a Specord 50 UV/vis spectrometer from Analytik Jena. Spectroscopic-grade solvents from VWR and quartz cuvettes by Hellma with a path length of 1 cm were used.

Luminescence Measurements (fixed temperature 77 K, r.t.) For steady-state emission spectroscopy solvents of spectroscopic grade were use. Steady-state emission spectra were recorded in 10 mm quartz cuvettes on a Jasco FP8300 or a Horiba Scientific FluoroMax-4 spectrometer. The solutions for the measurements under argon were degassed via the freeze-pump-thaw technique.

Variable temperature emission spectroscopy

VT-steady-state emission spectra were recorded with a FLS1000 spectrometer from Edinburgh Instruments equipped with a cooled photomultiplier detector N-G11 PMT-980 (250–980 nm). A xenon arc lamp Xe2 (450 W) was used for excitation. All samples were dissolved in a mixture of EtOH/MeOH (6 : 4 v/v) and purged with nitrogen for 20 min prior to use. VT-emission measurements were carried out using a liquid nitrogen cooled cryostat Optistat DN from Oxford Instruments.

Singlet Oxygen ($^1O_2$) phosphorescence. $^1O_2$ formation was observed using a FLS1000 spectrometer equipped with a cooled NIR sensitive photomultiplier detector N-G09 PMT-1700 (500–1700 nm) and a xenon arc lamp Xe2 (450 W) as excitation source. The samples were dissolved in MeCN and filled in a 10 mm quartz cuvette for the measurement.

Transient Absorption Spectroscopy

Transient absorption spectra were recorded with a time resolution of about 100 fs employing a pump-probe setup based on a Ti : sapphire laser system (Spitfire Ace PA, Spectra Physics), which operates at a centre wavelength of 800 nm and a repetition rate of 1 kHz.[27] The pump pulses with a center wavelength of 400 nm were obtained by frequency-doubling the Ti : sapphire output in a BBO crystal. For the probe pulses, a white light continuum is generated in a CaF_2 crystal. To avoid effects caused by orientational relaxation, the polarizations of the pump and probe pulses were set to magic angle with respect to each other. Behind the sample, the probe was dispersed by a prism and the spectrally resolved absorption changes were recorded by a CCD array detector. The compounds were dissolved in MeCN under argon and the sample solution was filled into a fused silica cuvette with a thickness of 1 mm.

Nanosecond laser flash photolysis (ns-LFP) and photostability

All solutions for the experiments in this section were prepared in quartz glass cuvettes (1.0 cm path length) using acetonitrile (Fisher Scientific, > 99 %, HPLC purity), purged with argon gas (Nippon 5.0) for 5 min and with the respective optical density adjusted to 0.2 at 355 nm unless otherwise stated in the figure captions.

UV/Vis was measured using a Perkin Elmer LAMBDA 365. For the laser flash photolysis (LFP) measurements an LP980-KS apparatus from Edinburgh Instruments was used. The energy of the 355 nm laser pulse (frequency-tripled Nd-YAG laser from Litron with ~5 ns pulses) was adjusted to 5–12 mJ and measured before and after each series of experiments. Further details are given in the figure captions. A beam expander (Thorlabs) was used to ensure homogenous excitation in the detection volume. Kinetic traces were recorded at a single wavelength with a photomultiplier tube and for measuring transient absorption (TA) or emission spectra an iCCD camera from Andor was employed. All TA spectra were time-integrated for 100 ns. The samples were measured at 20 C using the sample holder TC1 from Quantum Northwest. A 390 nm LED (Kessil Science, PR160 L-390 nm) was used for photostability measurements. The highest LED intensity was selected for these measurements (100 %, 399 mW/cm^2 in 1.0 cm distance).[35]

DFT calculations

All density functional theory (DFT) calculations were carried out using ORCA[36] version 5.0.3. Geometries were optimized using the B97-3c composite scheme.[37] In order to check whether the

ChemPhotoChem

Research Article
doi.org/10.1002/cptc.202300281

Chemistry Europe
European Chemical Societies Publishing

structure is a minimum structure, a frequency calculation was performed and checked for the absence of negative frequencies. UV/Vis spectra were calculated using the time-dependent DFT (TD-DFT) approach as implemented in ORCA. The calculations utilized all electron scalar relativistic basis sets of triple ζ quality,[37,38] and the ZORA[40] approach to account for relativistic effects. The functional of choice for all TD-DFT calculations was the PBE0[41] functional along with the ZORA-def2-TZVP basis set.[38] B3LYP was also tried, but PBE0 gave a better match with the UV/vis spectra. The RIJCOSX[42] approximation implemented in ORCA was used to speed up the hybrid calculations. The tight convergence criterion was imposed on all calculations and the D4 dispersion correction was employed.[43] Stick spectra have been subjected to Gaussian broadening with a fixed FWHM of 15 nm. Spatial distributions of orbitals were visualized using IboView.[44] The analysis of the individual fractions of the molecular orbitals is based on the Löwdin population analysis, which was extracted from the ORCA output file using MOAnalyzer (version 1.3).[45]

Supporting Information

General procedures, ligand synthesis, details of single crystal structure analysis, electrochemistry, additional computational information, additional transient absorption spectra are found in the Supporting Information. Crystallographic data have been deposited at the Cambridge Crystallographic Data Centre and assigned the deposition numbers 2039995 (C1), 2237754 (C2) and 2039996 (C3). Copies are available free of charge via www.ccdc.cam.ac.uk.

Author Contributions

Methodology, Writing – Original Draft, DFT Calculations and Analysis, Supporting Synthesis (Ref. [1]), L. F.; Synthesis (C1–C3), Writing – Prior Draft Y. V.; Femtosecond Transient Absorption Spectroscopy, Writing – Review & Editing M. L.; Variable Temperature Emission Spectroscopy, Singlet Oxygen Phosphorescence Measurements R. N.; Nanosecond Laser Flash Photolysis Measurements M.-S. B.; Femtosecond Transient Absorption Spectroscopy A. K.; Single-Crystal Measurements and Analyses R. S.; Prior DFT Calculations P. M.; Spectroelectrochemistry Measurements, A. N.; Supporting Synthesis (Ref. [3]) P. D.; Writing – Review & Editing S.L.; Writing – Review & Editing C. K.; Writing – Review & Editing K. H. Conceptual design of the study, Writing – Review & Editing, Project Administration M. B. All authors have read and agreed to the published version of the manuscript.

Acknowledgements

L. F. thanks the "Fonds der Chemischen Industrie" for a Kekulé grant. The German research foundation (DFG) is kindly acknowledged for financial support in the frame of the Priority programme SPP 2102 (BA 4467/7-2, HE2778/14-2 and LO 714/11-2) and for grant INST 247/1018-1 FUGG to K. H. The Paderborn Center for Parallel Computing PC2 is gratefully acknowledged for generous grants of computer time. Open Access funding enabled and organized by Projekt DEAL.

Conflict of Interests

The authors declare no conflict of interest.

Data Availability Statement

The data that support the findings of this study are available from the corresponding author upon reasonable request.

Keywords: Density functional calculations · Ruthenium complexes · Photophysics · Substituent effects · Time-resolved spectroscopy

[1] a) M. Baroncini, M. Canton, L. Casimiro, S. Corra, J. Groppi, M. La Rosa, S. Silvi, A. Credi, *Eur. J. Inorg. Chem.* **2018**, *42*, 4589–4603; b) P.-A. Blanche, *Materials* **2021**, *14*, 585; c) A. Jain, N. T. Garrett, Z. P. Malone, *Photochem. Photobiol.* **2021**, *98*, 6–16; d) N. Noma, T. Tsuzuki, Y. Shirota, *Adv. Mater.* **1995**, *7*, 647–648; e) L. Xu, F. Mou, H. Gong, M. Luo, J. Guan, *Chem. Soc. Rev.* **2017**, *46*, 6905–6926.
[2] V. Balzani, S. Campagna, *Photochemistry and Photophysics of Coordination Compounds I*, Springer, Berlin, Heidelberg, **2007**, Vol. 280.
[3] a) E. A. Medlycott, G. S. Hanan, *Chem. Soc. Rev.* **2005**, *34*, 133–142; b) M. Abrahamsson, H.-C. Becker, L. Hammarström, *Dalton Trans.* **2017**, *46*, 13314–13321; c) D. Kuciauskas, J. E. Monat, R. Villahermosa, H. B. Gray, N. S. Lewis, J. K. McCusker, *J. Phys. Chem. B* **2002**, *106*, 9347–9358.
[4] C. Kreitner, K. Heinze, *Dalton Trans.* **2016**, *45*, 13631–13647.
[5] M. Montalti, A. Credi, L. Prodi, M. T. Gandolfi, *Handbook of Photochemistry*, CRC Press, **2006**.
[6] a) A. Amini, A. Harriman, A. Mayeux, *Phys. Chem. Chem. Phys.* **2004**, *6*, 1157–1164; b) C. Kreitner, E. Erdmann, W. W. Seidel, K. Heinze, *Inorg. Chem.* **2015**, *54*, 11088–11104.
[7] a) E. C. Constable, C. E. Housecroft, A. C. Thompson, P. Passaniti, S. Silvi, M. Maestri, A. Credi, *Inorg. Chim. Acta* **2007**, *360*, 1102–1110; b) D. J. Wasylenko, C. Ganesamoorthy, M. A. Henderson, B. D. Koivisto, H. D. Osthoff, C. P. Berlinguette, *J. Am. Chem. Soc.* **2010**, *132*, 16094–16106; c) G. Albano, V. Balzani, E. C. Constable, M. Maestri, D. R. Smith, *Inorg. Chim. Acta* **1998**, *277*(2), 225–231; d) F. Barigelletti, L. Flamigni, G. Calogero, L. Hammarström, J.-P. Sauvage, Collin, Jean-Paul, *Chem. Commun.* **1998**, *7(21)*, 2333–2334.
[8] S. U. Son, K. H. Park, Y.-S. Lee, B. Y. Kim, C. H. Choi, M. S. Lah, Y. H. Jang, D.-J. Jang, Y. K. Chung, *Inorg. Chem.* **2004**, *43*, 6896–6898.
[9] H.-J. Park, Y. K. Chung, *Dalton Trans.* **2012**, *41*, 5678–5686.
[10] H.-J. Park, S. Yoo, I.-S. Shin, Y. K. Chung, J. Kim, *Electroanalysis* **2013**, *25*, 1111–1115.
[11] M. Poyatos, J. A. Mata, E. Falomir, R. H. Crabtree, E. Peris, *Organometallics* **2003**, *22*, 1110–1114.
[12] M. Maestri, N. Armaroli, V. Balzani, E. C. Constable, C. Thompson, M. W. Alexander, *Inorg. Chem.* **1995**, *34*, 2759–2767.
[13] H.-J. Park, K. H. Kim, S. Y. Choi, H.-M. Kim, W. I. Lee, Y. K. Kang, Y. K. Chung, *Inorg. Chem.* **2010**, *49*, 7340–7352.
[14] a) C. M. Boudreaux, N. P. Liyanage, H. Shirley, S. Siek, D. L. Gerlach, F. Qu, J. H. Delcamp, E. T. Papish, *Chem. Commun.* **2017**, *53*, 11217–11220; b) S. Das, R. R. Rodrigues, R. W. Lamb, F. Qu, E. Reinheimer, C. M. Boudreaux, C. E. Webster, J. H. Delcamp, E. T. Papish, *Inorg. Chem.* **2019**, *58*, 8012–8020; c) L.-H. Chung, K.-S. Cho, J. England, S.-C. Chan, K. Wieghardt, C.-Y. Wong, *Inorg. Chem.* **2013**, *52*, 9885–9896.
[15] a) T. Duchanois, L. Liu, M. Pastore, A. Monari, C. Cebrián, Y. Trolez, M. Darari, K. Magra, A. Francés-Monerris, E. Domenichini, M. Beley, X. Assfeld, S. Haacke, P. C. Gros, *Inorganics* **2018**, *6*, 63; b) S. Kaufhold, K. Wärnmark, *Catalysts* **2020**, *10*, 132; c) P. Dierks, Y. Vukadinovic, M. Bauer, *Inorg. Chem. Front.* **2022**, *9*, 206–220; d) O. S. Wenger, *Chemistry* **2019**, *25*, 6043–6052; e) L. H. M. de Groot, A. Ilic, J. Schwarz, K. Wärnmark, *J. Am. Chem. Soc.* **2023**, *145*, 9369–9388.

[16] a) W. A. Herrmann, *Angew. Chem. Int. Ed.* **2002**, *41*, 1290–1309; b) D. Enders, T. Balensiefer, *Acc. Chem. Res.* **2004**, *37*, 534–541; c) D. M. Khramov, V. M. Lynch, C. W. Bielawski, *Organometallics* **2007**, *26*, 6042–6049.
[17] a) A. Breivogel, M. Park, D. Lee, S. Klassen, A. Kühnle, C. Lee, K. Char, K. Heinze, *Eur. J. Inorg. Chem.* **2014**, *2014*(2) 288–295; b) A. Breivogel, M. Meister, C. Förster, F. Laquai, K. Heinze, *Chem. Eur. J.* **2013**, *19*, 13745–13760; c) G. J. Irvine, S. Rajesh, M. Georgiadis, W. A. Phillip, *Environ. Sci. Technol.* **2013**, *47*, 13745–13753; d) K. Heinze, K. Hempel, *Chem. Eur. J.* **2009**, *15*, 1346–1358.
[18] Y. Vukadinovic, L. Burkhardt, A. Päpcke, A. Miletic, L. Fritsch, B. Altenburger, R. Schoch, A. Neuba, S. Lochbrunner, M. Bauer, *Inorg. Chem.* **2020**, *59*, 8762–8774.
[19] L. Liu, T. Duchanois, T. Etienne, A. Monari, M. Beley, X. Assfeld, S. Haacke, P. C. Gros, *Phys. Chem. Chem. Phys.* **2016**, *18*, 12550–12556.
[20] E. J. Viere, A. E. Kuhn, M. H. Roeder, N. A. Piro, W. S. Kassel, T. J. Dudley, J. J. Paul, *Dalton Trans.* **2018**, *47*, 4149–4161.
[21] V. Balzani, A. Juris, M. Venturi, *Chem. Rev.* **1996**, *96*(2), 759–833.
[22] T. Duchanois, T. Etienne, C. Cebrián, L. Liu, A. Monari, M. Beley, X. Assfeld, S. Haacke, P. C. Gros, *Eur. J. Inorg. Chem.* **2015**, *2015*, 2469–2477.
[23] R. L. Lord, M. M. Allard, R. A. Thomas, O. S. Odongo, H. B. Schlegel, Y.-J. Chen, J. F. Endicott, *Inorg. Chem.* **2013**, *52*, 1185–1198.
[24] A. V. Lesikar, *J. Chem. Phys.* **1977**, *66*, 4263–4276.
[25] A. J. Lees, *Comments Inorg. Chem.* **1995**, *17*, 319–346.
[26] O. Stern, M. Volmer, *Phys. Z.* **1919**, *20*, 193–188.
[27] A. Päpcke, A. Friedrich, S. Lochbrunner, *J. Phys. Condens. Matter* **2019**, *32*, 153001.
[28] A. C. Sell, J. C. Wetzel, M. Schmitz, A. W. Maijenburg, G. Woltersdorf, R. Naumann, C. Kerzig, *Dalton Trans.* **2022**, *51*, 10799–10808.
[29] A. Juris, V. Balzani, F. Barigelletti, S. Campagna, P. Belser, A. von Zelewsky, *Coord. Chem. Rev.* **1988**, *84*, 85–277.
[30] A. R. Naziruddin, C.-L. Kuo, W.-J. Lin, W.-H. Lo, C.-S. Lee, B.-J. Sun, A. H. H. Chang, W.-S. Hwang, *Organometallics* **2014**, *33*, 2575–2582.
[31] D. Hernández-Castillo, R. E. P. Nau, M.-A. Schmid, S. Tschierlei, S. Rau, L. González, *Angew. Chem. Int. Ed.* **2023**, *62*, e202308803.
[32] G. M. Sheldrick, *Acta Crystallogr. Sect. A* **2008**, *64*, 112–122.
[33] a) J. Heinze, *Angew. Chem.* **1984**, *96*, 823–840; b) R. S. Nicholson, I. Shain, *Anal. Chem.* **1964**, *36*, 706–723.
[34] J. E. B. Randles, *Trans. Faraday Soc.* **1948**, *44*, 322.
[35] Kessil, to be found under https://kessil.com/products/science_PR160 L. php (accessed: 03. 08. 2023).
[36] a) F. Neese, *WIREs Comput. Mol. Sci.* **2012**, *2*, 73–78; b) F. Neese, *WIREs Comput. Mol. Sci.* **2018**, *8*, e1327.
[37] J. G. Brandenburg, C. Bannwarth, A. Hansen, S. Grimme, *J. Chem. Phys.* **2018**, *148*, 64104.
[38] F. Weigend, R. Ahlrichs, *Phys. Chem. Chem. Phys.* **2005**, *7*, 3297–3305.
[39] a) F. Weigend, *Phys. Chem. Chem. Phys.* **2006**, *8*, 1057–1065; b) D. A. Pantazis, X.-Y. Chen, C. R. Landis, F. Neese, *J. Chem. Theory Comput.* **2008**, *4*, 908–919; c) D. A. Pantazis, F. Neese, *J. Chem. Theory Comput.* **2009**, *5*, 2229–2238; d) D. A. Pantazis, F. Neese, *J. Chem. Theory Comput.* **2011**, *7*, 677–684; e) D. A. Pantazis, F. Neese, *Theor. Chem. Acc.* **2012**, 131.
[40] C. van Wüllen, *J. Chem. Phys.* **1998**, *109*, 392–399.
[41] C. Adamo, V. Barone, *The Journal of Chemical Physics* **1999**, *110*, 6158–6170.
[42] F. Neese, F. Wennmohs, A. Hansen, U. Becker, *Chem. Phys.* **2009**, *356*, 98–109.
[43] E. Caldeweyher, S. Ehlert, A. Hansen, H. Neugebauer, S. Spicher, C. Bannwarth, S. Grimme, *J. Chem. Phys.* **2019**, *150*, 154122.
[44] G. Knizia, J. E. M. N. Klein, *Angew. Chem.* **2015**, *127*, 5609–5613.
[45] M. U. Delgado-Jaime, S. DeBeer, *J. Comput. Chem.* **2012**, *33*, 2180–2185.

Manuscript received: October 31, 2023
Revised manuscript received: December 7, 2023
Accepted manuscript online: December 8, 2023
Version of record online: ■■, ■■

RESEARCH ARTICLE

Amine substitution in the backbone of a room temperature (r.t.) luminescent C^N^C ruthenium(II) complex alters the excited energy landscape such that at low temperature (l.t.) the typical luminescent relaxation of the ^{3}MLCT (metal-to-ligand charge transfer) to the ^{1}GS (ground state) can occur, but at r.t. a dark relaxation pathway across the ^{3}MC (metal centered) state is activated and a higher photostability is observed.

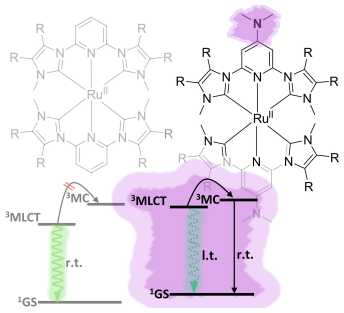

*L. Fritsch, Dr. Y. Vukadinovic, Dr. M. Lang, Dr. R. Naumann, M.-S. Bertrams, A. Kruse, Dr. R. Schoch, Dr. P. Müller, A. Neuba, Dr. P. Dierks, Prof. Dr. S. Lochbrunner, Prof. Dr. C. Kerzig, Prof. Dr. K. Heinze, Prof. Dr. M. Bauer**

1 – 12

Chemical and photophysical properties of amine functionalized bis-NHC-pyridine-Ru^{II} complexes

CHAPTER 3

IRON(III)-COMPLEXES WITH N-PHENYLPYRAZOLE-BASED LIGANDS

Noble metal complexes are prominent for their superior photophysical properties as it was shown in Chapter 2. However, especially from an economic and ecological point of view, the replacement of these metals by abundant metals such as iron is desirable. Nonetheless, the low ligand field splitting of the lighter 3d metals presents a challenging task for maintaining favorable photophysical properties, typically characterized by a short excited state lifetime and lack of fluorescence due to non-radiative deactivation by low-lying MC states. In this work, the influence of N-phenylpyrazole-based ligands on the electronic structure of the iron(III) centre was investigated using UV-Vis spectroscopy, cyclic voltammetry and advanced X-ray spectroscopy in combination with (TD-)DFT calculations. It was possible to show how different electron-withdrawing and donating groups in the backbone of the phenyl affect the different energy levels and thus the photochemical properties.

Participations in this publication

T. Hirschhausen: Methodology, synthesis, writing - original draft preparation;
L. Fritsch: DFT calculations, X-ray spectroscopy, writing;
F. Lux: supporting synthesis; J. Steube: writing-review;
R. Schoch: single-crystal measurements and analyses;
A. Neuba: spectroelectrochemistry measurements; H. Egold: NMR measurements;
M. Bauer: Writing - Review and Editing, Project Administration.

Reprinted from
Iron(III)-Complexes with N-Phenylpyrazole-Based Ligands
Tanja Hirschhausen, Lorena Fritsch, Franziska Lux, Jakob Steube, Roland Schoch, Adam Neuba, Hans Egold and Matthias Bauer, *Inorganics* **2023**, *11(7)*, 282, DOI:10.3390/inorganics11070282.

Supplementary Information for this publication is found in the Appendix A.2.

inorganics

MDPI

Article

Iron(III)-Complexes with *N*-Phenylpyrazole-Based Ligands

Tanja Hirschhausen [1,†], Lorena Fritsch [1,†], Franziska Lux [1], Jakob Steube [1], Roland Schoch [1], Adam Neuba [1], Hans Egold [1] and Matthias Bauer [1,2,*]

[1] Institute of Inorganic Chemistry, Paderborn University, 33098 Paderborn, Germany; tanja.hirschhausen@upb.de (T.H.); lorena.fritsch@upb.de (L.F.); lux.franziska@web.de (F.L.); jakob.steube@upb.de (J.S.); roland.schoch@upb.de (R.S.); adam.neuba@upb.de (A.N.); hans.egold@upb.de (H.E.)
[2] Center for Sustainable Systems Design, Paderborn University, 33100 Paderborn, Germany
* Correspondence: matthias.bauer@upb.de
† These authors contributed equally to this work.

Abstract: The use of iron as a replacement for noble metals in photochemical and photophysical applications is challenging due to the typically fast deactivation of short-lived catalytically active states. Recent success of a cyclometalated iron(III) complex utilizing a bis-tridentate ligand motif inspired the use of phenyl-1*H*-pyrazole as a bidentate ligand. Five complexes using the tris(1-phenylpyrazolato-*N*,C^2)iron(III) complex scaffold are presented. In addition to the parent complex, four derivatives with functionalization in the meta-position of the phenyl ring are thoroughly investigated by single crystal diffractometry, UV-Vis-spectroscopy, and cyclic voltammetry. Advanced X-ray spectroscopy in the form of X-ray absorption and emission spectroscopy allows unique insights into the electronic structure as well as DFT calculations. The ligand design leads to overlapping MLCT and LMCT absorption bands, and emissive behavior is suppressed by low-lying MC states.

Keywords: photosensitizer; iron(III) complex; cyclometalation; phenyl-1*H*-pyrazol

Citation: Hirschhausen, T.; Fritsch, L.; Lux, F.; Steube, J.; Schoch, R.; Neuba, A.; Egold, H.; Bauer, M. Iron(III)-Complexes with *N*-Phenylpyrazole- Based Ligands. *Inorganics* **2023**, *11*, 282. https://doi.org/10.3390/inorganics11070282

Academic Editor: László Kótai

Received: 5 June 2023
Revised: 20 June 2023
Accepted: 25 June 2023
Published: 29 June 2023

1. Introduction

Noble metal complexes based on ruthenium(II) [1,2], osmium(II) [3], and iridium(III) [4,5] show a long history of photophysical and photochemical applications due to their stability and activity. However, the scarcity and high costs of noble metals prevent a decentral application in water splitting or photocatalysis [6]. It may therefore be appropriate to shift the focus towards more abundant, less expensive, and, at best, more environmentally friendly alternatives. Iron is the dream candidate to fulfill these requirements. However, its use in photoactive complexes requires the development of new ligand designs for catalytically active states, since deactivation by the rapid population of inactive states usually occurs [7,8]. If this major problem can be solved, iron complexes could enable photocatalytic reactions through high-energy states with sufficiently long lifetimes. In d^6 systems, this is typically a metal-to-ligand charge transfer (MLCT) state [9]. These are the active states in octahedral noble metal complexes with polypyridyl-based ligands, such as $[Ru(tpy)_2]^{2+}$ (tpy = 2,6-Bis(2-pyridyl)pyridine) and $[Ru(bpy)_3]^{2+}$ (bpy = 2,2′-bipyridinyl) [10–12]. Analogous nitrogen-coordinated iron(II)-d^6 complexes suffer from short MLCT lifetimes in the 100 fs range due to fast relaxation into low-lying metal-centered (MC) states induced by the inherent small ligand field splitting of 3d-metals [13,14].

Consequently, strategies in ligand design target the stabilization of photoactive long-lived charge transfer states and the destabilization of MC states. Various attempts to achieve this goal employ a mix of strong σ-donor and π-acceptor ligands [14]. Strong σ-donating groups promote higher ligand field splitting by destabilization of the antibonding e_g*. In this context, *N*-heterocyclic carbenes (NHCs) were extensively applied due to their strong σ-donating character [15]. Starting from the bis-tridentate prototype NHC iron(II) complex

$[Fe(pbmi)_2]^{2+}$ (pbmi = 2,6-bis(imidazol-2-ylidene)pyridine), donor/acceptor properties could be modified by the introduction of different functional groups [14,16,17]. Nevertheless, the MLCT lifetimes of these complexes remain below 50 ps; therefore, a breakthrough using CˆNˆC ligands could barely be achieved [8].

In contrast, the substitution of the central pyridine in the CˆNˆC ligand scaffold by a phenylene to obtain a CˆCˆC ligand significantly alters the properties of the resulting complex. The cyclometalated bis-tridentate iron(III) complex $[Fe(ImP)_2][PF_6]$ (HImP = 1,1′-(1,3-phenylene)bis(3-methyl-1-imidazol-2-ylidene)) exhibits dual emission from ligand-to-metal charge transfer (^{2}LMCT) with a lifetime of 240 ps and a ^{2}MLCT state lifetime of over 4 ns [18]. In general, iron(III) complexes in a low-spin $^2T_2$-ground state and a strong donor environment lead to the population of ^{2}LMCT states, from which spin-allowed luminescence occurs [19,20]. $^{4/6}$MC states could interfere in this deactivation pathway if they are energetically favored [21,22].

Despite recent progress using bis-tridentate coordination environments, bidentate ligands offer complexes with higher symmetry, resulting in a stronger ligand field [8,19,23]. Accordingly, in Ru(II) complexes for example, a comparison of $[Ru(tpy)_2]^{2+}$ and $[Ru(bpy)_3]^{2+}$ reveals a prolonged and much more intense luminescence at room temperature for the bipyridine complex [24]. This is reflected in $[Fe(btz)_3]^{2+}$ (btz = 3,3′-dimethyl-1,1′-bis(p-tolyl)-4,4′-bis(1,2,3-triazol-5-ylidene)), a hexa-carbene iron(II) complex with a ^{3}MLCT lifetime of 528 ps, which is an order of magnitude longer than the lifetime of previously discussed bis-tridentate CˆNˆC complexes [25]. Its iron(III) congener $[Fe(btz)_3]^{3+}$ was the first iron complex to show the aforementioned ^{2}LMCT emission, with a lifetime of 100 ps [19].

Consequently, the transfer of the cyclometalation approach to bidentate ligands suggests phenylpyrazole (ppz) as one possible ligand. It was already successfully employed in iridium complexes, resulting in $Ir(ppz)_3$ [26]. Although the base–metal complexes $Co(ppz)_3$ and $Fe(ppz)_3$ have also been reported, no spectroscopic analyses were conducted for the latter [27,28]. Bridging this gap by revisiting this pristine complex and further investigating its functionalization in the meta-position of the phenyl ring relative to the iron center with electron-withdrawing trifluoromethyl groups and electron-donating methoxy groups, as well as the extension of the aromatic system with phenyl and naphthalene, is the key element of this study.

2. Results

2.1. Synthesis and Characterization

The ligands were synthesized as reported in the literature by a reaction between the functionalized phenyl-bromide and pyrazole in a copper-catalyzed *N*-arylation under mild conditions, resulting in high-yield product formation (>90%) [29,30]. The synthesis of the complexes is based on the literature and involves the two steps of orthometalation and transmetalation [27,28,31]. The orthometalated ligands were obtained by refluxing the proligand with an ethylmagnesium bromide solution (EtMgBr in THF) for 24 h in THF. $FeBr_2(THF)_{1.5}$ was used as the iron precursor, which was prepared in situ as described in the literature and added to the ligand solution at −80 °C, thereby initiating the transmetalation [32]. The synthesis is displayed in Figure 1 (top), exemplarily for tris(2-phenylpyrazolato-*N*,C^2)iron(III) (**Fe(ppz)$_3$**). Functionalized derivatives are also shown in Figure 1 (bottom).

Workup under atmospheric conditions with an aqueous ammonium chloride solution removed bromide-containing by-products and was followed by column chromatography. After isolation of the yellow (**Fe(ppz)$_3$, Fe(CF$_3$ppz)$_3$**) or red (**Fe(bppz)$_3$, Fe(naphpz)$_3$, Fe(MeOppz)$_3$**) solids, the air- and moisture-stable products were dried under vacuum and obtained in elemental-analysis purity, albeit in low yields (<15%). These can be explained firstly by the disproportion mechanism leading to the product formation and secondly by various, unstable coordination products apart from the desired complexes [26–28].

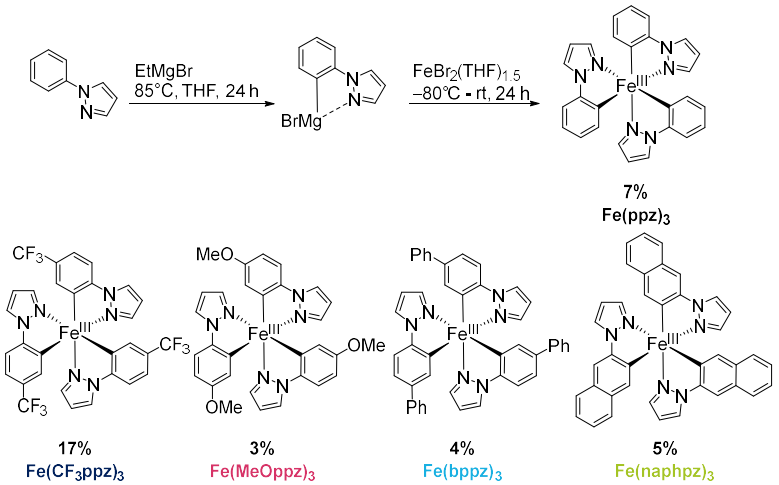

Figure 1. (**Top**) Reaction pathway for the synthesis of pyrazole-based iron(III) complexes, exemplary for tris(1-phenylpyrazolato-*N*,$C^{2'}$)iron(III) (**Fe(ppz)$_3$**). (**Bottom**) Structures of tris(1-(4-(trifluoromethyl)phenyl)pyrazolato-*N*,C^2)iron(III) (**Fe(CF$_3$ppz)$_3$**), tris(1-(([1,1′-biphenyl])-4-yl)phenyl)pyrazolato-*N*,C^2)iron(III) **(Fe(bppz)$_3$)**, tris(1-(naphthalen-2-yl)pyrazolato-*N*,C^2)iron(III) **Fe(naphpz)$_3$**, and tris(1-(4-methoxyphenyl)pyrazolato-*N*,C^2)iron(III) (**Fe(MeOppz)$_3$**), with their respective yields.

Single crystals suitable for X-ray diffraction were obtained by diffusion of cyclopentane into a solution of the respective complex in DCM. The exemplary crystal structure of **Fe(ppz)$_3$** is shown in Figure 2 (top), and crystallographic data for the other complexes are summarized in the Supplementary Information. All complexes show a distorted octahedral geometry with C_3 symmetry. While complexes with tris-bidentate ligands in general allow the formation of both facial (*fac*) and meridional (*mer*) isomers, only the formation of ***fac*-Fe(R-ppz)$_3$** is observed in all complexes' crystals [27,33,34]. This is most likely due to the trans effect, which leads to an enthalpically favored *fac*-isomer as in Co(ppz)$_3$ and other bidentate iridium, zinc, and iron complexes [27,35,36].

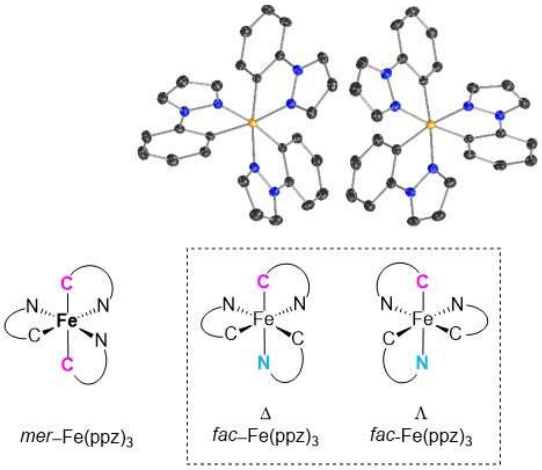

Figure 2. (**Top**) Single crystal structure of **Fe(ppz)$_3$**, displayed with 50% probability for the anisotropic displacement ellipsoids, hydrogen atoms omitted for clarity; (**Bottom**) *mer*-**Fe(ppz)$_3$** and *fac*-**Fe(ppz)$_3$** (with Δ- and Λ-enantiomers).

The *fac*-isomer allows for the formation of both Δ- and Λ-enantiomers, which were observed in direct adjacency within one unit cell. This was present in the structures of all complexes. Yet, it was not possible to isolate and quantify the enantiomer ratios.

Due to the racemic mixture, the three discrete phenylpyrazole-based ligands are crystallographically inequivalent, and the corresponding Fe-N and Fe-C bond lengths were therefore averaged. The key structural parameters are summarized in Table 1, which are in good agreement with the results obtained from DFT calculations (Table S17).

Table 1. Crystallographic data for the investigated iron(III) complexes; averaged over all binding distances.

Complex	$d_{Ø}$ (Fe-N) (Å)	$d_{Ø}$ (Fe-C) (Å)	∢Chelate Bite Angle (°)	∢$(C\text{-}Fe\text{-}N)_{axial}$ (°)
Fe(ppz)$_3$	2.0030(15)	1.9508(13)	87.07(7)	171.54(7)
Fe(CF$_3$ppz)$_3$	2.0075(15)	1.9520(16)	85.88(6)	170.46(6)
Fe(MeOppz)$_3$	2.0129(15)	1.9512(13)	94.52(5)	170.89(5)
Fe(bppz)$_3$	2.0122(7)	1.9536(7)	91.68(1)	172.90(1)
Fe(naphpz)$_3$	2.0134(12)	1.9530(17)	93.59(7)	169.99(7)

The Fe-C bonds of the presented complexes are about 0.05 Å shorter than the Fe-N bonds, probably due to the stronger donor properties plus π-accepting properties of the carbon. All bond lengths are approximately identical to those of $Co(ppz)_3$ [27]. Within the investigated set of compounds, the Fe-C bond lengths remain nearly identical; thus, the influence of the meta-substituents seems negligible. Nevertheless, the Fe-N bond length and chelate bite angles show slight variations in dependence of the different functional groups. The shortest Fe-N bonds and smallest bite angles are observed for **Fe(ppz)$_3$** (2.0030(15) Å, 87.07(7)°) and **Fe(CF$_3$ppz)$_3$** (2.0075(15) Å, 85.88°), while **Fe(MeOppz)$_3$** and **Fe(naphpz)$_3$** exhibit the longest Fe-N bonds (2.0129(15) Å and 2.0134(12) Å, respectively) and the largest bite angles (94.52(5)°, 93.59(7)°). Apparently, the resonance effect of the functional groups affects both Fe-N bond length and the chelate bite angle by altering electron density on the coordinating nitrogen. This would explain the similar bond lengths in **Fe(ppz)$_3$** and **Fe(CF$_3$ppz)$_3$**, since the trifluoromethyl group shows only minor resonance effects, whereas both the methoxy and naphthyl moieties show strong resonance effects. Therefore, the overall electron density on the ligand is increased, resulting in an elongated Fe-N bond and a higher chelate bite angle. In **Fe(bppz)$_3$** with a bite angle of 91.68(1)°, a rotation of the phenyl group to reduce the angular strain results in a weaker overlap of the π orbitals. Therefore, a less pronounced resonance effect is observed, resulting in shorter Fe-N bonds and smaller bite angles compared to **Fe(MeOppz)$_3$** and **Fe(naphpz)$_3$**. Influences due to steric effects are possible, but unlikely in this context. They may play a role in the C-Fe-N angle, which is largest in the unfunctionalized compound (171.54(7)°) and smallest in **Fe(naphpz)$_3$** (169.99(7)°), possibly due to repulsion of the ligands with the rigid naphthyl groups.

The presence of the +III oxidation state of iron could also be confirmed by NMR-spectroscopy (see Supplementary Information for further details), where relatively sharp resonances with a broad range of chemical shifts between 13.54 ppm and –75.20 ppm are observed. Assignment of ^{1}H- and ^{13}C-NMR signals could be achieved by various pulse sequences for paramagnetic compounds [37]. The chemical shifts of the complexes show an alternating pattern of the ^{13}C resonances for both rings equally. An influence of the electron density distribution (Figure S56), as well as a resonance effect, cannot be excluded. Drastic proton resonance shifts of up to –75.20 ppm are observed for the ortho-positions of the cyclometalating phenylene, directly adjacent to the paramagnetic center. Interestingly, strong shielding of the protons adjacent to cyclometalating functions is also observed in diamagnetic complexes due to the proximity to the metal center and can be used as an indicator for successful cyclometallation [38–42]. The protons on the pyrazolyl-moiety are less affected, presumably due to the nitrogen atoms inhibiting the effects of the unpaired

electron originating from the iron. Additionally, the pyrazole, contrary to the phenylene, is not bound covalently to the iron center, which may also reduce the paramagnetic effects.

2.2. Cyclic Voltammetry and Optical Spectroscopy

The redox properties of the investigated complexes were investigated by cyclic voltammetry in MeCN (Figure 3). The measured solutions (10^{-3} M) of the individual compounds contained tetrabutylammonium hexafluorophosphate ($[Bu_4N]PF_6$) in 0.1 M concentration as an electrolyte. The values reported in the following are referenced against Fc/Fc^+. The key results are summarized in Table 2.

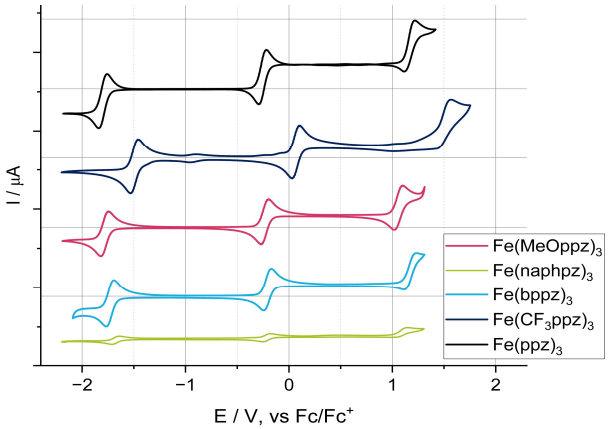

Figure 3. Cyclic voltammograms of the five investigated complexes (10^{-3} M) in MeCN with 0.1 M $[Bu_4N]PF_6$ as electrolyte at a scan rate of 100 mV/s under light exclusion.

Table 2. Electrochemical [a] and electronic [b] and properties of the complexes.

Complex	$E_{1/2}$ $Fe^{II/III}$ (V)	$E_{1/2}$ $Fe^{III/IV}$ (V)	$E_{1/2}$ (Ligand) (V)	ΔE_{LMCT} [e] (V)	$\lambda_{abs\text{-}max}$ (nm) (ε (cm^{-1} M^{-1}))
Fe(ppz)$_3$	−1.80 (rev)	−0.26 (rev)	1.17 (irrev)	2.97 (418 nm)	109 (6.18) 346 (1.63) 450 (0.64) (λ_{max} = 522) [c]
Fe(CF$_3$ppz)$_3$	−1.50 (rev)	0.07 (rev)	1.54 [d] (irrev)	3.04 (408 nm)	293 (2.82) 350 (0.61) 417 (0.38) (λ_{max} = 530) [c]
Fe(MeOppz)$_3$	−1.78 (rev)	−0.23 (rev)	1.11 (irrev)	2.89 (429 nm)	290 (6.45) 356 (0.62) 453 (0.39) (λ_{max} = 580) [c]
Fe(bppz)$_3$	−1.73 (rev)	−0.21 (rev)	1.17 (irrev)	2.90 (428 nm)	277 (2.99) 343 (0.68) 440 (0.45) (λ_{max} = 540) [c]
Fe(naphpz)$_3$	−1.68 (rev)	−0.22 (rev)	1.08 (irrev)	2.76 (449 m)	284 (3.35) 362 (0.93) 442 (0.68) (λ_{max} = 590) [c]

[a] Concentration of 10^{-3} M in MeCN with 0.1 M $[Bu_4N]PF_6$ as electrolyte. [b] Molarity of 10^{-5} M in BuCN. [c] λ_{max} = maximal value of absorption wavelength. [d] Anodic peak potential. [e] Calculated from the difference of $E_{1/2}$(ligand) and $E_{1/2}(Fe^{II/III})$.

Three redox processes were identified in the potential window for all complexes. In the range of −0.26 to 0.07 V, transitions are observed that can be attributed to an iron(III/IV) redox process [18,28,43]. These values are similar to those found for the aforementioned $[Fe(ImP)_2]^{2+}$ (0.08 V), a compound containing two cyclometalating moieties [18]. Functionalization of the meta-position in the phenyl unit does not result in significant changes in the

Inorganics **2023**, *11*, 282

iron(III/IV) redox potentials relative to **Fe(ppz)$_3$**, with the exception of **Fe(CF$_3$ppz)$_3$**. Here, an anodic shift of the oxidation potential is observed, in agreement with a stabilization of the metal-based levels by the electron-withdrawing CF_3 group. The same behavior is found for the iron(II/III) redox processes, which are observed between −1.50 and −1.80 V.

Above potentials of 1 V, irreversible ligand-based oxidation takes place. Although these processes are irreversible, the values can be used to discuss the influence of the different substituents on the electron density in the ppz ligand scaffold. While **Fe(bppz)$_3$** shows the same value as **Fe(ppz)$_3$**, the cathodically shifted oxidation potentials in **Fe(MeOppz)$_3$** and **Fe(naphpz)$_3$** indicate an increased electron density on the coordinating phenylene. This is consistent with the effects observed in the crystal structures, where increased electron density leads to increased Fe-N bond lengths. Consequently, **Fe(CF$_3$ppz)$_3$** shows the most anodically shifted ligand oxidation. From the difference in the ligand oxidation potential and the iron(II/III) transition, electrochemical bandwidths for an LMCT transition can be obtained. These band gaps reflect the same trends since all complexes exceed the band gap of $[Fe(ImP)_2]^{2+}$ (2.47 V) significantly. The highest ΔE values are observed for **Fe(ppz)$_3$** (2.97 V) and **Fe(CF$_3$ppz)$_3$** (3.04 V).

To confirm these results, UV-Vis spectra were recorded in butyronitrile (BuCN) due to the superior stability of the complexes in this solvent (vide infra) and are shown in Figure 4.

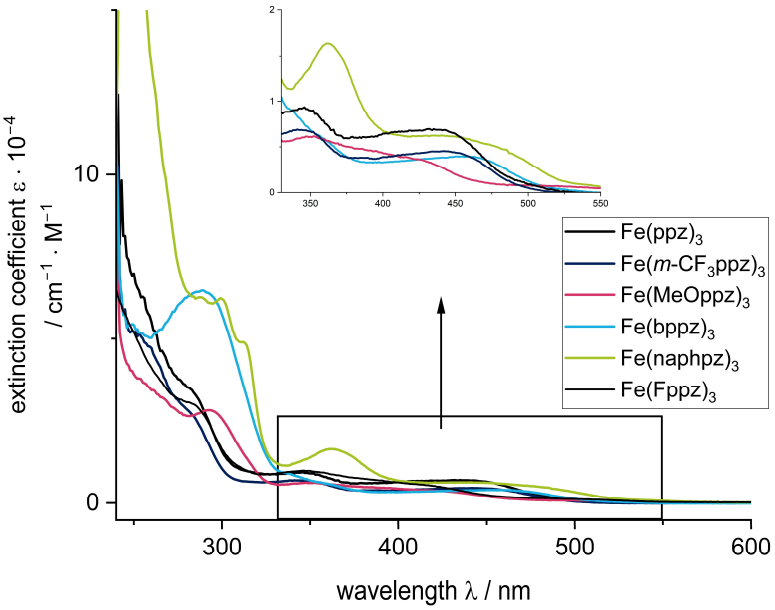

Figure 4. Absorption spectra in BuCN for the investigated compounds. Inset: Enhancement of the 330 to 550 nm absorption region.

The spectra can be divided into three regions. In the high-energy region below 325 nm, intense absorption bands can be observed. These are attributed to π–π* transitions. Consequently, **Fe(bppz)$_3$** and **Fe(naphpz)$_3$** show the highest intensities due to the extended π-systems.

Between 350 and 400 nm, the complexes exhibit a pronounced feature, which is the most intense for **Fe(naphpz)$_3$** at 362 nm. The remaining complexes show less intense, blue-shifted signals at 346 nm for **Fe(ppz)$_3$**, 350 nm for **Fe(CF$_3$ppz)$_3$**, 356 nm for **Fe(MeOppz)$_3$**, and 343 nm for **Fe(bppz)$_3$**. The origin of this absorption is presumably an MLCT [27].

Above 375 nm and 400 nm (for **Fe(naphpz)$_3$**), all complexes exhibit a broad absorption band. DFT calculations (vide infra, Figure 5) indicate that this band is composed of both MLCT and LMCT transitions, with a dominating MLCT character. This is unexpected, as

previously reported photoactive iron(III) complexes show an energetically lowest LMCT absorption and, in general, MLCT absorption only as an exception [18–20]. Therefore, the ligand design of this complex is responsible for this unexpected behavior. The interplay of pyrazole and phenylene as donors creates π and π^* orbitals, which are in the right energetic distance to the metal orbitals to enable the energetically lowest mixed MLCT/LMCT bands with a dominating MLCT character. This may also be the reason that these compounds do not exhibit a fluorescence as could be expected for iron(III) in this strong donor environment. As stated in the literature, the excited ^{2}MLCT states may undergo intersystem crossing (ISC) into a ^{4}MLCT state, which can possibly relax into energetically lower ^{4}MC states [22]. A possible explanation is that breathing and deformation modes in these bidentate complexes lead to this deactivation pathway, which is not possible in the more rigid tridentate $[Fe(ImP)_2]^+$, which shows emission from both ^{2}MLCT and ^{2}LMCT [18,44,45].

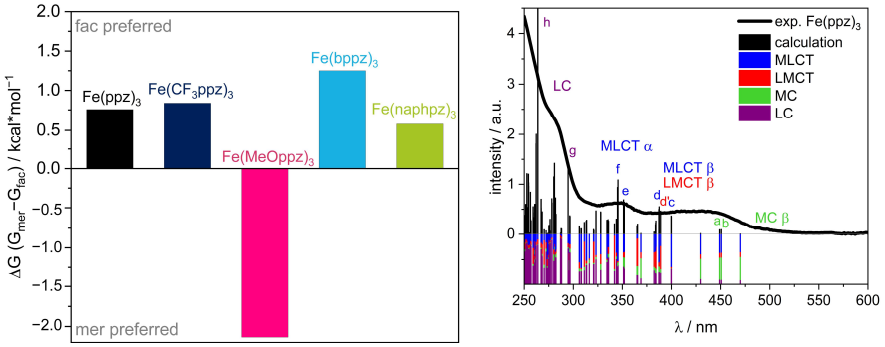

Figure 5. (**Left**) Gibbs energy difference (ΔG) between the *fac*- and *mer*-isomers of optimized geometries computed at the DFT/PBEh-3c level of theory. (**Right**) TPSSh-calculated vertical transitions for the *fac*-optimized structure of $Fe(ppz)_3$ in comparison with the experimental UV-Vis spectrum. Analysis of excited states is shown from 0 to −1. Further analysis of designated transitions a–h can be found in the Supporting Information (Table S18).

3. Computational Calculations

The formation of *fac*-isomers as a single product was confirmed by the crystal structure. This observation was further investigated by DFT calculations. For this purpose, the Gibbs free energy (G) for the optimized structures, using the PbEh-3c composite method, was calculated (Figure 5) [46]. For the complexes **Fe(ppz)$_3$, Fe(CF$_3$ppz)$_3$, Fe(bppz)$_3$**, and **Fe(naphpz)$_3$** the *fac*-isomer is energetically favored by 0.5–1.5 kcal·mol^{-1}. The higher stability is also reported for similar complexes such as $Co(ppz)_3$ and $Ir(ppy)_3$ and can be explained by the position of the phenyl groups, relative to the pyrazolyl groups, as elaborated on above [27,36]. Surprisingly, calculations suggest a higher thermodynamic stability for ***mer*-Fe(MeOppz)$_3$** despite the fact that it crystallizes in the *fac*-isomer. This indicates a significant kinetic inhibition for the transformation of the kinetic product ***fac*-Fe(MeOppz)$_3$** into the more stable ***mer*-Fe(MeOppz)$_3$**. Furthermore, the calculated bond lengths and angles of the optimized *fac*-isomers match the crystal structure, indicating a good agreement between the calculation and the experimental values (Table S17). Only the angles of the oppositely lying C-Fe-N atoms are diverging between the experiment and the theoretical calculation, showing a better approximation of a perfect octahedral structure which is typical for a gas-phase optimized structure in comparison to the solid crystal structure.

To further explain the experimental findings, TD-DFT calculations with the meta-hybrid TPSSh functional and the def2-TZVP basis set were conducted [47,48]. The energies of the resulting frontier orbitals are shown in Figure 6. The spatial distribution can be found in the Supporting Information (Figure S56). Since all complexes are open-shell systems and thus the electron density of up (α) and down (β) spin is separated in the calculations,

Inorganics **2023**, *11*, 282

two sets of singly occupied orbitals in the molecular orbital schemes are obtained. Due to the single Slater determinant in DFT as a reference function, such a multiconfigurational character is not well described, so the results must be considered with care.

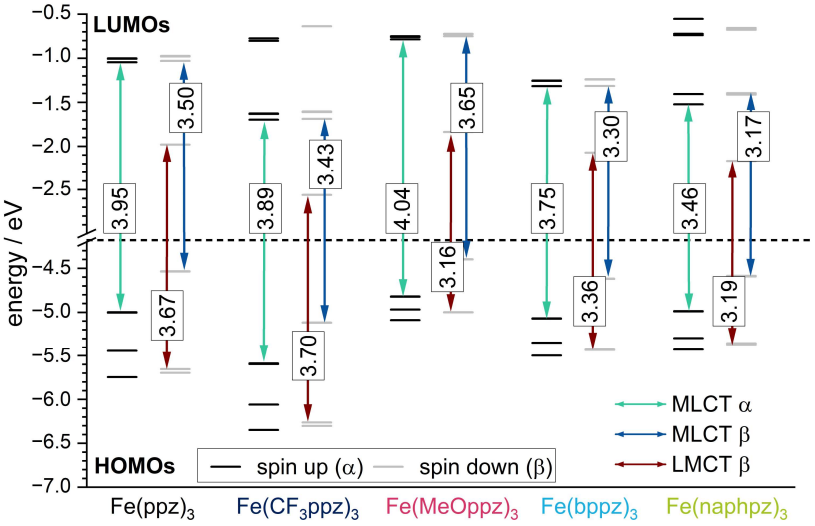

Figure 6. TPSSh-calculated molecular orbital schemes of all investigated complexes showing the HOMOs and LUMOs of the DFT-calculated spin-up and spin-down orbitals.

The β HOMO energy levels show mainly metal character (Figure S56) and can be correlated to the iron(III)/iron(IV) redox potentials. The trend of the energetic order of the calculated HOMOs follows the experimental CV data. In particular, **Fe(CF$_3$ppz)$_3$** shows the most stabilized HOMO at −5.12 eV, which is in line with the highest oxidation potential of 0.07 eV. For the remaining complexes, HOMO energy values with only small deviations of −4.40 eV, −4.54 eV, −4.59 eV, and −4.62 eV are obtained for **Fe(MeOppz)$_3$**, **Fe(ppz)$_3$**, **Fe(naphpz)$_3$**, and **Fe(bppz)$_3$**, respectively, which is in agreement with the small deviations for the experimental potentials of −0.23 eV, −0.26 eV, −0,22 eV, and −0.21 eV, respectively. The metal-based β LUMO can be correlated to the iron(II)/(III) redox potential. Since a lower negative potential for the reduction correlates with a lower orbital energy, **Fe(CF$_3$ppz)$_3$** shows the lowest negative potential of −1.50 eV and, as expected, has the lowest LUMO energy of −2.56 eV in the calculations. This is followed by slightly increasing calculated LUMO energies of **Fe(naphpz)$_3$** (−2.17 eV), **Fe(bppz)$_3$** (−2.07 eV), **Fe(MeOppz)$_3$** (−1.84 eV), and **Fe(ppz)$_3$** (−1.98 eV), reflecting the increasing negative potentials of −1.68 eV, −1.73 eV, −1.78 eV, and −1.80 eV, respectively. In addition, the lowest ground state (not including excited states) LMCT energies, which can be extracted from the energy differences of the HOMO−2 β and the LUMO β (Figure 6, red arrow), can be compared to the ΔE_{LMCT}, calculated from CV potentials. Although the consideration of the difference of the frontier orbitals always yields slightly higher values of 0.3–0.7 eV than the experimental potential differences, the order for **Fe(CF$_3$ppz)$_3$**, which has the highest expected LMCT energy of 3.70 eV (calculated) and 3.04 eV (experimental), **Fe(ppz)$_3$** (3.67 eV/2.97 eV), **Fe(bppz)$_3$** (3.36 eV/2.90 eV), and **Fe(naphpz)$_3$** (3.19 eV/2.76 eV) remains the same. Only **Fe(MeOppz)$_3$** (3.16 eV/2.89 eV) shows the smallest energy difference in the calculations, while for the experimental ΔE_{LMCT}, it shows the second smallest. To substantiate the assignment of the optical absorption bands, the first 150 vertical transitions (Figure S56) were calculated for the example of **Fe(ppz)$_3$** to determine the character of the bands in the UV-Vis spectrum. The lowest energy transitions in the visible area (a, b) originate from β HOMO to β LUMO+X transitions, with both orbitals having metal character, which is visualized in the Supporting Information (Table S18). Since the energy for the

vertical transitions is typically slightly overestimated, these transitions may be assigned to the shoulder at 500 nm in the experimental spectrum [49]. This is supported by the weak oscillator strength, characteristic of dipole-forbidden MC transitions. The broad band at about 425 nm can be assigned to both MLCT (c,d) and LMCT (d') transitions in the β-orbital set. This is consistent with almost equal energetic differences of the respective orbital levels shown in Figure 6, depicting the lowest-energy MLCT and LMCT states. Only for **Fe(MeOppz)$_3$** is the lowest LMCT energy below the MLCT energy, which explains the slightly changed experimental UV-Vis spectrum for this complex. The signal at 350 nm can be assigned to MLCT transitions (e, f) in the α-orbital set. For **Fe(naphpz)$_3$**, the red shift of the α MLCT band to 362 nm can be explained on the basis of the α HOMO-LUMO gap displaying the lowest-energy MLCT. Due to its large π-system leading to energetically low π* orbitals, the MLCT transition is significantly lower energetic in contrast to the remaining complexes. This is also reflected in the transitions below 300 nm, which can be assigned to ligand-centered (LC) transitions (g,h) and follow the general trend.

4. Hard X-ray Spectroscopy

The electronic structure of selected complexes was further investigated by synchrotron X-ray spectroscopy. X-ray absorption (XAS) and X-ray emission (XES) spectroscopy are useful methods to obtain structural and electronic information about metal complexes [50]. In the pre-edge of the X-ray absorption near edge structure (XANES) region, transitions from the 1s to the lowest unoccupied molecular orbital (LUMO) occur in K-edge spectra. For d^5 transition metals, the LUMO usually contains high fractions of the metal d orbitals. Since 1s → nd transitions are dipole-forbidden, intensity increases due to ligand-mediated hybridization with metal p-orbitals. Since the overlap depends on the geometry and symmetry of the complex, information about these factors is obtained [51]. The prepeak also provides information about the oxidation state by its energy. To enhance the experimental resolution, a specified emissive final state can be detected as the signal linewidth is inversely proportional to the lifetime of the measured final states (HERFD-XANES) [52,53]. XES examines the relaxation processes after the photoionization described above [54,55]. Core-to-core (CtC) XES spectra result from 3p → 1s transitions, where information about the spin state, the oxidation state of the metal, and the covalency of the bond between the ligand and metal is obtained due to the 3p–3d exchange interaction. 3d → 1s transitions are the origin of valence-to-core (VtC) XES spectra [56].

The XANES spectra of **Fe(ppz)$_3$**, **Fe(CF$_3$ppz)$_3$**, and **Fe(bppz)$_3$** shown in Figure 7a,b look nearly identical, indicating the very similar chemical and electronic structure in all three compounds. Due to the non-inversion symmetric character of the C_3-point group, hybridization leads to two prepeak signals at 7111 eV and 7114 eV. These two prepeaks imply accessible empty states in the non-degenerate ligand field states. TD-DFT calculations based on the TPSSh functional along with the def2-TZVPP basis set and the def2/J auxiliary basis set furthermore show that the first signal at 7111 eV can be ascribed to iron d_{xz}-orbitals as acceptor orbitals. The second signal at 7114 eV shows the transitions to the $d_{x2\text{-}y2/z2}$-orbital set. Due to the larger number of available holes in this d-orbital set, a much higher intensity can be observed here, indicating a low-spin state. This is also confirmed by CtC spectra (Figure S57), showing just a small splitting between the $Kb_{1,3}$ main line at around 7058 eV and the Kb' signal at 7045 eV for the three complexes. Furthermore, the signal in the XANES spectra does not shift for any of the complexes, confirming the same oxidation states. In the further course, two features appear at 7120 and 7124 eV. The first signal at 7120 eV emerges mainly from transitions into the pyrazole C_p-orbitals, and the signal at 7124 eV can be related to transitions into the phenyl C_p-orbitals. While the spectra at 7120 eV overlap exactly, small differences become apparent in the further course at 7124 eV. This can be attributed to the different substituents on the phenyl, shifting the C_p orbitals in energy. The slight shift to higher energy follows the order **Fe(CF$_3$ppz)$_3$** < **Fe(ppz)$_3$** < **Fe(bppz)$_3$** and shows the electron-withdrawing and -donating effects of CF_3^- and phenyl substituents, respectively.

Inorganics **2023**, *11*, 282

The VtC spectra shown in Figure 7c,d show a similar behavior. For analysis, DFT calculations using the TPSS functional along with the def2-TZVPP basis set and def2/J auxiliary basis set for the RI-J approximation were used. The calculated spectra correspond well to the experimental data. This allows the main peak at 7109 eV to be attributed to transitions from the phenyl C_p-orbital with an admixture of Fe_d orbitals (~20%) in all cases. The shoulder at 7106.5 eV can be attributed to transitions from the N_p orbitals of the pyrazole with an admixture of Fe_d orbitals. At lower energies, the cross-over transitions are located. From 7101 to 7105 eV, there are transitions from the phenyl and pyrazole p-orbitals, and around 7085 to 7100 eV, there are transitions from ligand s-orbitals.

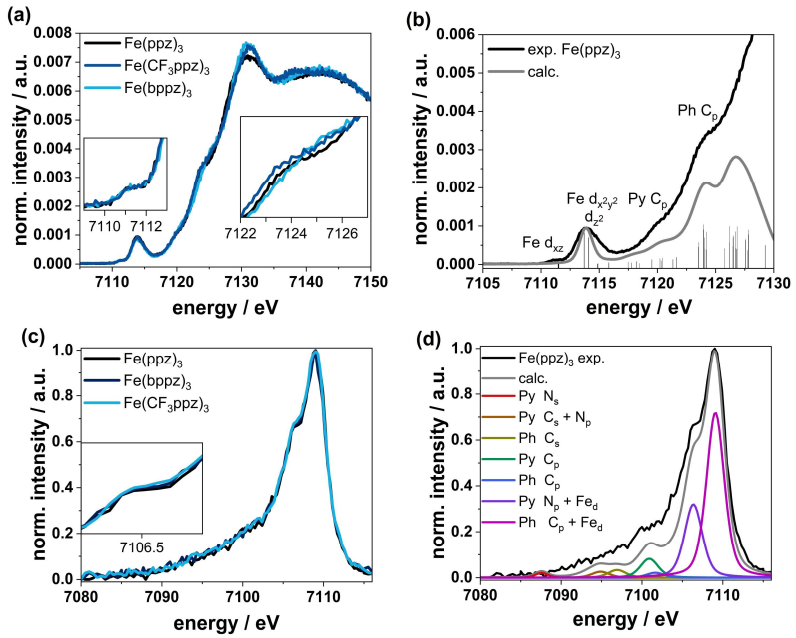

Figure 7. Experimental XANES (**a**) and VtC (**c**) spectra of $Fe(ppz)_3$, $Fe(bppz)_3$, and $Fe(CF_3ppz)_3$) and comparison of experimental and calculated XANES (**b**) and VtC (**d**) spectra exemplary for $Fe(ppz)_3$ with main character of acceptor (**b**) and donor (**d**) orbitals accountable for the peak (calculated transitions for $Fe(bppz)_3$ and $Fe(CF_3ppz)_3$ can be found in the Supporting Information Figure S58).

5. Behavior under Irradiation

To explore potential applications of the investigated complexes as photoactive compounds, their behavior under continuous irradiation was explored. Photodecomposition of all complexes is observed in acetonitrile under broadband irradiation (300 W xenon lamp, 390–800 nm) for 24 h (Figure S51). ^{1}H-NMR measurements of the resulting products showed signals attributed to a ligand-based product and an NMR-silent iron species. With assistance from mass spectroscopy (found: m/z_{exp} = 287.1268) and additional 2D-NMR spectra, the C-C-homocoupled ligand–dimer 2,2′-di(1*H*-pyrazol-1-yl)-1,1′-biphenyl (m/z_{theo} = 286.1218) was identified as the main decomposition product after illumination of **Fe(ppz)$_3$**. This behavior and the respective product of the reductive elimination can be observed for all complexes described here.

Accordingly, irradiated **Fe(ppz)$_3$** and the functionalized complexes undergo reductive ligand elimination. The C-C-coupling mechanism (Figure 8) is presumably close to the related $Co(ppz)_3$ complex, which was already investigated by Thompson et al. [27].

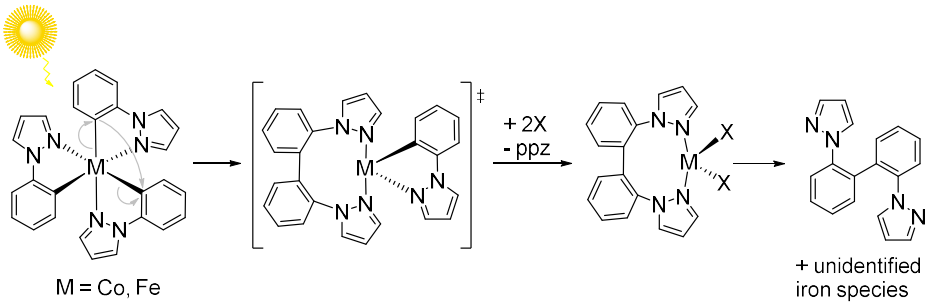

Figure 8. Proposed separation mechanism after illumination of the initial **Fe(ppz)$_3$** complex towards 2,2′-di(1H-pyrazol-1-yl)1,1′biphenyl. Adapted from [27].

To determine the rate constant of the ligand-separation process, time-dependent ^{1}H-NMR measurements were carried out, and the dynamic signals were referenced against TMS, exemplarily conducted for **Fe(ppz)$_3$**.

Within the first 5 h of irradiation, approximately 4% of the complex disintegrated; after 16 h, it was 15%. This means at least 85% of the complex is still intact even after 24 h under irradiation, following a first-order reaction (Figure 9, right) and a decomposition constant of k = -0.0144 h^{-1}.

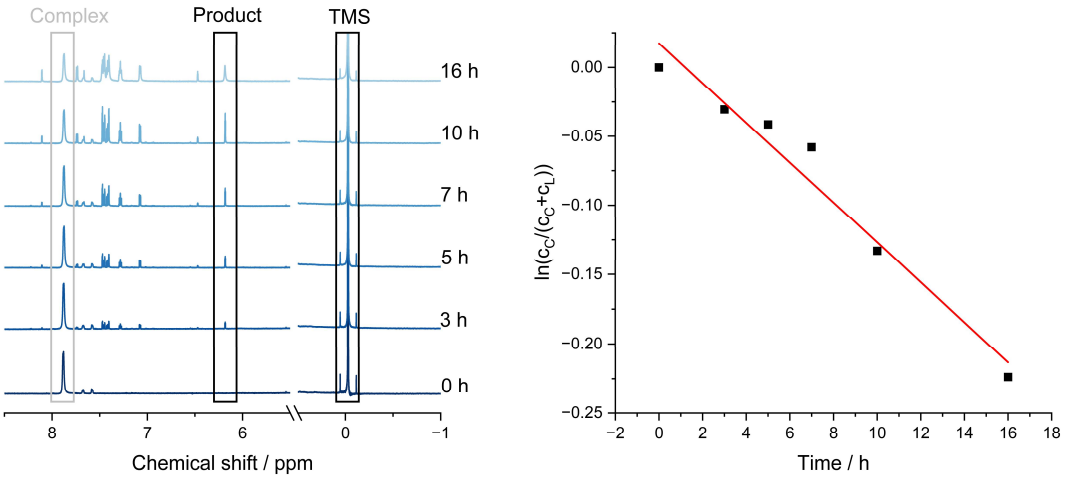

Figure 9. (**Left**) NMR spectra after irradiation for (from bottom to top) 0, 3, 5, 10, and 16 h, referenced against TMS; (**Right**) decomposition of **Fe(ppz)$_3$**, time against relative concentration of the signal at 6.21 ppm for two protons at the coupled ligand and 7.90 ppm, for three protons at the complex. Calculation included the relative intensity, multiplied by the fracture of the protons. The linear regression shows a slope of -0.0144 h^{-1} [57].

Additionally, the stability of **Fe(ppz)$_3$** under irradiation was also investigated in different solvents by ^{1}H-NMR spectroscopy. Measurements in acetone, DMSO, THF, dichloromethane, methanol, benzene, toluene, chloroform, butyronitrile (BuCN), and 2-methyltetrahydrofuran (2-MeTHF) (Figure S52) showed that the complex was only broadband-stable in the last two solvents. The reason for this behavior needs to be explored in the future. The UV-Vis spectra had to be accordingly recorded in BuCN, and the CV was conducted under light exclusion.

Finally, monitoring of the decomposition of **Fe(ppz)$_3$** at various wavelengths was analyzed (Figure S53). By the installation of bandwidth filters at 320, 360, and 390 nm, as

well as long-pass filters at 400 and 495 nm, wavelength-dependent measurements were enabled. Decomposition only occurred for wavelengths higher than 400 nm and lower than 495 nm. Therefore, excitation into the broad band composed of β ^{2}LMCT and β ^{2}MLCT transitions leads inevitably to the decomposition of the compound, whereas the ^{2}MC transitions do not lead to decomposition. A tentative explanation reiterates the explanation for the absence of luminescence: Excitation of the ^{2}MLCT state leads to ISC into the ^{4}MLCT state, which relaxes into a ^{4}MC state. Due to the population of the antibonding metal-based orbitals, the bonds of the pyrazole to the iron are elongated further or completely dissociated, as seen in photochemically induced ligand release, allowing the coordination of solvent molecules and possibly leading to reductive elimination [58]. This is supported by the optimized structure of the lowest quartet state. The spin density plot of this state (Figure S55) shows that it has a metal-centered character. In addition, a significant bond expansion of one Fe-N bond from 2.0 Å in the ^{2}GS to 2.4 Å in the ^{4}MC state occurs, which might indicate the first step of the decomposition process.

6. Conclusions

The synthesis of five different homoleptic iron(III) complexes with bidentate phenylpyrazole-based ligands was reported in this work, with functional groups on the 4-position of the phenyl ring, such as trifluoromethyl, methoxy, phenyl, and naphthyl groups, to compare the influence of electron-donating or -withdrawing groups on the electronic structure. All compounds were received purely as *fac*-isomers in low-spin iron(III) configuration. Despite the paramagnetism, the complete NMR signal assignments and substantiated DFT calculations could be performed.

The complexes show very low-lying oxidation potentials of −0.26 V for the parent **Fe(ppz)$_3$**, where the strong σ-donating capabilities of the phenyl moiety impact the redox behavior drastically compared to common polypyridyl complexes. The effect of electron-withdrawing moieties consequently shifts the potentials to 0.07 V in **Fe(CF$_3$ppz)$_3$**, whereas the reduction potentials are more affected by electron-donating groups.

The absorption behavior, as assigned by TDDFT, is dominated by LC transitions in the UV range, whereas two absorption bands are observed above 350 nm. The higher energy band around 350 nm can be attributed solely to α MLCT transitions, and the broad and featureless absorption band above 370 nm (400 nm for **Fe(naphpz)$_3$**) is assigned to a mixture of MLCT and LMCT transitions, with an MC transition as the lowest energy shoulder. This unexpected behavior is caused by the ligand design, incorporating both cyclometalating and pyrazole ligands, leading to isoenergetic π-E* and E-π* gaps, which finally causes overlapping LMCT and MLCT transitions.

No emission of the complexes is observed. Instead, decomposition by reductive elimination is caused by irradiation over a longer period in the energy range of 400–495 nm. Therefore, an excited state relaxation following a ^{2}MLCT → ^{4}MLCT → ^{4}MC cascade, leading to the population of a non-emissive and destructive ^{4}MC state, is most likely. There, elongated or dissociated bonds allow for the coordination of solvent molecules and the reductive elimination of two homocoupled ligands.

With the presented results, the first spectroscopic and theoretical characterization of tris-bidentate iron(III) complexes is provided. The introduction of further functional groups in different positions or exchanging the pyrazole for other donor groups would potentially suppress reductive elimination, and photostable and photoactive compounds may be obtained.

7. General Procedures

Complex Synthesis

The described synthetic procedure applies to all complexes.

Ligand (3 equiv) was suspended in tetrahydrofuran (THF) (10 mL) under an argon atmosphere. Ethylmagnesium bromide (4 equiv, 0.9 M in THF) was added dropwise and refluxed overnight. In a second flask, iron powder (12 equiv) was added to a THF solution

of iron(II) bromide (1.5 equiv) (40 mL) and refluxed overnight. After refluxing, the flask was cooled to room temperature, and the ligand solution was cooled in an ethanol–nitrogen bath to −80°C. The iron(II) bromide solution was added dropwise and slowly warmed to room temperature. To the reaction mixture, a solution of NH_4Cl (100 mL, 15 g/L) was added and extracted with dichloromethane (DCM) (3 × 100 mL). The combined organic phases were dried with $MgSO_4$ and concentrated under reduced pressure. Column chromatography with silica as solid phase and DCM as eluent was applied. The combined fractions were concentrated under reduced pressure and crystallized with slow diffusion of cyclopentane into the DCM-analyte solution. After removing the crystalline product and drying it at 50 °C under vacuum, the compound was received as an elemental-analysis pure product.

All experimental data can be found in the Supporting Information.

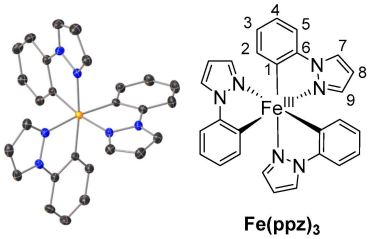

Tris(1-phenylpyrazolato-*N*,$C^{2'}$)iron(III)Fe(ppz)$_3$
The complex was obtained as a yellow powder (7.5%).
^{1}H-NMR (700.0 MHz, CD_3CN): δ = −75.20 (s, 1H, 2-*H*), −9.27 (s, 1H, 9-*H*), −5.25 (s, 1H, 4-*H*), −3.35 (s, 1H, 8-*H*), −1.15 (s, 1H, 5-*H*), 7.90 (s, 1H, 3-*H*), 13.04 (s, 1H, 7-*H*) ppm. **^{13}C-NMR** (176.1 MHz, CD_3CN): δ = −92.7 (1C, 3-*C*), −74.8 (1C, 5-*C*), 100.2 (1C, 7-*C*), 117.0 (1C, 8-*C*), 122.9 (1C, 9-*C*), 239.9 (1C, 4-*C*), 389.1 (1C, 2-*C*), 396.6 (1C, 6-*C*) ppm. **^{15}N-NMR** (70.96 MHz, CD_3CN): 70.4 ppm. (ESI in MECN): *m*/*z* 485.1160 (for $C_{27}H_{21}FeN_6$ calc. 485.1177) **Elemental analysis**: calc. for $C_{27}H_{21}FeN_6$ C: 66.82%, H: 4.36%, N: 17.32%, found: C: 66.77%, H: 4.56%, N: 17.25%. **IR** (ATR, $\tilde{\nu}$ [cm^{-1}]): 3139 w, 3041 w, 1573 w, 1506 w, 1461 m, 1434 m, 1417 m, 1398 m, 1328 w, 1270 m, 1236 w, 1193 w, 1153 w, 1099 w, 1064 m, 1043 m, 1012 m, 960 m, 918 w, 871 w, 825 w, 742s, 715 m, 698 m, 661 w, 644 w, 609 m.

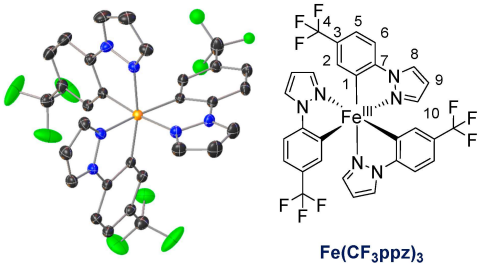

Tris(1-(4-(trifluoromethyl)phenyl)pyrazolato-*N*,C^2)iron(III)Fe(CF_3ppz)$_3$
The complex was obtained as a yellow powder (17.2%).
^{1}H-NMR (700.0 MHz, CD_3CN): δ = −75.17 (s, 1H, 2-*H*), −10.47 (s, 1H, 10-*H*), −3.39 (s, 1H, 9-*H*), −3.17 (s, 1H, 5-*H*), 0.27 (s, 1H, 6-*H*), 11.23 (s, 1H, 8-*H*) ppm. **MS** (ESI in MECN): *m*/*z* 689.0800 (for $C_{30}H_{18}F_9FeN_6$ calc. 689.0799). **^{13}C-NMR** (176.1 MHz, CD_3CN): δ = −93.4 (1C, 3-C), −68.6 (1C, 6-C), 108.9 (1C, 8-C), 112.6 (1C, 9-C), 126.5 (1C, dd, $^1J_{CF}$ = 272.85 Hz 275.09 Hz, 4-*C*), 132.8 (1C, 10-*C*), 229.9 (1C, 5-C), 361.9 (1C, 2-C), 382.0 (1C, 7-C) ppm. **^{15}N-NMR** (70.96 MHz, CD_3CN): 84.0 ppm. **^{19}F-NMR** (659.0 MHz, CD_3CN): δ = −71.5 (s, 3F) ppm. **Elemental analysis**: calc. for $C_{30}H_{18}F_9FeN_6$: C: 52.27%, H: 2.63%, N: 12.19%, found: C: 51.90%, H: 2.81%, N: 12.12%. **IR** (ATR, $\tilde{\nu}$ [cm^{-1}]): 3155 w, 3033 w, 2360 w, 2335 w, 1585 w, 1508 w, 1477 w, 1396 m, 1315s, 1272s, 1249 m, 1159 m, 1110s, 1066s, 1045s, 960 m, 900 m, 838 w, 821 w, 804 m, 746s, 702 m, 661 m, 607 w.

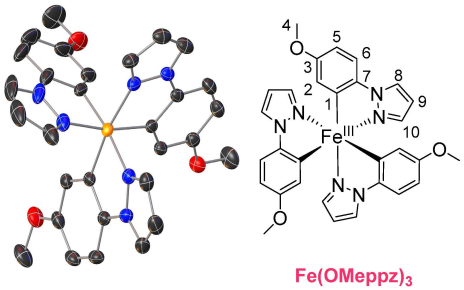

Fe(OMeppz)$_3$

Tris(1-(4-methoxyphenyl)pyrazolato-*N*,*C*^{2})iron(III) Fe(MeOppz)$_3$
The complex was obtained as a red powder (2.6%).
^{1}H-NMR (700 MHz, CD$_3$CN): δ = −79.93 (s, 1H, 2-*H*), −10.34 (s, 1H, 10-*H*), −5.36 (s, 1H, 6-*H*)), −5.12 (s, 1H, 5-*H*), −3.19 (s, 1H, 9-*H*), 1.44 (s, 3H, 4-*H*), 12.06 (s, 1H, 8-*H*) ppm. **^{13}C-NMR*** (176.1 MHz, CD$_3$CN): δ = −106.1 (1C, 156.6 Hz, 6-*C*), −93.0 (1C, 3-*C*), 49.1 (1C, 139.07 Hz, 4-*C*), 103.9 (1C, 182.9 Hz, 8-*C*), 114.1 (1C, 191.7 Hz, 9-*C*) 130.1 (1C, 182.9 Hz, 10-*C*), 232.4 (1C, 159.9 Hz, 5-C), 360.8 (1C, 129.6 Hz, 2-*C*), 403.2 (1C, 7-*C*) ppm. **^{15}N-NMR** (70.96 MHz, CD$_3$CN): 80.2 ppm. **MS** (ESI in MECN): *m*/*z* 575.1530 (for $C_{30}H_{27}FeN_6O_3$ calc. 575.1494).
Elemental analysis: calc. for $C_{30}H_{27}FeN_6O_3$: C: 62.62%, H: 4.73%, N: 14.61%, found: C:62.49%, H: 5.19%, N: 14.35%. **IR** (ATR, $\tilde{\nu}$ [cm^{-1}]): 3122 w, 3039 w, 3006 w, 2952 w, 2931 w, 2902 w, 2829 w, 1583 w, 1560s, 1506 w, 1469s, 1417s, 1315 m, 1276s, 1249 m, 1209s, 1174s, 1116 m, 1031s, 958 m, 879 m, 811 w, 784s, 744s, 661 w, 621 m, 609 m.
* not decoupled.

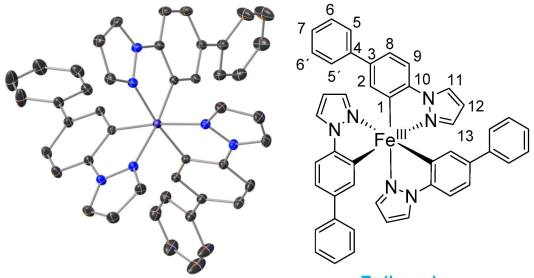

Fe(bppz)$_3$

Tris(1-([1,1′-biphenyl])-4-yl)phenyl)pyrazolato-*N*,*C*^{2})iron(III) Fe(bppz)$_3$
The complex was obtained as a red powder (3.9%).
^{1}H-NMR (700 MHz, CD$_3$CN): δ = −77.61 (1s, 1H, 2-*H*) −10.18 (s, 1H, 13-*H*), −4.64 (s, 1H, 8-*H*), −3.21 (s, 1H, 12-*H*), −1.74 (s, 1H, 9-*H*), 5.39 (d, $^3J_{HH}$ = 8.19 Hz, 2H, 5,5′-*H*), 5.75 (t, $^3J_{HH}$ = 7.60 Hz, 2H, 6,6′-*H*), 7.10 (t, $^3J_{HH}$ = 7.14 Hz, 1H, 6-H) 11.84 (s, 1H, 11-*H*) ppm. **^{13}C-NMR** (176.1 MHz, CD$_3$CN): δ = −79.6 (1C, 152.5 Hz, 9-C), −77.9 (1C, 3-C), 105.4 (1C, 185.7 Hz, 11-C), 114.4 (1C, 62.3 Hz, 12-C), 115.3 (2C, 89.03 Hz, 5,5′-C), 123.1 (1C, 162.9 Hz, 7-C), 130.9 (2C, 160.4 Hz, 6,6′-C), 131.9 (1C, 183.3 Hz, 13-C), 154.1 (1C, 4-C), 241.4 (1C, 158.8 Hz, 8-C), 370.5 (1C, 133.9 Hz, 2-C), 396.7 (1C, 10-C) ppm. **^{15}N-NMR** (70.96 MHz, CD$_3$CN): 71.0 ppm. **MS** (ESI in MECN): *m*/*z* 713.2150 (for $C_{45}H_{33}FeN_6$ calc. 713.6460). **Elemental analysis:** calc. for $C_{45}H_{33}FeN_6$ C: 75.74%, H: 4.66%, N: 11.78%, found: C: 71.15%, H: 4.84%, N: 10.78%. **IR** (ATR, $\tilde{\nu}$ [cm^{-1}]): 3108 w, 3056 w, 3020 w, 1598 w, 1564 w, 1502 w, 1465 m, 1400 m, 1373 w, 1330 w, 1261 m, 1112 w, 1064 m, 1047 m, 1016 w, 958 w, 916 w, 894 w, 808s, 757s, 734s, 694s, 663 w, 649 w, 607 w.

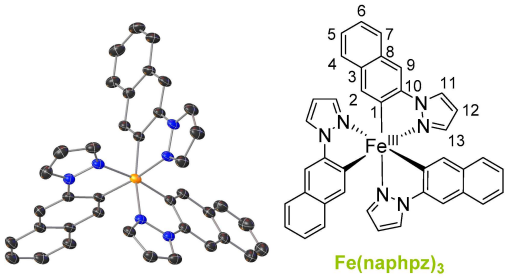

Tris(1-(naphthalen-2-yl)pyrazolato-*N*,C^2)iron(III) Fe(naphpz)$_3$
The complex was obtained as a red powder (5.3%).
^{1}H-NMR (700 MHz, DMSO-d6): δ = −85.19 (s, 1H, 2-*H*), −12.51 (s, 1H, 13-*H*), −1.68 (d, $^3J_{HH}$ = 6.3 Hz, 1H, 4-*H*), −1.31 (s, 1H, 12-*H*), 1.10 (s, 1H, 9-*H*), 1.25 (t, $^3J_{HH}$ = 7.10 Hz, 1H, 6-*H*), 8.12 (t, $^3J_{HH}$ = 6.30 Hz, 1H, 5-*H*), 11.15 (s, 1H, 11-*H*), 12.83 (d, $^3J_{HH}$ = 8.50 Hz, 1H, 7-*H*) ppm. **^{13}C-NMR*** (176.1 MHz, DMSO-d6): δ = −97.6 (1C, 3-*C*), −56.79 (1C, 150.66 Hz, 9-*C*), 80.3 (1C, 150.66 Hz, 7-*C*), 81.6 (1C, 160.34 Hz, 5-*C*), 99.4 (1C, 180.91 Hz, 12-*C*), 124.3 (2C, 188.74 Hz, 11-*C*), 126.6 (1C, 188.74 Hz, 13-*C*), 172.1 (2C, 157.98 Hz, 6-*C*), 180.5 (1C, 157.98 Hz, 4-*C*), 216.3 (1C, 8-*C*), 365.3 (1C, 2-*C*), 413.9 (1C, 10-*C*) ppm. **MS** (ESI in MECN): *m*/*z* 635.1640 (for $C_{39}H_{27}FeN_6$ calc. 635.1647). **Elemental analysis**: calc. for $C_{39}H_{27}FeN_6$: C: 73.71%, H: 4.28%, N: 13.22%, found: C: 74.29%, H: 5.10%, N: 12.42%. **IR** (ATR, $\tilde{\upsilon}$ [cm^{-1}]): 3126 w, 6047 w, 2917 w, 2854 w, 1585 w, 1593 w, 1560 w, 1510 w, 1486 w, 1459 m, 1405 m, 1332 w, 1313 w, 1251 w, 1197 w, 1134 w, 1107 w, 1062 m, 1037 w, 977 w, 935 w, 889 w, 856 m, 831 w, 736s, 682 w, 651 w.
* not decoupled.

8. Materials and Methods

Synthesis of ligands and complexes was carried out under standard Schlenk conditions, under inert and anhydrous conditions. Inert and pre-dried argon was used, and all applied glassware was heated under vacuum und flushed with inert gas three times. Anhydrous solvents were provided by a solvent drying plant from MBraun (MB SPS 800, München, Germany) and purged with argon prior to use. Used chemicals for all synthesis were commercially purchased from *Fischer Scientific* (Hampton, NH, USA), *Merck* (Rahway, NJ, USA), *Abcr* (Karlsruhe, Germany), and *TCI* (Chennai, India) and used without further purification. Ligand synthesis has been reported in [29,30].

8.1. NMR Spectroscopy

NMR spectra were recorded on a BRUKER Avance 700 (^{1}H, 700.1 MHz, Billerica, MA, USA) using deuterated solvents from *Deutero* (Kastellaun, Germany) without further purification. NMR signals were referenced to residual solvent signals relative to TMS. For the decomposition experiments a 300 W xenon lamp for irradiation was installed in front of an NMR sample of **Fe(ppz)$_3$**, exemplarily. To determine the percentage of intact complex, it was referenced against a calibrated TMS signal with the product species signal at 6.21 ppm, with common analytic calculations. Mass spectrometry was performed with a quadrupole time-of-flight mass spectrometer (MS) Synapt 2G from the company WATERS (Milford, MA, USA). Elemental analysis measurements were performed with a Micro Cube from ELEMENTAR (Langenselbold, Germany) and were compared with the theoretically calculated mass. A **PerkinElmer** (Waltham, MA, USA) Lambda 465 single-beam spectrophotometer was used for UV-Vis spectra. Solutions had a concentration of 10^{-5} M BuCN and were measured in a **Hellma** (Müllheim, Germany) quartz cuvette with a path length of 1 cm. For IR spectroscopy a Bruker Vertex 70, with the sample as solid powder and the ATR technique, was applied. Cyclic voltammograms were measured with a 10^{-3} M analyte and 0.1 M [*n*-Bu$_4$N](PF$_6$) concentration on a PGSTAT 101 potentiostat

from **Metrohm-Autolab** (Utrecht, The Netherlands). Emission spectra were recorded on an FLS1000 from **Edinburgh Instruments** (Livingston, UK) at room temperature.

8.2. Quantum Chemical Calculations

All calculations presented here were conducted with the ORCA quantum chemistry package (version 5.0.3) [59]. Unconstrained geometry optimization was performed using the PBEh-3c composite method [46], whereas a frequency calculation was performed and checked for the absence of negative values to confirm a minimum structure. Optimized structures were used as input for further calculations. Time-dependent (TD) DFT calculations for the extraction of orbital energies and the prediction of vertical transitions were conducted using the TPSSh functional [60] together with the def2-TZVP basis set, as well as the def2/J auxiliary basis set [61] and the RIJCOSX approximation [62] for the Hartree-Fock component. The tight convergence criterion was imposed on all calculations, and the D4 dispersion correction [62] was always employed when not using the PBEh-3c method. The conductor-like polarizable continuum model (CPCM) [63] for acetonitrile accounting for solvent effects was applied. For the simulation of the XANES and VtC XES spectra, the same settings except the CPCM model were used. For XANES, the TD-DFT approach with the TPSSh basis set and the expanded CP(PPP) basis set [64] only for iron was applied. VtC-XES spectra were calculated based on the DFT approach using the TPSS and CP(PPP) functional [60]. XANES transitions were plotted with linearly increasing broadening to higher energies, starting from 0.6 (fwhm) at the prepeak, and were shifted by 155.3 eV to match the experimental spectrum. VtC-XES transitions were broadened by 2.5 eV (fwhm), and all spectra were shifted by 170.6 eV. Ligand or atom projected VtC-XES spectra were created by taking only a set of donor orbitals with significant populations of a given atom or fragment into account. The analysis of the fractions of the molecular orbitals was based on the Löwdin population analysis, which was extracted from the ORCA output file using MOAnalyzer (version 1.3) and the TheoDORE package [65,66]. Spatial distributions of orbitals were visualized using IboView (version 20150427) [67].

8.3. X-ray Absorption and Emission Spectroscopy

X-ray absorption and emission experiments were performed at beamline ID26 at the European Synchrotron Radiation Facility (ESRF) in Grenoble [68]. The electron energy was 6.0 GeV, and the ring current varied between 180 and 200 mA. Incident energy calibration was performed using a Fe foil. For K-edge measurements, the solid samples were prepared as wafers using degassed cellulose as a binder to avoid self-absorption effects. The XANES spectra were monitored using a photodiode installed at about a 90° scattering angle and at 45° to the sample surface. To exclude radiation damage, fast measurements over the prepeak were carried out under the measurement conditions (attenuated beam, cryostat to cool the sample to 80 K). No signs of radiation damage could be detected. VtC-XES spectra were recorded at an excitation energy of 7300 eV measured with a Johann-type spectrometer [69].

8.4. Single-Crystal X-ray Diffraction

The presented X-ray single-crystal data were collected on a *Bruker Venture D8* three-cycle diffractometer equipped with a Mo K_α μ-source (λ = 0.71073 Å). Monochromatization of the radiation was obtained using *Incoatec* (Geesthacht, Germany) multilayer Montel optics, and a Photon III area detector was used for data acquisition. All crystals were kept at 120 K during measurement.

Data processing was carried out using the *Bruker* APEX 4 software package: This includes SAINT for data integration and SADABS for multi-scan absorption correction. Structure solution was obtained by direct methods, and the refinement of the structures using the full-matrix least squares method based on F^2 was achieved in SHELX [70,71]. All non-hydrogen atoms were refined anisotropically, and the hydrogen atom positions were refined at idealized positions riding on the carbon atoms with isotropic displacement

parameters $U_{iso}(H) = 1.2\ U_{eq}(C)$ and $1.5\ U_{eq}(\text{-}CH_3)$ and C-H bond lengths of 0.93–0.96 Å. All CH_3 hydrogen atoms were allowed to rotate but not to tip.

Crystallographic data were deposited at the Cambridge Crystallographic Data Centre and assigned the deposition numbers 2191100-2191104. Copies are available free of charge via www.ccdc.cam.ac.uk, accessed on 1 January 2020.

Supplementary Materials: The following supporting information can be downloaded at: https://www.mdpi.com/article/10.3390/inorganics11070282/s1, Figure S1: ^{1}H-NMR spectrum of complex Fe(ppz)$_3$ in CD_3CN; Figure S2: ^{13}C-NMR spectrum of complex Fe(ppz)$_3$ in CD_3CN; Figure S3: ^{15}N-HMBC spectrum of Fe(ppz)$_3$ in CD_3CN, second signal is the folded signal of non-deuterated solvent CH_3CN; Figure S4: ESI-MS spectrum of complex Fe(ppz)$_3$ in CH_3CN; Figure S5: Complete cyclovoltammetry spectra for complex Fe(ppz)$_3$ in CH_3CN; Figure S6: Plotted data of Randles-Sevcik-Equation Fe(ppz)$_3$ at different scan rates, first redox step; Figure S7: Plotted data of Randles-Sevcik-Equation Fe(ppz)$_3$ at different scan rates, second redox step; Figure S8: Plotted data of Randles-Sevcik-Equation Fe(ppz)$_3$ at different scan rates, third redox step; Figure S9: ATR-IR spectrum for complex Fe(ppz)$_3$; Figure S10: Change in the absorptive behaviour of Fe(ppz)$_3$ with an applied potential of 0.5–2 V in CH_3CN; Figure S11: Change in the absorptive behaviour of Fe(ppz)$_3$ with an applied potential of -0.5 V in CH_3CN; Figure S12: Change in the absorptive behaviour of Fe(ppz)$_3$ with an applied potential of -2.0–2.5 V in CH_3CN; Figure S13: ^{1}H-NMR spectrum of complex Fe(bppz)$_3$ in CD_3CN; Figure S14: ^{13}C-NMR spectrum of complex Fe(bppz)$_3$ in CD_3CN; Figure S15: ^{15}N-HMBC spectrum of Fe(bppz)$_3$ in CD_3CN; Figure S16: ESI-MS spectrum of complex Fe(bppz)$_3$ in CH_3CN; Figure S17: Cyclovoltammetry spectra of Fe(bppz)$_3$ in CH_3CN; Figure S18: Plotted data of Randles-Sevcik-Equation Fe(bppz)$_3$ at different scan rates, first redox step; Figure S19: Plotted data of Randles-Sevcik-Equation Fe(bppz)$_3$ at different scan rates, second redox step; Figure S20: Plotted data of Randles-Sevcik-Equation Fe(bppz)$_3$ at different scan rates, third redox step; Figure S21: ATR-IR- spectrum of complex Fe(bppz)$_3$; Figure S22:^{1}H-NMR spectra of complex Fe(CF_3ppz)$_3$ in CD_3CN; Figure S23: ^{13}C-NMR spectra of complex Fe(CF_3ppz)$_3$ in CD_3CN; Figure S24: ^{15}N-HMBC spectrum of the complex Fe(CF_3ppz)$_3$ in CD_3CN; Figure S25: ^{19}F-HMBC spectrum of the complex Fe(CF_3ppz)$_3$ in CD_3CN; Figure S26: ESI-MS of complex Fe(CF_3ppz)$_3$ in CH_3CN; Figure S27: Cyclovoltammetry spectra of Fe(CF_3ppz)$_3$ in CH_3CN; Figure S28: Plotted data of Randles-Sevcik-Equation Fe(CF_3ppz)$_3$ at different scan rates, first redox step; Figure 29: Plotted data of Randles-Sevcik-Equation Fe(CF_3ppz)$_3$ at different scan rates, first redox step; Figure S30: ATR-IR-spectrum of complex Fe(CF_3ppz)$_3$; Figure S31: ^{1}H-NMR spectrum of complex Fe(naphpz)$_3$ in DMSO-d^6; Figure S32: ^{13}C-NMR spectrum of complex Fe(naphpz)$_3$ in DMSO-d^6; Figure S33: ESI-MS spectrum of complex Fe(naphpz)$_3$ in CH_3CN; Figure S34: Cyclovoltammetry spectra of complex Fe(naphpz)$_3$ in CH_3CN; Figure S35: Plotted data of Randles-Sevcik-Equation Fe(naphpz)$_3$ at different scan rates, first redox step; Figure S36: Plotted data of Randles-Sevcik-Equation Fe(naphpz)$_3$ at different scan rates, second redox step; Figure S37: Plotted data of Randles-Sevcik-Equation Fe(naphpz)$_3$ at different scan rates, first redox step; Figure S38: ATR-IR-spectrum of complex Fe(naphpz)$_3$ in CH_3CN; Figure S39: Change in the absorptive behaviour of (Fe(naphpz)$_3$ with an applied potential of 0.8–2 V in CH_3CN; Figure S40: Change in the absorptive behaviour of (Fe(naphpz)$_3$ with an applied potential of -0.5–(-1.5) V in CH_3CN; Figure S41: Change in the absorptive behaviour of (Fe(naphpz)$_3$ with an applied potential of -2.5 V in CH_3CN; Figure S42: ^{1}H-NMR spectrum of complex Fe(MeOppz)$_3$ in CD_3CN; Figure S43: ^{13}C-NMR spectrum of complex Fe(MeOppz)$_3$ in CD_3CN; Figure S44: ^{15}N-HMBC spectrum of Fe(MeOppz)$_3$ in CD_3CN; Figure S45: ESI-MS spectrum of complex Fe(MeOppz)$_3$ in CH_3CN; Figure S46: Cyclovoltammetry spectra of complex Fe(MeOppz)$_3$ in CH_3CN; Figure S47: Plotted data of Randles-Sevcik-Equation Fe(MeOppz)$_3$ at different scan rates, first redox step; Figure S48: Plotted data of Randles-Sevcik-Equation Fe(MeOppz)$_3$ at different scan rates, second redox step; Figure S49: Plotted data of Randles-Sevcik-Equation Fe(MeOppz)$_3$ at different scan rates, third redox step; Figure S50: ATR-IR spectrum of complex Fe(MeOppz)$_3$; Figure S51: Experiments on complex stability in acetonitrile solution: before illumination of Fe(ppz)$_3$ (blue), after illumination of 24 h: Fe(ppz)$_3$ (red), Fe(CF_3ppz)$_3$ (green), Fe(MeOppz)$_3$ (purple), Fe(bppz)$_3$ (yellow), Fe)naphpz)$_3$ (orange, pure solubility decreases signal intensity); Figure S52: Experiments on complex stability exemplarily for Fe(ppz)$_3$, bottom blue: before illumination in toluene (blue), from there upwards after illumination: toluene (red), THF (green), DMSO (pruple), DCM (yellow), BuCN (orange), benzene (grey), acetone (red), 2Me-THF (blue); Figure S53: Decomposition of Fe(ppz)$_3$, with different filters. Blue: before irradiation; red: 320 nm bandwidth filter, green: 360 nm band-

width filter, purple: 390 bandwidth filter; yellow: 400 longpass filter, orang: 495 longpassfilter. At 7.90 ppm complex signal, additional diamagnetic species in yellow spectra is the product of the reductive elimination; Figure S54: Calculated slope of the decomposition of $Fe(ppz)_3$, based on the relative intensities of TMS, the product of the reductive illumination at 6.21 ppm and the complex resonance at 7.90 ppm; Figure S55: PBEh-3c optimized lowest quartet state of fac-$Fe(ppz)_3$. *Left*: Spin density plot. *Right*: Depicted Fe-ligand bond lengths; Figure S56: TPSSh/def2-TZVP calculated spatial distribution of the frontier orbitals of the respective complexes; Figure S57: Experimental CtC spectra of $Fe(ppz)_3$, $Fe(bppz)_3$, $Fe(CF_3ppz)_3$ with different substituents; Figure S58: Comparison of experimental and calculated XANES (a,b) and VtC (c,d) spectra with main character of acceptor (a,b) and donor (c,d) orbitals orbital components for Pyrazol (Py) and Phenyl (Ph) accountable for the peak. Table S1: Cyclovoltammetry data for $Fe(ppz)_3$ at different scan rates, first redox step; Table S2: Cyclovoltammetry data for $Fe(ppz)_3$ at different scan rates, second redox step: Table S3: Cyclovoltammetry data for $Fe(ppz)_3$ at different scan rates, third redox step; Table S4: Cyclovoltammetry data for $Fe(bppz)_3$ at different scan rates, first redox step; Table S5: Cyclovoltammetry data for $Fe(bppz)_3$ at different scan rates, second redox step; Table S6: Cyclovoltammetry data for $Fe(bppz)_3$ at different scan rates, third redox step; Table S7: Cyclovoltammetry data for $Fe(CF_3ppz)_3$ at different scan rates, first redox step; Table S8: Cyclovoltammetry data for $Fe(CF_3ppz)_3$ at different scan rates, second redox step; Table S9: Cyclovoltammetry data for $Fe(naphpz)_3$ at different scan rates, first redox step; Table S10: Cyclovoltammetry data for $Fe(naphpz)_3$ at different scan rates, second redox step; Table S11: Cyclovoltammetry data for $Fe(naphpz)_3$ at different scan rates, second redox step; Table S12: Cyclovoltammetry data for $Fe(MeOppz)_3$ at different scan rates, first redox step; Table S13: Cyclovoltammetry data for $Fe(MeOppz)_3$ at different scan rates, second redox step; Table S14: Cyclovoltammetry data for $Fe(MeOppz)_3$ at different scan rates, second redox step; Table S15: Differential Gibbs free energy of PbEh-3c optimized structures excluding and including the SMD model for MeCN and BuCN implemented in ORCA. Negative values account for higher stability; Table S16: Absolute an differential Gibbs free energy of PbEh-3c optimized structures of fac- and mer- isomers; Table S17: Comparison of the bond length and binding angles for the single crystal structure analysis and PBEh-3c geometry optimized fac-complexes. Table S18: Analysis of the main acceptor and donor orbital contribution to the TD-DFT calculated vertical transitions (Figure 5) of fac-$Fe(ppz)_3$. The lettering of the transitions a-h refers to the assigned transitions in Figure 5. Additionally, the calculated wavelength λ and oscillator strength f is given for the selected transitions. Figures S1–S50 and Tables S1–S14: Summarized data for complex analysis, including NMR-, IR, MS-spectra, as well as the complete CV data including reversibility determination after Randles-Sevcik; Figures S51–S54: NMR-spectra and caculations of the illumination experiments; Figures S55–S58 and Tables S15–S17: Computational data.

Author Contributions: Methodology, synthesis, writing—original draft preparation, T.H.; DFT calculations, writing, L.F.; supporting synthesis, F.L.; writing—review, J.S.; single-crystal measurements and analyses, R.S.; spectroelectrochemistry measurements, A.N.; NMR measurements, H.E.; writing—review and editing, M.B. All authors have read and agreed to the published version of the manuscript.

Funding: This research was funded by the German Research Council (Deutsche Forschungsgemeinschaft DFG), in the frame of priority program SPP 2102, grant number BA 4467/7-1 and BA 4467/7-2.

Data Availability Statement: Crystallographic data have been deposited at the Cambridge Crystallographic Data Centre and assigned the deposition numbers 2191100-2191104. Copies are available free of charge via www.ccdc.cam.ac.uk, accessed on 1 January 2020.

Acknowledgments: The European Synchrotron Radiation Facility (ESRF) and the beamline ID26 are acknowledged for the provision of beamtime and help during the experiment. Generous grants of computer time at the Paderborn Center for Parallel Computing PC2 are gratefully acknowledged. L.F. thanks the chemical industry fund ("Fonds der Chemischen Industrie") for a Kekulé PhD scholarship.

Conflicts of Interest: The authors declare no conflict of interest.

References

1. Balzani, V.; Campagna, S. *Photochemistry and Photophysics of Coordination Compounds I*; Springer: Berlin/Heidelberg, Germany, 2007; Volume 280. [CrossRef]
2. Prier, C.K.; Rankic, D.A.; MacMillan, D.W.C. Visible light photoredox catalysis with transition metal complexes: Applications in organic synthesis. *Chem. Rev.* **2013**, *113*, 5322–5363. [CrossRef] [PubMed]
3. Wenger, O.S. Long-range electron transfer in artificial systems with d^6 and d^8 metal photosensitizers. *Coord. Chem. Rev.* **2009**, *253*, 1439–1457. [CrossRef]
4. Goldsmith, J.I.; Hudson, W.R.; Lowry, M.S.; Anderson, T.H.; Bernhard, S. Discovery and high-throughput screening of heteroleptic iridium complexes for photoinduced hydrogen production. *J. Am. Chem. Soc.* **2005**, *127*, 7502–7510. [CrossRef]
5. Day, J.I.; Teegardin, K.; Weaver, J.; Chan, J. Advances in Photocatalysis: A Microreview of Visible Light Mediated Ruthenium and Iridium Catalyzed Organic Transformations. *Org. Process Res. Dev.* **2016**, *20*, 1156–1163. [CrossRef]
6. Corredor, J.; Rivero, M.J.; Rangel, C.M.; Gloaguen, F.; Ortiz, I. Comprehensive review and future perspectives on the photocatalytic hydrogen production. *J. Chem. Technol. Biot.* **2019**, *94*, 3049–3063. [CrossRef]
7. Wenger, O.S. Is Iron the New Ruthenium? *Chem. Eur. J.* **2019**, *25*, 6043–6052. [CrossRef] [PubMed]
8. Dierks, P.; Vukadinovic, Y.; Bauer, M. Photoactive iron complexes: More sustainable, but still a challenge. *Inorg. Chem. Front.* **2022**, *9*, 206–220. [CrossRef]
9. Cannizzo, A.; Milne, C.J.; Consani, C.; Gawelda, W.; Bressler, C.; van Mourik, F.; Chergui, M. Light-induced spin crossover in Fe(II)-based complexes: The full photocycle unraveled by ultrafast optical and X-ray spectroscopies. *Coord. Chem. Rev.* **2010**, *254*, 2677–2686. [CrossRef]
10. Sauvage, J.-P.; Collin, J.-P.; Chambron, J.-C.; Gullirez, S.; Coudret, C.; Balzani, V.; Barigelletti, F.; de Cola, L.; Flamigni, L. ChemInform Abstract: Ruthenium(II) and Osmium(II) Bis(terpyridine) Complexes in Covalently- Linked Multicomponent Systems: Synthesis, Electrochemical Behavior, Absorption Spectra, and Photochemical and Photophysical Properties. *Chem. Rev.* **1994**, *25*, 993–1019. [CrossRef]
11. Damrauer, N.H.; Cerullo, G.; Yeh, A.; Boussie, T.R.; Shank, C.V.; McCusker, J.K. Femtosecond Dynamics of Excited-State Evolution in. *Science* **1997**, *275*, 54–57. [CrossRef]
12. Jakubikova, E.; Chen, W.; Dattelbaum, D.M.; Rein, F.N.; Rocha, R.C.; Martin, R.L.; Batista, E.R. Electronic Structure and Spectroscopy of $[Ru(tpy)_2]^{2+}$, $[Ru(tpy)(bpy)(H_2O)]^{2+}$, and $[Ru(tpy)(bpy)(Cl)]^{+}$. *Inorg. Chem.* **2009**, *48*, 10720–10725. [CrossRef] [PubMed]
13. McCusker, J.K. Electronic structure in the transition metal block and its implications for light harvesting. *Science* **2019**, *363*, 484–488. [CrossRef] [PubMed]
14. Liu, Y.; Persson, P.; Sundström, V.; Wärnmark, K. Fe *N*-Heterocyclic Carbene Complexes as Promising Photosensitizers. *Acc. Chem. Res.* **2016**, *49*, 1477–1485. [CrossRef]
15. Kaufhold, S.; Wärnmark, K. Design and Synthesis of Photoactive Iron *N*-Heterocyclic Carbene Complexes. *Catalysts* **2020**, *10*, 132. [CrossRef]
16. Liu, Y.; Harlang, T.; Canton, S.E.; Chábera, P.; Suárez-Alcántara, K.; Fleckhaus, A.; Vithanage, D.A.; Göransson, E.; Corani, A.; Lomoth, R.; et al. Towards longer-lived metal-to-ligand charge transfer states of iron(II) complexes: An *N*-heterocyclic carbene approach. *Chem. Comm.* **2013**, *49*, 6412–6414. [CrossRef] [PubMed]
17. Lindh, L.; Chábera, P.; Rosemann, N.W.; Uhlig, J.; Wärnmark, K.; Yartsev, A.; Sundström, V.; Persson, P. Photophysics and Photochemistry of Iron Carbene Complexes for Solar Energy Conversion and Photocatalysis. *Catalysts* **2020**, *10*, 315. [CrossRef]
18. Steube, J.; Kruse, A.; Bokareva, O.S.; Reuter, T.; Demeshko, S.; Schoch, R.; Argüello Cordero, M.A.; Krishna, A.; Hohloch, S.; Meyer, F.; et al. Janus-type emission from a cyclometalated iron(III) complex. *Nat. Chem.* **2023**, *15*, 468–474. [CrossRef]
19. Chábera, P.; Liu, Y.; Prakash, O.; Thyrhaug, E.; Nahhas, A.E.; Honarfar, A.; Essén, S.; Fredin, L.A.; Harlang, T.C.B.; Kjær, K.S.; et al. A low-spin Fe(III) complex with 100-ps ligand-to-metal charge transfer photoluminescence. *Nature* **2017**, *543*, 695–699. [CrossRef]
20. Kjær, K.S.; Kaul, N.; Prakash, O.; Chábera, P.; Rosemann, N.W.; Honarfar, A.; Gordivska, O.; Fredin, L.A.; Bergquist, K.-E.; Häggström, L.; et al. Luminescence and reactivity of a charge-transfer excited iron complex with nanosecond lifetime. *Science* **2019**, *363*, 249–253. [CrossRef]
21. Koeberl, C.; Young, E.R.; Oldacre, A. Iron hits the mark. *Science* **2019**, *363*, 224–225. [CrossRef]
22. Chábera, P.; Lindh, L.; Rosemann, N.W.; Prakash, O.; Uhlig, J.; Yartsev, A.; Wärnmark, K.; Sundström, V.; Persson, P. Photofunctionality of iron(III) *N*-heterocyclic carbenes and related d transition metal complexes. *Coord. Chem. Rev.* **2021**, *426*, 213517. [CrossRef]
23. Liu, Y.; Kjaer, K.S.; Fredin, L.A.; Chábera, P.; Harlang, T.; Canton, S.E.; Lidin, S.; Zhang, J.; Lomoth, R.; Bergquist, K.-E.; et al. A heteroleptic ferrous complex with mesoionic bis(1,2,3-triazol-5-ylidene) ligands: Taming the MLCT excited state of iron(II). *Chem. Eur. J.* **2015**, *21*, 3628–3639. [CrossRef] [PubMed]
24. Medlycott, E.A.; Hanan, G.S. Designing tridentate ligands for ruthenium(II) complexes with prolonged room temperature luminescence lifetimes. *Chem. Soc. Rev.* **2005**, *34*, 133–142. [CrossRef] [PubMed]
25. Chábera, P.; Kjaer, K.S.; Prakash, O.; Honarfar, A.; Liu, Y.; Fredin, L.A.; Harlang, T.C.B.; Lidin, S.; Uhlig, J.; Sundström, V.; et al. FeII Hexa *N*-Heterocyclic Carbene Complex with a 528 ps Metal-to-Ligand Charge-Transfer Excited-State Lifetime. *J. Phys. Chem. Lett.* **2018**, *9*, 459–463. [CrossRef]

26. Nam, E.J.; Kim, J.H.; Kim, B.-O.; Kim, S.M.; Park, N.G.; Kim, Y.S.; Kim, Y.K.; Ha, Y. A Synthesis and Luminescence Study of Ir(ppz)$_3$ for Organic Light-Emitting Devices. *Bull. Chem. Soc. Jpn.* **2004**, *77*, 751–755. [CrossRef]
27. Ren, X.; Alleyne, B.D.; Djurovich, P.I.; Adachi, C.; Tsyba, I.; Bau, R.; Thompson, M.E. Organometallic complexes as hole-transporting materials in organic light-emitting diodes. *Inorg. Chem.* **2004**, *43*, 1697–1707. [CrossRef] [PubMed]
28. Drevs, H. Elektronenvariable σ-Organochelatkomplexe: Pyrazolylphenylkomplexe des Eisen(II), Eisen(III) und Eisen(IV). *Z. Chem.* **1979**, *19*, 31–32. [CrossRef]
29. Cristau, H.-J.; Cellier, P.P.; Spindler, J.-F.; Taillefer, M. Mild Conditions for Copper-Catalysed *N*-Arylation of Pyrazoles. *Eur. J. Org. Chem.* **2004**, *2004*, 695–709. [CrossRef]
30. Cristau, H.-J.; Cellier, P.P.; Spindler, J.-F.; Taillefer, M. Highly efficient and mild copper-catalyzed N- and C-arylations with aryl bromides and iodides. *Chem. Eur. J.* **2004**, *10*, 5607–5622. [CrossRef]
31. Marxer, A.; Siegrist, M. Über die Umsetzung von 1-Phenylpyrazol mit Äthylmagnesiumbromid. 8. Mitteilung über Grignard-Reaktionen [1]//Über die Umsetzung von 1-Phenylpyrazol mit Äthylmagnesiumbromid. *Helv. Chim. Acta* **1974**, *57*, 1988–2000. [CrossRef]
32. Cotton, F.; Luck, R.L.; Son, K.-A. New polynuclear compounds of iron(II) chloride with oxygen donor ligands Part I. $Fe_4Cl_8(THF)_6$: Synthesis and a single crystal X-ray structure determination. *Inorg. Chim. Acta* **1991**, *179*, 11–15. [CrossRef]
33. Tsuchiya, K.; Ito, E.; Yagai, S.; Kitamura, A.; Karatsu, T. Chirality in the Photochemical mer→fac Geometrical Isomerization of Tris(1-phenylpyrazolato,*N*,$C^{2\prime}$)iridium(III). *Eur. J. Inorg. Chem.* **2009**, *2009*, 2104–2109. [CrossRef]
34. Francés-Monerris, A.; Gros, P.C.; Assfeld, X.; Monari, A.; Pastore, M. Toward luminescent iron complexes: Unraveling the photophysics by computing potential energy surfaces. *ChemPhotoChem* **2019**, *3*, 666–683. [CrossRef]
35. Deorukhkar, N.; Besnard, C.; Guénée, L.; Piguet, C. Tuning spin-crossover transition temperatures in non-symmetrical homoleptic meridional/facial [Fe(didentate)$_3$]$^{2+}$ complexes: What for and who cares about it? *Dalton Trans.* **2021**, *50*, 1206–1223. [CrossRef]
36. Tamayo, A.B.; Alleyne, B.D.; Djurovich, P.I.; Lamansky, S.; Tsyba, I.; Ho, N.N.; Bau, R.; Thompson, M.E. Synthesis and characterization of facial and meridional tris-cyclometalated iridium(III) complexes. *J. Am. Chem. Soc.* **2003**, *125*, 7377–7387. [CrossRef]
37. Lehr, M.; Paschelke, T.; Trumpf, E.; Vogt, A.-M.; Näther, C.; Sönnichsen, F.D.; McConnell, A.J. A Paramagnetic NMR Spectroscopy Toolbox for the Characterisation of Paramagnetic/Spin-Crossover Coordination Complexes and Metal-Organic Cages. *Chem. Angew. Chem. Int. Ed.* **2020**, *59*, 19344–19351. [CrossRef]
38. Bomben, P.G.; Robson, K.C.D.; Sedach, P.A.; Berlinguette, C.P. On the viability of cyclometalated Ru(II) complexes for light-harvesting applications. *Inorg. Chem.* **2009**, *48*, 9631–9643. [CrossRef]
39. Kaneko, R.; Wu, G.; Sugawa, K.; Otsuki, J.; Islam, A.; Han, L.; Bedja, I.; Gupta, R.K. Cyclometalated ruthenium complexes with 6-(ortho-methoxyphenyl)-2,2′-bipyridine as panchromatic dyes for dye-sensitized solar cells. *J. Organomet. Chem.* **2017**, *833*, 61–70. [CrossRef]
40. Kisserwan, H.; Kamar, A.; Shoker, T.; Ghaddar, T.H. Photophysical properties of new cyclometalated ruthenium complexes and their use in dye sensitized solar cells. *Dalton Trans.* **2012**, *41*, 10643–10651. [CrossRef]
41. Motley, T.C.; Troian-Gautier, L.; Brennaman, M.K.; Meyer, G.J. Excited-State Decay Pathways of Tris(bidentate) Cyclometalated Ruthenium(II) Compounds. *Inorg. Chem.* **2017**, *56*, 13579–13592. [CrossRef]
42. Steube, J.; Burkhardt, L.; Päpcke, A.; Moll, J.; Zimmer, P.; Schoch, R.; Wölper, C.; Heinze, K.; Lochbrunner, S.; Bauer, M. Excited-State Kinetics of an Air-Stable Cyclometalated Iron(II) Complex. *Chem. Eur. J.* **2019**, *25*, 11826–11830. [CrossRef] [PubMed]
43. Prakash, O.; Chábera, P.; Rosemann, N.W.; Huang, P.; Häggström, L.; Ericsson, T.; Strand, D.; Persson, P.; Bendix, J.; Lomoth, R.; et al. A Stable Homoleptic Organometallic Iron(IV) Complex. *Chemistry* **2020**, *26*, 12728–12732. [CrossRef] [PubMed]
44. Ashley, D.C.; Jakubikova, E. Ray-Dutt and Bailar Twists in Fe(II)-Tris(2,2′-bipyridine): Spin States, Sterics, and Fe-N Bond Strengths. *Inorg. Chem.* **2018**, *57*, 5585–5596. [CrossRef] [PubMed]
45. Paulus, B.C.; Adelman, S.L.; Jamula, L.L.; McCusker, J.K. Leveraging excited-state coherence for synthetic control of ultrafast dynamics. *Nature* **2020**, *582*, 214–218. [CrossRef]
46. Grimme, S.; Brandenburg, J.G.; Bannwarth, C.; Hansen, A. Consistent structures and interactions by density functional theory with small atomic orbital basis sets. *Chem. Phys.* **2015**, *143*, 54107. [CrossRef]
47. Tao, J.; Perdew, J.P.; Staroverov, V.N.; Scuseria, G.E. Climbing the density functional ladder: Nonempirical meta-generalized gradient approximation designed for molecules and solids. *Phys. Rev. Lett.* **2003**, *91*, 146401. [CrossRef]
48. Weigend, F. Accurate Coulomb-fitting basis sets for H to Rn. *Phys. Chem. Chem. Phys.* **2006**, *8*, 1057–1065. [CrossRef]
49. Shoaf, A.L.; Bayse, C.A. TD-DFT and structural investigation of natural photosensitive phenanthroperylene quinone derivatives. *New J. Chem.* **2016**, *40*, 413–422. [CrossRef]
50. Atkins, A.J.; Bauer, M.; Jacob, C.R. The chemical sensitivity of X-ray spectroscopy: High energy resolution XANES versus X-ray emission spectroscopy of substituted ferrocenes. *Phys. Chem. Chem. Phys.* **2013**, *15*, 8095–8105. [CrossRef]
51. Burkhardt, L.; Holzwarth, M.; Plietker, B.; Bauer, M. Detection and Characterization of Hydride Ligands in Iron Complexes by High-Resolution Hard X-ray Spectroscopy and Implications for Catalytic Processes. *Inorg. Chem.* **2017**, *56*, 13300–13310. [CrossRef]
52. Atkins, A.J.; Jacob, C.R.; Bauer, M. Probing the electronic structure of substituted ferrocenes with high-resolution XANES spectroscopy. *Chem. Eur. J.* **2012**, *18*, 7021–7025. [CrossRef] [PubMed]

53. Bauer, M. HERFD-XAS and valence-to-core-XES: New tools to push the limits in research with hard X-rays? *Phys. Chem. Chem. Phys.* **2014**, *16*, 13827–13837. [CrossRef] [PubMed]
54. Glatzel, P.; Bergmann, U. High resolution 1s core hole X-ray spectroscopy in 3d transition metal complexes—Electronic and structural information. *Coord. Chem. Rev.* **2005**, *249*, 65–95. [CrossRef]
55. Bergmann, U.; Glatzel, P. X-ray emission spectroscopy. *Photosyn. Res.* **2009**, *102*, 255–266. [CrossRef]
56. Delgado-Jaime, M.U.; DeBeer, S.; Bauer, M. Valence-to-core X-ray emission spectroscopy of iron-carbonyl complexes: Implications for the examination of catalytic intermediates. *Chem. Eur. J.* **2013**, *19*, 15888–15897. [CrossRef]
57. Illanes, A. (Ed.) *Enzyme Biocatalysis: Principles and Applications*; Springer: Dordrecht, The Netherlands, 2008; ISBN 978-1-4020-8360-0.
58. Eastham, K.; Scattergood, P.A.; Chu, D.; Boota, R.Z.; Soupart, A.; Alary, F.; Dixon, I.M.; Rice, C.R.; Hardman, S.J.O.; Elliott, P.I.P. Not All ^{3}MC States Are the Same: The Role of ^{3}MCcis States in the Photochemical N^N Ligand Release from Ru(bpy)$_2$(N^N)$^{2+}$ Complexes. *Inorg. Chem.* **2022**, *61*, 19907–19924. [CrossRef]
59. Neese, F. The ORCA program system. *WIREs Comput. Mol. Sci.* **2012**, *2*, 73–78. [CrossRef]
60. Staroverov, V.N.; Scuseria, G.E.; Tao, J.; Perdew, J.P. Comparative assessment of a new nonempirical density functional: Molecules and hydrogen-bonded complexes. *Chem. Phys.* **2003**, *119*, 12129–12137. [CrossRef]
61. Weigend, F.; Ahlrichs, R. Balanced basis sets of split valence, triple zeta valence and quadruple zeta valence quality for H to Rn: Design and assessment of accuracy. *Phys. Chem. Chem. Phys.* **2005**, *7*, 3297–3305. [CrossRef]
62. Neese, F.; Wennmohs, F.; Hansen, A.; Becker, U. Efficient, approximate and parallel Hartree–Fock and hybrid DFT calculations. A 'chain-of-spheres' algorithm for the Hartree–Fock exchange. *Chem. Phys.* **2009**, *356*, 98–109. [CrossRef]
63. Cossi, M.; Rega, N.; Scalmani, G.; Barone, V. Energies, structures, and electronic properties of molecules in solution with the C-PCM solvation model. *J. Comput. Chem.* **2003**, *24*, 669–681. [CrossRef] [PubMed]
64. Neese, F. Prediction and interpretation of the ^{57}Fe isomer shift in Mössbauer spectra by density functional theory. *Inorg. Chim. Acta* **2002**, *337*, 181–192. [CrossRef]
65. Delgado-Jaime, M.U.; DeBeer, S. Expedited analysis of DFT outputs: Introducing MOAnalyzer. *J. Comput. Chem.* **2012**, *33*, 2180–2185. [CrossRef]
66. Plasser, F. TheoDORE: A toolbox for a detailed and automated analysis of electronic excited state computations. *Chem. Phys.* **2020**, *152*, 84–108. [CrossRef] [PubMed]
67. Knizia, G.; Klein, J.E.M.N. Electron flow in reaction mechanisms--revealed from first principles. *Angew. Chem. Int. Ed. Engl.* **2015**, *54*, 5518–5522. [CrossRef]
68. Gauthier, C.; Solé, V.A.; Signorato, R.; Goulon, J.; Moguiline, E. The ESRF beamline ID26: X-ray absorption on ultra dilute sample. *J. Synchrotron. Rad.* **1999**, *6*, 164–166. [CrossRef]
69. Johann, H.H. Die Erzeugung lichtstarker Röntgenspektren mit Hilfe von Konkavkristallen. *Z. Physik* **1931**, *69*, 185–206. [CrossRef]
70. Sheldrick, G.M. Crystal structure refinement with SHELXL. *Acta Crystallogr. C Struct. Chem.* **2015**, *71*, 3–8. [CrossRef]
71. Sheldrick, G.M. SHELXT—Integrated space-group and crystal-structure determination. *Acta Crystallogr. A Found. Adv.* **2015**, *71*, 3–8. [CrossRef]

CHAPTER 4

ISOSTRUCTURAL SERIES OF A CYCLOMETALATED IRON COMPLEX IN THREE OXIDATION STATES

Oxidation states are an important formalistic model to describe the electronic structure of molecules which can also be used to estimate stability and reactivity of complexes. In this chapter a cyclometallated iron complex which is stable in three different oxidation states is investigated by different ground and excited state techniques. The characterization demonstrates that the chemically induced oxidation and reduction from the parent iron(III) complex is centered at the metal and thus leads to the first isostructural row of homoleptic low-spin iron complexes in a d^6, d^5 and d^4 configuration which corresponds to spin states of S=0, S=0.5 and S=1 in the octahedral ligand field. This is especially shown by magnetic susceptibility measurements and X-ray absorption and emission spectroscopy.

Participations in this publication

Jakob Steube: Synthesis, characterization(NMR, MS, IR, UV-Vis), Writing;
L. Fritsch: X-ray spectroscopy and accompanying calculations, Writing;
Ayla Kruse, Stefan Lochbrunner: Transient absorption spectroscopy;
Serhiy Demeshko, Franc Meyer: SQUID and Mößbauer measurements;
Hossam Elgabarty, Mohammad Alaraby, Olga Bokareva, Thomas D. Kühne, Oliver Kühn : Theoretical calculations;
M. Bauer: Writing – review and editing, Project Administration.

Reprinted from
Isostructural series of a cyclometalated iron complex in three oxidation states
Jakob Steube, Lorena Fritsch, Ayla Kruse, Olga Bokareva. Serhiy Demeshko, Hossam Elgabarty, Roland Schoch, Mohammad Alaraby, Stephan Hohloch , Thomas D. Kühne, Franc Meyer, Oliver Kühn, Stefan Lochbrunner, Matthias Bauer*; *Inorg. Chem.*, **2023**, in revision.

Supplementary Information for this publication is found in the Appendix A.3.

Isostructural series of a cyclometalated iron complex in three oxidation states

Jakob Steube[1,2], Lorena Fritsch[1,2], Ayla Kruse[3,4], Olga Bokareva[3†], Serhiy Demeshko[5], Hossam Elgabarty[2,6], Roland Schoch[1,2], Mohammad Alaraby[2,6], Stephan Hohloch[1‡], Thomas D. Kühne[2,6], Franc Meyer[5], Oliver Kühn[3,4], Stefan Lochbrunner[3,4], Matthias Bauer[1,2*]

1: Institute for Inorganic Chemistry, Paderborn University, 33098 Paderborn, Germany

2: Center for Sustainable Systems Design (CSSD), Paderborn University, 33098 Paderborn, Germany

3: Department of Life, Light and Matter, University of Rostock, 18051 Rostock, Germany

4: Institute for Physics, University of Rostock, 18051 Rostock, Germany

5: Institute of Inorganic Chemistry, University of Göttingen, Göttingen, Germany

6: Institute for Theoretical Chemistry, Paderborn University, 33098 Paderborn, Germany

ABSTRACT: An isostructural series of Fe^{II}, Fe^{III} and Fe^{IV} complexes $[Fe(ImP)_2]^{0/+/2+}$ utilizing the ImP (1,1'-(1,3-phenylene)bis(3-methyl-1-imidazol-2-ylidene) ligand is presented. In these complexes, a uniquely strong donor ligand set is formed by the combination of four *N*-heterocyclic carbenes (NHCs) and two cyclometalating functions. These stabilize the high-valent Fe^{IV} oxidation state, but also keep the Fe^{II} oxidation state accessible from the parent Fe^{III} compound. Chemical oxidation of $[Fe(ImP)_2]^+$ with $NOPF_6$ yields stable $[Fe^{IV}(ImP)_2]^{2+}$. In contrast, $[Fe^{II}(ImP)_2]^0$, obtained by reduction with sodium amalgam, is highly sensitive towards oxygen. Exhaustive ground state characterization with a broad array of methods, namely single-crystal X-ray diffraction (scXRD), ^{1}H-NMR, Mössbauer spectroscopy, temperature-dependent magnetic measurements, a combination of X-ray absorption near edge structure (XANES) and Valence-to-Core, as well as Core-to-Core X-ray emission spectroscopy, complemented by detailed DFT analysis, reveals that the three complexes $[Fe(ImP)_2]^{0/+/2+}$ can be unequivocally attributed to low-spin d^6, d^5 and d^4 complexes, respectively, with spin-states of 0, ½ and 1. The excited state behavior of the Fe^{II} and the Fe^{IV} complexes, as characterized by transient optical spectroscopy, is radically different from the parent Fe^{III} complex. Short ^{3}MLCT and ^{3}LMCT excited state lifetimes of 5.1 and 1.4 ps, respectively, are revealed. An energetically low-lying MC state with a lifetime of 10.8 ps was identified in the relaxation cascade of $[Fe^{II}(ImP)_2]^0$, leading to the fast deactivation of the ^{3}MLCT state.

Introduction

The chemistry of iron offers a huge variety due to the broad range of possible formal oxidation states in its complex chemistry. From the -II state in Collman's reagent[1] up to the +VI state in either the ferrate anion (FeO_4^{2-})[2] or the recently published example of a bis(carbene) bis(imido) complex from the group of Smith *et al.*,[3] every formal oxidation state has been observed. However, isostructural series of more than two successive metal-based oxidation states are still rare,[4,5] often due to non-innocent ligand behavior.[6–12] Another important factor is the stabilization of higher oxidation states, which requires strong donor ligands. Typically, strong π-donors, such as oxo or imido ligands[13,14] but also corroles are employed for this purpose.[15,16] Besides such anionic nitrogen π-donors, anionic carbon ligands in the form of alkyl and aryl anions can also be used.[17,18] Here the σ-donor character dominates, but they also show a significant amount of π-donation in the case of aryl carbanions.[19–21] Therefore, compared to neutral nitrogen counterparts such as pyridines, higher oxidation states are more stabilized. Noteworthy examples are Au(III) and Pt(IV) compounds,[22,23] where cyclometalating functions play a role in stabilizing these high oxidation states. Another good example for the stabilization of higher oxidation states is a series of Os(II) complexes, based on $[Os(bpy)_3]^{2+}$ (bpy = 2,2'-bipyridine). Here, bpy ligands are exchanged for cyclometalating 2-phenylpyridine (ppy^-) ligands. Each ppy-ligand leads to a destabilization of the Os(II)-state of around 0.5 V.[24] Such a trend has also been observed in recently realized cyclometalated iron complexes. Substitution of one of the outer pyridines in the parent bis(terpyridine)iron(II) by a cyclometalating phenylene leads to a significant decrease of the $Fe^{II/III}$ redox potential by about 0.8 V.[25] This trend continues for the replacement of the two central pyridine rings in $[Fe(bimp)_2]^{2+}$ (bimp = (2,6-bis(3-methylimidazol-1-ylidene)pyridine))[26] by phenylene in $[Fe(ImP)_2]^+$ (ImP =1,1'-(1,3-phenylene)bis(3-methyl-1-imidazol-2-ylidene)), with a cathodic shift of the $Fe^{II/III}$ potential of around 1.5 V.[27] This complex is additionally characterized by a $Fe^{III/IV}$ transition

Table 1: Comparison of the important structural parameters of 1^-, 1 and 1^+ obtained from their crystal structures with their respective error in brackets.

Compound	1^- ($[Fe(ImP)_2]^0$)	1 ($[Fe(ImP)_2]^+$)	1^+ ($[Fe(ImP)_2]^{2+}$)
Fe-C_{CM} mean distance (Å)	1.918(2)	1.948(3)	1.955(7)
Fe-C_{NHC} mean distance (Å)	1.938(8)	1.983(3)	2.005(8)
C_{NHC}-Fe-C_{NHC} bite angle (°)	156.00(60)	155.36(15)	154.30(30)
Ligand/Ligand torsion angle (°)	90	86	88

at a potential of 0.1 V vs $Fc^{0/+}$. Accordingly, $[Fe(ImP)_2]^+$ shows a rather rare property of both a MLCT (metal-to-ligand charge-transfer) and LMCT (ligand-to-metal charge-transfer) optical absorption. As a unique feature in iron complex chemistry, an emission from both states is observed. Due to the ligand design combining *N*-heterocyclic carbenes (NHCs) with a cyclometalating functionality in the ImP-ligand, three oxidation states are in an accessible range. Therefore, a series of the isostructural homoleptic complexes $[Fe(ImP)_2]^{0/+/2+}$ was attempted in this work.

The electronic structure of the complexes was investigated with respect to the physical oxidation state of the iron center using various analytical and spectroscopic methods, including single crystal X-ray diffraction, Mössbauer and temperature dependent superconducting quantum interference device (SQUID) magnetization. Special emphasis was placed on synchrotron-based X-ray absorption (XAS) and emission spectroscopy (XES), as these provide high sensitivity to the local electronic structure of the iron center. The excited state dynamics were studied by transient optical absorption spectroscopy. Theoretical calculations were used to understand and consolidate the spectroscopic results.

Results and Discussion

Figure 1 shows the synthesis for the discussed complexes. The synthesis of $[Fe^{III}(ImP)_2]PF_6$ (HImP =1,1′-(1,3-phenylene)bis(3-methyl-1-imidazol-2-ylidene)) **1** was published recently.[27] From this, $[Fe^{II}(ImP)_2]$ **1^-** is obtained by reduction of **1** with sodium amalgam in THF. For better solubility in THF, **1** was converted to its BPh_4 salt prior to reduction (*cf.* Supporting Information, Synthesis). The orange compound was stored in the cold (-30°C) in the glovebox, since miniscule amounts of oxygen at room temperature led to reoxidation to the blue Fe^{III} counterpart, which is, as expected, faster in solution than in the solid. However, due to its instability towards atmospheric conditions, it was not possible to obtain meaningful results in elemental analysis. Yet, single crystals suitable for X-ray diffraction could be grown by diffusion of pentane into a DCM solution of **1^-**, confirming the structure of **1^-**.

Dark $[Fe^{IV}(ImP)_2](PF_6)_2$ **1^+** can be obtained by oxidation of **1** under inert conditions in acetonitrile (MeCN) using $NOPF_6$ (*cf.* Supporting Information, Synthesis for experimental detail). Fine crystals are yielded by diffusion of chloroform into a solution of **1^+** in acetone, while crystals suitable for X-ray diffraction were obtained by diffusion of diethyl ether into a methanol solution of **1^+**.

In table 1, selected structural parameters of **1^-** and **1^+** are compared to literature values of **1**.[27,28] The corresponding molecular structures are depicted in Figure 1. The bond lengths of **1^-** are generally similar, but shorter than those of the analogous Fe^{II} complex with pyridines in the center of the tridentate ligands (mean Fe-N distance: 1.929 Å, mean Fe-C distance: 1.962 Å).[26]

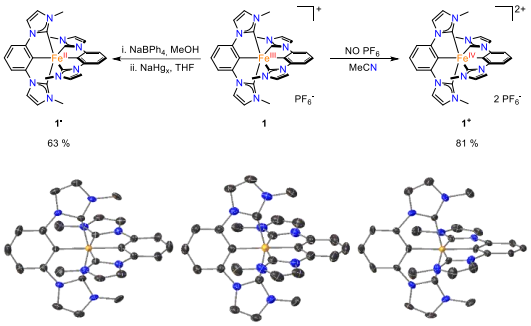

Figure 1: Synthesis of complexes **1^-** and **1^+** which are obtained by reduction via sodium amalgam (0.3 %) and oxidation via nitrosonium hexafluorophosphate, respectively, and the molecular structures of **1^-**, **1**[27,28] and **1^+** determined by scXRD (electron density on a 50% probability level).

The mean Fe-C_{NHC} bond-length is also shorter than in the $[Fe^{II}(btz)]^{2+}$ complex (btz =3,3′-dimethyl-1,1′-bis(*p*-tolyl)-4,4′-bis(1,2,3-triazol-5-ylidene)), where a similar mean Fe-C bond-length of 1.963 Å is observed.[29] The mean Fe-C_{NHC} bond-lengths of **1** and **1^+** are both comparable to the mean Fe-C bond-lengths of $[Fe(phtmeimb)_2]^+$ and $[Fe(phtmeimb)_2]^{2+}$ (phtmeimb) = [phenyl(tris(3-methylimidazolin-2-ylidene))borate]$^-$) (1.979 and 2.002 Å, respectively).[30,31] Therefore, comparison with literature-known compounds shows that the ligand type has a greater influence on the bond-length than the oxidation state, although slightly longer bonds are observed in higher oxidation states.

A comparison of the different oxidation states in the $[Fe^{n+}(ImP)_2]^{(n-2)+}$ series shows only minor structural changes (Table 1). While there seems to be a correlation between oxidation states and an increase in bond length, the changes between successive oxidation states are statistically non-significant. This leads to two conclusions: First, all complexes are in a low-spin environment, since high-spin complexes usually show longer bond lengths, which are typically at least 0.1 Å longer.[32,33] Second, the covalency of the iron-carbon bonds and the rigidity of the (ImP) ligand leads

to a stability of the structural motif, where only small structural changes are possible upon oxidation state change. Accordingly, only small structural reorganization energies between the different oxidation states are induced, allowing fast electron transfer processes, as described by Wärnmark *et al.*[30] This also explains the fast reaction of **1**$^-$ with oxygen, leading to reoxidation to **1**.

Therefore, acquisition of NMR data for **1**$^-$ was a challenging task. Nevertheless, NMR data matches the expectation of a low-spin Fe^{II} complex and does not show residues of **1** or protonated ligand (*cf.* Figure S12 and S13 in the Supporting Information). ^{1}H-NMR proved also useful for the examination of **1**$^+$, as again all signals except for the central proton in the phenyl backbone can be observed (*cf.* Figure S14). With the broadest peak showing reasonable FWHM values of 125 Hz/ 0.179 ppm and data indicating symmetric ligands, the NMR data supports that oxidation of **1** occurs on the metal center and **1**$^+$ is a low-spin Fe^{IV} compound.

More detailed insights into the electronic structure are provided by Mössbauer spectroscopy. The spectra of **1**$^-$ and **1**$^+$ in comparison to **1**[27] are shown in Figure 2.

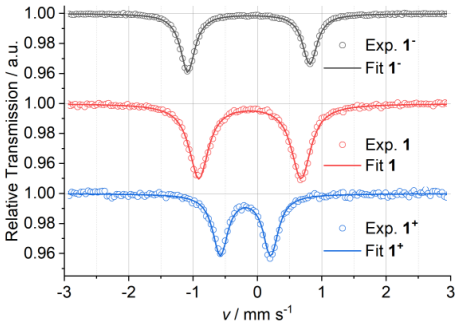

Figure 2: ^{57}Fe zero-field Mössbauer spectra of **1**$^-$ (black), **1** (red)[27] and **1**$^+$ (blue) at 80 K.

The Mössbauer spectra of the three compounds are all composed of doublets, characterized by their isomer shift and quadrupole splitting parameters. Usually, the isomer shift is a revealing parameter for the oxidation state of iron compounds. It is typically lower for higher oxidation states, as it reflects the contribution of the 4s electrons to the electron density at the Fe nucleus, which is mainly influenced by the 4s population and by shielding effects due to the 3d population.[34] On the other hand, the isomer shift depends strongly on the iron–ligand distances, i.e., shorter iron–ligand distances cause lower isomer shifts due to the decreased radial extension of the 4s-orbital.[35] After oxidation from **1** to **1**$^+$, the isomer shift decreases from –0.12 mm s^{-1} to –0.19 mm s^{-1}, as expected for the increased metal oxidation state, since the shielding effect of the 3d-electrons (less for **1**$^+$ compared to **1**) on the 3s- and 4s-electrons decreases while all Fe–C distances remain comparable upon going from **1** to **1**$^+$ (*cf.* Table 1). Hence, the difference in the isomer shift between **1** to **1**$^+$ follows the expected trend and can be attributed to the changes in 3d-orbital population. However, after reduction from **1** to **1**$^-$, the isomer shift decreases slightly from –0.12 mm s^{-1} to –0.14 mm s^{-1}. This counterintuitive isomer shift change can be explained by the significant contraction of the Fe–C distances in **1**$^-$ (*cf.* Table 1) due to enhanced π-backdonation, hence the data are still in line with metal-based reduction.[36] All three isomer shift values are quite low, in accordance with a low-spin configuration of the investigated compounds. The values for the quadrupole splitting reflect the non-cubic charge distribution of the surrounding electrons and in the case of strongly covalent anisotropic bonds, no simple correlation with the oxidation states can be made.

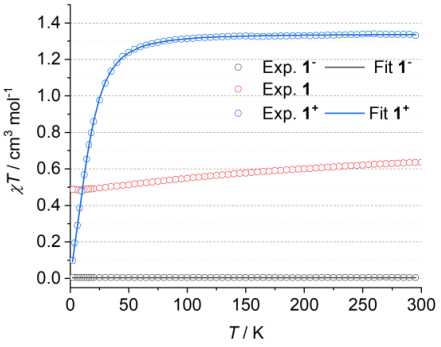

Figure 3: Temperature-dependent magnetic susceptibility measurements of **1**,[27] **1**$^-$, and **1**$^+$.

Temperature-dependent magnetic susceptibility measurements, which are shown in Figure 3, confirm these considerations. Experimental $\chi_M T$ values at room temperature are 0.005, 0.63[27] and 1.33 cm^{3}mol^{-1}K for **1**$^-$, **1**, and **1**$^+$, respectively, which are close to the theoretically expected spin-only values of 0, 0.375 and 1 cm^{3}mol^{-1}K for S = 0, ½ and 1, respectively, and indicative of some orbital contributions in case of **1** and **1**$^+$. For **1**$^+$, global fitting of the temperature dependent susceptibility data and the variable temperature – variable field measurements (*cf.* Figure S3 in the Supporting Information) allowed the determination of the zero-field splitting (ZFS) parameter D = +39.5 cm^{-1}. The D value is slightly higher than the typical values of +16 to + 35 cm^{-1} for Fe(IV) complexes,[14,30,37] although values up to 51 cm^{-1} have been observed.[12] Since the ZFS is inversely proportional to the energy gap between the triplet ground state and the first excited quintet state,[38] the relatively high D value for **1**$^+$ may be indicative of a rather low triplet-quintet separation.

Further analysis of the electronic structure is obtained by hard X-ray spectroscopy in form of X-ray absorption near-edge structure spectroscopy (XANES)[39–41] and X-ray emission spectroscopy (XES).[42–45] XANES spectra of 3d-metal complexes exhibit prepeak signals originating from 1s → LUMO transitions, thus probing typically nd/(n+1)p states. As pure s→d transitions are dipole forbidden and the resulting signal would be very weak, the prepeak intensity in these distorted octahedral complexes gain intensity from hybridization of the d-orbitals with ligand p-orbitals.[46,47]

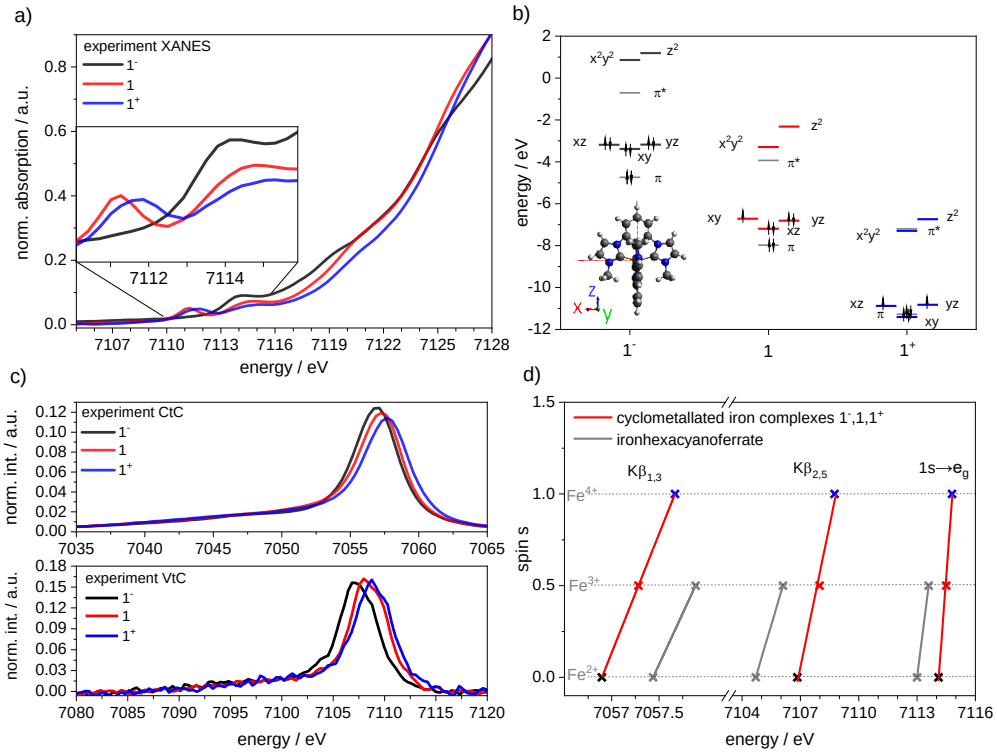

Figure 4: a) Experimental XANES spectra of complexes **1**$^{-}$, **1** and **1**$^{+}$. Inset: Magnification of the pre-edge region. b) Selected molecular orbital levels of d-orbitals, highest π and lowest π* orbital based on TPSS/def2-TZVPP DFT calculations. c) Experimental CtC (top) and VtC (bottom) spectra of complexes **1**$^{-}$, **1** and **1**$^{+}$. d) Plot spin vs. energy of the Kβ$_{1,3}$, Kβ$_{2,5}$ and pre-peak (1s→e$_g$) maxima of complexes **1**$^{-}$, **1** and **1**$^{+}$ in comparison to $Fe(CN)_6^{3+/4+}$. Parameters for linear regression are listed in Table S1.

Thus, the prepeaks can provide information about the coordination geometry and the electronic structure of the absorbing atom. Due to the isostructural nature of the investigated complexes, it is employed here to gain information on the local electronic structure at the iron centers. With increasing oxidation state from $[Fe(ImP)_2]^0$ to $[Fe(ImP)_2]^{2+}$, a higher prepeak energy is expected for purely metal-based oxidation events, which is indeed found in the experimental spectra of Figure 4. Only one prepeak in the range of 7110-7116 eV can be observed for complex **1**$^{-}$, whereas **1** and **1**$^{+}$ show two. Since the prepeaks result from excitations into the d-orbitals, the signal at higher energies around 7114 eV is assigned to transitions into the e$_g$ orbitals (d_{z^2} and $d_{x^2-y^2}$) and the one at lower energies at about 7112 eV to t$_{2g}$ orbitals. DFT calculations,[48,49] presented in Figure 4, confirm this assignment.

In complex **1**$^{-}$, no transitions to the latter final state are observed, as the t$_{2g}$ is fully occupied, confirming **1**$^{-}$ as low-spin Fe^{II}-d^6 complex. In contrast, both low-spin Fe^{III}-d^5 (**1**) and $[Fe(ImP)_2]^{2+}$ (**1**$^{+}$) exhibit t$_{2g}$ vacancies that cause the additional low energy prepeak signal. According to DFT results in Figure 4, a constant and nearly identical energy increase of both the t$_{2g}$ and e$_g$ levels with decreasing iron oxidation state is expected. Experimental values confirm this prediction: The t$_{2g}$ prepeak energy increases by 0.6 eV from $([Fe(ImP)_2]^{+})$ (**1**: 7111.3 eV) to $([Fe(ImP)_2]^{2+})$ (**1**$^{+}$: 7111.9 eV), while the e$_g$ prepeak energy increases by 0.4 and 0.3 eV respectively, from **1**$^{-}$ (7114.1 eV) to **1** (7114.5 eV) and **1**$^{+}$ (7114.8 eV). In particular, the last row of values suggests a constant change of charge at the iron center, or a stepwise iron-localized oxidation, supporting that the observed redox-events are metal-based and **1**$^{+}$ is indeed a low-spin Fe^{IV}-complex.

To further prove this stepwise oxidation state change on the metal-center, the more metal localized K-edge Core-to-Core X-ray emission spectroscopy (CtC-XES) is applied in the following. Here, the emission caused by radiative relaxation from the metal 3p to 1s orbital after excitation at energies above the absorption edge is observed. The resulting signal splits into two peaks: The intense Kβ mainline (Kβ$_{1,3}$), and a weaker peak shifted to lower energies, the Kβ satellite (Kβ'). The reason for the splitting and therefore the spectral shape is the 3p-3d exchange interaction. The higher the effective electron spin in the d orbitals, the larger the exchange interaction and thus the splitting.[44,45,50]

In the experimental CtC-XES spectra shown in Figure 4c, the first thing to notice is that the intensity of the Kβ' satellite is rather low. This indicates a small splitting and thus a small number of unpaired electrons in agreement with a low-spin

Table 2: Computed spin-up and spin-down orbital occupation numbers and the derived oxidation state of the iron center. The shaded boxes mark the occupied orbitals with n≈1. The atomic charges based on Mulliken and natural populations are also listed together with the corresponding spin populations.

	Spin	d-orbital occupation numbers					Configuration	Spin multiplicity	Natural charges (total/ per Spin)	Mulliken charge	Mulliken spin population	Natural spin population
1^-	α	0.33	0.36	0.99	0.99	0.99	d^6	0	-1.427	-0.0546	0	0
									α: -0.713			
	β	0.33	0.36	0.99	0.99	0.99			β: -0.713			
1	α	0.65	0.69	0.97	0.97	0.98	d^5	1	-0.969	0.765	1.189	0.96
									α: -0.975			
	β	0.19	0.69	0.73	0.95	0.95			β: 0.006			
1^+	α	0.75	0.81	0.98	0.98	0.99	d^4	2	-0.615	0.693	2.171	1.75
									α: -1.204			
	β	0.19	0.20	0.69	0.78	0.97			β : 0.590			

configuration for all complexes. Therefore, only the energy of the Kβ mainline can be used properly as parameter to describe the splitting.[45] Although the main line energy is not only dependent on the spin state but also on covalency, ligand and metal-metal interactions effects,[51,52] such influences can be nearly fully ruled out due to the isostructure of the complexes.

The $K\beta_{1,3}$ signal shows a linear correlation between the number of unpaired electrons and the main line energy (Figure 4d), as reported for purely ionic compounds with increasing oxidation states by Glatzel and Bergman.[45] Accordingly, these results support the prepeak analysis and the conclusion of a stepwise oxidation state change at the metal center, since a ligand centered oxidation will not have the exact same effect on the spin state as a metal centered oxidation. To further substantiate this claim, the identical analysis is shown in Figure 4d for Fe^{II} and Fe^{III} hexacyanoferrate. The slope of the spin-energy correlation is very similar to the investigated row of isostructural carbene complexes.

The hard X-ray investigation of the isostructural complex row is complemented by Valence-to-Core X-ray emission spectroscopy (VtC-XES). Here the emitted signal serves as a probe of valence levels including occupied 3d-orbitals and ligand-centered orbitals.[53] In the experimental VtC-XES spectra of Figure 4c a nearly constant shift of the $K\beta_{2,5}$ signal from 7107.0 (**1**$^-$) to 7108.0 eV (**1**) to 7108. 8 eV (**1**$^+$) is observed with increasing oxidation state, again supporting the previous findings. To further analyze the spectrum and explain the origin of this shift, DFT calculations were performed. The calculations show that the weak Kβ'' signal in the range of 7095-7102 eV originates from transitions of orbitals with mainly C-s and -p character, as well as N-p contributions from the imidazolylidene. In this range, the low energy transitions involve the s- and the higher energy transitions involve mainly the p-orbitals of carbon delocalized over the ligand. The $K\beta_{2,5}$ peak is composed by transitions from the C p-orbitals with a small admixture of Fe p-orbitals. As demonstrated in Figure S7, transitions from the NHC carbon constitute the lower energy side of the signal, while the higher-energy side is dominated by the phenyl fragment. It is important to note that according to the calculations the orbital composition of the transitions does not change (*cf.* Figure S7 and Figure S8/Table S3 in the Supporting Information). Instead, the metal orbitals are stabilized with higher oxidation state (Figure 4b), but the ligand based π-molecular orbitals are less affected, confirming the metal-based oxidation.

The quantum chemical characterization of **1**, **1**$^-$, and **1**$^+$ regarding their oxidation states and associated changes in the electronic charge densities was performed with DFT calculations on the isolated complexes (*cf.* Supporting Information: Computational details, "NBO, localized orbitals, and bond order analyses"). In molecular systems, as opposed to isolated ions, there is no correlation between formal charges invoked by oxidation states and the charge localized around the atomic center. The reason behind this widely reported observation was explained by Raebiger *et. al.*[54] (schematic depiction in Figure S10 in the Supporting Information). Whenever an electron is added or removed at the d-orbitals of a transition metal (TM) center, there is an inevitable adjustment in the energies of the d-orbitals. Consequently, the hybridization of the metal-ligand bonding orbitals changes, such that the contribution of the TM center to the bonding orbitals decreases or increases, respectively. This leads to a negative feedback charge self-regulation that stabilizes the amount of charge localized around the TM center.

For characterizing the oxidation state in each molecule, the wave function projection method suggested by Sit *et al.*[55] was chosen (*cf.* Supporting Information: Computational details, Characterization of the oxidation state). With this method the occupancy (n) of each iron atomic d-orbital in each complex can be obtained. As in the case of a free atom,

only fully occupied d-orbitals (n≈1) are relevant for determining the oxidation state of the TM. The oxidation state is determined by simply counting the fully occupied d-orbitals. All other d-orbitals with weaker occupations (n≈0) are due to ligand donation to empty d-orbitals and do not contribute to the determination of the oxidation state. The results are reported in Table 2, where it is indeed found that the oxidation state and electronic configuration of each molecule can be unambiguously identified, ranging from d^6 in the case of $\mathbf{1}^-$ down to d^4 in the case of $\mathbf{1}^+$.

Interestingly, the signature of the strong ligand field in these molecules also manifests in the analysis. The ideal case of n=1 for fully occupied and n=0 for vacant d-orbitals is only achieved in the limit of a weak-field ligand.[55,56] For strong-field ligands as it is the case here, the occupation numbers deviate from this ideal. The deviations mainly arise from the larger distortions in the atomic d-orbitals due to the stronger ligand field and larger orbital mixing. π-Backdonation from the ligand to the TM center contributes here as well (*cf.* Supporting Information: Computational details, NBO analysis results). Nevertheless, the assignment of the oxidation state in each case remains easy and non-ambiguous, with the occupied orbitals all having n > 0.95.

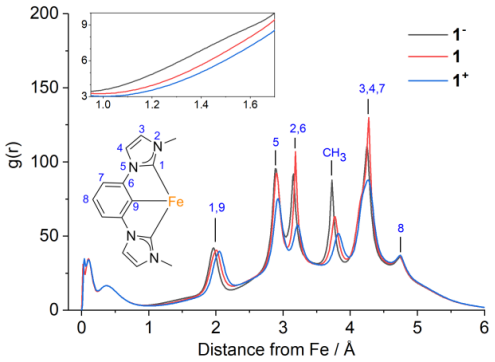

Figure 5: Radial distribution function of the electron density of the complex, with the iron at the center.

A common method for characterization of the charge distribution in a molecule is to compute partial atomic charges, which are obtained through a partitioning of the total electron density into atomic contributions. Because this partitioning can be accomplished in different ways, there is always an ambiguity in the definition of the charges and different methods can yield widely differing values. As already mentioned, they are a rather poor measure of the oxidation state, if a measure at all.[57,58] In most cases, because of the aforementioned negative feedback mechanism, first-principles quantum mechanical calculations show only negligible changes in the total charge localized around the TM center as the oxidation state is altered. A change of ±0.5 in any direction, or sometimes much less, is rather common.[59,60] It seems that transition metal atomic charges are rather more sensitive to the nature of the complexing ligand than to the formal oxidation state.[61] For compounds in a low oxidation state and coordinated to a highly electronegative ligand, a higher charge at the metal atom can be observed than for a complex with a higher oxidation state and a less electronegative ligand.[61]

The partial atomic charges and spin populations obtained from Mulliken and from natural bond orbital analyses (NBO[62,63]) are listed in Table 2. The atomic charges not only give information about the charge distribution but also carry the fingerprint of the charge self-regulation process. Upon oxidation of $\mathbf{1}^-$ to **1** (removing a spin-down electron), the Fe atom loses a natural charge of 0.7e from the beta (spin-down) channel, but concomitantly gains 0.25e in the alpha (spin-up) spin channel, leading to the more modest net loss of 0.45e. The difference between the natural spin populations however now amounts to almost one full electron, explaining the previously reported observation that spin populations usually perform much better than atomic charges in characterizing the oxidation state of a compound particularly in high spin states.[64,65] This is merely a consequence of the negative feedback charge regulation. The same behavior and arguments are also valid for the iron-center in $\mathbf{1}^+$, which loses 0.6e in one spin channel and gains back 0.25e in the other, a net loss of only 0.35e. Again, the charge self-regulation working in the different spin channel leads to a change in the spin population of almost 1e. We conclude that, for the same reason that partial atomic charges do not correlate with the oxidation state, the spin populations can be a very easy and efficient method for its characterization. This is also true for Mulliken population analysis, even though the Mulliken charges are known to occasionally have several problematic features like basis-set sensitivity and chemically non-intuitive values.[62]

For a more detailed understanding of the oxidation-induced charge reorganization in the three complexes, Figure 5 depicts the radial distribution function of the electron density, with the Fe atom at the origin. By far the most significant charge redistribution is taking place in the aromatic π-system at the second- and third- neighbor atoms to the Fe. At the vicinity of the Fe atom, oxidation leads to a depletion in the charge density at the bond between the metal atom and the six nearest neighbors. There is also radial charge redistribution at the Fe atom itself, particularly obvious in the case of $\mathbf{1}^+$, and consistent with a shrinking in the ionic radius at higher oxidation states.

Therefore, the theoretical approach also shows that the redox events of **1** lead to metal-centered reduction and oxidation, respectively, as judged by the populations of the d-orbitals in Table 2 and spectroscopic results. The overall observed effects, which may suggest partial ligand non-innocence, are due to charge redistribution within the system. A driving force behind this is the strong donor ligand, which is able to redistribute electron density from the ligand backbone into the metal-ligand bond. The characterization of the electronic structures of the complex in its three oxidation states thus concludes that the complexes $\mathbf{1}^-$, **1** and $\mathbf{1}^+$ are indeed iron +II, +III and +IV, respectively.

To get further information on the optical properties of this interesting compound class, electronic absorption spectra of $\mathbf{1}^-$, **1** and $\mathbf{1}^+$ were recorded in solutions of acetonitrile (Figure 6). The electronic transitions in $\mathbf{1}^-$, **1** and $\mathbf{1}^+$ were assigned using TD-DFT calculations (see reference 27 for **1**).

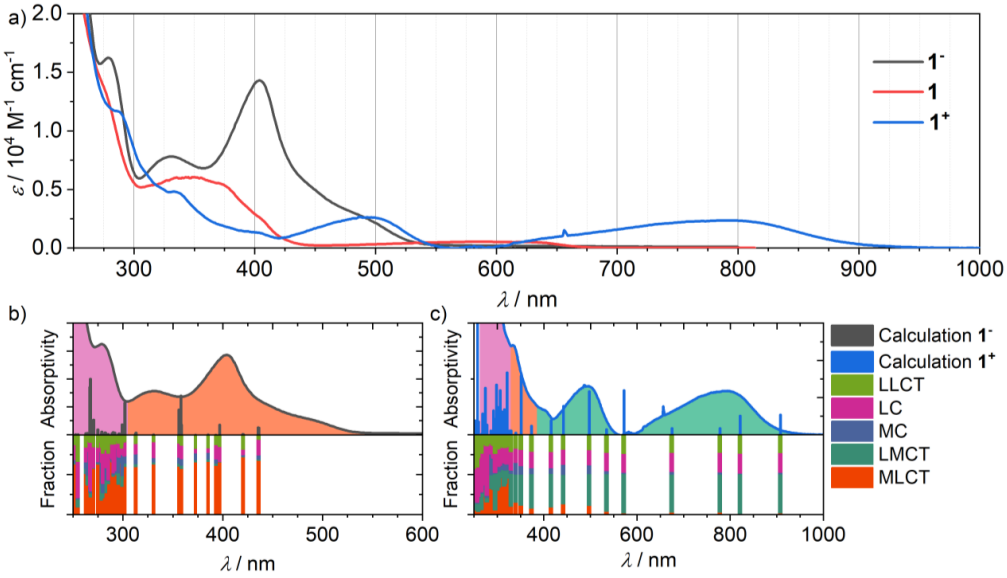

Figure 6: a) UV-Vis spectra of **1**$^{-}$, **1**[27] and **1**$^{+}$ in comparison (measured at 10^{-5} M for **1** and **1**$^{+}$ and 10^{-4} M for **1**$^{-}$ in MeCN). b) Calculated transitions of **1**$^{-}$ compared to and the fractional composition of the transitions. c) Calculated transitions of **1**$^{+}$ and the fractional composition of the transitions.

Because of the covalent cyclometalating bond, the orbitals contain electron density from both ligands and metals. This mixing results in LMCT and MLCT transitions with some LC, ILCT, and LLCT character and vice versa. In both **1** and **1**$^{+}$, LMCT transitions can be observed in the low energy part of the spectra above 450 and 380 nm (Figure 6c), respectively. Contrary to **1**, the Fe^{IV} complex **1**$^{+}$ shows two LMCT bands. The transitions are around five times more intense (ε_{791nm} = 0.24 10^4 M^{-1} cm^{-1} and ε_{496nm} = 0.26 10^4 M^{-1} cm^{-1}) than the LMCT transition in **1** (ε_{585nm} = 0.05 10^4 M^{-1} cm^{-1}).[27] MLCT transitions can be observed in all three oxidation states between 320 and 430 nm and for **1**$^{+}$ even above 500 nm.

However, in the Fe^{IV} compound **1**$^{+}$, the MLCT shows up just as a shoulder at 330 nm. The intensities of the MLCT band decrease with increasing oxidation state, as it is expected. The MLCT absorption of Fe^{II} **1**$^{-}$ shows a molar extinction of ε_{404nm} = 1.43 10^4 M^{-1} cm^{-1}, Fe^{III} as reported[27] ε_{351nm} = 0.60 10^4 M^{-1} cm^{-1} and Fe^{IV} ε_{333nm} = 0.48 10^4 M^{-1} cm^{-1}. Besides, a shift of the maximum towards higher energies is observed for increasing oxidation states. This is supported by the observation of a stabilization of the metal-orbitals relative to the ligand orbitals (Figure 4 b) in the VtC-spectra. Below 310 nm, ligand-based transitions are observed in all three compounds. Contrary to **1,** which exhibits a unique emission behavior with luminescence from both MLCT and LMCT states, no emission from **1**$^{-}$ and **1**$^{+}$ could be observed. Thus, the excited state dynamics could only be investigated with transient absorption spectroscopy (TA).

The transient absorption measurements of the $[Fe(ImP)_2]^0$ complex **1**$^{-}$ (Figure 7) show a negative signal in the range below 450 nm with a minimum beyond the UV edge of 400 nm of the detection window. At wavelengths longer than 450 nm, the signal is positive with a maximum at about 535 nm, which can be attributed to excited state absorption (ESA)

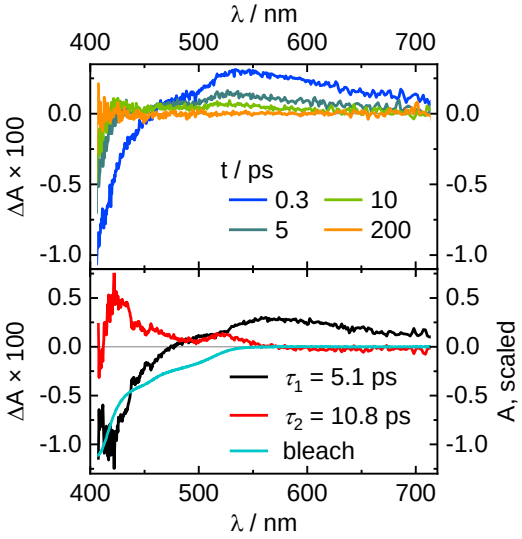

Figure 7: Transient absorption spectra (top) of **1**$^{-}$ in MeCN with polarizations set to magic angle at the given delay times after optical excitation at 400 nm and the obtained decay associated spectra (bottom) labelled by the corresponding time constants and compared to the bleach (negative, scaled absorption spectrum) for complex **1**$^{-}$.

A global fit of the transient absorption spectra reveals a biexponential decay with time components of 5.1 ps and 10.8 ps. The contribution of the ESA at longer wavelengths than 550 nm decays with the short time constant of 5.1 ps. At shorter wavelengths than 550 nm, the two decay associated spectra (DAS) obtained by the fit show a certain mirror symmetry. This may indicate that from the optically excited state an energetically lower intermediate state is populated with the short time constant. It is responsible for the ESA components between 400 and 550 nm and it subsequently relaxes to the ground state within the slower decay time of 10.8 ps. The bleach is clearly imprinted on the TA spectra at short times but is masked by the new ESA at longer delay times. The short decay time of 5.1 ps can be attributed to a ^{3}MLCT state, as the ESA red to the MLCT absorption (Figure 7) originates from the LMCT absorption of the oxidized metal center in the charge-separated state and is comparable to what is seen in the absorption spectrum of **1** (Figure 6). In contrast, the longer lifetime of 10.8 ps can be attributed to an MC state, most likely a ^{3}MC state. This is deduced from the absence of ESA components indicative for charge transfer character.

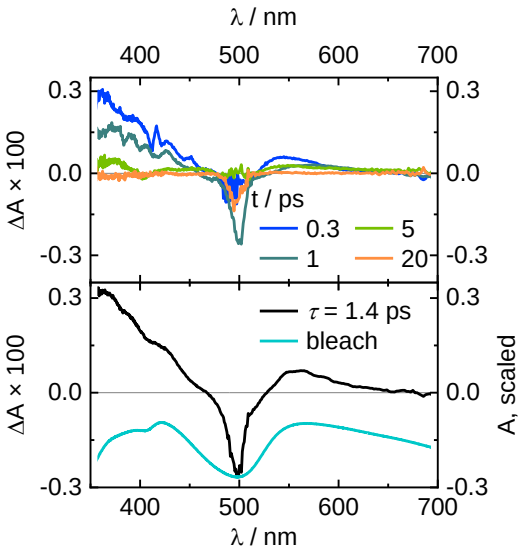

Figure 8: Transient absorption spectra (top) of complex **1**$^+$ in MeCN at different delay times after optical excitation at 490 nm and with polarizations set to magic angle and the decay associated spectrum (bottom) compared to the bleach (negative, scaled absorption spectrum).

In the transient absorption measurements of $[Fe(ImP)_2]^{2+}$ complex **1**$^+$ (Figure 8), a negative signal was observed in the range of 470-530 nm with a minimum at 500 nm. At this point, the bleach also shows a minimum. At shorter as well as longer wavelengths, the signal is positive with maxima at about 355 and 560 nm. The transient absorption decays rather fast and monoexponentially with a time constant of 1.4 ps. The spectrally narrow negative signal component at 500 nm is possibly related to scattered light, since the spectral position and band width match the excitation pulses. Ignoring the narrowband component, the impression arises that there is a broad ESA that spans the entire visible spectral range and on which the overlapping bleach is imprinted. The shape of the DAS obtained by the monoexponential fit indicates that it belongs to a ^{3}LMCT state, since the ESA fits well the absorption profile of **1** (*cf.* Figure 6). This is expected for an excited LMCT state of **1**$^+$, since it involves a reduction of the metal center ($Fe^{IV} \rightarrow Fe^{III}$) resulting in an absorption spectrum similar to that of **1**.

These results become even more interesting when compared to known compounds in different oxidation states. The Fe^{II}/Fe^{III} pair $[Fe(btz)_3]^{2/3+}$ is an ideal reference.[29,66] The MLCT lifetime of $[Fe(btz)_3]^{2+}$ with 0.5 ns is much longer than the LMCT lifetime in the Fe^{III} congener (0.1 ns), which is a diametrical behavior to the present results. $[Fe(ImP)_2]^+$ **1** shows an LMCT lifetime of 0.2 ns,[27] whereas the MLCT lifetime of the Fe^{II} compound is only 5.1 ps. This is also about half of the MLCT lifetime of the Fe^{II} complex from which **1**$^-$ is derived ($[Fe(bimp)_2]^{2+}$ with 9 ps MLCT lifetime).[26] A possible explanation is the destabilization of the MLCT states by the π-donor character of the cyclometalating moieties, which outweighs the σ-donor strength of the C^C^C donor-set, enabling energetically low MC-states. This can be further supported by the symmetry of the complex, since the cyclometalating moieties are in trans position. This enables an energetically low MC-state where the Fe-carbene bonds can be elongated. This is analogous to the calculations Dixon made on an $[Fe(NCN)_2]$ complex,[67] predicting exactly this behavior, even though Fe-carbene bonds should be harder to elongate than Fe-pyridine bonds presented in the work. Overall, an interplay of these two effects is believed to be the main cause for the short MLCT lifetime and a pronounced MC lifetime. The lifetime of the ^{3}LMCT state in the Fe^{IV} complex on the other hand is slightly longer than the only other known Fe^{IV} ^{3}LMCT lifetime (0.8 ps),[30] but still far from a region where most photophysical applications are possible.

Conclusions

The iron compound $[Fe(ImP)_2]^{0/+/2+}$ with the ImP = 1,1'-(1,3-phenylene)bis(3-methyl-1-imidazol-2-ylidene) ligand was fully characterized in three different oxidation states. With a multitude of spectroscopic and theoretical methods it could be unequivocally proven that the redox processes take exclusively place at the metal center and the ImP ligand is fully innocent. All complexes exhibit low-spin configurations of d^6 to d^4. Therefore, this is one of the very few isostructural series, showing solely metal-centered redox events and, to the best of our knowledge, the first isostructural series of homoleptic iron-carbene complexes. DFT calculations and NBO analysis suggest that charge-redistribution within the strong donor-ligand is responsible for effects which can be mistaken as ligand non-innocence. Nevertheless, based on the population of the d-orbitals, the experimental results of metal-centered redox events are supported. Optical characterization shows a panchromatic absorption of **1**$^+$ with the absorption ranging up until 900 nm. The excited states of **1**$^+$ and **1**$^-$ were investigated using tran-

sient absorption measurements. $\mathbf{1}^{+}$ exhibits a ^{3}LMCT lifetime of around a picosecond, which is slightly longer than the observed ^{3}LMCT lifetime in a comparable low-spin Fe^{IV} complex as previously reported. $\mathbf{1}^{-}$ on the other hand shows a very short-lived ^{3}MLCT state, contrary to the expectations from the strong donor ligands. This can be explained by an energetically more favorable MC state, which is caused by the destabilization of the MLCT state by the strong π-donating cyclometalating functions, outweighing the σ-donating capabilities. While this results in a dual-emissive compound with ns-lifetime in the +III oxidation state,[27] the effects on the +II and +IV oxidation states are not sufficient to lead to photoactive complexes.

Nevertheless, the metal-centered redox processes take place very fast due to structural similarity. Therefore, an application of $\mathbf{1}^{-}$ as a reductant with an oxidation potential close to cobaltocene (-1.16 V vs. -1.33 V)[27,68] can be envisioned, especially catalytically obtained via photoreduction of **1**. $\mathbf{1}^{+}$ on the other hand can act as a mild oxidant, with a reduction potential in the range of 2,3-Dichloro-5,6-dicyano-1,4-benzoquinone (DDQ, 0.08 V vs. 0.13 V).[68] Consequently, this series of compounds shows the versatility of the compound class based on the (ImP) ligand framework, which allows the complexes to exist isostructural and stable in three different oxidation states.

ASSOCIATED CONTENT

Supporting Information. Synthesis and experimental details, spectra and computational details.
This material is available free of charge via the Internet at http://pubs.acs.org

AUTHOR INFORMATION

Corresponding Author

* Matthias Bauer; Email: matthias.bauer@upb.de

Present Addresses

† Institute of Physics, University of Kassel, Kassel, Germany
‡ Institute of General, Inorganic and Theoretical Chemistry, University of Innsbruck, Innsbruck, Austria

Author Contributions

The manuscript was written through contributions of all authors. All authors have given approval to the final version of the manuscript.

Notes

The authors declare no competing financial interest.

ACKNOWLEDGMENT

J.S. thanks the German Federal Environmental Foundation (Deutsche Bundesstiftung Umwelt - DBU) for a PhD scholarship. Wolfgang Caliebe and Aleksandr Kalinko of Petra III-beamline P64 (Deutsches Elektronensynchrotron Desy, Hamburg) is acknowledged for support and provision of beamtime. The grant of computer time at the Paderborn Center for Parallel Computing PC2 is acknowledged. This work was performed in the framework of the SPP 2102 funded by the Deutsche Forschungsgemeinschaft (BA 4467/7-1 and BA 4467/7-2, KU 952/12-1 and KU 952/12-2, LO 714/11-1 and LO 714/11-2, ME 1313/15-1).

REFERENCES

(1) Collman, J. P. Disodium tetracarbonylferrate, a transition metal analog of a Grignard reagent. *Acc. Chem. Res.* **1975**, *8* (10), 342–347. DOI: 10.1021/ar50094a004.

(2) Sharma, V. K. Potassium ferrate(VI): an environmentally friendly oxidant. *Advances in Environmental Research* **2002**, *6* (2), 143–156. DOI: 10.1016/S1093-0191(01)00119-8.

(3) Martinez, J. L.; Lutz, S. A.; Yang, H.; Xie, J.; Telser, J.; Hoffman, B. M.; Carta, V.; Pink, M.; Losovyj, Y.; Smith, J. M. Structural and spectroscopic characterization of an Fe(VI) bis(imido) complex. *Science* **2020**, *370* (6514), 356–359. DOI: 10.1126/science.abd3054.

(4) Lee, Y.; Mankad, N. P.; Peters, J. C. Triggering N(2) uptake via redox-induced expulsion of coordinated NH(3) and N(2) silylation at trigonal bipyramidal iron. *Nat. Chem.* **2010**, *2* (7), 558–565. DOI: 10.1038/nchem.660. Published Online: May. 16, 2010.

(5) Keilwerth, M.; Mao, W.; Jannuzzi, S. A. V.; Grunwald, L.; Heinemann, F. W.; Scheurer, A.; Sutter, J.; DeBeer, S.; Munz, D.; Meyer, K. From Divalent to Pentavalent Iron Imido Complexes and an Fe(V) Nitride via N-C Bond Cleavage. *Journal of the American Chemical Society* **2023**, *145* (2), 873–887. DOI: 10.1021/jacs.2c09072. Published Online: Dec. 30, 2022.

(6) Keilwerth, M.; Hohenberger, J.; Heinemann, F. W.; Sutter, J.; Scheurer, A.; Fang, H.; Bill, E.; Neese, F.; Ye, S.; Meyer, K. A Series of Iron Nitrosyl Complexes {Fe-NO}6-9 and a Fleeting {Fe-NO}10 Intermediate en Route to a Metalacyclic Iron Nitrosoalkane. *Journal of the American Chemical Society* **2019**, *141* (43), 17217–17235. DOI: 10.1021/jacs.9b08053. Published Online: Oct. 17, 2019.

(7) Akbar Ali, M.; Bernhardt, P. V.; Brax, M. A. H.; England, J.; Farlow, A. J.; Hanson, G. R.; Yeng, L. L.; Mirza, A. H.; Wieghardt, K. The trivalent copper complex of a conjugated bis-dithiocarbazate Schiff base: stabilization of Cu in three different oxidation states. *Inorg. Chem.* **2013**, *52* (3), 1650–1657. DOI: 10.1021/ic302596h. Published Online: Jan. 16, 2013.

(8) Kosog, B.; La Pierre, H. S.; Denecke, M. A.; Heinemann, F. W.; Meyer, K. Oxidation state delineation via U L(III)-edge XANES in a series of isostructural uranium coordination complexes. *Inorg. Chem.* **2012**, *51* (14), 7940–7944. DOI: 10.1021/ic3011234. Published Online: Jul. 5, 2012.

(9) Wittwer, B.; Dickmann, N.; Berg, S.; Leitner, D.; Tesi, L.; Hunger, D.; Gratzl, R.; van Slageren, J.; Neuman, N. I.; Munz, D.; Hohloch, S. A mesoionic carbene complex of manganese in five oxidation states. *Chem. Commun.* **2022**, *58* (41), 6096–6099. DOI: 10.1039/d2cc00097k. Published Online: May. 20, 2022.

(10) Garai, A.; Sobottka, S.; Schepper, R.; Sinha, W.; Bauer, M.; Sarkar, B.; Kar, S. Chromium Complexes with Oxido and Corrolato Ligands: Metal-Based Redox Processes versus Ligand Non-Innocence. *Chem. Eur. J.* **2018**, *24* (48), 12613–12622. DOI: 10.1002/chem.201801452. Published Online: Jul. 19, 2018.

(11) Sinha, W.; Sommer, M. G.; Deibel, N.; Ehret, F.; Bauer, M.; Sarkar, B.; Kar, S. Experimental and Theoretical Investigations of the Existence of Cu(II), Cu(III), and Cu(IV) in Copper Corrolato Complexes. *Angew. Chem. Int. Ed.* **2015**, *54* (46), 13769–13774. DOI: 10.1002/anie.201507330. Published Online: Sep. 25, 2015.
(12) Gravogl, L.; Heinemann, F. W.; Munz, D.; Meyer, K. An Iron Pincer Complex in Four Oxidation States. *Inorg. Chem.* **2020**, *59* (8), 5632–5645. DOI: 10.1021/acs.inorgchem.0c00355. Published Online: Apr. 9, 2020.
(13) Bigi, J. P.; Harman, W. H.; Lassalle-Kaiser, B.; Robles, D. M.; Stich, T. A.; Yano, J.; Britt, R. D.; Chang, C. J. A high-spin iron(IV)-oxo complex supported by a trigonal nonheme pyrrolide platform. *Journal of the American Chemical Society* **2012**, *134* (3), 1536–1542. DOI: 10.1021/ja207048h. Published Online: Jan. 4, 2012.
(14) Meyer, S.; Klawitter, I.; Demeshko, S.; Bill, E.; Meyer, F. A tetracarbene-oxoiron(IV) complex. *Angew. Chem. Int. Ed.* **2013**, *52* (3), 901–905. DOI: 10.1002/anie.201208044. Published Online: Nov. 28, 2012.
(15) Zou, H.-B.; Yang, H.; Liu, Z.-Y.; Mahmood, M. H. R.; Mei, G.-Q.; Liu, H.-Y.; Chang, C.-K. Iron(IV)-Corrole Catalyzed Stereoselective Olefination of Aldehydes with Ethyl Diazoacetate. *Organometallics* **2015**, *34* (12), 2791–2795. DOI: 10.1021/acs.organomet.5b00069.
(16) Simkhovich, L.; Goldberg, I.; Gross, Z. Iron(III) and iron(IV) corroles: synthesis, spectroscopy, structures, and no indications for corrole radicals. *Inorg. Chem.* **2002**, *41* (21), 5433–5439. DOI: 10.1021/ic020118b.
(17) Bower, B. K.; Tennent, H. G. Transition metal bicyclo[2.2.1]hept-1-yls. *Journal of the American Chemical Society* **1972**, *94* (7), 2512–2514. DOI: 10.1021/ja00762a056.
(18) Lewis, R. A.; Smiles, D. E.; Darmon, J. M.; Stieber, S. C. E.; Wu, G.; Hayton, T. W. Reactivity and Mössbauer spectroscopic characterization of an Fe(IV) ketimide complex and reinvestigation of an Fe(IV) norbornyl complex. *Inorg. Chem.* **2013**, *52* (14), 8218–8227. DOI: 10.1021/ic401096p. Published Online: Jun. 21, 2013.
(19) Casitas, A.; Rees, J. A.; Goddard, R.; Bill, E.; DeBeer, S.; Fürstner, A. Two Exceptional Homoleptic Iron(IV) Tetraalkyl Complexes. *Angew. Chem., Int. Ed.* **2017**, *56* (34), 10108–10113. DOI: 10.1002/anie.201612299. Published Online: Mar. 2, 2017.
(20) Dixon, I. M.; Khan, S.; Alary, F.; Boggio-Pasqua, M.; Heully, J.-L. Probing the photophysical capability of mono and bis(cyclometallated) Fe(ii) polypyridine complexes using inexpensive ground state DFT. *Dalton. Trans.* **2014**, *43* (42), 15898–15905. DOI: 10.1039/c4dt01939c.
(21) Kreitner, C.; Heinze, K. Excited state decay of cyclometalated polypyridine ruthenium complexes:Insight from theory and experiment. *Dalton. Trans.* **2016**, *45* (35), 13631–13647. DOI: 10.1039/c6dt01989g.
(22) Kumar, R.; Nevado, C. Cyclometalated Gold(III) Complexes: Synthesis, Reactivity, and Physicochemical Properties. *Angew. Chem. Int. Ed.* **2017**, *56* (8), 1994–2015. DOI: 10.1002/anie.201607225. Published Online: Jan. 23, 2017.
(23) Newman, C. P.; Casey-Green, K.; Clarkson, G. J.; Cave, G. W. V.; Errington, W.; Rourke, J. P. Cyclometallated platinum(II) complexes: oxidation to, and C-H activation by, platinum(IV). *Dalton Trans.* **2007** (29), 3170–3182. DOI: 10.1039/b705609e. Published Online: Jun. 15, 2007.
(24) Cerón-Camacho, R.; Hernández, S.; Le Lagadec, R.; Ryabov, A. D. Cyclometalated Os(C-N)x(N-N)(3-x)m+ mimetics of tris(2,2'-bipyridine)osmium(II): covering a 2 V potential range by known (x = 0, 1) and new (x = 2, 3) species (C-N = o-2-phenylpyridinato). *Chem. Commun.* **2011**, *47* (10), 2823–2825. DOI: 10.1039/c0cc04582a. Published Online: Jan. 14, 2011.
(25) Steube, J.; Burkhardt, L.; Päpcke, A.; Moll, J.; Zimmer, P.; Schoch, R.; Wölper, C.; Heinze, K.; Lochbrunner, S.; Bauer, M. Excited-State Kinetics of an Air-Stable Cyclometalated Iron(II) Complex. *Chem. Eur. J.* **2019**, *25* (51), 11826–11830. DOI: 10.1002/chem.201902488.
(26) Liu, Y.; Harlang, T.; Canton, S. E.; Chábera, P.; Suárez-Alcántara, K.; Fleckhaus, A.; Vithanage, D. A.; Göransson, E.; Corani, A.; Lomoth, R.; Sundström, V.; Wärnmark, K. Towards longer-lived metal-to-ligand charge transfer states of iron(II) complexes: an N-heterocyclic carbene approach. *Chem. Comm.* **2013**, *49* (57), 6412–6414. DOI: 10.1039/C3CC43833C.
(27) Steube, J.; Kruse, A.; Bokareva, O. S.; Reuter, T.; Demeshko, S.; Schoch, R.; Argüello Cordero, M. A.; Krishna, A.; Hohloch, S.; Meyer, F.; Heinze, K.; Kühn, O.; Lochbrunner, S.; Bauer, M. Janus-type emission from a cyclometalated iron(III) complex. *Nat. Chem.* **2023**, *15* (4), 468–474. DOI: 10.1038/s41557-023-01137-w. Published Online: Feb. 27, 2023.
(28) *CCDC database, entry 2002774*.
(29) Chabera, P.; Kjær, K. S.; Prakash, O.; Honarfar, A.; Liu, Y.; Fredin, L. A.; Harlang, T. B.; Lidin, S.; Uhlig, J.; Sundstrom, V.; Lomoth, R.; Persson, P.; Wärnmark, K.; Chábera, P.; Kjaer, K. S.; Harlang, T. C. B.; Sundström, V. A FeII Hexa N-Heterocyclic Carbene Complex with a 528 ps Metal-to-Ligand Charge-Transfer Excited-State Lifetime // FeII Hexa N-Heterocyclic Carbene Complex with a 528 ps Metal-to-Ligand Charge-Transfer Excited-State Lifetime. *J. Phys. Chem. Lett.* **2018**, *9* (3), 459–463. DOI: 10.1021/acs.jpclett.7b02962.
(30) Prakash, O.; Chábera, P.; Rosemann, N. W.; Huang, P.; Häggström, L.; Ericsson, T.; Strand, D.; Persson, P.; Bendix, J.; Lomoth, R.; Wärnmark, K. A Stable Homoleptic Organometallic Iron(IV) Complex. *Chem. Eur. J.* **2020**, *26* (56), 12728–12732. DOI: 10.1002/chem.202002158. Published Online: Sep. 11, 2020.
(31) Kjær, K. S.; Kaul, N.; Prakash, O.; Chábera, P.; Rosemann, N. W.; Honarfar, A.; Gordivska, O.; Fredin, L. A.; Bergquist, K.-E.; Häggström, L.; Ericsson, T.; Lindh, L.; Yartsev, A.; Styring, S.; Huang, P.; Uhlig, J.; Bendix, J.; Strand, D.; Sundström, V.; Persson, P.; Lomoth, R.; Wärnmark, K. Luminescence and reactivity of a charge-transfer excited iron complex with nanosecond lifetime. *Science* **2019**, *363* (6424), 249–253. DOI: 10.1126/science.aau7160.
(32) Toftlund, H. Spin equilibria in iron(II) complexes. *Coord. Chem. Rev.* **1989**, *94*, 67–108. DOI: 10.1016/0010-8545(89)80045-1.
(33) Constable, E. C.; Baum, G.; Bill, E.; Dyson, R.; van Eldik, R.; Fenske, D.; Kaderli, S.; Morris, D.; Neubrand, A.; Neuburger, M.; Smith, D. R.; Wieghardt, K.; Zehnder, M.; Zuberbühler, A. D. Control of Iron(II) Spin States in 2,2′:6′,2″-Terpyridine Complexes through Ligand Substitution. *Chem. Eur. J.* **1999**, *5* (2), 498–508. DOI: 10.1002/(SICI)1521-3765(19990201)5:2<498:AID-CHEM498>3.0.CO;2-V.

(34) Gütlich, P. Fifty Years of Mössbauer Spectroscopy in Solid State Research - Remarkable Achievements, Future Perspectives. *Z. Anorg. Allg. Chem.* **2012**, *638* (1), 15–43. DOI: 10.1002/zaac.201100416.

(35) Neese, F. Prediction and interpretation of the 57Fe isomer shift in Mössbauer spectra by density functional theory. *Inorg. Chim. Acta* **2002**, *337*, 181–192. DOI: 10.1016/S0020-1693(02)01031-9.

(36) Ye, S.; Bill, E.; Neese, F. Electronic Structures of the Fe(N2)(SiP(iPr)3)(+1/0/-1) Electron Transfer Series: A Counterintuitive Correlation between Isomer Shifts and Oxidation States. *Inorg. Chem.* **2016**, *55* (7), 3468–3474. DOI: 10.1021/acs.inorgchem.5b02908. Published Online: Mar. 11, 2016.

(37) McDonald, A. R.; Que, L. High-valent nonheme iron-oxo complexes: Synthesis, structure, and spectroscopy. *Coord. Chem. Rev.* **2013**, *257* (2), 414–428. DOI: 10.1016/j.ccr.2012.08.002.

(38) Schöneboom, J. C.; Neese, F.; Thiel, W. Toward identification of the compound I reactive intermediate in cytochrome P450 chemistry: a QM/MM study of its EPR and Mössbauer parameters. *Journal of the American Chemical Society* **2005**, *127* (16), 5840–5853. DOI: 10.1021/ja0424732.

(39) Zimmer, P.; Burkhardt, L.; Schepper, R.; Zheng, K.; Gosztola, D.; Neuba, A.; Flörke, U.; Wölper, C.; Schoch, R.; Gawelda, W.; Canton, S. E.; Bauer, M. Towards Noble-Metal-Free Dyads: Ground and Excited State Tuning by a Cobalt Dimethylglyoxime Motif Connected to an Iron N-Heterocyclic Carbene Photosensitizer. *Eur. J. Inorg. Chem.* **2018**, *2018* (48), 5203–5214. DOI: 10.1002/ejic.201800946.

(40) Bauer, M. HERFD-XAS and valence-to-core-XES:New tools to push the limits in research with hard X-rays? *Phys. Chem. Chem. Phys.* **2014**, *16* (27), 13827–13837. DOI: 10.1039/C4CP00904E.

(41) Bunker, G. *Introduction to XAFS*; Cambridge University Press, 2010. DOI: 10.1017/CBO9780511809194.

(42) Burkhardt, L.; Vukadinovic, Y.; Nowakowski, M.; Kalinko, A.; Rudolph, J.; Carlsson, P.-A.; Jacob, C. R.; Bauer, M. Electronic Structure of the Hieber Anion Fe(CO)3(NO)- Revisited by X-ray Emission and Absorption Spectroscopy. *Inorg. Chem.* **2020**, *59* (6), 3551–3561. DOI: 10.1021/acs.inorgchem.9b02092. Published Online: Mar. 3, 2020.

(43) Burkhardt, L.; Holzwarth, M.; Plietker, B.; Bauer, M. Detection and Characterization of Hydride Ligands in Iron Complexes by High-Resolution Hard X-ray Spectroscopy and Implications for Catalytic Processes. *Inorg. Chem.* **2017**, *56* (21), 13300–13310. DOI: 10.1021/acs.inorgchem.7b02063.

(44) Bergmann, U.; Glatzel, P. X-ray emission spectroscopy. *Photosynthesis research* **2009**, *102* (2-3), 255–266. DOI: 10.1007/s11120-009-9483-6.

(45) Glatzel, P.; Bergmann, U. High resolution 1s core hole X-ray spectroscopy in 3d transition metal complexes—electronic and structural information. *Coord. Chem. Rev.* **2005**, *249* (1-2), 65–95. DOI: 10.1016/j.ccr.2004.04.011.

(46) Yamamoto, T. Assignment of pre-edge peaks in K-edge x-ray absorption spectra of 3d transition metal compounds: electric dipole or quadrupole? *X-Ray Spectrom.* **2008**, *37* (6), 572–584. DOI: 10.1002/xrs.1103.

(47) Matthias Bauer; Helmut Bertagnolli. X-Ray Absorption Spectroscopy – the Method and Its Applications. In *Methods in Physical Chemistry*; John Wiley & Sons, Ltd, 2012; pp 231–269. DOI: 10.1002/9783527636839.ch7.

(48) Weigend, F.; Ahlrichs, R. Balanced basis sets of split valence, triple zeta valence and quadruple zeta valence quality for H to Rn: Design and assessment of accuracy. *Phys. Chem. Chem. Phys.* **2005**, *7* (18), 3297–3305. DOI: 10.1039/b508541a.

(49) Staroverov, V. N.; Scuseria, G. E.; Tao, J.; Perdew, J. P. Comparative assessment of a new nonempirical density functional: Molecules and hydrogen-bonded complexes. *The Journal of Chemical Physics* **2003**, *119* (23), 12129–12137. DOI: 10.1063/1.1626543.

(50) Kenjiro Tsutsumi; Hiroo Nakamori; Kouichi Ichikawa. X-ray Mn Kβ emission spectra of manganese oxides and manganates. *Phys. Rev. B* **1976**, *13* (2), 929. DOI: 10.1103/PhysRevB.13.929.

(51) Kowalska, J. K.; Hahn, A. W.; Albers, A.; Schiewer, C. E.; Bjornsson, R.; Lima, F. A.; Meyer, F.; DeBeer, S. X-ray Absorption and Emission Spectroscopic Studies of [L2Fe2S2]n Model Complexes: Implications for the Experimental Evaluation of Redox States in Iron–Sulfur Clusters. *Inorganic Chemistry* **2016**, *55* (9), 4485–4497. DOI: 10.1021/acs.inorgchem.6b00295.

(52) Pollock, C. J.; Delgado-Jaime, M. U.; Atanasov, M.; Neese, F.; DeBeer, S. Kβ mainline X-ray emission spectroscopy as an experimental probe of metal-ligand covalency. *J. Am. Chem. Soc.* **2014**, *136* (26), 9453–9463. DOI: 10.1021/ja504182n.

(53) Lee, N.; Petrenko, T.; Bergmann, U.; Neese, F.; DeBeer, S. Probing valence orbital composition with iron Kbeta X-ray emission spectroscopy. *J. Am. Chem. Soc.* **2010**, *132* (28), 9715–9727. DOI: 10.1021/ja101281e.

(54) Raebiger, H.; Lany, S.; Zunger, A. Charge self-regulation upon changing the oxidation state of transition metals in insulators. *Nature* **2008**, *453* (7196), 763–766. DOI: 10.1038/nature07009.

(55) Sit, P. H.-L.; Car, R.; Cohen, M. H.; Selloni, A. Simple, unambiguous theoretical approach to oxidation state determination via first-principles calculations. *Inorg. Chem.* **2011**, *50* (20), 10259–10267. DOI: 10.1021/ic2013107. Published Online: Sep. 16, 2011.

(56) Knizia, G. Intrinsic Atomic Orbitals: An Unbiased Bridge between Quantum Theory and Chemical Concepts. *J. Chem. Theory Comput.* **2013**, *9* (11), 4834–4843. DOI: 10.1021/ct400687b. Published Online: Oct. 17, 2013.

(57) Walsh, A.; Sokol, A. A.; Buckeridge, J.; Scanlon, D. O.; Catlow, C. R. A. Electron Counting in Solids: Oxidation States, Partial Charges, and Ionicity. *J. Phys. Chem. Lett.* **2017**, *8* (9), 2074–2075. DOI: 10.1021/acs.jpclett.7b00809.

(58) Walsh, A.; Sokol, A. A.; Buckeridge, J.; Scanlon, D. O.; Catlow, C. R. A. Oxidation states and ionicity. *Nature materials* **2018**, *17* (11), 958–964. DOI: 10.1038/s41563-018-0165-7. Published Online: Oct. 1, 2018.

(59) Chaudhari, A.; Lee, S.-L. Theoretical study of 3d-metal mononitrides using DFT method. *Int. J. Quantum Chem.* **2007**, *107* (1), 212–218. DOI: 10.1002/qua.21060.

(60) Štekláč, M.; Breza, M. On the relation between oxidation states and d-electron populations of the 1st row transition metal complexes I. Tetrachloro complexes. *Polyhedron* **2021**, *201*, 115172. DOI: 10.1016/j.poly.2021.115172.
(61) Aullón, G.; Alvarez, S. Oxidation states, atomic charges and orbital populations in transition metal complexes. *Theor Chem Acc* **2009**, *123* (1-2), 67–73. DOI: 10.1007/s00214-009-0537-9.
(62) Reed, A. E.; Curtiss, L. A.; Weinhold, F. Intermolecular interactions from a natural bond orbital, donor-acceptor viewpoint. *Chem. Rev.* **1988**, *88* (6), 899–926. DOI: 10.1021/cr00088a005.
(63) Glendening, E. D.; Landis, C. R.; Weinhold, F. Natural bond orbital methods. *WIREs Comput Mol Sci* **2012**, *2* (1), 1–42. DOI: 10.1002/wcms.51.
(64) Thom, A. J. W.; Sundstrom, E. J.; Head-Gordon, M. LOBA: a localized orbital bonding analysis to calculate oxidation states, with application to a model water oxidation catalyst. *Physical chemistry chemical physics : PCCP* **2009**, *11* (47), 11297–11304. DOI: 10.1039/b915364k. Published Online: Oct. 19, 2009.
(65) Fredin, L. A.; Pápai, M.; Rozsályi, E.; Vankó, G.; Wärnmark, K.; Sundström, V.; Persson, P. Exceptional Excited-State Lifetime of an Iron(II)-N-Heterocyclic Carbene Complex Explained. *J. Phys. Chem. Lett.* **2014**, *5* (12), 2066–2071. DOI: 10.1021/jz500829w.
(66) Chabera, P.; Liu, Y.; Prakash, O.; Thyrhaug, E.; Nahhas, A. E.; Honarfar, A.; Essen, S.; Fredin, L. A.; Harlang, T. C. B.; Kjaer, K. S.; Handrup, K.; Ericson, F.; Tatsuno, H.; Morgan, K.; Schnadt, J.; Haggstrom, L.; Ericsson, T.; Sobkowiak, A.; Lidin, S.; Huang, P.; Styring, S.; Uhlig, J.; Bendix, J.; Lomoth, R.; Sundstrom, V.; Persson, P.; Wärnmark, K. A low-spin Fe(iii) complex with 100-ps ligand-to-metal charge transfer photoluminescence. *Nature* **2017**, *543* (7647), 695–699. DOI: 10.1038/nature21430.
(67) Dixon, I. M.; Alary, F.; Boggio-Pasqua, M.; Heully, J.-L. The (N4C2)2- donor set as promising motif for bis(tridentate) iron(II) photoactive compounds. *Inorg. Chem.* **2013**, *52* (23), 13369–13374. DOI: 10.1021/ic402453p.
(68) Connelly, N. G.; Geiger, W. E. Chemical Redox Agents for Organometallic Chemistry. *Chem. Rev.* **1996**, *96* (2), 877–910. DOI: 10.1021/cr940053x.

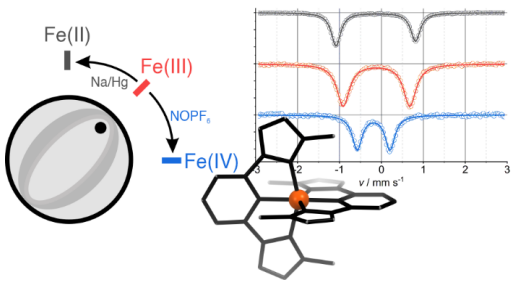

CHAPTER 5

DETECTION AND CHARACTERIZATION OF HYDRIDE LIGANDS IN COPPER COMPLEXES BY HARD X-RAY SPECTROSCOPY

Hydrides play an important role in various catalytic processes. Cu-hydrides are potential candidates as catalysts for CO_2 hydrogenation reactions. For the investigation of the working principles, insights into the geometric and electronic properties are indispensable. In this study two Cu-hydride complexes and one non-hydride complex are investigated by HERFD-XANES and VtC-XES to uncover the potential of X-ray spectroscopic methods for answering corresponding questions. It could be shown that VtC-XES provides a direct instrument to detect hydride ligands, whereas XANES is very sensitive to the coordination geometry and thus can provide additional indirect information about a hydride coordination.

Participations in this publication

L. Fritsch: Methodology, Analysis, Writing;
P. Rehsies: Synthesis Cu_3H; W. Barakat: Synthesis Cu-I;
D. P. Estes: Writing - review and editing.
M. Bauer: Writing - review and editing, Project administration.

Reprinted from
Detection and Characterization of Hydride Ligands in Copper Complexes by Hard X-ray Spectroscopy
Lorena Fritsch, Pia Rehsies, W. Barakat, Deven P. Estes , Matthias Bauer*; *Chem. Eur. J.*, **2024**, accepted, DOI: 10.1002/chem.202400357.

Supplementary Information for this publication is found in the Appendix A.4.

WILEY-VCH

RESEARCH ARTICLE

Detection and Characterization of Hydride Ligands in Copper Complexes by Hard X-ray Spectroscopy

Lorena Fritsch,[a] Pia Rehsies,[a] Wael Barakat,[b] Deven P. Estes,[b] and Matthias Bauer*[a]

[a] Lorena Fritsch, Pia Rehsies, Prof. Dr. M. Bauer
Institute of Inorganic Chemistry and Center for Sustainable Systems Design (CSSD), Paderborn University
Warburger Straße 100, 33098 Paderborn, Germany
E-mail: matthias.bauer@upb.de, http://www.chemie.upb.de/bauer

[b] Dr. Wael Barakat, Jun. Prof. Dr. Deven Estes
Institute of Technical Chemistry, University of Stuttgart
Pfaffenwaldring 55, 70569 Stuttgart, Germany

Abstract: Transition metal complexes, particularly copper hydrides, play an important role in various catalytic processes and molecular inorganic chemistry. This study employs synchrotron hard X-ray spectroscopy to gain insights into the geometric and electronic properties of copper hydrides as potential catalysts for CO_2 hydrogenation. The potential of high energy resolution X-ray absorption near-edge structure (HERFD-XANES) and valence-to-core X-ray emission (VtC-XES) is demonstrated with measurement on Stryker's reagent (**Cu_6H_6**) and $[Cu_3(\mu_3\text{-}H)(dpmppe)_2](PF_6)_2$ (**Cu_3H**), alongside a non-hydride copper compound ICu(dtbppOH) (**Cu-I**). The XANES analysis reveals that coordination geometries strongly influence the spectra, providing only indirect details about hydride coordination. The VtC-XES analysis exhibits a distinct signal around 8975 eV, offering a diagnostic tool to identify hydride ligands. Theoretical calculations support and extend these findings by comparing hydride-containing complexes with their hydride-free counterparts.

Introduction

Metal hydrides are essential components in a variety of chemical processes, including organometallic catalysis, energy conversion or hydrogen storage.[1] In catalytic hydrogenation reactions, for instance, C-H bond activation and functionalization processes, transfer hydrogenation and olefin isomerization, they play key roles as intermediates to transfer hydrides to unsaturated substrates.[2] Also, in energy conversion, electrochemical reduction and protonation of catalysts can generate metal hydrides that can undergo hydride transfer reactions with proton or carbon dioxide sources to generate H_2 or carbon-based fuels.[3] In particular CO_2 hydrogenation could play a crucial role to decelerate global warming by CO_2 removal from the atmosphere and valorization. While such reactions in solution are well known and can be studied mainly by NMR which also allows a precise identification of hydride species[4], heterogeneous gas-solid reactions are much less explored and require other spectroscopic approaches.

To understand the mechanistic principles of heterogenized molecular catalysts, it is crucial to have experimental methods available that can access geometric and electronic information of formed and involved hydride species under rather harsh in situ environments and reaction conditions. Vibrational spectroscopy is a powerful tool to access both types of information, however often the investigated vibrations in case of metal hydrides are usually too weak and often overlap with ligand, solvent, or co-reactant frequencies.[5] While NMR spectroscopy is sensitive to hydride ligands, it is often difficult to access ^{1}H NMR data for solid state catalysts under harsh conditions. Neutron diffraction requires selective deuteration and X-ray scattering is typically not applicable for immobilized molecular complexes. It could be recently shown by our group that X-ray absorption (XAS)[6] and X-ray emission spectroscopy (XES)[7] using hard X-rays are well-suited to detect hydride coordination in iron complexes, to investigate the HOMO and LUMO details of hydride complexes, and to follow the fate of the hydride in the course of catalytic reactions.[8] Hard X-ray radiation has several beneficial properties such as complete penetration of radiation into the sample so that metal centers can be examined independently of surface effects or the matrix, which makes the use of various measurement cells for solid, liquid or gas phase samples possible.[9]

XAS can be divided into the XANES (X-ray absorption near-edge structure) region, including the pre-peak signal, and the EXAFS

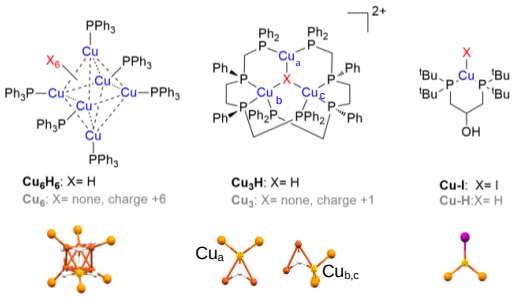

Figure 1: Top: Structures of complexes under investigation (black fond: experimental, grey fond: hypothetical). Bottom: For a better representation of the coordination geometry, the (different) copper centers of the optimized structures are shown only with their direct neighbor atoms. Cu (orange, investigated/different ones marked with a yellow grid), P (dark yellow), I (purple), H (white).

(extended X-ray absorption fine structure) region. While K-edge XANES investigates the excitation of the 1s electron of a specific atom, usually a metal center, into unoccupied bound states, EXAFS measures the absorption probability oscillating due to the influence of different backscattering neighbor atoms.[6a] However, in EXAFS, the signal of hydride ligands suffers from minimal backscattering amplitude, which makes it hard to detect hydride contributions. XES splits up into the Core-to-Core (CtC) and Valence-to-Core (VtC) transitions where the emission process of core states (e.g.: 2p or 3p, in the case of a 3d transition metal) and valence states (VtC) into the 1s orbital as a relaxation after the absorption process are studied. CtC-XES reflects the spin state and covalency at the metal center caused by the p-d exchange interaction. The splitting of the $K\beta_{1,3}$ and Kβ′ feature becomes larger with increasing 3p−3d exchange interactions and thus the region is suitable for oxidation state investigations. The signals in the VtC region are assigned to those from the valence orbitals which have mainly ligand *n*p and *n*s character with metal 3d mixing. Thus, VtC is a powerful tool to track ligand effects in the highest occupied molecular orbitals (HOMOs) since it is sensitive to ligand type, distance, and their coordination geometry. With the combination of XANES and VtC, both HOMO and LUMO levels can be investigated in combination with (TD)-DFT (time-dependent density functional theory) methods allowing conclusions to be drawn about the ligand environment of a central atom.[7c]

However, Kβ-XES and HERFD-XANES studies at Cu centers are relatively rare compared to other 3d transition metal sites like Fe. Typical studies investigate monovalent complexes with respect to their chemical signatures, or use the methodic combination for oxidation state, electronic structure determinations or catalytic investigations.[10] So far it was not used to investigate Cu-H species.[10a,11] Here, we measured and analyzed experimental and (TD-)DFT calculated X-ray spectroscopy data of two Cu hydrides (Stryker's reagent (**Cu_6H_6**) and $[Cu_3(\mu_3\text{-}H)(dpmppe)_2](PF_6)_2$ with dpmppe= $Ph_2PCH_2P(Ph)(CH_2)_2P(Ph)CH_2PPh_2$ (**Cu_3H**)) and one non-hydride Cu compound ICu(dtbppOH) with dtbppOH = $(^tBu)_2PCH_2CH(OH)CH_2P(^tBu)_2$ (**Cu-I**) which are shown in Figure 1. To be able to compare corresponding (non)-hydride references of those three complexes with a similar coordination environment, three further model compounds were considered on a purely theoretical basis to verify the conclusions on the analysis of the experimental data (see Figure 1, grey). For this purpose, theoretical XANES and VtC calculations for **Cu_6**, **Cu_3** and **Cu-H** were carried out and compared with the three main complexes.

Results and Discussion

Experimental Results

Figure 1 shows the structures of compounds under investigation. Stryker's reagent **Cu_6H_6** is a hexameric copper complex with one PPh_3 ligand on each Cu center in which six of the eight faces were originally thought to be covered by hydride ligands.[12] However, a revision in 2014 could show that there are six short and six long Cu-Cu edges and the hydrides bridge the short edges.[13] Thus, the approximated geometry of a distorted capped trigonal prism is obtained around one Cu center. Overall, the copper centers all exhibit a very similar coordination environment, with an average of one hydride ligand per copper. In the case of **Cu_3H**, this ratio is reduced to 1:3 since there is only one hydride ligand in the center of a trinuclear cuprous cluster. In addition, two different types of copper centers are found here, which is evident from the coordination of three phosphine ligands in the case for two copper centers ($Cu_{b,c}$) and the coordination of only two phosphine ligands for the third one (Cu_a). For those different Cu centers also a varying hydride bond length of 1.86 Å in the first case and only 1.48 Å in the second case is observed.[14] Not considering a possible metal-metal bond (average distance of 2.88 Å) the symmetry can be approximated by a tetrahedral coordination in the first case and a trigonal planar one in the second case. The

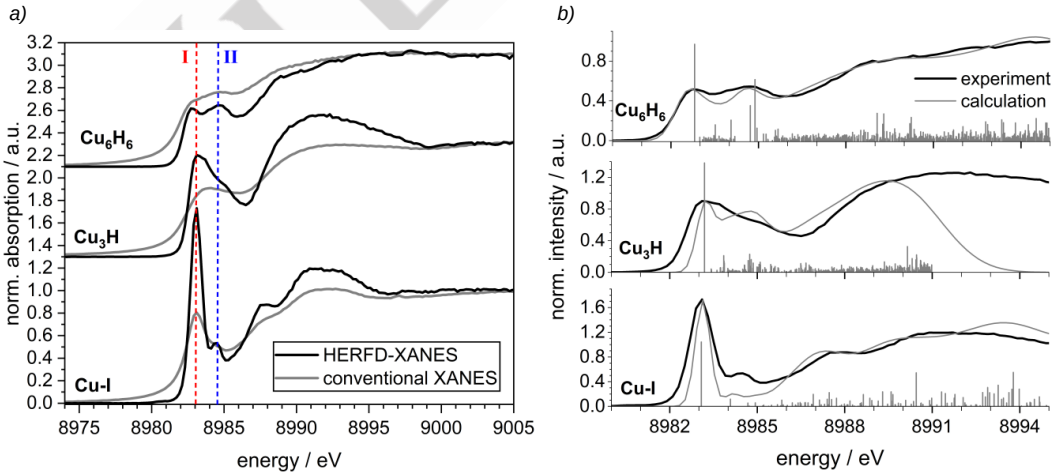

Figure 2: a) Comparison of experimental conventional XANES and HERFD-XANES spectra of C_6H_6, Cu_3H and Cu-I. b) Experimental (black, normalized) and TD-DFT calculated (grey) first 500 transitions as sticks and broadened as a spectrum of **C_6H_6**, **Cu_3H** and **Cu-I.**

iodide complex **Cu-I** serves as experimentally accessible hydride-free reference. It was chosen as halides can be considered as valence-isoelectronic to hydride ligands, both carrying a single negative charge. Investigation of Cu-X vs. Cu-H thus allows a more precise assignment of spectral signatures and avoids misinterpretations. In **Cu-I** the employed bidentate phosphine ligand results in the formation of a trigonal planar coordination geometry. All complexes are characterized by a formal oxidation state of +I, which is reflected by the identical edge position in the XANES spectra and the equal shape of Kβ CtC-XES spectra (Figure 2 and Figure S1). All Cu^{I} compounds under investigation show a similar spectral shape in the Kβ CtC-XES, while Cu^{II} species like $CuCl_2$ and CuO show a shift for the $K\beta_{1,3}$ signal to lower energies and a higher intensity for the Kβ' satellite due to the different p-d exchange interaction resulting from the unpaired d-electron.[7a,15]

HERFD-XANES

To investigate the impact of hydride ligands on the LUMO states, first the spectroscopic signatures of the experimental XANES spectra will be discussed. Figure 2a compares conventional XANES and HERFD-XANES spectra. It should be emphasized here that due to the used concentration slight self-absorption effects in the conventional XANES spectra might occur and additionally the normalization procedure for HERFD-XANES is not unambiguous due to the short energy range. However, in HERFD-XANES self-absorption can be excluded and the fine structure is visible due to the improved resolution, which allows for more thorough analysis of the contributing sites. When comparing the experimental HERFD-XANES spectra of **Cu_6H_6** with a Cu:Hydride ratio of 1:1 with **Cu_3H** characterized by the ratio of 3:1 and **Cu-I** containing no Hydrides, the edge energy remains the same, but differences become particularly apparent in the intensity of the two signals at 8983 eV (I) and 8985 eV (II). While the intensity of the second signal remains almost the same at around 0.5, the first signal varies in intensity. For **Cu_6H_6**, the intensity of I and II is approximately the same, whereas for **Cu_3H** the signal intensity of I increases by around one third. For **Cu-I** this effect becomes even more pronounced. Here, the intensity of I is more than three times higher than II. Transitions in this region are typically assigned to have 1s→ 4p character whereas the two signals might arise from degenerated 4p orbitals with variable ligand mixing.[16] Thus, also mixing with hydride ligand orbitals might play a role here.

However, in literature reports of Cu^{I} complexes it was also noted that the intensity of this signal region depends on the coordination geometry and number. For planar geometry in general a higher intensity is found than for tetrahedral coordination.[11a,17] This can be explained by a ligand field picture with molecular orbital considerations. In a trigonal-planar complex, the $4p_x$ orbital is stabilized in contrast to the $4p_{y,z}$ leading to one low energy p orbital. In the tetrahedral case all 4p orbitals are degenerate and energetically slightly lower than the $4p_{y,z}$ of the trigonal planar case (Figure 3).[17] This leads to a low energy signal with a high intensity for trigonal planar complexes and a slight shift to higher energies of this signal for tetrahedral complexes. Since the investigated complexes also show different coordination geometries and numbers of the Cu centers either, this consideration also applies and is evident here. For the complexes with (partially) planar geometry a higher intensity of the signal in general can be observed due to a low-lying p orbital. Thus, the differences in intensity of signal I of the three complexes mentioned above can be explained by their geometry, since **Cu-I** shows the highest intensity (1.7 a.u.) of signal I and has pure trigonal planar geometry, **Cu_3H** shows a decrease in intensity (0.9 a.u.) and has 1/3 of approximate trigonal planar geometry and 2/3 of approximate tetrahedral geometry. **Cu_6H_6** has the lowest intensity (0.5 a.u.) and no planar geometry. Even if not the hydride coordination itself, but more the complex geometry plays a role for this feature, it could be used to track changes in coordination geometry during catalytic reactions.

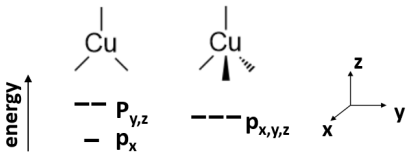

Figure 3: Schematic representation of the ligand field splitting of the Cu 4p orbitals in trigonal planar and tetrahedral geometry.

VtC-XES

For hydride complexes of iron it has been shown that a typical hydride signature can be observed in VtC XES while geometric factors are less dominating and thus the probed HOMO states of a higher chemical specificity towards hydride ligands.[8] The experimental spectra of **Cu_6H_6**, **Cu_3H** and **Cu-I** in Figure 4a show an intense signal A at around 8979 eV and a very weak cross-over area C below 8972 eV. Additionally, a shoulder B at around 8976 eV is observed for the two Hydride containing complexes. The higher energy features above 8983 eV are found in all published Cu VtC-XES spectra collected well above the edge and can be ascribed to double ionization features.[11b,11c,18] Literature suggests that signal A could be assigned to transitions from bonding combinations of copper 3d with ligand p to the copper 1s orbital.[11a] The energy of this band is almost the same for all complexes, with a slight shift of +0.3 eV for **Cu-I** in contrast to the hydride containing complexes. The crossover signals C typically are caused by transitions from ligand s-orbitals without significant metal contribution to the copper 1s orbital which explains the low transition probability. Signal B reflects transitions from ligand p-orbitals with increasing metal contribution. This distinct shoulder is usually not present in covalent Cu^{I} complex compounds like **Cu-I**.[11a,16] However, a similar signal can be found in ionic Cu^{I} compounds like Cu_2O, CuI and CuH at the same energy or Cu^{II} peroxo complexes, here as a sign of an of a O−O group at 8971 eV.[11c,19] Moreover, in the case of iron hydrides, the hydride signal was found at the same position, about 3 eV below the Fe 3d signal. This suggests that in the case of copper, a hydride signal might be also present in region B, which is supported by the increasing intensity for **Cu_3H** and **Cu_6H_6** with higher hydride ligand contribution in the complexes. Theoretical calculations in the following section will be used to substantiate the interpretation of this signal.

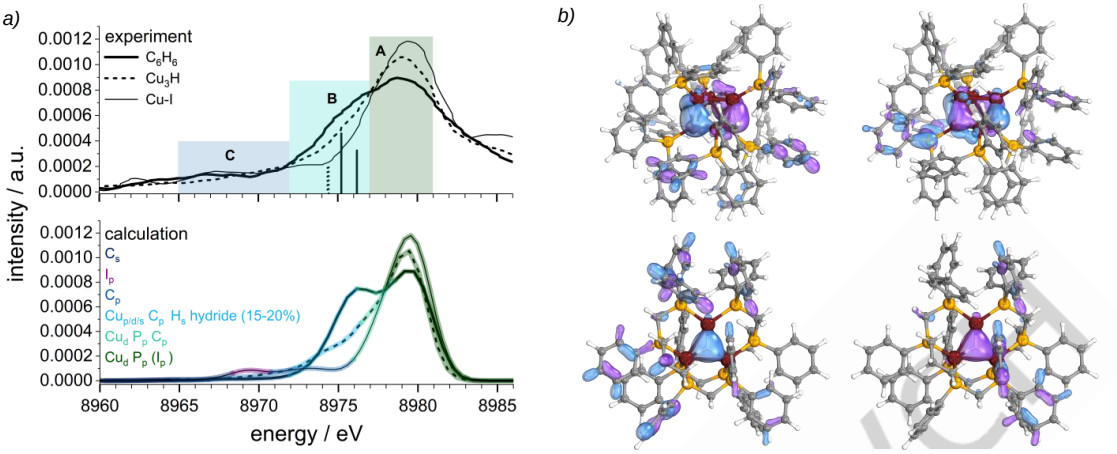

Figure 4: a) Experimental (top, not normalized) and DFT calculated (bottom) VtC spectra of **C_6H_6**, **Cu_3H** and **Cu-I**. More detailed analysis of the transitions can be found in Fig. S1. In the top spectrum two selected transitions with high Hydride contribution are shown for Cu_6H_6 and Cu_3H, respectively which are marked in Tab. S1. b) Spatial distribution of specific donor orbitals from transitions marked in Fig. 4a, top with high hydride contribution (Cu_6H_6 orbital 398/429, Cu_3H orbital 278/282) causing signal B.

Theoretical Results

So far, the HERFD and VtC-XES spectra were only analyzed quantitatively based on literature reports of related compounds, either copper complexes or hydride complexes of other metals. For a more detailed analysis and understanding of the molecular orbital origins of observed transitions, (TD-)DFT calculations are applied. Geometry optimizations of all three complexes were performed using the PBEh-3c composite method serving as an input for theoretical calculations in the following section.[20] The obtained structures (theo) show a good agreement with crystal structures and neutron diffraction (exp) and the edge-bridging hydride binding mode in **Cu_6H_6** is reproduced. This is shown by the six short Cu-Cu edges ($d_{Ø,exp}$ 2.52 Å; $d_{Ø,theo}$ 2.57 Å) and six long Cu-Cu edges ($d_{Ø,exp}$ 2.68 Å; $d_{Ø,theo}$ 2.65 Å).[12,13] Also the binding mode of the Cu to the Hydride ligands is reproduced showing a short bond length to two hydride ligands ($d_{Ø,exp}$ 1.67 Å; $d_{Ø,theo}$ 1.69 Å) and one significantly longer to the third one (d_{exp} 1.99 Å; $d_{,theo}$ 2.30 Å). The trinuclear copper hydride complex **Cu_3H** shows average experimental Cu-Cu bond lengths of $d_{Ø,exp}$ 2.95 Å and slightly shorter bonds in the theory with $d_{Ø,theo}$ 2.88 Å whereas also one shorter Cu_a-H ($d_{Ø,exp}$ 1.56 Å; $d_{Øtheo}$ 1.62 Å) and the longer $Cu_{b,c}$-H bond length is reproduced ($d_{Ø,exp}$ 1.79 Å; $Ø_{theo}$ 1.70 Å).[14] In **Cu-I** the Cu-I bond length of d_{exp} 2.50 Å is reproduced with d_{theo} 2.51 Å . Based on these geometries a very good agreement between theoretical and experimental HERFD-XANES and VtC-XES spectra is achieved which is shown in Figures 2b and 4a.

HERFD-XANES

The first 500 XANES transitions were calculated by TD-DFT using the TPSSh functional. (Figure 2b) The intensity ratio of the signals I and II is well reproduced and the calculated transitions are even able to model the quasi-continuum at higher energies, which are typically hard to reproduce due to the localized character of DFT.[11a,11d] This is also why only the first two signals are analyzed. In all cases the signal I is based on a single transition where the acceptor orbital is built from mainly Cu p-, P d- and C p-orbitals with different fractions (see Table S1). It is noticeable that with increasing transition probability from **Cu_6H_6** to **Cu_3H** to **Cu-I**, the proportion of Cu p-orbitals in the acceptor orbitals of signal I also increases (18.5 %, 22.8 % and 29.4 % respectively) whereas the C p-proportion decreases (40.6 %, 27.9 % and 25.2 % respectively). A participation of the Hydride s-orbitals cannot be observed here. Thus, although the direct informative value about the hydride is limited here, information about geometric changes can be also obtained and modeled by TD-DFT calculations to obtain indirect information about hydride and ligand coordination in general.

This gets especially visible when calculating the XANES spectrum of the two different Cu centers (Cu_a and $Cu_{b,c}$) in **Cu_3H** (Figure S2). While for Cu_a with a trigonal planar structure signal I at 8983 eV is particularly intense and signal II only gets visible as a weak shoulder at 8985 eV, for the more tetrahedrally coordinated $Cu_{b,c}$ solely signal II is present at 8985 eV with only a slightly higher intensity as the shoulder mentioned before (Figure S1). The higher intensity of I for planar coordination geometry fits to the reported literature findings and represents the p-orbital splitting shown in Figure 3.[11a,17] Furthermore, it appears that signal II is less dependent on the coordination geometry since the intensity hardly varies here. This signal results from several transitions where the Cu p-orbital fraction is lower than for signal I. Especially **Cu_3H** and **Cu-I** have a Cu p-orbital contribution of less than 10 % explaining the lower dependence from geometry-based p-orbital splitting (see Table S1).

WILEY VCH

RESEARCH ARTICLE

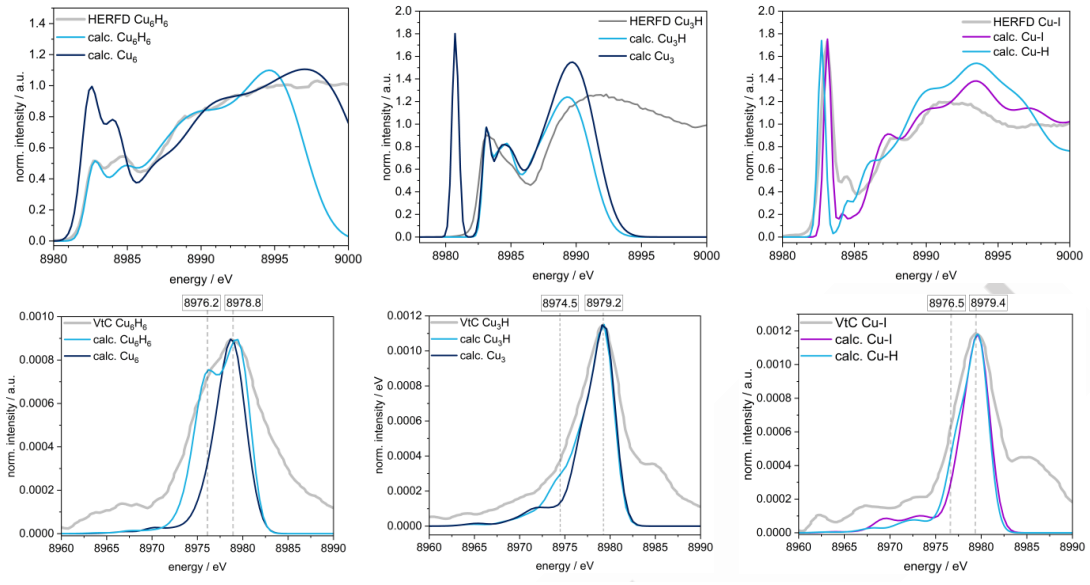

Figure 5: Comparison of calculated XANES (top) and VtC (bottom) spectra of the experimentally and theoretically investigated hydride (light blue), non-hydride (dark blue) and halide (purple) complexes.

VtC-XES

Also, DFT calculated VtC transitions represent the spectra and especially the prominent shoulder at 8976 eV very well (Figure 4a). The lowest energy and very weak signals in area C at about 8964 eV originate from C s- to the metal 1s-orbital transitions for all three complexes, but for **Cu-I** a slight increased intensity at 8969 eV gets visible due to transitions from the I s-orbital (Table S1). From 8970 eV onwards, the signal is dominated by C p-orbitals for all complexes. These transitions also contain a small contribution from H s-orbitals of organic ligands, but not those of the hydride ligands. Since the signal at 8975 eV in area B increases with increasing number of hydride ligands, this was assumed to be a signature of hydride ligands. In fact, the calculations for this signal show a strong proportion of hydride H s-orbitals in combination with C p-orbitals. With **Cu_6H_6** there are two transitions at 8975.2 eV and 8976.2 eV (Figure 4a, Table S1) which have a high hydride portion. The spatial distribution of the donor orbitals of those transitions are shown in Fig. 4b, where it can also be seen that the hydrides have a major influence on the orbitals. In the case of **Cu_6H_6**, the hydride contribution of up to 21 % for the signal at 8975.2 eV is twice as large as for **Cu_3H** (12 % at 8974.4 eV) which agrees well with the experimental signal intensity. For **Cu_3H** there are two very close transitions with a high hydride content at 8974.3 and 8974.4 eV. The spatial distribution of the donor orbitals is also shown in Figure 4b. Even if there are differences between the copper centers in **Cu_3H**, both transitions exist for all three centers, although the transition probability for Cu_a as the acceptor orbital is slightly increased in contrast to $Cu_{b,c}$. **Cu-I** does not show any noticeable transitions in this region, which underlines the dependence of the signal intensity on the presence of hydride ligands. The intense signal at 8979 eV in area A originates mainly from Cu d-orbitals with admixture of Cu and ligand p-orbitals. The experimentally observed intensity decrease from **Cu-I** to **Cu_3H** to **Cu_6H_6** is well reproduced by DFT-calculations.

Further theoretical spectroscopy

While the results obtained by analysis of experimental data with theoretical calculations are already convincing, purely theoretical considerations are used in the following to further substantiate these results by comparison of the spectra of the investigated complexes with the hypothetical non-hydride and hydride counterpart complexes. This means that on the one hand, **Cu_6H_6** and **Cu_3H** are compared with structures **Cu_6** and **Cu_3**, respectively, in which only the hydrides have been removed and replaced by (six or three, respectively) positive charges to account for a similar geometry and oxidation state at the Cu centers. Furthermore, **Cu-I** is compared with the potential Cu-Hydride (**Cu-H**) in which the iodine is exchanged by a hydride (cf. Figure 1). In all cases the oxidation state is Cu^{I}. As such the purely theoretical spectra generated here can be compared to the experimental data.

In case of HERFD-XANES spectra the geometry modification by removal of hydride ligands is observed (Figure 5). The theoretical spectrum of **Cu_6** obviously differs from the experimental data for **Cu_6H_6** in the intensity ratio of the white line and continuum signals. In the experiment and the calculation for **Cu_6H_6** the ratio is 1:2 while in the case of **Cu_6** it is about 1. This can be attributed to the change in geometry here. **Cu_6H_6** corresponds to a distorted capped trigonal prism whereas **Cu_6** corresponds more to a distorted square pyramid, increasing the whiteline intensity. For **Cu_3** a very intense signal at 8981 eV gets visible in contrast to the experimental spectrum of **Cu_3H**. Analysis of this signal (Fig. S3)

shows that this is also a 1s→ 4p transition with high Cu p-orbital portion. The change in geometry and the reduction in the number of ligands results in a change in p orbital splitting which leads to the low-energetic signal. Since for **Cu-I** and **Cu-H** no geometry change is present, the first signal at 8983 eV overlaps. In the further course only minor differences are observed.

In the VtC spectra, signals with significant hydride contributions were found around 8975 eV. This is supported by consideration of the respective hypothetical reference in Figure 5. In case of **Cu_6H_6** the intense signal at 8976 eV is immediately noticeable, where a high hydride content was detected in the previous chapter. Accordingly, the signal for the hydride-free reference **Cu_6** is completely absent. As expected, **Cu_6H_6** reproduces the experiment significantly better than **Cu_6**. The same effect is also found with **Cu_3H** and **Cu_3**, albeit significantly weaker, which can be attributed to the low hydride content of the complex. The hydride signal is also relatively weak for **Cu-H**, but there are also differences to **Cu-I** visible. In particular, a transition at 8977.8 eV (see Table S1, marked) with a hydride content of 23 % is responsible for the additional shoulder of the hydride containing complex. This hypothetical observation further supports the experimental and theoretical results, that VtC offers a possibility to clearly identify hydride coordination in copper complexes.

Conclusion

In this study, we have employed hard X-ray spectroscopy techniques in the form of high energy resolution fluorescence detected X-ray absorption near-edge structure (HERFD-XANES) and valence-to-core X-ray emission spectroscopy (VtC-XES), to investigate the electronic structure of three different Cu hydrides. It was shown that the HERFD-XANES spectra of the differently coordinated species do not provide direct information about the hydride ligands but are very sensitive to coordination geometries which was particularly evident from the intensity of a pre-edge signal at 8983 eV and can provide indirect details about the presence of hydride coordination. Furthermore, the VtC-XES analysis provided valuable information on the HOMO states, with a focus on the presence and contribution of hydride ligands. A distinct signal at around 8975 eV observed in the VtC-XES spectra demonstrated the potential of this technique to identify hydride ligands in those complexes. Theoretical considerations were also employed to support and extend our findings by comparing the hydride-containing complexes with their hydride-free counterparts.

In conclusion, the potential of hard X-ray spectroscopy to detect and characterize hydride ligands in copper complexes could be demonstrated and a protocol for this purpose could be established, which includes simulation of hypothetical structures as well. Especially the complementarity of both VtC-XES and HERFD-XANES allows the identification of changes in geometry and ligand type, which is extremely important for mechanistic studies on catalytic systems under operando conditions. The combination of experimental and theoretical approaches could provide a comprehensive understanding of the electronic and structural properties of the studied copper hydride complexes. These findings not only contribute to the broader knowledge of transition metal chemistry but also pave the way for the development of advanced catalysts with tailored reactivity for various chemical transformations by in-situ and operando studies using hard X-rays.

Experimental Section

Materials

Strykers reagent Cu_6H_6 was bought from Sigma-Aldrich.

Synthesis of $[Cu_3(\mu_3\text{-}H)(dpmppe)_2](PF_6)_2$: Cu_3H was synthesized according to reported procedures[14]: To a solution of meso-dpmppe (200 mg, 0.311 mmol) and CuCl (46.2 mg, 0.467 mmol) in DCM (8.3 ml) and methanol (8.3 ml) was added NH_4PF_6 (77.1 mg, 0.473 mmol) and $NaBH_4$ (60 mg, 1.59 mmol) and the reaction mixture was stirred for 3 h under argon at room temperature. The solvent was removed under reduced pressure, and the residue was extracted with DCM (30 ml). This solution was passed through a membrane filter (0.2 µm) and the solvent was removed again. This residue was extracted with MeCN (10 ml) and passed again through a membrane filter (0,2 µm) before removing the solvent under reduced pressure. ^{1}H-NMR (700 MHz, MeCN-d_6): δ 7.90-6.85 (m, 68H), 3.64 (d, J_{HH} = 14.7 Hz, 2H), 3.31 (d, J_{HH} = 14.2 Hz, 2H), 2.65 (m, 4H), 2.51 (m, 2H), 2.07 (d, J_{HH} = 13.8 Hz, 2H), 1.75 (t, J_{HH} = 13.7 Hz, 2H), 1.65 (td, J_{HH} = 14.2 Hz, J_{HH} = 3.8 Hz, 2H), -0.59 (s, 1H, hydride). ^{31}P-NMR (150 MHz, MeCN-d_6): 4.1 (s, 6P), -3.0 (s, 2P), -144.5 (sept, 2P). ESI-MS (in MeCN): m/z 738.091 (z2, $[Cu_3H(dpmppe)_2]^{2+}$ (738.091)).

Synthesis of (^{t}Bu$_2$P)$_2$C$_3$H$_5$OH (1): The P-ligand for Cu-I was synthesized based on a similar literature procedure for the PPh_2 derivative.[21] 1.027 g of HP^tBu_2 (7.02 mmol, 2 eq) was diluted in distilled THF (9 mL) under argon. 4.9 mL of nBuLi (7.02 mmol, 2 eq) in hexane was added dropwise to this solution at room temperature resulting in a color change to bright yellow. After stirring for 1h, this solution was added dropwise (up to 30 min) to a solution of rac-epichlorhydrin (0.324 g, 3.51 mmol, 1 eq) in distilled THF (6 mL) at 0 °C. The yellow color of the phosphide solution was quickly lost upon addition to the epichlorhydrin until 1 eq had been added, after which the yellow color remained and intensified with addition of the rest of the solution. The solution was stirred for a further 2 h at room temperature until the solution was fully colorless. The solution was quenched with degassed water (12 mL), the water removed under Ar by syringe, and the solvent removed under vacuum, giving an off white solid. This was dissolved in CH_2Cl_2 (6 mL), the remaining solid filtered away by cannula filtration, washed with a further 3 mL CH_2Cl_2, concentrated in vacuum to roughly 1/3 the volume, and crystallized overnight at -25 °C, yielding 1.015 g of off-white crystals with a total yield (83%). **^{1}H NMR** (δ, C_6D_6, 400 MHz) 3.95 (*m*,1H), 3.12 (*m*, 1H), 2.06 (*dd, J* = 4.1, 5.6 Hz, 1H), 2.02 (*dd, J* = 4.1, 5.6 Hz, 1H), 1.77 (*ddd*, *J* = 1.9, 3.4, 7.6 Hz, 1H), 1.73 (*ddd*, *J* = 1.9, 3.4, 7.6, 1H), 1.13 (*d*, *J* = 3.35 Hz, 18H), 1.10 (*d*, *J* = 3.5 Hz, 18H). **^{31}P NMR** (δ, C_6D_6, 161.9 MHz) 16.96 (s). **^{13}C NMR** (δ, C_6D_6, 161.9 MHz) 71.67 *(t*, *J* = 25 Hz), 31.90 (*d*, *J* = 7.7 Hz), 31.71

(*d*, *J* = 7.7 Hz), 31.26 (*d*, *J* = 20.8 Hz), 30.87 (*d, J* = 20.2 Hz), 29.52 (*d*, *J* = 7.7 Hz), 29.38 (*d*, *J* = 7.7 Hz).

Synthesis of ICu(dtbppOH) (2): For Synthesis of Cu-I, ligand **1** (207 mg, 0.594 mmol) was added to a solution of CuI (113.1 mg, 0.594 mmol) in DMF (1 mL) and the mixture stirred for 1 h over which time the solution became transparent with no insoluble material. After this time, 20 mL of acetonitrile was added resulting in a white precipitate. This was stored at -35 °C overnight. The remaining liquid was removed by filtration and the solid dried in vacuo to yield complex **2** as a white solid (230 mg, 71 % yield). **^{1}H NMR** (δ, thf-d_8, 400 MHz) 4.11 ppm (*m***,** 1H), 4.04 ppm (*m*, **1**H), 2.12 ppm (*m***,** 2H), 1.63 ppm (*m*, 2H, overlapping with solvent peak), 1.22 ppm (*m*, 18H), 1.17 ppm (*m*, 18H). **^{31}P {^{1}H} NMR** (δ, thf-d_8, 161.9 MHz) 10.14 ppm (s). **^{13}C {^{1}H} NMR** (δ, thf-d_8, 100.6 MHz) 69.40 ppm (*vt*, *J* = 10.95 Hz), 34.15 ppm (*vt*, *J* = 5.13 Hz), 33.36 ppm (*vt*, *J* = 6.6 Hz), 30.45 ppm (s), 29.41 ppm (*vt*, J = 4.00 Hz), 28.50 ppm (*vt*, *J* = 4.05 Hz). **IR** (KBr): 3427, 2945, 1474, 1368, 1282, 1179. **EA**: anal. calc. for $C_{19}H_{42}CuIOP_2$ C 42.34, H 7.86 found: C 42.11 H 7.79.

X-ray crystal structure of (2)

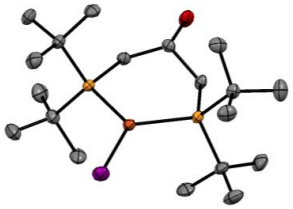

A single X-ray structure of **2** obtained from crystal grown by slow evaporation of a solution of **2** in DMF, chloroform, and THF under argon at room temperature. O: red, P: light yellow, Cu: orange, I: purple.

Single crystal X-ray diffraction was measured on a Bruker Kappa APEXII Duo diffractometer with Mo K_α-radiation at 145 K and refined with the software SHELXL-2014-7.

Hard X-ray spectroscopy

For (HERFD)-XANES and XES measurements, the investigated compound powders were diluted with dry BN, pressed to wafers, and sealed with Kapton tape. For the HERFD XANES the concentration was calculated according to an edge jump of 0.3 to avoid self-absorption and for XES and conventional XANES the concentration was chosen according to an edge jump of 1.2. Handling of all samples was performed under an inert atmosphere in a glovebox. X-ray spectroscopic measurements were conducted at Beamline P64 at DESY (Deutsches Elektronen Synchrotron) with a von Hamos type X-ray emission spectrometer.[22] The incident energy was selected using the ⟨311⟩ reflection from a double Si crystal monochromator and had a flux of 1*10^12 photons/s. HERFD spectra were obtained by scanning the incident energy and for XES measurements a fixed incident energy of 9300 eV was used. The emission energy was selected using the Si⟨444⟩ reflection of ten crystals. Calibration of the position sensitive detector was performed using the elastic scattering lines. The conventional XANES was recorded by monitoring the total fluorescence yield. The energy resolution of the monochromator is 0.3 eV whereas the spectrometer resolution is 1 eV. The lifetime broadening of the Cu 1s hole in the conventional XANES amounts to 1.78 eV whereas the 2p hole in the HERFD-XANES has typically a reduced lifetime-broadening of around 0.5 eV.[23] All measurements were carried out with the sample placed at around 90 K in a N_2 cryostat and short XANES spectra were conducted to check for radiation damage. 1.9 mm glassy carbon filters and the measurement time of 90 s for Cu_6H_6, 180 s for Cu_3H and 30 s for Cu-I were adjusted so that no changes in the K-edge could be detected during measurement time.

DFT calculations

All density functional theory (DFT) calculations were carried out using ORCA version 5.0.3.[24] Geometries of Cu_6H_6, Cu_3H, Cu-I and Cu-H were optimized using the PBEh-3c composite scheme.[20] In order to check whether the structure is a minimum structure, a frequency calculation was performed and checked for the absence of negative frequencies. For hypothetical complexes Cu_6 and Cu_3 no separate optimization was done to maintain the same geometry except for the hydrides. For this purpose, the hydride ligands were removed from the optimized original complexes Cu_6H_6 and Cu_3H. In order to model the same oxidation state as before, the corresponding number of charges was added for the spectra calculations. Since different copper centers are only present in the case of Cu_3H and Cu_3, all centers were included in the spectra calculation. In the case of Cu_6H_6 and Cu_6, the spectra calculation was limited to the transitions from one Cu center due to the equality. All XANES spectra were calculated using the time-dependent DFT (TD-DFT) approach as implemented in ORCA.[25] The calculations utilized all electron scalar relativistic basis sets of triple-ζ quality[26]. The functional of choice for all XANES-TD-DFT calculations was the TPSSh functional and for VtC-DFT calculations the TPSS functional along with the def2-TZVP basis set[26a,27]. The core properties of the Cu centers were described by triple-ζ basis set CP(PPP).[28] The tight convergence criterion was imposed on all calculations and the D4 dispersion correction was employed.[29] The single-energy transitions of the calculated XANES spectra have been subjected to Gaussian broadening, linearly rising with increasing excitation energy. The calculated VtC transitions are broadened with constantly 2.5 eV. The calculated spectra have been shifted to match the copper K-edge. For that a shift of 202 eV was required for XANES and 219 eV for VtC spectra. Furthermore, all spectra have been adjusted in intensity to match the experimental spectrum. Spatial distributions of orbitals were visualized using IboView.[30] The analysis of the individual fractions of the molecular orbitals is based on the Löwdin population analysis, which was extracted from the ORCA output file using MOAnalyzer (version 1.3).[31]

Supporting Information

Additional information theoretical calculated XANES and VtC-XES spectra can be found in the supporting information.

Acknowledgements

L.F. thanks the “Fonds der Chemischen Industrie” for a Kekulé grant. The Paderborn Center for Parallel Computing PC^2 is gratefully acknowledged for generous grants of computer time.

Keywords: X-ray absorption spectroscopy • X-ray emission spectroscopy • Hydrides

[1] a) N. Klopčič, I. Grimmer, F. Winkler, M. Sartory, A. Trattner, J. Energy Storage **2023**, 72, 108456; b) M. Peruzzini, R. Poli, Eds, Recent advances in hydride chemistry; Elsevier Science Ltd, Amsterdam, New York, **2007**.

[2] a) M. Orchin, AIP conf. proc. **1966**, 16, 1–47; b) C. P. Casey, H. Guan, J. Am. Chem. Soc. **2007**, 129, 5816–5817; c) K. Goldberg, Ed, Activation and functionalization of C-H bonds; American Chemical Society, Washington D.C, **2004**.

[3] a) W.-H. Wang, Y. Himeda, J. T. Muckerman, G. F. Manbeck, E. Fujita, Chem. Rev. **2015**, 115, 12936–12973; b) F. Bertini, N. Gorgas, B. Stöger, M. Peruzzini, L. F. Veiros, K. Kirchner, L. Gonsalvi, ACS Catal. **2016**, 6, 2889–2893.

[4] a) C.-Y. Liu, S.-F. Yuan, S. Wang, Z.-J. Guan, D.-E. Jiang, Q.-M. Wang, Nat. Commun. **2022**, 13, 2082; b) C. M. Zall, J. C. Linehan, A. M. Appel, J. Am. Chem. Soc. **2016**, 138, 9968–9977.

[5] a) X. Wang, L. Andrews, L. Manceron, C. Marsden, J. Phys. Chem. A **2003**, 107, 8492–8505; b) L. Andrews, X. Wang, J. Am. Chem. Soc. **2003**, 125, 11751–11760.

[6] a) M. Bauer, H. Bertagnolli in Methods in Physical Chemistry; (Eds. R. Schäfer, P. C. Schmidt), Wiley, **2012**, pp. 231–269; b) A. J. Atkins, M. Bauer, C. R. Jacob, Phys. Chem. Chem. Phys. **2013**, 15, 8095–8105.

[7] a) U. Bergmann, P. Glatzel, Photosynth. Res. **2009**, 102, 255–266; b) P. Glatzel, U. Bergmann, Coord. Chem. Rev. **2005**, 249, 65–95; c) M. Bauer, Phys. Chem. Chem. Phys. **2014**, 16, 13827–13837.

[8] L. Burkhardt, M. Holzwarth, B. Plietker, M. Bauer, Inorg. Chem. **2017**, 56, 13300–13310.

[9] M. Bauer, U. Bentrup, J. B. Priebe, A. Brückner in Contemporary Catalysis: Science, Technology, and Applications; (Eds. P. C. J. Kamer, D. Vogt, J. Thybaut), The Royal Society of Chemistry, **2017**, pp. 549–588.

[10] a) B. L. Geoghegan, Y. Liu, S. Peredkov, S. Dechert, F. Meyer, S. DeBeer, G. E. Cutsail, J. Am. Chem. Soc. **2022**, 144, 2520–2534. b) K. Kvande, B. Garetto, G. Deplano, M. Signorile, B. G. Solemsli, S. Prodinger, U. Olsbye, P. Beato, S. Bordiga, S. Svelle, E. Borfecchia, *Chem. Sci.* **2023**, *14*, 9704–9723; c) D. K. Pappas, A. Martini, M. Dyballa, K. Kvande, S. Teketel, K. A. Lomachenko, R. Baran, P. Glatzel, B. Arstad, G. Berlier, C. Lamberti, S. Bordiga, U. Olsbye, S. Svelle, P. Beato, E. Borfecchia, *J. Am. Chem. Soc.* **2018**, *140*, 15270–15278.

[11] a) N. J. Vollmers, P. Müller, A. Hoffmann, S. Herres-Pawlis, M. Rohrmüller, W. G. Schmidt, U. Gerstmann, M. Bauer, Inorg. Chem. **2016**, 55, 11694–11706; b) V. Martin-Diaconescu, K. N. Chacón, M. U. Delgado-Jaime, D. Sokaras, T.-C. Weng, S. DeBeer, N. J. Blackburn, Inorg. Chem. **2016**, 55, 3431–3439; c) J. R. Vegelius, K. O. Kvashnina, M. Klintenberg, I. L. Soroka, S. M. Butorin, J. Anal. At. Spectrom. **2012**, 27, 1882. d) P. Müller, K. Karhan, M. Krack, U. Gerstmann, W.G. Schmidt., M. Bauer and T.D. Kühne, J. Comput. Chem. **2019**, 40, 712–716.

[12] R. C. Stevens, M. R. McLean, R. Bau, T. F. Koetzle, J. Am. Chem. Soc. **1989**, 111, 3472–3473.

[13] E. L. Bennett, P. J. Murphy, S. Imberti, S. F. Parker, Inorg. Chem. **2014**, 53, 2963–2967.

[14] T. Nakajima, Y. Kamiryo, K. Hachiken, K. Nakamae, Y. Ura, T. Tanase, Inorg. Chem. **2018**, 57, 11005–11018.

[15] a) P. Glatzel, R. Alonso‐Mori, D. Sokaras in X‐Ray Absorption and X‐Ray Emission Spectroscopy; (Eds. J. A. van Bokhoven, C. Lamberti), Wiley, **2016**, pp. 125‐153; b) K. Tsutsumi, J. Phys. Soc. Jpn. **1959**, 14, 1696‐1706.

[16] Y. Liu, S. G. Resch, I. Klawitter, G. E. Cutsail, S. Demeshko, S. Dechert, F. E. Kühn, S. DeBeer, F. Meyer, Angew. Chem. Int. Ed. **2020**, 59, 5696–5705.

[17] J. Rudolph, C. R. Jacob, Inorg. Chem. **2018**, 57, 10591–10607.

[18] a) P. Glatzel in AIP Conf. Proc. **2003**, pp. 250–255; b) T. Günter, H. W. P. Carvalho, D. E. Doronkin, T. Sheppard, P. Glatzel, A. J. Atkins, J. Rudolph, C. R. Jacob, M. Casapu, J.-D. Grunwaldt, Chem. Commun. **2015**, 51, 9227–9230.

[19] G. E. Cutsail, N. L. Gagnon, A. D. Spaeth, W. B. Tolman, S. DeBeer, Angew. Chem. Int. Ed. 2019, 58, 9114–9119.

[20] S. Grimme, J. G. Brandenburg, C. Bannwarth, A. Hansen, J. Chem. Phys. 2015, 143, 54107.

[21] J. Scherer, G. Huttner, M. Büchner, Chem. Ber. 1996, 129, 697–713.

[22] a) W. A. Caliebe, V. Murzin, A. Kalinko, M. Görlitz in AIP Conf. Proc, p .60031; b) A. Kalinko, W. A. Caliebe, R. Schoch, M. Bauer, J. Synchrotron Radiat. 2020, 27, 31–36;

[23] H. Hayashi, Y. Udagawa, W. A. Caliebe, C.-C. Kao, *Chem. Phys. Lett.* **2003**, *371*, 125–130.

[24] a) F. Neese, WIREs Comput. Mol. Sci. 2012, 2, 73–78; b) F. Neese, WIREs Comput. Mol. Sci. **2022**, 12;

[25] a) S. DeBeer George, T. Petrenko, F. Neese, J. Phys. Chem. A **2008**, 112, 12936–12943; b) S. DeBeer George, T. Petrenko, F. Neese, Inorg. Chim. **2008**, 361, 965–972.

[26] a) F. Weigend, R. Ahlrichs, Phys. Chem. Chem. Phys. **2005**, 7, 3297–3305; b) F. Weigend, Phys. Chem. Chem. Phys. **2006**, 8, 1057–1065; c) D. A. Pantazis, X.-Y. Chen, C. R. Landis, F. Neese, J. Chem. Theory Comput. **2008**, 4, 908–919; d) D. A. Pantazis, F. Neese, J. Chem. Theory Comput. **2009**, 5, 2229–2238; e) D. A. Pantazis, F. Neese, J. Chem. Theory Comput. **2011**, 7, 677–684; f) D. A. Pantazis, F. Neese, Theor. Chem. Acc. **2012**, 131, 1292.

[27] V. N. Staroverov, G. E. Scuseria, J. Tao, J. P. Perdew, J. Chem. Phys. **2003**, 119, 12129–12137.

[28] F. Neese, Inorg. Chim. **2002**, 337, 181–192.

[29] E. Caldeweyher, S. Ehlert, A. Hansen, H. Neugebauer, S. Spicher, C. Bannwarth, S. Grimme, J. Chem. Phys. **2019**, 150, 154122.

[30] G. Knizia, J. E. M. N. Klein, Angew. Chem. **2015**, 127, 5609–5613.

[31] M. U. Delgado-Jaime, S. DeBeer, J. Comput. Chem. **2012**, 33, 2180–2185.

WILEY-VCH

RESEARCH ARTICLE

Entry for the Table of Contents

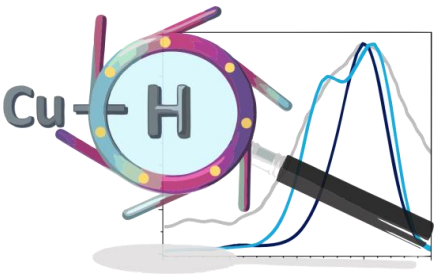

Discover how X-ray absorption and X-ray emission spectroscopy analyses unveil insights into the geometric and electronic properties of copper hydride complexes. The integration of experimental and theoretical approaches offers a holistic approach in detecting and characterizing hydride ligands in copper complexes.

Institute and/or researcher Twitter usernames: @BauerResearch

CHAPTER 6

FINAL CONCLUSION & OUTLOOK

The combination of experimental electron spectroscopy and theoretical calculations has been shown to be a versatile tool for many different questions in the investigation of TM complexes and the aim of getting deep insight into the different systems was reached. The focus here was particularly on X-ray spectroscopy which, in combination with theoretical calculations, allowed conclusions to be drawn about the geometric and electronic structure of different complexes used for sustainable chemistry applications. Furthermore, the analysis of UV-Vis and photoluminescence spectroscopy, as well as cyclic voltammetry, was substantiated and elucidated through theoretical calculations.

The effects of backbone amine functionalization in three homoleptic CˆNˆC type Ru^{II} complexes bearing a tridentate bis-imidazole-2-ylidene pyridine ligand framework were analyzed. Cyclic voltammetry, optical spectroscopy and transient absorption spectroscopy revealed that functionalization by dimethylamine groups at the 4-position on the pyridine backbone led to a decrease in photoluminescence quantum yield and a shortened excited state lifetime, while improving photostability and increasing the molar absorption coefficient of the MLCT bands. Ab initio DFT calculations were able to attribute these effects to the different orbital levels and excited state energies enabling the population of a dark relaxation pathway at room temperature.

Furthermore, different backbone functionalizations of photophysically challenging homoleptic bidentate Fe^{III} complexes using the phenyl-1H-pyrazole as a ligand motive were examined. In addition to cyclic voltammetry and UV-Vis-spectroscopy, X-ray absorption and emission spectroscopy were also used here to get insights into the electronic structure. The good π-acceptor properties of a trifluoromethyl substituted ligand or the more electron-donating properties of the methoxy substitution were demonstrated. Also here, the spectra were analyzed using DFT calculations, which additionally enabled structural predictions to be made about the facial or meridional conformation of the possible isomers of the bidentate

species.

Moreover, it could be shown that the strong donor ligand ImP (1,1'-(1,3-phenylene)bis(3-methyl-1-imidazol-2-ylidene) using a combination of four N-heterocyclic carbenes (NHCs) and two cyclometalating functions is able to not only build the stable literature known Fe^{III} complex but is also able to stabilize the Fe^{II} and Fe^{IV} species. With the help of X-ray spectroscopy, the spin and the oxidation state could be clearly assigned to substantiate that the ligand is able to stabilize all three oxidation states of iron.

Lastly, it was demonstrated that X-ray spectroscopy can serve as a suitable tool for detecting hydride ligands in Cu complexes which are known for their catalytic activity in CO_2 hydrogenation. The potential of high energy resolution X-ray absorption near-edge structure (HERFD-XANES) and valence-to-core X-ray emission (VtC-XES) could be demonstrated to probe geometric factors and a specific hydride signal to contribute indirectly and directly as a diagnostic tool to identify hydride ligands. DFT calculations also play a major role here, which were indispensable for determining the character of the specific signal. The measurements shown were stationary measurements in solid state. A further step would be to use the shown methods for in-situ measurements. Additionally, pursuing pump-probe experiments represents the next step in understanding electron transfer reactions, including those in photocatalytic processes.

Overall, this work has shown how transition metal complexes can be understood by sophisticated experimental and theoretical techniques in order to derive a correlation between the structure and the properties. This knowledge should help to design optimal properties for certain processes. Furthermore, the potential and good agreement between the experiments and quantum chemical calculations were demonstrated in the work. In the future such calculations might be used even more as a predictive tool for stability and properties prognoses of potential complexes.

APPENDIX A

APPENDIX

A.1 Supporting Information of "Chemical and photophysical properties of amine functionalized bis-NHC-pyridine Ru^{II} complexes"

ChemPhotoChem

Supporting Information

Chemical and photophysical properties of amine functionalized bis-NHC-pyridine-Ru^{II} complexes

Lorena Fritsch, Yannik Vukadinovic, Moritz Lang, Robert Naumann, Maria-Sophie Bertrams, Ayla Kruse, Roland Schoch, Patrick Müller, Adam Neuba, Philipp Dierks, Stefan Lochbrunner, Christoph Kerzig, Katja Heinze, and Matthias Bauer*

SUPPORTING INFORMATION

Chemical and photophysical properties of amine functionalization bis-NHC-pyridine-Ru^{II} complexes

Lorena Fritsch,[a] Yannik Vukadinovic,[a] Moritz Lang,[c] Robert Naumann,[b] Maria-Sophie Bertrams,[b] Ayla Kruse,[c] Roland Schoch,[a] Patrick Müller,[a] Adam Neuba,[a] Philipp Dierks,[a] Stefan Lochbrunner,[c] Christoph Kerzig,[b] Katja Heinze,[b] and Matthias Bauer *[a]

[a]Institute of Inorganic Chemistry and Center for Sustainable Systems Design (CSSD), Paderborn University, Warburger Straße 100, 33098 Paderborn, Germany

Email: matthias.bauer@upb.de, http://www.chemie.upb.de/bauer

[b]Department of Chemistry, Johannes Gutenberg University Mainz, Duesbergweg 10-14, 55128 Mainz, Germany

[c]Institute for Physics and Department of Life, Light and Matter, University of Rostock, 18051 Rostock, Germany

TABLE OF CONTENTS

1. General Remarks

General Procedures: All reactions and subsequent manipulations were performed under argon atmosphere using standard Schlenk techniques. The used solvents were dried and degassed prior to use. All chemicals were purchased from Sigma Aldrich, TCI, Fischer Scientific or abcr. NMR spectra were recorded with a Bruker Avance 500 (^{1}H, 500.1 MHz; ^{13}C, 125.8 MHz) and Bruker Avance 700 (^{1}H, 700.1 MHz; ^{13}C, 176.0 MHz), using different solvents purchased by *Deutero.* The NMR signals were referenced to residual solvents measured relative to TMS as internal standard. ESI-Mass spectra were recorded by a Waters Synapt 2G (QTOF). UV/Vis spectra were recorded with a Varian Cary 50, IR with a Bruker Vertex 70 and Cyclovoltammmograms with the PAR101 Potentiostat from Metrohm. Elemental analyses were performed with a vario MICRO Cube Elementar.

2. Synthesis

The preparation of the tridentate ligand structures was achieved by the reaction protocol shown in scheme S1. Precursor **1** was established following a reaction protocol reported by BREIVOGEL et al.[1] For further functionalization of product **1** a modified instruction by VIRICEL et al.[2] was followed. This reaction step was followed by the nucleophilic substitution of the diazole derivates. Therefore, we modified a reaction sequence reported by BROWN et al.[3] Further alkylation of the ligand precursor with methyl iodide in MeCN leads to the ligands **L1-L3**.

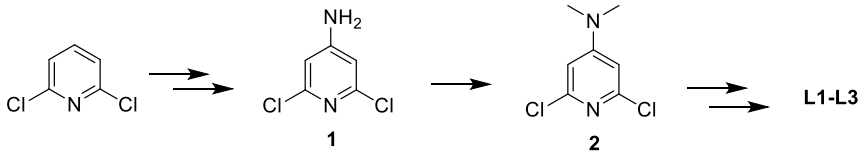

Scheme S1: Reaction pathway to for tridentate ligand structures **L1**-**L3**.

Synthesis of **2**

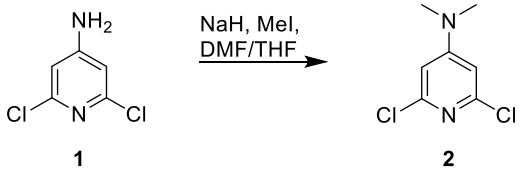

2,6-Dichloropyridine-4-amine (1 eq.; 12.02 mmol) was added to a cooled solution of NaH (3 eq.; 36.06 mmol) in a mixture of DMF/THF (1:1; 30:30 ml) under argon atmosphere and was stirred at this temperature for 1 h. After addition of MeI (3 eq., 36.06 mmol) the mixture was heated at 80 °C for 5 h. Then the mixture is cooled to r.t. and quenched with a saturated aqueous solution of K_2CO_3. The obtained solution is extracted three times with hexane

(3x100 mL). The collected hexane phases are dried over Na_2SO_4 and the solvent is evaporated under vacuum. The raw product is purfied by column chromatographie on silica using DCM:Hexan 2:1 as eluent. Yield: 70-80%

^{1}H-NMR (500 MHz, 30 °C, $CDCl_3$, δ [ppm]): 6.39 (s, 2H, CH); 2.99 (s, 6H; CH_3). **^{13}C-NMR** (500 MHz, 30 °C, $CDCl_3$, δ [ppm]): 157.6 (Cq); 151.0 (Cq); 108.0 (CH); 39.8 (CH_3). **ESI-MS** (m/z (%)) (MeOH): 191.0 (100) [M+H$^+$]; 212.9 (28) [M+Na$^+$].

Synthesis of **L1**

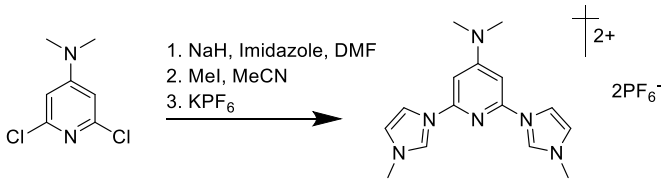

2 **L1**

Under argon atmosphere imidazole (2.8 eq., 16.4 mmol) was slowly added to an ice-cold solution of NaH (3 eq., 17.5 mmol) in DMF (50 mL). The reaction mixture was stirred at 0 °C for 1 h and was then allowed to warm to r.t. 2,6-Dichloropyridine-4-dimethylamine (1 eq., 8 mmol) was added portion wise and the solution was heated to 130 °C for 72 h. After cooling to r.t. the reaction mixture was given to an ice/water mixture (500 mL) and stirred for additional 10 minutes. The precipitate is filtered, washed with diethylether (300 mL) and dried under vacuum. Yield: 65 %.

^{1}H-NMR (500 MHz, 30 °C, DMSO, δ [ppm]): 8.65 (t, 2H, CH); 8.06 (t, 2H, CH); 7.09 (s, 2H, CH); 6.83 (s, 2H, CH); 3.12 (s, 6H, CH_3). **^{13}C-NMR** (500 MHz, 30 °C, DMSO, δ [ppm]): 158.6 (Cq); 148.6 (Cq); 135.6 (CH); 129.7 (CH); 117.0 (CH); 92.5 (CH); 39.6 (CH_3). **ESI-MS** (m/z (%))(MeCN): 255.13 (100) [M+H$^+$]

Under argon atmosphere 2,6-bisimidazol-1-yl-N,N-dimethylpyridin-4-amine (1 eq.; 3.8 mmol) was dissolved in dry MeCN (40 mL). To the solution methyl iodide (4 eq.; 15.2 mmol) was added and the reaction mixture was heated to reflux for 16 h. After cooling to r.t. the solvent was removed under vacuum and the residual solid was dissolved in a minimum amount of water and added dropwise to a saturated aqueous solution of KPF_6. The resulting white precipitate was filtered and dried under vacuum. Yield: 79 %

^{1}H-NMR (500 MHz, 30 °C, DMSO, δ [ppm]): 10.13 (s, 2H, CH); 8.68 (t, 2H, CH); 7.98 (t, 2H, CH); 7.22 (s, 2H, CH); 3.99(s, 6H, CH_3); 3.21 (s, 6H, CH_3). **^{13}C-NMR** (125 MHz, 30 °C, DMSO, δ [ppm]): 158.8 (Cq); 146.1 (Cq); 135.9 (CH); 124.7 (CH); 119.2 (CH); 95.1 (CH); 39.9 (CH_3); 36.5 (CH_3).**ESI-MS** (m/z (%))(MeCN): 142.08 (100) [M^{2+}].

Synthesis of **L2**

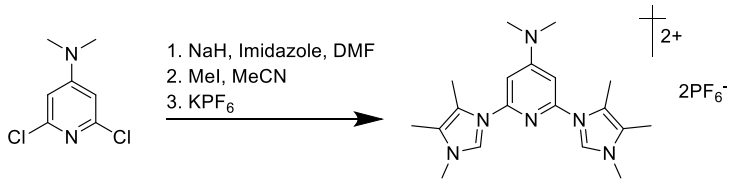

2 **L2**

Under argon atmosphere 4,5-dimethylimidazole (3.4 eq., 18.2 mmol) was slowly added to an ice-cold solution of NaH (3.5 eq., 18.7 mmol) in DMF (40 mL). The reaction mixture was stirred at 0 °C for 1 h and was then allowed to warm to r.t. 2,6-Dichloropyridine-4-dimethylamine (1 eq., 5.3 mmol) was added portion wise and the solution was heated to 130 °C for 72 h. After cooling to r.t. the reaction mixture was given to an ice/water mixture (500 mL) and stirred for additional 10 minutes. The precipitate is filtered, washed with diethylether (300 mL) and dried under vacuum. Yield: 76 %.

^{1}H-NMR (500 MHz, 30 °C, $CDCl_3$, δ [ppm]): 7.82 (s, 2H, CH); 6.42 (s, 2H, CH); 3.12 (s, 6H, CH_3); (s, 6H, CH_3). 2.22 (s, 6H, CH_3). **^{13}C-NMR** (500 MHz, 30 °C, $CDCl_3$, δ [ppm]): 158.0 (Cq); 150.4 (Cq); 135.3 (Cq); 134.9 (CH); 122.06 (Cq); 98.2 (CH); 39.9 (CH_3); 12.7 (CH_3); 10.5 (CH_3). **ESI-MS** (m/z (%))(MeCN): 311.13 (100) [$M+H^+$]

Under argon atmosphere 2,6-bis(4,5-dimethylimidazol-1-yl)-N,N-dimethylpyridin-4-amine (1 eq.; 4 mmol) was dissolved in dry MeCN (40 mL). Methyl iodide (3.5 eq.; 14 mmol) was added to the solution and the reaction mixture was heated to reflux for 24 h. After cooling to r.t. the solvent was removed under vacuum and the residual solid was dissolved in a minimum amount of water and added dropwise to a saturated aqueous solution of KPF_6. The resulting white precipitate was filtered and dried under vacuum. Yield: 83 %

^{1}H-NMR (500 MHz, 30 °C, DMSO, δ [ppm]): 9.75 (s, 2H, CH); 7.28 (s, 2H, CH); 4.02 (s, 6H, CH_3); 3.47 (s, 2H, CH); 3.32 (s, 6H, CH_3); 2.65 (s, 3H, CH_3). **^{13}C-NMR** (125 MHz, 30 °C, DMSO, δ [ppm]): 158.0 (Cq); 146.7 (Cq); 135.6 (CH); 127.9 (Cq); 125.9 (Cq); 102.6 (CH); 39.67 (CH_3); 33.9 (CH_3); 9.4 (CH_3); 7.8 (CH_3) **ESI-MS** (m/z (%))(MeCN): 170.20 (100) [M^{2+}].

Synthesis of **L3**

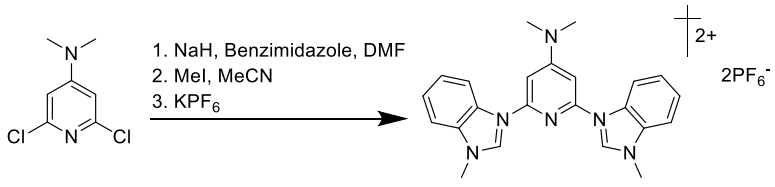

2 **L3**

Under argon atmosphere benzimidazole (3.2 eq., 16 mmol) was slowly added to an ice-cold solution of NaH (3.5 eq., 17.5 mmol) in DMF (50 mL). The reaction mixture was stirred at 0 °C for 1 h and was then allowed to warm to r.t.. 2,6-Dichloropyridine-4-dimethylamine (1 eq., 5 mmol) was added portion wise and the solution was heated to 130 °C for 72 h. After cooling to r.t. the reaction mixture was given to an ice/water mixture (500 mL) and stirred for 10 minutes. The precipitate is filtered, washed with diethyl ether (300 mL) and dried under vacuum. Yield: 75 %.

^{1}H-NMR (500 MHz, 30 °C, DMSO, δ [ppm]): 9.03 (s, 2H, CH); 8.20 (dd, 2H, CH); 7.79 (dd, 2H, CH); 7.34 (m; 4H; CH); 7.03 (s, 2H, CH); 3.21 (s, 6H, CH3).**^{13}C-NMR** (125 MHz, 30 °C, DMSO, δ [ppm]): 158.6 (Cq); 149.9 (Cq); 144.7 (Cq), 143.1 (Cq), 132.6 (CH), 124.3 (CH), 123.4 (CH), 120.4 (CH), 114.2 (CH), 95.6 (CH), 39.8 (CH3).**ESI-MS** (m/z (%)) (MeCN): 355.1 (100) [$M+H^+$].

Under argon atmosphere 2,6-bis-benzimidazol-1-yl-N,N-dimethylpyridin-4-amine (1 eq.; 2 mmol) was dissolved in dry MeCN (20 mL). Methyl iodide (4 eq.; 8 mmol) was added to the solution and the reaction mixture was heated to reflux for 16 h. After cooling to r.t. the solvent was removed under vacuum and the residual solid was dissolved in a minimum amount of water and added dropwise to a saturated aqueous solution of KPF_6. The resulting white precipitate was filtered and dried under vacuum. Yield: 60 %

^{1}H-NMR (500 MHz, 30 °C DMSO, δ [ppm]): 10.49 (s, 2H, CH); 8.39 (d, 2H, CH); 8.17 (d, 2H, CH); 7.81 (t, 2H; CH); 7.73 (t, 2H, CH); 7.36 (s, 2H; CH); 4.25 (s, 6H; CH_3); 3.28 (s, 6H; CH_3). **^{13}C-NMR** (125 MHz, 30 °C DMSO, δ [ppm]):158.8 (Cq); 147.6 (Cq); 143.4 (CH); 132.6 (Cq); 130.0 (Cq); 128.1 (CH); 127.6 (CH); 116.1 (CH); 114.4 (CH); 100.2 (CH); 39.99 (CH_3); 34.2 (CH_3). **ESI-MS** (m/z (%))(MeCN): 192.1 [M^{2+}] (100); 401.2 [M^++OH] (22); 383.2 [M^+] (4).

3. Details of single crystal structure analysis

[Ru(bip^{NMe2})$_2$] [PF$_6$]$_2$ (C1)

($C_{30}H_{36}N_{12}Ru$) 2(PF_6) 3(C_2H_3N), M_r = 1078.88 Da, yellow block, size 0.48 x 0.40 x 0.30 mm³, monoclinic space group C2/c with Z = 8, a = 28.6848(15) Å, b = 11.6015(6) Å, c = 27.7843(14) Å, β = 108.0270(10)°, V = 8792.4(8) Å³, D_c = 1.630 mg/m³, μ = 0.529 mm^{-1}, F(000) = 4384, θ_{max} = 31.173°, reflections collected: 51128, independent reflections: 13349, R_{int} = 0.0353, refinement converged at R1 = 0.0451 [I>2σ(I)], wR2 = 0.1171 [all data], min./max. ΔF = -0.73 eÅ³ (0.44 Å from F111) / 1.05 eÅ³ (0.57 Å from F112).

Table S1. Crystal data and structure refinement for [Ru(bip^{NMe2})$_2$] [PF$_6$]$_2$ **(C1)**:

CCDC code	2039995	
Empirical formula	C36 H45 F12 N15 P2 Ru	
Formula weight	1078.88	
Temperature	130(2) K	
Wavelength	0.71073 Å	
Crystal system	Monoclinic	
Space group	C2/c	
Unit cell dimensions	a = 28.6848(15) Å	α= 90°.
	b = 11.6015(6) Å	β = 108.0270(10)°.
	c = 27.7843(14) Å	γ = 90°.
Volume	8792.4(8) Å^3	
Z	8	
Density (calculated)	1.630 Mg/m^3	
Absorption coefficient	0.529 mm^{-1}	
F(000)	4384	
Crystal size	0.480 x 0.400 x 0.300 mm^3	
Theta range for data collection	1.493 to 31.173°.	
Index ranges	-40<=h<=39, -16<=k<=16, -39<=l<=37	
Reflections collected	51128	
Independent reflections	13349 [R(int) = 0.0353]	
Completeness to theta = 25.242°	99.9 %	
Refinement method	Full-matrix least-squares on F^2	
Data / restraints / parameters	13349 / 37 / 638	
Goodness-of-fit on F^2	1.039	
Final R indices [I>2sigma(I)]	R1 = 0.0451, wR2 = 0.1061	
R indices (all data)	R1 = 0.0604, wR2 = 0.1171	
Extinction coefficient	n/a	
Largest diff. peak and hole	1.048 and -0.726 e.Å^{-3}	

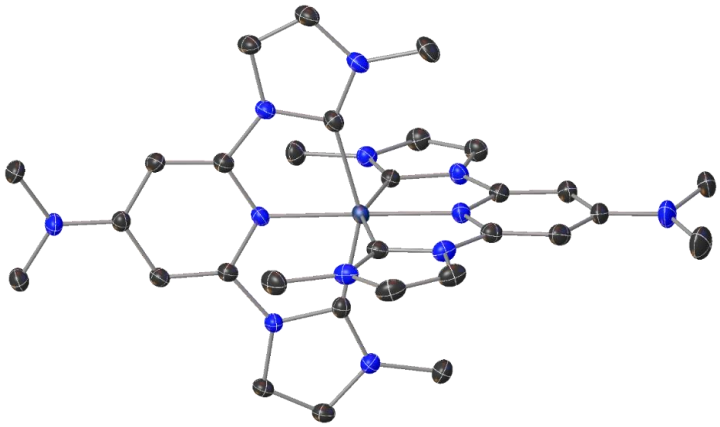

Figure S1: Single crystal structure of **C1** drawn with anisotropic displacement ellipsoids at a 50% probability level. Hydrogen atoms and counterions are omitted for clarity.

[Ru(bdmip^{NMe2})$_2$] [PF$_6$]$_2$ (C2)

($C_{38}H_{52}N_{12}Ru$) 2(PF_6) 1(C_2H_3N), M_r = 1108.88 Da, yellow block, size 0.48 x 0.40 x 0.30 mm³, monoclinic space group C2/c with Z = 8, a = 9.8309(5) Å, b = 14.1968(8) Å, c = 17.9474(10) Å, β = 108.0270(10)°, V = 8792.4(8) Å³, D_c = 1.630 mg/m³, μ = 0.529 mm^{-1}, F(000) = 4384, θ_{max} = 31.173°, reflections collected: 28348, independent reflections: 13959, R_{int} = 0.0294, refinement converged at R1 = 0.0391 [I>2σ(I)], wR2 = 0.0947 [all data], min./max. ΔF = -0.73 eÅ³ (0.72 Å from F111) / 1.05 eÅ³ (0.57 Å from F112).

Table S2. Crystal data and structure refinement for [Ru(bdmip^{NMe2})$_2$] [PF$_6$]$_2$ **(C2)**:

Identification code	2237754	
Empirical formula	C40 H55 F12 N13 P2 Ru	
Formula weight	1108.98	
Temperature	130(2) K	
Wavelength	0.71073 Å	
Crystal system	Triclinic	
Space group	P-1	
Unit cell dimensions	a = 9.8309(5) Å	a= 73.0170(10)°.
	b = 14.1968(8) Å	b= 84.8800(10)°.
	c = 17.9474(10) Å	g = 85.1250(10)°.
Volume	2381.5(2) Å^3	
Z	2	
Density (calculated)	1.546 Mg/m^3	
Absorption coefficient	0.489 mm^{-1}	
F(000)	1136	
Crystal size	0.440 x 0.260 x 0.220 mm^3	
Theta range for data collection	1.503 to 31.083°.	
Index ranges	-14<=h<=13, -20<=k<=20, -26<=l<=25	
Reflections collected	28348	
Independent reflections	13959 [R(int) = 0.0294]	
Completeness to theta = 25.242°	100.0 %	
Absorption correction	Semi-empirical from equivalents	
Refinement method	Full-matrix least-squares on F^2	
Data / restraints / parameters	13959 / 0 / 630	
Goodness-of-fit on F^2	1.041	
Final R indices [I>2sigma(I)]	R1 = 0.0391, wR2 = 0.0871	
R indices (all data)	R1 = 0.0503, wR2 = 0.0947	
Extinction coefficient	n/a	
Largest diff. peak and hole	0.721 and -0.508 e.Å^{-3}	

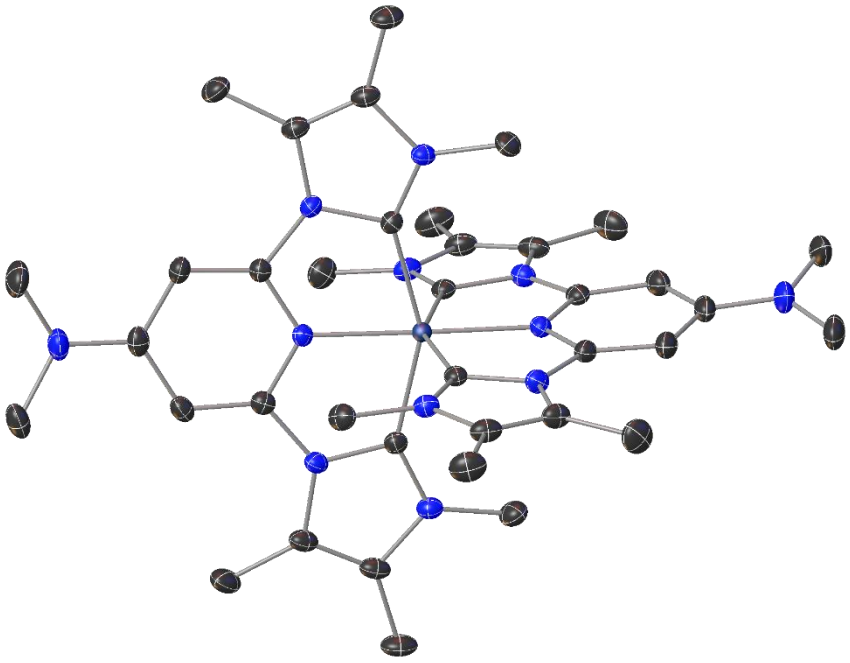

Figure S2: Single crystal structure of **C2** drawn with anisotropic displacement ellipsoids at a 50% probability level. Hydrogen atoms, counterions and solvent molecule are omitted for clarity.

[Ru(bbp^{NMe2})$_2$] [PF$_6$]$_2$ (C3)

($C_{46}H_{44}N_{12}Ru$) 2(PF_6) 2(C_2H_3N) , M_r = 1238.05 Da, yellow plate, size 0.28 x 0.24 x 0.08 mm³, triclinic space group $P\bar{1}$ with Z = 2, a = 12.963(7) Å, b = 14.714(8) Å, c = 16.481(9) Å, α = 80.219(18)°, β = 68.341(17)°, γ = 71.591(18)°, V = 2767(3) Å³, D_c = 1.486 mg/m³, μ = 0.431 mm^{-1}, F(000) = 1260, θ_{max} = 31.971°, reflections collected: 303983, independent reflections: 19002, R_{int} = 0.0809, refinement converged at R1 = 0.0489 [I>2σ(I)], wR2 = 0.1374 [all data], min./max. ΔF = -1.36 eÅ³ (0.69 Å from Ru1) / 1.38 eÅ³ (0.57 Å from F241).

Table S3. Crystal data and structure refinement for [Ru(bbp^{NMe2})$_2$] [PF$_6$]$_2$ **(C2)**:

CCDC code	2039996	
Empirical formula	C50 H50 F12 N14 P2 Ru	
Formula weight	1238.05	
Temperature	120(2) K	
Wavelength	0.71073 Å	
Crystal system	Triclinic	
Space group	P-1	
Unit cell dimensions	a = 12.963(7) Å	α= 80.219(18)°.
	b = 14.714(8) Å	β = 68.341(17)°.
	c = 16.481(9) Å	γ = 71.591(18)°.
Volume	2767(3) Å^3	
Z	2	
Density (calculated)	1.486 Mg/m^3	
Absorption coefficient	0.431 mm^{-1}	
F(000)	1260	
Crystal size	0.280 x 0.240 x 0.080 mm^3	
Theta range for data collection	2.540 to 31.971°.	
Index ranges	-19<=h<=19, -21<=k<=21, -24<=l<=24	
Reflections collected	303983	
Independent reflections	19002 [R(int) = 0.0809]	
Completeness to theta = 25.242°	99.9 %	
Refinement method	Full-matrix least-squares on F^2	
Data / restraints / parameters	19002 / 0 / 759	
Goodness-of-fit on F^2	1.089	
Final R indices [I>2sigma(I)]	R1 = 0.0489, wR2 = 0.1163	
R indices (all data)	R1 = 0.0743, wR2 = 0.1374	
Extinction coefficient	n/a	
Largest diff. peak and hole	1.376 and -1.361 e.Å^{-3}	

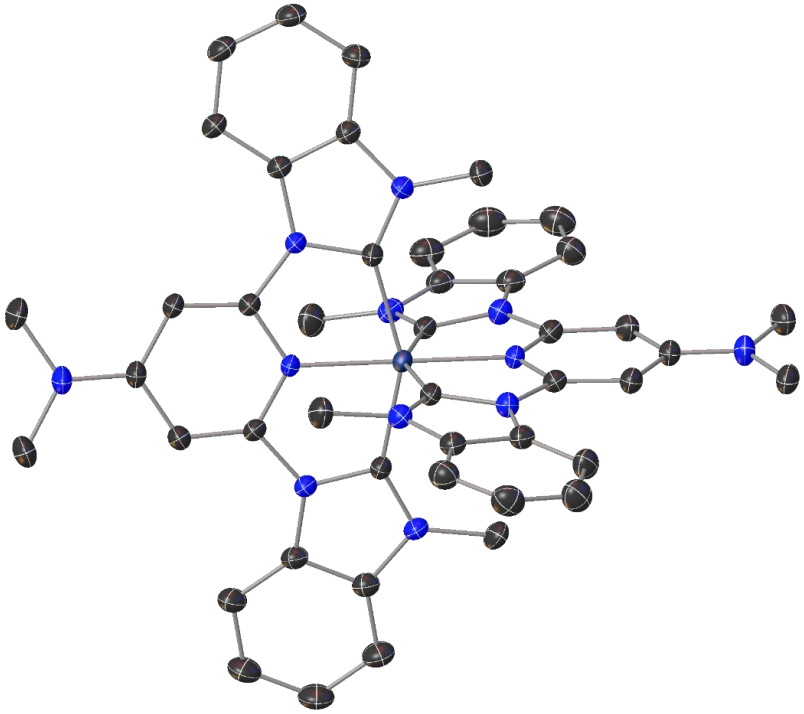

Figure S3: Single crystal structure of **C3** drawn with anisotropic displacement ellipsoids at a 50% probability level. Hydrogen atoms and counterions are omitted for clarity.

4. Electrochemistry

Cyclic- and square wave voltammograms at r.t. were performed in deoxygenated MeCN using a PGSTAT 101 potentiostat from Metrohm-Autolab. An analyte concentration of 10^{-3} M and a [nBu_4N][PF_6] concentration of 0.1 M as inert electrolyte were used with a three electrode arrangement: A Pt working electrode (1 mm diameter), Ag/ 0.01 M $AgNO_3$, 0.1 M Bu_4NPF_6 in MeCN as reference and a Pt wire as counter electrode. Ferrocene was added as internal standard after the measurement and all potentials are referenced relative to the Fc/Fc^+ couple. The cyclic and square wave voltammograms were analyzed with the software NOVA Version 2.1.3 from Metrohm.

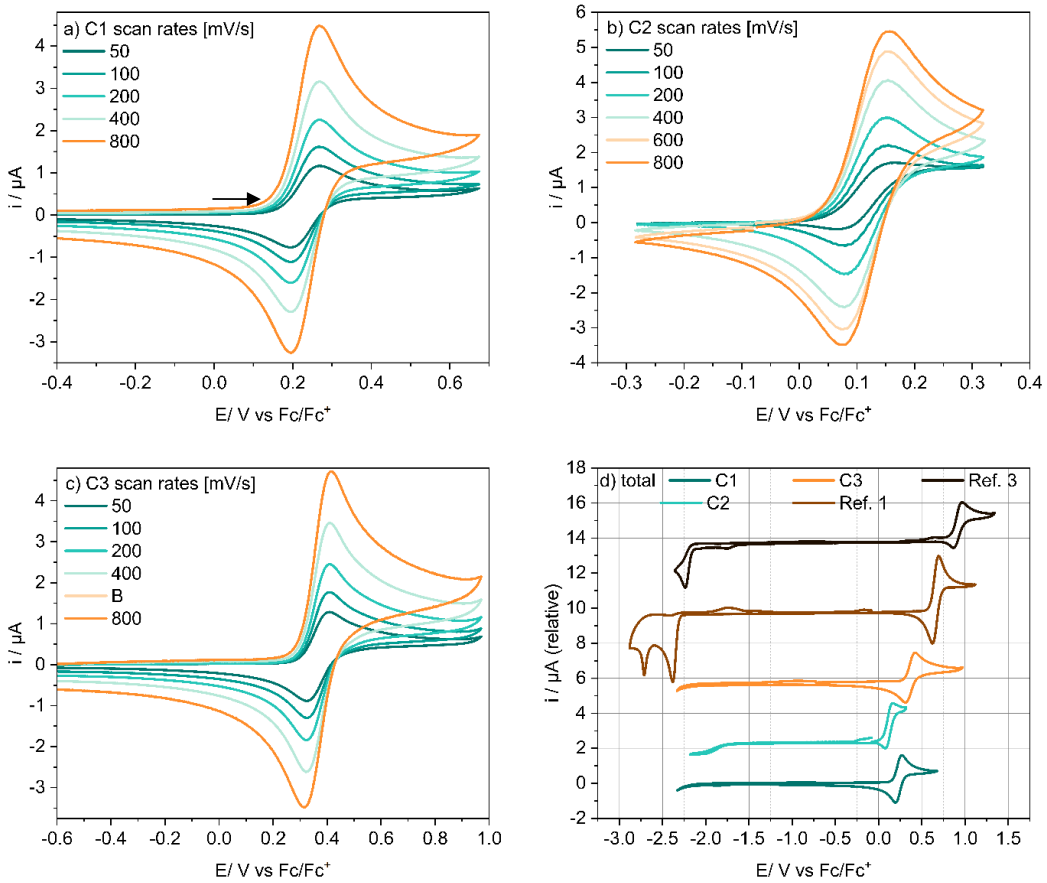

Figure S4: Cyclic voltammograms of **C1** (a), **C2** (b) **and C3** (c) with different scan rates and total cyclic voltammogram of **C1-C3** and **Ref. 1 + Ref. 3** (d).

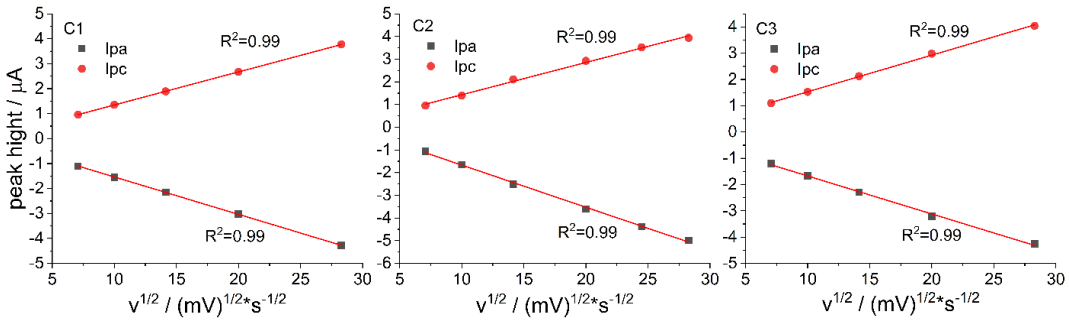

Figure S5: Linear increase of the peak current with the square root of the scan rate of **C1-C3**, indicating an electrochemically reversible electron transfer process according to the Randles-Sevcik-equation.[4]

Table S4: Electrochemical data for the reversible oxidation ($E^0_{1/2}$ vs. Fc/Fc^+) for complex **C1-C3.**

C1	**V [mV s^{-1}]**	**50**	**100**	**200**	**400**	**600**	**800**
	E_{pc} [V]	0.265	0.265	0.262	0.265	-	0.265
	E_{pa} [V]	0.194	0.196	0.196	0.194	-	0.194
	$E_{1/2}$ [V]	0.229	0.231	0.229	0.229	-	0.229
	ΔE [mV]	71	68	66	71	-	71
	I_{pa} [10^{-6} A]	1.10	1.55	2.15	3.02	-	4.29
	I_{pa}/I_{pc}	1.15	1.14	1.14	1.13	-	1.14
	$I_{pa}/v^{0.5}$	4.93E-06	4.89E-06	4.81E-06	4.78E-06	-	4.79E-06
C2	**V [mV s^{-1}]**	**50**	**100**	**200**	**400**	**600**	**800**
	E_{pc} [V]	0.142	0.142	0.139	0.142	0.142	0.144
	E_{pa} [V]	0.071	0.078	0.076	0.076	0.078	0.074
	$E_{1/2}$ [V]	0.106	0.110	0.107	0.109	0.110	0.109
	ΔE [mV]	71	63	63	66	64	70
	I_{pa} [10^{-6} A]	1.06	1.66	2.51	3.60	4.38	4.98
	$\|I_{pa}\|/I_{pc}$	1.10	1.19	1.19	1.23	1.24	1.26
	$I_{pa}/v^{0.5}$	4.73E-06	5.24E-06	5.62E-06	5.69E-06	5.66E-06	5,57E-06
C3	**V [mV s^{-1}]**	**50**	**100**	**200**	**400**	**600**	**800**
	E_{pc} [V]	0.406	0.404	0.409	0.409	-	0.411
	E_{pa} [V]	0.326	0.326	0.326	0.326	-	0.319
	$E_{1/2}$ [V]	0.366	0.365	0.367	0.367	-	0.365
	ΔE [mV]	81	78	83	83	-	93
	I_{pa} [10^{-6} A]	1.20	1.67	2.30	3.21	-	4.25
	I_{pa}/I_{pc}	1.09	1.09	1.08	1.08	-	1.05
	$I_{pa}/v^{0.5}$	5.37E-06	5.27E-06	5.14E-06	5.08E-06	-	4.75E-06

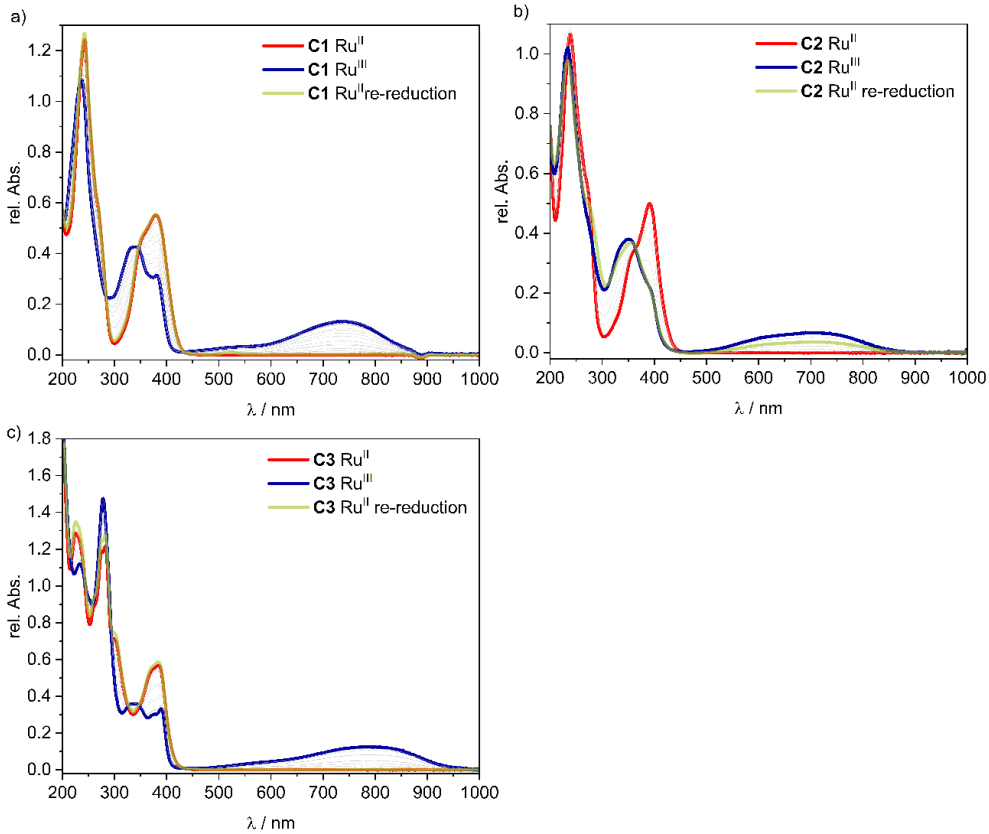

Figure S6: Chronoamperometric absorption spectra of **C1** (a), **C2** (b) and **C3** (c) in acetonitrile at r.t. with an applied potential of 0.47 V (**C1**), 0.8 V (**C2**) and 0.66 V (**C3**).

5. Emission spectroscopy

Singlet Oxygen Emission:

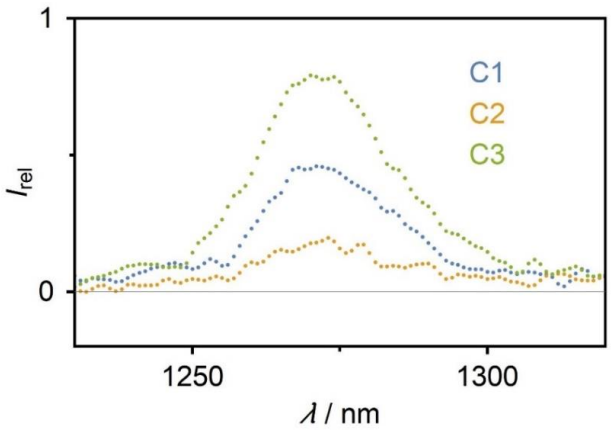

Figure S7: Characteristic $^1O_2$ emission at 1270 nm resulting from a sample of complexes **C1-C3** in deuterated acetonitrile (excitation at 380, 385 and 390 nm for C1, C3 and C2, respectively).

R.t. emission spectra:

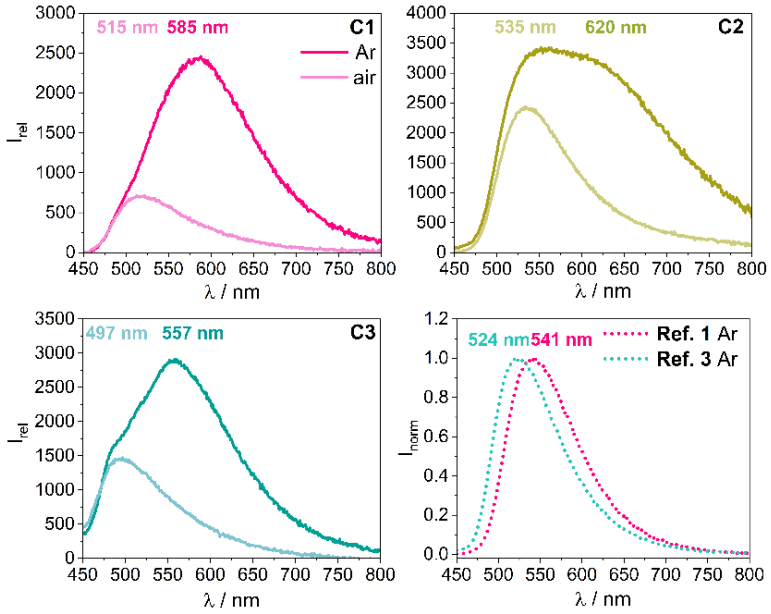

Figure S8: Emission spectra of **C1-C3** and obtained in a degassed MeCN solution under argon (darker colour) and a non-degassed MeCN solution (lighter colour) at r.t. with an excitation wavelength of 380 nm (not normalized to illustrate the overlap of two bands) in comparison to normalized emission spectra of **Ref.1** and **Ref. 3**.

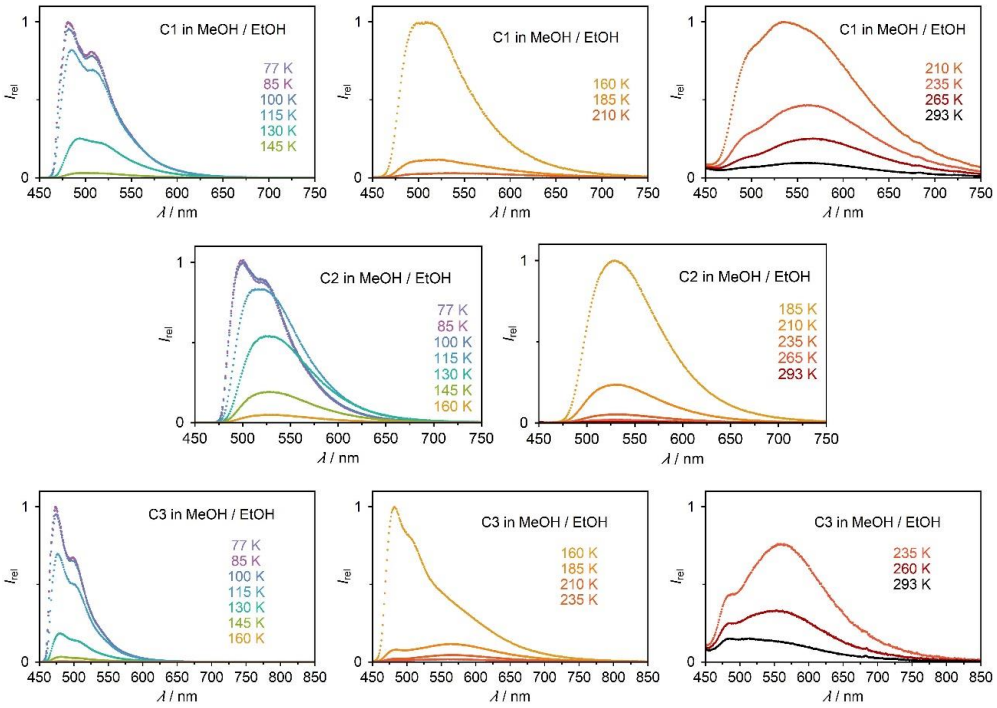

Figure S9: *Emission intensity of **C1-C3** at low temperature (77K) to room temperature (293 K) in MeOH:EtOH (40/60 v/v) with an excitation wavelength of 390 nm.*

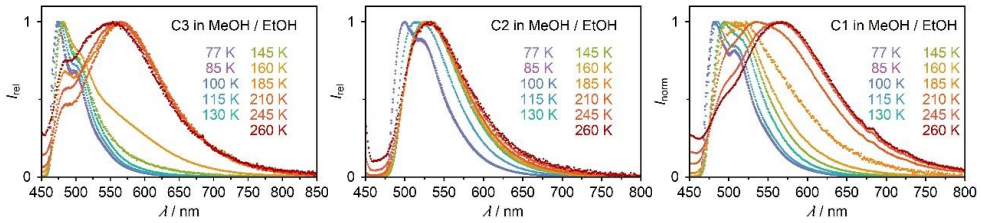

Figure S10: Normalized Emission spectra of **C1-C3** at low temperature (77K) to (260 K) in MeOH:EtOH (40/60 v/v) with an excitation wavelength of 390 nm.

Excitation spectra:

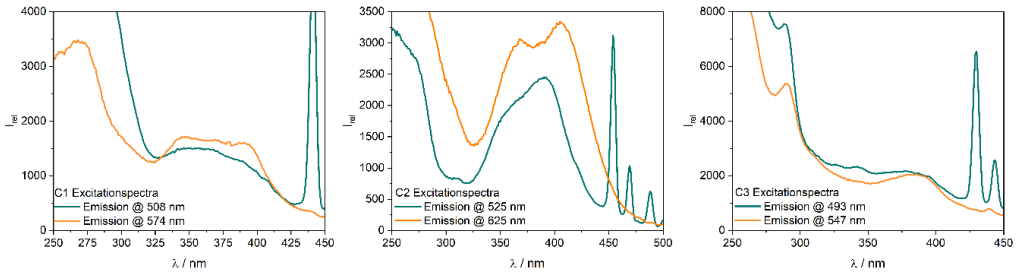

Figure S11*:* Excitation spectra of **C1-C3** in a purged MeCN solution at r.t. at two different emission energies.

6. Time resolved spectroscopy

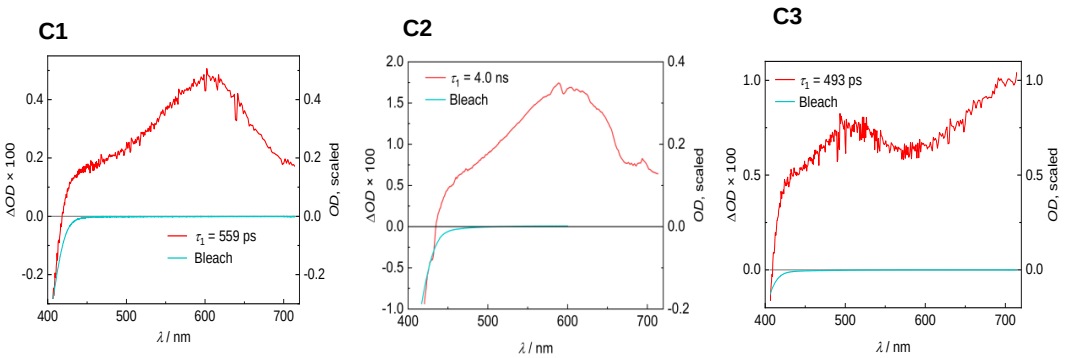

Figure S12: Decay associated difference spectra (DADS) obtained from a global fit of the transient absorption data of complexes **C1**-**C3** and labelled by the corresponding time constants. The experiments were conducted with magic angle between the polarizations of the pump and probe beam. The cyan colored spectrum is the bleach, i.e., the scaled negative ground state absorption.

Figure S12 shows the decay associated difference spectra (DADS) of the Ruthenium complexes **C1**, **C2** and **C3** measured in magic angle polarization. The decay dynamics of all three complexes can be described with a monoexponential decay. Figure S13 shows the DADS for parallel and perpendicular polarizations exemplarily for **C3**. Here a component with a lifetime in the range of tens of picoseconds arises. It can clearly be seen that this component is mirrored for the perpendicular polarization compared to the parallel polarization and vanishes completely for the magic angle polarization. This is a clear indication that this component is due to rotational diffusion of the excited molecules and can therefore be neglected in our considerations.

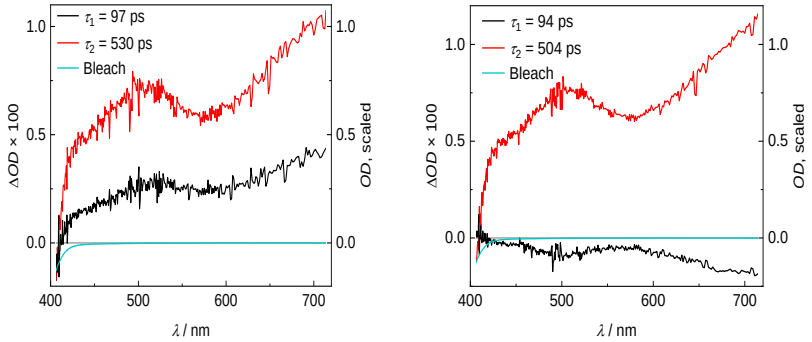

Figure S13: DADS of **C3** for parallel (left) and perpendicular (right) polarizations. The component with the short time constant (loss of anisotropy due to parallel or perpendicular polarization) is depicted in black and depends on the relative angle of the polarizations of the pump and probe beam.

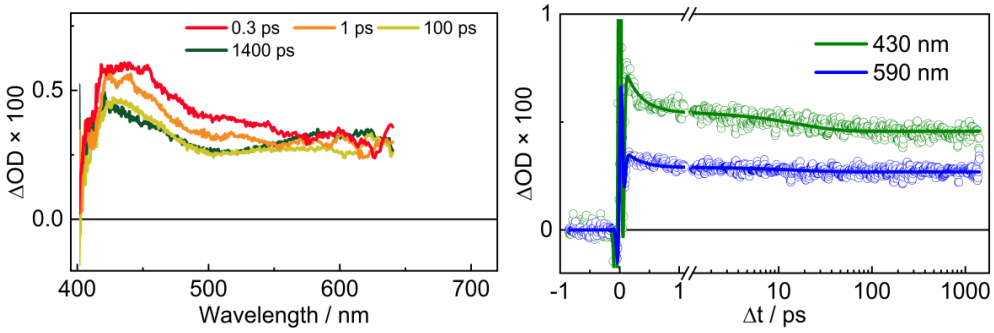

Figure S14: Transient absorption of **Ref. 3**. Left: Spectra at different delay times. Right: Time evolution at characteristic wavelengths. The lifetime exceeds the experimental time window.

For comparison, time resolved absorption spectra were also measured for the reference complex **Ref. 3** (Figure S14). The transient absorption measurement shows that the excited state lifetime exceeds by far the time window of the experiment. Therefor a time constant significantly longer than 1 ns can be expected. At shorter times an additional dynamic with a lifetime of several ps is visible. This can be ascribed to vibrational relaxation processes. In time resolved luminescence experiments the lifetime was determined to be 920 ns (Figure S15).

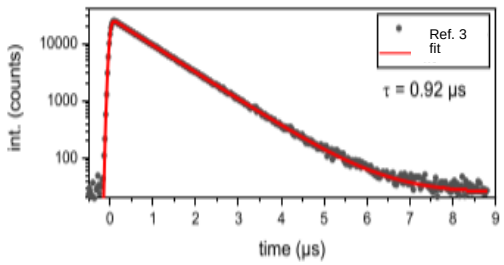

Figure S15: Time resolved emission of **Ref. 3** obtained from streak camera experiments. The emission lifetime is ca. 920 ns.

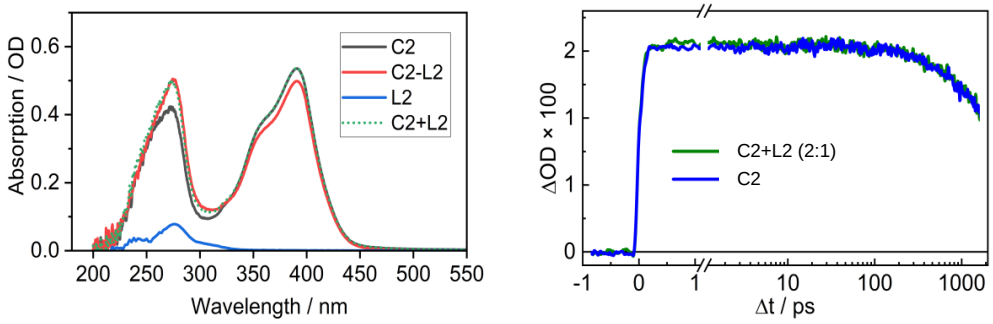

Figure S16: Left: Absorption spectra of the complex **C2**, a mixture of **C2** and **L2** (**C2**-**L2**), the pure pro-ligand **L2** and the added absorption spectra of **C2** and **L2** (**C2**+**L2**). Right: Time evolution of the excited state signal, observed at ca. 600 nm.

To exclude that an interaction between the Ru-complexes, which could act as a photobase, and residual free ligands, that act as an acid and could therefore quench the excited state very efficiently, might influence the observed dynamics, the transient absorption of the complex **C2** was again measured in the presence of the respective pro-ligand **L2** in a proportion of 2:1. The samples were degassed under Argon for 15 min prior to the experiment. The time evolution shows clearly that there is no influence of the pro-ligand on the excited state dynamics (Figure S16 right). This is also reflected in the analysis of the data. The data is again essentially monoexponential. The lifetimes of the two solutions do not differ within the uncertainty of the experiment.

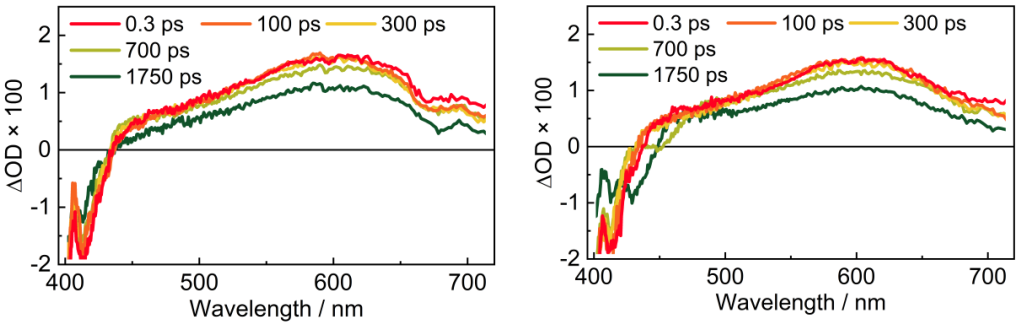

Figure S17: Transient absorption spectra at selected delay times of the pure complex **C2** (left) and the mixture **C2**-**L2** (right).

7. Computational chemistry

Geometry Optimization:

Table S5: Bond lengths and angles of the B97-3c geometry optimized and crystal structures.

Complex	Ru-N_{exp} av[a]	Ru-N_{cal} av[b]	Ru-C_{exp} av[a]	Ru-C_{cal} av[b]	N-Ru-N_{exp}[c]	N-Ru-N_{cal}[d]	C-Ru-C_{exp}[c]	C-Ru-C_{cal}[d]
C1	2.020(2)	2.028	2.044(2)	2.042	178.70(7)	180.0	153.51(9)	153.2
C2	2.018(2)	2.025	2.042(2)	2.034	178.85(6)	179.9	153.20(8)	153.2
C3	2.031(1)	2.026	2.044(3)	2.033	179.21(7)	179.7	153.855(7)	153.6
Ref. 1	2.019(2)	2.023	2.051(2)	2.046	175.78(6)	179.9	153.69(8)	153.8
Ref. 2[e]	-	2.021	-	2.037	-	179.9	-	154.3

[a] Average of all bonding sites. [b] Average of all bonding sites of the geometric optimized structure.[c] Trans angle. [d] Trans angle of the geometric optimized structure. [e] No crystal structure available.

Frontier orbital analysis

Table S6: *Contribution of the metal and ligand fragments to the frontier orbitals [%]. PBE0 / ZORA-def2-TZVP based TD-DFT calculations.*

	Orbital	**Energy / eV**	**Ru**	**Pyridine + NMe_2**	**NMe_2**	**NHC**
C1	HOMO (170)	-5.65	44.6 (xz)	26.3	11.8	11.6
	-1	-5.66	44.4 (yz)	26.3	11.8	11.6
	-2	-5.77	41.5 (xy)	6.6	0.0	35.0
	-X	-7.01 (X= 5)	0	30.2	0	53.8
	-X	-7.40 (X=-6)	3.2	47.2	0	31.4
	LUMO (171)	-1.20	0.0	47.5	0.8	25.4
	+1	-1.14	4.4	46	0.8	23.1
	+2	-1.12	6.6	42.7	5.9	25.9
	+3	-1.12	6.6	49.5	5.9	23.9
C2	HOMO (202)	-5.45	35.9 (xy)	5.6	0.1	39.3
	-1	-5.47	43.9 (yz)	23.3	10.3	14.3
	-2	-5.47	43.7(xz)	33.1	10.1	14.3
	-X	-7.05 (X=-7)	16.8	35.0	23.3	29.0
	-X	-7.34 (X=-9)	0.0	38.3	0.0	42.2
	LUMO (203)	-1.03	6.7	43.5	0.1	23.1
	+1	-1.02	6.8	43.7	6.0	22.8
	+2	-0.96	0.0	50.3	6.0	21.3
	+3	-0.89	4.4	49.3	0.2	18.9
C3	HOMO (222)	-5.85	39.8 (yz)	30.5	14.0	11.0
	-1	-5.85	39.8 (xz)	30.9	14.2	10.9
	-2	-6.13	35.2 (xy)	6.8	0.0	40.4
	-X	-7.01 (X=-6)	1.6	22.7	0.0	55.7
	-X	-8.15 (X=-12)	0.2	29.5	0.0	54.1
	LUMO (223)	-1.37	6.3	21.7	2.7	47.1
	+1	-1.37	6.3	21.8	2.7	47.2
	+2	-1.28	0.0	39.3	0.3	33.1
	+3	-1.20	4.8	40.4	0.2	27.1
Ref. 1	HOMO (146)	-5.98	40.3	6.8	-	36.6
	-1	-6.23	54.0	11.8	-	19.0
	-2	-6.26	54.5	11.5	-	18.9
	LUMO (147)	-1.83	7.0	55.2	-	12.6
	+1	-1.80	7.6	55.4	-	11.9
	+2	-1.38	0.0	47.9	-	24.6
Ref. 3	HOMO (198)	-6.29	32.1	7.0	-	41.4
	-1	-6.46	47.4	10.5	-	26.0
	-2	-6.50	49.9	10.1	-	23.7
	LUMO (199)	-2.03	6.3	52.8	-	14.9
	+1	-1.95	7.8	52.6	-	13.9
	+2	-1.41	0.1	42.7	-	29.9

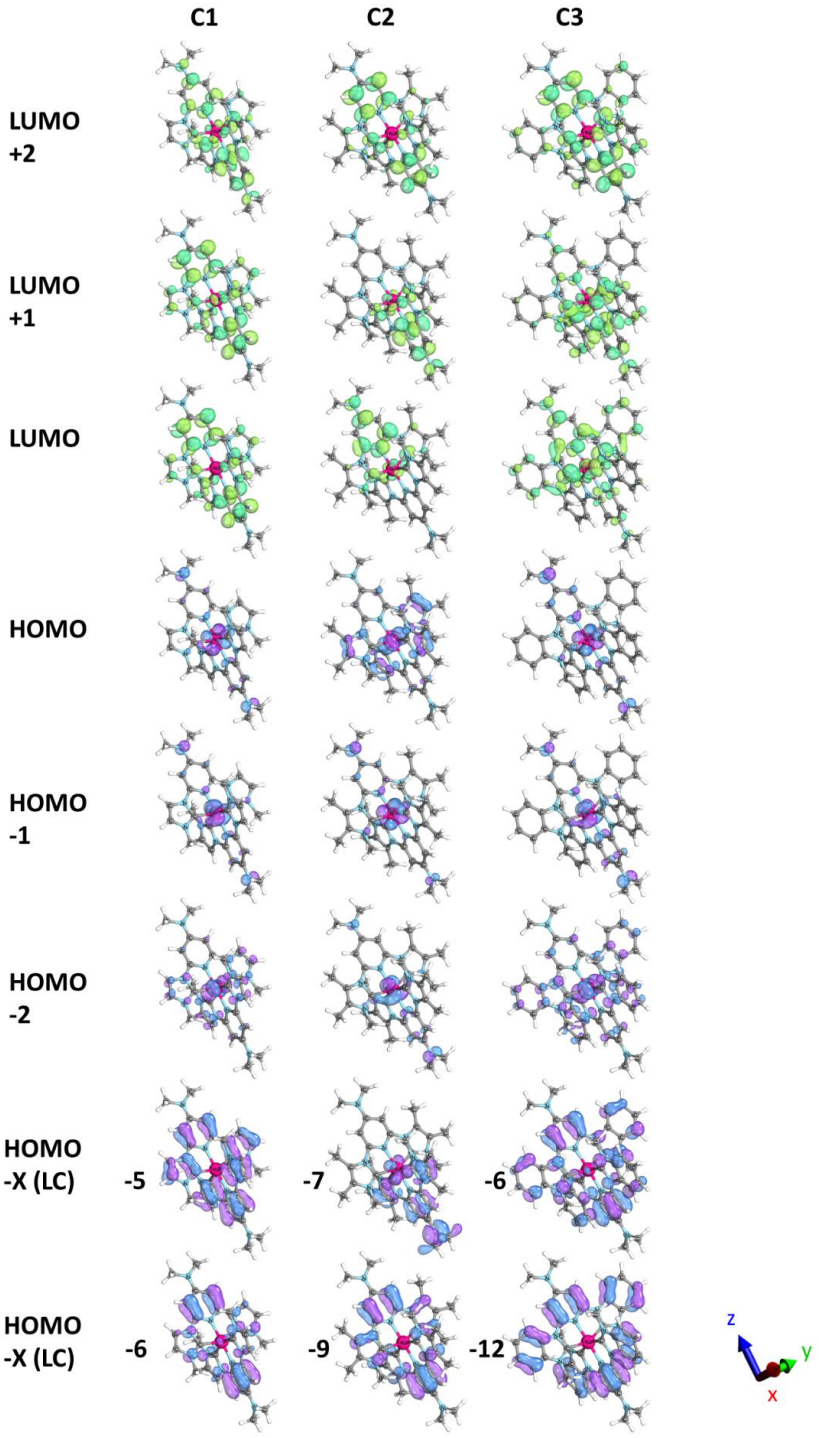

Figure S18: Spatial distribution of the first three HOMO and LUMO orbitals of **C1**-**C3**. PBE0 / ZORA-def2-TZVP based TD-DFT calculations.

Calculated UV/Vis spectra:

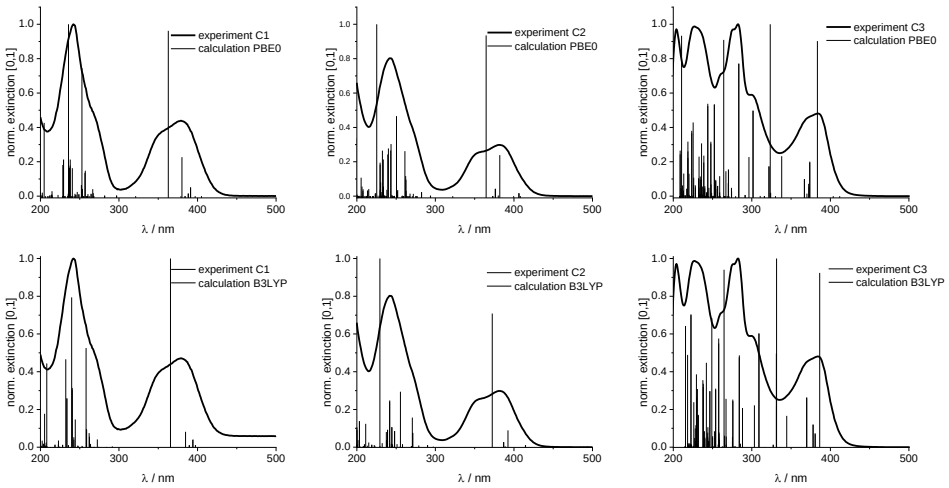

Figure S19: Experimental spectra together with the PBE0 (25 % HF) and B3LYP (20 % HF) / ZORA-def2-TZVP calculated UV/Vis transitions (first 150 singlet-singlet transitions) for the optimized geometries of complex **C1-C3** with the CPCM model for acetonitrile. Sticks shifted by -3000 cm^{-1}(PBE0) and -2000 cm^{-1}(B3LYP) to fit the spectrum.

Calculated state energies

Table S7: Main theoretical (PBE0) electronic **singlet-singlet** transition energies (ΔE) with corresponding oscillator strengths (f) and assignment to the ligand fragments of the two Ligands L1 and L2 (%).

C1												
State	**ΔE (nm)**	**f**	**Donor**					**Acceptor**				
			Ru	**Pyr L1**	**NHC L1**	**Pyr L2**	**NHC L2**	**Ru**	**Pyr L1**	**NHC L1**	**Pyr L2**	**NHC L2**
S_1	361.1	0.00001	45	13	6	13	6	7	22	12	22	12
S_2	354.7	0.00001	45	13	6	13	6	7	22	12	22	12
S_3	350.1	0.04878	42	3	18	3	18	7	18	11	25	14
S_5	347.9	0.01486	45	13	6	14	6	4	23	12	23	12
S_9	341.2	0.21752	44	10	10	10	10	5	22	12	22	13
S_{11}	327.2	0.92484	42	3	18	3	18	0	24	13	24	13
S_{14}	272.6	0.00306	45	13	6	14	6	45	8	9	8	9
S_{15}	259.8	0.00436	10	25	10	25	11	2	23	12	23	12
C2												
State	**ΔE (nm)**	**f**	**Donor**					**Acceptor**				
			Ru	**Pyr L1**	**NHC L1**	**Pyr L2**	**NHC L2**	**Ru**	**Pyr L1**	**NHC L1**	**Pyr L2**	**NHC L2**
S_1	370.4	0.00034	44	12	7	12	7	7	22	12	22	12
S_2	369.1	0.01638	36	3	20	3	20	7	2	4	42	19
S_5	348.7	0.23082	36	3	20	3	20	0	24	10	27	12
S_7	344.1	0.04103	44	7	8	17	7	4	26	10	23	9
S_{11}	334.2	0.90323	36	3	19	3	20	0	24	10	27	12
S_{16}	273.7	0.00263	0	6	34	6	34	7	42	19	2	4

C3												
State	ΔE (nm)	f	Donor					Acceptor				
			Ru	Pyr $_{L1}$	NHC $_{L1}$	Pyr $_{L2}$	NHC $_{L2}$	Ru	Pyr $_{L1}$	NHC $_{L1}$	Pyr $_{L2}$	NHC $_{L2}$
S_1	366.5	0.00012	40	15	5	15	5	6	11	34	11	24
S_3	343.9	0.47515	40	15	5	15	5	6	11	34	11	24
S_5	336.1	0.10576	40	11	6	20	5	5	20	14	20	14
S_7	335.0	0.03777	37	11	10	11	10	4	15	15	15	21
S_{11}	306.9	0.12245	35	3	20	3	20	0	20	17	20	16
S_{25}	268.0	0.00321	40	19	5	11	6	30	8	19	8	19

Table S8: PBE0 TD-DFT calculated state energies [eV] for complex **C1-C3**, **Ref. 1**and **Ref. 3** performed on PBE0 / ZORA-def-2-TZVP level on the ground state optimized geometry (S_0). (H=HOMO, L= LUMO)

TDDFT states	Energy (eV) main acceptor orbital – main donor orbital				
state	**C1**	**C2**	**C3**	**Ref. 1**	**Ref. 3**
^{1}MLCT (1)	3.433 H-1→L+2	3.347 H→2-L	3.383 H→L	3.081 H→L	3.285 H→L
^{1}MLCT ("state") highest oscillator strength	3.790 (11) H-2→L+1 3.634 (9) H-2→L+1	3.710 (11) H→L+2 3.556 (5) H-1→L	3.605 (3) H-1→L+1 3.689 (4) H→L+3 3.751 (9) H-2→L	3.836 (7) H→L+2 3.542 (5) H-1→L+1	3.625 (5) H-1→L 4.120 (10) H→L+2
^{3}MLCT (1)	2.943 H-1→L+2	2.863 H-1→L	2.955 H-1→L	2.770 H-1→L+1	2.856 H-1→L
First ^{3}MC ("state")	4.106 (14) H→L+12	4.129 (16) H-1→L+16	4.201 (25) H-1→L+16	4.297 (19) H-1→L+11	4.344 (29) H-1→L+12

8. Nanosecond laser laser flash photolysis (ns-LFP) and photostability

Photostability of the complexes:

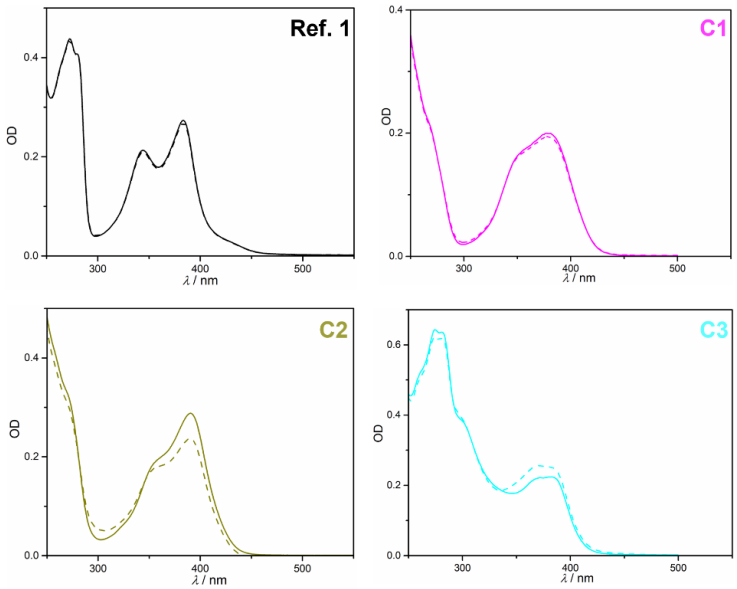

Figure S20: UV/Vis spectra of **Ref. 1** (upper left, after ~135 pulses), **C1** (upper right after ~515 pulses), C2 (lower left, after ~135 pulses), and **C3** (lower right, after ~210 pulses) before (straight) and after (dashed) the ns-LFP measurement using 10 mJ 355 nm pulses of ~5 ns duration.

The UV/Vis spectra of complexes **Ref. 1**, **C1**, **C2** and **C3** were recorded during ns-LFP measurements (Figure S20). Complexes **Ref. 1** and **C1** remained essentially stable and no significant changes in the absorption bands were observed comparing the spectra before and after the LFP measurements. The spectra of complexes **C2** and **C3** clearly differ before and after the laser measurement, and this fast decomposition did not allow us to generate reproducible transient absorption data sets for these two complexes.

Ns-LFP for Ref. 1:

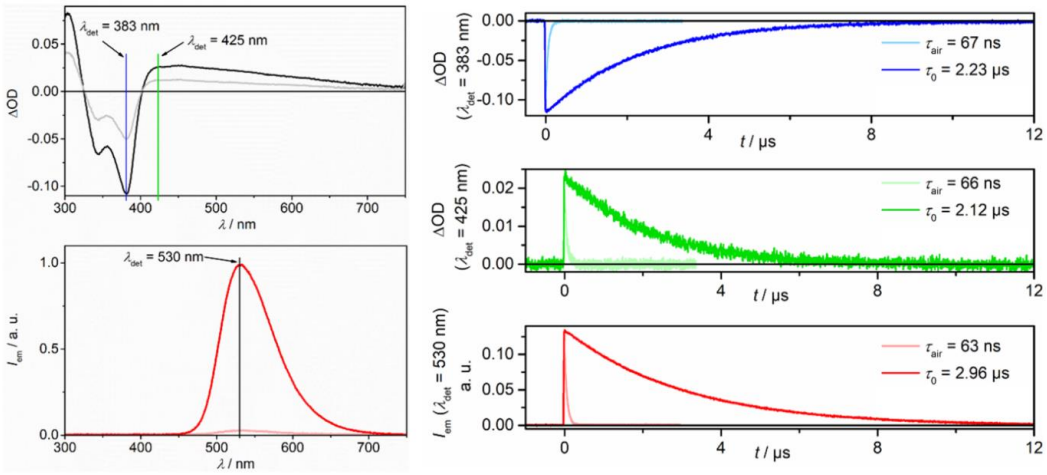

Figure S21: Ns-LFP data for complex **Ref. 1** in MeCN at 20 °C, using a 355 nm pulsed laser for excitation. Upper left: TA spectra of **Ref. 1** after purging with Ar (black) or under air (gray), with a time delay of 10 ns after the laser pulse and integrated over 100 ns. Lower left: Emission spectra of **Ref. 1** after purging with Ar (red) or under air (light red), with a time delay of 10 ns after the laser pulse and integrated over 20 µs. Right: Kinetic traces of **Ref. 1** (wavelengths for the detection are color-coded and indicated in the corresponding spectra in the left part of the figure), under air (with light coloring) or after degassing with argon together with the corresponding lifetimes.

The TA spectrum of **Ref.1** shows a GSB (below 400 nm) and a broad ESA in the visible region of the spectrum. The transient absorption signals and the ^{3}MLCT emission at 530 nm decay with an average lifetime of 2.4 µs. Even though the maximum of the emission is located at 530 nm, which agrees well with the literature, the lifetime measured here exceeds that of Son *et al.*[5] by a factor of ~3. Quenching of the excited state with oxygen was investigated with solutions under air and the rate constant was determined using the Stern-Volmer equation comparing lifetimes in air- and Ar-saturated solutions (with 1.9 mM of dissolved oxygen in MeCN at 20°C).[6] The estimated quenching rate constant amounts to 8×10^9 M^{-1} s^{-1} from the three independent measurements shown in Fig. S21.

Comparative ns-LFP for C1 and Ref. 1:

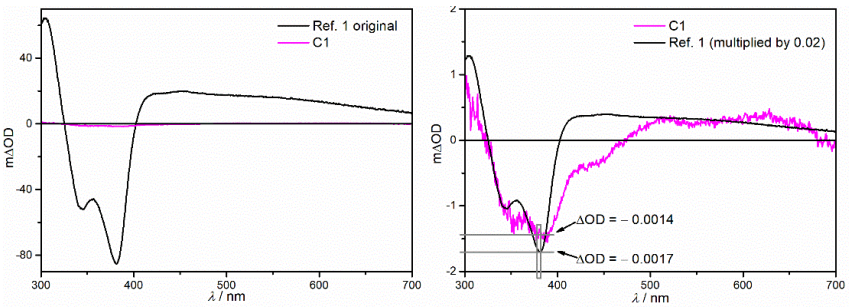

Figure S22: Comparison of the ΔOD spectra for **C1** (magenta, time delay 10 ns) and **Ref. 1** (black, time delay 20 ns) after 355 nm laser excitation. The general conditions for the measurement were almost identical (laser intensity ~10 mJ, same absorption at the excitation wavelength 355 nm, argon-saturated). On the left side are the original TA spectra. On the right side, the TA spectrum for **Ref. 1** has been multiplied by 0.002 as a scaling factor. The gray box indicates the window, which was used to average the ΔOD values (gray lines).

Figure S22 shows the TA spectra of **C1** (magenta) and Ref. 1 (black, scaled by 0.02) under essentially identical excitation and detection conditions, allowing conclusions about the triplet excited states of the two complexes. The solutions of **C1** and **Ref. 1** in MeCN were prepared and measured under identical conditions, except for the delay time after the laser pulse, which was 10 ns for **C1** and 20 ns for Ref. 1 (identical spectra are expected for **Ref. 1** for both delay times due to its long lifetime). The ΔOD was averaged between 375 nm and 385 nm to avoid inaccuracies originating from noise effects. Including the scaling factor of 0.02 for **Ref. 1** the final ΔOD values for comparison are -0.0014 for C1 and -0.0017 for **Ref. 1**. The ~sixty-fold signal increase from C1 to **Ref. 1** is a further indicator for the much more efficient excited-state deactivation in **C1** (*via* the ^{3}MC), compared to the reference complex. However, the very weak signals observed for **C1** could be due to impurities. Assuming similar extinction coefficients for the excited states, the remaining signal for the **C1** sample in ns-LFP experiments might originate from photoactive impurities with a similar structure as **Ref. 1**.

Ns-LFP data for **C1**:

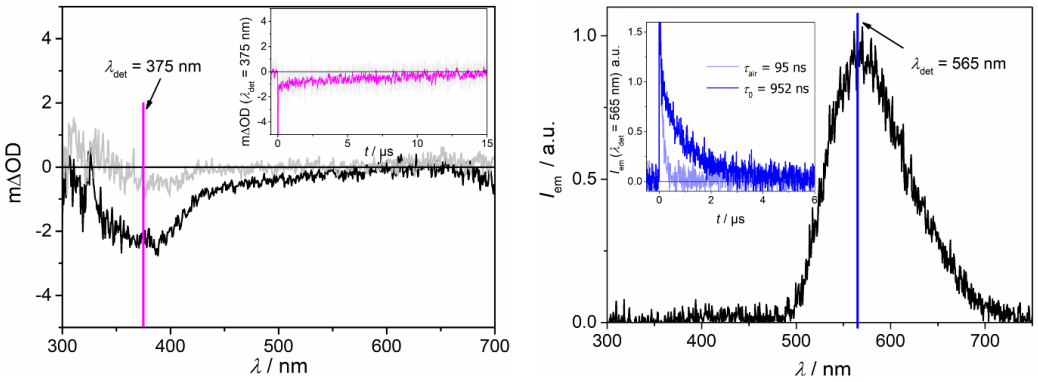

Figure S23: Ns-LFP data for complex **C1**, using a 355 nm pulsed laser for excitation. Left: TA spectra after 50 ns (black) and 5.0 µs (gray) integrated over 100 ns (after 5 min degassing with argon); Inset: Kinetic trace detected at 375 nm for the same solution (gray corresponds to original data, the pink data set was additionally averaged). Right: Emission spectrum after 50 ns delay and integrated over 10 µs; Inset: Kinetic trace of the emission detected at 565 nm under inert conditions (blue) and under air (light blue) together with the corresponding lifetimes.

The complex **C1** (see main part, section *Luminescence Properties* for more details) allowed acquisition of ns-LFP only under highly optimized conditions. The TA-spectra show a weak GSB below 430 nm (left part of Figure S23). The emission (right part of Figure S23) is clearly quenched if the solution is not degassed as also evidenced by the spectral data of **C1** in Figure S9. The time delay (50 ns) does not allow the observation of the short-lived species around 500 nm (see also Figure S9).

Photostability under LED (390 nm) conditions:

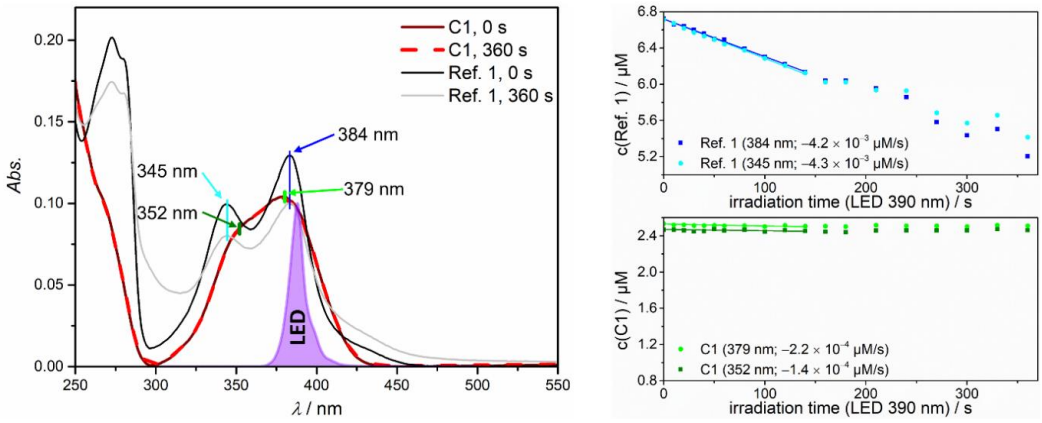

Figure S24: Left: UV/Vis spectra of the complexes **Ref. 1** (black) and C1 (dark red) in acetonitrile and of the same solutions after 6 minutes of irradiation (gray for **Ref. 1** and dashed red for **C1**) with a 390 nm LED (violet spectrum, scaled intensity). Right: Concentrations of complexes **Ref. 1** (upper panel, blue) and **C1** (lower panel, green) plotted vs. the irradiation time, together with linear fits for the decomposition and the corresponding slopes.

The photostability of complexes **Ref. 1** and **C1** was investigated by irradiating the complexes, dissolved in MeCN (2.5 mL, degassed with argon for 5 min) with a 390 nm LED (100 %, see left part of Figure 5) under standardized conditions (very similar OD at peak LED wavelength). Both solutions were irradiated for 6 × 10 s, 6 × 20 s, and 6 × 30 s and the decomposition was monitored by UV/Vis spectroscopy. The concentrations of the complexes after the different irradiation times were calculated using the extinction coefficients (see Table 2 of the main paper). The linear fits are limited to a time frame such that > 90% of the initial concentration of Ref. 1 are still present, assuming only minor contributions to the UV/Vis absorption of decomposition species.[7] Under these conditions, **Ref. 1** decomposes faster compared to **C1** by over one order of magnitude (see Figure S24 right part). This finding is in line with the low emission quantum yield of **C1** (compared to **Ref. 1**, see main part), which prohibits the decomposition of the complex via a dark state ^{3}MC.

9. NMR Spectra

NMR-spectra of **C1**

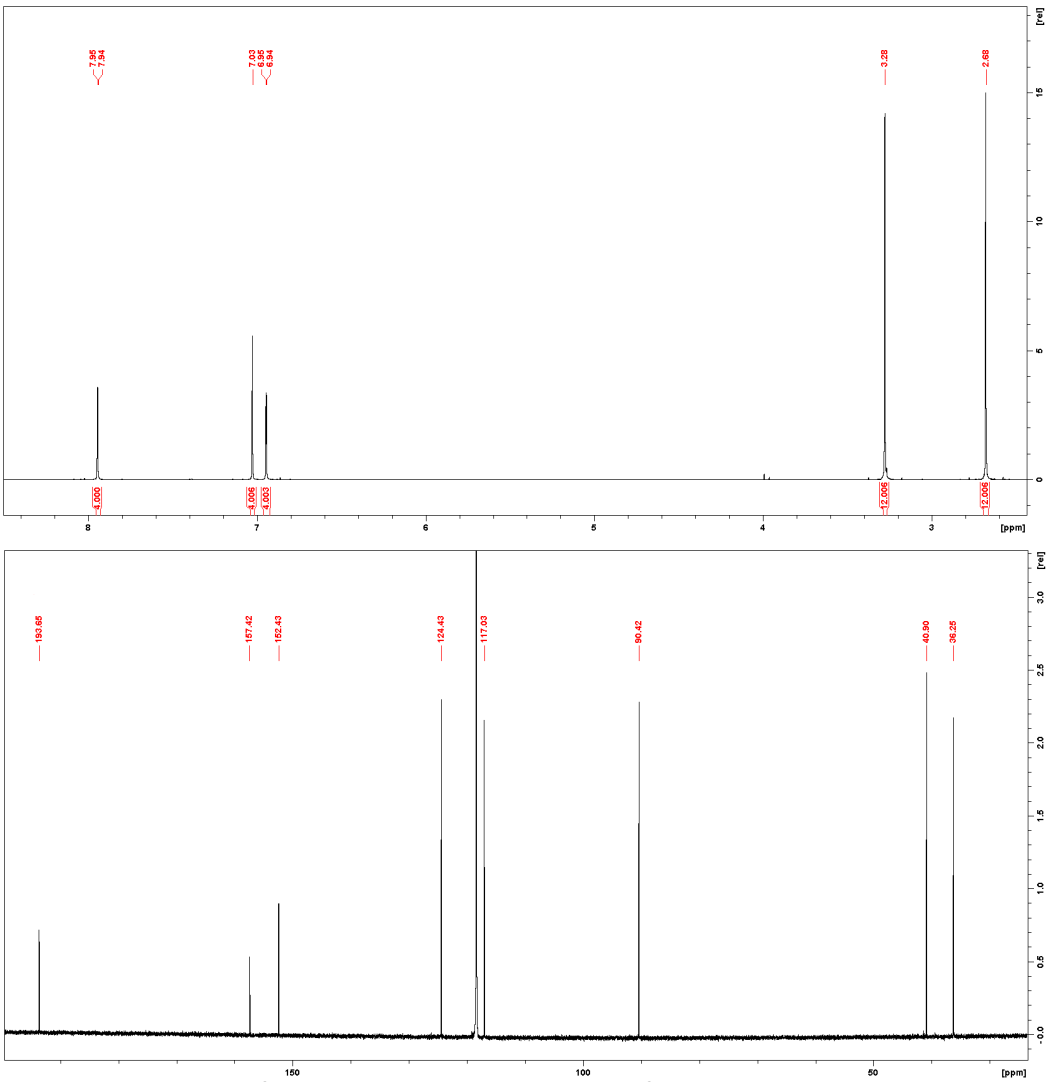

Figure S25: ^{1}H- (top) and ^{13}C-NMR spectra (bottom) of **[Ru(bip^{NMe2})$_2$][PF$_6$]$_2$ (C1)** in CD_3CN at 303 K.

NMR-spectra of **C2**

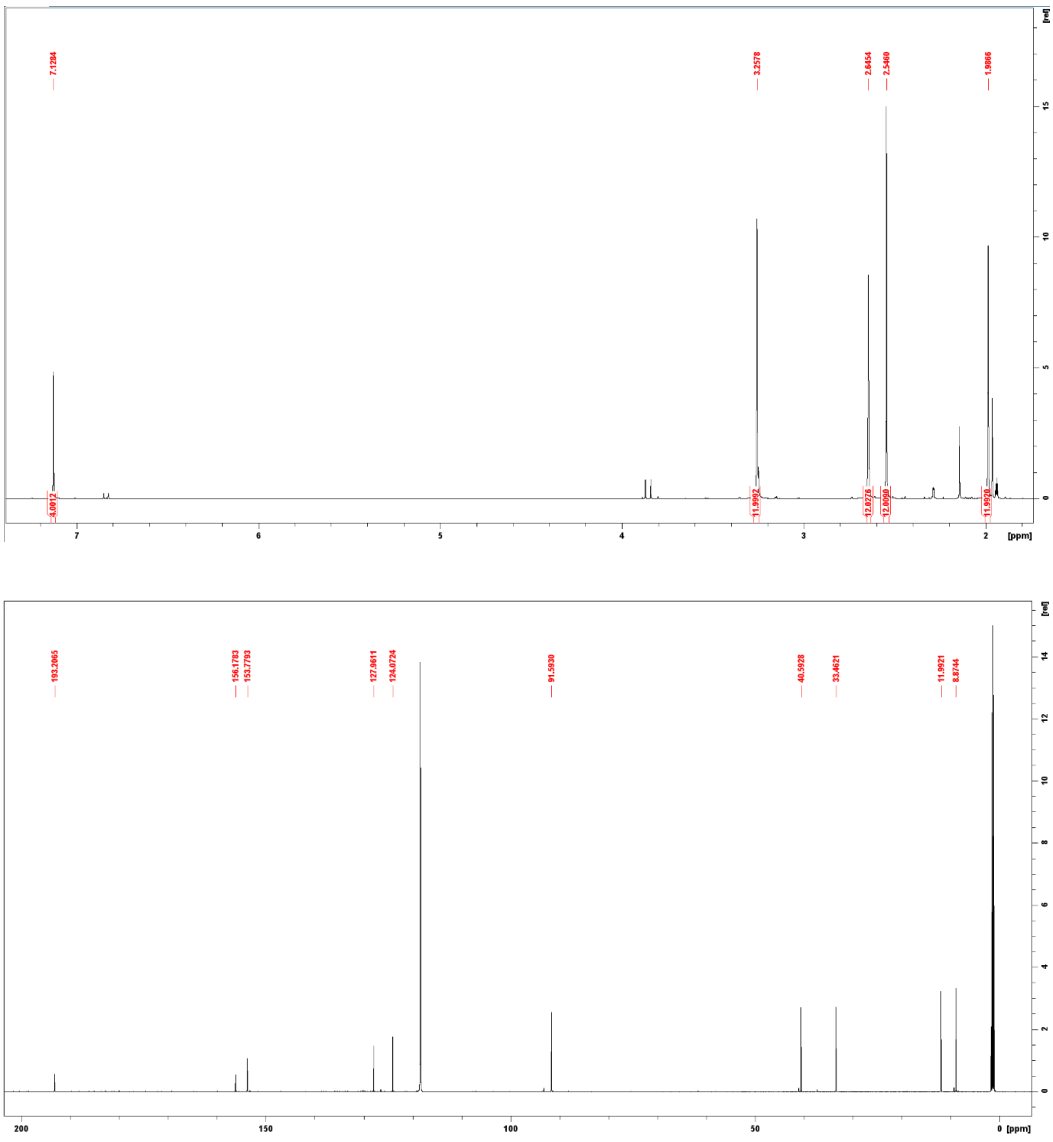

FigureS26: ^{1}H- (top) and ^{13}C-NMR spectra (bottom) of **[Ru(bdmip^{NMe2})$_2$][PF$_6$]$_2$ (C2)** in CD_3CN at 303 K.

NMR-spectra of **C3**

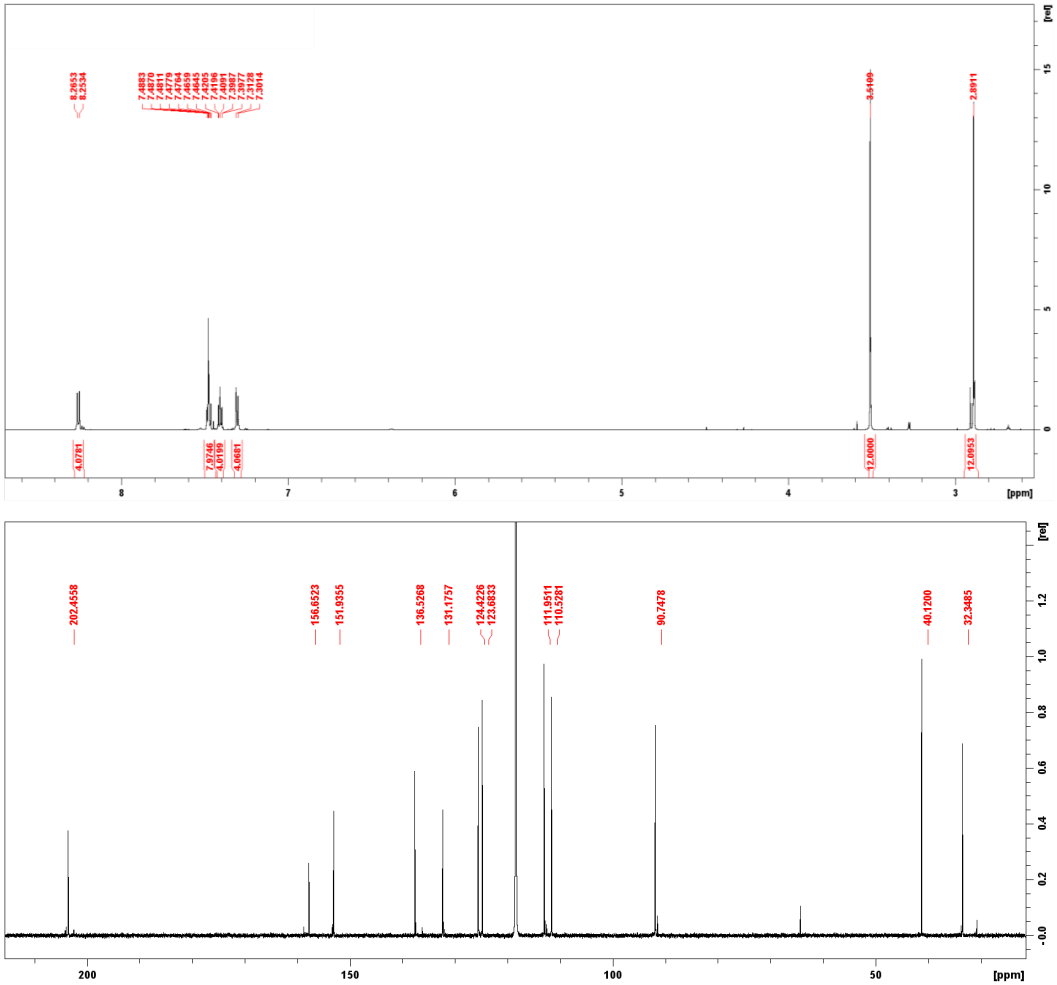

FigureS27: ^{1}H- (top) and ^{13}C-NMR spectra (bottom) of **[Ru(bbp^{NMe2})$_2$][PF$_6$]$_2$ (C3)** in CD_3CN at 303 K.

^{1}H-NMR-spectrum of **Ref.1**

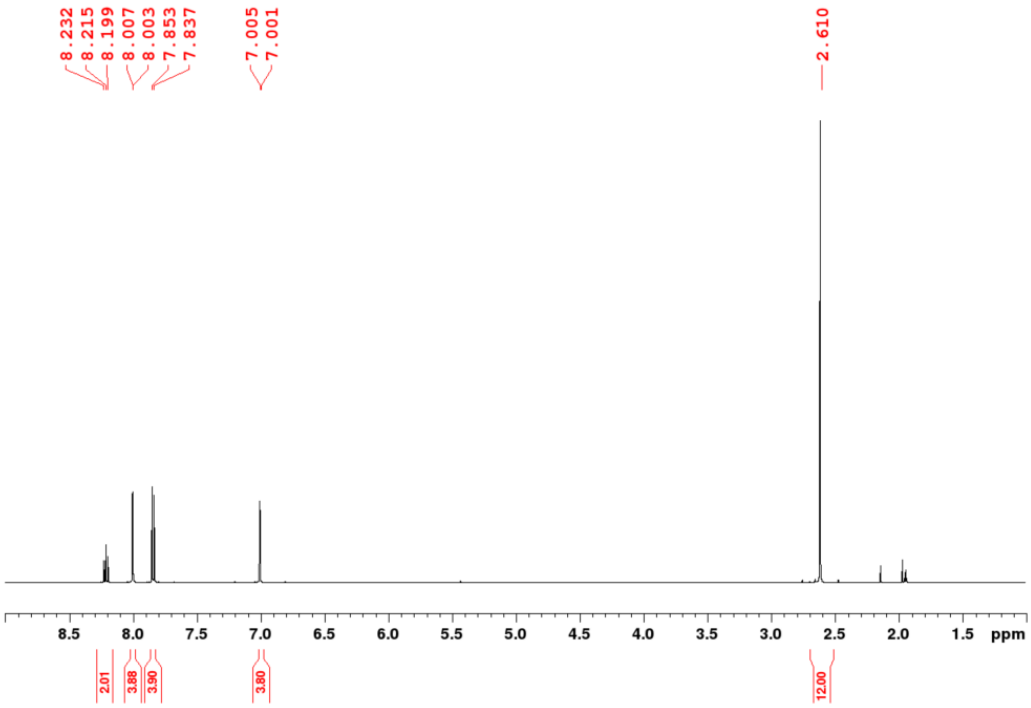

FigureS28: ^{1}H-NMR spectrum of **[Ru(bip)$_2$][PF$_6$]$_2$** (**Ref.1**) in CD_3CN at 303 K.

NMR-spectra of **Ref.3**

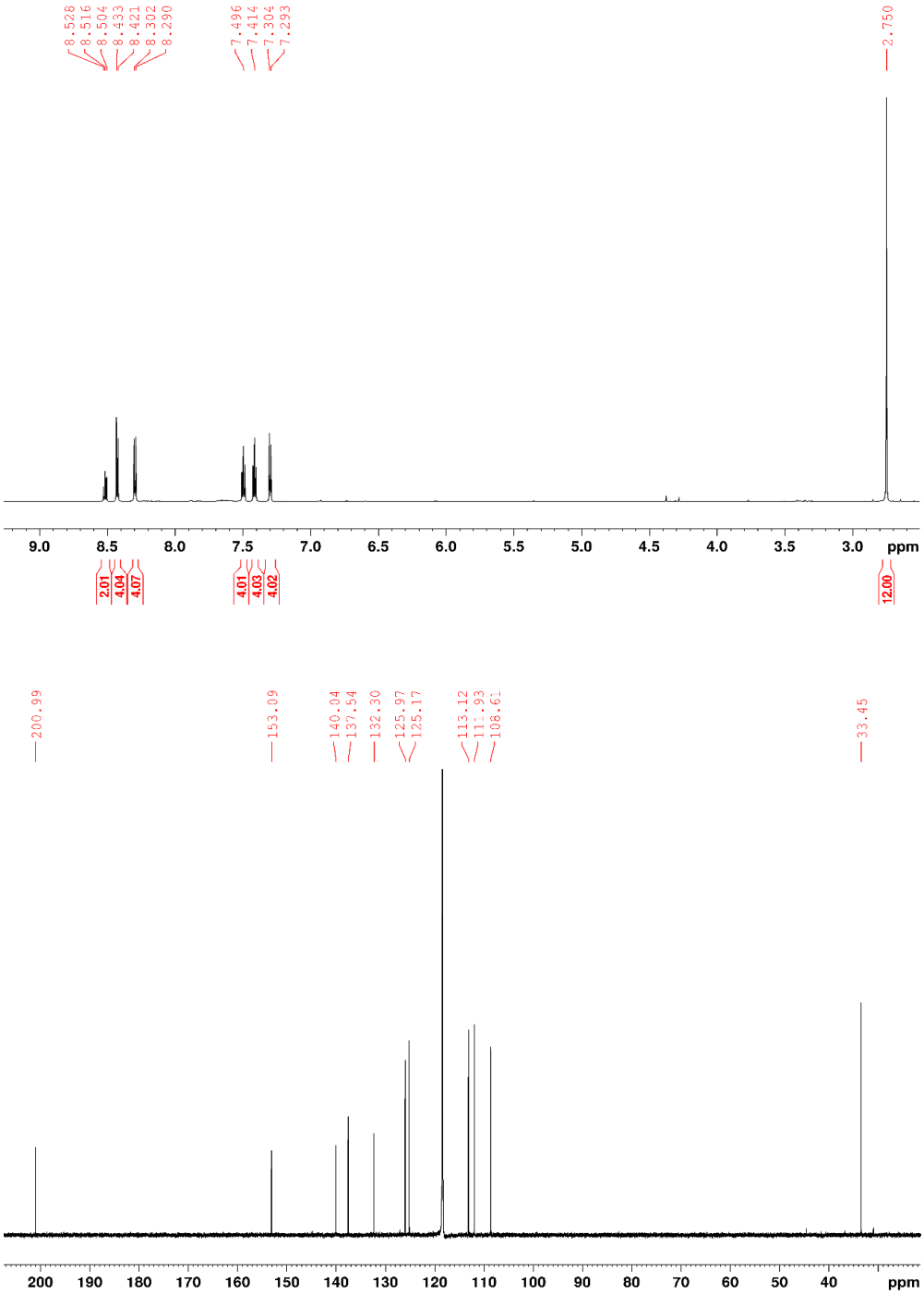

FigureS29: ^{1}H- (top) and ^{13}C-NMR spectra (bottom) of **[Ru(bbp)$_2$][PF$_6$]$_2$** (**Ref.3**) in CD_3CN at 303 K.

References

[1] A. Breivogel, M. Meister, C. Förster, F. Laquai, K. Heinze, *Chem. Eur. J.* **2013**, *19*, 13745–13760.
[2] W. Viricel, A. Mbarek, J. Leblond, *Angew. Chem.* **2015**, *54*, 12743–12747.
[3] D. H. Brown, G. L. Nealon, P. V. Simpson, B. W. Skelton, Z. Wang, *Organometallics* **2009**, *28*, 1965–1968.
[4] J. E. B. Randles, *Trans. Faraday Soc.* **1948**, *44*, 322.
[5] S. U. Son, K. H. Park, Y.-S. Lee, B. Y. Kim, C. H. Choi, M. S. Lah, Y. H. Jang, D.-J. Jang, Y. K. Chung, *Inorg. Chem.* **2004**, *43*, 6896–6898.
[6] M. Montalti, A. Credi, L. Prodi, M. T. Gandolfi, *Handbook of Photochemistry*, CRC Press, **2006**.
[7] a) W. R. Kitzmann, M.-S. Bertrams, P. Boden, A. C. Fischer, R. Klauer, J. Sutter, R. Naumann, C. Förster, G. Niedner-Schatteburg, N. H. Bings et al., *J. Am. Chem. Soc.* **2023**, *145*, 16597–16609; b) J. Castellanos-Soriano, T. J. B. Zähringer, J. C. Herrera-Luna, M. C. Jiménez, C. Kerzig, R. Pérez-Ruiz, *Phys. Chem. Chem. Phys.* **2023**, *25*, 12041–12049;

A.2 Supporting Information of "Iron(III)-Complexes with N-Phenylpyrazole-based ligands"

Supporting Information

Iron^{III}-Complexes with *N*-Phenylpyrazole-based Ligands

Tanja Hirschhausen1†, Lorena Fritsch1†, F. Lux [1], J. Steube[1], R. Schoch [1], A. Neuba [1], H. Egold[1] and M. Bauer [1,2]*

[1] Institute of Inorganic Chemistry, Paderborn University, Paderborn, Germany.
[2] Center for Sustainable Systems Design, Paderborn University, Paderborn, Germany
* Correspondence: matthias.bauer@upb.de
† These authors contributed equally to this work.

Contents

General procedure

Synthesis of ligands and complexes were carried out under standard Schlenk conditions, under inert and anhydrous conditions. Inert and pre-dried argon was used, and all applied glass wear was heated and re-filled with argon at least three times. Water free solvents were provided by a solvent drying-plant by MBraun (MB SPS 800) and purged with argon prior use. Used chemicals for all synthesis were commercially purchased by the following providers*: Fischer Scientific, Merck, Abcr*, and *TCI*, and used without further purification. Ligand synthesis has been reported in literature.[1,2]

NMR spectra were recorded on a BRUKER Avance 700 (^{1}H, 700.1 MHz) using deuterated solvents by *Deutero* without further purification. NMR signals were referred to residual solvent signals relative to TMS. Mass spectrometry was measured with a quadrupol time-of-flight mass spectrometer (MS) Synapt 2G by the company WATERS. Elemental analysis measurements were performed with a Micro Cube by ELEMENTAR and were compared with the theoretical calculated mass. A **PerkinElmer** Lambda 465 single beam spectrophotometer was used for Uv-Vis spectra. Concentrations contained a 10^{-5} M complex solution in BuCN, and were filled in a **Hellma** quartz cuvette with a pathlength of 1 cm. For IR spectroscopy a Bruker Vertex 70, with the sample as solid powder and the ATR-technique, was applied. Cylovoltamogramms were measured with a 10^{-3} M analyte and 0.1 M [*n*-Bu$_4$N](PF$_6$) concentration on

a PGSTAT 101 potentiostat from **Metrohm-Autolab**. Emission spectra were recorded on a FLS1000 from **Edinburgh Instruments** at room-temperature.

General procedure of complex synthesis

Under Argon atmosphere respective ligand (3 equiv) was suspended in tetrahydrofuran (THF) (10 mL). Ethylmagnesium bromide (4 equiv, 0.9 M in THF) was added dropwise and refluxed overnight. In a second round button flask, iron powder (12 equiv) was added to THF solution of iron(II) bromide (1.5 equiv) (40 mL) and refluxed overnight. After refluxing, the flask was cooled to room-temperature and the ligand-solution was cooled in an ethanol-nitrogen bath to -80°C. The iron(II) bromide solution was added dropwise and slowly warmed to room temperature under an argon atmosphere. To the reaction mixture a solution of NH_4Cl (100 mL, 15 g/L) was added, and extracted with dichloromethane (DCM) (3x100 mL). The combined organic portions were dried with $MgSO_4$ and concentrated under reduced pressure. Column chromatography with silica as solid phase and DCM as eluent was applied. The combined fractions were concentrated under reduced pressure and crystallized with slow diffusion of cyclopentane into the DCM-analyte solution. After removing the crystalline product and drying at 50°C at high vacuum, the compound was received as elemental analysis pure product.

$Fe(ppz)_3$

The complex was obtained as yellow powder (7.5%)

^{1}H-NMR (700.0 MHz, CD_3CN): δ = -75.20 (s, 1H, 2-*H*), -9.27 (s, 1H, 9-*H*), -5.25 (s, 1H, 4-*H*), -3.35 (s, 1H,8-*H*), -1.15 (s, 1H, 5-*H*), 7.90 (s, 1H, 3-*H*), 13.04 (s, 1H, 7-*H*) ppm.

^{13}C-NMR (176.1 MHz, CD_3CN): δ = -92.7 (1C, 3-*C*), -74.8 (1C, 5-*C*), 100.2 (1C, 7-*C*), 117.0 (1C, 8-*C*), 122.9 (1C, 9-*C*), 239.9 (1C, 4-*C*), 389.1 (1C, 2-*C*), 396.6 (1C, 6-*C*) ppm.

^{15}N-NMR (70.96 MHz, CD_3CN): 70.4 ppm. (ESI in MECN): m/z 485.1160 (for $C_{27}H_{21}FeN_6$ calc. 485.1177)

Elemental analysis: calc. for $C_{27}H_{21}FeN_6$ C: 66.82%, H: 4.36%, N: 17.32%, found: C: 66.77%, H: 4.56%, N: 17.25%.

IR (ATR, $\tilde{\upsilon}$ [cm^{-1}]): 3139w, 3041w, 1573w, 1506w, 1461m, 1434m, 1417m, 1398m, 1328w, 1270m, 1236w, 1193w, 1153w, 1099w, 1064m, 1043m, 1012m, 960m, 918w, 871w, 825w, 742s, 715m, 698m, 661w, 644w, 609m.

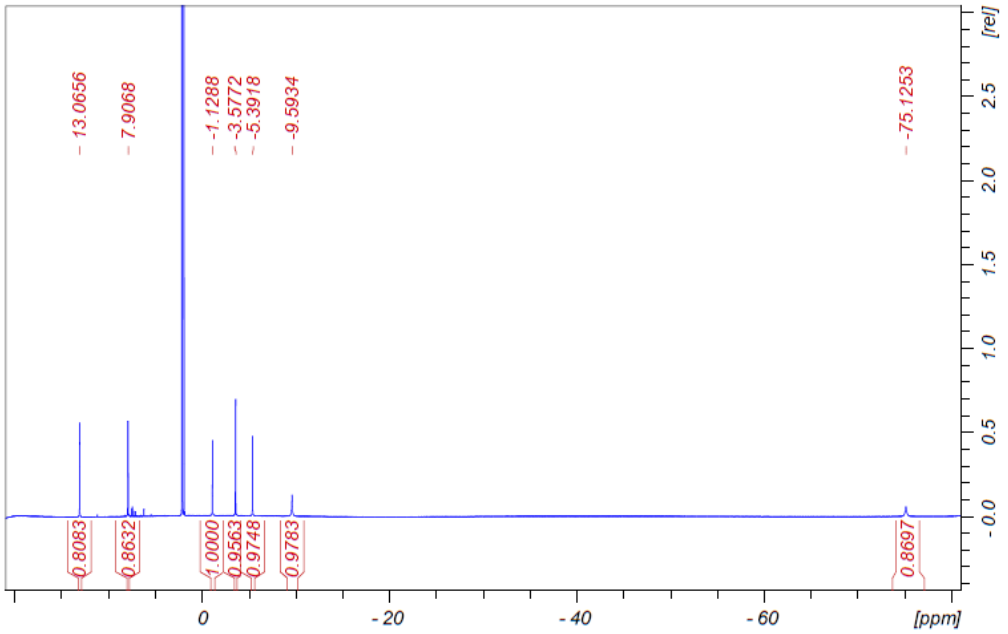

Figure S1: ^{1}H-NMR spectrum of complex Fe(ppz)$_3$ in CD_3CN

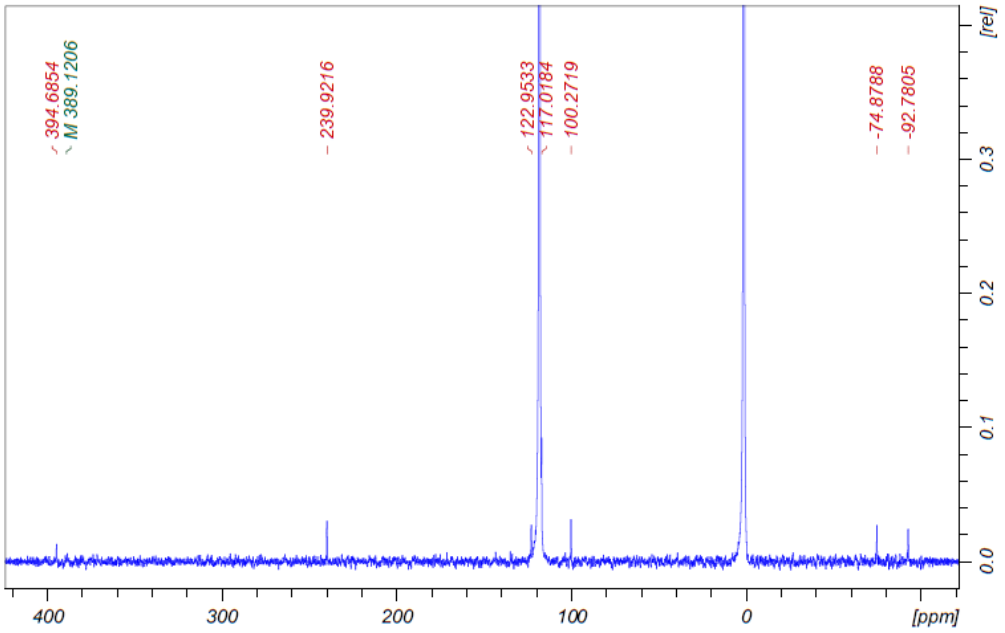

Figure S2: ^{13}C-NMR spectrum of complex Fe(ppz)$_3$ in CD_3CN

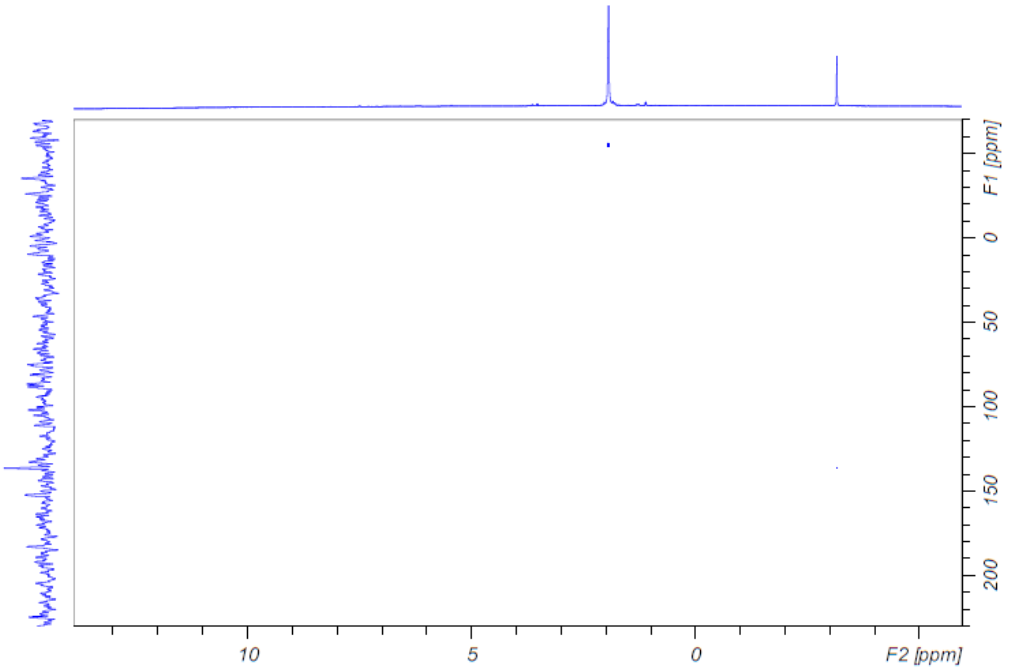

Figure S3: ^{15}N-HMBC spectrum of $Fe(ppz)_3$ in CD_3CN, second signal is the folded signal of non-deuterated solvent CH_3CN

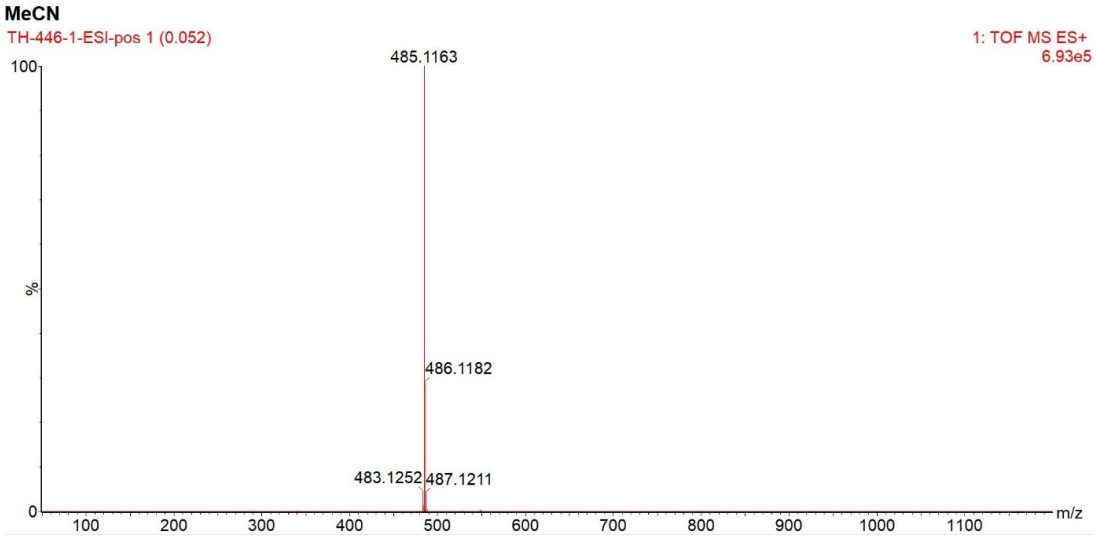

Figure S4: ESI-MS spectrum of complex $Fe(ppz)_3$ in CH_3CN

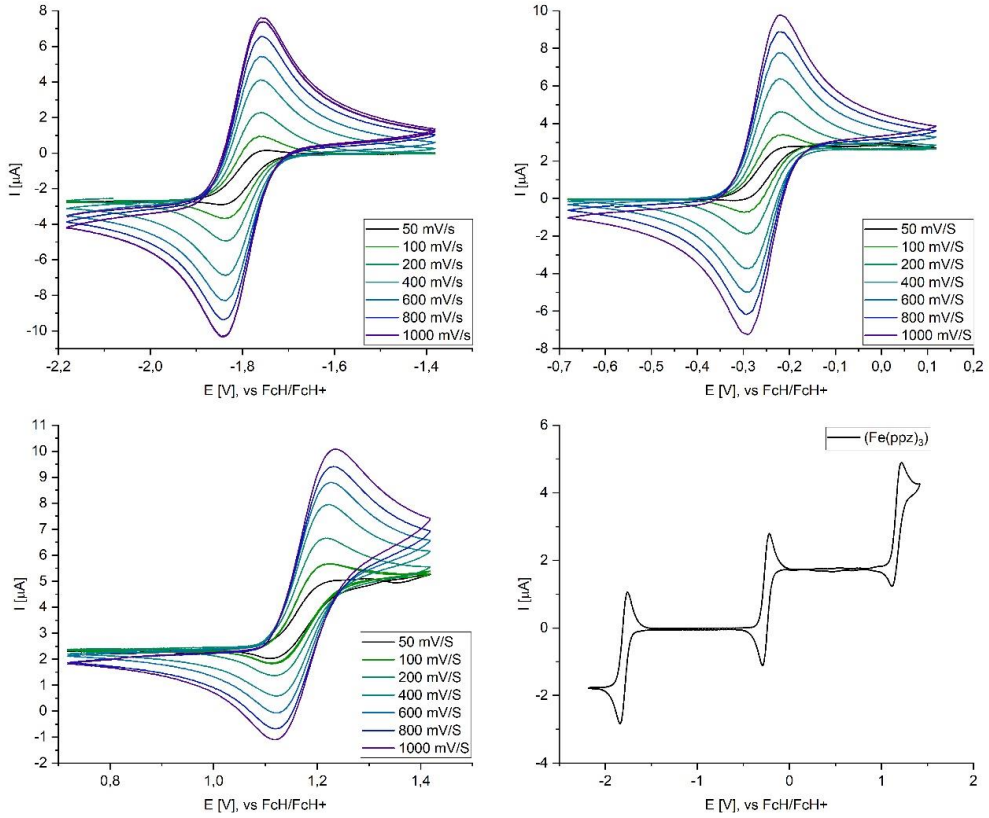

Figure S5: Complete cyclovoltammetry spectra for complex $Fe(ppz)_3$ in CH_3CN

Table S1: Cyclovoltammetry data for $Fe(ppz)_3$ at different scan rates, first redox step

SCANRATE	[MV/S]	50	100	200	400	600	800	1000
E_{PC}	[V]	-1,835	-1,828	-1,833	-1,835	-1,835	-1,840	-1,838
E_{PA}	[V]	-1,762	-1,765	-1,759	-1,762	-1,760	-1,760	-1,762
$E_{1/2}$	[V]	-1,80	-1,80	-1,80	-1,80	-1,80	-1,80	-1,80
ΔE	[V]	0,073	0,063	0,074	0,073	0,076	0,081	0,076
I_{PA}	[µA]	-1,68	-2,73	-4,11	-5,76	-7,11	-8,17	-9,07
I_{PC}	[µA]	1,64	2,78	4,11	5,87	7,14	8,24	9,14
I_{PA}/I_{PC}		-0,98	-1,02	-1,00	-1,02	-1,00	-1,01	-1,01

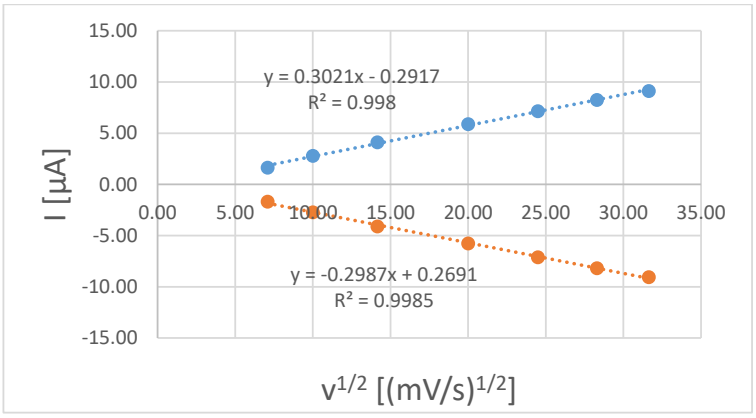

Figure S6: Plotted data of Randles-Sevcik-Equation $Fe(ppz)_3$ at different scan rates, first redox step

Table S2: Cyclovoltammetry data for $Fe(ppz)_3$ at different scan rates, second redox step

SCANRATE	[MV/S]	50	100	200	400	600	800	1000
E_{PC}	[V]	-0,296	-0,286	-0,289	-0,289	-0,289	-0,294	-0,291
E_{PA}	[V]	-0,223	-0,225	-0,223	-0,223	-0,225	-0,223	-0,223
$E_{1/2}$	[V]	-0,26	-0,26	-0,26	-0,26	-0,26	-0,26	-0,26
ΔE	[V]	0,073	0,061	0,066	0,066	0,063	0,071	0,068
I_{PA}	[µA]	-1,88	-2,65	-3,80	-5,43	-6,88	-8,00	-9,00
I_{PC}	[µA]	1,55	2,41	3,80	5,53	6,69	7,79	8,72
I_{PA}/I_{PC}		-0,83	-0,91	-1,00	-1,02	-0,97	-0,97	-0,97

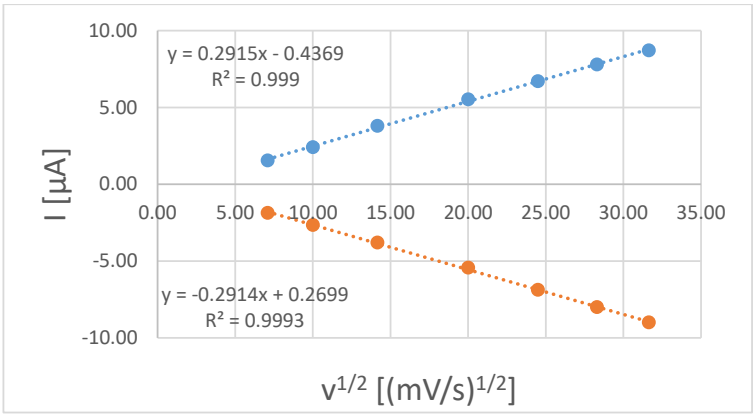

Figure S7: Plotted data of Randles-Sevcik-Equation $Fe(ppz)_3$ at different scan rates, second redox step

Table S3: Cyclovoltammetry data for $Fe(ppz)_3$ at different scan rates, third redox step

SCANRATE	[MV/S]	50	100	200	400	600	800	1000
E_{PC}	[V]	1,126	1,131	1,123	1,128	1,128	1,128	1,126
E_{PA}	[V]	1,211	1,209	1,209	1,216	1,216	1,221	1,226
$E_{1/2}$	[V]	1,17	1,17	1,17	1,17	1,17	1,17	1,18
ΔE	[V]	0,085	0,078	0,085	0,088	0,088	0,093	0,100
I_{PA}	[µA]	-1,70	-1,88	-2,77	-3,77	-4,57	-5,17	-5,73
I_{PC}	[µA]	1,35	2,02	2,92	3,97	4,64	5,12	5,52
I_{PA}/I_{PC}		-0,80	-1,08	-1,06	-1,05	-1,01	-0,99	-0,96

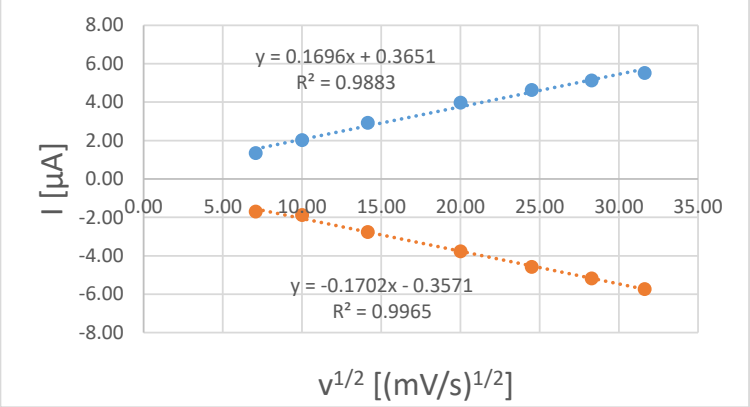

Figure S8: Plotted data of Randles-Sevcik-Equation $Fe(ppz)_3$ at different scan rates, third redox step

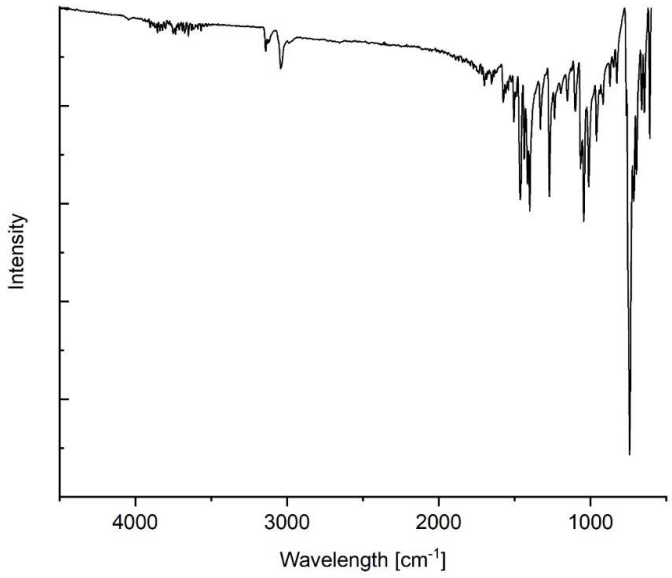

Figure S9: ATR-IR spectrum for complex $Fe(ppz)_3$

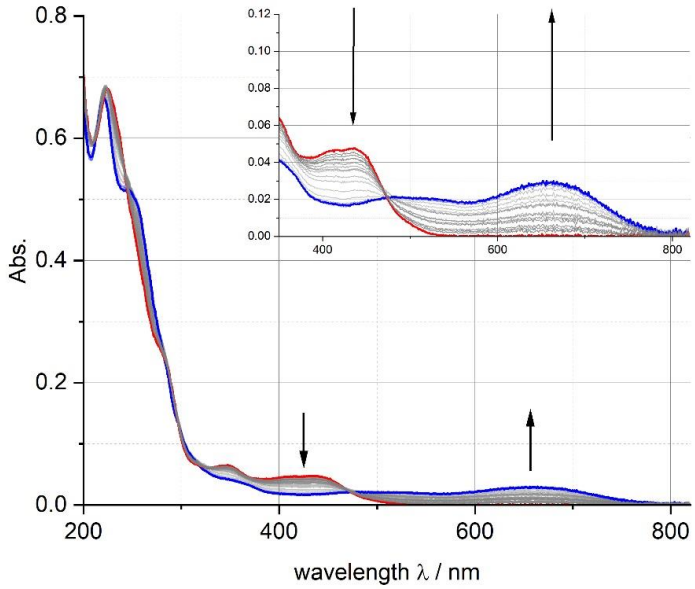

Figure S10: Change in the absorptive behaviour of $Fe(ppz)_3$ with an applied potential of 0.5-2 V in CH_3CN

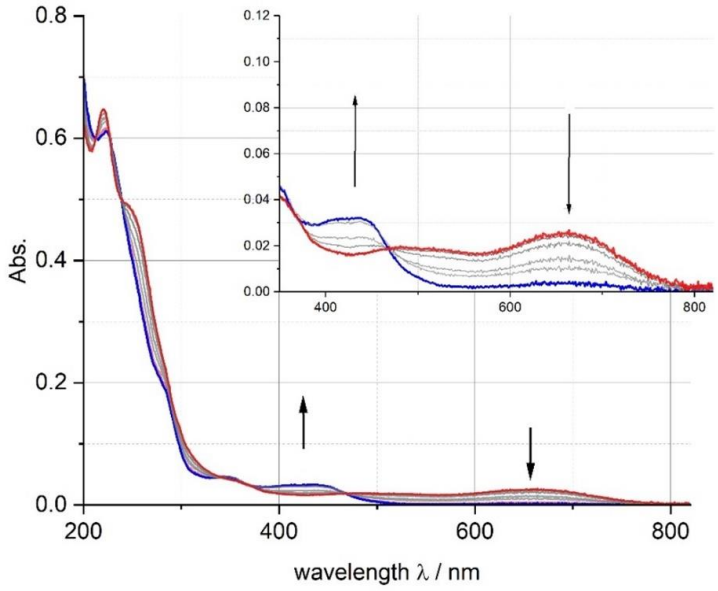

Figure S11: Change in the absorptive behaviour of $Fe(ppz)_3$ with an applied potential of -0.5 V in CH_3CN

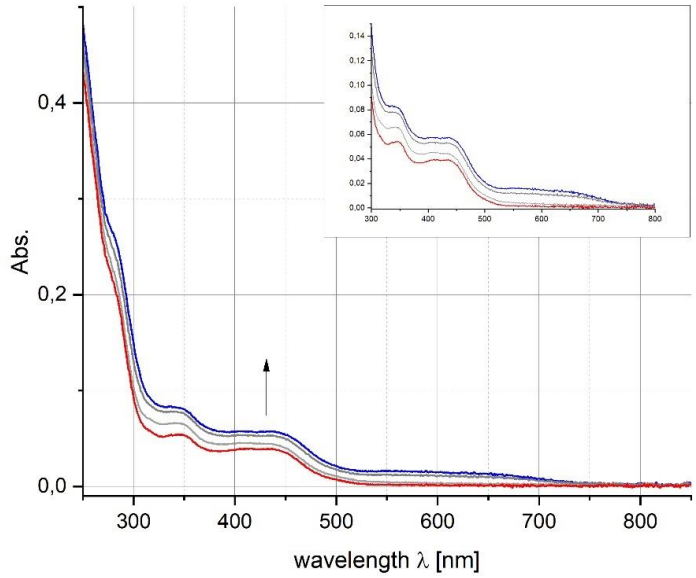

Figure S12: Change in the absorptive behaviour of $Fe(ppz)_3$ with an applied potential of -2.0-2.5 V in CH_3CN

$Fe(bppz)_3$

The complex was obtained as red powder (3.9%).

^{1}H-NMR (700 MHz, CD_3CN): δ = -77.61 (1s, 1H, 2-*H*) -10.18 (s, 1H, 13-*H*), -4.64 (s, 1H, 8-*H*), -3.21 (s, 1H, 12-*H*), -1.74 (s, 1H, 9-*H*), 5.39 (d, $^3J_{HH}$ = 8.19 Hz, 2H, 5,5´-*H*), 5.75 (t, $^3J_{HH}$ = 7.60 Hz, 2H, 6,6´-*H*), 7.10 (t, $^3J_{HH}$ = 7.14 Hz, 1H, 6-H) 11.84 (s, 1H, 11-*H*) ppm.).

^{13}C-NMR (176.1 MHz, CD_3CN): δ = -79.6 (1C, 152.5 Hz, 9-*C*), -77.9 (1C, 3-*C*), 105.4 (1C, 185.7 Hz, 11-*C*), 114.4 (1C, 62.3 Hz, 12-*C*), 115.3 (2C, 89.03 Hz, 5,5´-*C*), 123.1 (1C, 162.9 Hz, 7-*C*), 130.9 (2C, 160.4 Hz, 6,6´-*C*), 131.9 (1C, 183.3 Hz, 13-*C*), 154.1 (1C, 4-*C*), 241.4 (1C, 158.8 Hz, 8-*C*), 370.5 (1C, 133.9 Hz, 2-*C*), 396.7 (1C, 10-*C*) ppm.

^{15}N-NMR (70.96 MHz, CD_3CN): 71.0 ppm.

MS (ESI in MECN): m/z 713.2150 (for $C_{45}H_{33}FeN_6$ calc. 713.6460).

Elemental analysis: calc. for $C_{45}H_{33}FeN_6$ C: 75.74%, H: 4.66%, N: 11.78%, found: C: 71.15%, H: 4.84%, N: 10.78%.

IR (ATR, $\tilde{\upsilon}$ [cm^{-1}]): 3108w, 3056w, 3020w, 1598w, 1564w, 1502w, 1465m, 1400m, 1373w, 1330w, 1261m, 1112w, 1064m, 1047m, 1016w, 958w, 916w, 894w, 808s, 757s, 734s, 694s, 663w, 649w, 607w.

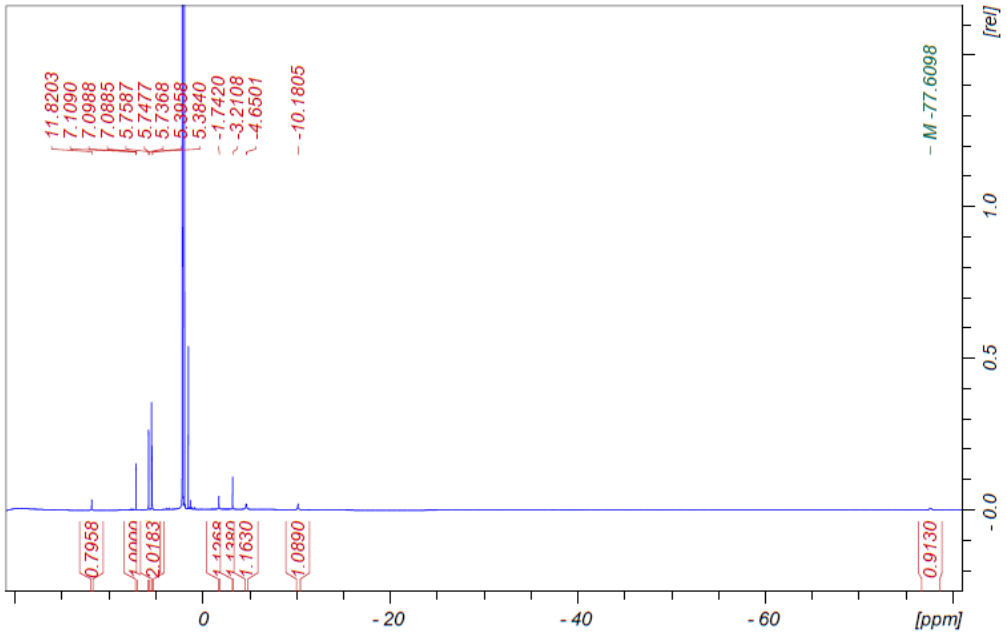

Figure S13: ^{1}H-NMR spectrum of complex Fe(bppz)$_3$ in CD_3CN

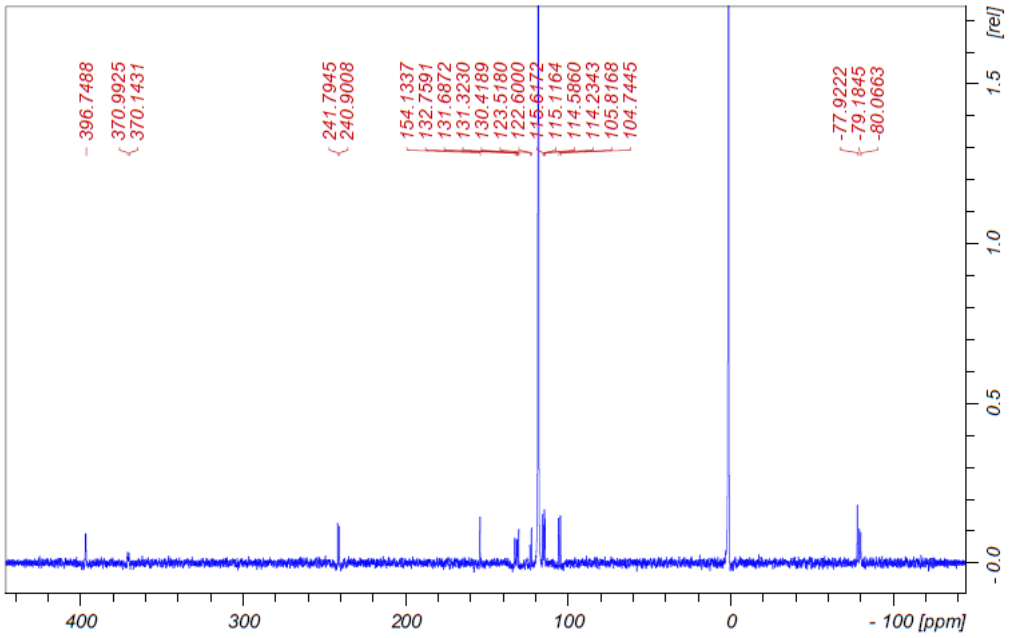

Figure S14: ^{13}C-NMR spectrum of complex Fe(bppz)$_3$ in CD_3CN

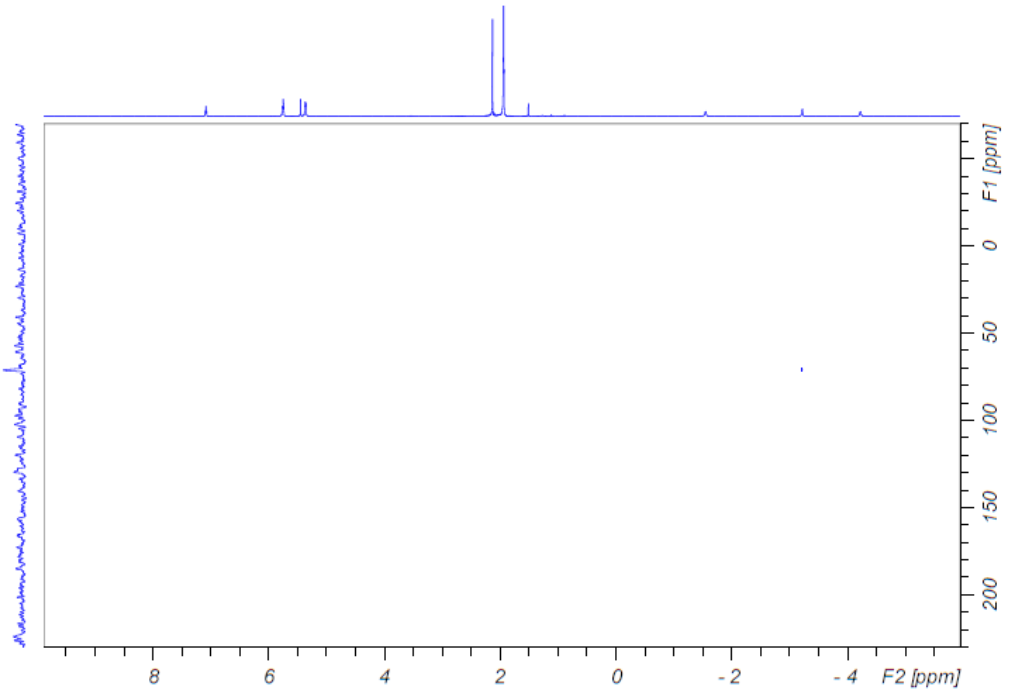

Figure S15: ^{15}N-HMBC spectrum of Fe(bppz)$_3$ in CD_3CN

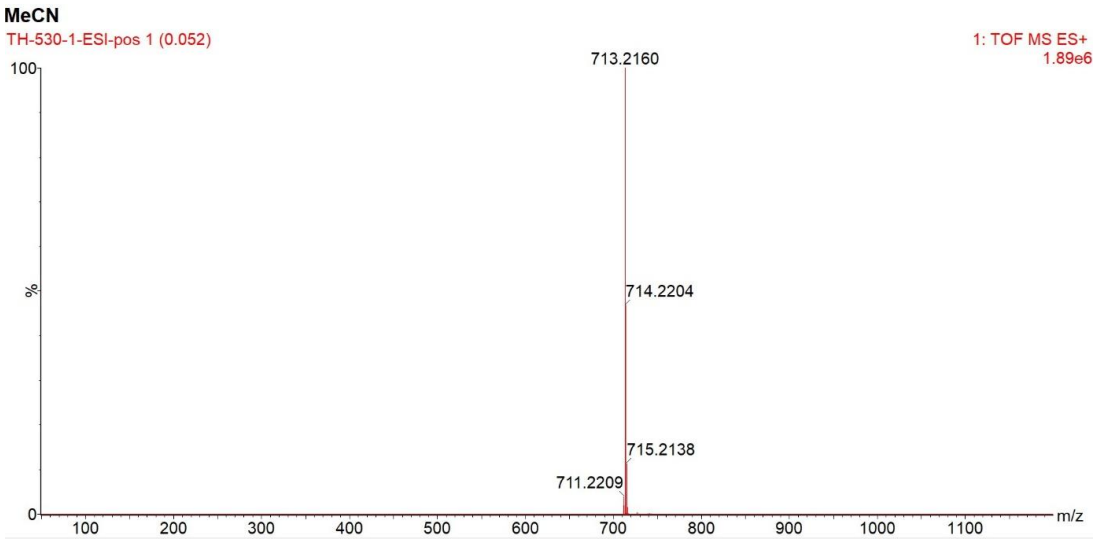

Figure S16: ESI-MS spectrum of complex Fe(bppz)$_3$ in CH_3CN

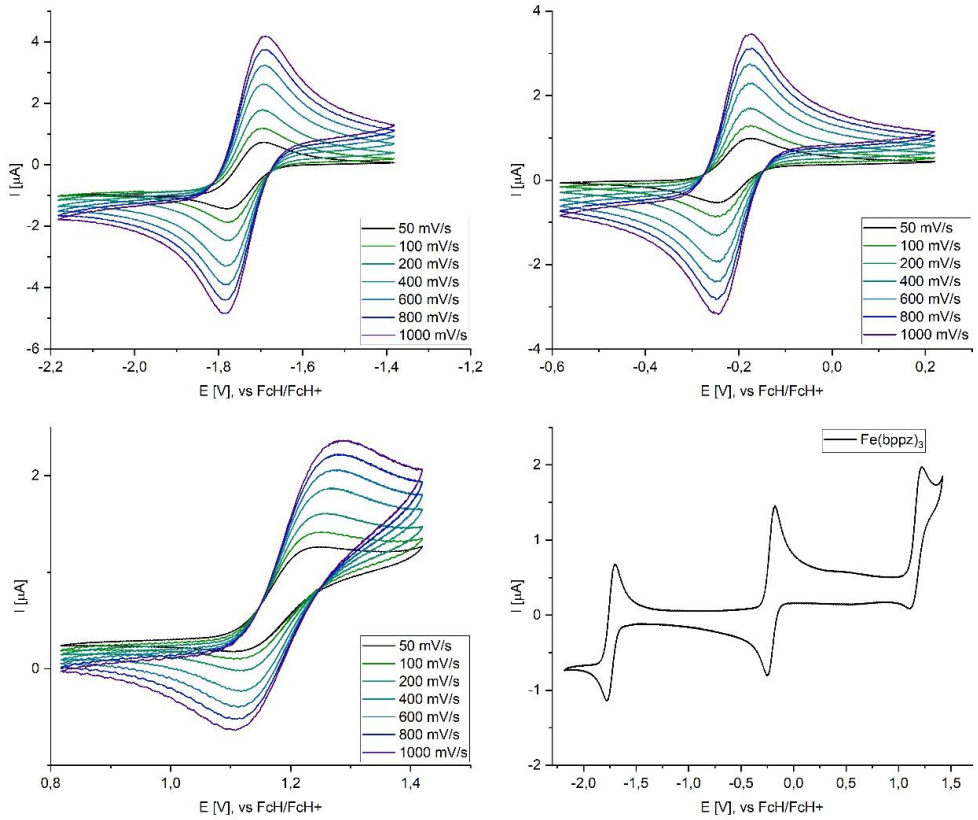

Figure S17: Cyclovoltammetry spectra of $Fe(bppz)_3$ in CH_3CN

Table S4: Cyclovoltammetry data for $Fe(bppz)_3$ at different scan rates, first redox step

SCANRATE	[MV/S]	50	100	200	400	600	800	1000
E_{PC}	[V]	-1,774	-1,777	-1,772	-1,777	-1,777	-1,779	-1,777
E_{PA}	[V]	-1,699	-1,699	-1,696	-1,694	-1,699	-1,696	-1,696
$E_{1/2}$	[V]	-1,74	-1,74	-1,73	-1,74	-1,74	-1,74	-1,74
ΔE	[V]	0,076	0,078	0,076	0,083	0,078	0,083	0,081
I_{PC}	[µA]	-1,12	-1,58	-2,24	-3,10	-3,76	-4,27	-4,75
I_{PA}	[µA]	1,36	1,67	2,19	2,95	3,54	4,01	4,43
I_{PA}/I_{PC}		-1,21	-1,06	-0,98	-0,95	-0,94	-0,94	-0,93

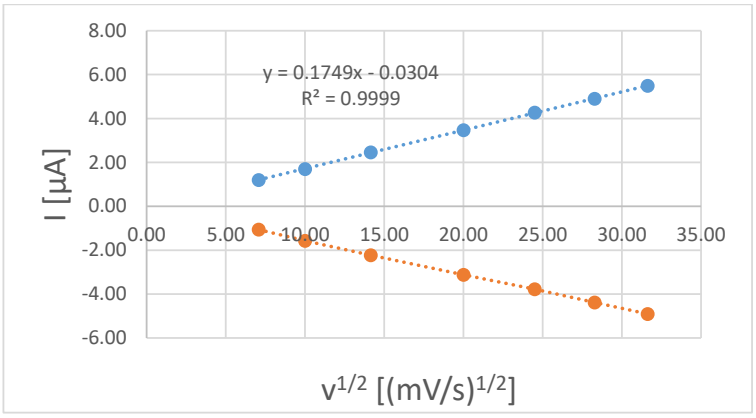

Figure S18: Plotted data of Randles-Sevcik-Equation $Fe(bppz)_3$ at different scan rates, first redox step

Table S5: Cyclovoltammetry data for $Fe(bppz)_3$ at different scan rates, second redox step

SCANRATE	[MV/S]	50	100	200	400	600	800	1000
E_{PC}	[V]	-0,241	-0,241	-0,246	-0,241	-0,241	-0,249	-0,244
E_{PA}	[V]	-0,175	-0,175	-0,180	-0,180	-0,175	-0,183	-0,173
$E_{1/2}$	[V]	-0,21	-0,21	-0,21	-0,21	-0,21	-0,22	-0,21
ΔE	[V]	0,066	0,066	0,066	0,061	0,066	0,066	0,071
I_{PC}	[µA]	-0,75	-1,09	-1,55	-2,18	-2,62	-3,04	-3,41
I_{PA}	[µA]	0,87	1,14	1,60	2,21	2,69	3,08	3,43
I_{PA}/I_{PC}		-1,17	-1,05	-1,04	-1,01	-1,03	-1,01	-1,01

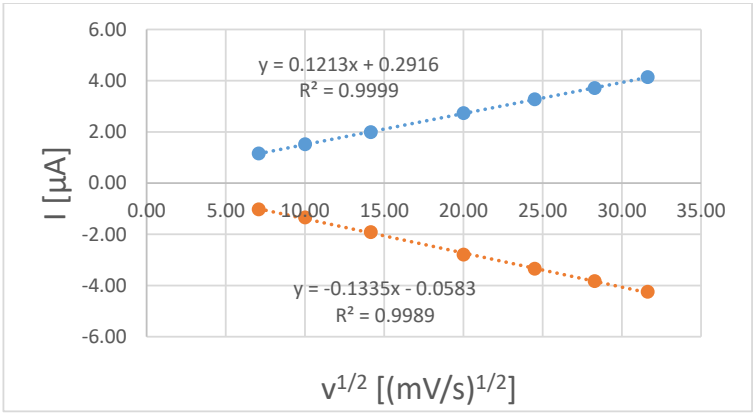

Figure S19: Plotted data of Randles-Sevcik-Equation $Fe(bppz)_3$ at different scan rates, second redox step

Table S6: Cyclovoltammetry data for $Fe(bppz)_3$ at different scan rates, third redox step

SCANRATE	[MV/S]	50	100	200	400	600	800	1000
E_{PC}	[V]	1,129	1,127	1,134	1,132	1,124	1,122	1,110
E_{PA}	[V]	1,217	1,222	1,232	1,239	1,244	1,246	1,261
$E_{1/2}$	[V]	1,17	1,17	1,18	1,19	1,18	1,18	1,19
ΔE	[V]	0,088	0,095	0,098	0,107	0,120	0,125	0,151
I_{PC}	[µA]	-0,49	-0,58	-0,71	-0,95	-1,21	-1,33	-1,44
I_{PA}	[µA]	0,53	0,64	0,76	0,88	1,02	1,08	1,13
I_{PA}/I_{PC}		-1,08	-1,10	-1,07	-0,92	-0,84	-0,82	-0,78

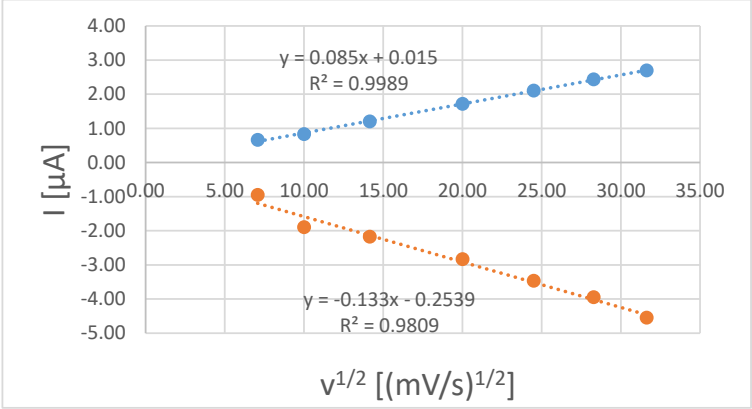

Figure S20: Plotted data of Randles-Sevcik-Equation $Fe(bppz)_3$ at different scan rates,third redox step

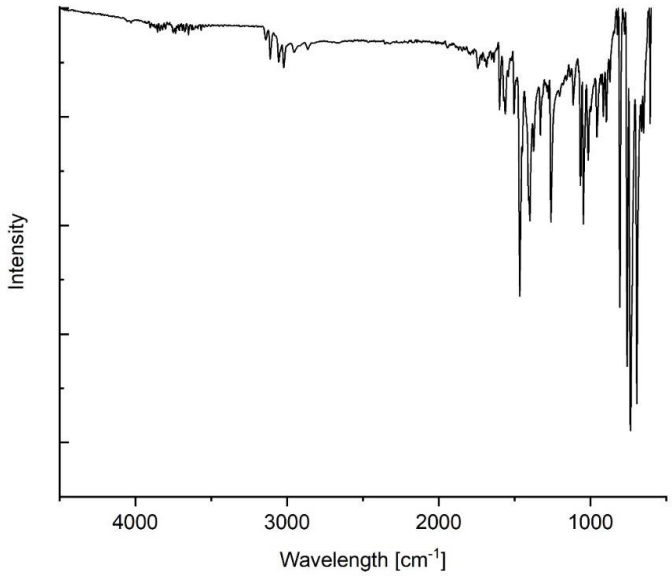

Figure S21: ATR-IR- spectrum of complex $Fe(bppz)_3$

Fe(CF_3ppz)$_3$

The complex was obtained as yellow powder (17.2%).

^{1}H-NMR (700.0 MHz, CD_3CN): δ = -75.17 (s, 1H, 2-*H*), -10.47 (s, 1H, 10-*H*), -3.39 (s, 1H, 9-*H*), -3.17 (s, 1H, 5-*H*), 0.27 (s, 1H, 6-*H*), 11.23 (s, 1H, 8-*H*) ppm.

^{13}C-NMR (176.1 MHz, CD_3CN): δ = -93.4 (1C, 3-*C*), -68.6 (1C, 6-*C*), 108.9 (1C, 8-*C*), 112.6 (1C, 9-*C*), 126.5 (1C, dd, $^1J_{CF}$ = 272.85 Hz 275.09 Hz, 4-*C*), 132.8 (1C, 10-*C*), 229.9 (1C, 5-*C*), 361.9 (1C, 2-*C*), 382.0 (1C, 7-*C*) ppm.

^{15}N-NMR (70.96 MHz, CD_3CN): 84.0 ppm.

^{19}F-NMR (659.0 MHz, CD_3CN): δ = -71.5 (s, 3F) ppm.

MS (ESI in MECN): m/z 689.0800 (for $C_{30}H_{18}F_9FeN_6$ calc. 689.0799).

Elemental analysis: calc. for $C_{30}H_{18}F_9FeN_6$: C: 52.27%, H: 2.63%, N: 12.19%, found: C: 51.90%, H: 2.81%, N: 12.12%.

IR (ATR, $\tilde{\nu}$ [cm^{-1}]): 3155w, 3033w, 2360w, 2335w, 1585w, 1508w, 1477w, 1396m, 1315s, 1272s, 1249m, 1159m, 1110s, 1066s, 1045s, 960m, 900m, 838w, 821w, 804m, 746s, 702m, 661m, 607w.

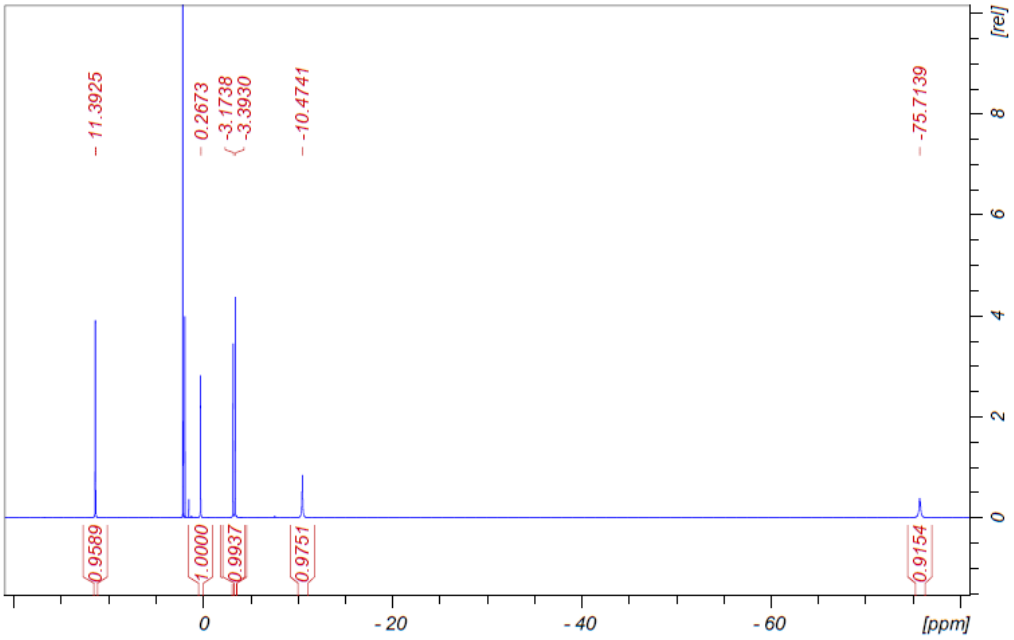

Figure S22:^{1}H-NMR spectra of complex Fe(CF_3ppz)$_3$ in CD_3CN

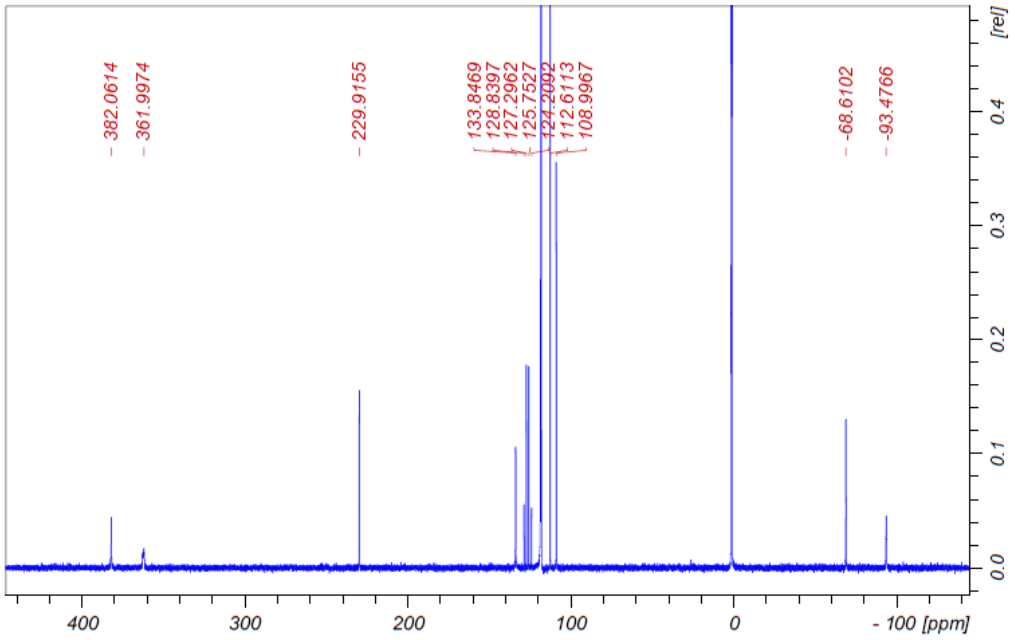

Figure S23: ^{13}C-NMR spectra of complex Fe(CF_3ppz)$_3$ in CD_3CN

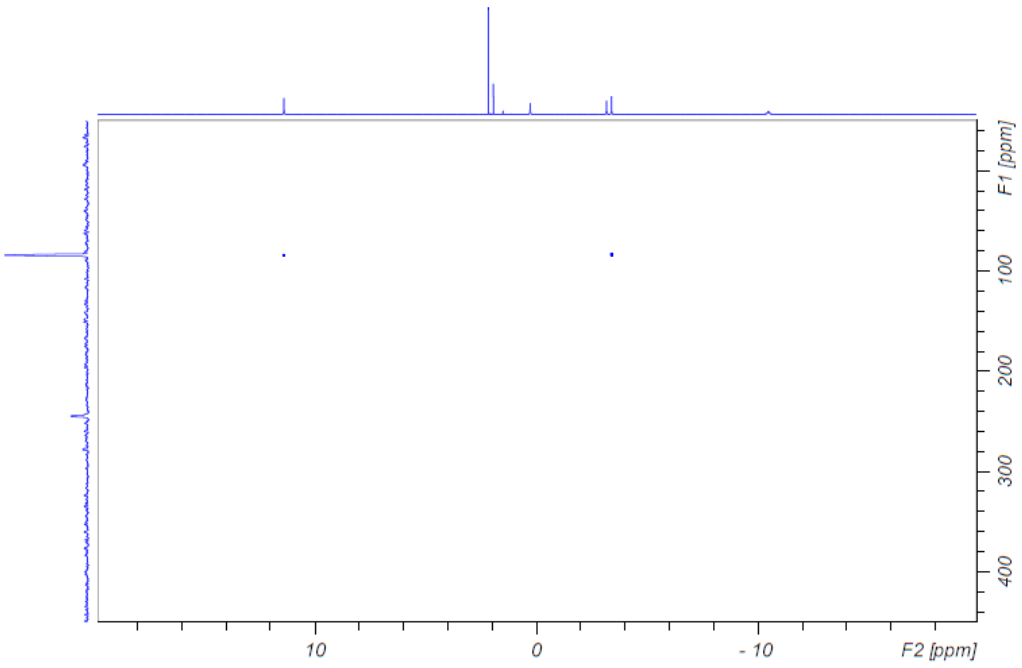

Figure S24: ^{15}N-HMBC spectrum of the complex Fe(CF_3ppz)$_3$ in CD_3CN

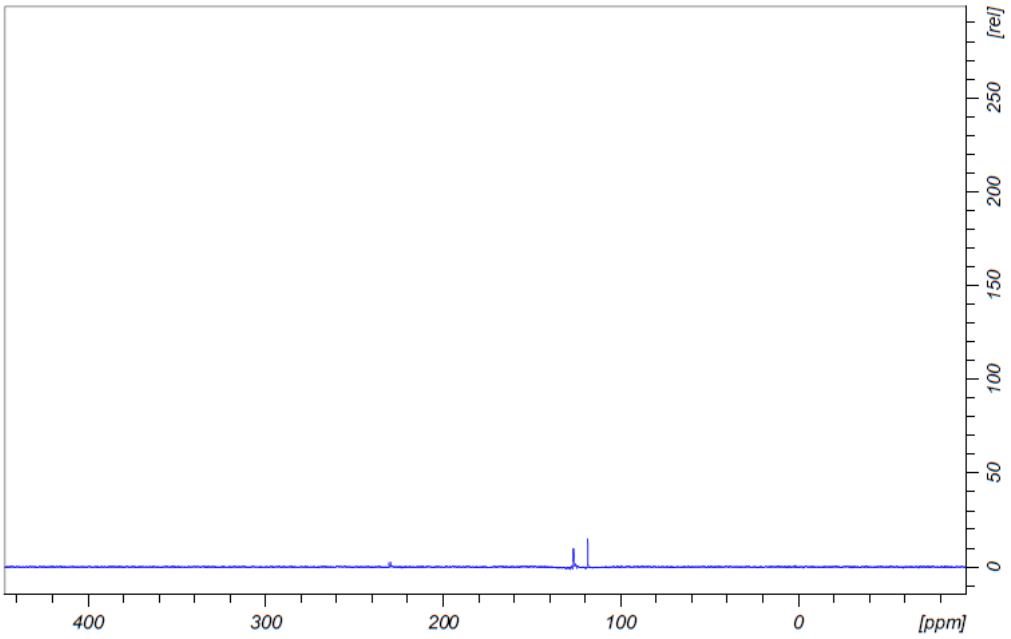

Figure S25:^{19}F-HMBC spectrum of the complex Fe(CF_3ppz)$_3$ in CD_3CN

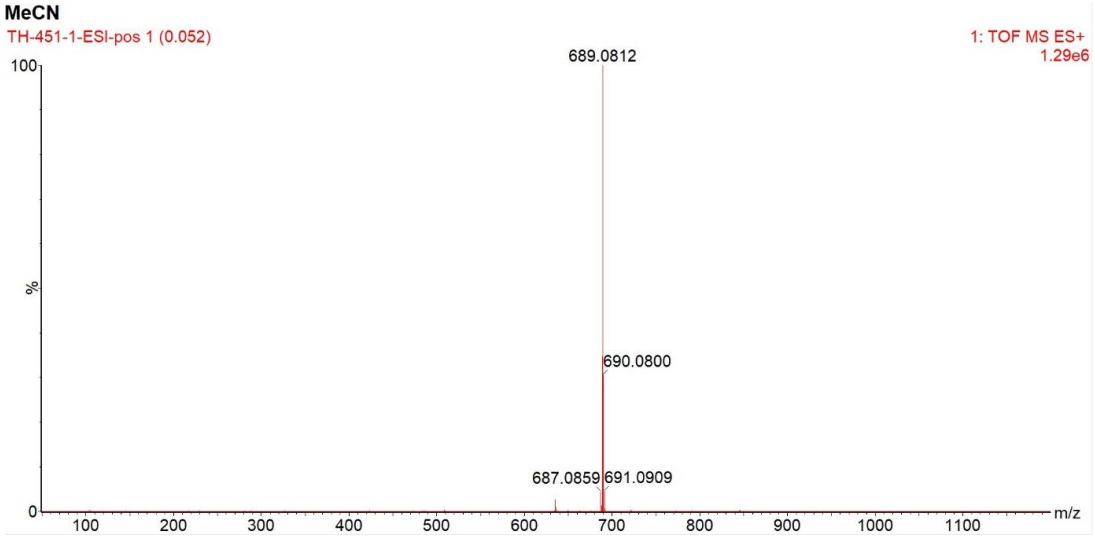

Figure S26: ESI-MS of complex Fe(CF_3ppz)$_3$ in CH_3CN

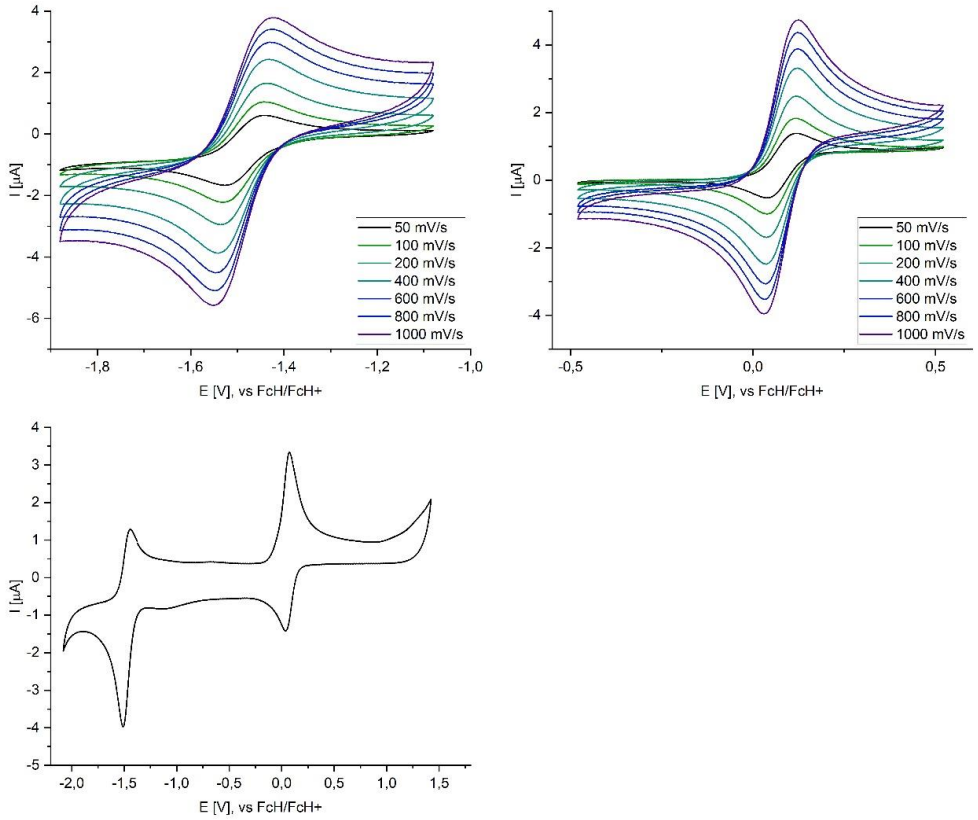

Figure S27: Cyclovoltammetry spectra of $Fe(CF_3ppz)_3$ in CH_3CN

Table S7: Cyclovoltammetry data for $Fe(CF_3ppz)_3$ at different scan rates, first redox step

SCANRATE	[MV/S]	50	100	200	400	600	800	1000
E_{PC}	[V]	-1,522	-1,524	-1,531	-1,539	-1,541	-1,544	-1,541
E_{PA}	[V]	-1,448	-1,443	-1,441	-1,439	-1,436	-1,439	-1,434
$E_{1/2}$	[V]	-1,48	-1,48	-1,49	-1,49	-1,49	-1,49	-1,49
ΔE	[V]	0,073	0,081	0,090	0,100	0,105	0,105	0,107
I_{PC}	[µA]	-1,13	-1,59	-2,25	-2,99	-3,50	-3,95	-4,24
I_{PA}	[µA]	1,10	1,48	2,02	2,63	3,03	3,35	3,63
I_{PA}/I_{PC}		-0,97	-0,93	-0,90	-0,88	-0,86	-0,85	-0,86

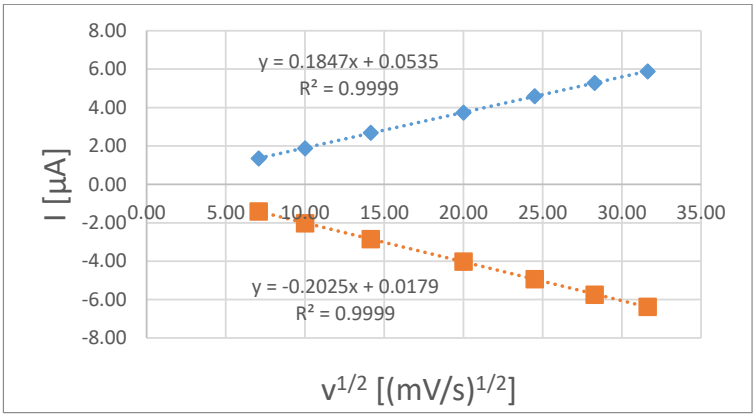

Figure S28: Plotted data of Randles-Sevcik-Equation $Fe(CF_3ppz)_3$ at different scan rates, first redox step

Table S8: Cyclovoltammetry data for $Fe(CF_3ppz)_3$ at different scan rates, second redox step

SCANRATE	[MV/S]	50	100	200	400	600	800	1000
E_{PC}	[V]	0,045	0,040	0,037	0,037	0,035	0,037	0,033
E_{PA}	[V]	0,113	0,113	0,118	0,120	0,123	0,118	0,118
$E_{1/2}$	[V]	0,08	0,08	0,08	0,08	0,08	0,08	0,08
ΔE	[V]	0,068	0,073	0,081	0,083	0,088	0,081	0,085
I_{PC}	[µA]	-1,11	-1,55	-2,22	-3,02	-3,63	-4,11	-4,54
I_{PA}	[µA]	1,03	1,47	2,04	2,79	3,33	3,77	4,13
I_{PA}/I_{PC}		-0,93	-0,95	-0,92	-0,92	-0,92	-0,92	-0,91

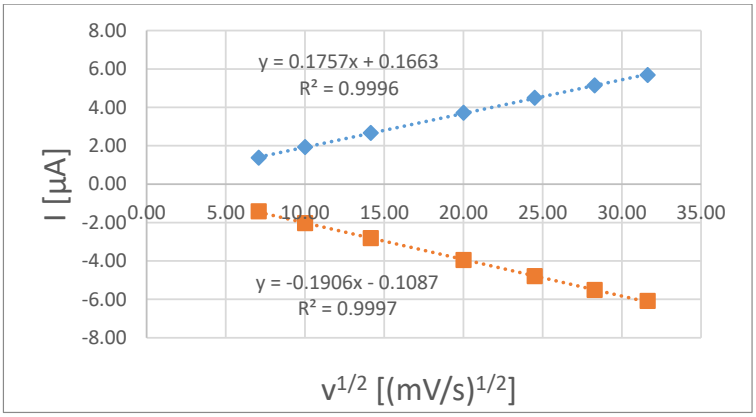

Figure 29: Plotted data of Randles-Sevcik-Equation $Fe(CF_3ppz)_3$ at different scan rates, first redox step

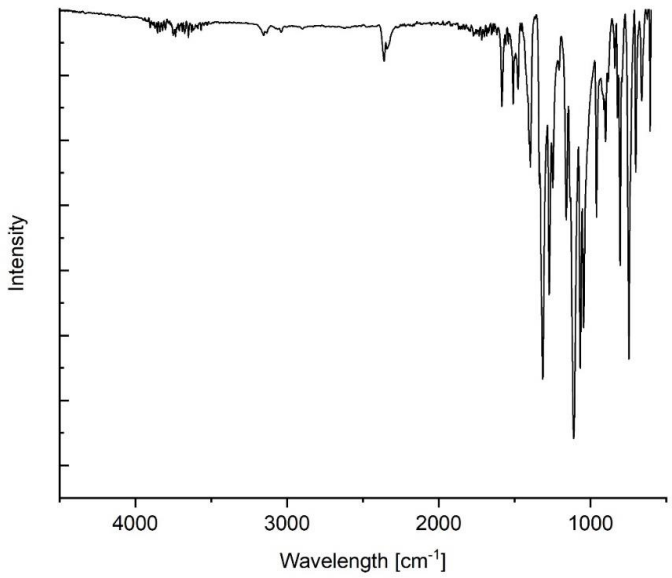

Figure S30: ATR-IR-spectrum of complex $Fe(CF_3ppz)_3$

Fe(naphpz)$_3$

The complex was obtained as red powder (5.3%).

^{1}H-NMR (700 MHz, DMSO-d6): δ = -85.19 (s, 1H, 2-*H*), -12.51 (s, 1H, 13-*H*), -1.68 (d, $^3J_{HH}$ = 6.3 Hz, 1H, 4-*H*), -1.31 (s, 1H, 12-*H*), 1.10 (s, 1H, 9-*H*), 1.25 (t, $^3J_{HH}$ = 7.10 Hz, 1H, 6-*H*), 8.12 (t, $^3J_{HH}$ = 6.30 Hz, 1H, 5-*H*), 11.15 (s, 1H, 11-*H*), 12.83 (d, $^3J_{HH}$ = 8.50 Hz, 1H, 7-*H*) ppm.

^{13}C-NMR* (176.1 MHz, DMSO-d6): δ = -97.6 (1C, 3-*C*), -56.79 (1C, 150.66 Hz, 9-*C*), 80.3 (1C, 150.66 Hz, 7-*C*), 81.6 (1C, 160.34 Hz, 5-*C*), 99.4 (1C, 180.91 Hz, 12-*C*), 124.3 (2C, 188.74 Hz, 11-*C*), 126.6 (1C, 188.74 Hz, 13-*C*), 172.1 (2C, 157.98 Hz, 6-*C*), 180.5 (1C, 157.98 Hz, 4-*C*), 216.3 (1C, 8-*C*), 365.3 (1C, 2-*C*), 413.9 (1C, 10-*C*) ppm.

MS (ESI in MECN): m/z 635.1640 (for $C_{39}H_{27}FeN_6$ calc. 635.1647).

Elemental analysis: calc. for $C_{39}H_{27}FeN_6$: C: 73.71%, H: 4.28%, N: 13.22%, found: C: 74.29%, H: 5.10%, N: 12.42%. **IR** (ATR, $\tilde{\upsilon}$ [cm^{-1}]): 3126w, 6047w, 2917w, 2854w, 1585w, 1593w, 1560w, 1510w, 1486w,

1459m, 1405m, 1332w, 1313w, 1251w, 1197w, 1134w, 1107w, 1062m, 1037w, 977w, 935w, 889w, 856m, 831w, 736s, 682w, 651w.

*not decoupled

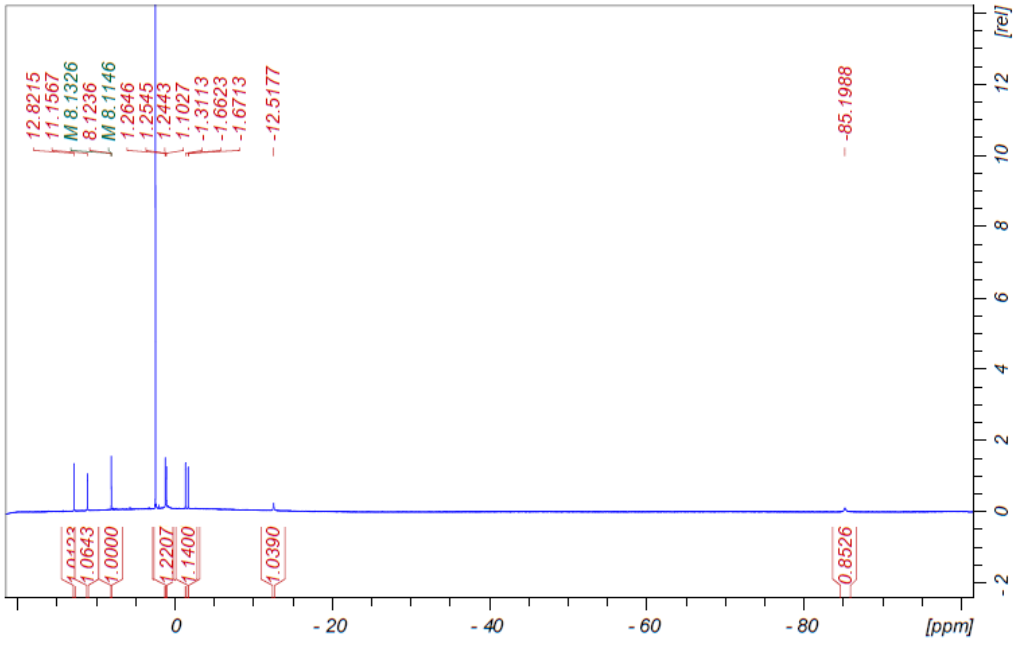

Figure S31: ^{1}H-NMR spectrum of complex Fe(naphpz)$_3$ in DMSO-d^6

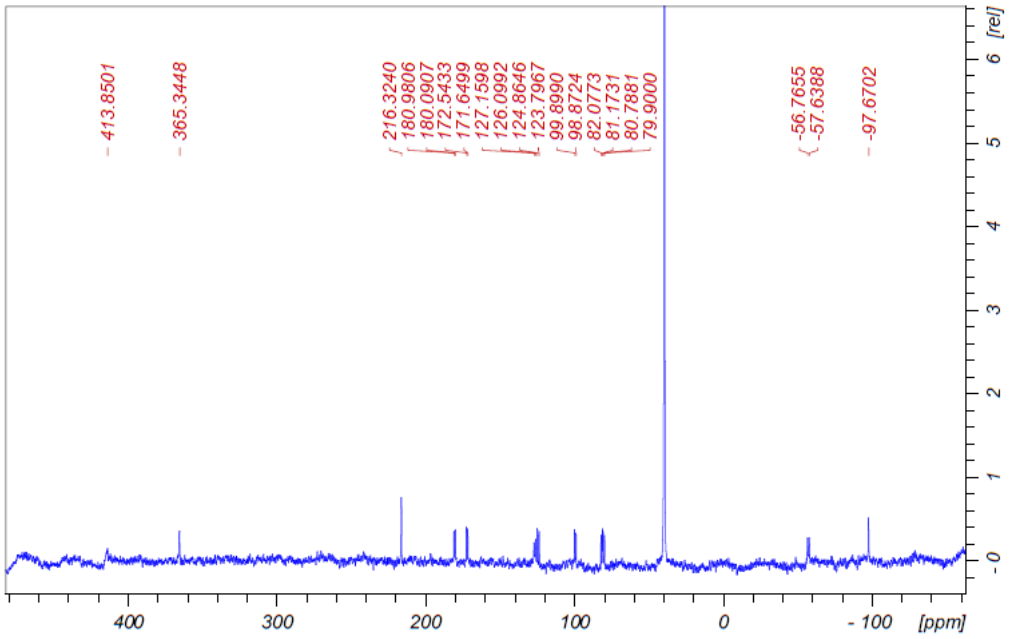

Figure S32: ^{13}C-NMR spectrum of complex Fe(naphpz)$_3$ in DMSO-d^6

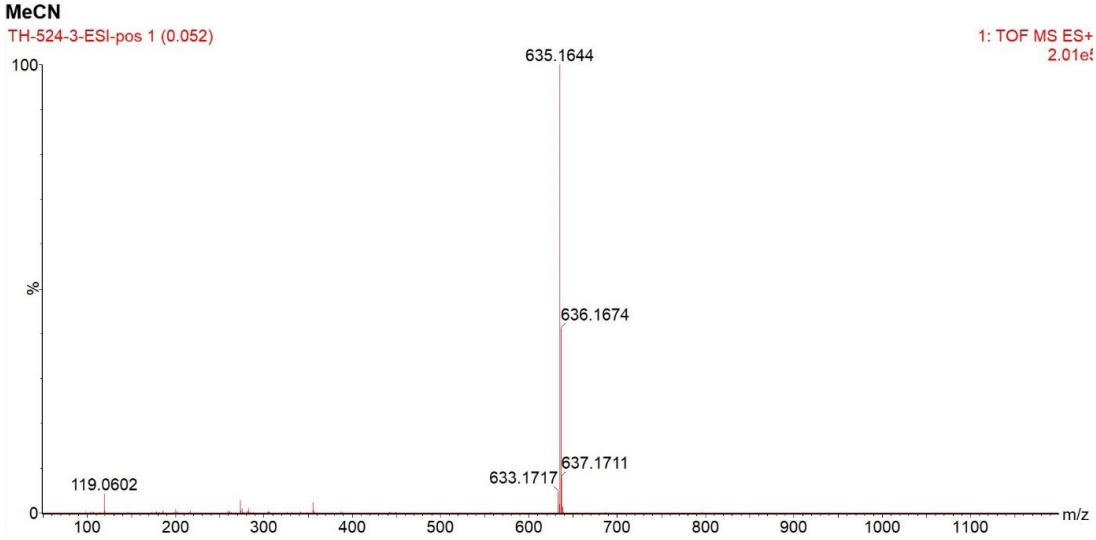

Figure S33: ESI-MS spectrum of complex Fe(naphpz)$_3$ in CH_3CN

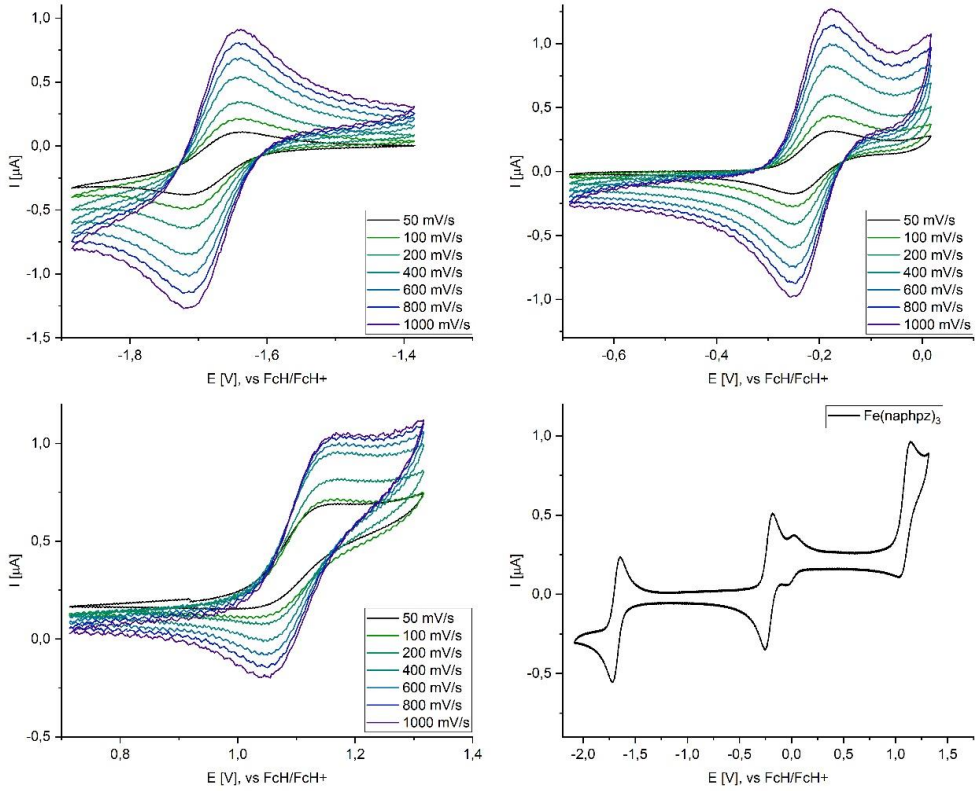

Figure S34: Cyclovoltammetry spectra of complex Fe(naphpz)$_3$ in CH_3CN

Table S9: Cyclovoltammetry data for $Fe(naphpz)_3$ at different scan rates, first redox step

SCANRATE	[MV/S]	50	100	200	400	600	800	1000
E_{PC}	[V]	-1,712	-1,712	-1,712	-1,717	-1,714	-1,709	-1,714
E_{PA}	[V]	-1,638	-1,641	-1,648	-1,643	-1,648	-1,648	-1,643
$E_{1/2}$	[V]	-1,68	-1,68	-1,68	-1,68	-1,68	-1,68	-1,68
ΔE	[V]	0,073	0,071	0,064	0,073	0,066	0,061	0,071
I_{PC}	[µA]	-0,18	-0,21	-0,39	-0,53	-0,59	-0,77	-0,81
I_{PA}	[µA]	0,18	0,25	0,37	0,56	0,62	0,75	0,88
I_{PA}/I_{PC}		-1,02	-1,18	-0,95	-1,05	-1,04	-0,98	-1,08

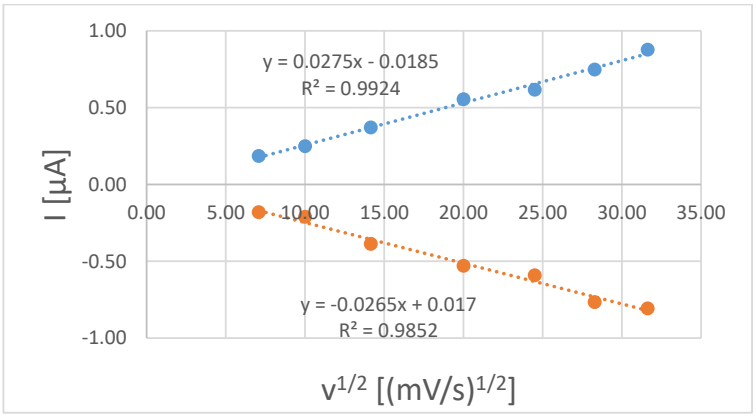

Figure S35: Plotted data of Randles-Sevcik-Equation $Fe(naphpz)_3$ at different scan rates, first redox step

Table S10: Cyclovoltammetry data for $Fe(naphpz)_3$ at different scan rates, second redox step

SCANRATE	[MV/S]	50	100	200	400	600	800	1000
E_{PC}	[V]	-0,248	-0,251	-0,246	-0,251	-0,257	-0,243	-0,253
E_{PA}	[V]	-0,177	-0,182	-0,182	-0,192	-0,191	-0,190	-0,185
$E_{1/2}$	[V]	-0,21	-0,22	-0,21	-0,22	-0,22	-0,22	-0,22
ΔE	[V]	0,071	0,068	0,063	0,059	0,066	0,054	0,068
I_{PC}	[µA]	-0,15	-0,22	-0,35	-0,65	-0,83	-0,71	-0,79
I_{PA}	[µA]	0,17	0,19	0,32	0,52	0,65	0,55	0,60
I_{PA}/I_{PC}		-1,10	-0,86	-0,91	-0,80	-0,79	-0,76	-0,76

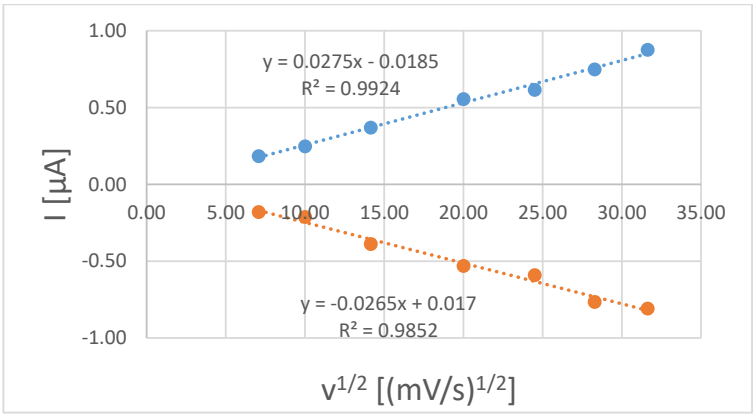

Figure S36: Plotted data of Randles-Sevcik-Equation $Fe(naphpz)_3$ at different scan rates, second redox step

Table S11: Cyclovoltammetry data for $Fe(naphpz)_3$ at different scan rates, second redox step

SCANRATE	[MV/S]	50	100	200	400	600	800	1000
E_{PC}	[V]	1,037	1,035	1,057	1,049	1,057	1,059	1,062
E_{PA}	[V]	1,125	1,130	1,127	1,140	1,130	1,127	1,125
$E_{1/2}$	[V]	1,08	1,08	1,09	1,09	1,09	1,09	1,09
ΔE	[V]	0,088	0,095	0,071	0,090	0,073	0,068	0,063
I_{PC}	[µA]	-0,18	-0,30	-0,37	-0,44	-0,51	-0,54	-0,61
I_{PA}	[µA]	0,20	0,25	0,35	0,43	0,46	0,50	0,52
I_{PA}/I_{PC}		-1,07	-0,84	-0,94	-0,98	-0,90	-0,92	-0,86

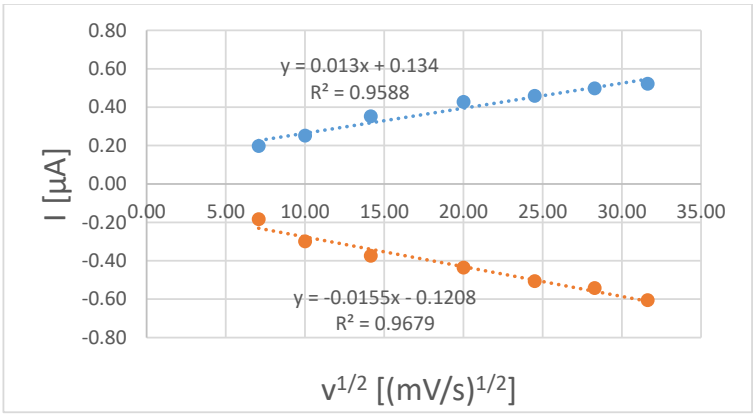

Figure S37: Plotted data of Randles-Sevcik-Equation $Fe(naphpz)_3$ at different scan rates, first redox step

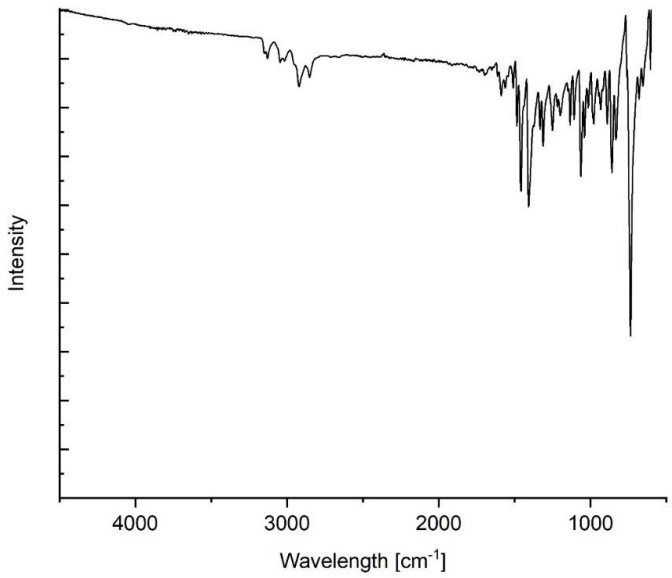

Figure S38: ATR-IR-spectrum of complex $Fe(naphpz)_3$ in CH_3CN

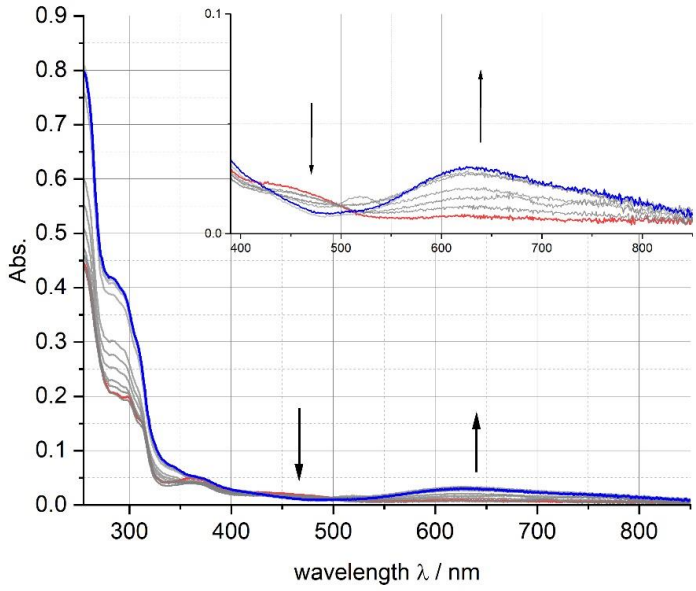

Figure S39: Change in the absorptive behaviour of $(Fe(naphpz)_3$ with an applied potential of 0.8-2 V in CH_3CN

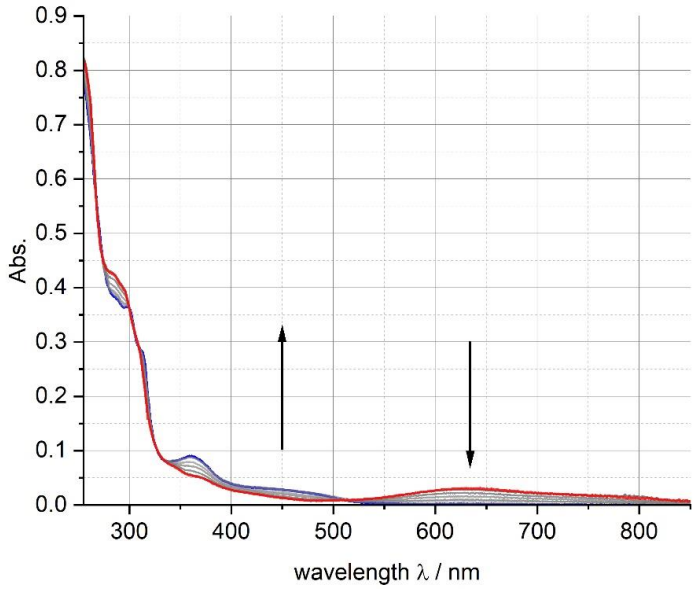

Figure S40: Change in the absorptive behaviour of $(Fe(naphpz)_3$ with an applied potential of -0.5-(-1.5) V in CH_3CN

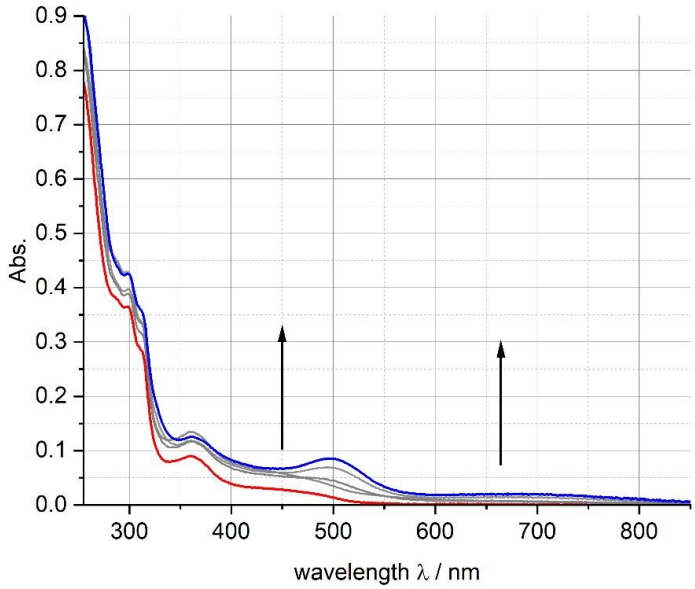

Figure S41: Change in the absorptive behaviour of $(Fe(naphpz)_3$ with an applied potential of -2.5 V in CH_3CN

Fe(MeOppz)$_3$

The complex was obtained as red powder (2.6%).

^{1}H-NMR (700 MHz, CD_3CN): δ = -79.93 (s, 1H, 2-*H*), -10.34 (s, 1H, 10-*H*), -5.36 (s, 1H, 6-*H*)), -5.12 (s, 1H, 5-*H*), -3.19 (s, 1H, 9-*H*), 1.44 (s, 3H, 4-*H*), 12.06 (s, 1H, 8-*H*) ppm.

^{13}C-NMR* (176.1 MHz, CD_3CN): δ = -106.1 (1C, 156.6 Hz, 6-*C*), -93.0 (1C, 3-*C*), 49.1 (1C, 139.07 Hz, 4-*C*), 103.9 (1C, 182.9 Hz, 8-*C*), 114.1 (1C, 191.7 Hz, 9-*C*) 130.1 (1C, 182.9 Hz, 10-*C*), 232.4 (1C, 159.9 Hz, 5-*C*), 360.8 (1C, 129.6 Hz, 2-*C*), 403.2 (1C, 7-*C*) ppm.

^{15}N-NMR (70.96 MHz, CD_3CN): 80.2 ppm.

MS (ESI in MECN): m/z 575.1530 (for $C_{30}H_{27}FeN_6O_3$ calc. 575.1494).

Elemental analysis: calc. for $C_{30}H_{27}FeN_6O_3$: C: 62.62%, H: 4.73%, N: 14.61%, found: C:62.49%, H: 5.19%, N: 14.35%.

IR (ATR, $\tilde{\upsilon}$ [cm^{-1}]): 3122w, 3039w, 3006w, 2952w, 2931w, 2902w, 2829w, 1583w, 1560s, 1506w, 1469s, 1417s, 1315m, 1276s, 1249m, 1209s, 1174s, 1116m, 1031s, 958m, 879m, 811w, 784s, 744s, 661w, 621m, 609m.

*not decoupled

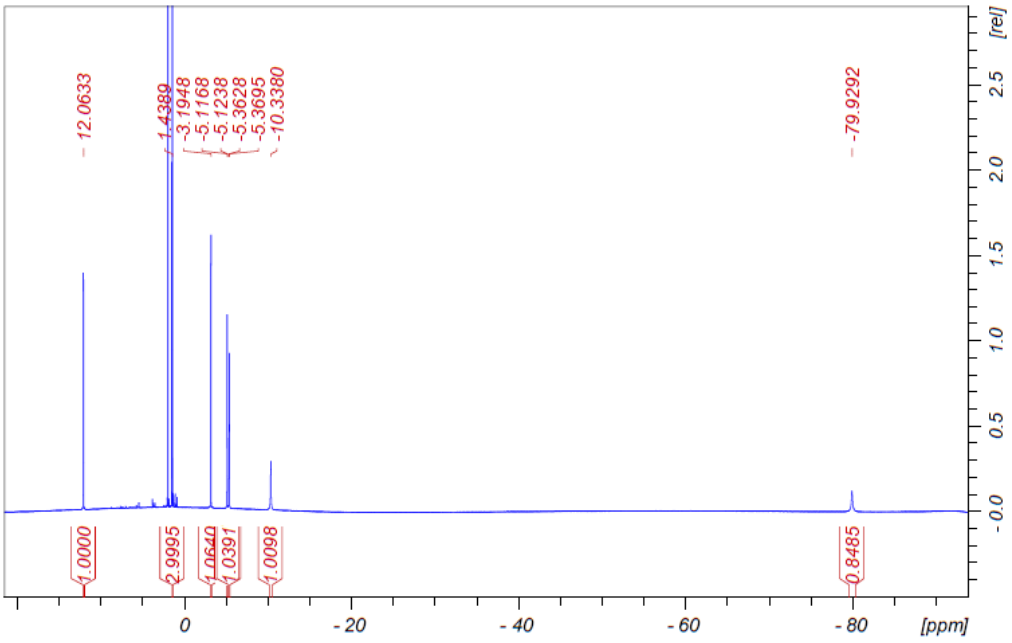

Figure S42: ^{1}H-NMR spectrum of complex Fe(MeOppz)$_3$ in CD_3CN

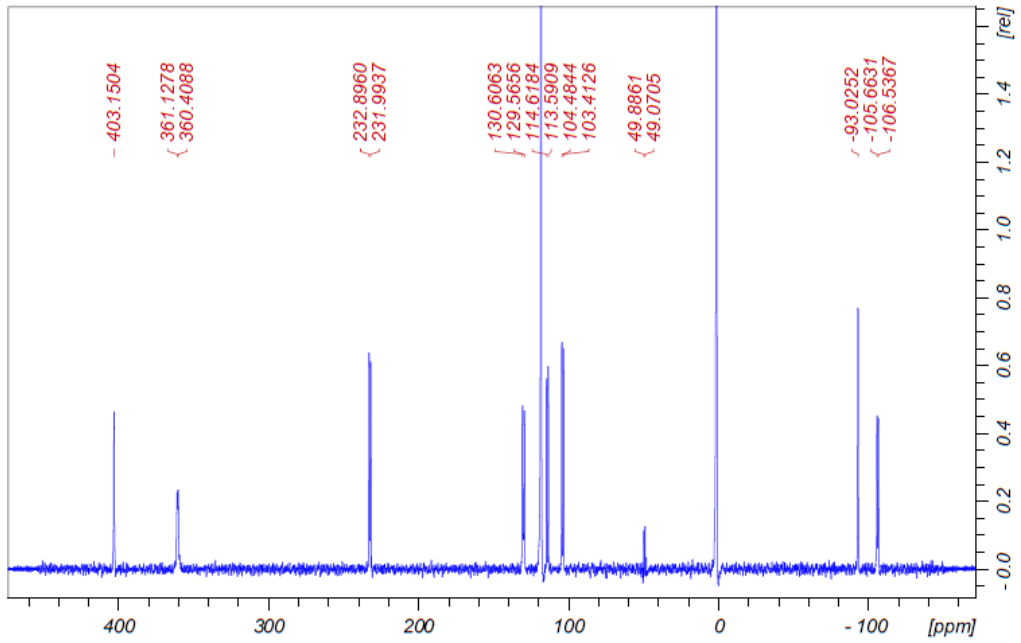

Figure S43: ^{13}C-NMR spectrum of complex Fe(MeOppz)$_3$ in CD_3CN

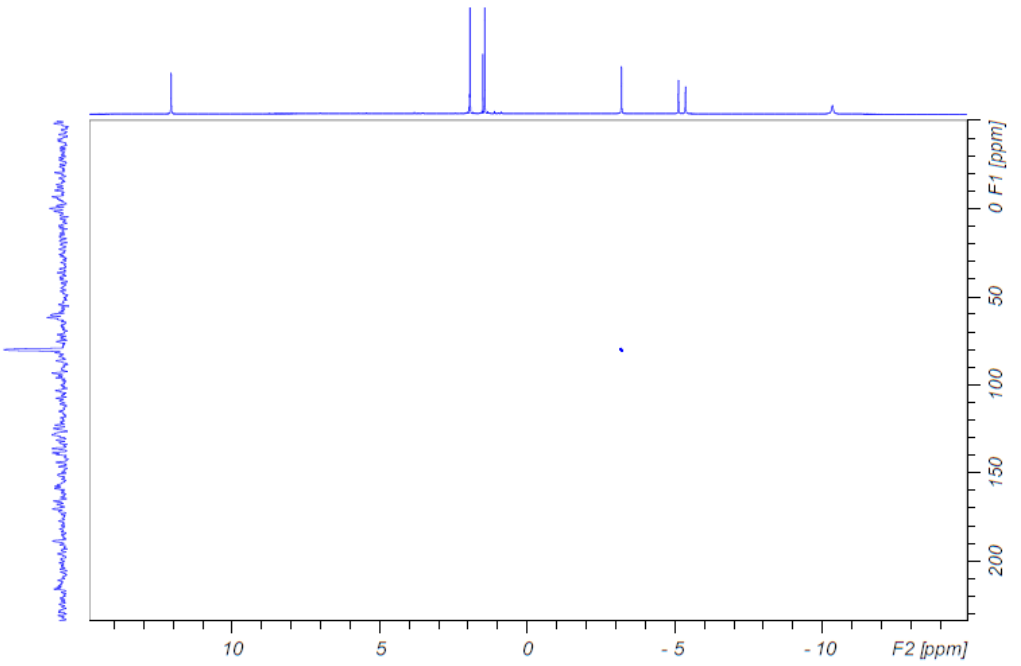

Figure S44: ^{15}N-HMBC spectrum of Fe(MeOppz)$_3$ in CD_3CN

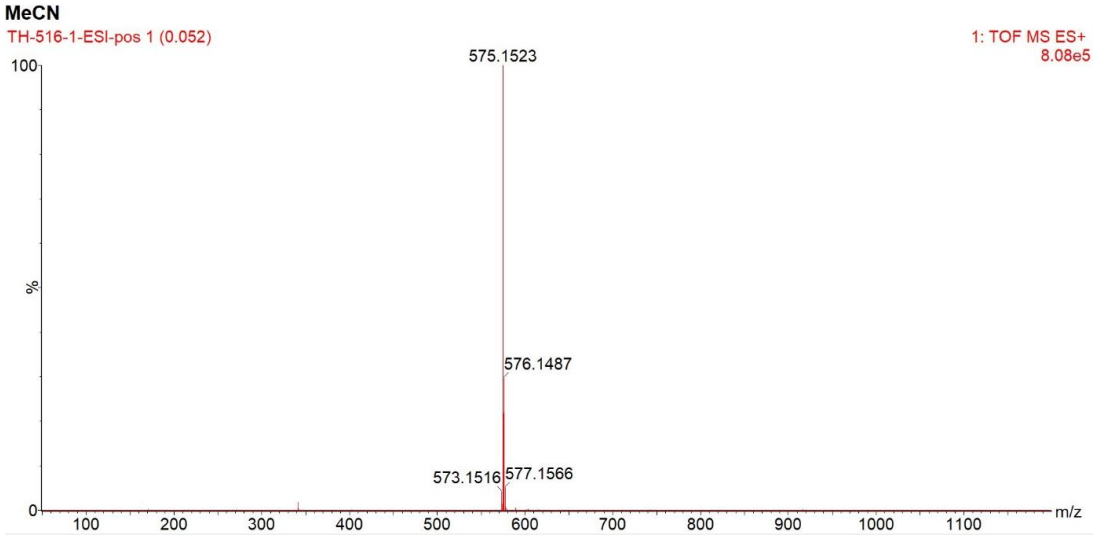

Figure S45: ESI-MS spectrum of complex Fe(MeOppz)$_3$ in CH_3CN

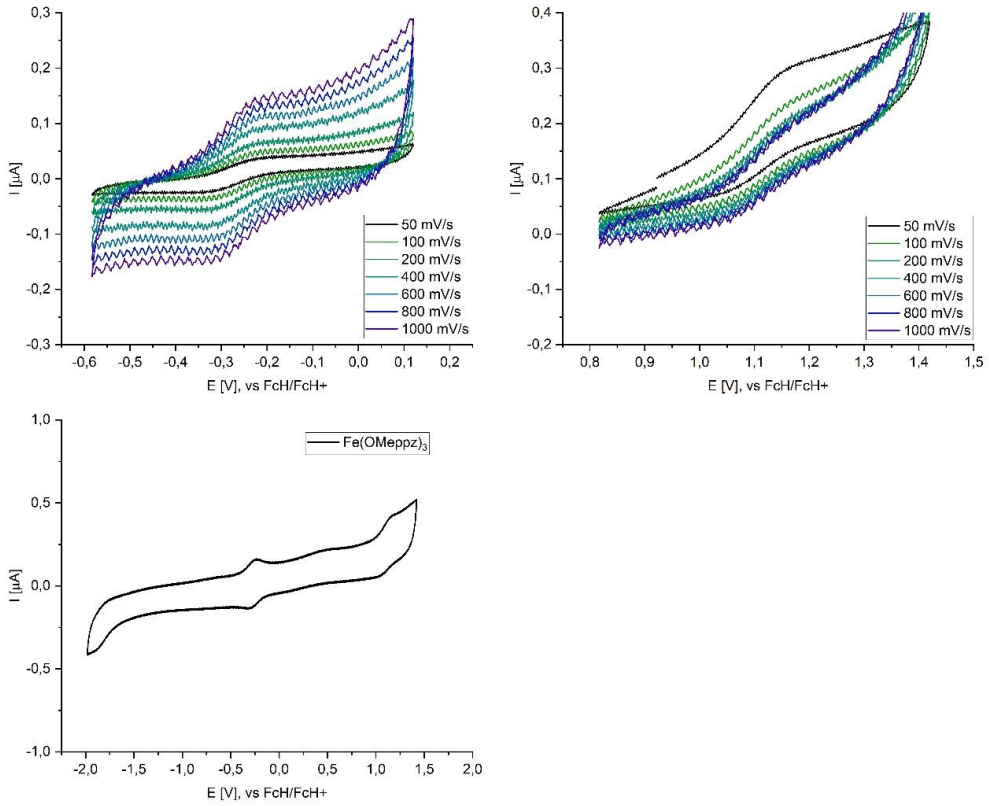

Figure S46: Cyclovoltammetry spectra of complex Fe(MeOppz)$_3$ in CH_3CN

Table S12: Cyclovoltammetry data for $Fe(MeOppz)_3$ at different scan rates, first redox step

SCANRATE	[MV/S]	50	100	200	400	600	800	1000
E_{PC}	[V]	-1,746	-1,753	-1,751	-1,748	-1,751	-1,748	-1,751
E_{PA}	[V]	-1,814	-1,812	-1,814	-1,812	-1,817	-1,814	-1,819
$E_{1/2}$	[V]	-1,78	-1,78	-1,78	-1,78	-1,78	-1,78	-1,78
ΔE	[V]	-0,068	-0,059	-0,063	-0,063	-0,066	-0,066	-0,068
I_{PC}	[µA]	-1,18	-1,61	-2,34	-3,35	-4,11	-4,71	-5,33
I_{PA}	[µA]	1,27	1,80	2,52	3,59	4,37	5,03	5,57
I_{PA}/I_{PC}		-1,08	-1,12	-1,08	-1,07	-1,06	-1,07	-1,04

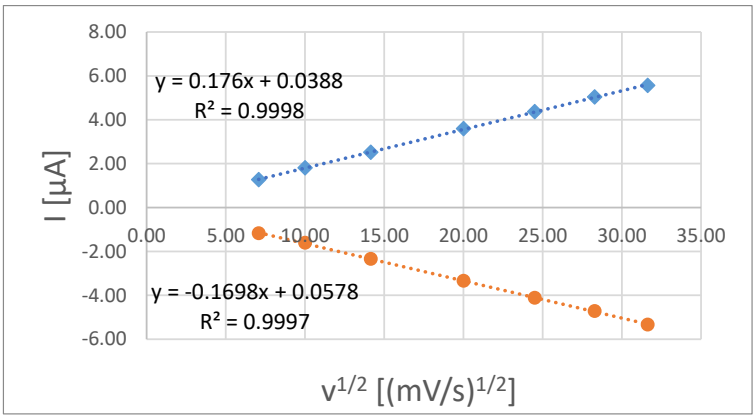

Figure S47: Plotted data of Randles-Sevcik-Equation $Fe(MeOppz)_3$ at different scan rates, first redox step

Table S13: Cyclovoltammetry data for $Fe(MeOppz)_3$ at different scan rates, second redox step

SCANRATE	[MV/S]	50	100	200	400	600	800	1000
E_{PC}	[V]	-0,268	-0,265	-0,265	-0,275	-0,268	-0,265	-0,265
E_{PA}	[V]	-0,207	-0,204	-0,197	-0,199	-0,197	-0,199	-0,207
$E_{1/2}$	[V]	-0,24	-0,23	-0,23	-0,24	-0,23	-0,23	-0,24
ΔE	[V]	0,061	0,061	0,068	0,076	0,071	0,066	0,059
I_{PC}	[µA]	-1,28	-1,72	-2,54	-3,62	-4,41	-5,05	-5,62
I_{PA}	[µA]	1,27	1,82	2,56	3,52	4,35	5,06	5,61
I_{PA}/I_{PC}		-0,99	-1,06	-1,01	-0,97	-0,99	-1,00	-1,00

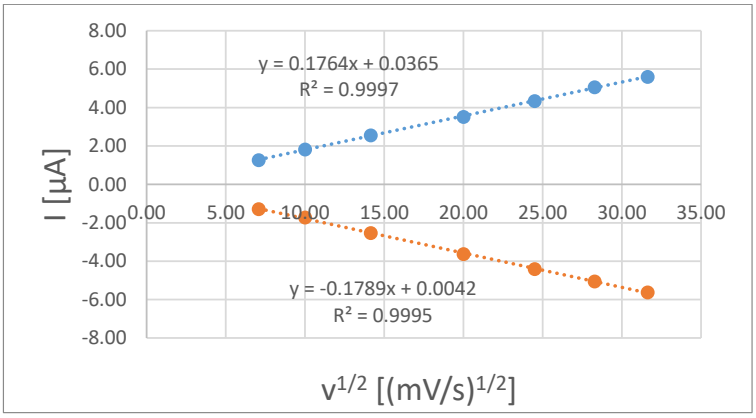

Figure S48: Plotted data of Randles-Sevcik-Equation $Fe(MeOppz)_3$ at different scan rates, second redox step

Table S14: Cyclovoltammetry data for $Fe(MeOppz)_3$ at different scan rates, second redox step

SCANRATE	[MV/S]	50	100	200	400	600	800	1000
E_{PC}	[V]	1,023	1,023	1,027	1,018	1,018	1,013	1,013
E_{PA}	[V]	1,091	1,088	1,096	1,093	1,103	1,103	1,106
$E_{1/2}$	[V]	1,06	1,06	1,06	1,06	1,06	1,06	1,06
ΔE	[V]	0,068	0,066	0,068	0,076	0,086	0,090	0,093
I_{PC}	[µA]	-1,29	-1,73	-2,10	-3,24	-3,84	-4,31	-4,72
I_{PA}	[µA]	0,94	1,38	1,90	2,71	3,27	3,67	4,05
I_{PA}/I_{PC}		-0,73	-0,80	-0,91	-0,84	-0,85	-0,85	-0,86

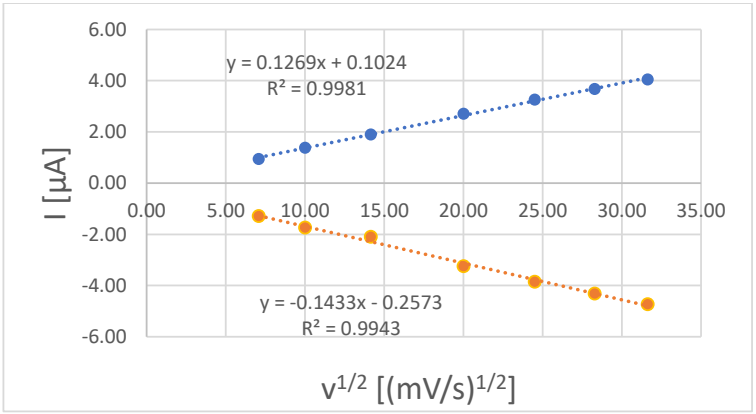

Figure S49: Plotted data of Randles-Sevcik-Equation $Fe(MeOppz)_3$ at different scan rates, third redox step

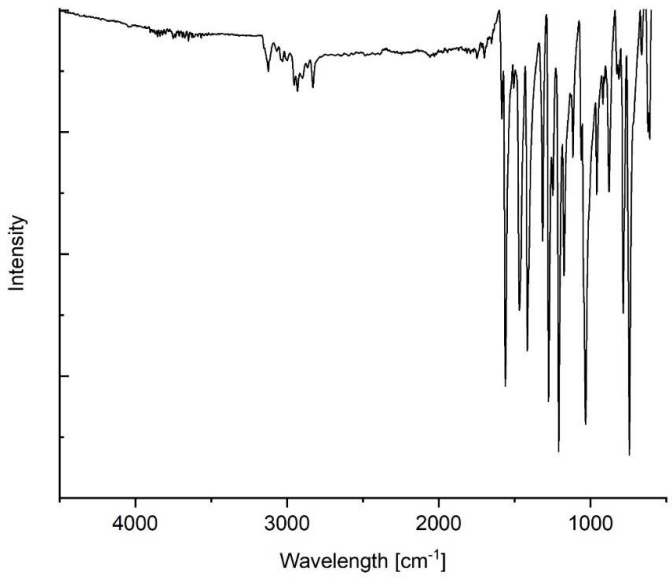

Figure S50: ATR-IR spectrum of complex $Fe(MeOppz)_3$

Illumination Experiments

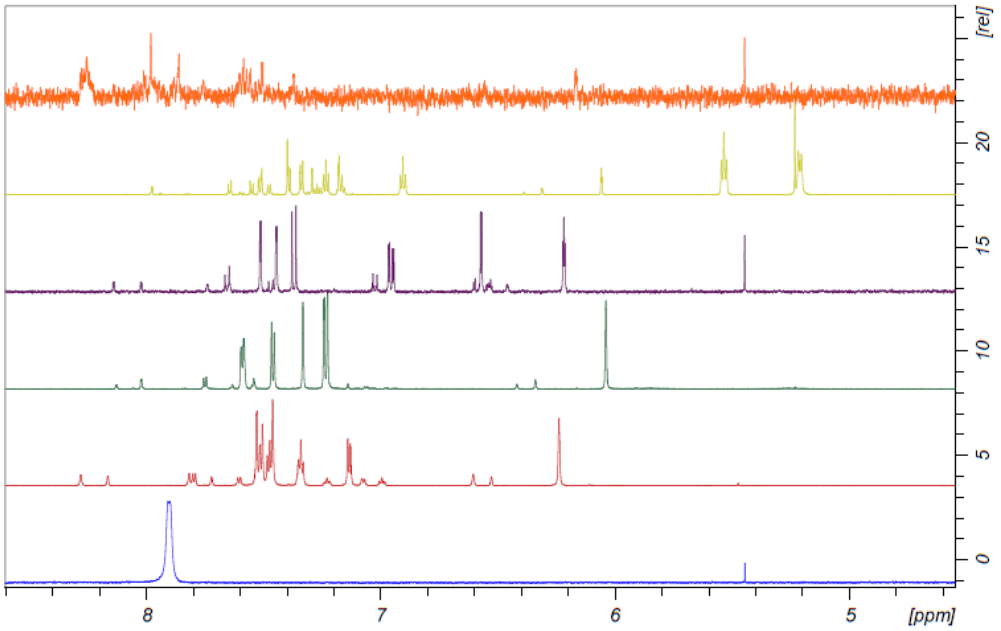

Figure S51: Experiments on complex stability in acetonitrile solution: before illumination of $Fe(ppz)_3$ (blue), after illumination of 24 h: $Fe(ppz)_3$ (red), $Fe(CF_3ppz)_3$ (green), $Fe(MeOppz)_3$ (purple), $Fe(bppz)_3$ (yellow), Fe)naphpz)$_3$ (orange, pure solubility decreases signal intensity)

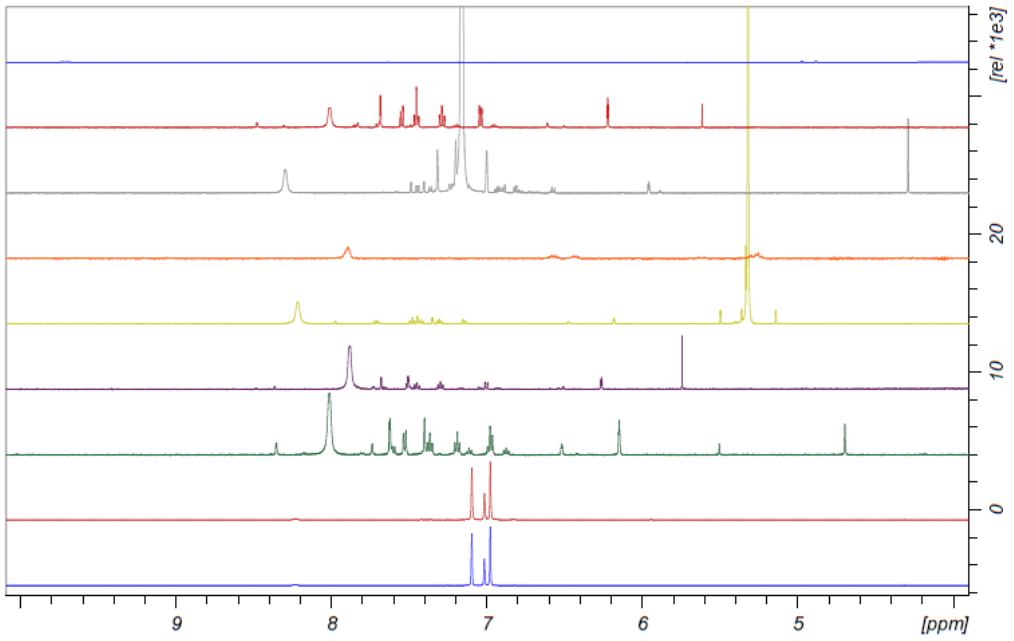

Figure S52: Experiments on complex stability exemplarily for $Fe(ppz)_3$, bottom blue: before illumination in toluene (blue), from there upwards after illumination: toluene (red), THF (green), DMSO (pruple), DCM (yellow), BuCN (orange), benzene (grey), acetone (red), 2Me-THF (blue).

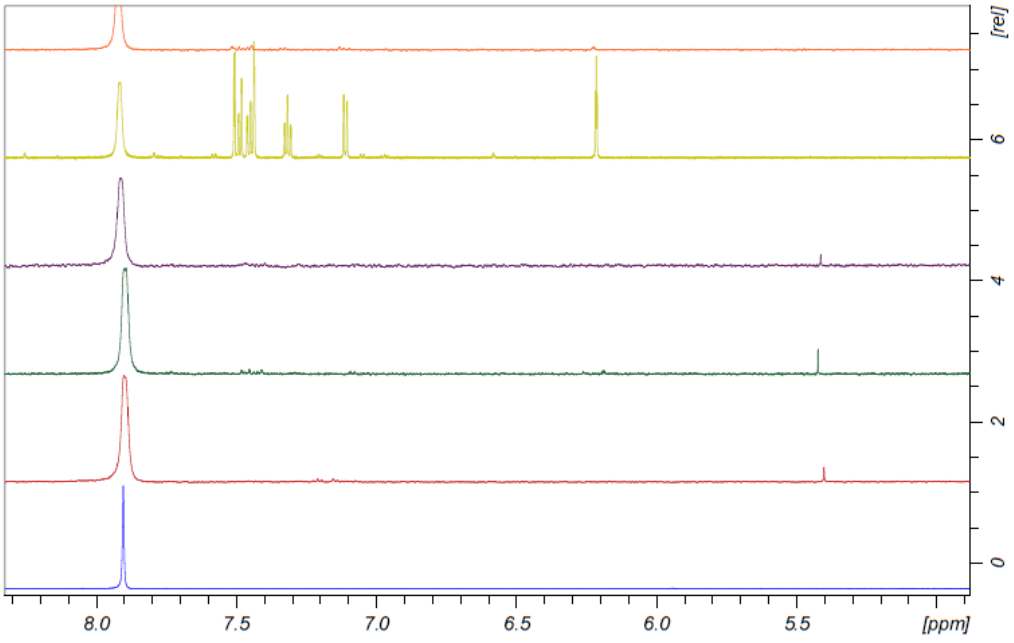

Figure S53: Decomposition of $Fe(ppz)_3$, with different filters. Blue: before irradiation; red: 320 nm bandwidth filter, green: 360 nm bandwidth filter, purple: 390 bandwidth filter; yellow: 400 longpass filter, orang: 495 longpassfilter. At 7.90 ppm complex signal, additional diamagnetic species in yellow spectra is the product of the reductive elimination.

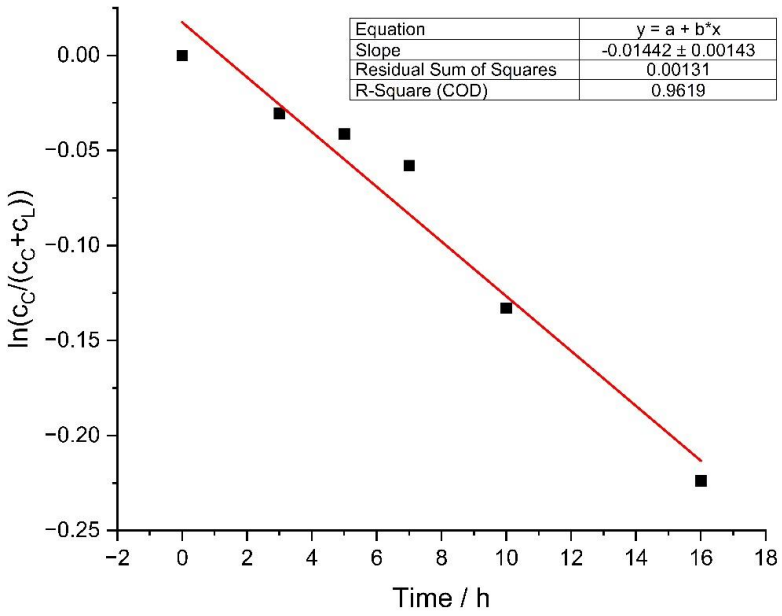

Figure S54: Calculated slope of the decomposition of $Fe(ppz)_3$, based on the relative intensities of TMS, the product of the reductive illumination at 6.21 ppm and the complex resonance at 7.90 ppm.

Computational

Table S15: Differential Gibbs free energy of PbEh-3c optimized structures excluding and including the SMD model for MeCN and BuCN implemented in ORCA. Negative values account for higher stability.

	Δ Gibbs free energy [kcal/mol]		
solvent	none	MeCN	BuCN
***fac*-Co(ppz)$_3$**	0	-30.67	-32.05
***fac*-Fe(ppz)$_3$**	0	-31.35	-32.73
Co(II) species	0	-58.16	-59.10
Fe(II) species	0	-58.9	-59.91

Table S16: Absolute an differential Gibbs free energy of PbEh-3c optimized structures of fac- and mer- isomers.

	Gibbs energy [kcal·mol^{-1}]		
	***fac*-isomer**	***mer*-isomer**	**Δ(fac-mer)**
Fe(naphpz)$_3$	-1946262.77	-1946262.19	-0.58
Fe(bppz)$_3$	-2092187.62	-2092186.16	-1.46
Fe(MeOppz)$_3$	-1872534.07	-1872536.20	2.13
Fe(CF$_3$ppz)$_3$	-2292413.78	-2292412.94	-0.84
Fe(ppz)$_3$	-1656600.74	-1656600.11	-0.63

Table S17: Comparison of the bond length and binding angles for the single crystal structure analysis and PBEh-3c geometry optimized fac-complexes.

	Experimental data			**Computational data**		
complex	Ø Fe-N [Å]	Ø Fe-C [Å]	∢ C-Fe-N [°]	Ø Fe-N [Å]	Ø Fe-C [Å]	∢ C-Fe-N$_{(ax)}$ [°]
Fe(naphpz)$_3$	2.0134(12)	1.9530(17)	169.99(7)	2.019	1.952	174.5
Fe(bppz)$_3$	2.0122(7)	1.9536(7)	172.90(1)	2.018	1.952	174.8
Fe(MeOppz)$_3$	2.0129(15)	1.9512(13)	170.89(5)	2.020	1.956	174.3
Fe(CF$_3$ppz)$_3$	2.0075(15)	1.9520(16)	170.46(6)	2.015	1.956	174.5
Fe(ppz)$_3$	2.0030(15)	1.9508(13)	171.54(7)	2.020	1.954	173.7

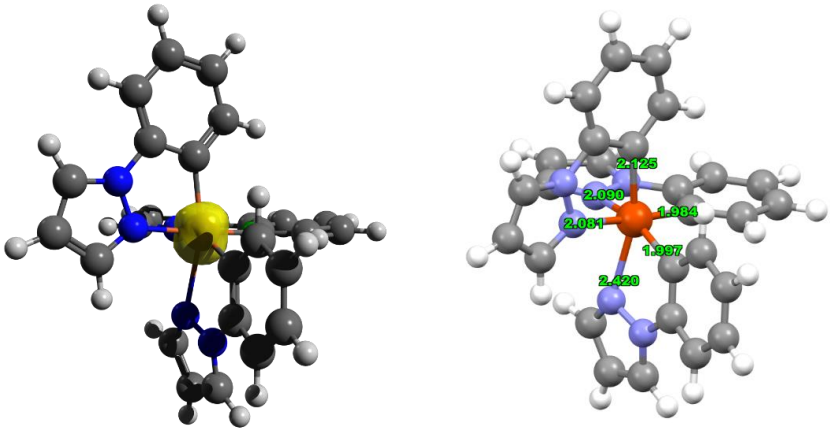

Figure S55: PBEh-3c optimized lowest quartet state of fac-**Fe(ppz)$_3$**. *Left*: Spin density plot. *Right*: Depicted Fe-ligand bond lengths.

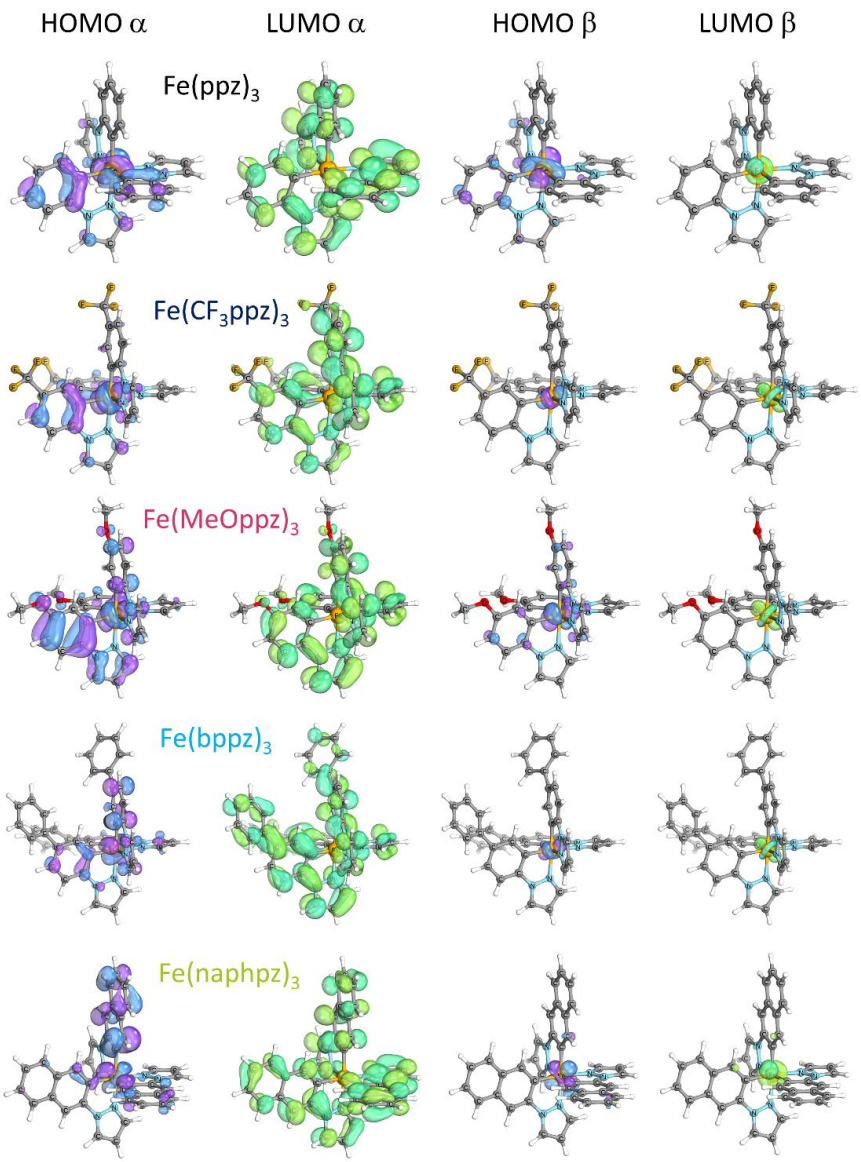

Figure S56: TPSSh/def2-TZVP calculated spatial distribution of the frontier orbitals of the respective complexes.

Table S18: Analysis of the main acceptor and donor orbital contribution to the TD-DFT calculated vertical transitions (Fig. 5) of fac-Fe(ppz)$_3$. The lettering of the transitions a-h refers to the assigned transitions in Fig. 5. Additionally, the calculated wavelength λ and oscillator strength *f* is given for the selected transitions.

Transition	Main Donor Orbitals	Main Acceptor Orbitals	Contribution to the transition
a *λ = 451 nm,* *f = 0.0022*	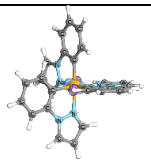 HOMO β	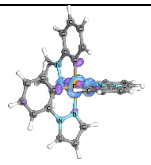 LUMO+8 β	13%
	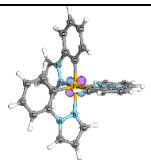 HOMO-1 β	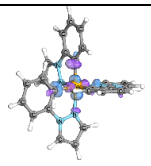 LUMO+7 β	11%
	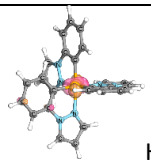 HOMO α	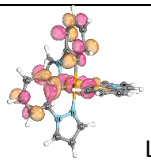 LUMO+5 α	10%
b *λ = 449 nm* *f = 0.0022*	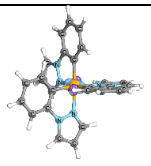 HOMO β	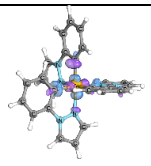 LUMO+7 β	13%
	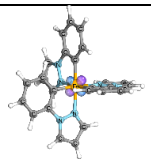 HOMO-1 β	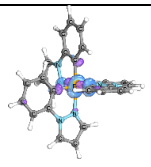 LUMO+8 β	11%
	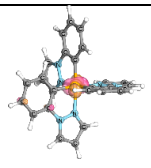 HOMO α	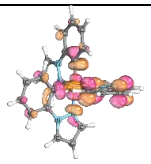 LUMO+3 α	10%
c *λ = 400 nm* *f = 0.0085*	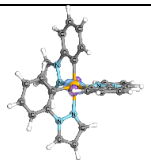 HOMO β	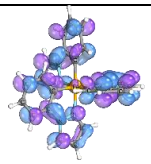 LUMO+1 β	84%
d *λ = 388 nm* *f = 0.0128*	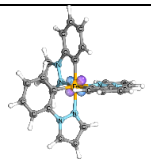 HOMO-1 β	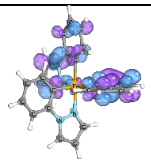 LUMO+3 β	30%
	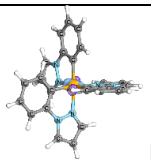 HOMO β	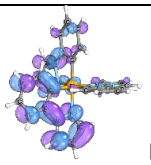 LUMO+2 β	30%

d' *λ = 389 nm* *f = 0.0108*	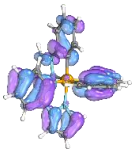 HOMO-2 β	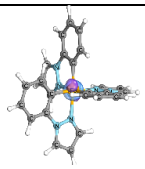 LUMO β	58%
e *λ = 351 nm* *f = 0.0159*	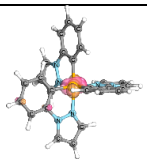 HOMO α	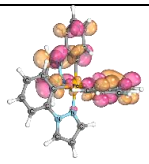 LUMO+3 α	15%
	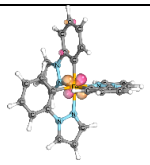 HOMO-1 α	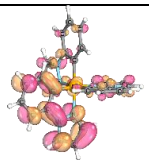 LUMO+1 α	12%
	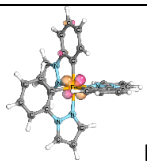 HOMO-1 α	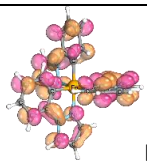 LUMO α	10%
f *λ = 346 nm* *f = 0.0251*	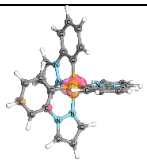 HOMO α	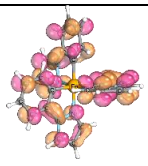 LUMO α	68%
g *λ = 281 nm* *f = 0.0328*	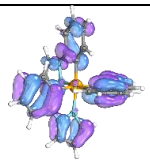 HOMO-2 β	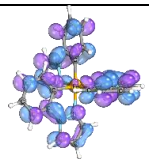 LUMO+1 β	26%
	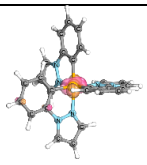 HOMO α	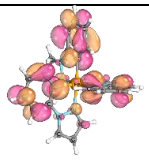 LUMO+5 α	16%
	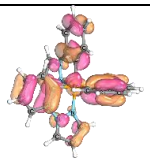 HOMO-2 α	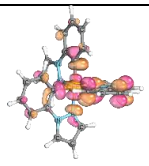 LUMO+3 α	7%
h *λ = 264 nm* *f = 0.2085*	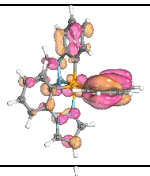 HOMO-4 α	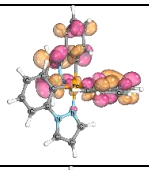 LUMO+2 α	10%
	 HOMO-3 α	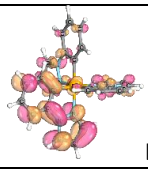 LUMO+1 α	9%

	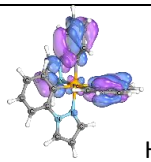 HOMO-4 β	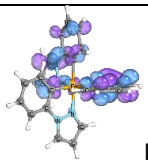 LUMO+3 β	7%
	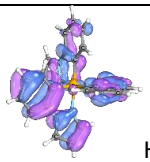 HOMO-3 β	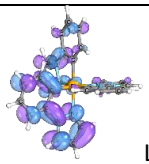 LUMO+2 β	7%
	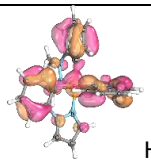 HOM-5 α	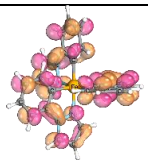 LUMO α	6%

X-ray emission spectroscopy

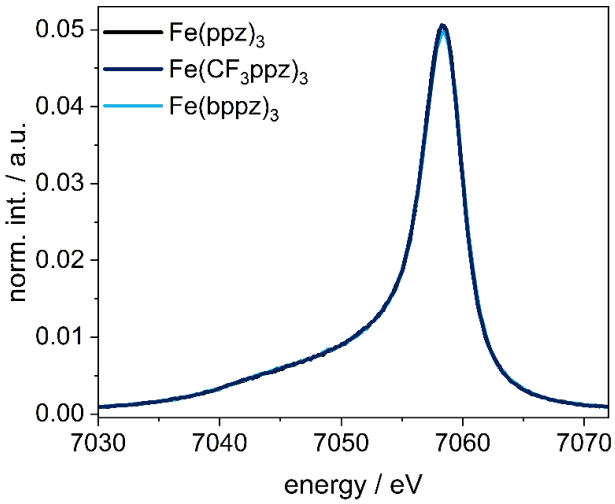

Figure S57: Experimental CtC spectra of $Fe(ppz)_3$, $Fe(bppz)_3$, $Fe(CF_3ppz)_3$ with different substituents.

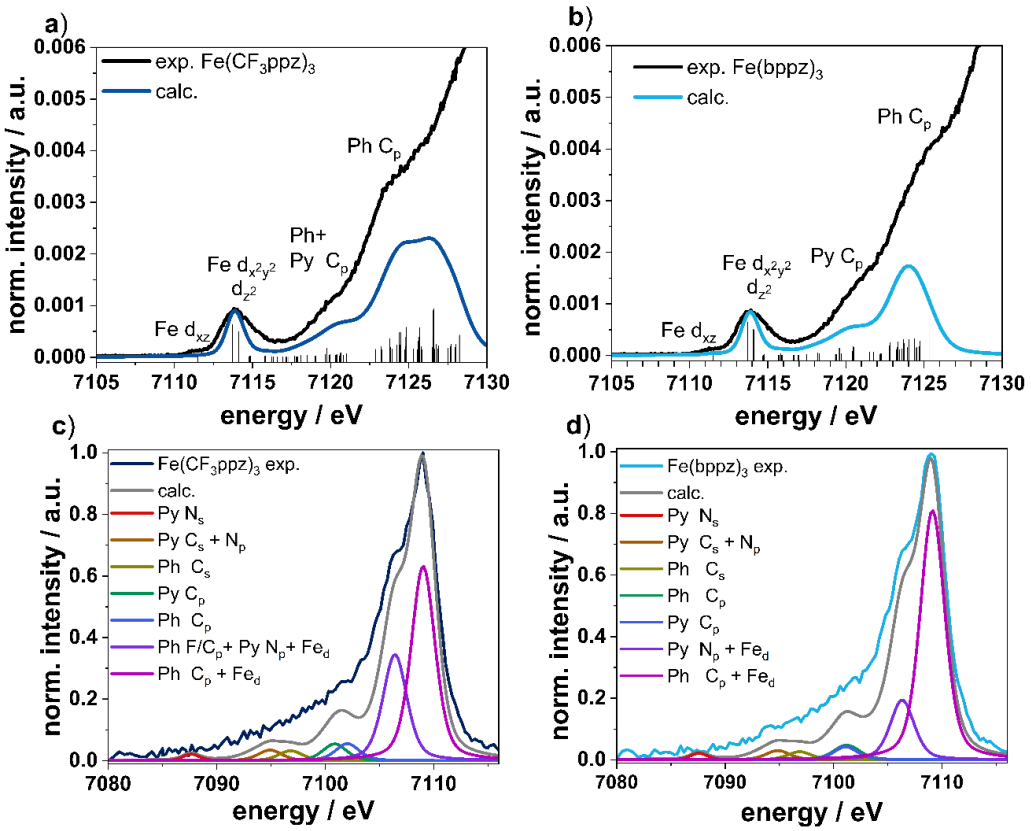

Figure S58: Comparison of experimental and calculated XANES (a, b) and VtC (c,d) spectra with main character of acceptor (a,b) and donor (c,d) orbitals orbital components for Pyrazol (Py) and Phenyl (Ph) accountable for the peak.

Single Crystal X-Ray Diffraction

The presented X-ray single crystal data were collected on a *Bruker Venture D8* three-cycle diffractometer equipped with a Mo K_α μ-source (λ=0.71073 Å). Monochromatization of the radiation was obtained using *Incoatec* multilayer Montel optics and a Photon III area detector was used for data acquisition. All crystals were kept at 120 K during measurement.

Data processing was carried out using the *Bruker* APEX 4 software package: This includes SAINT for data integration and SADABS for a multi-scan absorption correction. Structure solution was obtained by direct methods and the refinement of the structures using full-matrix least squares method based on F^2 were achieved in SHELX.[3,4] All non-hydrogen-atoms were refined anisotropically and the hydrogen atom positions were refined at idealized positions riding on the carbon atoms with isotropic displacement parameters $U_{iso}(H)=1.2\ U_{eq}(C)$ resp. $1.5\ U_{eq}(-CH_3)$ and C-H bond lengths of 0.93-0.96 Å. All CH_3 hydrogen atoms were allowed to rotate but not to tip.

Crystallographic data have been deposited at the Cambridge Crystallographic Data Centre assigned to the deposition numbers 2191100-2191104**. Copies are available free of charge via** www.ccdc.cam.ac.uk**.**

Crystallographic data

Tris(2-phenylpyrazolato-*N,C*^{2})iron(III) Fe(ppz)$_3$

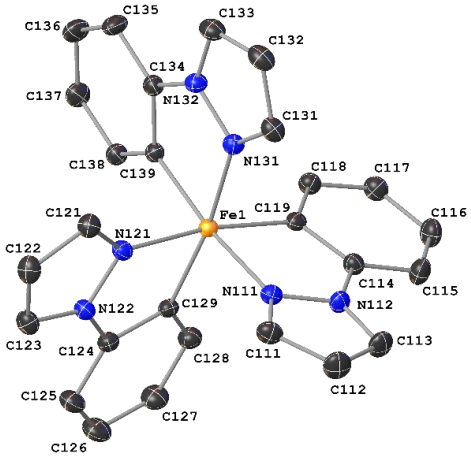

CCDC number	2191100
Empirical formula	C55 H44 Cl2 Fe2 N12
Moiety formula	C27 H21 N6 Fe
Formula weight	1055.62 Da
Color	brown
Shape	needle
Temperature	119(2) K
Wavelength	0.71073 Å
Crystal system	Orthorhombic
Space group	$P2_12_12_1$
Unit cell dimensions	a = 13.6656(7) Å
	b = 15.4759(8) Å
	c = 22.6671(11) Å
Volume	4793.8(4) Å^3
Z	4
Density (calculated)	1.463 mg/m^3
Absorption coefficient	0.770 mm^{-1}
F(000)	2176
Crystal size	0.300 x 0.060 x 0.020 mm^3
Theta range for data collection	2.182 to 30.524°
Index ranges	-19≤h≤19, -22≤k≤22, -32≤l≤32
Reflections collected	144195
Independent reflections	14658 [R(int) = 0.0379]
Completeness to theta = 25.242°	99.8 %
Absorption correction	Semi-empirical from equivalents
Refinement method	Full-matrix least-squares on F^2
Data / restraints / parameters	14658 / 0 / 641
Goodness-of-fit on F^2	1.075
Final R indices [I>2σ(I)]	R1 = 0.0270, wR2 = 0.0694
R indices (all data)	R1 = 0.0321, wR2 = 0.0737
Absolute structure parameter	0.397(10)
Largest diff. peak and hole	0.499 e/Å^3 (0.51 Å from H223) and -0.367 e/Å^3 (0.52 Å from Fe1)

The structure was refined as an inversion twin (BASF=0.39746)

Tris(1-(([1,1'-biphenyl])-4-yl)phenyl)pyrazolato-*N,C*^{2})iron(III) Fe(bppz)$_3$

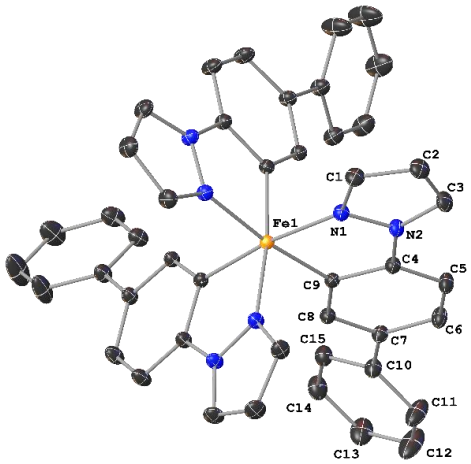

CCDC number	2191101
Empirical formula	C46.20 H35.40 Cl2.40 Fe N6
Moiety formula	C45 H33 Fe N6
Formula weight	815.53 Da
Color	red
Shape	prism
Temperature	120(2) K
Wavelength	0.71073 Å
Crystal system	Trigonal
Space group	R-3
Unit cell dimensions	a = 14.3819(5) Å
	b = 14.3819(5) Å
	c = 32.0647(16) Å
Volume	5743.7(5) Å^3
Z	6
Density (calculated)	1.415 mg/m^3
Absorption coefficient	0.605 mm^{-1}
F(000)	2528
Crystal size	0.200 x 0.200 x 0.180 mm^3
Theta range for data collection	2.833 to 36.372°
Index ranges	-23≤h≤24, -24≤k≤23, -53≤l≤53
Reflections collected	198137
Independent reflections	6215 [R(int) = 0.0423]
Completeness to theta = 25.242°	99.7 %
Absorption correction	Semi-empirical from equivalents
Refinement method	Full-matrix least-squares on F^2
Data / restraints / parameters	6215 / 0 / 157
Goodness-of-fit on F^2	1.046
Final R indices [I>2σ(I)]	R1 = 0.0332, wR2 = 0.0909
R indices (all data)	R1 = 0.0368, wR2 = 0.0940
Largest diff. peak and hole	0.538 e/Å^3 (0.65 Å from C4) and -0.355 e/Å^3 (0.53 Å from Fe1)

For refinement, two partially occupied dichloromethane molecules were treated with SQUEEZE from the PLATON software package.[5]

Tris(1-(4-(trifluoromethyl)phenyl)pyrazolato-*N,C*^{2})iron(III) Fe(CF$_3$ppz)$_3$

CCDC number	2191102
Empirical formula	C67 H44 F18 Fe2 N12
Moiety formula	C30 H18 F9 Fe N6
Formula weight	1470.84 Da
Color	yellow
Shape	plate
Temperature	120(2) K
Wavelength	0.71073 Å
Crystal system	Triclinic
Space group	P-1
Unit cell dimensions	a = 13.5555(9) Å b = 16.6300(10) Å c = 16.8788(10) Å α= 104.514(2)° β= 108.952(2)° γ = 109.287(2)°
Volume	3111.8(3) Å^3
Z	2
Density (calculated)	1.570 mg/m^3
Absorption coefficient	0.575 mm^{-1}
F(000)	1488
Crystal size	0.100 x 0.100 x 0.020 mm^3
Theta range for data collection	2.339 to 32.121°
Index ranges	-20≤h≤20, -24≤k≤24, -25≤l≤25
Reflections collected	314702
Independent reflections	21751 [R(int) = 0.0566]
Completeness to theta = 25.242°	99.9 %
Absorption correction	Semi-empirical from equivalents
Refinement method	Full-matrix least-squares on F^2
Data / restraints / parameters	21751 / 163 / 987
Goodness-of-fit on F^2	1.080
Final R indices [I>2σ(I)]	R1 = 0.0447, wR2 = 0.1024
R indices (all data)	R1 = 0.0694, wR2 = 0.1226
Largest diff. peak and hole	1.147 e/Å^3 (0.77 from F21D) and -0.789 e/Å^3 (0.49 Å from F12I)

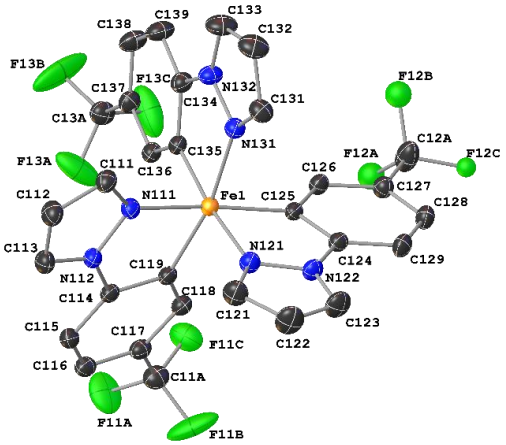

The asymmetric unit of the structure contains two complex molecules. Four CF$_3$-groups tend to rotate and could be refined splitted in two positions, a fifth one in three positions. Due to this disorder, not all splitted atom groups could be refined anisotropically.

Tris(1-(naphthalen-2-yl)pyrazolato-*N,C*^{2})iron(III) Fe(naphpz)$_3$

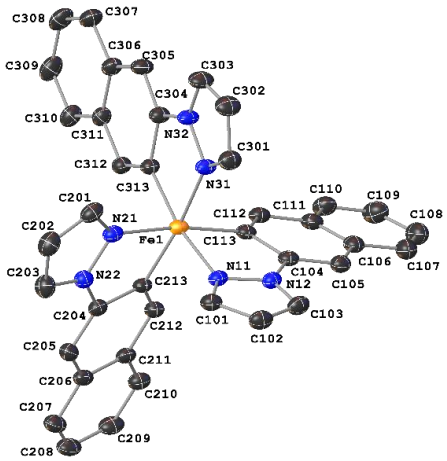

CCDC number	2191103
Empirical formula	C52 H37 Fe N8
Moiety formula	C39 H27 Fe N6
Formula weight	829.74 Da
Color	orange
Shape	plate
Temperature	120(2) K
Wavelength	0.71073 Å
Crystal system	Monoclinic
Space group	$P2_1/n$
Unit cell dimensions	a = 11.3521(10) Å
	b = 30.655(3) Å
	c = 12.3313(11) Å
	β= 110.723(2)°
Volume	4013.7(6) Å^3
Z	4
Density (calculated)	1.373 mg/m^3
Absorption coefficient	0.425 mm^{-1}
F(000)	1724
Crystal size	0.280 x 0.180 x 0.100 mm^3
Theta range for data collection	2.030 to 30.546°
Index ranges	-16≤h≤16, -43≤k≤43, -17≤l≤17
Reflections collected	190973
Independent reflections	12271 [R(int) = 0.0682]
Completeness to theta = 25.242°	99.9 %
Absorption correction	Semi-empirical from equivalents
Refinement method	Full-matrix least-squares on F^2
Data / restraints / parameters	12271 / 0 / 550
Goodness-of-fit on F^2	1.131
Final R indices [I>2σ(I)]	R1 = 0.0455, wR2 = 0.1075
R indices (all data)	R1 = 0.0734, wR2 = 0.1274
Largest diff. peak and hole	1.196 e/Å^3 (0.63 Å from H405) and -0.698 e/Å^3 (0.69 Å from Fe1)

Tris(1-(4-methoxyphenyl)pyrazolato-*N,C*^{2})iron(III) Fe(MeOppz)$_3$

CCDC number	2191104
Empirical formula	C30 H27 Fe N6 O3
Moiety formula	C30 H27 Fe N6 O3
Formula weight	575.42 Da
Color	red
Shape	block
Temperature	120(2) K
Wavelength	0.71073 Å
Crystal system	Trigonal
Space group	R-3
Unit cell dimensions	a = 19.9138(11) Å
	b = 19.9138(11) Å
	c = 48.704(4) Å
Volume	16727(2) Å^3
Z	24
Density (calculated)	1.371 mg/m^3
Absorption coefficient	0.584 mm^{-1}
F(000)	7176
Crystal size	0.18 x 0.18 x 0.10 mm^3
Theta range for data collection	2.400 to 32.048°
Index ranges	-29≤h≤29, -29≤k≤29, -72≤l≤72
Reflections collected	660843
Independent reflections	12775 [R(int) = 0.0674]
Completeness to theta = 25.242°	96.8 %
Absorption correction	Semi-empirical from equivalents
Refinement method	Full-matrix least-squares on F^2
Data / restraints / parameters	12775 / 0 / 505
Goodness-of-fit on F^2	1.143
Final R indices [I>2σ(I)]	R1 = 0.0350, wR2 = 0.0834
R indices (all data)	R1 = 0.0530, wR2 = 0.0997
Largest diff. peak and hole	0.701 e/Å^3 (2.28 Å from H13D) and -0.556 e/Å^3 (0.64 Å from Fe1)

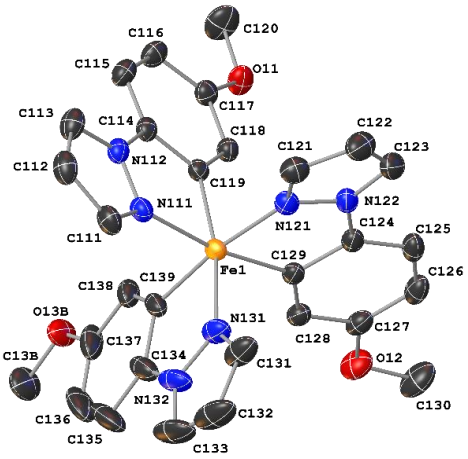

One methoxy group of the structure is disordered over two positions and could be refined anisotropically. Furthermore, two water molecules are only partially occupied (SOF<0.2), could not be refined and were therefore treated using SQUEEZE from the PLATON software package.[5]

References

(1) Cristau, H.-J.; Cellier, P. P.; Spindler, J.-F.; Taillefer, M. Mild Conditions for Copper-Catalysed *N*-Arylation of Pyrazoles. *Eur. J. Org. Chem.* **2004**, *2004* (4), 695–709. DOI: 10.1002/ejoc.200300709.

(2) Cristau, H.-J.; Cellier, P. P.; Spindler, J.-F.; Taillefer, M. Highly efficient and mild copper-catalyzed N- and C-arylations with aryl bromides and iodides. *Chem. Eur. J.* **2004**, *10* (22), 5607–5622. DOI: 10.1002/chem.200400582.

(3) Sheldrick, G. M. Crystal structure refinement with SHELXL. *Acta crystallographica. Section C, Structural chemistry* **2015**, *71* (Pt 1), 3–8. DOI: 10.1107/S2053229614024218. Published Online: Jan. 1, 2015.

(4) Sheldrick, G. M. SHELXT - integrated space-group and crystal-structure determination. *Acta crystallographica. Section A, Foundations and advances* **2015**, *71* (Pt 1), 3–8. DOI: 10.1107/S2053273314026370. Published Online: Jan. 1, 2015.
(5) Spek, A. L. PLATON SQUEEZE: a tool for the calculation of the disordered solvent contribution to the calculated structure factors. *Acta crystallographica. Section C, Structural chemistry* **2015**, *71* (Pt 1), 9–18. DOI: 10.1107/S2053229614024929. Published Online: Jan. 1, 2015.

A.3 Supporting Information of "Isostructural series of a cyclometalated iron complex in three oxidation states"

Supporting Information for

Isostructural series of a cyclometalated iron complex in three oxidation states

Jakob Steube[1,2], Lorena Fritsch[1,2], Ayla Kruse[3,4], Olga Bokareva[3†], Serhiy Demeshko[5], Hossam Elgabarty[2,6], Roland Schoch[1,2], Mohammad Alaraby[2,6], Stephan Hohloch[1‡], Thomas D. Kühne[2,6], Franc Meyer[5], Oliver Kühn[3,4], Stefan Lochbrunner[3,4], Matthias Bauer[1,2*]

1: Institute for Inorganic Chemistry, Paderborn University, 33098 Paderborn, Germany

2: Center for Sustainable Systems Design (CSSD), Paderborn University, 33098 Paderborn, Germany

3: Department of Life, Light and Matter, University of Rostock, 18051 Rostock, Germany

4: Institute for Physics, University of Rostock, 18051 Rostock, Germany

5: Institute of Inorganic Chemistry, University of Göttingen, Göttingen, Germany

6: Institute for Theoretical Chemistry, Paderborn University, 33098 Paderborn, Germany

† Present Address: Institute of Physics, University of Kassel, Kassel, Germany

‡ Present Address: Institute of General, Inorganic and Theoretical Chemistry, University of Innsbruck, Innsbruck, Austria

Table of contents

Synthesis

All reactions under inert conditions were either performed under standard schlenk techniques using argon as inert gas or in an argon filled glovebox. Dry and degassed solvents were obtained by dynamic drying of the respective solvent over molar sieves in an MBraun SPS solvent purifying system, subsequent degassing by bubbling argon through it and storage over molar sieves. The solvent for the reduction was additionally degassed using three freeze-pump-thaw cycles. All chemicals were used without further purification. NMR spectra were recorded on a Bruker Ascent 700 spectrometer. Assignments were done using 2D spectra. Mass spectra were recorded on a Waters Synapt G2 quadrupole TOF spectrometer with Acetonitrile as solvent. Elemental Analysis was performed on a vario MicroCube by elementar. $[Fe(ImP)_2]PF_6$ **1** was synthesized according to literature procedures.[1]

$[Fe(ImP)_2]$ (**1**$^-$)

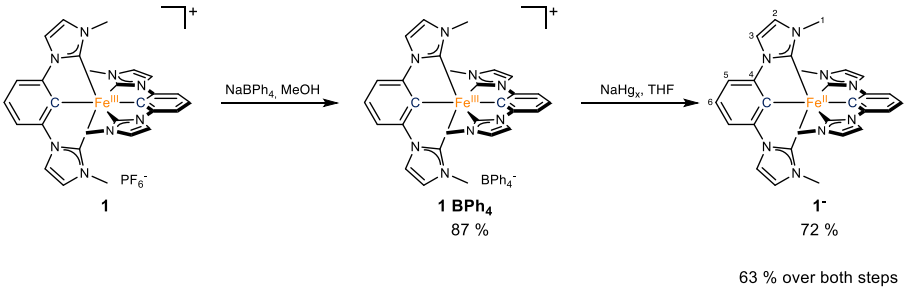

Scheme S1: Synthesis of **1**$^-$.

The synthesis of **1**$^-$ started with the preparation of the BPh_4^- salt of **1**, **1 BPh$_4$**. For this, the starting compound (100 mg, 0.148 mmol) was dissolved in a minimal amount of methanol. $NaBPh_4$ (101 mg, 0.296 mmol, 2 eq.) was added to the dark blue solution and stirred. The dark suspension was filtered, the solids were washed with cold methanol and then washed out of the filter using dichloromethane. After removal of the solvent and thoroughly drying, **1 BPh$_4$** was obtained as a dark blue powder (109 mg, 0.128 mmol, 87 %) and used without further purification.

1 BPh$_4$ (102 mg, 0.12 mmol) was dissolved in dry and degassed THF (15 mL in total) and then transferred to Sodium Amalgam (1.3 %, 849 mg, 0.48 mmol, 4 eq.) under THF (3 mL) in a schlenk flask while stirring. The solution quickly turned green and then slowly orange. After 2h of vigorous stirring, no further change in color was noticeable and the solvent of the orange solution was evaporated off under vacuum. The flask was transferred into a glovebox for further purification. There, the solids were washed with toluene and filtered to obtain an orange solution. The solvent was evaporated off to obtain **3** as fine orange crystals (45 mg, 0.085 mmol, 72 %). Crystals suitable for single crystal analysis were obtained by diffusion of pentane into a solution of **1**$^-$ in dichloromethane, where the orange crystals could be easily separated from residues of **1** which formed due to deterioration of the solution.

Note on the NMR-data: The coordinating carbon atoms were not observed in the ^{13}C-NMR.

^{1}H-NMR: (700 MHz, THF-d_8) δ (ppm) =7.40 (d, *J* = 7.3 Hz, 4H, **5-H**), 7.39 (d, *J* = 2.0 Hz, 4H, **3-H**), 6.44 (d, *J* = 1.9 Hz, 4H, **2-H**), 6.32 (t, *J* = 7.8 Hz, 2H, **6-H**), 2.36 (s, 12H, **1-H**).

^{13}C-NMR: (700 MHz, Acetonitrile-d_3) δ (ppm) =154.72 (**4-C**), 121.96 (**5-C**), 121.27 (**2-C**), 112.35 (**3-C**), 98.66 (**6-C**), 35.07(**1-C**).

$[Fe(ImP)_2](PF_6)_2$ (**1**$^+$)

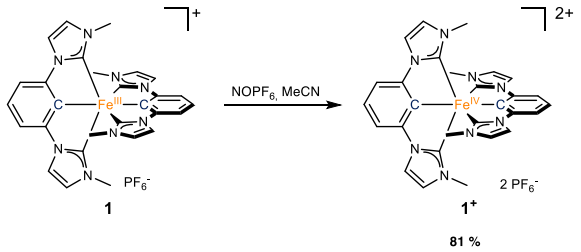

Scheme S2: Synthesis of **1**$^+$.

In a Schlenk flask, **1** (71.5 mg, 0.106 mmol) was first degassed thoroughly under a vacuum (10^{-3} mbar) for 1 h and then dissolved in dry and degassed acetonitrile (5 mL). To the blue solution, $NOPF_6$ (20 mg, 0.114 mmol, 1.08 eq.) was added. The solution was stirred under argon overnight, before 1 mL of methanol was added to quench the reaction. The solution was stirred for another 15 minutes under atmosphere. The volatiles were removed at the rotary evaporator. The dark solid was washed thoroughly with chloroform until the blue color disappeared. The purple solid was purified by diffusion of chloroform into a solution of **1**$^+$ in acetone to yield fine purple needles (70 mg, 0.085 mmol, **81 %**). Crystals suitable for single crystal X-Ray analysis were obtained by diffusion of diethyl ether into a solution of **1**$^+$ in methanol, which were also used for Mössbauer spectroscopy and magnetic measurements.

^{1}H-NMR: (700 MHz, Acetonitrile-d_3) δ (ppm) = 38.91 (12H), 26.74 (4H), 8.53 (4H), -35.56 (4H).

ESI-MS: (m/z) $[M\text{-}2PF_6]^{2+}$ 265.0813 (calculated for $C_{28}H_{26}FeN_8^{2+}$: 265.0809), $[M\text{-}2PF_6]^+$ 530.1635 (calculated for $C_{28}H_{26}FeN_8^+$: 530.1630), $[M\text{-}PF_6]^+$ 675.1281 (calculated for $C_{28}H_{26}F_6FeN_8P^+$: 675.1272).

Elemental Analysis: (%) Found (calculated for $C_{28}H_{26}F_{12}FeN_8P_2$): C: 40.93 (41.00) H: 3.42 (3.19) N: 13.50 (13.66).

Single Crystal X-Ray Analysis

X-ray single crystal data of **1**$^-$ and **1**$^+$ were recorded using a Bruker SMART CCD area-detector diffractometer equipped with a graphite monochromator at 120 K. The data were integrated with SAINT and afterwards a multi-scan absorption correction was applied using SADABS.[2] Structure solution was achieved by direct methods in SHELXT[3] and structure refinement was conducted using full-matrix least squares refinement based on F^2.[3] All non-hydrogen-atoms were refined anisotropically and the hydrogen atom positions were refined at idealized positions riding on the carbon atoms with isotropic displacement parameters $U_{iso}(H)=1.2\ U_{eq}(C)$ and C-H bond lengths of 0.93-0.96 Å. In the case of **1**$^-$ one dichloromethane and of **1**$^+$ one methanol molecule could not be modelled due to significant disorders and therefore were treated using SQUEEZE from the Platon software package.[4,5] The crystal structure of **1** is already published in Steube *et al.*[1]

The Cambridge Crystallographic Data Centre provides the presented structures free of charge via www.ccdc.cam.ac.uk assigned to the deposition numbers 2002774 (**1**), 2108627 (**1**$^-$) and 2108628 (**1**$^+$).

1$^-$: ($C_{28}H_{26}N_8Fe$), M_r = 530.42 Da, orange plate, size 0.30 x 0.16 x 0.02 mm^3, tetragonal space group $I\bar{4}$ with Z=2, a=8.327(2) Å, b=8.327(2) Å, c=17.946(3) Å, V=1244.4(6) $Å^3$, D_c=1.416 mg/m^3, μ=0.640 mm^{-1}, F(000)=552, θ_{max}=33.721°, reflections collected: 85875, independent reflections: 2474, R_{int}=0.0553, refinement converged at R1=0.0312 [I>2σ(I)], wR2=0.0655 [all data], min./max. ΔF: -0.450 $eÅ^3$ (0.75 Å from C1A) / 0.474 $eÅ^3$ (0.75 Å from Fe1), **CCDC No.: 2108627.**

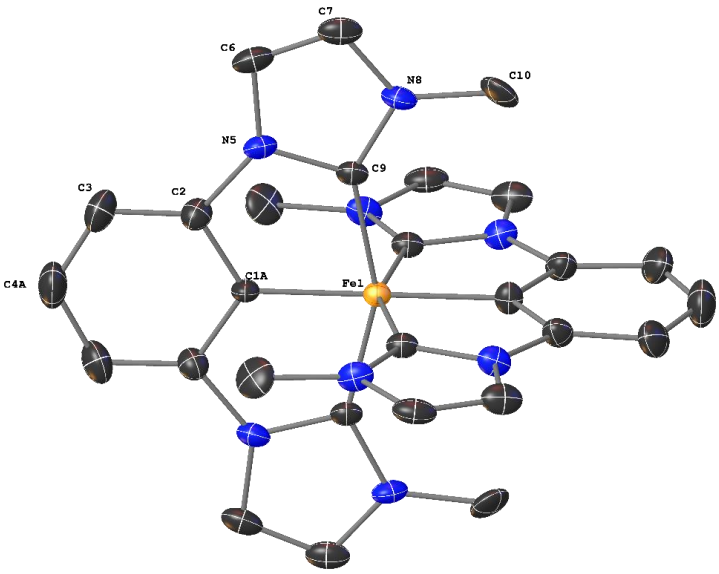

Figure S1: Molecular structure of **1**$^{+}$. determined by scXRD. Thermal ellipsoids are drawn at the 50 % probability level. Hydrogen atoms omitted for clarity.

1^{+}**:** $(C_{28}H_{26}N_8Fe)(PF_6)_2$ $[CH_4O]$, M_r = 852.40 Da, black needle, size 0.48 x 0.18 x 0.14 mm^3, trigonal space group $P3_221$ with Z=3, a=b=10.869(3) Å, c=25.087(7) Å, V=2566.4(15) Å^3, D_c=1.655 mg/m^3, μ=0.639 mm^{-1}, F(000)=1296, θ_{max}=27.110°, reflections collected: 9276, independent reflections: 3765, R_{int}=0.0476, refinement converged at R1=0.0662 [I>2σ(I)], wR2=0.1391 [all data], min./max. ΔF: -0.476 eÅ^3 (1.07 Å from F2) / 0.623 eÅ^3 (1.04 Å from C114), **CCDC No.: 2108628.**

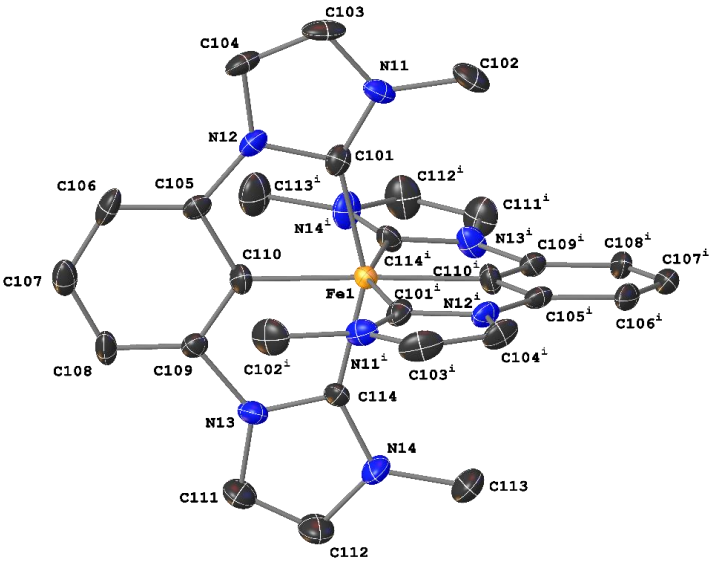

Figure S2: Molecular structure of **1**$^{+}$. determined by scXRD. Thermal ellipsoids are drawn at the 50 % probability level. Hydrogen atoms and counter ions omitted for clarity.

Mössbauer Spectroscopy

Mössbauer spectra were recorded with a ^{57}Co source in a Rh matrix using an alternating constant acceleration *Wissel* Mössbauer spectrometer operated in the transmission mode and equipped with a *Janis* closed-cycle helium cryostat. Isomer shifts are given relative to iron metal at ambient temperature.

Simulation of the experimental data was performed with the *Mfit* program using Lorentzian line doublets: E. Bill, Max-Planck Institute for Chemical Energy Conversion, Mülheim/Ruhr, Germany.

Magnetic Measurements

Temperature-dependent magnetic susceptibility measurements for **1**$^{-}$ and **1**$^{+}$ were carried out with a Quantum-Design MPMS3 SQUID magnetometer equipped with a 7 Tesla magnet in the range from 295 to 2.0 K at a magnetic field of 0.5 T. The powdered samples were contained in a polycarbonate capsule and fixed in a non-magnetic sample holder. Each raw data file for the measured magnetic moment was corrected for the diamagnetic contribution of the sample holder and the polycarbonate capsule. The molar susceptibility data were corrected for the diamagnetic contribution.

Experimental temperature dependent and VTVH (variable temperature – variable field) data for **1**$^{+}$ were simultaneously modelled by using a fitting procedure to the spin Hamiltonian for Zeeman splitting and zero-field splitting, equation (1).

$$\hat{H} = g\mu_B \vec{B}\vec{S} + D\left[\hat{S}_z^2 - \frac{1}{3}S(S+1)\right] \quad (1)$$

For **1**$^{-}$, the simulation was done for a diamagnetic S =0 spin state assuming 0.1 % impurity with $S = 5/2$.

Simulations of the experimental magnetic data was performed with the *julX_2s* program: E. Bill, Max-Planck Institute for Chemical Energy Conversion, Mülheim/Ruhr, Germany. Temperature-independent paramagnetism (*TIP*) was included according to $\chi_{calc} = \chi + TIP$ ($TIP = 300 \cdot 10^{-6}$ cm^{3}mol^{-1}).

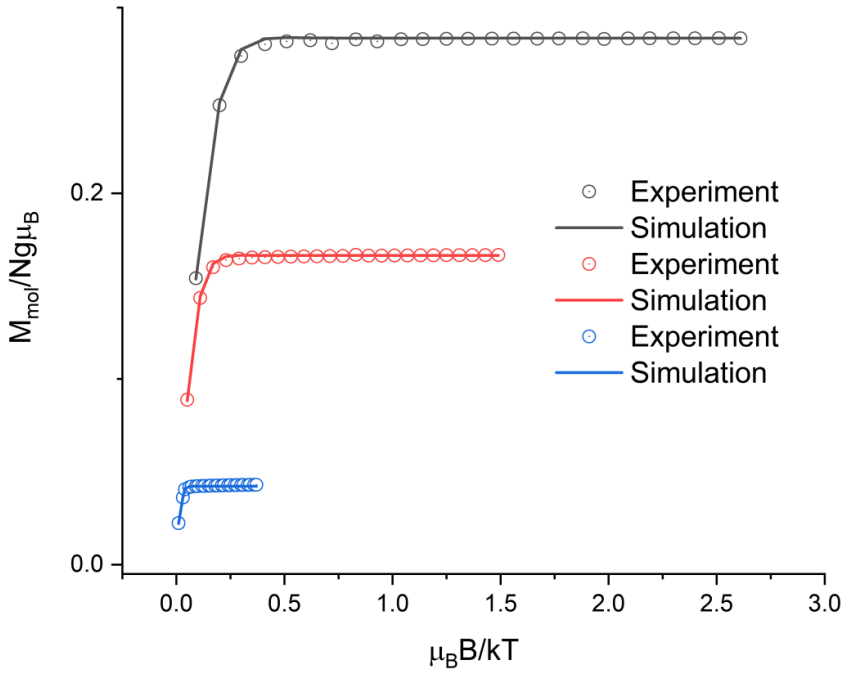

Figure S3: Plot of variable temperature – variable field magnetization measurements for **1**$^{+}$ at 1 T (blue circles), 4 T (red circles) and 7 T (black circles). The corresponding solid lines represent the global fit with the best parameters g = 2.32 and D = *+39.5 cm*$^{-1}$ *for* S = *1.*

XANES and Kβ emission data collection, processing, and analysis

All XANES and XES spectra were collected at Beamline P64 of Petra III at DESY (Hamburg, Germany).[6,7] The electron energy of the storage-ring was 6.0 GeV, the ring current was 100 mA. The incident energy was selected using the (311) reflection from a Si double-crystal monochromator using Fe foil for energy calibration. The samples were measured as pure powder at room temperature sealed with Kapton tape against air contact. XANES spectra were recorded in fluorescence mode for 60 s. To obtain reasonable data, 12 spectra, each on a new sample spot, were collected. XES spectra were recorded off-resonant at an excitation energy of 7300 eV in the range of 6930 to 7120 eV with the von Hamos spectrometer of P64, using six Si crystals in the (440) reflection. Also 12 spectra (300 s per scan) were recorded, using a different sample spot for each scan. Comparing XANES spectra before and after irradiation of 300 s no radiation damage can be observed (no change in the spectrum). The VtC-XES spectra are super-imposed by the high-energy slope of the $K\beta_{1,3}$ emission line and were background-corrected by fitting the slope and subtracted it from the raw spectrum. All spectra were area normalized. Values for the peak maxima of $Fe(CN)_6$ are measured in the same way as for complex row 1 in case of $K\beta_{1,3}$. For $K\beta_{2,5}$ and the pre-peak literature values were used.[8]

Table S1: Parameters of the linear regression between the peak maxima of $K\beta_{1,3}$, $K\beta_{2,5}$ and the $1s \rightarrow e_g$ pre-peak respectively shown in Fig.4.

Line	complex row	function	R^2	corrected R^2
$K\beta_{1,3}$	1	f(x) = 1.29 x - 9129.2	1	1
$K\beta_{1,3}$	$Fe(CN)_6$	f(x) = 1.11 x - 7859.1	-	-
$K\beta_{2,5}$	1	f(x) = 0.52 x - 3670.5	0.988	0.976
$K\beta_{2,5}$	$Fe(CN)_6$	f(x) = 0.35 x - 2537.4	-	-
Pre-peak	1	f(x) = 1.42 x - 10094.4	0.993	0.987
Pre-peak	$Fe(CN)_6$	f(x) = 0.83 x - 5927.5	-	-

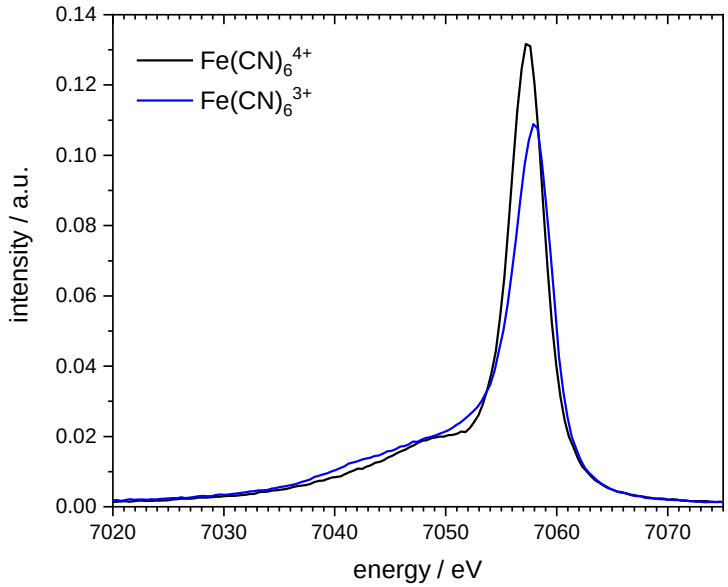

Figure S4: Experimental $K\beta_{1,3}$ spectra of the $Fe(CN)_6^{3+/4+}$ references.

Computational details

Due to the quite rigid structure, the computed geometries only slightly depend on the applied computational protocol within the variety of tested functionals. All minima computed with (U)DFT for differently charged species have been checked for the absence of negative frequencies. Computation of VtC-XES and XANES spectra were performed with ORCA 4.2.1 quantum chemistry package[9], whereas TDDFT calculations of absorption spectra and NBO analysis were done using Gaussian software.[10,11]

VtC-XES and XANES. For the unconstrained geometry optimization the B97-3c method was used.[12] For calculation of VtC-XES spectra, TPSS[13]/def2-TZVP[14] has been chosen. The TPSSh[13]/def2-TZVP was used to calculate the XANES spectra. Auxiliary basis set def2/J[14] and RIJCOSX approximation[15] for the Hartree-Fock component were used. In all cases, the D3BJ dispersion correction[16] and CP(PPP) basis set[17] for iron were applied. TPPS(h) functionals were previously shown to deliver good performance for XES/XANES spectra.[18–21]

XES spectra were plotted with ORCA Mapspc, using the uniform broadening of 2.5 eV. For the XANES spectra, a linearly increasing broadening to higher energies was chosen, starting from 0.6 (fwhm) at the prepeak. The calculated spectra were shifted to match the prepeak (XANES) or the $K\beta_{2,5}$ peak (VtC-XES) and were normalized to these maxima. The analysis of the individual fractions of the molecular orbitals is based on the Löwdin population analysis, which was extracted from the ORCA output file using MOAnalyzer (version 1.3).[22] Using this, only orbitals with a significant fraction (>10%) were selected for fragment projections of the XES spectra.

For plotting the d-orbital splitting (Fig. 4), the Löwdin population analysis was performed. The energy was chosen from the molecular orbital with the highest contribution of a certain d-orbital around the HOMO-LUMO gap, whereas for open shell systems α and β orbitals are averaged. The Kohn-Sham orbitals were visualized with IboView (vers. 20150427).[23]

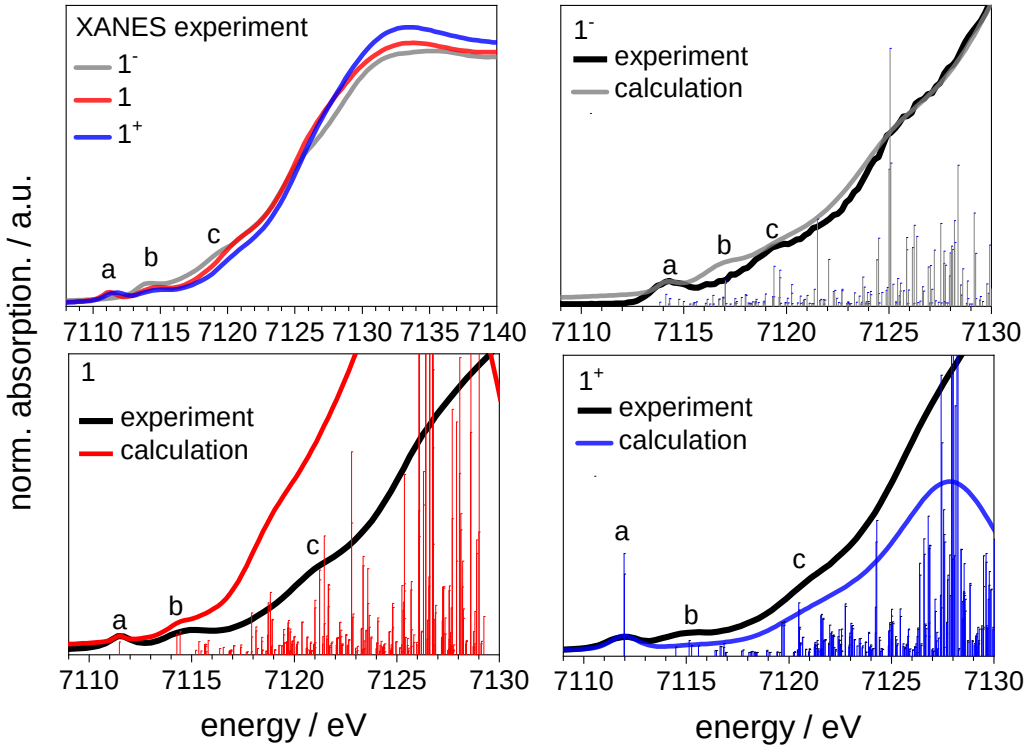

Figure S5: Comparison of experimental and calculated XANES spectra of **1**⁻,**1** and **1**⁺. Single transitions are potted as sticks, whereas the acceptor orbital of the main peaks (a,b,c) are analyzed in Table S2

Table S2: Calculated fractions of the individual atomic contributions of the acceptor orbitals (XANES) of the most intense transitions. Indication of the orbital fractions in %.

	Peak	acceptor orbital	C		H		N		Fe	
			s	p	s	p	s	p	p	d
1⁻ (Fe^{2+})	a	152	10	17	28	3	0	0	1	28
	b	160	6	27	42	5	0	1	8	0
	c	186	15	26	17	4	0	5	0	0
		191	0	59	3	3	0	3	0	1
1 (Fe^{3+})	a	137 β	0	17	0	0	0	15	0	50
	b	142 α	10	20	1	0	1	2	0	50
		142 β	9	20	1	0	1	3	0	50
	c	186 α	9	42	12	2	1	4	1	0
		186 β	10	43	13	2	1	4	1	0
1⁺ (Fe^{4+})	a	136 β	0	19	0	0	0	4	1	61
		137 β	0	18	0	0	0	4	1	62
	b	140 β	5	38	0	0	0	6	0	29
		142 β	6	32	1	0	0	5	0	36
	c	159 α	5	25	40	6	2	1	1	0
		159 β	6	24	43	7	2	1	1	0

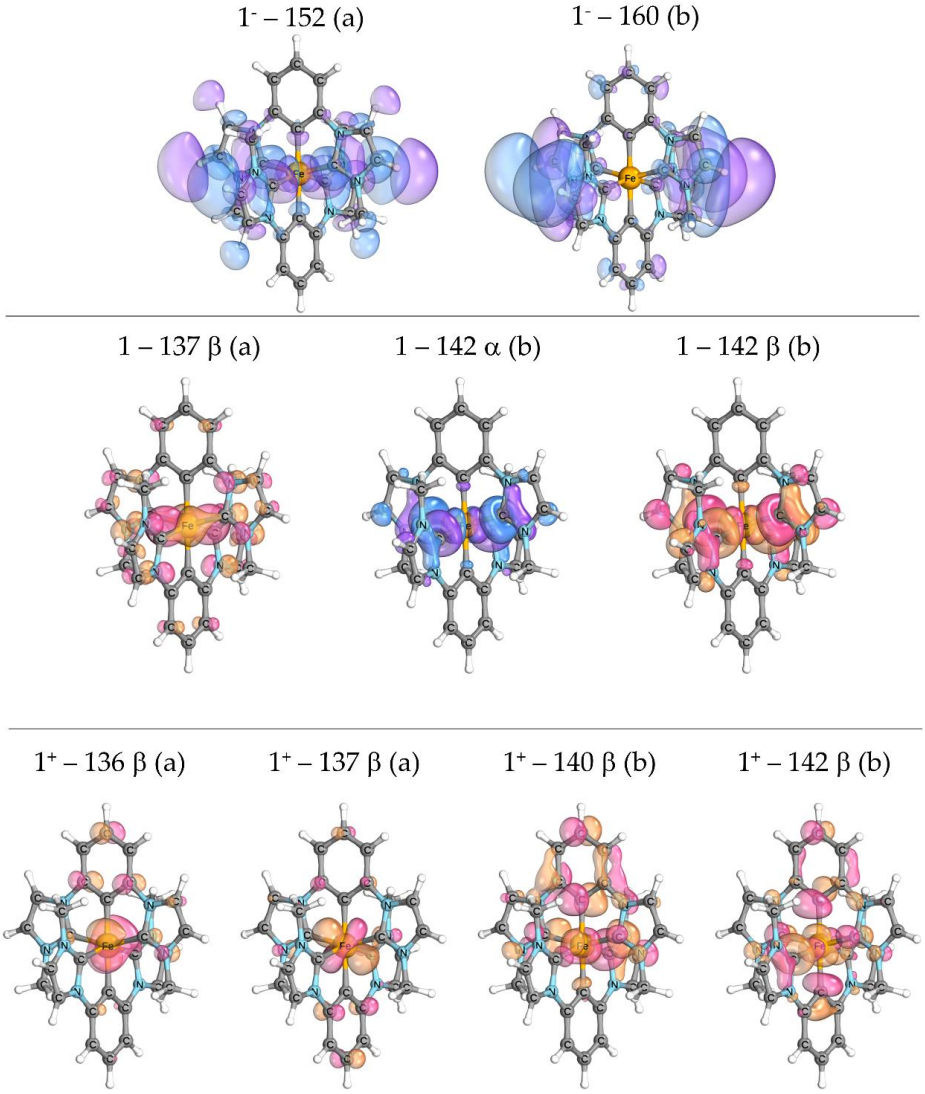

Figure S6: Calculated spatial contribution of the acceptor orbitals (XANES, Table S2) of the transitions of the prepeaks (a,b).

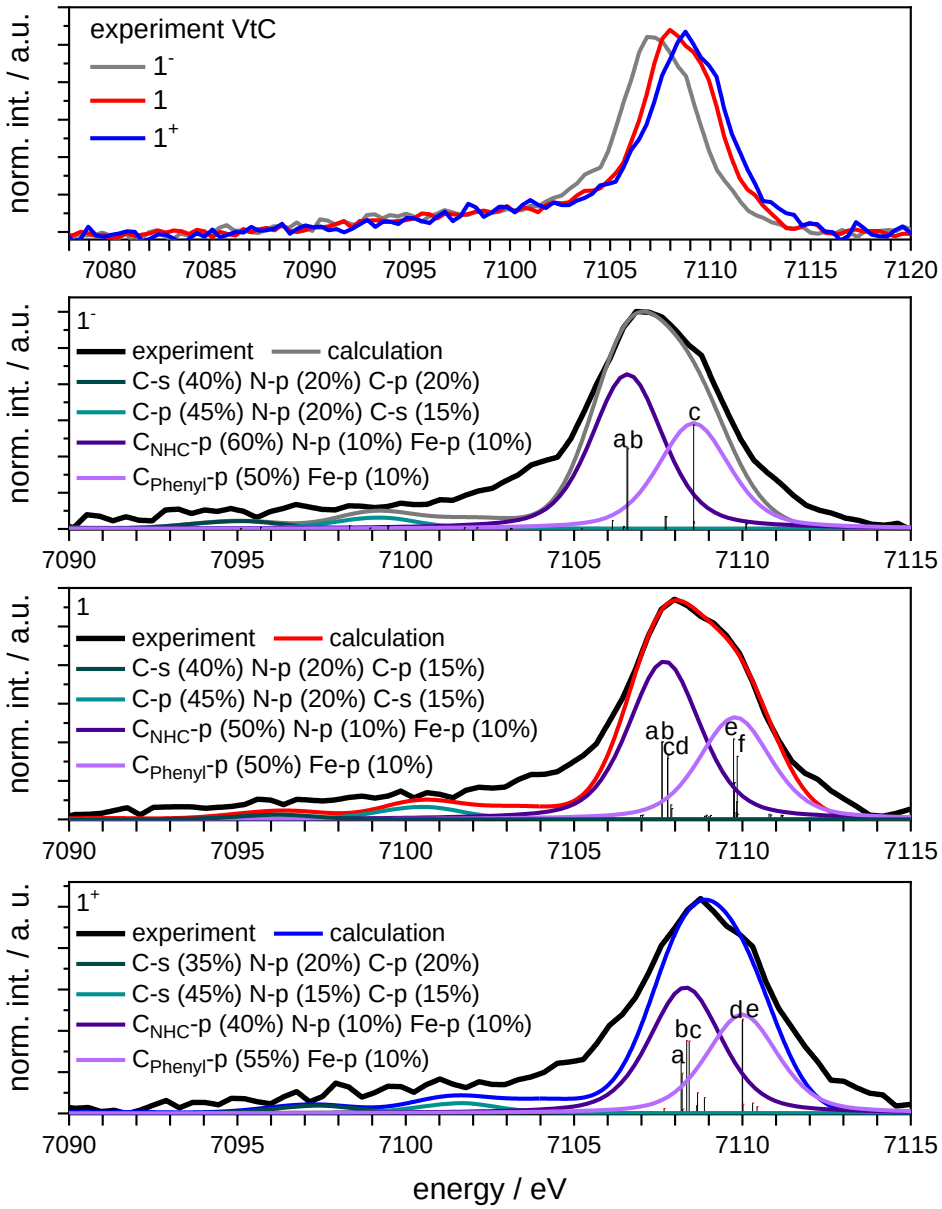

Figure S7: Experimental and calculated VtC spectra of **1**$^{-}$,**1** and **1**$^{+}$ including the analysis of the peak contributions (threshold 10%, rounded on 5%).

Table S3: Calculated fractions of the individual atomic contributions of donor orbitals (VtC) of the most intense transitions. Indication of the orbital fractions in %.

	signal / eV	donor orbital	C		H		N		Fe	
			s	p	s	p	s	p	p	d
1- (Fe2+)	7095	59	39	12	11	0	0	26	1	0
		60	39	13	11	2	0	25	1	0
		63	37	26	10	2	2	10	3	0
	7099	72	17	44	11	2	3	16	1	0
		75	12	46	13	2	2	19	1	0
		76	12	45	13	2	2	19	1	0
	7103	84	3	51	27	0	1	6	1	0
		91	6	40	20	0	0	20	1	0
	7106	123 (a)	8	52	1	0	1	11	12	1
		124 (b)	8	52	1	0	1	12	12	1
	7109	134 (c)	5	56	1	0	1	3	12	4
1 (Fe3+)	7096	59 β	39	11	10	1	0	27	1	0
		60 β	39	11	10	2	0	27	1	0
		63 β	38	25	11	2	2	10	1	0
	7100	72 β	17	43	11	1	4	16	1	0
		75 β	13	46	12	2	2	18	2	0
		76 β	13	46	12	2	2	18	2	0
	7103	81 β	8	52	19	0	1	9	0	0
		82 α	8	53	19	0	1	9	0	0
		91 α	6	38	20	0	0	21	1	0
	7107	121 α (a)	8	52	1	0	0	12	13	2
		121 β (b)	8	52	1	0	0	11	13	1
		122 α (c)	7	57	1	1	0	8	11	1
		122 β (d)	8	58	0	1	0	8	11	1
	7109	131 β (e)	4	60	1	1	0	3	10	2
		134 α (f)	3	60	1	1	0	5	8	3
1+ (Fe4+)	7097	59 β	40	13	9	2	0	26	1	0
		60 β	40	12	9	2	0	26	1	0
		63 β	34	23	14	3	3	12	1	0
	7102	71 β	16	43	12	2	3	17	1	0
		75 β	13	46	11	2	2	17	1	0
		76 β	13	46	11	2	3	17	1	0
	7104	81 α	8	52	19	2	1	9	0	0
		82 α	8	52	19	2	1	10	0	0
		89 β	8	37	20	1	0	19	1	0
	7108	123 α (a)	5	37	2	0	0	7	8	24
		122 β (b)	8	52	1	0	1	9	13	4
		123 β (c)	9	53	1	0	1	8	13	4
	7110	129 α (d)	4	58	2	0	1	3	12	3
		129 β (e)	4	58	2	0	0	2	12	4

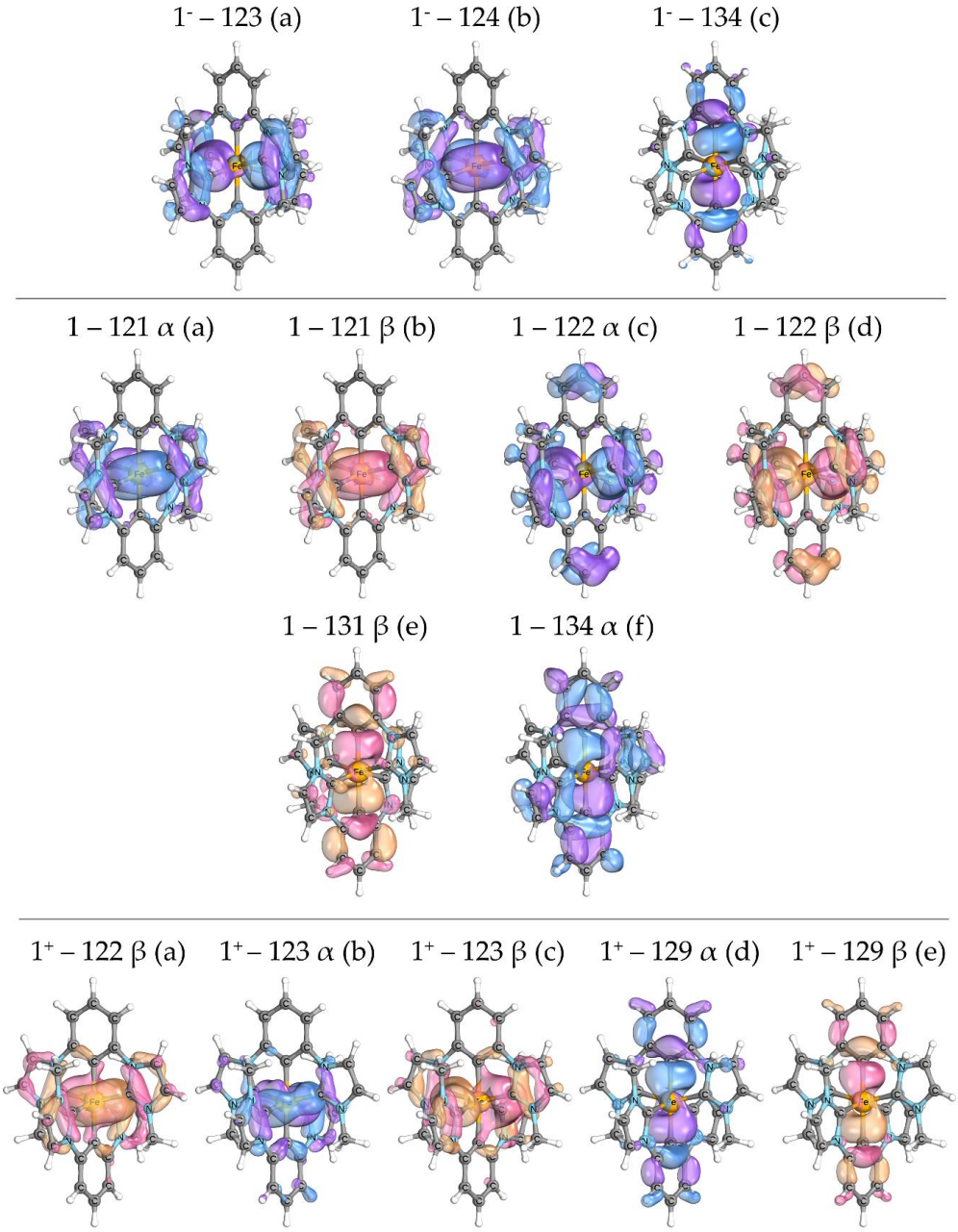

Figure S8: Spatial contribution of the donor orbitals (VtC, Table S3) of most intense transitions (a-f) marked in the spectrum Figure S7.

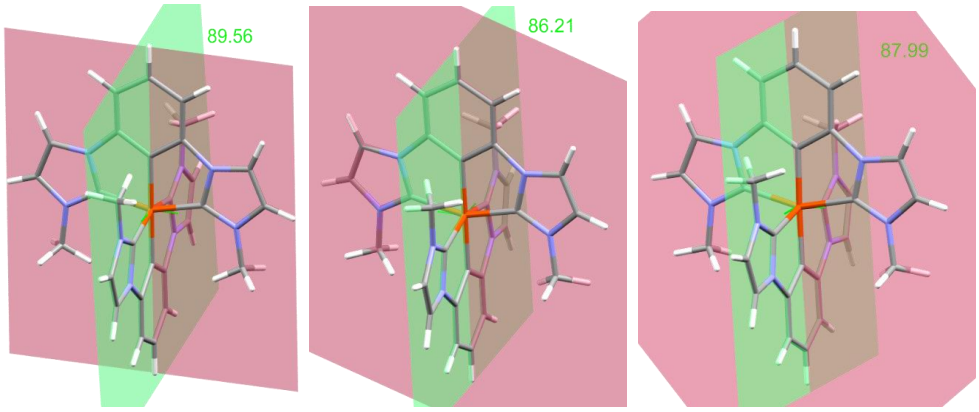

Figure S9: Ligand/ligand torsion angle of the gas phase geometry optimized molecular structures of 1^- (89.56°), 1 (86.21°) and 1^+ (87.99°).

NBO, localized orbitals, and bond order analyses. Analysis of the bonding structure and charge distribution in the three complexes was performed using natural bond orbitals (NBO)[24,25] version 3.1 as implemented in Gaussian 16.[10,26] The geometries of the complexes were optimized with the TPSSh functional and def2-TZVP basis set, and the NBO analysis was performed on the optimized geometries with the same functional and basis set. Table S4 lists the important geometric parameters in the three complexes.

Table S4: Geometric parameters of the optimized geometries of the three complexes. The numbers between brackets indicate the range of the obtained values (maximum minus minimum). Values reported without a range have a span of less than 1 ppm.

	1^-	**1**	**1^+**
Fe-C_{CM}	1.932	1.943	1.953 (0.054)
Fe-C_{NHC}	1.970	2.013	2.062 (0.006)
Bite angle	155.2	155.4	156.6 (4.3)

Characterization of the oxidation state by projection of the wave function.[27]

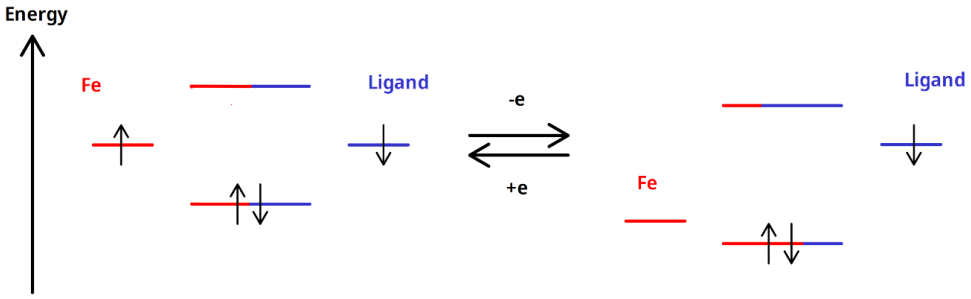

Figure S10: Schematic depiction of the negative feedback charge self-regulation.[28]

For a free ion the assignment of the oxidation state is trivial, and the occupation numbers of the orbitals are either 1 or 0. Here, we take the free Fe atom, with its 5 d-orbitals (ϕ_m), as a reference to facilitate the identification of the oxidation states of the complexes. We now construct a 5 x 5 occupation matrix ($n^{\sigma}_{m,m'}$),

obtained by projecting the occupied Kohn-Sham orbitals of the complex (ψ_i^σ) onto the atomic d-orbitals of the reference free atom, where the label σ accounts for spin in spin-polarized (open shell) cases:

$$n_{m,m'}^{\sigma} = \sum_i \langle \psi_i^\sigma | \phi_{m'} \rangle \langle \phi_m | \psi_i^\sigma \rangle$$

The 5 occupation numbers of the d-orbitals in the complex are then obtained as the eigenvalues of the occupation matrix. This procedure is obviously not sensitive to the choice of the basis set, unlike many of the population analysis methods. As long as the overlap of the d-orbitals with the ligand orbitals is not very strong, only those d-orbitals that would be initially occupied in our reference free ion remain fully occupied (n≈1), all other d-orbital occupations are due to ligand donation to previously empty d-orbitals and are expected to be very low (n≈0). Thus, like in the case of a free atom, only the fully occupied d-orbitals are relevant for determining the oxidation state of the TM in the complex. The oxidation state can be found by simply counting the fully occupied d-orbitals.

NBO analysis results. NBO methods represent chemical structures in a manner that is usually very close to Lewis structures and thus amenable to intuitive chemical reasoning.[25,29,30] Natural bond orbitals are high-occupancy (n≈2) orbitals localized on one center (lone pairs) or two centers (chemical bonds) in the molecule, in a manner that is very similar to Lewis dot-diagrams. The basic idea is to construct a set of orthogonal natural atomic orbitals NAOs (unlike the atomic orbital basis functions, which are generally not orthogonal). The occupancy of these NAOs is the basis of natural population analysis and natural atomic charges. After constructing the NAOs, a search is performed over all possible bonding patterns for these high-occupancy Lewis-type orbitals, leading to the optimal natural Lewis structure pattern and associated natural bond orbitals (NBOs) that optimally describe the total electron density ρ_l. The error of the natural Lewis structure description is quantified by the occupancy (ρ_{nl}) of residual non-Lewis orbitals, which complement the dominant contribution of Lewis orbitals. The higher this error, the less "perfect" is the description of the molecule in terms of a single Lewis structure, for example due to the molecule have other important resonance structures that need to be accounted for.

Natural electron configuration.

Table S5: Natural electron configuration.

		Natural electron configuration
1$^-$		[core] $4S^{0.33}$ $3d^{7.78}$ $4p^{1.29}$
1	Total	[core] $4S^{0.35}$ $3d^{7.32}$ $4p^{1.27}$
	Spin up	[core] $4S^{0.18}$ $3d^{4.14}$ $4p^{0.64}$
	Spin down	[core] $4S^{0.17}$ $3d^{3.18}$ $4p^{0.63}$
1$^+$	Total	[core] $4S^{0.37}$ $3d^{6.96}$ $4p^{1.26}$
	Spin up	[core] $4S^{0.19}$ $3d^{4.35}$ $4p^{0.65}$
	Spin down	[core] $4S^{0.18}$ $3d^{2.60}$ $4p^{0.62}$

Contribution of non-Lewis energy. For a simple covalently-bonded molecule, the occupied NBOs often account for more than 99.9% of the total energy of the molecule. As observable in Table S6, **1** and **1**$^+$ have a Lewis energy around 96%, due to extensive donor-acceptor interactions between bonding and antibonding NBOs and back-donation from the ligand to the metal.

Table S6: The percentage contribution of Lewis energy to the total energy of each complex.

Molecule	%E (Lewis)
1^{-}	99.320 %
1	96.284 %
1^{+}	96.167 %

Contribution of the Fe atom to the six hybrid metal-ligand bonding orbitals.

Table S7: The percentage contribution of the iron to the metal-ligand bonding orbitals.

Complex		Fe-C_{CM}		Fe-C_{NHC}	
		Fe %	Ligand C %	Fe %	Ligand C %
1^{+}		**23%** 4s(30%) 4p(3%) 3d(67%)	**77%** 2s(38%) 2p(62%)	**24%** 4s(38%) 4p(2%) 3d(58%)	**76%** 2s(54%) 2p(46%)
1	Spin up	**35.0%** 4s(33%) 3d(67%)	**65.0%** 2s(32%) 2p(68%)	**31%** 4s(33%) 3d(67%)	**69%** 2s(46%) 2p(54%)
	Spin down	**31%** 4s(33%) 3d(67%)	**69%** 2s(38%) 2p(62%)	**28%** 4s(33%) 3d(67%)	**72%** 2s(45%) 2p(55%)
1^{-}	Spin up	**40%** 4s(34%) 3d(66%)	**60%** 2s(28%) 2p(72%)	**32%** 4s(33%) 3d(67%)	**68%** 2s(39%) 2p(61%)
	Spin down	**33%** 4s(28%) 3d(72%)	**67%** 2s(30%) 2p(70%)	**32.19%** 4s(31%) 3d(69%)	**67.81%** 2s(42%) 2p(58%)

Localized orbital bonding analysis (LOBA):[31]

The LOBA method is a population analysis projected on localized molecular orbitals (LMOs). One defines a threshold value, typically ~50%. The oxidation state of an atom is then simply calculated from the number of electrons sufficiently localized on that atom, i.e. above the given threshold.

The results of the analysis are presented in the following table:

Table S8: Results from the LOBA-method.

Complex	LOBA Oxidation state*
1^{-}	2
1	6
1^{+}	7

*Based on a threshold of 60%.

LOBA correctly gives the oxidation state of Fe in 1-, and the value is stable over a wide range of threshold values. However the method drastically overestimates the oxidation state in the **1** and **1+** complexes. No common value for the threshold was found that would simultaneously yield the correct oxidation state for all the three complexes. For **1**$^{+}$ an oxidation state of 4 could be obtained, but only for a threshold < 40%, while for **1**, a threshold between 42%-48% is required to give an oxidation state of 3.

Bond order analysis

For the six bonds between the Fe and its nearest neighbors, the bond orders were computed using the Mulliken[32] and the Mayer[33] methods. The results are presented in the following table. All values are averages over all the equivalent bonds.

Table S9: Results from bond order analysis.

Method	Bond	**1**$^{-}$	**1**	**1**$^{+}$
Mulliken	Fe-C_{CM}	1.22	-0.37	-0.55
	Fe-C_{NHC}	-4.70	0.24	0.16
Mayer	Fe-C_{CM}	0.29	0.44	0.57
	Fe-C_{NHC}	0.49	0.68	0.65

No correlation was found between the oxidation state and the bond orders. As is well known, the Mulliken method does not give bond orders strictly in the range between 0 and 2. Here negative bond orders have no physical meaning and should be interpreted as essentially a bond order of zero.

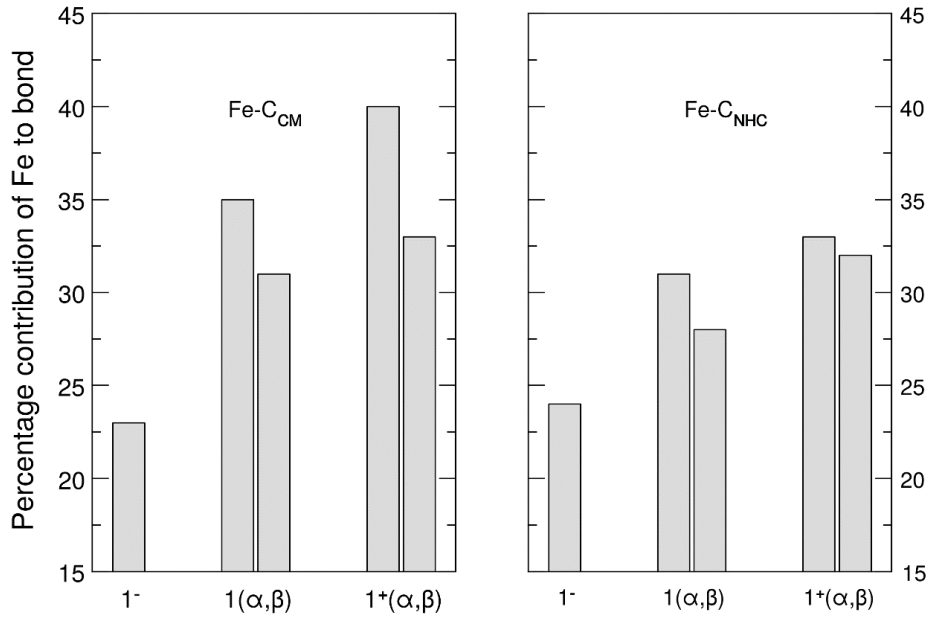

Figure S11: Percentage contribution of the Fe d-orbitals in different complexes to hybrid metal-ligand orbitals. Left: the two Fe-C_{CM} bonds, right: the four Fe-C_{NHC} bonds.

TDDFT absorption spectra. As reliable description of long-range MLCT and LMCT transitions represents a challenge for conventional DFT,[34,35] the non-empirical system-dependent tuning of functional was applied to recover the fundamental properties of exchange-correlation functional and to improve the description of these states. The two-parameter optimal tuning of LC-BLYP was done via the ΔSCF method,[36–38] the details

of the present setup can be found in the previous studies.[1,39] The range separation parameters α=0.0 and ω=0.15 $Bohr^{-1}$ were taken for all charged species.

Absorption spectra were computed with the linear-response time-dependent density functional theory (TDDFT) using the optimally-tuned LC-BLYP functional with the solvent effects (acetonitrile) modeled by the polarizable continuum model (PCM)[40]. The 6-31G(d) basis set was used for tuning procedure, while a larger basis set (def2-TZVP on iron and 6-311G(d,p) on other atoms) was employed for calculations of absorption spectra. The broadening of resulting stick spectra was done with Gaussians of FWHM 0.20 eV. Excited state analysis was done using the TheoDORE package,[41] which enables automatic quantitative wavefunction analysis and localization of excitations at predefined molecular moieties. Pre- and post-processing of data was done with homemade programs.

UV-Vis spectroscopy

UV-Vis spectra were recorded at around 10^{-5} M (**1**$^{+}$) and around 10^{-4} M (**1**$^{-}$) on a PerkinElmer Lambda 465 single-beam spectrophotometer. Acetonitrile used for **3** was of HPLC quality from fisher, which was passed over activated neutral alumina and subsequently degassed using three freeze-pump-thaw cycles. The acetonitrile used for **1**$^{+}$ was of spectroscopic quality from VWR.

Transient Absorption Spectroscopy

Transient absorption measurements were realized using a titanium sapphire laser system (CPA-2001, Clark MXR for **1**$^{+}$ or Spitfire® ACE™ PA, Spectra-Physics® for **1**$^{-}$) with a fundamental wavelength of 800 nm and a repetition rate of 1 kHz. For complex **1**$^{+}$ a noncollinear parametric amplifier (NOPA) was applied to obtain the excitation wavelength of 490 nm. The dispersion of the NOPA pulses was minimized by a compressor based on fused silica prisms. The excitation wavelength of 400 nm for complex **1**$^{-}$ was reached by frequency doubling the fundamental wavelength with a BBO-crystal. For probing, a white light continuum was generated with a CaF_2-crystal. To avoid effects caused by orientational relaxation, the polarizations of the pump and probe pulses were set to magic angle with respect to each other. Pump and probe beam were focused onto the sample to overlapping spots with diameters of 530 µm and 120 µm, respectively. Behind the sample, the white light continuum was dispersed by a prism and the changes in the sample were spectrally resolved recorded by an array detector. The compounds were dissolved in MeCN under argon and the sample solution was filled into a fused silica cuvette with a thickness of 1 mm. For complex **1**$^{-}$ a glovebox was used to transfer the complex into the cuvette.

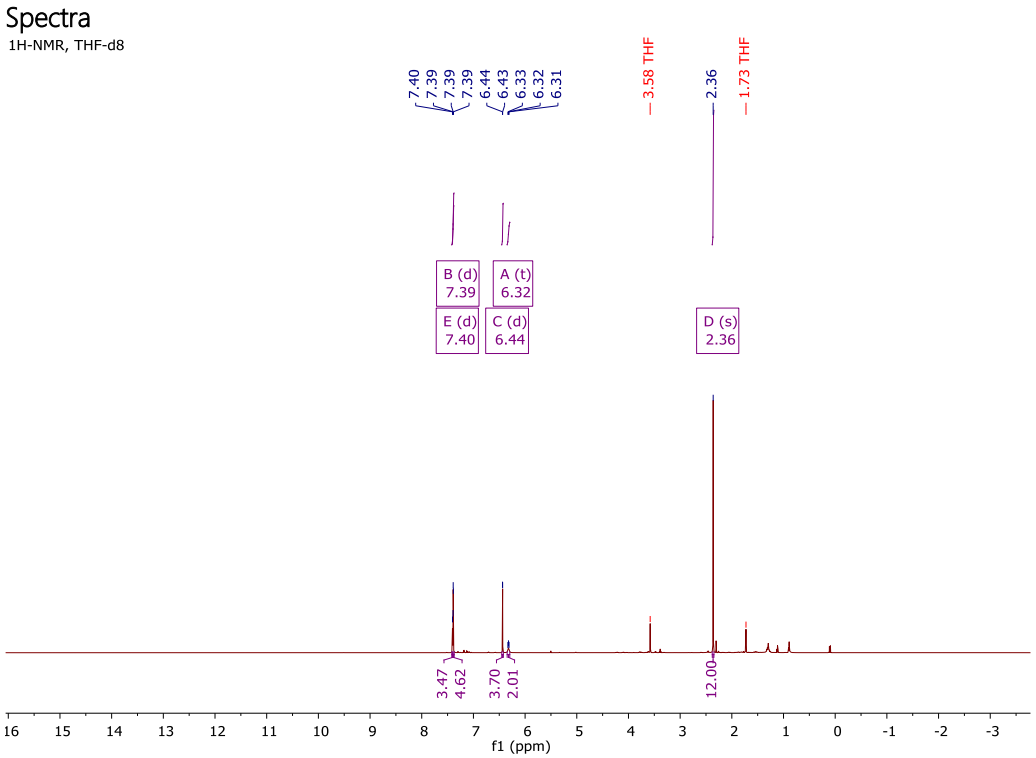

Figure S12: ^{1}H-NMR Spectrum of **1**$^{\cdot}$ in THF-d$_8$

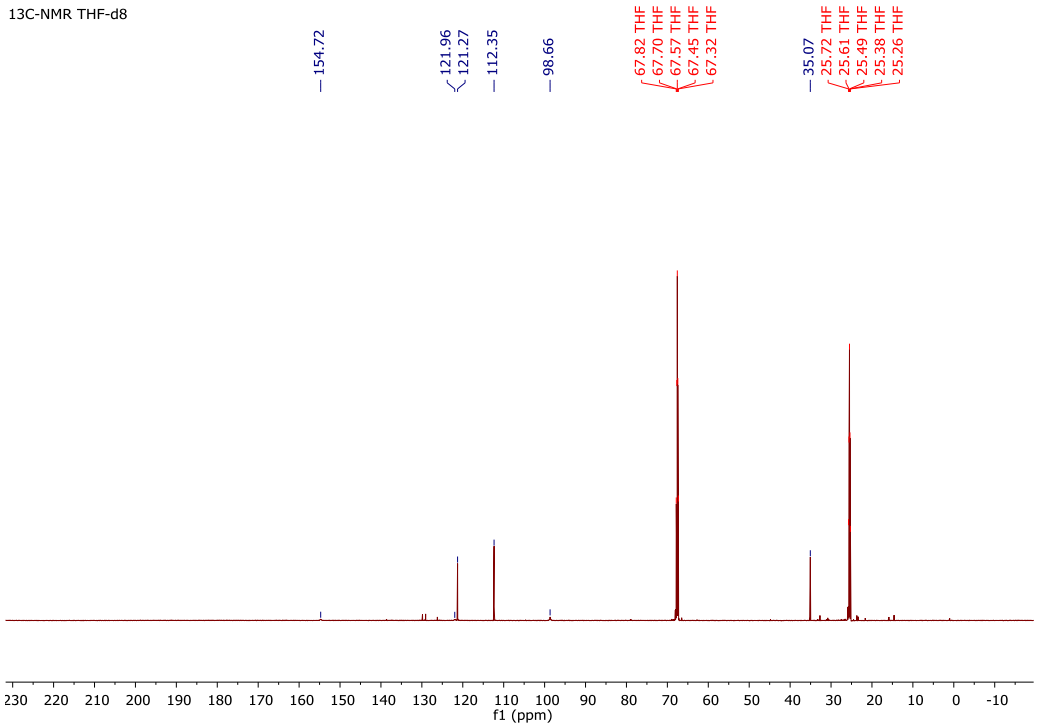

Figure S13: ^{13}C-NMR Spectrum of **1**$^{\cdot}$ in THF-d$_8$

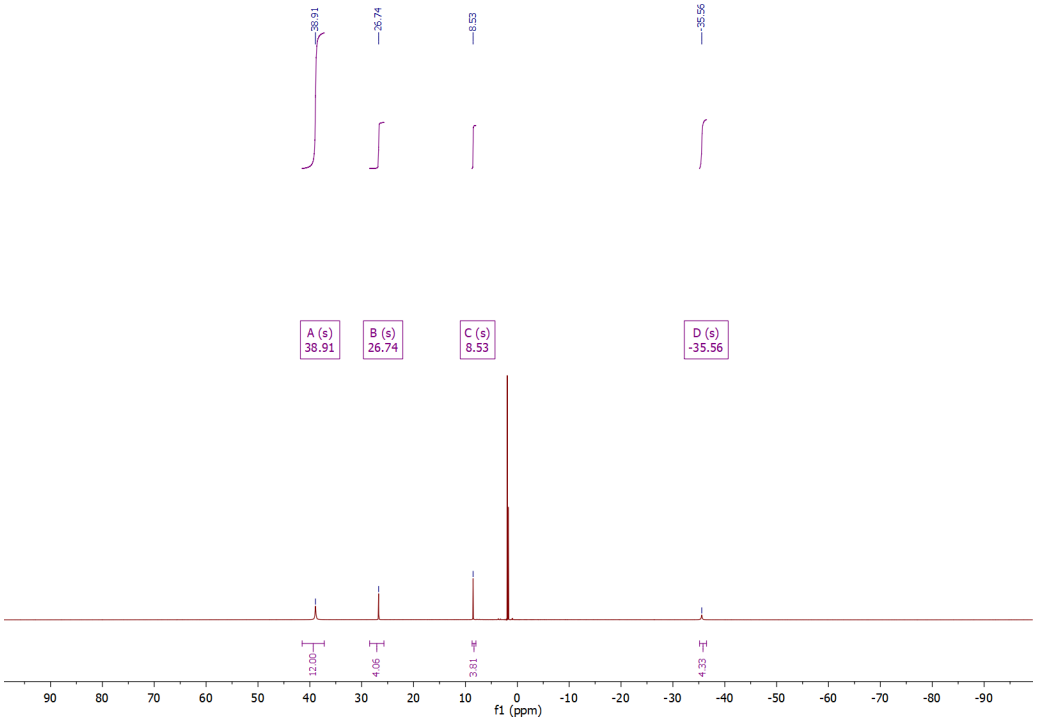

Figure S14: ^{1}H-NMR Spectrum of **1**$^{+}$ in MeCN-d_3.

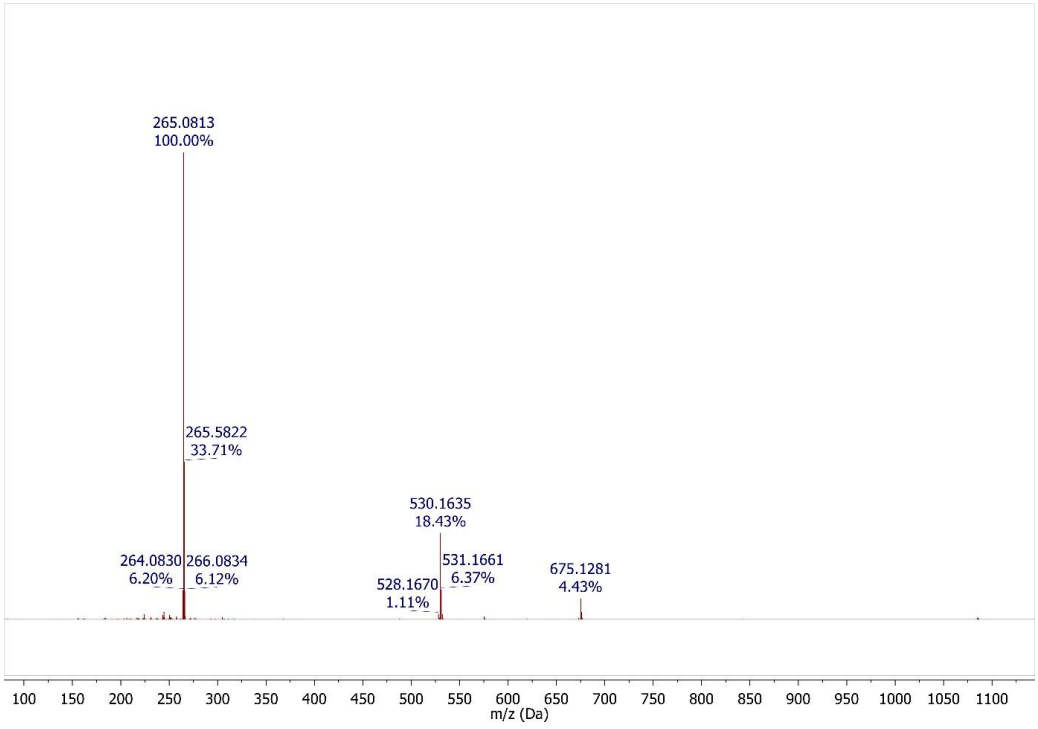

Figure S15: ESI-MS spectrum of **1**$^{+}$.

REFERENCES

(1) Steube, J.; Kruse, A.; Bokareva, O. S.; Reuter, T.; Demeshko, S.; Schoch, R.; Argüello Cordero, M. A.; Krishna, A.; Hohloch, S.; Meyer, F.; Heinze, K.; Kühn, O.; Lochbrunner, S.; Bauer, M. Janus-type emission from a cyclometalated iron(III) complex. *Nat. Chem.* **2023**, *15* (4), 468–474. DOI: 10.1038/s41557-023-01137-w. Published Online: Feb. 27, 2023.

(2) Krause, L.; Herbst-Irmer, R.; Sheldrick, G. M.; Stalke, D. Comparison of silver and molybdenum microfocus X-ray sources for single-crystal structure determination. *J Appl Crystallogr* **2015**, *48* (1), 3–10. DOI: 10.1107/S1600576714022985.

(3) Sheldrick, G. M. SHELXT – Integrated space-group and crystal-structure determination. *Acta Crystallogr A Found Adv* **2015**, *71* (1), 3–8. DOI: 10.1107/S2053273314026370.

(4) Spek, A. L. Structure validation in chemical crystallography. *Acta Crystallogr. D* **2009**, *65* (Pt 2), 148–155. DOI: 10.1107/S090744490804362X.

(5) Spek, A. L. PLATON SQUEEZE: a tool for the calculation of the disordered solvent contribution to the calculated structure factors. *Acta Crystallogr. C Struct. Chem.* **2015**, *71* (Pt 1), 9–18. DOI: 10.1107/S2053229614024929.

(6) Caliebe, W. A.; Murzin, V.; Kalinko, A.; Görlitz, M. High-flux XAFS-beamline P64 at PETRA III. In ; Author(s), 2019; p 60031. DOI: 10.1063/1.5084662.

(7) Kalinko, A.; Caliebe, W. A.; Schoch, R.; Bauer, M. A von Hamos-type hard X-ray spectrometer at the PETRA III beamline P64. *Journal of synchrotron radiation* **2020**, *27* (Pt 1), 31–36. DOI: 10.1107/S1600577519013638. Published Online: Jan. 1, 2020.

(8) Ross, M.; Andersen, A.; Fox, Z. W.; Zhang, Y.; Hong, K.; Lee, J.-H.; cordones, A.; March, A. M.; Doumy, G.; Southworth, S. H.; Marcus, M. A.; Schoenlein, R. W.; Mukamel, S.; Govind, N.; Khalil, M. Comprehensive Experimental and Computational Spectroscopic Study of Hexacyanoferrate Complexes in Water: From Infrared to X-ray Wavelengths. *J. Phys. Chem. B* **2018**, *122* (19), 5075–5086. DOI: 10.1021/acs.jpcb.7b12532. Published Online: May. 9, 2018.

(9) Neese, F.; Wennmohs, F.; Becker, U.; Riplinger, C. The ORCA quantum chemistry program package. *J. Chem. Phys.* **2020**, *152* (22), 224108. DOI: 10.1063/5.0004608.

(10) Frisch, M. J.; Trucks, G. W.; Schlegel, H. B.; Scuseria, G. E.; Robb, M. A.; Cheeseman, J. R.; Scalmani, G.; Barone, V.; Petersson, G. A.; Nakatsuji, H.; Li, X.; Caricato, M.; Marenich, A. V.; Bloino, J.; Janesko, B. G.; Gomperts, R.; Mennucci, B.; Hratchian, H. P.; Ortiz, J. V.; Izmaylov, A. F.; Sonnenberg, J. L.; Williams; Ding, F.; Lipparini, F.; Egidi, F.; Goings, J.; Peng, B.; Petrone, A.; Henderson, T.; Ranasinghe, D.; Zakrzewski, V. G.; Gao, J.; Rega, N.; Zheng, G.; Liang, W.; Hada, M.; Ehara, M.; Toyota, K.; Fukuda, R.; Hasegawa, J.; Ishida, M.; Nakajima, T.; Honda, Y.; Kitao, O.; Nakai, H.; Vreven, T.; Throssell, K.; Montgomery Jr., J. A.; Peralta, J. E.; Ogliaro, F.; Bearpark, M. J.; Heyd, J. J.; Brothers, E. N.; Kudin, K. N.; Staroverov, V. N.; Keith, T. A.; Kobayashi, R.; Normand, J.; Raghavachari, K.; Rendell, A. P.; Burant, J. C.; Iyengar, S. S.; Tomasi, J.; Cossi, M.; Millam, J. M.; Klene, M.; Adamo, C.; Cammi, R.; Ochterski, J. W.; Martin, R. L.; Morokuma, K.; Farkas, O.; Foresman, J. B.; Fox, D. J. *Gaussian 16 Rev. C.01*, 2016.

(11) Mao, Y.; Ge, Q.; Horn, P. R.; Head-Gordon, M. On the Computational Characterization of Charge-Transfer Effects in Noncovalently Bound Molecular Complexes. *J. Chem. Theory Comput.* **2018**, *14* (5), 2401–2417. DOI: 10.1021/acs.jctc.7b01256.

(12) Brandenburg, J. G.; Bannwarth, C.; Hansen, A.; Grimme, S. B97-3c: A revised low-cost variant of the B97-D density functional method. *J. Chem. Phys.* **2018**, *148* (6), 64104. DOI: 10.1063/1.5012601.

(13) Staroverov, V. N.; Scuseria, G. E.; Tao, J.; Perdew, J. P. Comparative assessment of a new nonempirical density functional: Molecules and hydrogen-bonded complexes. *The Journal of Chemical Physics* **2003**, *119* (23), 12129–12137. DOI: 10.1063/1.1626543.

(14) Weigend, F.; Ahlrichs, R. Balanced basis sets of split valence, triple zeta valence and quadruple zeta valence quality for H to Rn: Design and assessment of accuracy. *Phys. Chem. Chem. Phys.* **2005**, *7* (18), 3297–3305. DOI: 10.1039/b508541a.

(15) Neese, F.; Wennmohs, F.; Hansen, A.; Becker, U. Efficient, approximate and parallel Hartree–Fock and hybrid DFT calculations. A 'chain-of-spheres' algorithm for the Hartree–Fock exchange. *Chemical Physics* **2009**, *356* (1-3), 98–109. DOI: 10.1016/j.chemphys.2008.10.036.

(16) Becke, A. D.; Johnson, E. R. A density-functional model of the dispersion interaction. *J. Chem. Phys.* **2005**, *123* (15), 154101. DOI: 10.1063/1.2065267.

(17) Neese, F. Prediction and interpretation of the 57Fe isomer shift in Mössbauer spectra by density functional theory. *Inorg. Chim. Acta* **2002**, *337*, 181–192. DOI: 10.1016/S0020-1693(02)01031-9.

(18) Chakraborty, U.; Bügel, P.; Fritsch, L.; Weigend, F.; Bauer, M.; Jacobi von Wangelin, A. Planar Iron Hydride Nanoclusters: Combined Spectroscopic and Theoretical Insights into Structures and Building Principles. *ChemistryOpen* **2021**, *10* (2), 265–271. DOI: 10.1002/open.202000307.

(19) Schoch, A.; Burkhardt, L.; Schoch, R.; Stührenberg, K.; Bauer, M. Hard X-ray spectroscopy: an exhaustive toolbox for mechanistic studies (?). *Faraday Discuss.* **2019**, *220* (0), 113–132. DOI: 10.1039/c9fd00070d.

(20) Besley, N. A. Modeling of the spectroscopy of core electrons with density functional theory. *WIREs Comput Mol Sci* **2021**, *11* (6). DOI: 10.1002/wcms.1527.

(21) Burkhardt, L.; Holzwarth, M.; Plietker, B.; Bauer, M. Detection and Characterization of Hydride Ligands in Iron Complexes by High-Resolution Hard X-ray Spectroscopy and Implications for Catalytic Processes. *Inorg. Chem.* **2017**, *56* (21), 13300–13310. DOI: 10.1021/acs.inorgchem.7b02063.

(22) Delgado-Jaime, M. U.; DeBeer, S. Expedited analysis of DFT outputs: introducing MOAnalyzer. *Journal of computational chemistry* **2012**, *33* (27), 2180–2185. DOI: 10.1002/jcc.23028.

(23) Knizia, G. Intrinsic Atomic Orbitals: An Unbiased Bridge between Quantum Theory and Chemical Concepts. *J. Chem. Theory Comput.* **2013**, *9* (11), 4834–4843. DOI: 10.1021/ct400687b. Published Online: Oct. 17, 2013.

(24) Foster, J. P.; Weinhold, F. Natural hybrid orbitals. *Journal of the American Chemical Society* **1980**, *102* (24), 7211–7218. DOI: 10.1021/ja00544a007.

(25) Reed, A. E.; Weinstock, R. B.; Weinhold, F. Natural population analysis. *The Journal of Chemical Physics* **1985**, *83* (2), 735–746. DOI: 10.1063/1.449486.

(26) E. D. Glendening, A. E. Reed, J. E. Carpenter, F. Weinhold. *NBO Version 3.1*.

(27) Sit, P. H.-L.; Car, R.; Cohen, M. H.; Selloni, A. Simple, unambiguous theoretical approach to oxidation state determination via first-principles calculations. *Inorg. Chem.* **2011**, *50* (20), 10259–10267. DOI: 10.1021/ic2013107. Published Online: Sep. 16, 2011.

(28) Raebiger, H.; Lany, S.; Zunger, A. Charge self-regulation upon changing the oxidation state of transition metals in insulators. *Nature* **2008**, *453* (7196), 763–766. DOI: 10.1038/nature07009.

(29) Reed, A. E.; Curtiss, L. A.; Weinhold, F. Intermolecular interactions from a natural bond orbital, donor-acceptor viewpoint. *Chem. Rev.* **1988**, *88* (6), 899–926. DOI: 10.1021/cr00088a005.

(30) Glendening, E. D.; Landis, C. R.; Weinhold, F. Natural bond orbital methods. *WIREs Comput Mol Sci* **2012**, *2* (1), 1–42. DOI: 10.1002/wcms.51.

(31) Thom, A. J. W.; Sundstrom, E. J.; Head-Gordon, M. LOBA: a localized orbital bonding analysis to calculate oxidation states, with application to a model water oxidation catalyst. *Physical chemistry chemical physics : PCCP* **2009**, *11* (47), 11297–11304. DOI: 10.1039/b915364k. Published Online: Oct. 19, 2009.

(32) Mulliken, R. S. Electronic Population Analysis on LCAO–MO Molecular Wave Functions. I. *J. Chem. Phys.* **1955**, *23* (10), 1833–1840. DOI: 10.1063/1.1740588.

(33) Mayer, I. Charge, bond order and valence in the AB initio SCF theory. *Chemical Physics Letters* **1983**, *97* (3), 270–274. DOI: 10.1016/0009-2614(83)80005-0.

(34) Dreuw, A.; Head-Gordon, M. Single-reference ab initio methods for the calculation of excited states of large molecules. *Chem. Rev.* **2005**, *105* (11), 4009–4037. DOI: 10.1021/cr0505627.

(35) Peach, M. J. G.; Benfield, P.; Helgaker, T.; Tozer, D. J. Excitation energies in density functional theory: an evaluation and a diagnostic test. *The Journal of Chemical Physics* **2008**, *128* (4), 44118. DOI: 10.1063/1.2831900.

(36) Livshits, E.; Baer, R. A density functional theory for symmetric radical cations from bonding to dissociation. *The journal of physical chemistry. A* **2008**, *112* (50), 12789–12791. DOI: 10.1021/jp803606n.

(37) Stein, T.; Kronik, L.; Baer, R. Reliable prediction of charge transfer excitations in molecular complexes using time-dependent density functional theory. *J. Am. Chem. Soc.* **2009**, *131* (8), 2818–2820. DOI: 10.1021/ja8087482.

(38) Stein, T.; Kronik, L.; Baer, R. Prediction of charge-transfer excitations in coumarin-based dyes using a range-separated functional tuned from first principles. *J. Chem. Phys.* **2009**, *131* (24), 244119. DOI: 10.1063/1.3269029.

(39) Zobel, J. P.; Kruse, A.; Baig, O.; Lochbrunner, S.; Bokarev, S. I.; Kühn, O.; González, L.; Bokareva, O. S. Can range-separated functionals be optimally tuned to predict spectra and excited state dynamics in photoactive iron complexes? *Chem. Sci.* **2023.** DOI: 10.1039/D2SC05839A.

(40) Tomasi, J.; Mennucci, B.; Cammi, R. Quantum mechanical continuum solvation models. *Chem. Rev.* **2005**, *105* (8), 2999–3093. DOI: 10.1021/cr9904009.

(41) Plasser, F. TheoDORE: A toolbox for a detailed and automated analysis of electronic excited state computations. *J. Chem. Phys.* **2020**, *152* (8), 84108. DOI: 10.1063/1.5143076.

A.4 Supporting Information of "Detection and Characterization of Hydride Ligands in Copper Complexes by Hard X-ray Spectroscopy"

SUPPORTING INFORMATION

Detection and Characterization of Hydride Ligands in Copper Complexes by Hard X-ray Spectroscopy

Lorena Fritsch, [a] Pia Rehsies, [a], Wael Barakat,[b] Deven P. Estes,[b] and Matthias Bauer*[a]

[a] L Fritsch, Pia Rehsies, Prof. Dr. M. Bauer
Institute of Inorganic Chemistry and Center for Sustainable Systems Design (CSSD), Paderborn University
Warburger Straße 100, 33098 Paderborn, Germany
E-mail: matthias.bauer@upb.de, http://www.chemie.upb.de/bauer

[b] Dr. Wael Barakat, Jun. Prof. Dr. Deven Estes
Institute of Technical Chemistry, University of Stuttgart
Pfaffenwaldring 55, 70569 Stuttgart, Germany

Table S1: *Analysis of atomic contribution to selected acceptor orbitals of TD-DFT calculated XANES transitions and donor orbitals of DFT calculated VtC-transitions. H^a is the Cu bound Hydride, H^b refers to the C bound H. In case of Cu-I where no H is present, column is replaced by I p-orbital contribution. (Grey marked: High Hydride contribution)*

Compound	**Transition no. / Energy (eV)**	**Acceptor orbital / %**							
		No. (donor)	**Cu p**		**H^as (I p)**	**H^b s**	**P p**	**P d**	**Cp**
Cu_6H_6	01/ 8982.8	504	18.5		0	0	3.4	8.9	40.6
	38/ 8984.7	541	16.5		2.9	16.3	6.6	8.0	14.6
	39/ 8984.9	542	18.0		2.4	13.8	7.4	10.9	16.1
Cu_3H	01/ 3983.2	$389_{(0)}$	22.8		0	2.1	7.2	15.3	27.9
	63/ 8984.7	$411_{(0)}$	6.6		0	1.2	1.1	2.6	55.8
	68/ 8984.7	$414_{(2)}$	9.4		0.1	2.0	9.0	13.5	33.9
	71/ 8984.8	$415_{(1)}$	6.0		0.5	4.4	13.1	17.3	25.2
Cu-I	01/ 8983.1	124	29.4		2.8	6.0	9.8	18.8	11.6
	02/ 8984.1	125	1.5		1.1	40.8	7.7	9.2	10.8
Compound	**Transition no. / Energy (eV)**	**Donor orbital / %**							
		No. (acc.)	**Cu p**	**Cu d**	**H^as (I p)**	**H^b s**	**P s**	**P p**	**Cs**	**Cp**
Cu_6H_6	193/ 8961.9	193	0.5	0	0	6.9	2.3	0.8	67.5	13.9
	210/ 8964.3	210	0.8	0	0	5.8	7.7	0.9	43.4	31.7
	246/8967.5	246	0.8	0	0	1.2	13.9	0.2	20.1	48.4
	282/ 8969.9	282	0.3	0	0	16.4	5.5	0	10.5	57.8
	300/ 8971.5	300	0.1	0	0	26.3	4.5	0.3	7.5	45.7
	362/ 8973.8	362	4.5	0.2	5.9	14.7	0	5.9	0	47.9
	398/8975.2	398	15.6	10.3	21.3	5.6	0.1	2.4	0	25.3
	429/ 8976.2	429	8.6	24.3	17.5	4.8	0	6.9	0	24.3
	432/ 8976.5	432	5.8	22.1	5.7	1.3	1.1	21.3	0.1	27.7
	480/ 8978.5	480	11.3	54.1	0.7	0	0.8	21.3	0	25.6
	499/ 8979.9	499	19.4	56.1		0.2	0.2	1.8	0	1.1
	502/8980.3	502	13.7	56.0	7.8	0	1.5	7.6	0	2.7
Cu_3H	482/ 8964.2	$162_{(b)}$	2.6	0	0	17.9	6.7	3.4	49.5	10.4
	489/ 8964.7	$164_{(a)}$	2.6	0	0	10.7	13.4	4.0	39.2	21.6
	575/ 8968.3	$194_{(c)}$	1.1	0	0	7.7	16.7	0.4	18.8	45.5
	657/ 8970.6	$220_{(a)}$	0.5	0	0	14.8	6.9	0.3	11.9	56.1
	667/ 8970.9	$224_{(c)}$	1.4	0	0	20.4	7.6	1.7	8.5	50.8
	694/ 8972.0	$232_{(a)}$	0.9	0	0	24.3	3.0	5.2	2.8	51.9
	829-831/ 8974.3	278 (a,b,c)	4.4	3.5	8.0	18.3	0.6	2.4	0	46.9
	841-843/ 8974.4	282 (a,b,c)	4.1	7.1	12.5	16.3	0.0	2.8	0.3	39.9
	1036/ 8977.3	$347_{(c)}$	2.7	45.7	0	5.0	1.1.	19.2	0	14.5
	1040/ 8977.3	$348_{(b)}$	3.0	43.4	0	5.3	1.1	19.1	0.1	15.7
	1148/ 8979.4	$384_{(b)}$	15.0	37.9	0	2.5	2.1	18.9	0.9	9.6
	1152/ 8979.5	$385_{(a)}$	13.1	40.2	0	1.3	2.0	16.8	0.6	14.3
	1160/ 8980.1	$388_{(b)}$	5.9	48.2	0	0.6	4.6	21.9	0	7.4
Cu-I	50/8963.4	50	1.9	0	0	17.0	5.1	1.7	54.9	13.7
	66/8969.5	66	9.3	0.8	83 (I_s)	0.5	0.1	0.3	0.5	0.5
	70/8971.7	70	1.4	0.3	0	20.5	5.4	0.8	11.8	52.1
	79/8973.4	79	0.6	0.1	0	22.8	0.2	3.2	0.4	65.0
	114/8977.7	114	3.6	43.4	0.3	3.3	1.0	24.4	0	13.7
	116/8978.3	116	3.1	52.1	35.1	0.3	0.2	2.9	0	2.0
	120/8979.4	120	9.3	20.0	52.8	1.2	0.6	7.5	0.3	3.5
	121/8979.8	121	9.3	36.8	38.4	0.9	0.4	4.0	0.5	2.8
Cu-H	104/8977.2	104	3.6	26.8	0	2.3	1.1	23.8	0	14.2
	106/8977.8	106	7.1	57.6	22.5	0.4	0.3	5.5	0	3.0

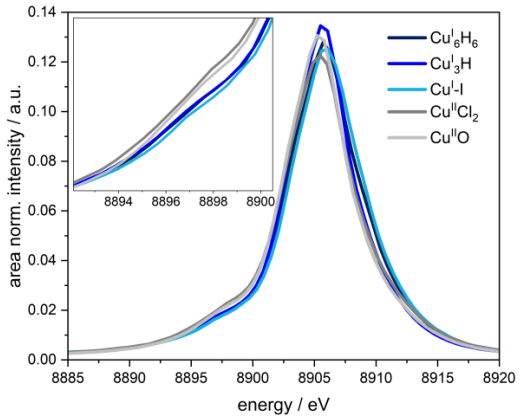

Figure S1: Experimental CtC spectra of Cu^{I} species Cu_6H_6, Cu_3H and Cu-I in comparison to Cu^{II} references $CuCl_2$ and CuO.

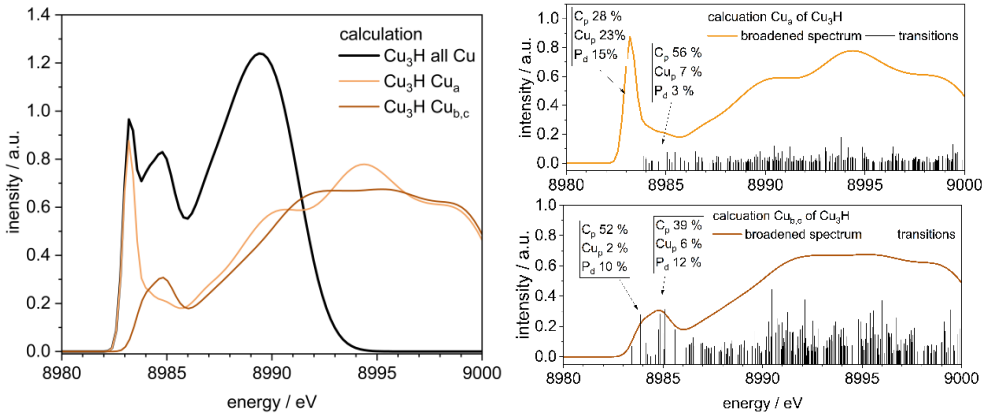

Figure S2: TD-DFT calculated XANES spectra of different Cu centers in Cu_3H in comparison to all Cu centers combined in one calculation (left) and the respective spectra with individual analyzed transitions (right).

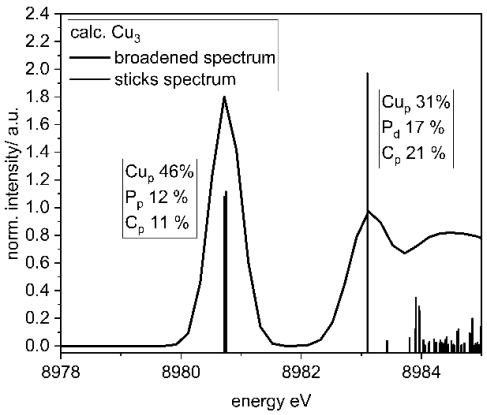

Figure S3: TD-DFT calculated XANES transitions (sticks) and resulting broadened spectrum of Cu_3. The analysis of the atomic orbital contribution is given for transitions at 8981 eV and 8983 eV.

BIBLIOGRAPHY

[1] N. Klopčič, I. Grimmer, F. Winkler, M. Sartory, A. Trattner. A review on metal hydride materials for hydrogen storage. *Journal of Energy Storage* **2023**, *72*, 108456.

[2] M. Peruzzini, R. Poli (Eds.), *Recent advances in hydride chemistry*, Elsevier Science Ltd, Amsterdam and New York, **2007**.

[3] C. P. Casey, H. Guan. An efficient and chemoselective iron catalyst for the hydrogenation of ketones. *Journal of the American Chemical Society* **2007**, *129*, 5816–5817.

[4] K. Goldberg (Ed.), *Activation and functionalization of C-H bonds*, Vol. 885 of *ACS Symposium Series*, Washington DC, **2004**.

[5] W.-H. Wang, Y. Himeda, J. T. Muckerman, G. F. Manbeck, E. Fujita. CO_2 Hydrogenation to Formate and Methanol as an Alternative to Photo- and Electrochemical CO_2 Reduction. *Chemical Reviews* **2015**, *115*, 12936–12973.

[6] L. Andrews, X. Wang. Infrared spectra and structures of the stable CuH_2^-, AgH_2^-, AuH_2^-, and AuH_4^- anions and the AuH_2 molecule. *Journal of the American Chemical Society* **2003**, *125*, 11751–11760.

[7] X. Wang, L. Andrews, L. Manceron, C. Marsden. Infrared Spectra and DFT Calculations for the Coinage Metal Hydrides MH, H_2MH, MH_2, M_2H, M_2H^- , and H_2CuHCu in Solid Argon, Neon, and Hydrogen. *The Journal of Physical Chemistry A* **2003**, *107*, 8492–8505.

[8] J. R. Lakowicz (Ed.), *Solvent and Environmental Effects*, Springer US, Boston, MA, **2006**, pp. 205–235.

[9] F. Hinderer, *UV/Vis-Absorptions- und Fluoreszenz-Spektroskopie: Einführung in die spektroskopische Analyse mit UV- und sichtbarer Strahlung 1st ed.*, of *essentials*, Springer, Wiesbaden, **2020**.

[10] L. H. Gade, *Koordinationschemie*, John Wiley & Sons, Hoboken, **2012**.

[11] P. W. Atkins, J. de Paula, *Atkins' physical chemistry 8th ed.*, Oxford University Press, Oxford, **2006**.

[12] G. G. Stokes. *Philosophical Transactions of the Royal Society of London* **1852**, *142*, 463–562.

[13] G. N. Lewis, M. Kasha. Phosphorescence and the Triplet State. *Journal of the American Chemical Society* **1944**, *66*, 2100–2116.

[14] A. M. Brouwer. Standards for photoluminescence quantum yield measurements in solution (IUPAC Technical Report). *Pure and Applied Chemistry* **2011**, *83*, 2213–2228.

[15] N. Mardirossian, M. Head-Gordon. Thirty years of density functional theory in computational chemistry: an overview and extensive assessment of 200 density functionals. *Molecular Physics* **2017**, *115*, 2315–2372.

[16] N. Lee, T. Petrenko, U. Bergmann, F. Neese, S. DeBeer. Probing valence orbital composition with iron Kb X-ray emission spectroscopy. *Journal of the American Chemical Society* **2010**, *132*, 9715–9727.

[17] M. A. Beckwith, M. Roemelt, M.-N. Collomb, C. DuBoc, T.-C. Weng, U. Bergmann, P. Glatzel, F. Neese, S. DeBeer. Manganese Kb X-ray emission spectroscopy as a probe of metal-ligand interactions. *Inorganic chemistry* **2011**, *50*, 8397–8409.

[18] N. A. Besley. Density Functional Theory Based Methods for the Calculation of X-ray Spectroscopy. *Accounts of Chemical Research* **2020**, *53*, 1306–1315.

[19] E. Runge, E. K. U. Gross. Density-Functional Theory for Time-Dependent Systems. *Phys. Rev. Lett.* **1984**, *52*, 997–1000.